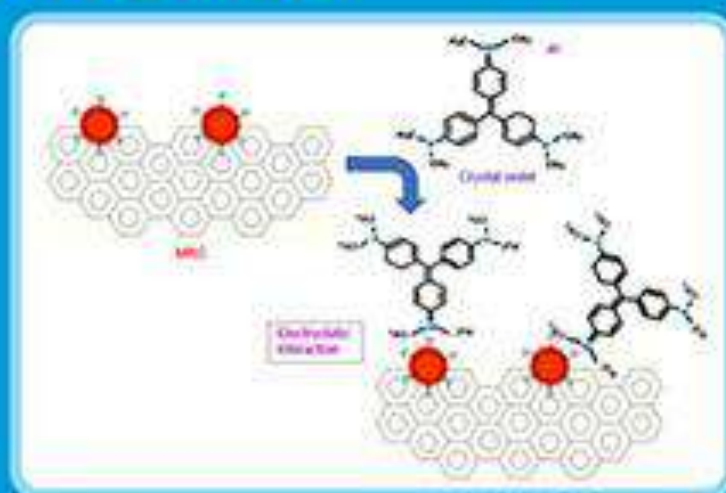


iSSN: 1411-9420 (print); 2460-1578 (online)

Indonesian Journal of Chemistry

Vol. 23, No. 1, February 2023



Approved by RISTEK, RI
No. 65/MENP/2020

Indones. J. Chem.

Vol. 23

No. 1

PP 1-284

Yogyakarta
February 2023

ISSN 1411-9420 (print)
2460-1578 (online)

Synthesis of Reduced Graphene Oxide-Bentonite Composite and Its Application as a Lead(II) Ion Adsorbent

Bartholomeus Lavelim, Lia Destiarti*, Adhitiyawarman Adhitiyawarman, and Risya Sasri

Department of Chemistry, Faculty of Mathematics and Natural Sciences, Universitas Tanjungpura,
Jl. Prof. Dr. Hadari Nawawi, Pontianak 78114, West Kalimantan, Indonesia

* **Corresponding author:**

tel: +62-81345208035

email: lia.destiarti@chemistry.untan.ac.id

Received: July 28, 2022

Accepted: December 4, 2022

DOI: 10.22146/ijc.67993

Abstract: The use of reduced graphene oxide (rGO) as an adsorbent has challenges to overcome. Although rGO has a large surface area, its solubility in water is very low. In this study, bentonite is added to reduce the use of rGO mass and increase the dispersibility of the adsorbent. The rGO-bentonite (rGOB) was characterized by XRD, FTIR, SEM-EDX, and XRF. The adsorption activity was tested in a Pb ion solution, derived from AAS. The XRD pattern of GO, rGO, and rGOB of 2θ were observed at 10.90° , 24.88° , and 26.66° , respectively. The FTIR spectrum showed that GO has C=C, C-O, C=O, and O-H, while in rGO, C=O disappears, and there was a significant decrease in the O-H and C-O peaks. The rGOB has identical spectra with rGO and yet has an additional peak from bentonite O-Si-O. The GO and rGO form agglomerate while rGOB looks more dispersed. The C/O ratio increases from GO to rGO because of the reduction process. The bentonite is Ca-bentonite with main components Al_2O_3 , SiO_2 , and CaO. The results showed that the rGOB composite could reduce the use of rGO by up to 80% and have an adsorption performance similar to rGO with an adsorption capacity of 217 mg/g.

Keywords: adsorption; bentonite; lead; reduced graphene oxide; reduced graphene oxide-bentonite

■ INTRODUCTION

Lead (Pb) is a toxic metal that leads to various environmental problems that need removal from wastewater. Reduced graphene oxide (rGO) is a material that has the potential as an adsorbent for Pb ion due to its large surface area but has poor dispersibility and is relatively difficult to produce. Lead is one of the most dangerous heavy metals that can cause various environmental problems. The agency for toxic substances and disease registry (ATSDR) even placed Pb in second place on the 2019 substance priority list regarding its amount in the environment, potential human exposure, and potential threats to human health [1]. The extensive use of lead in various industrial fields causes pollution by lead to be unavoidable, so more efforts are needed to reduce lead pollutants in industrial waste before entering the environment. Different methods have been used to reduce the Pb concentration in industrial wastewater,

such as chemical precipitation, ion exchange, adsorption, membrane filtration, coagulation and flocculation, flotation, and electrochemistry. However, adsorption is the most effective and economical process because of its ease of design and operation [2]. Many materials have been tested as Pb(II) adsorbents [3-5]. Still, most of them cannot be used effectively because of their low adsorption capacity, long equilibrium time, or high prices, so various materials are continuously being developed to get better adsorbents.

Because of its enormous surface area, rGO is a promising material as a Pb(II) adsorbent. However, in an aqueous solution, rGO presents in an aggregate [6], reducing its adsorption capacity. Besides, the rGO material is quite challenging to be produced, leading to its use as an adsorbent on a large scale becoming ineffective. Therefore, the rGO will be composited with bentonite to reduce its use in the adsorbent. High

dispersibility bentonite [7] is expected to increase the dispersibility of rGO. Bentonite was chosen because this material has a high abundance, relatively low prices, and is environmentally friendly [8].

Furthermore, compared to many other natural materials, bentonite has a large surface area and cation exchange capacity [9]. Therefore, the bentonite in the adsorbent would contribute to adsorbing Pb(II) and increase the overall adsorbent ability. So far, there is no publication found related to the application of reduced graphene oxide-bentonite (rGOB) as a Pb adsorbent.

In this work, graphene oxide was prepared from commercial synthetic graphite powder using a modified Hummer method which will then be reduced using hydrazine to form rGO [10]. Subsequently, an rGOB composite was made by combining the rGO and bentonite through a radical reaction [11]. The rGOB composites will be synthesized with two rGO/bentonite ratio variations to determine a better adsorbent composition. The rGOB composites were then characterized using XRD, FTIR, SEM-EDX, and XRF. The adsorption capability of synthesized material on Pb(II) solution that uses a batch adsorption system was evaluated using AAS.

■ EXPERIMENTAL SECTION

Materials

Ammonium persulfate ($(\text{NH}_4)_2\text{S}_2\text{O}_8$) (98%), commercial natural bentonite, commercial synthetic graphite (98.6%), demineralized water (H_2O), ethylene glycol ($\text{C}_2\text{H}_6\text{O}_2$) (99.5%), hydrazine (N_2H_4) (98% purity), hydrogen peroxide (H_2O_2) (30%), lead (Pb) stock solution (1000 ppm concentration), nitric acid (HNO_3) (65%), phosphoric acid (H_3PO_4) (85%), potassium permanganate (KMnO_4) (99.0%), sodium bisulfate (NaHSO_4) (99.0%), sodium hydroxide (NaOH) (98.0%), sulfuric acid (H_2SO_4) (95–97%). All substances are derived from Merck.

Procedure

Synthesis of graphene oxide

Graphene oxide was prepared using synthetic graphite obtained commercially based on the Hummer

method modified by Husnah et al. [10]. A 2.5 g of graphite powder was added into a beaker containing 57.5 mL $\text{H}_2\text{SO}_4/\text{H}_3\text{PO}_4$ (9:1) in an ice bath. The mixture was stirred until the temperature reached ± 10 °C. Next, 7.5 g of KMnO_4 was slowly added to the suspension while stirring, and the temperature was kept below 20 °C. The suspension was then heated to 50 °C while stirring for 40 min.

Furthermore, the suspension was slowly poured into 125 mL of demineralized water. The oxidation process was stopped by adding 2.5 mL hydrogen peroxide 30%. The suspension was then filtered through a Whatman paper, and the solid obtained was washed with demineralized water. The graphene oxide obtained was dried at 60 °C for 12 h.

Synthesis of reduced graphene oxide

Reduced graphene oxide was prepared by reducing GO using hydrazine via microwave heating by following the method developed by Husnah et al. [10]. Graphene oxide (2 g) was dispersed in 100 mL ethylene glycol with 2 h of sonication, followed by an hour of magnetic stirring. Then, 2 mL of hydrazine (N_2H_4) is added dropwise while stirring. The reduction process was completed by introducing the suspension into microwave heating at 100 °C for 20 min. The suspension was then filtered and washed with demineralized water. The reduced graphene oxide was dried at 60 °C for 12 h before being grounded into a powder and then sieved (325 mesh).

Synthesis of reduced graphene oxide-bentonite composites

Reduced graphene oxide-bentonite (rGOB) composites were prepared using a persulfate/bisulfate initiator [11]. The rGO suspension was prepared by dispersing 0.4 g of rGO in 150 mL of demineralized water after 2 h of sonication. At the same time, the rGOB suspension was prepared by dispersing an amount of rGO with a varied amount of bentonite (2 and 4 wt.%) in 100 mL demineralized water for 2 h stirring. After that, 16 mL of 40% NaOH aqueous solution, 16 mL of 1% $(\text{NH}_4)_2\text{S}_2\text{O}_8$, and 16 mL of 1% NaHSO_4 were added to the suspension and heated at 65 °C for 2 h while stirring. It was then cooled at room temperature before

being filtered by a Whatman paper. The rGOB solid (rGOB (1:2) and rGOB (1:4)) obtained was then washed with demineralized water before being dried at 60 °C for 12 h. It was grounded into a powder and sieved (325 mesh).

Characterization of materials

The X-ray powder diffraction data were collected with X-ray Diffraction Spectrometer X'Pert Powder PW 30/40 using a Cu-sealed tube (CuK α X-rays of 0.15406 nm, operating at 40 kV and 30 mA). Each system was measured in the scattering 2 θ range of 5° to 100° with a step of 0.026° and scan step time of 7.14 s. Spectra of dried graphite, bentonite, graphene oxide, reduced graphene oxide, and reduced graphene oxide-bentonite obtained by Fourier Transform Infrared Spectrometer Nicolet Avatar 360 IR, pellet KBr, from 4000–400 cm⁻¹ of the spectral region, and functional groups of materials can be observed. The morphology of the synthesized sample was observed by SEM JSM-6510 LA, using Au coating. The composition of bentonite was measured using XRF Rigaku-NexQC+QuanTEX.

Pb(II) adsorption

A total of 0.01 g of rGO, rGOB (1:2), or rGOB (1:4) was added to 50 mL of 50 ppm of Pb (II) solution (pH 1). The solution was then stirred with a magnetic stirrer for 60 min at room temperature (26 ± 2 °C). After that, the solution was filtered with Whatman filter paper, and the obtained filtrate was measured. The adsorption test was carried out three times for each adsorbent. Pb has measured the solution using an atomic absorption spectrometer graphite furnace 240Z AA Agilent Technologies. The source of the Pb hollow lamp is 217 nm, slit width 1.0 nm, 20–60 µg/L range of standard solution. The removal efficiency (R) and adsorption capacity (Q) using Eq. (1) and (2).

$$R = \frac{C_i - C_f}{C_i} \times 100\% \quad (1)$$

$$Q = \frac{(C_i - C_f) \times V}{W} \quad (2)$$

where C_i = initial concentration of Pb solution (mg/L), C_f = final concentration of Pb solution (mg/L), V = volume of solution (L), and W = mass of adsorbent (g)

RESULTS AND DISCUSSION

Graphene oxide is prepared using synthetic graphite obtained commercially *via* the modified Hummer method by Husnah et al. [10]. The temperature was kept below 20 °C when graphite contacted H₂SO₄/H₃PO₄ and KMnO₄ to prevent explosions because the reaction between KMnO₄ and H₂SO₄ would produce Mn₂O₇ which was very reactive and could cause an explosion at temperatures above 55 °C [12]. Graphite will react with H₂SO₄ in the presence of KMnO₄ to produce intercalated graphite [13]. The temperature escalation in the reaction causes more oxygen functional groups to be formed, and the oxidizers begin to enter the interlayer, which causes an increase in the graphite interlayer distance [14]. H₃PO₄ prevents excessive oxidation, which causes defects in the graphene layer [15]. The oxidation process was quenched by adding 30% H₂O₂, which will reduce the remaining KMnO₄ to MnSO₄ [16].

Reduced graphene oxide was made by reducing GO using hydrazine with the assistance of a microwave [10]. Graphene oxide is suspended in ethylene glycol using sonication to reduce particle agglomeration. Besides that, it can weaken the Van der Waals bonds between the graphene layers so that GO will be exfoliated [17]. Hydrazine is added to the suspension to reduce the oxygen functional group on GO.

The GO reduction process is completed by heating GO using a microwave at a temperature of 100 °C. The oxygen functional group in GO will be reduced thermally during heating. The suspension was then filtered, and the rGO obtained was washed with demineralized water, dried at 60 °C for 12 h, then ground into powder and sieved with a 325-mesh sieve.

The reduced graphene oxide-bentonite composite was prepared using a radical reaction with the help of a persulfate/bisulfate initiator. Suspension of rGO and bentonite were dispersed in demineralized water by a magnetic stirrer in the persulfate/bisulfate redox system. Ammonium persulfate and sodium bisulfate act as initiators and will form free radicals on the bentonite hydroxyl group so that bentonite can form bonds with rGO [11]. Sodium hydroxide was used to increase the

pH and initiate the initiation reaction. The reaction begins by heating the suspension at 65 °C while stirring with a magnetic stirrer. At this stage, the initiator will cause the formation of free radicals on some of the bentonite hydroxyl groups, which will then form bonds with rGO [11]. The suspension was then cooled to room temperature to stop the entire reaction process, filtered, and washed with demineralized water at 60 °C for 12 h. The materials used in this research are described in Fig. 1.

XRD Characterization

Graphite, GO, and rGO XRD diffractograms (Fig. 2) have diffraction peaks (002) at $2\theta = 26.37^\circ$ (graphite), $2\theta = 10.90^\circ$ (GO), and $2\theta = 24.88^\circ$ (rGO) which shows the distance between the graphene layers and the 2-dimensional diffraction peaks (10) at $2\theta = 42.63^\circ$ (GO) and $2\theta = 43.41^\circ$ (rGO) which shows the short-range order of the graphene stack [18].

Fig. 2 shows the diffraction patterns, which were processed using OriginPro *via* fitting to the Gaussian function. The diffraction peak (002) was applied to the Bragg equation to calculate the distance between the graphene layers (d) and laid into the Scherrer equation with a constant of 0.9 (Eq. (3)) to calculate the average height of the graphene stack (H) so that the number of graphene layers (n) could be estimated (Eq. (4)). The 2-dimensional diffraction peak (10) was applied into the Scherrer equation with a Warren constant of 1.84 (Eq. (5)) to estimate the mean diameter (D) of GO and rGO [18].

$$H = \frac{0.9\lambda}{\beta \cos \theta} \quad (3)$$

$$n = \frac{H}{d} \quad (4)$$

$$D = \frac{1.84\lambda}{\beta \cos \theta} \quad (5)$$

where λ = wavelength (nm), β = full width at half maximum (rad), and θ = angle of light (rad)

Table 1 shows the calculated crystal size of graphite, GO, and rGO. Graphite crystals have a graphene

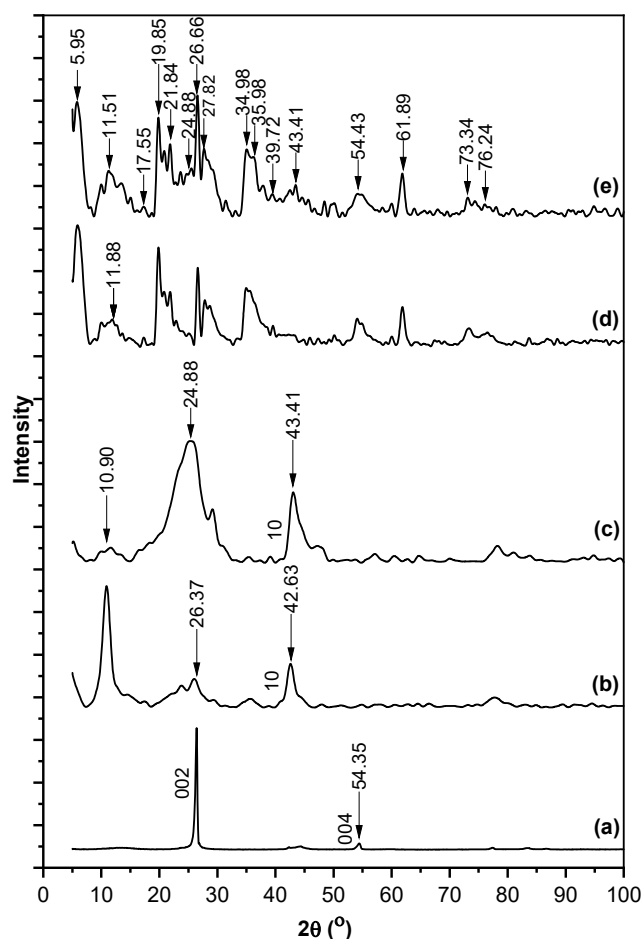


Fig 2. XRD diffractograms of graphite (a), GO (b), rGO (c), bentonite (d), and rGOB (e)

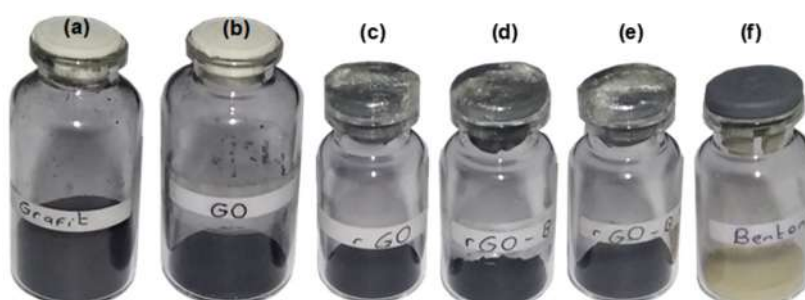


Fig 1. The visualization of samples of graphite (a), GO (b), rGO (c), rGOB (1:2) (d), rGOB (1:4) (e), and bentonite (f)

Table 1. The results of calculating the crystal size of graphite, GO and rGO

	Peak (002)				
	2 θ (°)	FWHM (°)	H (nm)	d (nm)	N
Graphite	26.37	0.4258	19.16	0.34	56–57
GO	10.90	1.7597	4.54	0.81	5–6
rGO	24.88	6.2327	1.31	0.36	3–4
	Peak (10)				
	2 θ (°)	FWHM (°)	D (nm)		
GO	42.63	1.4920	11.69		
rGO	43.41	2.2971	7.61		

interlayer distance of 0.34 nm and increase to 0.81 nm in GO due to the oxygen functional groups in the graphene interlayer. The graphene interlayer distance at rGO decreases again to 0.36 nm, indicating that GO has been successfully reduced and the structure of the graphene layer has been restored [19]. Besides, the number of graphene stacks was also reduced from 56–57 in graphite to 5–6 in GO and 3–4 in rGO. Based on the calculation results, GO crystals have an average size of 11.69 nm \times 4.54 nm, while in rGO, the average size of the crystals decreases to 7.61 nm \times 1.31 nm. The smaller the crystal size, the larger the surface area of the crystal, and it will increase its adsorption ability.

The diffractogram of bentonite (Fig. 2(d)) has characteristic peaks at 2 θ = 5.95°, 11.88°, 17.55°, 19.85°, 27.82°, 34.98°, 35.98°, 54.43°, 61.89°, 73.24°, 76.24° (montmorillonite), 21.84°, 26.66°, 39.72° (quartz), and 21.84° (cristobalite) [20,21]. On the rGOB diffractogram (Fig. 2(e)), the peaks of 11.88° and 27.82° shifted to 11.51° and 28.44°. Also, there are new peaks at 2 θ = 24.88° and 43.41° from the characteristic peaks of rGO.

FTIR Analysis

Fig. 3 shows a broad peak at 3430 cm⁻¹ (stretching OH) due to the adsorbed water and peaks at 1630 cm⁻¹ and 1550 cm⁻¹ (stretching C=C) due to the vibrations of the graphite domain. The peak at 3430 cm⁻¹ may appear because the drying process could be better, so water molecules are still trapped in the graphite powder. The intensity of the peak at 3430 cm⁻¹ vastly increased, and there are two new peaks at 1712 cm⁻¹ (stretching C=O) and 1050 cm⁻¹ (stretching C-O) in the GO spectra (Fig. 3(b)),

which indicated the presence of many oxygens functional groups after the oxidation process. The new peaks at 2925 cm⁻¹ and 2850 cm⁻¹ (stretching C-H) showed the presence of CH₂ groups in GO samples. The graphite domain vibrational peak on GO also shifted to 1615 cm⁻¹ and 1572 cm⁻¹. At rGO spectra (Fig. 3(c)), the peak intensity at 3430 cm⁻¹ and 1050 cm⁻¹ decreased significantly, while the peak at 1712 cm⁻¹ did not appear, indicating that all carbonyl and carboxylate groups and some hydroxyl and epoxide groups were successfully reduced. The peaks at 2925 cm⁻¹ and 2850 cm⁻¹ still found on rGO told that the graphite domain frame was not successfully recovered. The vibrational peaks of the graphite domain frame also shifted to 1645 cm⁻¹ and 1550 cm⁻¹ [22-23].

The FTIR spectra of bentonite (Fig. 3(d)) have a peak at 3450 cm⁻¹ (OH stretching) and 1640 cm⁻¹ (bending OH) from adsorbed water. The 3450 cm⁻¹ peak can come from the OH group on the rGO that failed to reduce and water molecules trapped in bentonite due to the imperfect drying process. Two peaks at 3630 cm⁻¹ (OH stretching) and 912 cm⁻¹ (bending OH) due to Si-OH in the tetrahedral bentonite layer. Peaks at 1040 cm⁻¹ correlated to the stretching of Si-O, while 522 cm⁻¹ and 466 cm⁻¹ for bending Si-O from Si-O-Si in the tetrahedral layer of bentonite. The peak characteristic of bentonite was also seen at 795 cm⁻¹ [20,22,24]. In the rGOB spectra (Fig. 3(e)), the peak intensity at 3630 cm⁻¹ and 912 cm⁻¹ decreased because some of the hydroxyl groups in bentonite formed bonds with rGO [11]. The peak of rGO characteristics did not appear in the rGOB spectra because the characteristic peaks of bentonite covered it.

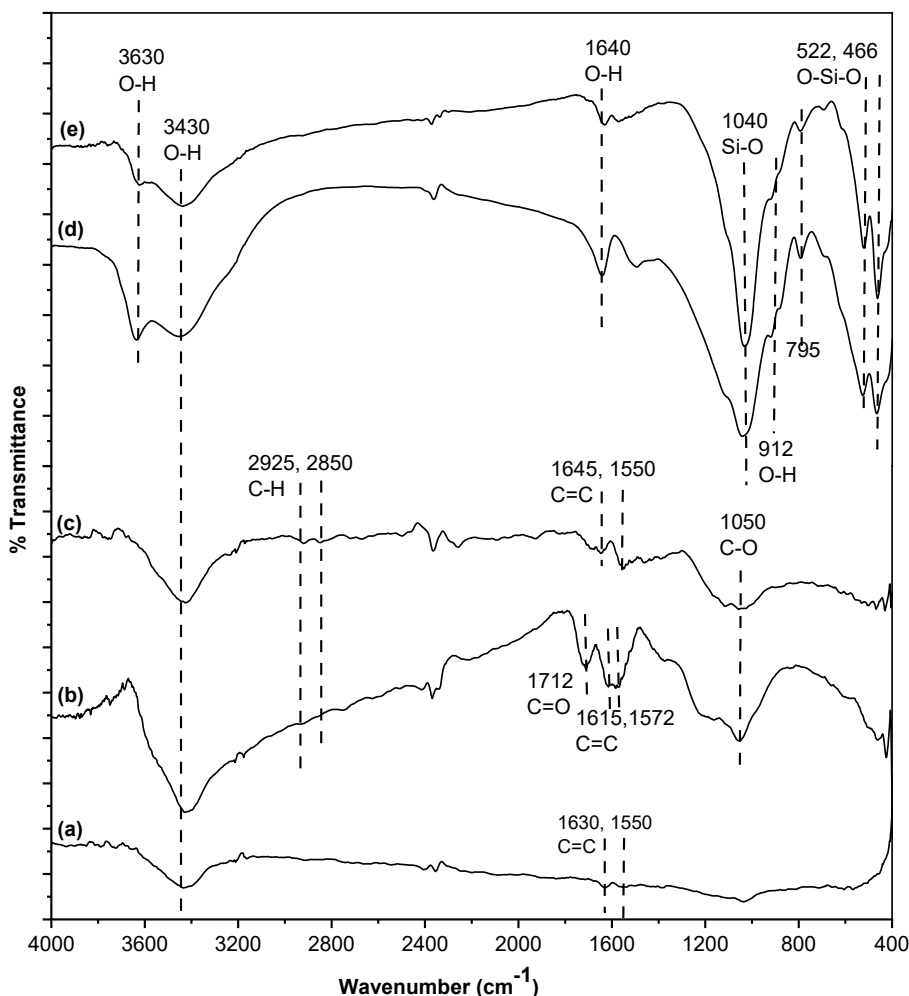


Fig 3. FTIR spectra of graphite (a), GO (b), rGO (c), bentonite (d), and rGOB (e)

SEM-EDX Analysis

Micrograph SEM (Fig. 4) of GO showed a layered structure with a rough surface and flaking flakes. The presence of these flakes indicates that the graphene surface has been successfully oxidized to GO. The results of the EDX analysis also showed the presence of oxygen atoms as much as 27.61%, which proved that the oxidation process was successful. After being reduced to rGO, the shape looks like small pieces with a wrinkled and folded surface, a characteristic of rGO materials [14,25]. In addition, the results of the EDX analysis (Fig. 4) also showed a decrease in the number of oxygen atoms from 27.61% in GO to 15.48% in rGO, indicating that the reduction process had been successfully carried out.

Both GO and rGO appear to form clumps, which could be due to prolonged heating [14]. The clumping

form can cause the adsorption ability of the material to be reduced. However, when rGO was composited with bentonite, it was seen that rGO adhered to the bentonite surface. The EDX results also showed the presence of Si and Al, which are the main components of bentonite. Based on the micrograph, bentonite does not appear to form large clumps, and rGO spreads on the bentonite surface. So that when used in the adsorption process, the material can be evenly dispersed in the solution and has a better adsorption ability.

XRF of Bentonite

Table 2 shows the composition of bentonite XRF determination. The results of the XRF test showed that there was a relatively high content of SiO_2 and Al_2O_3 . Both are the main ingredients of bentonite. The presence

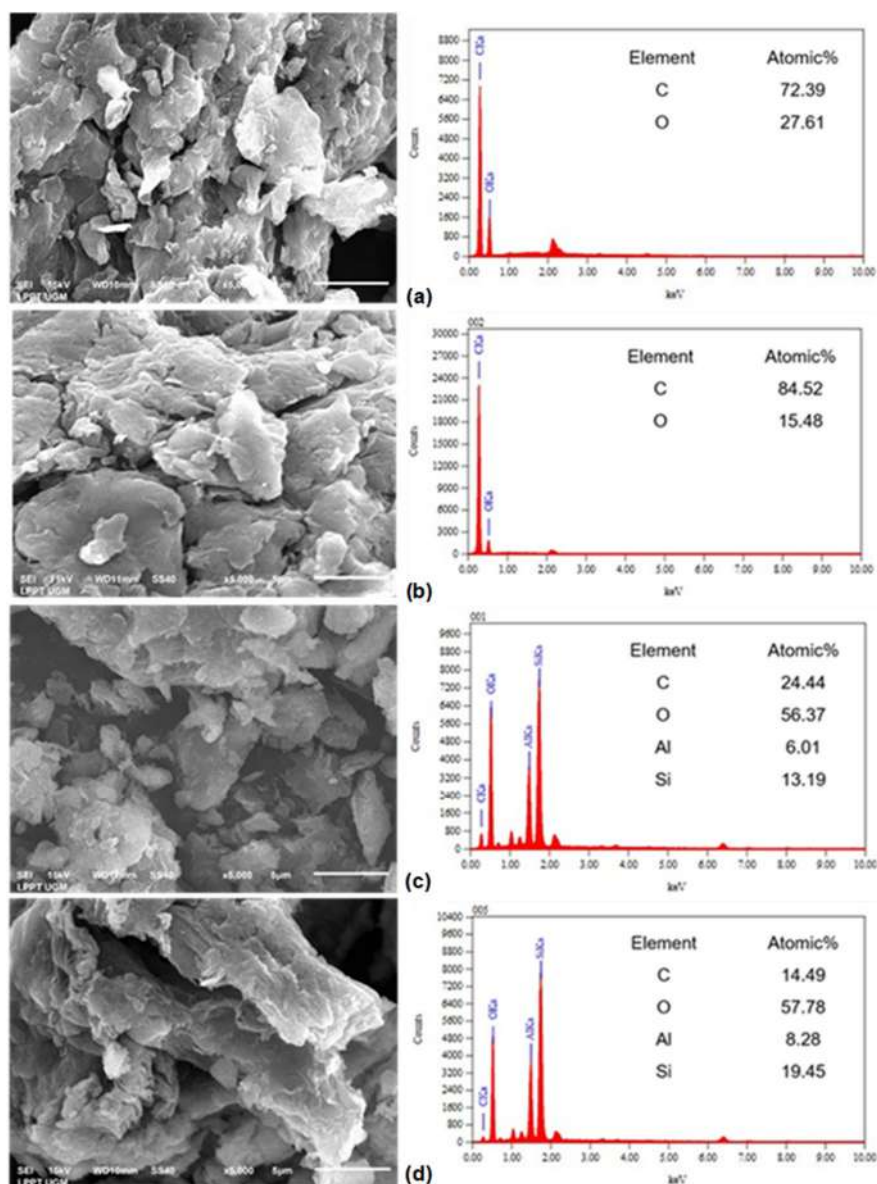


Fig 4. Micrograph SEM and EDX analysis of GO (a), rGO (b), rGOB 1:2 (c), and rGOB 1:4 (d)

Table 2. Bentonite composition from XRF result

Component	% Mass
Al ₂ O ₃	10.85
SiO ₂	63.33
CaO	25.82

of CaO indicates that the bentonite used is Ca-Bentonite. Many studies have been conducted to test the ability of bentonite as an adsorbent for heavy metals due to its abundant availability, relatively low price, environmentally friendly [8], and large surface area and cation exchange capacity [9]. However, the results showed

that the adsorption capacity of bentonite to Pb ion was not very high, only 19–85 mg/g [26–28].

Pb(II) Adsorption Activity Test

Table 3 shows the application of synthesized material as an adsorbent for Pb ion. The adsorption test was carried out on a 50 ppm (pH 1) Pb(II) solution with the batch adsorption method. The results showed that the rGO adsorbent had the highest adsorption capacity with an average adsorption capacity of 218 mg/g, followed by rGOB (1:4) of 217 mg/g, and finally, rGOB (1:2) of 216 mg/g. However, the results of the t-test with

Table 3. The results of the adsorption test on the Pb(II) solution

Adsorbent	Pb concentration after adsorption (ppm)	Removal efficiency (%)	Adsorption capacity (mg/g)
rGO	6.688	87	217
	6.537	87	217
	6.129	88	219
Average \pm SD		87	218 \pm 1.45
rGOB (1:2)	6.459	87	218
	7.452	85	213
	6.586	87	217
Average \pm SD		86	216 \pm 2.70
rGOB (1:4)	6.872	86	216
	6.316	88	218
	6.757	86	216
Average \pm SD		87	217 \pm 1.47

Table 4. The adsorption capacity of some adsorbents to Pb(II) at room temperature

Adsorbent Material	pH	Adsorption capacity (mg/g)	Ref.
Activated carbon	7	31–59	[29]
Natural bentonite	5.5	71	[27]
Porous cellulosic	6	52	[30]
Magnetic graphene oxide functionalized cyanopropyl nanocomposite	5	111	[31]
Halloysite nanotube-rich carboxyl carbon	6	184	[32]
Magnetic Fe ₃ O ₄ -encapsulated C ₃ N ₃ S ₃ polymer/reduced graphene oxide	6	270	[33]
Reduced graphene oxide-bentonite composite*	1	217	Present work

*Optimization of adsorption conditions has not been carried out

a 95% confidence interval showed that the removal efficiency for each adsorbent did not have a significant difference. The rGOB composite has the same efficiency as rGO, but the rGOB composite (1:2) can reduce the use of rGO by 66%, and even at rGOB (1:4), it can reduce the use of rGO by 80%.

Table 4 shows the comparison of some adsorbents to Pb ions. The rGOB composites can reduce the use of rGO very significantly but still have an equivalent adsorption capability. It is because, in a suspended state, rGO will form an aggregate [6] so that it will significantly reduce its adsorption capacity. The bentonite added to the adsorbent is a highly dispersed material [34]. The rGOB adsorbent produced also has good dispersibility and

causes the ability of the rGOB adsorbent not to decrease when compared to the rGO adsorbent. In addition, bentonite is also a heavy metal adsorbent, so it also contributes to the adsorption of Pb(II). The rGOB composites synthesized in this study have a high adsorption ability, so they have the potential to be used as heavy metal adsorbents.

■ CONCLUSION

The reduced graphene oxide-bentonite was successfully synthesized. The diffractogram of XRD shows the identity of GO, rGO, and bentonite. The FTIR spectrum described the functional group of materials qualitatively. The SEM-EDX confirms the morphology

and composition of the material. The XRF of bentonite sure the compound in it. The adsorption activity of the materials against Pb ion in the sample shows that the materials can run as an adsorbent well. The resulting rGOB composites can reduce the use of rGO by up to 80%, but they still have an adsorption capability similar to rGO. The rGOB adsorbent can adsorb Pb up to 87% and has an adsorption capacity of 217 mg/g.

■ ACKNOWLEDGMENTS

This work was supported by grants from Mathematics and Natural Sciences Faculty, Universitas Tanjungpura Pontianak, under DIPA UNTAN Grant No. SP DIPA-042.01.2.400955/2019. The authors express great gratitude for that support.

■ AUTHOR CONTRIBUTIONS

Bartholomeus Lavelim conducted the experiment and wrote the manuscript draft, Lia Destiarti concept the methodology and revised the manuscript, Adhitiyawarman wrote and revised the manuscript, and Risya Sasri checked the data accuracy. All authors agreed to the final version of this manuscript.

■ REFERENCES

- [1] Agency for Toxic Substances and Disease Registry, 2019, *ATSDR's Substance Priority List*, <https://www.atsdr.cdc.gov/spl/index.html>, accessed on April 7, 2021.
- [2] Fu, F., and Wang, Q., 2011, Removal of heavy metal ions from wastewaters: A review, *J. Environ. Manage.*, 92 (3), 407–418.
- [3] Asuquo, E., Martin, A., Nzerem, P., Siperstein, F., and Fan, X., 2017, Adsorption of Cd(II) and Pb(II) ions from aqueous solutions using mesoporous activated carbon adsorbent: Equilibrium, kinetics and characterisation studies, *J. Environ. Chem. Eng.*, 5 (1), 679–698.
- [4] Ibrahim, H.S., Ammar, N.S., Soylak, M., and Ibrahim, M., 2012, Removal of Cd(II) and Pb(II) from aqueous solution using dried water hyacinth as a biosorbent, *Spectrochim. Acta, Part A*, 96, 413–420.
- [5] Salem, A., and Sene, R.A., 2011, Removal of lead from solution by combination of natural zeolite–kaolin–bentonite as a new low-cost adsorbent, *Chem. Eng. J.*, 174 (2-3), 619–628.
- [6] Stankovich, S., Dikin, D.A., Piner, R.D., Kohlhaas, K.A., Kleinhammes, A., Jia, Y., Wu, Y., Nguyen, S.T., and Ruoff, R.S., 2007, Synthesis of graphene-based nanosheets via chemical reduction of exfoliated graphite oxide, *Carbon*, 45 (7), 1558–1565.
- [7] Nakamura, A., Ozaki, M., and Murakami, K., 2020, Elucidation of the aggregation mechanism of bentonite with cationic guar gum as flocculant and application to filtration, *Colloids Surf., A*, 596, 124660.
- [8] Zhang, Z., Luo, H., Jiang, X., Jiang, Z., and Yang, C., 2015, Synthesis of reduced graphene oxide–montmorillonite nanocomposite and its application in hexavalent chromium removal from aqueous solutions, *RSC Adv.*, 5 (59), 47408–47417.
- [9] Yener, N., Biçer, C., Önal, M., and Sarikaya, Y., 2012, Simultaneous determination of cation exchange capacity and surface area of acid activated bentonite powders by methylene blue sorption, *Appl. Surf. Sci.*, 258 (7), 2534–2539.
- [10] Husnah, M., Fakhri, H.A., Rohman, F., Aimon, A.H., and Iskandar, F., 2017, A modified Marcano method for improving electrical properties of reduced graphene oxide (rGO), *Mater. Res. Express*, 4 (6), 064001.
- [11] Liu, H., Xie, S., Liao, J., Yan, T., Liu, Y., and Tang, X., 2018, Novel graphene oxide/bentonite composite for uranium(VI) adsorption from aqueous solution, *J. Radioanal. Nucl. Chem.*, 317 (3), 1349–1360.
- [12] Dreyer, D.R., Park, S., Bielawski, C.W., and Ruoff, R.S., 2010, The chemistry of graphene oxide, *Chem. Soc. Rev.*, 39, 228–240.
- [13] Johansen, I., 2014, Wet Chemical Synthesis of Graphene for Battery Applications, *Thesis*, Norwegian University of Science and Technology, Trondheim.
- [14] Cao, N., and Zhang, Y., 2015, Study of reduced graphene oxide preparation by Hummers' method and related characterization, *J. Nanomater.*, 2015, 168125.

- [15] Sohail, M., Saleem, M., Ullah, S., Saeed, N., Afridi, A., and Khan, M., 2017, Modified and improved Hummer's synthesis of graphene oxide for capacitors applications, *Mod. Electron. Mater.*, 3 (3), 110–116.
- [16] Yoo, M.J., and Park, H.B., 2019, Effect of hydrogen peroxide on properties of graphene oxide in Hummers method, *Carbon*, 141, 515–522.
- [17] Zainuddin, M.F., Nik Raikhan, N.H., Othman, N.H., and Abdullah, W.F.H., 2018, Synthesis of reduced Graphene Oxide (rGO) using different treatments of Graphene Oxide (GO), *IOP Conf. Ser.: Mater. Sci. Eng.*, 358, 012046.
- [18] Stobinski, L., Lesiak, B., Malolepszy, A., Mazurkiewicz, M., Mierzwa, B., Zemek, J., Jiricek, P., and Bieloshapka, I., 2014, Graphene oxide and reduced graphene oxide studied by the XRD, TEM and electron spectroscopy methods, *J. Electron Spectrosc. Relat. Phenom.*, 195, 145–154.
- [19] Park, S., An, J., Potts, J.R., Velamakanni, A., Murali, S., and Ruoff, R.S., 2011, Hydrazine-reduction of graphite- and graphene oxide, *Carbon*, 49 (9), 3019–3023.
- [20] Ikhtiyarova, G.A., Özcan, A.S., Gök, Ö., and Özcan, A., 2012, Characterization of natural- and organo-bentonite by XRD, SEM, FT-IR and thermal analysis techniques and its adsorption behaviour in aqueous solutions, *Clay Miner.*, 47 (1), 31–44.
- [21] Vryzas, Z., Wubulikasimu, Y., Gerogiorgis, D.I., and Kelessidis, V.C., 2016, Understanding the temperature effect on the rheology of water-bentonite suspensions, *Annu. Trans. - Nord. Rheol. Soc.*, 24, 199–208.
- [22] Derrick, M.R., Stulik, D., and Landry, J.M., 1999, *Infrared Spectroscopy in Conservation Science*, The Getty Conservation Institute, Los Angeles.
- [23] Ren, P.G., Yan, D.X., Ji, X., Chen, T., and Li, Z.M., 2011, Temperature dependence of graphene oxide reduced by hydrazine hydrate, *Nanotechnology*, 22 (5), 055705.
- [24] Anirudhan, T.S., Jalajamony, S., and Sreekumari, S.S., 2012, Adsorption of heavy metal ions from aqueous solutions by amine and carboxylate functionalised bentonites, *Appl. Clay Sci.*, 65–66, 67–71.
- [25] Hidayah, N.M.S., Liu, W.W., Lai, C.W., Noriman, N.Z., Khe, C.S., Hashim, U., and Lee, H.C., 2017, Comparison on graphite, graphene oxide and reduced graphene oxide: Synthesis and characterization, *AIP Conf. Proc.*, 1892, 150002.
- [26] Anna, B., Kleopas, M., Constantine, S., Anestis, F., and Maria, B., 2014, Adsorption of Cd(II), Cu(II), Ni(II) and Pb(II) onto natural bentonite: Study in mono- and multi-metal systems, *Environ. Earth Sci.*, 73 (9), 5435–5444.
- [27] Hamidpour, M., Kalbasi, M., Afyuni, M., Shariatmadari, H., and Furrer, G., 2011, Sorption of lead on Iranian bentonite and zeolite: Kinetics and isotherms, *Environ. Earth Sci.*, 62 (3), 559–568.
- [28] Nava, Y.F., Ulmanu, M., Anger, I., Maranon, E., and Castrillon, L., 2011, Use of granular bentonite in the removal of mercury (II), cadmium (II) and lead (II) from aqueous solutions, *Water, Air, Soil Pollut.*, 215 (1-4), 239–249.
- [29] Song, M., Wei, Y., Cai, S., Yu, L., Zhong, Z., and Jin, B., 2018, Study on adsorption properties and mechanism of Pb²⁺ with different carbon based adsorbents, *Sci. Total Environ.*, 618, 1416–1422.
- [30] Barsbay, M., Kavaklı, P.A., Tilki, S., Kavaklı, C., and Güven, O., 2018, Porous cellulosic adsorbent for the removal of Cd(II), Pb(II) and Cu(II) ions from aqueous media, *Radiat. Phys. Chem.*, 142, 70–76.
- [31] Gabris, M.A., Jume, B.H., Rezaali, M., Shahabuddin, S., Nodeh, H.R., and Saidur, R., 2018, Novel magnetic graphene oxide functionalized cyanopropyl nanocomposite as an adsorbent for the removal of Pb(II) ions from aqueous media: Equilibrium and kinetic studies, *Environ. Sci. Pollut. Res.*, 25 (27), 27122–27132.
- [32] Wang, P., Tang, Y., Liu, Y., Wang, T., Wu, P., and Lu, X.Y., 2018, Halloysite nanotube@carbon with rich carboxyl groups as a multifunctional adsorbent for the efficient removal of cationic Pb(II), anionic Cr(VI) and methylene blue (MB), *Environ. Sci.: Nano*, 5 (10), 2257–2268.

- [33] Fu, W., Wang, X., and Huang, Z., 2019, Remarkable reusability of magnetic Fe₃O₄-encapsulated C₃N₃S₃ polymer/reduced graphene oxide composite: A highly effective adsorbent for Pb and Hg ions, *Sci. Total Environ.*, 659, 895–904.
- [34] Shaikh, S.M.R., Nasser, M.S., Magzoub, M., Benamor, A., Hussein, I.A., El-Naas, M.H., and Qiblawey, H., 2018, Effect of electrolytes on electrokinetics and flocculation behavior of bentonite-polyacrylamide dispersions, *Appl. Clay Sci.*, 158, 46–54.

Colorimetric Chemosensor for Sulfide Anion Detection Based on Symmetrical Nitrovanillin Azine

Diana Lestari, Tutik Dwi Wahyuningsih, and Bambang Purwono*

Department of Chemistry, Faculty of Mathematics and Natural Sciences, Universitas Gadjah Mada, Sekip Utara, Yogyakarta 55281, Indonesia

* Corresponding author:

email: purwono.bambang@ugm.ac.id

Received: December 15, 2021

Accepted: September 28, 2022

DOI: 10.22146/ijc.71259

Abstract: The nitrovanillin azine (NA) has been successfully synthesized and examined as a colorimetric chemosensor for sulfide anion detection. The NA was synthesized using two steps reaction. Vanillin was reacted with concentrated nitric acid to form 5-nitrovanillin (NV) then the NV was condensed with hydrazine hydrate to produce the NA. The NA was obtained and fully elucidated by FTIR, ¹H-NMR, ¹³C-NMR, and GC-MS spectrometer. The NA activity for anionic chemosensor was then carried out on several anions such as F⁻, Cl⁻, Br⁻, I⁻, S²⁻, CN⁻, HCO₃⁻, AcO⁻, H₂PO₄⁻, N₃⁻, NO₂⁻, SCN⁻, ClO₃⁻, and NO₃⁻. The chemosensor tests showed NA was only selective for S²⁻ in DMF:HEPES buffer (9:1, v/v, 10 mM, pH = 7.4) giving color change from light yellow to dark green. The LOD value was 1.43×10^{-5} M and the interaction model of NA-S²⁻ indicated deprotonation mode between the -OH group with sulfide anion in a ratio of 1:1. The NA chemosensor can be applied for qualitatively analysis of sulfide anion using filter paper strips and quantitatively analysis of sulfide anion in tap water.

Keywords: 5-nitrovanillin; hydrazine; azine; colorimetric; chemosensor

■ INTRODUCTION

Hydrogen sulfide (H₂S) is one of the most toxic, corrosive, and flammable gases with the characteristic odor of rotten eggs. In high concentrations, this gas causes serious problems such as hypertension, diabetes, liver cirrhosis, chronic kidney, Down Syndrome, and Alzheimer's disease [1-3]. According to the National Institute of Occupational Safety and Health, the concentration of H₂S harmful to life or health is up to 150 ppm, and the recommended exposure limit is 10 ppm for a maximum duration of 10 min [4]. Hydrogen sulfide is also involved in pathological and physiological functions, including inhibition of insulin signaling, regulation of inflammation, and relaxation of the smooth muscle of blood vessels [5]. Several methods for detecting sulfides are potentiometry [6], chromatography [7], and electrochemistry [8]. However, the use of those instruments requires a complicated sample preparation, expensive, and difficult to operate. Therefore, it is necessary to develop simple, efficient, and faster methods

with a high level of sensitivity and selectivity. The colorimetric chemosensor is the most often used to detect anions through color changes [9]. Visually, the detection process is more profitable because it can provide qualitative and quantitative information in a relatively short time [10], and it is possible to be seen directly with the naked eye. This method is not expensive and easy to operate their instruments [11].

Chemosensor compounds have two main parts: signal site in the form of chromophore groups acting as color carrier such as azine (RHC=N-N=CHR) [12], and binding sites such as -OH playing a role in interacting with anions through hydrogen bonding or deprotonation [13]. Research for anion chemosensor in recent years continues to grow. Acetophenone azine derivative has been synthesized as a colorimetric and fluorescence sensor to detect CN⁻, F⁻, and AcO⁻ in DMSO [14]. Azines from vanillin and 2-hydroxy-5-phenylazo-benzaldehyde have been used as a colorimetric sensor of S²⁻ anion in DMF:HEPES (v/v = 9:1, 10 mM HEPES, pH = 7.4) [15-16]. Another unsymmetrical azine of dicyanoisophorone-

based derivatives has been designed as a colorimetric and fluorescence of Cu^{2+} toward S^{2-} in DMSO/HEPES buffer ($v/v = 2:1$, 20 Mm HEPES, $\text{pH} = 7.4$) [17].

In this study, we synthesized the nitrovanillin azine (NA) from vanillin as a sulfide anion colorimetric chemosensor. Investigation for NA colorimetric chemosensor was carried out by sensing properties measurement to various anion, time interaction, anion interferences, pH effect, reversibility, and LOD. A qualitative test of sulfide anion has also been performed with a filter paper strip, while a quantitative analysis of sulfide anion in tap water shows the application of NA.

■ EXPERIMENTAL SECTION

Materials

Materials used for the synthesis were vanillin, nitric acid 37%, dichloromethane (DCM), hydrazine hydrate 80%, methanol, ethanol, chloroform, dimethyl sulfoxide (DMSO), dimethylformamide (DMF), HEPES buffer solution (HBS) in deionized water, acetone, acetonitrile, aquadest, sodium fluoride, sodium chloride, sodium bromide, sodium iodide, sodium sulfide, sodium cyanide, sodium hydrogen carbonate, sodium acetate, sodium dihydrogen phosphate, sodium azide, sodium nitrite, potassium thiocyanate, potassium chlorate, and potassium nitrate. All materials used have a Merck p.a quality, while deionized water is from Onemed.

Instrumentation

The characteristics of the synthesized compounds were carried out using a melting point determination apparatus (Electrothermal-9100), FTIR spectrophotometers (Shimadzu Prestige-21), $^1\text{H-NMR}$ (Agilent, 500 MHz and JEOL JNM ECA-500, 500 MHz), $^{13}\text{C-NMR}$ (Agilent, 125 MHz), GC-MS and DI-MS (Shimadzu QP-2010S). The color change was measured using a UV-Vis spectrophotometer (Shimadzu UV-1800).

Procedure

Synthesis of 5-nitrovanillin (5-NV)

The 5-nitrovanillin (5-NV) was synthesized based on previous methods [18]. Vanillin (13.79 g, 70 mmol) was dissolved in 55 mL of dichloromethane ($0-5^\circ\text{C}$) and 12 mL of HNO_3 was added dropwise at $0-5^\circ\text{C}$. The

reaction mixture was stirred at room temperature for 20 min and then cold distilled water (25 mL) was added and left for 2 h. Subsequently, the solid was filtered and recrystallized with ethanol. The synthesized product was obtained as a pale-yellow powder in yield of 72.1% (m.p. $176-178^\circ\text{C}$). FTIR (KBr) (cm^{-1}): 3209 (-OH group), 3078 ($\text{Csp}^2\text{-H}$), 2887 ($\text{Csp}^3\text{-H}$), 1681 (C=O), 1543 ($-\text{NO}_2$), 1612 and 1465 (C=C aromatic), 1111 and 1049 (C-O-C). m/z [M^+] = 197.

Synthesis of nitrovanillin azine (NA)

The synthesis of NA compound is based on a previous method with some modifications [15]. The 5-NV (0.390 g, 1 mmol) was dissolved in 25 mL of ethanol and mixed with (0.5 mmol) hydrazine hydrate 80% in 5 mL of ethanol. The reaction mixture was stirred at room temperature for overnight and the progress of reaction was monitored by TLC. The solid was filtered and washed with ethanol several times and then crystallized with ethanol:DMSO (2:1). The product was obtained as a yellow solid in yield of 76.14% (m.p. $293-394^\circ\text{C}$). FTIR (KBr) (cm^{-1}): 3448 (-OH group), 3078 ($\text{Csp}^2\text{-H}$), 2947 ($\text{Csp}^3\text{-H}$), 1627 ($-\text{C=N-}$), 1543 ($-\text{NO}_2$), 1472 (C=C aromatic), 1273 (C-O-C). m/z [M^+] = 390. $^1\text{H-NMR}$ (500 MHz, $\text{DMSO-}d_6$) (δ) (ppm): 3.96 (3H, s, OCH_3), 7.74 (1H, s, ArH), 7.96 (1H, d, ArH), 8.71 (1H, s, $-\text{CH=N-}$), 11.16 (1H, s, ArOH). $^{13}\text{C-NMR}$ (δ) (ppm): 56.69 (OCH_3), 112.73 (C_{aryl}), 118.19 (C_{aryl}), 124.10 (C_{aryl}), 137.18 ($\text{C}_{\text{aryl-NO}_2}$), 145.72 ($\text{C}_{\text{aryl-OH}}$), 150.03 ($-\text{C=N-}$), 160.10 ($\text{C}_{\text{aryl-OCH}_3}$).

Study of NA selectivity as anion chemosensor

A solution of NA (2×10^{-5} M) was prepared in DMF:HBS (9:1, v/v , 10 mM HEPES, $\text{pH} = 7.4$) and solution of anion (0.2 M) such as F^- , Cl^- , Br^- , I^- , S^{2-} , CN^- , HCO_3^- , AcO^- , H_2PO_4^- , N_3^- , NO_2^- , SCN^- , ClO_3^- , and NO_3^- in HEPES Buffer Solution (HBS). The 4 mL of NA were placed in a cuvette and each (150 μL) anion solution was added. The color change was recorded and determined with a UV-Vis spectrophotometer.

Study of competition of sulfide anions with different anions

A solution of NA (2×10^{-5} M) was prepared in DMF:HBS (9:1, v/v , 10 mM HEPES, $\text{pH} = 7.4$) and

different anion solutions with a concentration of 0.2 M in HBS. The 4 mL of NA were put in a cuvette and different anions (0.2 M, 100 μ L) of F⁻, Cl⁻, Br⁻, I⁻, CN⁻, HCO₃⁻, AcO⁻, H₂PO₄⁻, N₃⁻, NO₂⁻, SCN⁻, ClO₃⁻, and NO₃⁻ were added, then into each mixture added S²⁻ (100 μ L). Color changes were recorded and monitored at a wavelength of 613 nm.

Sensitivity study of NA as a sulfide anion sensor

A solution of NA (2×10^{-5} M) was prepared in DMF:HBS (9:1, v/v, 10 mM HEPES, pH = 7.4) and a solution of S²⁻ (0.2 M) in HBS. The 4 mL of NA was put in a cuvette and added S²⁻ (0–100 μ L). The color change for each addition of S²⁻ was recorded and monitored at a wavelength of 613 nm. Determination of detection limit using the $3\sigma/m$ equation [19].

Study of interaction time of NA-sulfide anions

The 4 mL of NA solution (2×10^{-5} M) was prepared in DMF:HBS (9:1, v/v, 10 mM HEPES, pH = 7.4) and a solution of S²⁻ (0.2 M, 115 μ L) was added in HBS. Changes in UV-Vis absorbance were monitored at wavelengths of 613 nm with different time intervals at room temperature.

Reversibility study of NA toward sulfide anions

The 4 mL of NA solution (2×10^{-5} M) was prepared in DMF:HBS (9:1, v/v, 10 mM HEPES, pH = 7.4) and a solution of S²⁻ (0.2 M, 116 μ L) was added in HBS followed by the addition of HCl (2 M, 23 μ L). Changes in UV-Vis absorbance were monitored at wavelengths of 613 nm before and after adding S²⁻ and HCl several times with different time intervals at room temperature.

pH Dependent study of NA toward sulfide anions

A solution of NA (2×10^{-5} M) was prepared in DMF:HBS (9:1, v/v, 10 mM HEPES, pH = 3, 5, 7.4, 9 and 11) and a solution of S²⁻ (0.2 M) in HBS. The 4 mL of NA with various pH was placed in a cuvette and added S²⁻

(150 μ L). Changes in UV-Vis absorbance were monitored at wavelengths of 613 nm before and after the addition of S²⁻.

Determination of NA-S²⁻ interaction through Job's Plot

A solution of NA in DMF:HBS (9:1, v/v, 10 mM HEPES, pH = 7.4) and solution of S²⁻ in HBS were prepared in a constant concentration of 7×10^{-5} M. Host-Guest solution comparison (1:9–9:1) were prepared by mixing of 0.4–3.6 mL of NA solution (Host) with 3.6–0.4 mL of S²⁻ (Guest) with a total solution of 4 mL. Changes in UV-Vis absorbance were monitored at wavelengths of 613 nm and plotted as [G]/[H] vs absorbance.

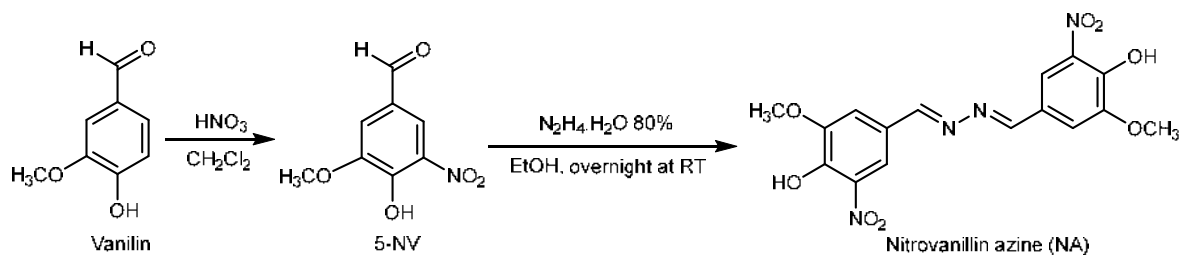
Filter paper strip study of NA toward sulfide anions

Filter paper strip (Whatman no. 42) with a size of 1 \times 3 cm were immersed in a solution of NA 1×10^{-3} M in DMF:HBS (9:1, v/v, 10 mM HEPES, pH = 7.4) for 2 h. The paper strip was dried in an oven, and then two drops of S²⁻ solution (0.2 M) in HBS were added to the paper strip and allowed to react. Color change was recorded visually and under a 366 nm UV lamp.

RESULTS AND DISCUSSION

Chemosensor NA was synthesized by condensation reaction between 5-NV with 80% hydrate hydrazine (Scheme 1) and purified through recrystallization from a solvent mixture of ethanol:DMSO (2:1) to produce a golden yellow solid. All products of synthesis are agreed with spectroscopy data.

Chemosensor NA has a binding site in the form of phenol groups that can interact strongly with anions through the hydrogen bond interaction. Here, the -OH group can be deprotonated with strong basic anions such



Scheme 1. Schematic formation of the reaction of NA Chemosensor

as CN^- , HCO_3^- , and AcO^- [20]. Sulfide anion also has basic properties that allow the same deprotonation mechanism. Hydrogen sulfide (H_2S) dissolves in water and dissociates to form H^+ , HS^- and S^{2-} . Under physiological conditions, it forms about 20% as H_2S and 80% as $\text{HS}^-/\text{S}^{2-}$. In this study, sulfide anion (S^{2-}) is a mixture of $\text{H}_2\text{S} + \text{HS}^- + \text{S}^{2-}$ in solution [21].

Selectivity and Sensitivity of NA toward S^{2-}

Chemosensor NA in DMF:HBS (9:1, v/v, 10 mM, pH = 7.4) has interacted with different anions such as F^- , Cl^- , Br^- , I^- , S^{2-} , CN^- , HCO_3^- , AcO^- , H_2PO_4^- , N_3^- , NO_2^- , SCN^- , ClO_3^- , and NO_3^- . The color changes were recorded and confirmed using a UV-Vis spectrophotometer. The addition effect of each anion showed that only the S^{2-} anion gave a color change from light yellow to dark green, whereas other anions did not give a significant color change. The absorbance spectra of NA showed two peaks at 388 and 459 nm. After addition of S^{2-} showed a bathochromic shift with the appearance of a new absorbance at 613 nm. This shift indicated the interaction of NA with S^{2-} . The phenol group of NA experienced deprotonation and then followed by delocalization of π electrons to produce a color change (Fig. 1) and emerging

wavelength at λ_{max} 613 nm (Fig. 2).

Detection Limit Calculation

The NA sensitivity was confirmed using a UV-Vis titration. Changes in UV-Vis absorbance after the addition of S^{2-} (0–5 mM) in DMF:HBS showed an increase in absorbance with increasing S^{2-} concentration at λ_{max} 613 nm (Fig. 3(a)).

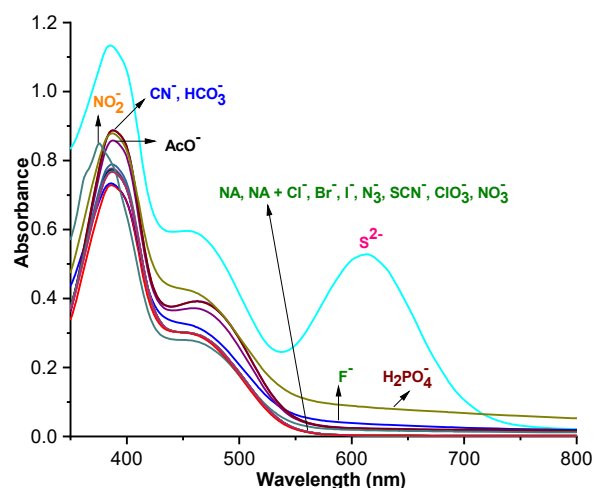


Fig 2. UV-Vis absorbance spectra of NA (2×10^{-5} M) with several anions in DMF:HBS (9:1, v/v, 10 mM, pH = 7.4)

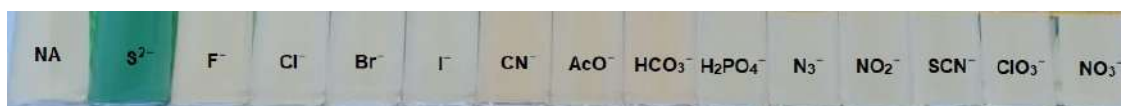


Fig 1. Color change of NA solution (2×10^{-5} M) with several anions

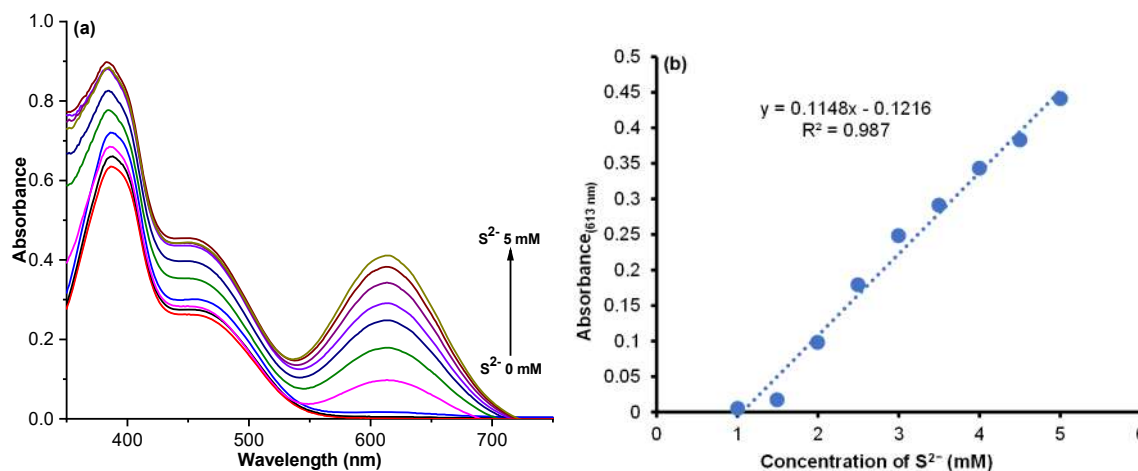


Fig 3. (a) Absorbance spectra of NA (2×10^{-5} M) after the addition of concentration variations S^{2-} and (b) Linear regression curve of NA with S^{2-}

The calculation of the detection limit used equation $3\sigma/m$, where the σ is the standard deviation obtained from an empty signal without S^{2-} and m is the slope value of the calibration curve [19]. The ratiometric calibration curve has an R^2 of 0.987 (Fig. 3(b)), so the detection limit value (LOD) S^{2-} is 1.43×10^{-5} M (14.3 μ M). This NA value is smaller than previous LOD values reported by Kaushik et al. [15] and Rokhmah et al. [16].

Competition Study with Other Anions

Examination of possible interference S^{2-} with other anions such as F^- , Cl^- , Br^- , I^- , CN^- , HCO_3^- , AcO^- , $H_2PO_4^-$, N_3^- , NO_2^- , SCN^- , ClO_3^- , and NO_3^- was studied. The results showed that almost all other anions have no interference effect in detecting S^{2-} anions except for CN^- and HCO_3^- (Fig. 4). These anions, CN^- and HCO_3^- are strong bases which interfere sulfide detection process [22]. Sulfide with CN^- and HCO_3^- competes with each other in interacting with the binding site of the chemosensor. Therefore, there is a slight increase in absorbance. This indicates that S^{2-} is not bound to the NA binding site due to the presence of CN^- and HCO_3^- , which causes no color change to occur.

Study of Interaction Time Effect of NA- S^{2-}

The study of the interaction time effect of NA- S^{2-} was monitored at λ_{max} 613 nm for 30 min (Fig. 5). The measurement results showed that the absorbance change at the peak of 613 nm occurred within one minute after the addition of S^{2-} and reached a maximum absorbance in 15 min and then decreased over time. The absorbance

decreases occurred because the S^{2-} was in another form after 15 min. This study confirmed that NA toward S^{2-} has a reasonably fast response.

Reversibility Study

The study of NA reversibility was examined by adding S^{2-} followed by the addition of a dilute acid solution of HCl (2 M) at λ_{max} 613 nm. Absorbance at λ_{max} 613 nm is a form of NA deprotonation by S^{2-} , and then after the addition of dilute acid, the absorbance at λ_{max} 613 nm is lost (NA is not deprotonated). Based on the absorbance at λ_{max} 613 nm, NA chemosensor can be used as a sulfide sensor with repeatability for up to four cycles (Fig. 6). This shows that NA has good reversibility to S^{2-} and H^+ ions.

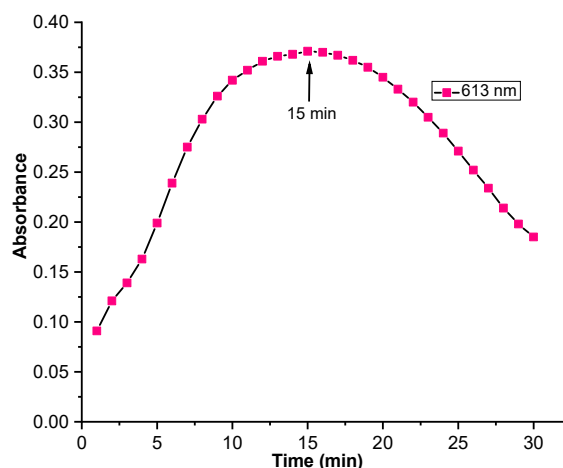


Fig 5. Interaction time and absorbance relationship curve at λ 613 nm of NA (2×10^{-5} M) to S^{2-}

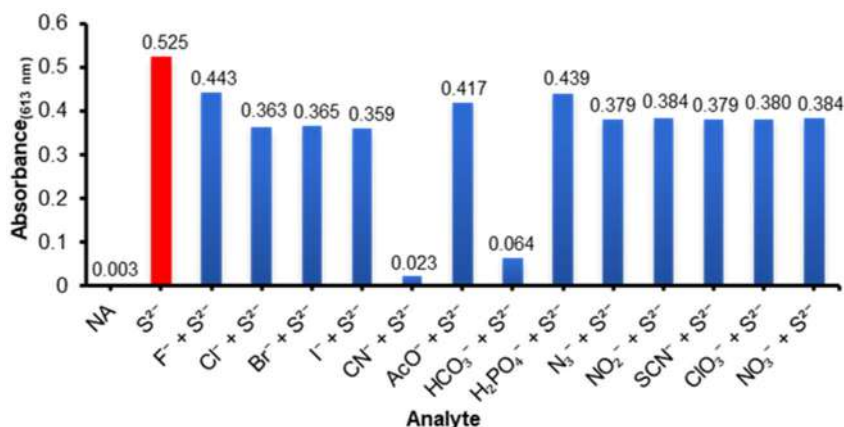


Fig 4. Bar diagram of the competition of several anions with S^{2-}

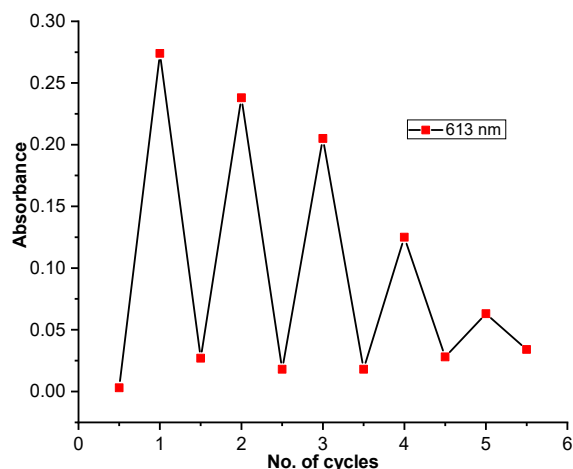


Fig 6. Reversibility absorbance spectra of NA with S^{2-} after the addition of HCl (2 M)

pH Effect Study

The pH effect in DMF:HEPES buffer (9:1, v/v, 10 mM HEPES, pH = 3, 5, 7, 4, 9, and 11) was carried out to determine the feasibility of working sensor at different pH. The UV-Vis spectra before the addition of S^{2-} showed two absorptions at 393 and 464 nm for pH of 7.4, 9, and 11. While at pH 3 and 5 produced absorptions at 336 and 337 nm, respectively (Fig. 7(a)). After the addition of S^{2-} at a pH of 7.4 produced the highest maximum absorbance at 613 nm, while at pH 9 and 11, there was no color change and wavelength shifts (Fig. 7(b)).

This shows that NA works effectively to detect S^{2-} at a solvent pH 3–8 because the main sulfide species at an acidic pH is H_2S , and pH > 7 is dominant in the form of

HS^- from the equilibrium of the S^{2-} species from the salt solution which allows to bind to the NA binding site [23]. At pH 9–11, H_2S is in the form of HS^- . The presence of excess HS^- causes higher basicity so that the sulfide interaction with the NA binding site does not occur, similar to the interferent of CN^- and HCO_3^- .

Job's Plot Study and NMR Titration

This experiment was conducted to determine the stoichiometric ratio of interactions between NA (host) and S^{2-} using the Continuous Variant methods (Job's Plot) [24]. The results from Job's Plot curve showed the ratio of 1:1 (Fig. 8). The NA- S^{2-} interaction was also studied by 1H -NMR titration in DMSO- d_6 (Fig. 9). The results showed that the addition of S^{2-} (1 eq.) in D_2O

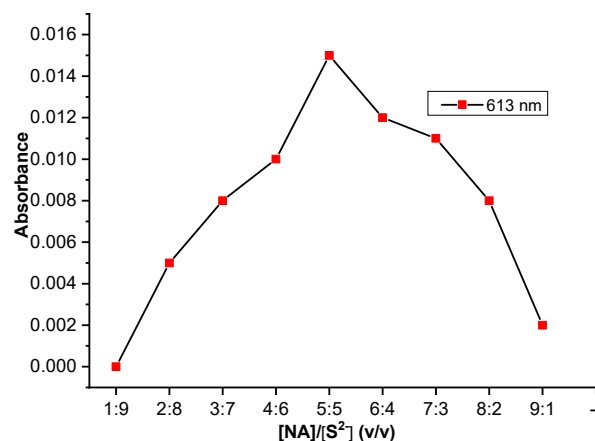


Fig 8. Job's Plot curve of NA titration toward the addition of S^{2-}

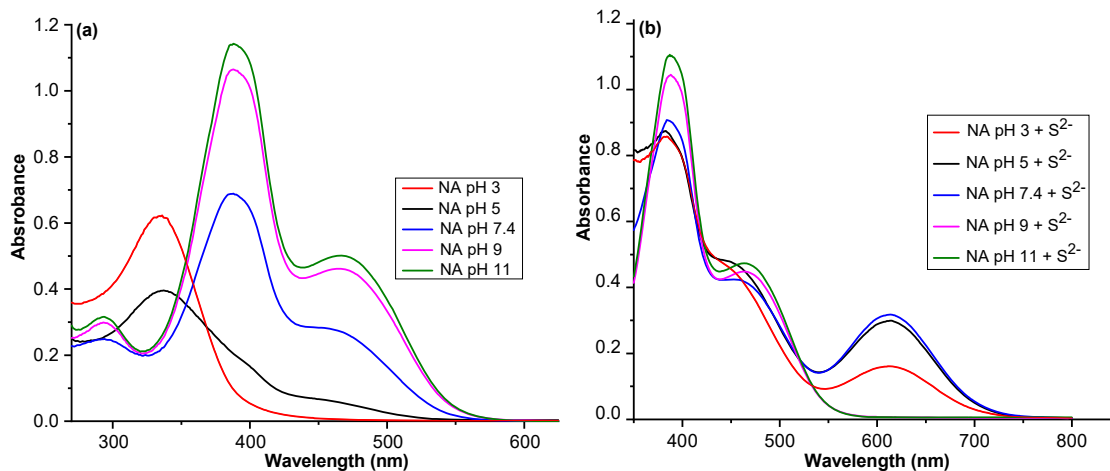


Fig 7. (a) Absorbance spectra of NA (2×10^{-5} M) at different pH and (b) Absorbance spectra of NA (2×10^{-5} M) after the addition of S^{2-} to different pH

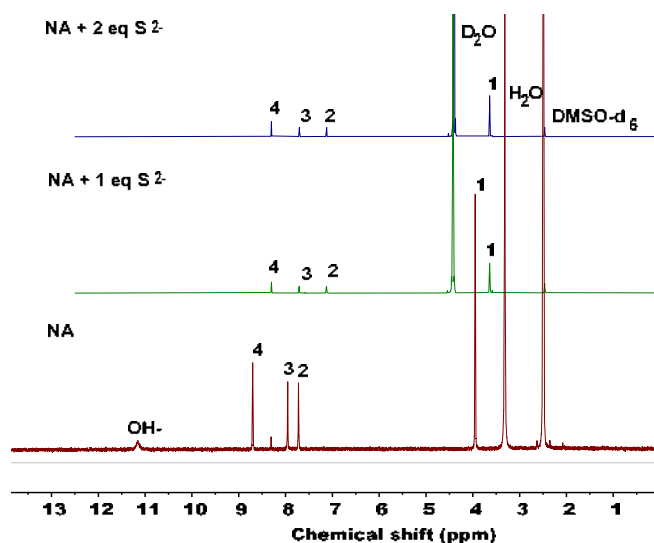
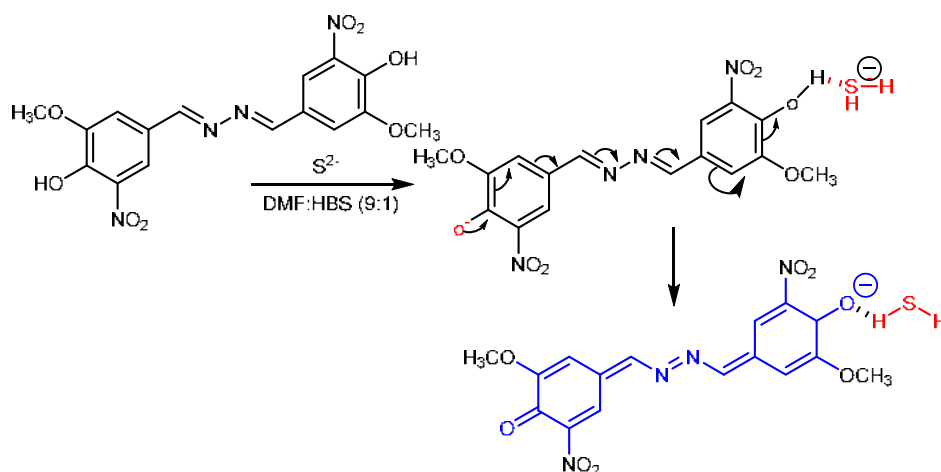


Fig 9. $^1\text{H-NMR}$ spectra titration of NA with S^{2-}

causes the $-\text{OH}$ signal at δ 11.16 ppm to disappear completely, followed by the proton of imine and aromatic ring shifting simultaneously to the up-field area. The addition of S^{2-} (2 eq.) has shifted more up-field than the addition of 1 eq. This shift is caused by $-\text{OH}$ deprotonation produced by a resonance phenomenon.



Scheme 2. The interaction model of NA- S^{2-}

Table 1. Determination of sulfides in tap water samples

Sample	Na_2S added (mM)	Na_2S found (mM)	RSD (%)	Recovery (%)
Tap water	1	1.085 ± 0.02	1.8	108.5
	3	2.958 ± 0.21	3.0	98.6
	5	4.587 ± 0.09	4.6	91.5

The electron density of the aromatic ring increases due to the disconnection of charges in the conjugation system. From the stoichiometric ratio stating one molecule of the binding site ($-\text{OH}$) interacting with one molecule of S^{2-} can be made an interaction model of NA- S^{2-} (Scheme 2).

Application of NA Chemosensor in Tap Water Samples Analysis

Determination of % recovery was carried out for quantitative analysis of sulfide in tap water samples. Tap water was added S^{2-} (1, 3, and 5 mM), and then NA was used as the reagent for quantitative analysis using UV-Vis. Using calibration curves ($y = 0.1148x - 0.1216$), the % recovery values are 108.5, 98.6 and 91.5%, respectively (Table 1). These results indicate that NA can be used to detect S^{2-} with a concentration range of 1–5 mM. From the obtained analysis data of a range % recovery (80–108%) and % RSD (6%) [25], it can be said that NA can be used for quantitative analysis by UV-Vis spectrophotometer. The results of % recovery and % RSD values are shown in (Table 1).



Fig 10. Change in the color of paper strip soaked in NA (1×10^{-3} M) after the addition of S^{2-} (0.2 M)

Qualitative Analysis Using Filter Paper Strips

To examine the rapid response of NA to S^{2-} , a qualitative analysis was performed using filter paper. Whatman filter paper No. 42 immersed in NA solution (1×10^{-3} M), was added two drops of S^{2-} and dried (Fig. 10). The color of paper strip changes from light pink to yellow. Furthermore, the paper strip was monitored under a 366 nm UV lamp and indicated no luminescence both before and after the addition of S^{2-} . The results indicated that NA could be used to detect sulfides in colorimetric analysis.

CONCLUSION

We have successfully synthesized a nitrovanillin azine (NA) through the condensation reactions of 5-nitrovanillin (5-NV) with hydrazine hydrate. Properties of NA chemosensor gave high selectivity toward S^{2-} in DMF:HBS (9:1, v/v, 10 mM, pH = 7.4) with color change from light yellow to dark green. The colorimetric LOD of NA was $14.3 \mu\text{M}$, and the interaction model between host-guests (NA- S^{2-}) is in a 1:1 ratio. A filter paper strip for qualitative and quantitative analysis of S^{2-} in tap water samples indicated that NA has potential as a sulfide anion colorimetric chemosensor.

ACKNOWLEDGMENTS

The author thanked to Faculty of Mathematics and Natural Sciences, Universitas Gadjah Mada, for the funding to this research with contract number of 165/J01.1.28/PL.06.02/2021.

REFERENCES

- [1] Hammers, M.D., Taormina, M.J., Cerda, M.M., Montoya, L.A., Seidenkranz, D.T., Parthasarathy, R., and Pluth, M.D., 2015, A bright fluorescent probe for H_2S enables analyte-responsive, 3d imaging in live zebrafish using light sheet fluorescence microscopy, *J. Am. Chem. Soc.*, 137 (32), 10216–10223.
- [2] Han, Y., Qin, J., Chang, X., Yang, J., and Du, J., 2006, Hydrogen sulfide and carbon monoxide are in synergy with each other in the pathogenesis of recurrent febrile seizures, *Cell. Mol. Neurobiol.*, 26 (1), 101–107.
- [3] Lou, Z., Li, P., and Han, K., 2015, “Selenium as a Versatile Center in Fluorescence Probe for the Redox Cycle Between HClO Oxidative Stress and H_2S Repair” in *Advanced Protocols in Oxidative Stress III*, Eds. Armstrong, D., Springer New York, 97–110.
- [4] Chan, Y.H., Lock, S.S.M., Wong, M.K., Yiin, C.L., Loy, A.C.M., Cheah, K.W., Chai, S.Y.W., Li, C., How, B.S., Chin, B.L.F., Chan, Z.P., and Lam, S.S., 2022, A state-of-the-art review on capture and separation of hazardous hydrogen sulfide (H_2S): Recent advances, challenges and outlook, *Environ. Pollut.*, 314, 120219.
- [5] Dufton, N., Natividad, J., Verdu, E.F., and Wallace, J.L., 2012, Hydrogen sulfide and resolution of acute inflammation: A comparative study utilizing a novel fluorescent probe, *Sci. Rep.*, 2 (1), 499.
- [6] Pol, R., Céspedes, F., Gabriel, D., and Baeza, M., 2019, Fully integrated screen-printed sulfide-selective sensor on a 3D-printed potentiometric microfluidic platform, *Sens. Actuators, B*, 290, 364–370.
- [7] Shu, J., Qiu, Z., and Tang, D., 2018, Self-referenced smartphone imaging for visual screening of H_2S using Cu_xO -polypyrrole conductive aerogel doped with graphene oxide framework, *Anal. Chem.*, 90 (16), 9691–9694.
- [8] Satheskumar, A., El-Mossalamy, E.H., Manivannan, R., Parthiban, C., Al-Harbi, L.M., Kosa, S., and Elango, K.P., 2014, Anion induced azo-hydrazone tautomerism for the selective colorimetric sensing of fluoride ion, *Spectrochim. Acta, Part A*, 128, 798–805.

- [9] Wang, Q., Wang, Y., Guan, M., Zhu, S., Yan, X., Lei, Y., Shen, X., Luo, L., and He, H., 2020, A multicolor colorimetric assay for sensitive detection of sulfide ions based on anti-etching of triangular gold nanoplates, *Microchem. J.*, 159, 105429.
- [10] Mergu, N., Singh, A.K., and Gupta, V.K., 2015, Highly sensitive and selective colorimetric and off-on fluorescent reversible chemosensors for Al^{3+} based on the rhodamine fluorophore, *Sensors*, 15 (4), 9097–9111.
- [11] Rajamanikandan, R., and Ilanchelian, M., 2022, Simple smartphone merged rapid colorimetric platform for the environmental monitoring of toxic sulfide ions by cysteine functionalized silver nanoparticles, *Microchem. J.*, 174, 107071.
- [12] Tiwari, K., Kumar, S., Kumar, V., Kaur, J., Arora, S., and Mahajan, R.K., 2018, An azine based sensor for selective detection of Cu^{2+} ions and its copper complex for sensing of phosphate ions in physiological conditions and in living cells, *Spectrochim. Acta, Part A*, 191, 16–26.
- [13] Pei, P.X., Hu, J.H., Chen, Y., Sun, Y., and Qi, J., 2017, A novel dual-channel chemosensor for CN^- using asymmetric double-azine derivatives in aqueous media and its application in bitter almond, *Spectrochim. Acta, Part A*, 181, 131–136.
- [14] Irmı, M.N., Purwono, B., and Anwar, C., 2021, Synthesis of symmetrical acetophenone azine derivatives as colorimetric and fluorescent cyanide chemosensors, *Indones. J. Chem.*, 21 (6), 1337–1347.
- [15] Kaushik, R., Ghosh, A., Singh, A., and Jose, D.A., 2018, Colorimetric sensor for the detection of H_2S and its application in molecular half-subtractor, *Anal. Chim. Acta*, 1040, 178–186.
- [16] Rokhmah, N.V., Mardjan, M.I.D., and Purwono, B., 2022, Synthesis vanillin-azine as colorimetric chemosensor of sulfide anion, *Indones. J. Chem.*, 22 (6), 1490–1500.
- [17] Li, J.Z., Leng, T.H., Wang, Z.Q., Zhou, L., Gong, X.Q., Shen, Y.J., and Wang, C.Y., 2019, A large Stokes shift, sequential, colorimetric fluorescent probe for sensing $\text{Cu}^{2+}/\text{S}^{2-}$ and its applications, *J. Photochem. Photobiol., A*, 373, 146–153.
- [18] Rahmawati, R., Purwono, B., and Matsjeh, S., 2018, A naked-eye colorimetric receptor for anions based on nitro group featuring with benzimidazole unit, *Asian J. Chem.*, 30 (9), 1933–1936.
- [19] Li, Q., Cai, Y., Yao, H., Lin, Q., Zhu, Y.R., Li, H., Zhang, Y.M., and Wei, T.B., 2015, A colorimetric and fluorescent cyanide chemosensor based on dicyanovinyl derivatives: Utilization of the mechanism of intramolecular charge transfer blocking, *Spectrochim. Acta, Part A*, 136, 1047–1051.
- [20] Ghosh, T., and Mishra, S., 2020, A natural cyanobacterial protein C-phycoerythrin as an HS^- selective optical probe in aqueous systems, *Spectrochim. Acta, Part A*, 239, 118469.
- [21] Tan, B., Jin, S., Sun, J., Gu, Z., Sun, X., Zhu, Y., Huo, K., Cao, Z., Yang, P., Xin, X., Liu, X., Pan, L., Qiu, F., Jiang, J., Jia, Y., Ye, F., Xie, Y., and Zhu, Y.Z., 2017, New method for quantification of gas transmitter hydrogen sulfide in biological matrices by LC-MS/MS, *Sci. Rep.*, 7, 46278.
- [22] Kamli, S., Orojloo, M., and Amani, S., 2021, Design and synthesis of a novel chemosensor for simultaneous detection of CN^- , HCO_3^- and AcO^- anions and Fe^{2+} cation in an organic-aqueous environment: An experimental and Density Functional Theory studies, *J. Mol. Struct.*, 1234, 130708.
- [23] Migdisov, A.A., Williams-Jones, A.E., Lakshatnov, L.Z., and Alekhin, Y.V., 2002, Estimates of the second dissociation constant of H_2S from the surface sulfidation of crystalline sulfur, *Geochim. Cosmochim. Acta*, 66 (10), 1713–1725.
- [24] Kang, J.H., Chae, J.B., and Kim, C., 2018, A multi-functional chemosensor for highly selective ratiometric fluorescent detection of silver(I) ion and dual turn-on fluorescent and colorimetric detection of sulfide, *R. Soc. Open Sci.*, 5 (6), 180293.
- [25] Official Methods of Analysis of AOAC International, 2019, *AOAC Guidelines for Single-Laboratory Validation of Chemical Methods for Dietary Supplements and Botanicals*, AOAC International, Gaithersburg, MD, USA, 1–15.

Identification of *Sida rhombifolia* from Its Related Plants Using Thin-Layer Chromatographic Analysis

Mohamad Rafi^{1,2*}, Sefni Reza Yolanda³, Dewi Anggraini Septaningsih^{2,4}, Maria Bintang³, Nanik Siti Aminah⁵, Muhamad Insanu⁶, and Abdul Rohman⁷

¹Department of Chemistry, Faculty of Mathematics and Natural Sciences, IPB University, Jl. Tanjung Kampus IPB Dramaga, Bogor 16680, Indonesia

²Tropical Biopharmaca Research Center - Institute of Research and Community Services, IPB University, Jl. Taman Kencana No. 3 Kampus IPB Taman Kencana, Bogor 16128, Indonesia

³Department of Biochemistry, Faculty of Mathematics and Natural Sciences, IPB University, Jl. Tanjung Kampus IPB Dramaga, Bogor 16680, Indonesia

⁴Advanced Research Laboratory - Institute of Research and Community Services, IPB University, Jl. Palem Raya Kampus IPB Dramaga, Bogor 16680, Indonesia

⁵Department of Chemistry, Faculty of Science and Technology, Universitas Airlangga, Jl. Mulyorejo Kampus C Unair, Surabaya 60286, Indonesia

⁶School of Pharmacy, Institut Teknologi Bandung, Jl. Ganesha No. 10, Bandung 40132, Indonesia

⁷Department of Pharmaceutical Chemistry, Faculty of Pharmacy, Universitas Gadjah Mada, Sekip Utara, Yogyakarta 55281, Indonesia

* **Corresponding author:**

email: mra@apps.ipb.ac.id

Received: February 16, 2022

Accepted: October 25, 2022

DOI: 10.22146/ijc.73077

Abstract: *Sida rhombifolia* belongs to the Malvaceae family and is often used to treat gout in Indonesia. *S. rhombifolia* has many efficacies and contains many different chemical components. The abundance and variation of chemical content and chemical compounds in this medicinal plant are challenging factors in ensuring medicinal plants' safety and quality control. Thin-layer chromatography (TLC) fingerprint analysis derived from *S. rhombifolia* extract can also be used for the medicinal plant's quality control. This research aimed to develop the optimum condition for the chemical fingerprint analysis of *S. rhombifolia* using a TLC fingerprint analysis. A total of 11 bands were produced with optimum separation using silica gel 60 F₂₅₄ TLC plate, a mixed mobile phase condition with chloroform, ethyl acetate, and methanol (6.5:2:1.5). This fingerprint analysis performed an excellent separation in the TLC plate at 366 nm with sulfuric acid as reagent derivatization. In general, the results of the analysis validation, including stability, specificity, precision, and robustness of TLC fingerprints, met the acceptance criteria. The TLC fingerprint of *S. rhombifolia* can be distinguished from 2 related plants with similar leaf shapes, *Turnera ulmifolia* L. and *Hibiscus rosa-sinensis*. The developed method was validated, so it could be used to control *S. rhombifolia* quality.

Keywords: fingerprint analysis; identification; *Sida rhombifolia*; thin-layer chromatography

■ INTRODUCTION

Sida rhombifolia, known as arrowleaf sida or *sidaduri* in Indonesia belongs to the Malvaceae family. *S.*

rhombifolia is one of the 200 species in *Sida* distributed throughout tropical and subtropical regions worldwide. *S. rhombifolia* is known for its wide range of medicinal uses, for instance, treating stings and bites of a scorpion,

snakes, and wasps (its flower), skin diseases and sores (stem), treating stomach disorders, stomach pain, digestion problems (roots and leaves), diabetes (leaves), chickenpox, blood cleaning, and fatigue [1]. *S. rhombifolia* is also widely used in Indonesia to treat gout [2]. Several natural flavonoid compounds in *S. rhombifolia* have been reported as xanthine oxidase inhibitors and promise greater use to reduce the excess uric acid production in the human body.

Many commercial herbal products in Indonesia or other countries use plant extracts in their compositions. However, there are some problems with variability and the bioactive compounds' concentration level from plant extracts in herbal medicines' production. Medicinal plant quality also depends on several factors, such as environmental growth, harvest, and postharvest, which cause its consistency in its biological activity [3]. Adulteration is another source of the medicinal plant's biological activity's inconsistency and becomes one of the most significant drawbacks in promoting herbal products. This can occur intentionally by substituting partially or entirely a herbal drug with other inferior products due to morphological resemblance to the authentic herb. An unintentional adulteration can be caused by herbal suppliers' carelessness, such as the inconsistency in the herb collection process and the confusion of common names for different plants [4]. The adulteration process in herbal medicine would lead to an increased risk for consumer health due to the differences in the chemical composition that could affect its biological and toxicity activity [5]. In contrast with the component-based method that needs to measure the marker compound's content, fingerprint analysis offers an alternative way to evaluate all the detectable compounds without the necessity to characterize all the compounds.

Identifying accurate marker compounds is very difficult for all traditionally used plant materials. The thin-layer chromatography (TLC) fingerprints can accurately certify and identify plant materials, even if the amount of active material is not the same for different samples. Therefore, it is essential to obtain a reliable TLC fingerprint representing the bioactive compounds and

chemically distinct components of plant materials [6]. The fingerprint analysis evaluation could compare the similarity or dissimilarity of the plant sample with a certain reference and present it as a fingerprint pattern. This could be used to identify the actual herbal plant and the false one. TLC fingerprint pattern analysis is an effective way to evaluate and control the quality of raw materials and their preparation process [7]. This method offers an advantage such as ease of sample preparation and could provide fundamental data on the herbal product's consistency, stability, and quality control [8]. The fingerprint analysis with TLC has been performed to identify and authenticate herbal plants such as *Wedelia chinensis*, *Psidium guajava*, *Curcuma mangga*, *Eugenia uniflora*, *Orthosiphon stamineus*, *Melastoma malabathricum* [9-14] and also differentiation of *C. longa*, *C. xanthorrhiza*, and *Zingiber cassumunar* [15].

Several papers have used TLC to analyze *S. rhombifolia* [1,16-18]. However, the profile information presented in the previously cited paper was not validated in terms of specificity according to the validation guidelines. Method validation needs to be done so that the developed method can evaluate the quality and stability of *S. rhombifolia*. Method validation which includes analyte stability, specificity, precision, and ruggedness, was also carried out to validate the developed Sidaguri TLC fingerprint method. The focus is on validating the qualitative TLC method, namely the R_f value, fingerprint profile, and band zone color. This paper describes our new cost-effective and simple TLC fingerprint analysis of *S. rhombifolia* to identify and authenticate its originality. Our result showed that the developed method could identify and discriminate *S. rhombifolia* from its related plants with the same leaf morphology, such as *Turnera ulmifolia* L. and *Hibiscus rosa-sinensis*.

■ EXPERIMENTAL SECTION

Materials

Materials used in this study involved *S. rhombifolia*, *T. ulmifolia*, and *H. rosa-sinensis* leaves obtained and identified by Mr. Taopik Ridwan from the medicinal plant garden Tropical Biopharmaca Research

Center LPPM IPB University. Sulfuric acid, methanol, ethanol, ethyl acetate, *n*-hexane, chloroform, dichloromethane, and 1-butanol were purchased from Merck (Darmstadt, Germany) and used without further purification.

Instrumentation

The instruments used in this study involved TLC semiautomatic CAMAG Linomat 5 (Muttentz, Switzerland), Densitometer CAMAG Reprostar 3 (Muttentz, Switzerland), CAMAG WinCATS software (Muttentz, Switzerland), ultrasonicator Branson 1510 (Dietzenbach, Germany), TLC plate silica gel F254 (Merck, Darmstadt, Germany), and analytical balance XT 220A (Precisa Gravimetrics, Switzerland).

Procedure

Sample preparation and extraction

All the sample leaves (100 g) were dried in the oven at 50 °C for 3 d, then pulverized into a powder, and then sieved with 100 mesh particle size. About 1 g of samples were macerated with 10 mL methanol using an ultrasonicator at 42 kHz for 30 min. After the extraction process was completed, the solution was filtered and diluted with methanol to obtain a 10% w/v concentration.

TLC separation condition

The extract of *S. rhombifolia* leaves was applied to the silica gel F₂₅₄ plate as a band 8 mm in length with TLC semiautomatic Camag Linomat 5 equipped with WinCATS software. The sample (20 µL) was applied at a speed of 70 nL/s, and the distance between the band was 4 mm. Then, the TLC plate was placed into a chromatography chamber with the mobile phase to obtain the separation process. After the separation was completed, the TLC plate's chromatogram was documented using a Densitometer Camag Reprostar 3.

The selection of the TLC mobile phase

About 10 mL of each solvent (methanol, ethanol, ethyl acetate, chloroform, dichloromethane, and *n*-hexane) was added into the chromatography chamber and saturated for 30 min. First, we eluted the *S. rhombifolia* extract with a single solvent for TLC separation. Then the selected solvent (2–3 solvents) was

mixed with another solvent to obtain the mobile phase mixture's best for the chromatography separation. After the separation process, the staining procedure at the TLC plate was performed using sulfuric acid to derivatize components in the extract of *S. rhombifolia* leaves. The sulfuric acid reagent was prepared by mixing 10 mL concentrated sulfuric acid with 90 mL cold methanol. Component detection was performed by exposing the TLC plate to 254 and 366 nm UV light. The TLC plate was then dried in the oven at 110 °C for 10 min to obtain a noticeable band color.

Validation method of TLC fingerprint

The validation method used to evaluate the TLC fingerprint of *S. rhombifolia* leaves extract involves several parameters: stability, specificity, precision, and robustness. The validation method has been developed following the previous procedure from Reich and Schibli [19]. The stability was evaluated by observing analyte separation during the separation process on the TLC plate and visualized by taking a photograph at 2nd, 5th, 10th, 30th, and 60th min. The specificity was checked by comparing the TLC fingerprint derived from the leaves extract of *T. ulmifolia* and *H. rosa-sinensis* with the TLC fingerprint extract of *S. rhombifolia* leaves. The robustness was investigated by observing the two distances of solvent development at the TLC plate (7 and 8 cm) in two chambers (twin-through and flat-bottom). The precision was evaluated by repeating a similar procedure three times a day and performing it on three different days.

Analyte stability during two-dimensional solvent development. About 4 µL of the leaves extract was applied as a spot with 0.6 mm width using an automatic TLC sampler at the bottom right corner of the 10 × 10 cm TLC plate. Then, the solvent was developed at the TLC plate using a twin-through chamber, and the TLC plate was dried afterward. Next, the TLC plate was rotated 90° clockwise, and the separation was repeated using a fresh solvent for the development process. The TLC plate obtained from the two-step solvent development process was then documented before and after the derivatization. The analyte stability at the TLC plate can be evaluated when all components in the

extract emerge in a diagonal line in two-dimensional solvent development.

Analyte stability in the sample solution. Evaluation of analyte stability in the sample solution was performed by applying 20 μL of the sample extract in 4 lines at the TLC plate. The first line consists of the fresh solution extract of *S. rhombifolia* leaves was applied to the TLC plate and left for 3 h. Then, the fresh extract of *S. rhombifolia* leaves was kept for 3 h and applied to the TLC plate as a third line. The second and fourth lines consist of the fresh extract of *S. rhombifolia* leaves and are applied to the TLC plate before the elution. After that, the TLC plate was placed into the twin-through chamber to separate the components. The documentation was performed before and after using sulfuric acid's sample derivatization process. If the difference of R_f value ≤ 0.05 between the spot at the TLC plate, it can be concluded that the extract of *S. rhombifolia* leaves was stable at both the stationary phase and the extract solution.

Analyte stability with visualization. The analyte's visualization stability was evaluated by applying 20 μL of *S. rhombifolia* leaves extract into the TLC plate and then placed into the twin-through chamber. After the solvent development, the TLC plate was then derivatized using sulfuric acid and visualized by visible and UV light at 366 nm. The observation was performed on the 2nd, 5th, 10th, 20th, 30th, 60th min.

Specificity test. Specificity was evaluated by applying 20 μL of the extract of *S. rhombifolia*, *T. ulmifolia*, and *H. rosa-sinensis* into the TLC plate as lines 1, 2, and 3 consecutively. Then, the TLC plate was eluted with a solvent using a twin-through chamber. After the solvent development process, the TLC plate was then documented before and after the sulfuric acid's derivatization process.

Precision evaluation. The sample of *S. rhombifolia* leaves was extracted by sonication process in triplicate, with each 20 μL extract applied to the TLC plate. The assessment was performed using three TLC plates in a twin-through chamber on a similar day. The acceptance criteria for TLC fingerprint derived from *S. rhombifolia* extract were given identical parameters in terms of number, position, color, intensity, and R_f value ≤ 0.02 .

Intermediate precision has also been evaluated using three different TLC plates on three days (one TLC plate per day).

Robustness of chamber type. For the robustness evaluation of chamber type, 20 μL of the leaves extracts of *S. rhombifolia*, *T. ulmifolia*, and *H. rosa-sinensis* were applied into a 5.5 \times 10 cm TLC plate with the extract concentration of 10% w/v. Each extract's solvent development was performed using two chambers: twin-through and flat-bottom. After the solvent development was completed, the TLC plate was documented before and after the sulfuric acid's derivatization. The acceptance criteria for the TLC fingerprint derived from each extract gave identical parameters in terms of number, position, color, intensity, and R_f value ≤ 0.05 .

Distance robustness of the solvent development. Evaluation of the robustness by measuring the distance in the solvent development was performed by 20 μL of *S. rhombifolia*, *T. ulmifolia*, and *H. rosa-sinensis* leaves extracts were applied to a 5.5 \times 10 cm TLC plate with the extract concentration of 10% w/v. Then, each extract's solvent development was performed using a twin-through chamber with two different solvent development distances of 7 and 8 cm. After the solvent development was completed, the TLC plate was documented before and after the sulfuric acid's derivatization process. The acceptance criteria for the TLC fingerprint derived from each extract gave identical parameters in terms of number, position, color, intensity, and R_f value ≤ 0.05 .

■ RESULTS AND DISCUSSION

TLC Fingerprint Mobile Phase

TLC fingerprint analysis is an analytical technique used to identify a medicinal plant. TLC will generally consist of a stationary and mobile phase, a medium for separating chemical components in a sample. In this study, silica gel 60 F₂₅₄ was used as the stationary phase and optimizing the mobile phase composition to obtain maximum separation of components. Generally, optimizing the mobile phase in TLC is mostly by trial and error. We used eight solvents with different polarity levels ranging from nonpolar, semipolar, and polar to

get an optimum mobile phase that could be mixed to maximize separation. Besides the mobile phase, the number of bands produced is also influenced by the detection type. This study used sulfuric acid as a derivatized reagent because it could react with almost all chemical components. After derivatization with sulfuric acid, a separate band of the components can be seen under 366 nm UV light with more apparent in the band's color.

The mobile phase optimization is an important parameter for obtaining the optimum separation pattern of the TLC fingerprint obtained from the extract of *S. rhombifolia* leaves. In the first step, eight single mobile phases were used, and chloroform (CHCl₃), ethyl acetate (EtOAc), and methanol (MeOH) were the best mobile phase. These single mobile phases exhibited the most significant number of bands and the best separation of zones on the TLC plate (Fig. 1). About 6, 5, and 4 bands were produced by CHCl₃, EA, and MeOH, respectively. The detection of bands on the TLC plate was performed using UV light at 366 nm. These solvents were mixed in different ratio compositions. Eight types of combinations in the different ratios were deduced, and CHCl₃:EtOAc:MeOH in both compositions of (6.5:2:1.5) and (7:1.5:1.5) showed a suitable solvent system producing 11 bands on the TLC plate (Fig. 2). However, after a further investigation of both ratios of the solvent system, it was obtained that the (6.5:2:1.5) composition

gave a better resolution factor rather than the (7:1.5:1.5) composition (Table 1). Therefore, CHCl₃:EtOAc:MeOH in the ratio of (6.5:2:1.5) was then selected as a solvent system for developing the TLC fingerprint from the extract of *S. rhombifolia* leaves. This solvent ratio composition exhibited 11 bands after derivatized with sulfuric acid reagent under 366 nm UV light.

We found a mixture of chloroform, ethyl acetate, and methanol solvents with a ratio (of 6.5:2:1.5) as the optimum mobile phase for separating *S. rhombifolia* components. Using this mobile phase, about 11 bands

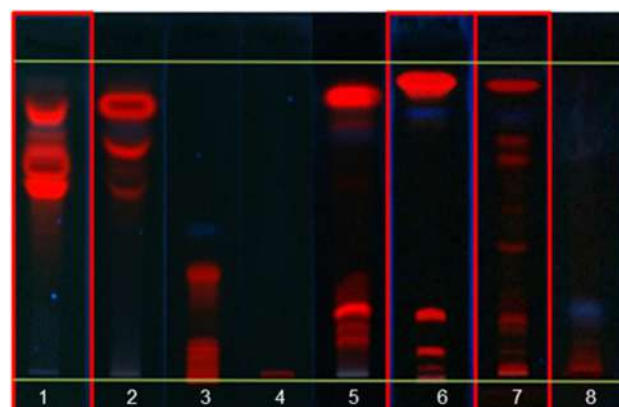


Fig 1. TLC chromatogram of *Sida rhombifolia* extract using single mobile phase: (1) methanol, (2) ethanol, (3) dichloromethane, (4) *n*-hexane, (5) *n*-butanol, (6) ethyl acetate, (7) chloroform, (8) water. The documentation was taken using UV light at 366 nm

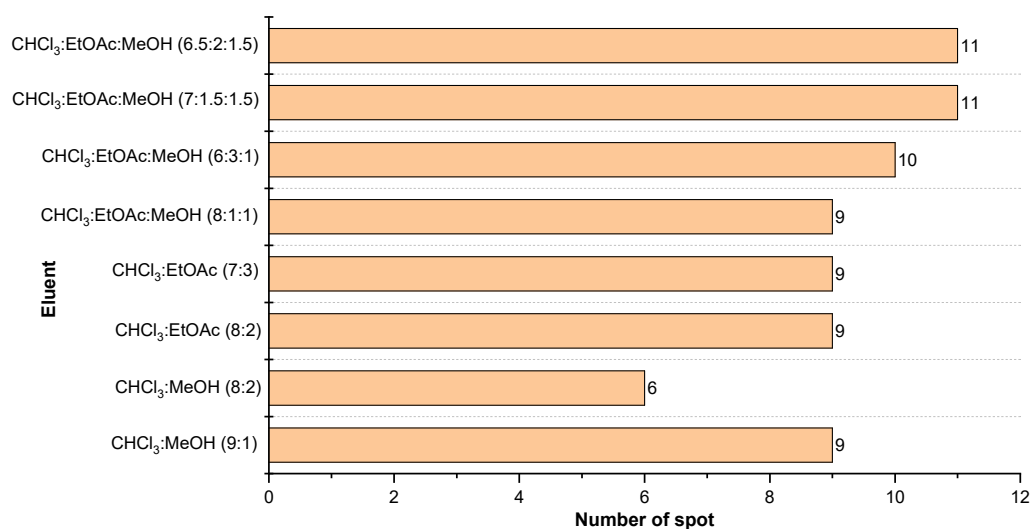


Fig 2. The number of bands obtained from the TLC fingerprint of *Sida rhombifolia* leaves extract with the solvent mixture and its visualization using UV 366 nm

Table 1. The resolution obtained from *S. rhombifolia* leaves extract using a mobile phase mixture of chloroform:ethyl acetate:methanol in two different compositions ratio (7:1.5:1.5) and (6.5:2.1:1.5) using UV 366 nm as detection wavelength

Chloroform:ethyl acetate:methanol (7 :1.5:1.5)					Chloroform:ethyl acetate:methanol (6.5:2:1.5)				
Band	Band distance (cm)	Band width (cm)	R _f	R _s	Band	Band distance (cm)	Band width (cm)	R _f	R _s
1	7.68	0.3	0.96		1	7.68	0.3	0.96	
				2.8					2.8
2	7.12	0.1	0.89		2	7.12	0.1	0.89	
				17.6					18.4
3	5.36	0.1	0.67		3	5.28	0.1	0.66	
				5.6					4.0
4	4.80	0.1	0.60		4	4.88	0.1	0.61	
				2.4					3.2
5	4.56	0.1	0.57		5	4.56	0.1	0.57	
				2.4					2.4
6	4.32	0.1	0.54		6	4.32	0.1	0.54	
				3.2					2.6
7	4.00	0.1	0.50		7	4.00	0.1	0.50	
				1.1					1.6
8	3.84	0.2	0.48		8	3.92	0.2	0.49	
				4.8					4.2
9	2.64	0.3	0.33		9	2.72	0.3	0.34	
				5.6					5.6
10	1.52	0.1	0.19		10	1.60	0.1	0.20	
				10.4					11.2
11	0.48	0.1	0.06		11	0.48	0.1	0.06	

appeared with a good resolution. The optimum mobile phase obtained is between semipolar and polar solvents. The semipolar solvent (chloroform) used has a large ratio to polar solvents, namely ethyl acetate and methanol. This aims to reduce the solvent's polarity and balance the resulting band position. The more polar a solvent or solvent mixture is, the farther the solvent moves the polar compound up from the starting point of the dotting while the nonpolar compound is held down.

Most components were separated between semipolar and nonpolar solvents (chloroform-ethyl acetate-methanol). The developed method of TLC fingerprint analysis of *S. rhombifolia* L. leaves is for a qualitative purpose only, and we could not precisely know the name of the separated components. However, from a previous study using chloroform and methanol as eluent,

it is known that *S. rhombifolia* leaves have an alkaloid compound at an R_f value of 0.92 with a brownish-yellow color [20]. Flavonoid compounds usually appear as fluorescent zone under UV 366 nm. So maybe the TLC fingerprint chromatogram of *S. rhombifolia* contains some alkaloid or flavonoid compound because the R_f value is near the previous study.

Validation of the Developed TLC Fingerprint Method

According to Reich and Schibli [19], we must do a validation method as formal evidence that a method is suitable for analysis. The TLC fingerprint's developed method was validated by determining the analyte stability on the TLC plate in the extract solution and during the chromatography process, the analyte stability of derivatized zones, specificity, repeatability,

intermediate precision, and robustness. The focus on validating the developed HPTLC qualitative method for identifying *S. rhombifolia* leaves was fingerprint profiles, such as R_f value and bands color. The results obtained from the validation step are evaluated according to the criteria described by Reich and Schibli [19].

Stability

Due to the TLC system's nature, studying the analytes' stability before and during the chromatography process is crucial. Before the chromatography process, the analyte stability was determined by developing the extract of *S. rhombifolia* leaves prepared at different times. The expected results should not differ in position and band color. Fig. 3 shows *S. rhombifolia* extract's stability in the solution and on the TLC plate visualized with 366 nm UV light. The R_f values of the 3 bands were observed to see the stability of the TLC results represented by the upper (X) R_f 0.71, middle (Y) R_f 0.55, and lower (Z) R_f 0.21 in the leaf extract of *S. rhombifolia*. There is no distinct difference in position and color bands between the four lanes on the TLC plate. Therefore, it can be concluded that the sample of *S. rhombifolia* extract is considered stable for at least 3 h in solution and the TLC plate.

During the chromatography process, the sample stability of *S. rhombifolia* extract was also investigated by 2-D solvent development on the TLC plate. Two-dimensional (2D) solvent development was carried out to determine the analyte's stability during the chromatography process. If the sample is stable during chromatography separation, all components should be detected on the diagonal line indicating spot movement in two-dimensional solvent development on the TLC plate. Fig. 4 shows no difference in two-dimensional solvent development on TLC fingerprint from the extract of *S. rhombifolia* leaves visualized with 366 nm UV light. This result indicated that the analytes remained stable for 3 h before the chromatography separation began, both on the TLC plate and the extract solution. In terms of sample derivatization, the chromatographic results' stability was determined by observing the zones' color for 60 min. Fig. 5 shows that the number and color of the zones were stable for 60 min. Therefore, it can be concluded that the

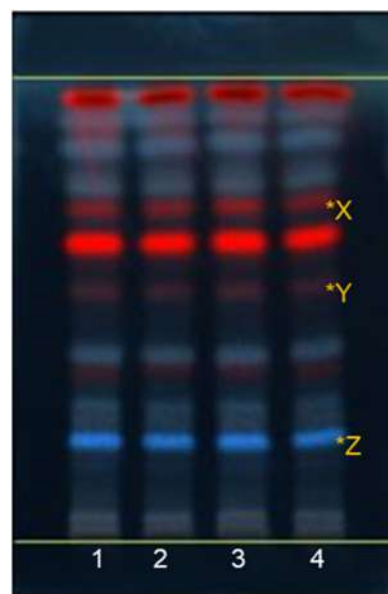


Fig 3. The TLC chromatogram of *S. rhombifolia* leaves extract for evaluation of analyte stability for 3 h and visualized with UV light 366 nm. (1) the extract of *Sida rhombifolia* leaves was left for 3 h, (2 and 4) the fresh extract of *S. rhombifolia* leaves was applied immediately to the TLC plate before the separation process, (3) the fresh extract of *S. rhombifolia* leaves was kept for 3 h and then applied to the TLC plate

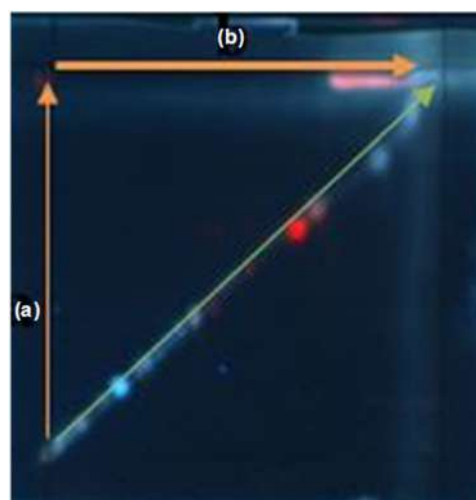


Fig 4. The TLC chromatogram derived from the extract of *S. rhombifolia* leaves extract with two-dimensional solvent development processes. (a) First solvent development process and (b) second development process and documented using UV light at 366 nm with the sulfuric acid reagent



Fig 5. The TLC chromatogram of *S. rhombifolia* leaves extract after (1) 2nd, (2) 5th, (3) 10th, (4) 20th, (5) 30th, (6) 60th min using UV light 366 nm with the sulfuric acid derivatization reagent

chromatogram was stable for at least 1 h after sample derivatization.

Specificity

The specificity of the TLC fingerprint analysis was evaluated by comparing the separation profile of *S. rhombifolia* and its related plants, like *T. ulmifolia* and *H. rosa-sinensis*, due to their leaves' physical and morphological similarities. Herbal medicinal products are generally used raw materials in powdered. So, it will make difficult to distinguish between the three plants if they are present in powdered form. We choose *T. ulmifolia* and *H. rosa-sinensis* as potential adulteration of *S. rhombifolia*. The specificity was performed by applying each plant extract on the TLC plates in different lanes. We can compare TLC fingerprint similarity during the specificity tests according to the number of bands, color, intensity, and band position.

The chromatogram results identifying *S. rhombifolia* extracts compared with the extract from *T. ulmifolia* and *H. rosa-sinensis* showed different patterns detected with sulfuric acid derivatization under 366 nm (Fig. 6). Based on the specificity evaluation, *S. rhombifolia* leaves are considered specific because they have different patterns, positions, quantities, colors, and intensities of the resulting bands. The extract from *S. rhombifolia*, *T. ulmifolia*, and *H. rosa-sinensis* produced 11, 10, and 12

bands on the TLC plate, respectively. However, these extracts have band similarities in terms of R_f values at 0.95, 0.89, 0.81, and 0.69 (Table 2). The TLC fingerprint of *S. rhombifolia* extracts had a marker band (blue color) at 0.28, which can be used to distinguish and specify only

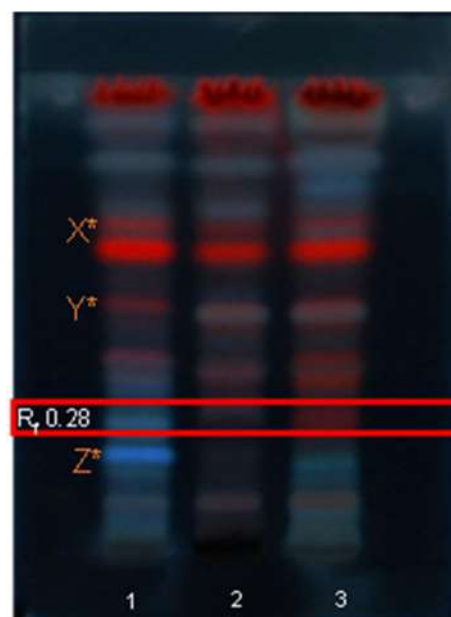


Fig 6. The TLC chromatogram obtained from the leaves extract of (1) *S. rhombifolia*, (2) *T. ulmifolia*, (3) *H. rosa-sinensis* using UV light at 366 nm with sulfuric acid as derivatization reagent

Table 2. Specific R_f value of *S. rhombifolia*, *T. ulmifolia*, *H. rosa-sinensis* extract using sulfuric acid as derivatization reagent followed by detection at UV light 366 nm

Band	R_f		
	<i>S. rhombifolia</i>	<i>T. ulmifolia</i>	<i>H. rosa-sinensis</i>
1	0.95	0.95	0.95
2	0.89	0.89	0.89
3	0.81	0.81	0.81
4	0.72	0.72	0.76
5	0.69	0.69	0.69
6	0.52	0.51	0.51
7	0.41	0.38	0.41
8	0.36	0.32	0.37
9	0.28	0.22	0.28
10	0.21	0.11	0.26
11	0.11		0.20
12			0.11

to this plant. Therefore, it can be concluded that the developed method can be used to differentiate *S. rhombifolia* from its related plant used in this study.

Precision and intermediate precision

Precision was performed on the same day using similar laboratory equipment, while intermediate precision was done in a similar laboratory using different equipment (tools and reagents) [21]. The precision was evaluated using plant extracts with three different TLC plates on a similar day, while intermediate precision was performed consecutively on three different days. Each extract was applied to the TLC plate, and its TLC chromatogram pattern was observed after separating the components. TLC fingerprint pattern criteria for the precision test were the number of bands, the band's position, color intensity, and the difference of R_f value between 3 bands on the TLC plate maximum at 0.02 ($\Delta R_f \leq 0.02$). For intermediate precision, the difference in R_f value from 3 bands at the TLC plate should be no more than 0.05 ($\Delta R_f \leq 0.05$) [19]. The intermediate precision requirement is higher than the precision parameter because we cannot maintain the laboratory's stable environment during the experiment.

Fig. 7 shows the pattern of the TLC fingerprint from *S. rhombifolia* extracts for precision evaluation, while Fig. 8 shows the TLC pattern for intermediate precision. Based on this observation, it can be seen from Fig. 7 that $\Delta R_f \leq 0.02$ was obtained from 3 bands at the TLC plate for precision evaluation, while the TLC fingerprint (Fig. 8) has $\Delta R_f \leq 0.05$ at the TLC plate for intermediate precision evaluation. R_f value's difference due to high humidity and

temperature causes poor separation and produces a low-resolution value. The resolution factor's low value is affected by the mobile phase's saturation and causes poor separation on the TLC plate. Therefore, it can be concluded that the criteria for precision and intermediate precision can be accepted based on the chromatogram pattern in Fig. 7 and 8.

Robustness

Robustness was evaluated by the chromatography chamber type and the solvent development distance on the TLC plate during the separation of components. The accepted criteria of robustness parameter include the constant TLC fingerprint profile in terms of number, position, bands' color, and R_f value difference of no more than 0.05 [19]. This evaluation was performed by developing the extract of *S. rhombifolia*, *T. ulmifolia*, and

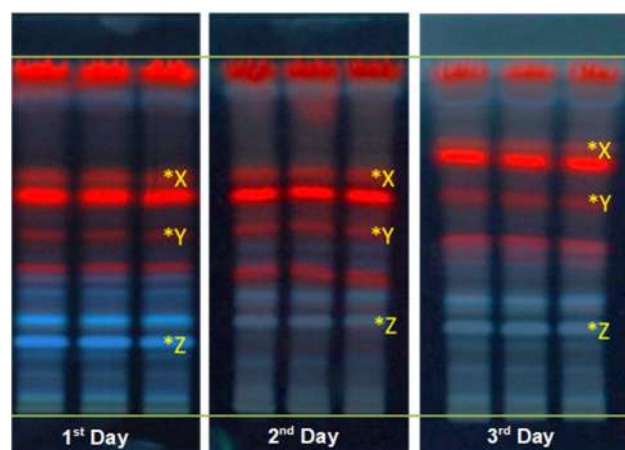


Fig 8. The three different TLC chromatograms obtained from the extract of *S. rhombifolia* leaves on (1) the first day, (2) the second day, and (3) the third day

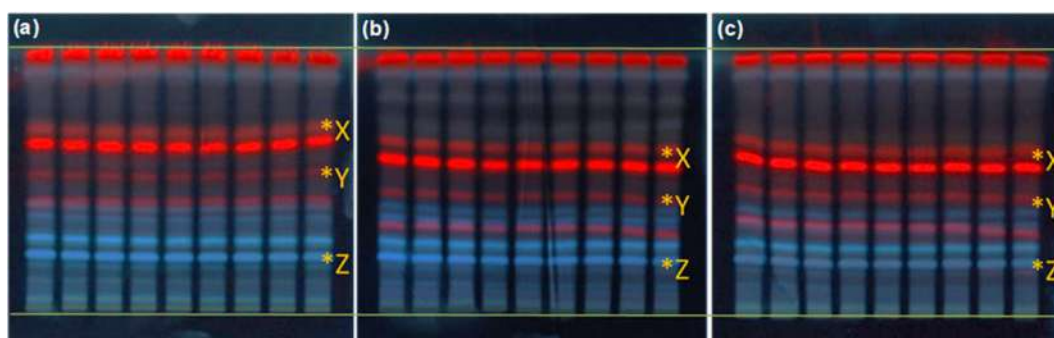


Fig 7. The three different TLC chromatograms obtained from the extract of *S. rhombifolia* leaves (a) first plate, (b) second plate, and (c) third plate

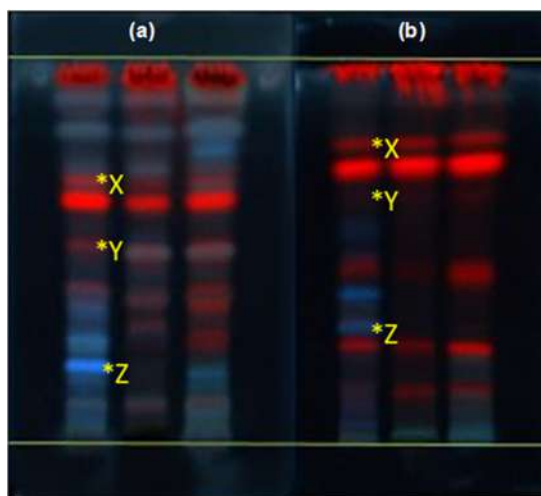


Fig 9. The TLC chromatogram of two different TLC plates using the extract of *S. rhombifolia* (line 1), *T. ulmifolia* (line 2), *H. rosa-sinensis* (line 3) from 2 different types of chamber chromatography (a) twin-through and (b) flat-bottom

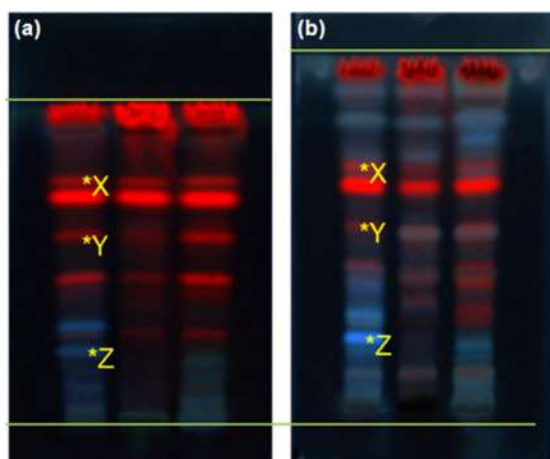


Fig 10. The TLC chromatogram of two different TLC plates from two different distances of solvent development at the twin-through chamber (a) 7 cm and (b) 8 cm

H. rosa-sinensis using the twin-through and flat-bottom with a different surface area and two different solvent development distances of 7 and 8 cm. Fig. 9 shows the chromatogram results from two chromatography chamber types that produce distinct differences between two TLC plates. The difference in R_f value was obtained more than 0.05 from 3 bands represented by top (X), middle (Y), and bottom (Z) in the extract of *S. rhombifolia*

leaves. The chromatography chamber's flat bottom gave a higher R_f value (ΔR_f) difference than the twin-through chamber. Based on this result, the robustness parameter still does not meet its acceptance level regarding the chromatography chamber type. Fig. 10 shows the chromatogram with two distances of solvent development with different TLC fingerprint patterns obtained from the extract of *S. rhombifolia* leaves. The difference in R_f values from the X, Y, and Z bands was obtained at more than 0.05 and still did not meet the quality control standard.

Fig. 9 and 10 show a distinct difference in the number of bands, position, and R_f value. This is due to relative humidity and mobile phase saturation changes and causes an increase in R_f value. The mobile phase's development process using a flat-bottom and twin-through chamber needs different times regarding its surface area. Therefore, this method is specific only for the twin-through chamber with an 8 cm distance of solvent development. This method could not maintain the fingerprint profile's stability when it changes to different solvent development and chamber type.

■ CONCLUSION

In conclusion, the TLC fingerprint analysis of *S. rhombifolia* fingerprints showed that all chromatographic conditions were applied, the most suitable of which was an aluminum plate coated with silica gel 60 F₂₅₄ as the stationary phase and a mixture of chloroform, ethyl acetate, and methanol (6.5:2:1.5) (v/v) as the mobile phase with sulfuric acid derivatization under UV visualization at 366 nm. The leaf fingerprint profile of *S. rhombifolia* produced 11 bands with good resolution. This fact confirms that the specificity of the proposed method is reliable with specificity, accuracy, precision, and robustness. This fingerprint analysis method has met the acceptance criteria for method validation and can be used to identify and control the quality of *S. rhombifolia* leaves.

■ ACKNOWLEDGMENTS

The authors gratefully acknowledged the Ministry of Research, Technology, and Higher Education of the

Republic of Indonesia through the World Class University Program of IPB University for financial support of this research by *Riset Kolaborasi Indonesia* Grant 2020 (No: 1757/IT3.L1/PN/2020/IT3.L1/PN/2020).

■ REFERENCES

- [1] Woldeyes, S., Adane, L., Tariku, Y., Muleta, D., and Begashaw, T., 2012, Evaluation of antibacterial activities of compounds isolated from *Sida rhombifolia* Linn. (Malvaceae), *Nat. Prod. Chem. Res.*, 1 (1), 1000101.
- [2] Iswantini, D., Yulian, M., Mulijani, S., and Trivadila, T., 2014, Inhibition kinetics of *Sida rhombifolia* L. extract toward xanthine oxidase by electrochemical method, *Indones. J. Chem.*, 14 (1), 71–77.
- [3] Ncube, B., Finnie, J.F., and Van Staden, J., 2012, Quality from the field: The impact of environmental factors as quality determinants in medicinal plants, *S. Afr. J. Bot.*, 82, 11–20.
- [4] Hernadi, E., Rohaeti, E., Rafi, M., Wahyuni, W.T., Putri, S.P., and Fukusaki, E., 2019, HPLC fingerprinting coupled with linear discriminant analysis for the detection of adulteration in *Orthosiphon aristatus*, *J. Liq. Chromatogr. Relat. Technol.*, 42 (15-16), 513–520.
- [5] Galvin-King, P., Haughey, S.A., and Elliott, C.T., 2018, Herb and spice fraud: The drivers, challenges, and detection, *Food Control*, 88, 85–97.
- [6] Zahiruddin, S., Parveen, A., Khan, W., Parveen, R., and Ahmad, S., 2021, TLC-based metabolite profiling and bioactivity-based scientific validation for use of water extracts in AYUSH formulations, *Evidence-Based Complementary Altern. Med.*, 2021, 2847440.
- [7] Parys, W., Dołowy, M., and Pyka-Pająk, A., 2022, Significance of chromatographic techniques in pharmaceutical analysis, *Processes*, 10 (1), 172.
- [8] Rafi, M., and Septaningsih, D.A., 2017, “Kendali Mutu Tumbuhan Obat Menggunakan Kromatografi Lapis Tipis” in *Atlas Kromatografi Lapis Tipis Tumbuhan Obat Indonesia*, Eds. Rafi, M., Heryanto, R., and Septaningsih, D.A., Volume 1, IPB Press, Bogor, Indonesia, 21–36.
- [9] Banu, R.H., and Nagarajan, N., 2014, TLC and HPTLC fingerprinting of leaf extracts of *Wedelia chinensis* (Osbeck) Merrill, *J. Pharmacogn. Phytochem.*, 2 (6), 29–33.
- [10] Astuti, M., Darusman, L.K., and Rafi, M., 2017, High performance thin layer chromatography fingerprint analysis of guava (*Psidium guajava*) leaves, *J. Phys.: Conf. Ser.*, 835, 012018.
- [11] Syafi’i, M., Rohaeti, E., Wahyuni, W.T., Rafi, M., and Septaningsih, D.A., 2018, Analisis sidik jari kromatografi lapis tipis rimpang temu mangga (*Curcuma mangga*), *Jurnal Jamu Indonesia*, 3 (3), 109–115.
- [12] Bezerra, I.C.F., Ramos, R.T.M., Ferreira, M.R.A., and Soares, L.A.L., 2018, Chromatographic profiles of extractives from leaves of *Eugenia uniflora*, *Rev. Bras. Farmacogn.*, 28 (1), 92–101.
- [13] Kartini, K., Dewi, E.R., Achmad, F., Jayani, N.I.E., Hadiyat, M.A., and Avanti, C., 2020, Thin layer chromatography fingerprinting and clustering of *Orthosiphon stamineus* Benth. from different origins, *Pharmacogn. J.*, 12 (1), 79–87.
- [14] Mayasari, D., Murti, Y.B., Pratiwi, S.U.T., Sudarsono, S., Hanna, G., and Hamann, M.T., 2022, TLC-based fingerprinting analysis of the geographical variation of *Melastoma malabathricum* in inland and archipelago regions: A rapid and easy-to-use tool for field metabolomics studies, *J. Nat. Prod.*, 85 (1), 292–300.
- [15] Rafi, M., Rohaeti, E., Miftahudin, A., and Darusman, L.K., 2011, Differentiation of *Curcuma longa*, *Curcuma xanthorrhiza* and *Zingiber cassumunar* by thin layer chromatography fingerprint analysis, *Indones. J. Chem.*, 11 (1), 71–74.
- [16] Chaves, O.S., Teles, Y.C., de Oliveira Monteiro, M.M., Mendes Junior, L.G., Agra, M.F., Braga, V.A., Silva, T.M.S., and de Souza, M.F.V., 2017, Alkaloids and phenolic compounds from *Sida rhombifolia* L. (Malvaceae) and vasorelaxant activity of two indoquinoline alkaloids, *Molecules*, 22 (1), 94.
- [17] Avula, B., Joshi, V., Wang, Y.H., Jadhav, A.N., and Khan, I.A., 2008, Quantitative determination of

- ecdysteroids in *Sida rhombifolia* L. and various other *Sida* species using LC-UV, and their anatomical characterization, *Nat. Prod. Commun.*, 3 (5), 705–710.
- [18] Sari, E.R., Suharti, N., Ismed, F., and Putra, D.P., 2021, Inventory, Morphological and Antioxidant Profile of the Sumatera Sidaguri (*Sida* spp.) Plants, *Proceedings of the 2nd International Conference on Contemporary Science and Clinical Pharmacy 2021 (ICCSCP 2021)*, Atlantis Press, 65–74.
- [19] Reich, E., and Schibli, A., 2007, *High Performance Thin Layer Chromatography for the Analysis of Medicinal Plants*, Thieme Medical Publishers Inc., New York.
- [20] Lenny, S., Barus, T., and Sitopu, E.Y., 2010, Isolasi senyawa alkaloid dari daun sidaguri (*Sida rhombifolia* L.), *Jurnal Kimia Mulawarman*, 8 (1), 40–43.
- [21] Shivatare, R.S., Nagore, D.H., and Nipanikar, S.U., 2013, “HPTLC” an important tool in standardization of herbal medical product: A review, *J. Sci. Innovative Res.*, 2 (6), 1086–1096.

Flocculation Performance of Industrial Sugarcane Juice by Acrylamide-Based Anionic Flocculant

Eva Oktavia Ningrum^{1*}, Agung Subyakto¹, Wirawan Ciptonugroho², Shania Lorensa¹, Devianti Anggraini Ramadhani¹, and Agus Surono¹

¹Department of Industrial Chemical Engineering, Faculty of Vocational Studies, Institut Teknologi Sepuluh Nopember, Kampus ITS Sukolilo, Surabaya, 60111, Indonesia

²Department of Chemical Education, Faculty of Teacher Training and Education, Universitas Sebelas Maret, Jl. Ir. Sutami 36A, Kentingan, Surakarta 57126, Indonesia

* **Corresponding author:**

email: eva-oktavia@chem-eng.its.ac.id

Received: February 19, 2022

Accepted: December 24, 2022

DOI: 10.22146/ijc.73150

Abstract: Despite the widespread use of ionic polymer flocculants in sugar refineries, there is still insufficient knowledge on the relationship between the polymer properties and the efficiency of flocculation. This paper describes the performance of poly(sodium acrylate-co-acrylamide) (poly(SA-co-AAm)) as an anionic flocculant in the flocculation-coagulation of sugarcane juice from the sugar factory Gempolkrep PTPN X Mojokerto. Poly(SA-co-AAm) was successfully prepared via free radical polymerization of sodium acrylate and acrylamide with respective molar ratios of 40:60, 50:50, and 60:40, and compared with the commercial flocculant Accofloc. It was found that the mud height of the sugarcane decreased with increasing SA:AAm ratio. However, mud height increase was observed with further increasing SA:AAm ratio. Furthermore, increasing the flocculant dosage did not induce any significant change in the mud height and pH. The total dissolved solids (TDS) significantly decreased when the ratio of sodium acrylate:acrylamide was changed from 40:60 to 50:50, whereas a further change to 60:40 increased the TDS value again. It is also noticed that the tendency of turbidity is consistent with the TDS value. These results demonstrate that poly(SA-co-AAm) is a feasible alternative to the commercial flocculant owing to its good flocculation-coagulation performance with an optimum SA:AAm ratio of 50:50.

Keywords: flocculation; flocculant; polymers; sugarcane

■ INTRODUCTION

Sugarcane is a primary raw material for the production of high-purity sucrose, which is vastly used in daily consumption and the food industry. In addition, sugar and sugarcane production plays an important role in the rural economy through agricultural income, job creation, and support for the rural economy [1]. In Indonesia, the demand for raw sugar for food and beverages is continuously increasing; in 2017, 6.32 million tons of sugar were consumed, and the demand increased by 6% in 2018 [2]. With an annual population growth of 1.3%, the growth in sugar consumption has averaged 4.3% per year since 2008, which has resulted in a large gap between production and sugar demand. The current

sugar production in the form of white crystal sugar shows a deficit of 100,000 to 300,000 tons per year or 3 to 10% of consumption. As a result, Indonesia became the world's largest sugar importer in 2017–2018 with 4.45 million tons imported [3].

Sugarcane is first milled after being harvested to collect the primary juice, which is further processed to obtain sucrose as the final product. Sugarcane juice is a complex liquid medium that contains many insoluble and suspended organic and inorganic constituents in a colloidal solution. This colloid is composed of sucrose (810–870 g/kg Brix), reducing sugar (30–60 g/kg Brix), oligosaccharides (0.6–6 g/kg Brix), polysaccharides including gums and dextrans (2–8 g/kg Brix), inorganic

salts (15–37 g/kg Brix), organic non-sugar substances (16.8–52 g/kg Brix), and insolubles (1.5–10 g/kg Brix) [4]. Apart from sucrose, the other constituents must be removed to obtain a refined juice with low turbidity [5]. The removal of suspended solids and non-sucrose impurities can be achieved by clarification [6-7]. Clarification can be conducted by adding lime milk ($\text{Ca}(\text{OH})_2$) followed by passing SO_2 (sulfidation) or CO_2 gas (carbonation) through the juice to generate insoluble calcium phosphate flocs ($\text{Ca}_3(\text{PO}_4)_2$), which can be readily separated by decantation. Decantation can also facilitate the formation of phosphate flocs by adding lime (CaO) to adjust the pH of the juice heated at 75 °C to 7.8 and boiling the limed juice [8]. It has been reported that the settling rate and the strength of the flocs formed can be accelerated by introducing an anionic copolymer [9-10]. Copolymers are also known to accelerate the flocs enlargement, leading to faster precipitation [11].

Anionic acrylamide copolymer flocculants are charged copolymers due to the presence of carboxylate, sulfonate, or phosphonate functional groups [12-13]. These copolymers can be prepared by copolymerizing acrylamide with another vinyl-type monomer bearing the corresponding functional groups or with another chemically modified polyacrylamide [14]. Six different polymerization approaches can be applied to synthesize anionic polyacrylamide (APAM), i.e., homopolymerization posthydrolysis, homopolymerization cohydrolysis, copolymerization, inverse emulsion polymerization, precipitation polymerization, and radiation polymerization [15-17]. The flocculant properties of the obtained APAM, including reactivity, hydrophobicity or hydrophilicity, and formation of hydrogen bonds, depending on the constituent monomers. The solution pH also affects the formation and reactivity of flocculant molecules. The intrinsic viscosity and solubility properties, which determine the molecular weight of APAM, are the most critical parameters during polymerization [18]. The APAM chains stretched under high charge densities induce an increase in the adsorption capacity and bridging effects that contribute to the efficient removal of organic particles. A combination of P_2O_5 and APAM flocculant has been shown to efficiently

improve the clarification of sugarcane juice [19]. Doherty et al. showed that the combination of acrylamide copolymers and quaternary ammonium compounds of trimethylammonium ethyl methacrylate (TMAEMAC) or cationic trimethylammonium ethyl acrylate chloride copolymers are more effective in flocculating sugarcane juice than TMAEMAC homopolymers [11]. The patch charge mechanism responsible for the residual turbidity in clarified juice using an anionic flocculant is minor and has a high negative charge. Six different starch-based anionic copolymers were synthesized and tested by Khalil and Aly [20] as flocculants in ferric laurate suspensions, finding that the flocculation performance of the copolymers was determined by the type of acid groups, the length of the alkyl chain bearing the carboxyl group, the chemical structure of the flocculant, the flocculant molar mass, and the pH of the suspension. In cane sugar juice, binding of copolymer microflocs most likely proceeds primarily by the attraction of the negatively charged acrylate groups to dipositive ionic bridges (e.g., Ca^{2+}), which are adsorbed to negative charges on the microfloc particles. However, it is still possible that they may proceed by two other mechanisms i.e., attraction of the negatively charged acrylate groups to positive charges on the surface of the microfloc particles and hydrogen or dipolar bonding between the acrylamide groups and the microfloc particles [21-25].

Although ionic polymer flocculants are essential in the sugar refinery, systematic studies to correlate the polymer properties and the efficiency in the flocculation have rarely been reported. With this aim, this paper describes the synthesis and characterization of different poly(sodium acrylate-*co*-acrylamide)s (poly(SA-*co*-AAM)s) as flocculating agents. Since ionic content is one of the most important parameters that affect flocculation performance, knowledge of the acrylamide/acrylate ratio in these copolymers is a subject of interest. Therefore, the performance of the copolymers to settle sugarcane juice collected from a sugar refinery in various acrylamide/acrylate ratios is evaluated by means of the floc settling rate and size, turbidity analysis, total dissolved solids (TDS), and final pH.

■ EXPERIMENTAL SECTION

Materials

Acrylamide 99%, acrylic acid 99%, and ammonium persulfate > 98% were purchased from Sigma Aldrich Co. USA, and were used without any further modifications. Sodium acrylate (NaAc) was prepared by neutralization of acrylic acid (AAM) with 12 mL of 2 N NaOH solution by the addition of active carbon (PT. Mapalus Makawanua Charcoal Industry) and 5 g of sodium carbonate (Na_2CO_3 , Merck, Germany). A clear solution of sodium acrylate was obtained for further synthesis of poly(SA-co-AAM). All materials were used as received. Distilled water was used throughout all experiments.

Instrumentation

Scanning electron microscopy (SEM)

The surface morphology of acrylamide, acrylic acid, and the poly(SA-co-AAM) flocculant samples was observed using a scanning electron microscope (HITACHI, FLEXSEM 1000, Japan).

Fourier transform infrared (FTIR) spectroscopy

The functional groups of acrylamide, sodium acrylate, and the poly(SA-co-AAM) flocculant samples with various concentrations were identified using FTIR spectroscopy. The FTIR spectra were obtained using a 550 Series II IR spectrometer (METTLER TOLEDO Instrument Co., Ltd., Switzerland) in a range of 500–4000 cm^{-1} by using ATR method.

Proton nuclear magnetic resonance ($^1\text{H-NMR}$) spectroscopy

$^1\text{H-NMR}$ spectroscopy (MR400 DD2, Agilent, USA) was employed to determine the chemical structure of the poly(SA-co-AAM) gel. To measure the spectra, the gels (20 mg) were dissolved in 1 mL of D_2O as a solvent.

Procedure

The preparation of the anionic flocculant poly(SA-co-AAM) consisted of two consecutive steps, i.e., the synthesis of sodium acrylate followed by the synthesis of poly(SA-co-AAM). For the first step, 8.8 mg of sodium carbonate (Na_2CO_3), 5 g of activated carbon, and 3.170 g of acrylic acid were charged into a glass beaker.

Subsequently, 12 mL of 2 N NaOH was added to neutralize the acrylic acid and to generate sodium acrylate. The resulting product mixture was filtered to obtain a clear solution of sodium acrylate. Next, the as-obtained sodium acrylate was mixed with 4.69 g of acrylamide and 30 mL of distilled water in a three-necked round bottom flask. After a homogeneous solution was obtained, the solution was purged with N_2 gas and then heated to 50 °C. Subsequently, 0.03 g of ammonium persulfate was introduced as an initiator to conduct the free radical polymerization reaction for 3 h under an N_2 atmosphere. Once the reaction was completed, a transparent polymer was obtained with a 95% yield. The polymer product was then collected and washed three times with 100 mL of ethanol. The polymer was then dried in an oven at 50 °C for three days. Following this procedure, three different samples of poly(SA-co-AAM) were prepared using initial concentration ratios of sodium acrylate and acrylamide of 40:60, 50:50, and 60:40.

Analysis of coagulation-flocculation

The coagulation-flocculation experiments were performed using a conventional jar apparatus or flocculator (VELP Scientifica Srl, Flocculator JLT6, Italy). This apparatus allowed four beakers to be agitated simultaneously. Meanwhile, sugarcane juice was provided by the Gempolkrep Mojokerto (PTPN X) sugar factory located in East Java, Indonesia which was taken before entering the clarifiers. This sugarcane juice's maximum $\text{Ca}(\text{OH})_2$ content is 1200 ppm. For each test, 1000 mL of sugar juice was charged into a glass beaker. The juice was subsequently heated to 70 °C followed by the addition of the anionic flocculant at various concentrations and dosages (0, 2, 4, and 6 ppm). Stirring at 120 rpm for 1 min (rapid stirring) was applied to promote the coagulation process. After 15 min, the stirring rate was lowered to 10 rpm. Subsequently, the beakers were carefully removed from the flocculator, and the flocs were allowed to settle for a certain time (0–60 min) before the analysis. To provide a comparison, commercial flocculant Accofloc was used as a reference. The most commonly used anionic flocculant with high molecular weight in sugar factories in Indonesia is

Accofloc A-110. The chemical constituent of this flocculant is anionic polyacrylamide.

Analysis of TDS

The TDS of sugarcane juice was determined by performing three repetitions for each sodium acrylate to acrylamide ratio. The flocculant-treated sugar juice (50 mL) was placed into an Erlenmeyer, and the TDS was measured using a conductivity meter (Eutech Instrument, CON 700, Singapore).

Analysis of turbidity

The juice turbidity is a valuable parameter to determine the effectiveness of the clarification process. Therefore, the turbidity of the sugarcane juice was measured before and after adding the poly(SA-co-AAm) flocculant using a turbidimeter (Eutech Instruments, TN-100, Singapore) and repeated three times.

Analysis of pH

The pH was measured using a pH meter (Trans Instruments, BP3001, Singapore) before and after adding the poly(SA-co-AAm) flocculant.

RESULTS AND DISCUSSION

Investigation of the Surface Morphology by SEM

Fig. 1 presents an SEM micrograph with 500×

magnification showing the surface morphology of the three poly(SA-co-AAm) samples, in which clear differences with the commercial flocculant Accofloc can be observed. Thus, at a low concentration of sodium acrylate compared with that of acrylamide, the morphology surface appears flat, and neither aggregation nor pores are observed (Fig. 1(a)). With increasing the sodium acrylate concentration to a sodium acrylate:acrylamide ratio of 50:50, the surface morphology remains flat (Fig. 1(b)). However, upon further increasing the ratio to 60:40, a layer and fold region on the surface with some holes is observed (Fig. 1(c)). By further increasing the concentration of the sodium acrylate:acrylamide ratio up to 80:20 (data is not shown) the pores are clearly observed throughout the surface of the synthesized flocculant. In contrast, the SEM image of Accofloc shows aggregation (Fig. 1(d)).

Identification of the Functional Groups by FTIR Spectroscopy

FTIR spectroscopy was performed to identify the functional groups present in poly(SA-co-AAm), and the corresponding spectra are displayed in Fig. 2. In the spectrum of sodium acrylate, the bands at 1694.01, 1634.45, and 1429.86 cm^{-1} correspond to the C=O groups of acrylic acid, the OH of water, and the COO^- groups of

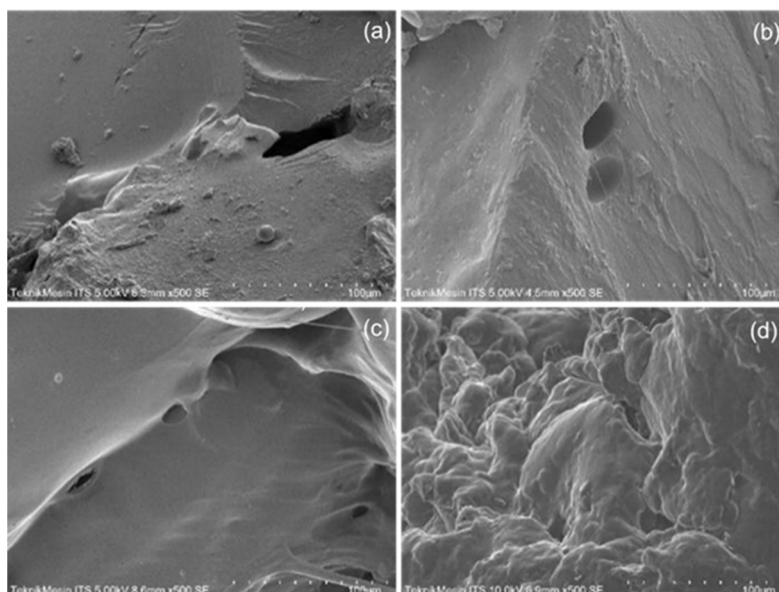


Fig 1. Scanning electron microscopy micrographs of poly(sodium acrylate-co-acrylamide) prepared with acrylic acid and acrylamide monomer ratios of (a) 40:60, (b) 50:50, and (c) 60:40 and (d) commercial flocculant Accofloc

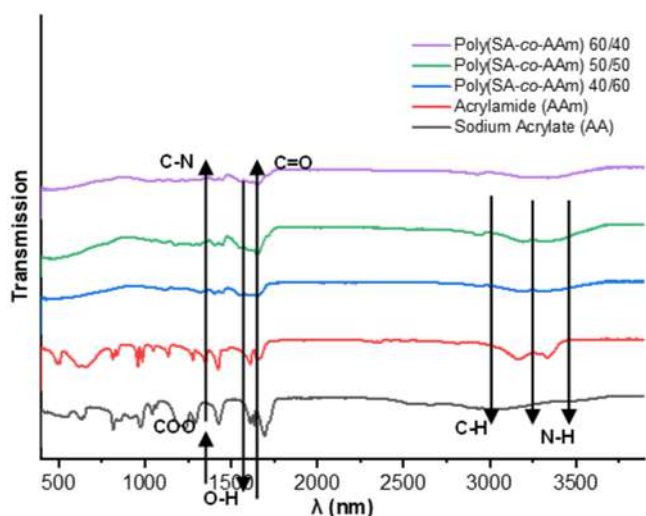


Fig 2. Fourier transform infrared spectra of sodium acrylate, acrylamide, and poly(sodium acrylate-*co*-acrylamide) (poly(SA-*co*-AAm)) samples prepared with sodium acrylate:acrylamide ratios of 40:60, 50:50, and 60:40

acrylate, respectively. In the spectrum of acrylamide, the bands at 3333.46 and 3164.33 cm^{-1} correspond to the NH_2 group, and the band at 2812.07 cm^{-1} indicates the presence of CH and CH_2 groups. The C=O groups and OH of water give rise to bands at 1651.91 and 1610.73 cm^{-1} , respectively. The slight difference of OH in various concentrations indicate the presence of adsorbed water as a solvent detected in the measurement. N-H bond corresponds to the characteristic of the acrylamide unit, with increasing SA to AAm ratio compared to the band of pure Acrylamide (red line) the peak appears weakened. On the contrary, the C-H bond attributes to the sodium acrylate unit which appears sharper and clearly observed with increasing SA to AAm ratio.

In addition, the CN groups of acrylamide produce a band at 1424.54 cm^{-1} [26]. Meanwhile, the spectra of the poly(SA-*co*-AAm) samples with a monomer ratio of 40:60, 50:50, and 60:40 show the bands corresponding to the N-H bond of the acrylamide unit at 3178.85 , 3338.26 , and 3337.80 cm^{-1} , respectively, and those attributable to the CH and CH_2 groups appear at 2894.269 , 2929.05 , and 2923.92 cm^{-1} , respectively. Moreover, the bands of the C=O groups of acrylamide and the OH of water are superposed, appearing at 1651.85 , 1648.18 , and 1654.59 cm^{-1} , respectively. The presence of the COO^-

groups of sodium acrylate or CN groups of acrylamide is evidenced by the peaks at 1444.85 , 1448.81 , and 1448.46 cm^{-1} , respectively. The blue line shows that poly(SA-*co*-AAm) samples with a monomer ratio of 40:60 have a lower and weak band at 1600 cm^{-1} compared to other concentrations. This indicates that the small fraction of the COOH group of acrylic acid during its reaction with NaOH is not completely neutralized while forming the sodium acrylate.

Confirmation of the Chemical Structure by ^1H -NMR Spectroscopy

^1H -NMR spectra were recorded to confirm the chemical structure of the resulting copolymers. Fig. 3 shows the spectrum of the copolymer prepared with a sodium acrylate:acrylamide ratio of 40:60. Two distinct broad peaks are observable in the regions of 1.23–1.86 and 1.97–2.36 ppm. These two ^1H -NMR signals can be ascribed to the presence of protons associated with $-\text{CH}(\text{CONH}_2)-$ and $-\text{CH}_2-$ groups, respectively, and are indicative of the formation of single bonds connecting the monomers to create a copolymer backbone. Mansri et al. reported a similar feature in the ^1H NMR spectra of polyacrylamide prepared via radical copolymerization in an aqueous solution, in which two multiplets appeared at 1.4–1.8 and 2–2.4 ppm [27]. For sodium acrylate, the proton bonded to the secondary carbon resonates at around 1.5–2.0 ppm, whereas the proton attached to the tertiary carbon gives rise to a peak at 2.38 ppm. In the present work, the $-\text{CH}_2-$ signal attributed to acrylate in the copolymer is hard to identify due to its overlap with the predominant peak of polyacrylamide. Nevertheless, the presence of the CH group from sodium polyacrylate is evidenced by the appearance of a weak peak at around 2.55 ppm. According to this result, the polyacrylamide segment is more predominant in the copolymer, which is expected considering the initial sodium acrylate:acrylamide monomer ratio. In addition, the spectrum around 3.6 ppm (multiplet) and around 1.1 ppm (triplet) appear because the copolymers are not pure compounds but show a broad molar weight distribution and possibly due to impurities in the comonomer.

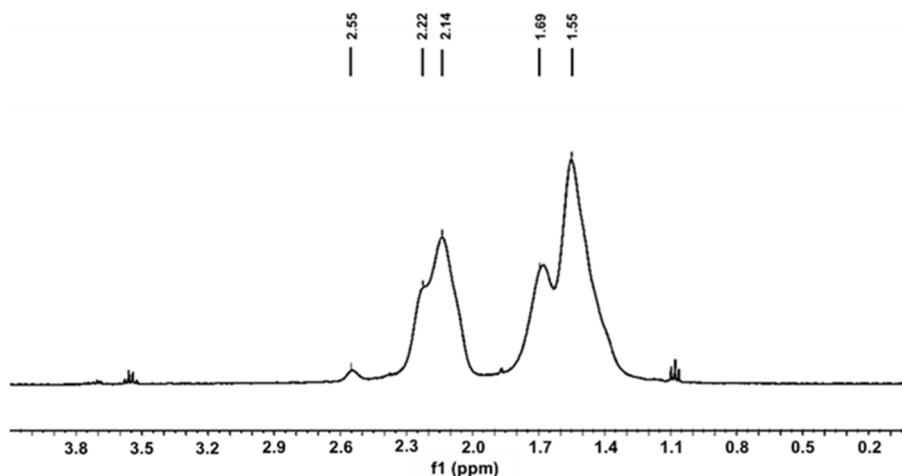


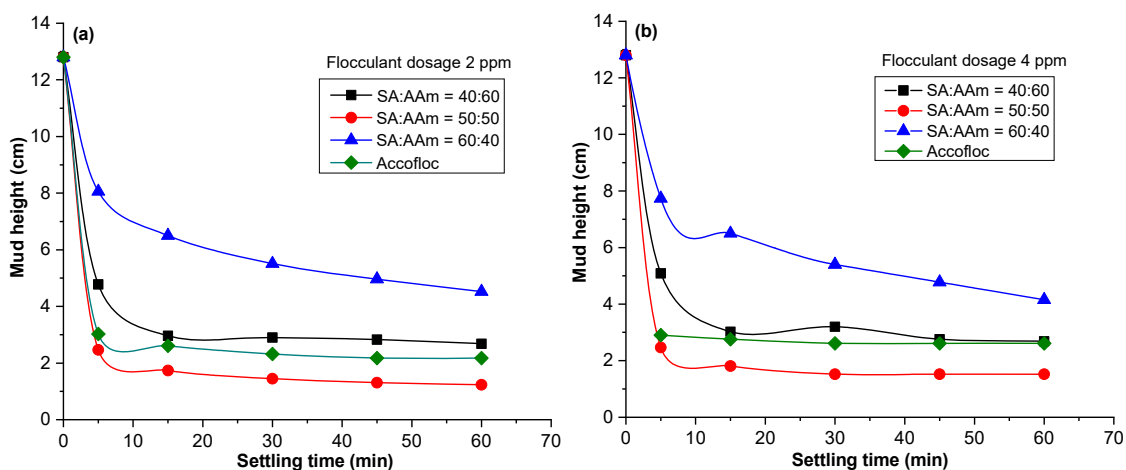
Fig 3. ^1H -Nuclear magnetic resonance spectra of poly(sodium acrylate-*co*-acrylamide) prepared with a sodium acrylate:acrylamide ratio of 40:60

Influence of Monomer Concentration of Flocculants on Mud Height

It is noteworthy that the shrinking volume of the settling with time could be attributed to the filling of the cavities between flocs leading to the sediment with a more compact arrangement. Fig. 4 shows the change in the mud height with time at various flocculant dosages and monomer ratios. Compared to the commercial flocculant of Accofloc, the mud heights were larger with the introduction of the copolymer flocculant. In general, at any dosage and at a lower settling time from 0–20 min, the concentration of SA in poly(SA-*co*-AAm) significantly influenced the initial mud height. For instance, at a flocculant concentration of 2 ppm, the mud volume decreased along with the intensified SA:AAM ratio from

40:60 to 50:50 ppm, which is caused by the decrease in the size of the cavities between flocs, shortening the distance between flocs as a result rendering them more compact. However, an appreciable increase in mud height was observable when increasing the SA:AAM ratio to 60:40; the mud height tends to increase significantly. This volume enlargement is caused by the formation of bigger flocs at a higher SA ratio and the presence of nonuniform cavities between the flocs. Higher floc formed with the presence of sufficiently high anion concentration required to facilitate the bridging [28]. Bridging is one of the flocculation mechanisms occurring when using a polymer flocculant, and the preferred one for polymers with long chains.

Fig. 4 also indicates that after 30 min, in all flocculant



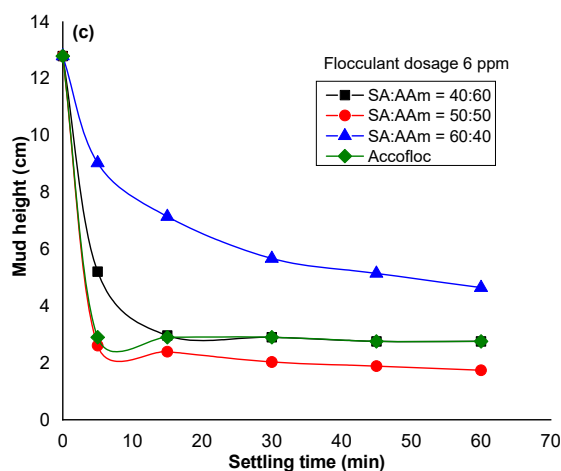


Fig 4. Effect of monomer concentration on the mud height upon addition of poly(sodium acrylate-*co*-acrylamide) dosage (a) 2 ppm, (b) 4 ppm, and (c) 6 ppm in comparison with commercial flocculant

dosage, the highest mud height was obtained when using poly(SA-*co*-AAM) with a monomer ratio of 60:40. Moreover, the commercial flocculant of Accofloc and flocculant with SA:AAM of 40:60 displayed a similar mud volume throughout the settling time and flocculant dosage. Furthermore, the effect of flocculant dosage was also investigated, suggesting a relatively insignificant improvement in the resulting mud heights. These results imply that the loading of SA in the copolymer is more essential to initiate the formation of larger flocs leading to a greater volume of the sediment.

The Influence of SA Content and Flocculant Dosage on the Acidity of Sugarcane Juice

Fig. 5 presents the change in the pH of the sugarcane juice with the flocculant dosage at various monomer ratios. Generally, the increase in the flocculant dosage decreased the pH value of the sugarcane juice. Moreover, the pH decreased gradually with increasing monomer ratio from 40:60 to 50:50, whereas it increased slightly with a further increase in the monomer ratio to 60:40. The addition of the commercial flocculant Accofloc also decreased the pH.

The increase in the poly(SA-*co*-AAM) dosage decreased the pH value. In the absence of a flocculant, the pH was 7.34. Meanwhile, when the flocculant was added, no drastic decrease was found on pH since the alkaline concentration provided was sufficient. In this case, FTIR has previously stated that only a small fraction of the COOH

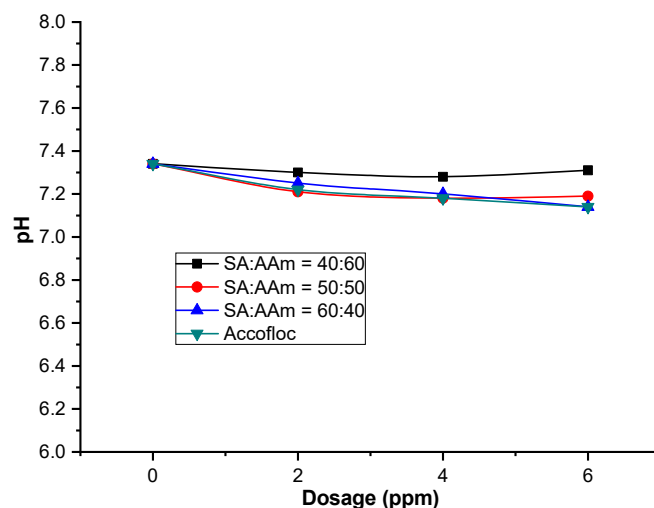


Fig 5. Effect of the flocculant dosage on the pH of a sugarcane juice suspension

group of acrylic acid neutralized NaOH while forming the sodium acrylate. Therefore, the decrease in the pH value did not significantly affect the sugarcane juice. After the addition of the flocculant, the sugarcane juice had a pH of 7.14–7.34. This value is within the optimal pH range for the sugarcane juice purification process in the sugar factory, which is 7–7.3.

Analysis of TDS

The TDS of flocculant with altered monomer ratios and different dosages is given in Fig. 6. The introduction of flocculant with 40:60 SA:AAM ratio insignificantly reduced the TDS at any given dosage.

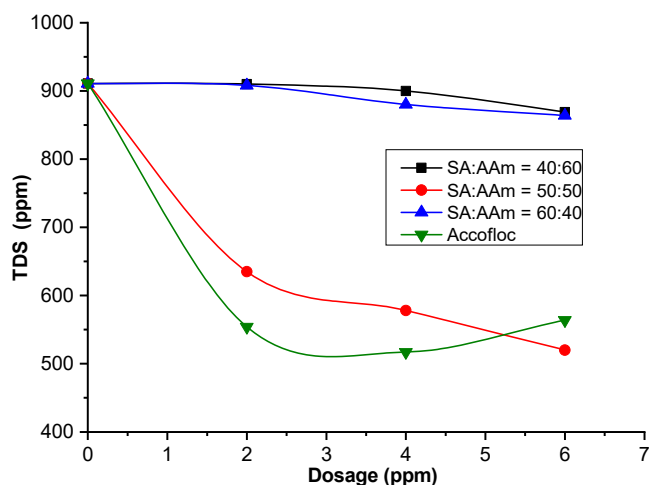


Fig 6. Effect of the flocculant dosage on total dissolved solids (TDS)

A remarkable TDS reduction was achieved once a higher SA:AAM ratio of 50:50 was applied to the sugarcane suspension. At this ratio, the TDS consistently declined from 900 to 520 ppm along with the enriched dosage from 0 to 6 ppm, respectively. Further enrichment of SA:AAM ratio to 60:40 increased the TDS again resembling the resulting TDS from SA:AAM ratio of 40:60. In fact, the SA:AAM ratio can be associated with the concentration of Na^+ cation in the suspension. This can be explained by the fact that an increase in the sodium acrylate concentration increases the number of flocs formed; however, an excessive amount of flocs may cause a collision between aggregated particles, which would then redisperse in the suspension, as previously reported by Mishra et al. [29] and Chan and Chiang [30]. It has been reported by Chan and Chiang [30] that on one hand, the Na^+ cation in the suspension could suppress the electric double layer of a particle favorable to the formation of larger flocs, but on the other hand, the excessive amounts of cations would resist the expansion of polymer chain unfavorable for bridging the interparticle. The minor influence of flocculant dosing at SA:AAM ratio of 40:60 could be reasoned by the insufficient cations available to initiate the flocculation. Meanwhile, the presence of Na^+ became too much at the highest monomer ratio of 60:40 preventing the generation of larger flocs. Furthermore, the addition of 2 ppm Accofloc depressed the TDS as low as 454 ppm before it gradually increased from 517 to

564 ppm following the introduction of the Accofloc from 4 to 6 ppm, respectively. According to Mishra et al., an increase in the flocculant dosage in a sugarcane juice suspension promotes the attraction among impurities and eventually reduces the concentration of dissolved solids in the suspension [29].

Suspension Turbidity

Fig. 7 illustrates the effect of the poly(SA-co-AAm) dosage and monomer ratio on the turbidity. In general, the turbidity fell significantly following the addition of the flocculant at 2 ppm because the impurities in the sugarcane juice were adsorbed by the flocculants leading to the precipitation. Furthermore, the turbidity remained constant as the dosage was intensified from 2 to 6 ppm. The addition of flocculants can adsorb the impurities enabling the formation of greater particles. Nevertheless, excessive addition of flocculants may cover the previously formed particles initiating particle redispersion and hindering the formation of larger flocs.

Furthermore, the influence of different flocculants on turbidity was also studied. At any given dosage, the turbidity declined with the increase of the SA:AAM ratio from 40:60 to 50:50. The result was in good agreement with previous studies on phosphate and anionic polyacrylamide flocculant (APF) for sugar cane juice clarification. Further enrichment of the SA ratio to 60:40

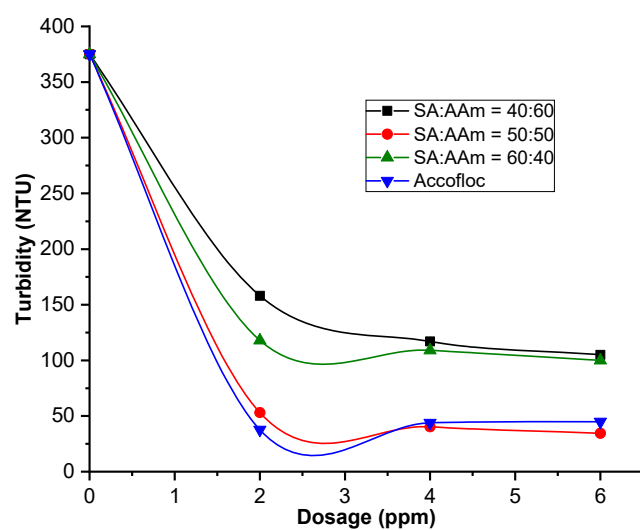


Fig 7. Effect of the flocculant dosage on the turbidity of a sugarcane juice suspension

gave rise to the turbidity as high as copolymer with SA:AAM ratio of 40:60. This also implies that the optimum ratio of 50:50 is responsible for the lowest turbidity of the suspension. The presence of an optimum ratio is due to the copolymer with 50:50 ratio that could provide a sufficient anion concentration for the flocculation without excessively covering the formed particles and bringing about their redispersion in the suspension. Moreover, the turbidity of Accofloc resembled that of the poly(SA-co-AAM) with 50:50 ratio. This infers that the SA-co-AAM with optimized SA:AAM ratio could assist flocculation as efficiently as the commercial flocculant.

It is noticed that the tendency of turbidity in this figure is also consistent with the TDS result as shown in Fig. 6. Total dissolved solids (TDS) contribute to the measurement of turbidity. The lower the TDS, the less turbidity of the supernatant since most of the particle settled as a consequence of the mud height increase.

■ CONCLUSION

Poly(SA-co-AAM) was successfully synthesized as an anionic flocculant for sugarcane juice from sugar factories owned by PT. Perkebunan Nusantara (PTPN) Indonesia. FTIR and NMR analysis showed that the anionic flocculant poly(SA-co-AAM) contained all the expected constituent monomer groups. Compared to the commercial flocculant of Accofloc, the mud heights were found to be larger with the introduction of the copolymer flocculant. In general, at any dosage and at a lower settling time from 0–20 min, the concentration of SA in poly(SA-co-AAM) significantly influenced the initial mud height. The mud volume decreased along with the intensified SA:AAM ratio from 40:60 to 50:50 ppm. However, an appreciable increase in mud height was observable when increasing SA:AAM ratio to 60:40; the mud height tends to increase significantly. The poly(SA-co-AAM) increase caused an insignificant decrease in the pH value and mud height. Concerning the TDS value, a significant decrease was observed upon increasing the sodium acrylate:acrylamide ratio from 40:60 to 50:50, whereas further increase in the monomer ratio to 60:40 increased the TDS value again. Overall, the poly(SA-co-AAM)

flocculant obtained with a sodium acrylate: acrylamide ratio of 50:50 and a dosage of 6 ppm afforded better results than the commercial flocculant with a dosage of 4 ppm. Although 6 ppm is a relatively higher dosage than that commonly used in sugar plants, this result demonstrates that poly(SA-co-AAM) can effectively replace the commercial flocculant due to its good flocculation-coagulation performance. Future work will focus on investigating the flocculation-coagulation performance of poly(SA-co-AAM) with a wider range of monomer ratios for the clarification of sugarcane juice.

■ ACKNOWLEDGMENTS

The authors gratefully acknowledge financial support from the Institut Teknologi Sepuluh Nopember for this work, under the project scheme of the Publication Writing and IPR Incentive Program (PPHKI) 2022.

■ AUTHOR CONTRIBUTIONS

Shania Lorensa and Devianti Anggraini Ramadhani conducted the experiment, Agung Subyakto and Agus Surono conducted the data calculations. Eva Oktavia Ningrum and Wirawan Ciptonugroho wrote and revised the manuscript. All authors agreed to the final version of this manuscript.

■ REFERENCES

- [1] Nandhini, T.S.K.D., and Padmavathy, V., 2017, A study on sugarcane production in India, *Int. J. Adv. Res. Bot.*, 3 (2), 13–17.
- [2] Reuters, 2017, *Indonesia Raw Sugar Consumption for Food, Beverages Seen Edging up in 2018*, <https://www.reuters.com/article/indonesia-sugar-idUSJ9N1I400Q>, accessed on February 10, 2022.
- [3] Sulaiman, A.A., Sulaeman, Y., Mustikasari, N., Nursyamsi, D., and Syakir, A.M., 2019, Increasing sugar production in Indonesia through land suitability analysis and sugar mill restructuring, *Land*, 8 (4), 61.
- [4] Xiao, Z., Liao, X., and Guo, S., 2017, Analysis of sugarcane juice quality indexes, *J. Food Qual.*, 2017, 1746982.

- [5] de Mello, M.L., Barros, N.Z., Sperança, M.A., and Pereira, F.M.V., 2022, Impurities in raw sugarcane before and after biorefinery processing, *Food Anal. Methods*, 15 (1), 96–103.
- [6] Meng, Y., Yu, S., Qiu, Z., Zhang, J., Wu, J., Yao, T., and Qin, J., 2021, Modeling and optimization of sugarcane juice clarification process, *J. Food Eng.*, 291, 110223.
- [7] Umesh Kumar, P.K., and Chand, K., 2015, Application of response surface method as an experimental design to optimize clarification process parameters for sugarcane juice, *J. Food Process. Technol.*, 6 (2), 1000422.
- [8] Shi, C., Rackemann, D.W., Moghaddam, L., Wei, B., Li, K., Lu, H., Xie, C., Hang, F., and Doherty, W.O.S., 2019, Ceramic membrane filtration of factory sugarcane juice: Effect of pretreatment on permeate flux, juice quality and fouling, *J. Food Eng.*, 243, 101–113.
- [9] Dao, V.H., Mohanarangam, K., Fawell, P.D., Simic, K., Iyer, R., Cameron, N.R., and Saito, K., 2020, Enhanced flocculation efficiency in a high-ionic-strength environment by the aid of anionic ABA triblock copolymers, *Langmuir*, 36 (6), 1538–1551.
- [10] Deniz, V., 2015, Dewatering of barite clay wastewater by inorganic coagulants and co-polymer flocculants, *Physicochem. Probl. Miner. Process.*, 51 (1), 351–364.
- [11] Doherty, W.O.S., Fellows, C.M., Gorjian, S., Senogles, E., and Cheung, W.H., 2003, Flocculation and sedimentation of cane sugar juice particles with cationic homo- and copolymers, *J. Appl. Polym. Sci.*, 90 (1), 316–325.
- [12] Bakir, H., Denman, J.A., and Doherty, W.O.S., 2020, Slow settling behaviour of soil nano-particles in water and synthetic sugarcane juice solutions, *J. Food Eng.*, 279, 109978.
- [13] Guan, G., Gao, T., Wang, X., and Lou, T., 2021, A cost-effective anionic flocculant prepared by grafting carboxymethyl cellulose and lignosulfonate with acrylamide, *Cellulose*, 28 (17), 11013–11023.
- [14] Rabiee, A., 2010, Acrylamide-based anionic polyelectrolytes and their applications: A survey, *J. Vinyl Addit. Technol.*, 16 (2), 111–119.
- [15] Zheng, H., Ma, J., Ji, F., Tang, X., Chen, W., Zhu, J., Liao, Y., and Tan, M., 2013, Synthesis and application of anionic polyacrylamide in water treatment: A review, *Asian J. Chem.*, 25 (13), 7071–7074.
- [16] Ma, J., Zheng, H., Tan, M., Liu, L., Chen, W., Guan, Q., and Zheng, X., 2013, Synthesis, characterization, and flocculation performance of anionic polyacrylamide P (AM-AA-AMPS), *J. Appl. Polym. Sci.*, 129 (4), 1984–1991.
- [17] Feng, L., Zheng, H., Gao, B., Zhang, S., Zhao, C., Zhou, Y., and Xu, B., 2017, Fabricating an anionic polyacrylamide (APAM) with an anionic block structure for high turbidity water separation and purification, *RSC Adv.*, 7 (46), 28918–28930.
- [18] Zheng, H., Ma, J., Zhu, C., Zhang, Z., Liu, L., Sun, Y., and Tang, X., 2014, Synthesis of anion polyacrylamide under UV initiation and its application in removing dioctyl phthalate from water through flocculation process, *Sep. Purif. Technol.*, 123, 35–44.
- [19] Mohammed, H., Solomon, W.K., and Bultosa, G., 2016, Optimization of phosphate and anionic polyacrylamide flocculant (APF) level for sugar cane juice clarification using central composite design, *J. Food Process. Preserv.*, 40 (1), 67–75.
- [20] Khalil, M.I., and Aly, A.A., 2002, Preparation and evaluation of some anionic starch derivatives as flocculants, *Starch-Stärke*, 54 (3-4), 132–139.
- [21] Shen, C.C., Petit, S., Li, C.J., Li, C.S., Khatoon, N., and Zhou, C.H., 2020, Interactions between smectites and polyelectrolytes, *Appl. Clay Sci.*, 198, 105778.
- [22] Rabiee, A., Ershad-Langroudi, A., and Zeynali, M.E., 2015, A survey on cationic polyelectrolytes and their applications: Acrylamide derivatives, *Rev. Chem. Eng.*, 31 (3), 239–261.
- [23] Thai, C.C.D., Bakir, H., and Doherty, W.O.S., 2012, Insights to the clarification of sugar cane juice expressed from sugar cane stalk and trash, *J. Agric. Food Chem.*, 60 (11), 2916–2923.
- [24] Pal, P., Pandey, J.P., and Sen, G., 2018, Grafted sesbania gum: A novel derivative for sugarcane juice clarification, *Int. J. Biol. Macromol.*, 114, 349–356.

- [25] Thai, C.C.D., and Doherty, W.O.S., 2013, Effect of Trash on the Coagulation and Flocculation of Sugarcane Juice, Australia, *Proceedings of the 35th Conference of the Australian Society of Sugar Cane Technologists*, Townsville, Queensland, Australia, April 16-18, 2013.
- [26] Magalhães, A.S.G., Almeida Neto, M.P., Bezerra, M.N., Ricardo, N.M.P.S., and Feitosa, J.P.A., 2012, Application of FTIR in the determination of acrylate content in poly(sodium acrylate-co-acrylamide) superabsorbent hydrogels, *Quim. Nova*, 35 (7), 1464–1467.
- [27] Mansri, A., Bendraoua, A., Benmoussa, A., and Benhabib, K., 2015, New polyacrylamide [PAM] material formulations for the coagulation/flocculation/decantation process, *J. Polym. Environ.*, 23 (4), 580–587.
- [28] Craciun, G., Ighigeanu, D., Manaila, E., and Stelescu, M.D., 2015, Synthesis and characterization of poly(acrylamide-co-acrylic acid) flocculant obtained by electron beam irradiation, *Mater. Res.*, 18 (5), 984–993.
- [29] Mishra, A., Agarwal, M., and Yadav, A., 2003, Fenugreek mucilage as a flocculating agent for sewage treatment, *Colloid Polym. Sci.*, 281 (2), 164–167.
- [30] Chan, W.C., and Chiang, C.Y., 1995, Flocculation of clay suspensions with water-insoluble starch grafting acrylamide/sodium allylsulfonated copolymer powder, *J. Appl. Polym. Sci.*, 58 (10), 1721–1726.

Influence of Al and Cu Doping on the Structure, Morphology, and Optical Properties of ZnO Thin Film

Faras Afifah^{1,2}, Arif Tjahjono², Aga Ridhova³, Pramitha Yuniar Diah Maulida⁴,
Alfian Noviyanto^{4,5*}, and Didik Aryanto^{1**}

¹Research Center for Advanced Materials, National Research and Innovation Agency,
Kawasan Puspiptek Serpong, Tangerang Selatan, Banten 15314, Indonesia

²Department of Physics, Universitas Islam Negeri Syarif Hidayatullah, Jl. Ir. H. Juanda, Cempaka Putih, Jakarta 15412, Indonesia

³Research Center for Metallurgy and Materials, National Research and Innovation Agency,
Kawasan Puspiptek Serpong, Tangerang Selatan, Banten 15314, Indonesia

⁴Nano Center Indonesia, Jl. Puspiptek, Tangerang Selatan, Banten 15314, Indonesia

⁵Department of Mechanical Engineering, Mercu Buana University, Jl. Meruya Selatan, Kebun Jeruk, Jakarta 11650, Indonesia

* **Corresponding author:**

email: a.noviyanto@nano.or.id*;
didi021@brin.go.id**

Received: February 23, 2022

Accepted: October 3, 2022

DOI: 10.22146/ijc.73234

Abstract: In this study, ZnO thin films doped with Al (AZO) and Cu (CZO) were fabricated on a glass substrate via sol-gel spin coating. The influence of 1 atomic % Al and Cu doping on the structure, morphology, as well as optical properties of ZnO thin film was then analyzed with X-ray diffraction (XRD), atomic force microscopy (AFM), and UV-Vis spectroscopy. XRD analysis revealed that all samples possessed hexagonal wurtzite crystal structures with 3 to 4 preferred orientations. Al and Cu doping caused a decrease in crystal size, while the lattice strain (ϵ) and dislocation density (ρ) were increased. AFM indicated that Al and Cu doping reduced the surface roughness of the ZnO thin film. Optical measurement showed that all samples exhibited high transmittance ($> 80\%$) in the visible light region. Transmittance was reduced after doping, while the band gaps for ZnO, AZO, and CZO thin films are 3.26, 3.28, and 3.23 eV. This study showed that an addition of 1 atomic % transition metal (Al and Cu) greatly influences the structure, morphology, and optical properties of ZnO thin film.

Keywords: doping; morphology; optical properties; structure; thin film

■ INTRODUCTION

Zinc oxide (ZnO) is a semiconductor II-VI with a bandgap of 3.2-3.3 eV and a strong excitation binding energy (60 MeV) at room temperature [1-3]. ZnO is a polycrystalline material and could exist in wurtzite, zinc-blende, and cubic rock salt form, with wurtzite being the most abundant due to it being the most stable [4]. In addition, ZnO is known to be non-toxic, eco-friendly, easy to process, and possesses high chemical stability [1-2,5-8]. In thin-film form, ZnO has high optical transmittance, high electron mobility, and thermal conductivity [9-10]. These properties make ZnO suitable for many applications, such as solar cells [11], transparent

conductive oxide (TCO) [12], light-emitting diode [13], and photocatalysts [6,14]. Therefore, various improvements in ZnO thin film have been the subject of much research.

The doping process is a promising way to modify the microstructure and both optical and electronic properties of ZnO. Some studies have reported that elements from the III group (Al, In, Ga) [5,7,15] and transition metals (Ti, V, Cr, Mn, Fe, Co, Ni, Cu) [10,16-17] are suitable dopant candidates for ZnO thin film. A previous study by Asikuzun et al. showed that doping ZnO thin film with Cu increased the surface roughness, lowered the optical transmittance, and lowered the optical band gap [18]. A similar result was reported by

Nimbalkar and Patil [13], who confirmed that the band gap, as well as the activation energy of ZnO thin film, were decreased after Cu doping.

On the other hand, Al doping has been reported to lower the crystal quality and band gap of ZnO thin film. However, lattice strain and Seebeck coefficient were conserved [19]. Another study found that band gap, lattice parameter, and grain size decreased after Al was added [20]. According to the studies mentioned earlier, the addition of Al and Cu could affect the morphology and optical properties of ZnO thin film.

From the chemical and physical perspectives, Cu is a more suitable candidate as a dopant for ZnO, as Cu has similar atomic properties to Zn, particularly in terms of atomic radius and electron shell [18]. The substitution of Cu^{2+} into Zn^{2+} is thought not to cause a notable change in lattice parameters, seeing as the radii of Cu^{2+} and Zn^{2+} are estimated to be around 0.073 and 0.074 nm [21]. In contrast, Al with an ionic radius of 0.053 nm is expected to cause a significant alteration in the lattice parameter, owing to the large radius difference. A previous study of Al- and/or Cu- doped ZnO thin film has been conducted [11-14,18-19,21-28]. However, the investigation focuses on the effect of only one doping (Al or Cu) in the ZnO thin film. Bakhtiargobandi et al. [29] investigated the effect of Al and Cu doping on the photoelectrochemical properties of ZnO thin films, nevertheless, the amount of dopants is large, i.e., 6 wt.%. To the best of our knowledge, there has been no report on the small number of dopants (Cu and Al) on the structure, morphology, and optical properties of ZnO thin films. The addition of small doping with different ionic radii on the structure, morphology and optical properties of ZnO becomes the focus of the present study, where ion radii of Cu are closer to that of Zn compared to ion radii of Al. In general, the least amount of reported doping of Cu or Al on ZnO is 1 atomic %. The interesting finding is that it has an effect on the properties of the thin films, especially with the addition of two different dopant atomic radii with Zn.

In this research, ZnO thin film was doped with Al and Cu, each with a concentration of 1%. The thin films were deposited onto a glass substrate using a sol-gel spin coating. This method was used due to its being safe, easy

to operate, and low cost [1-2] when compared to other methods such as pulsed laser deposition (PLD), chemical vapor deposition (CVD), sputtering [7], spray pyrolysis [21], chemical bath deposition, electrochemical deposition, and hydrothermal [13]. The influence of 1% Al and Cu doping on ZnO thin film's morphology, structure, and optical properties were evaluated thoroughly using X-ray diffraction (XRD), atomic force microscopy (AFM), and UV-Vis spectroscopy.

■ EXPERIMENTAL SECTION

Materials

The materials used in this research were zinc acetate dihydrate ($\text{Zn}(\text{CH}_3\text{COO})_2 \cdot 2\text{H}_2\text{O}$) (CAS number 5970-45-6, Merck KGaA), isopropanol (CAS number 67-63-0, Merck KGaA), ethanolamine ($\text{NH}_2\text{CH}_2\text{CH}_2\text{OH}$) (CAS number 141-43-5, Merck KGaA), Copper(II) acetate monohydrate ($\text{Cu}(\text{CH}_3\text{COO})_2 \cdot \text{H}_2\text{O}$) (CAS number 6046-93-1, Merck KGaA), and aluminum acetate ($\text{C}_4\text{H}_7\text{AlO}_5$) (CAS number 142-03-0, Sigma-Aldrich) were used in this study.

Instrumentation

VTC-100 spin coater was used to fabricate the thin film. Phase analysis was conducted by X-ray diffraction (XRD, Smartlab, Rigaku, Japan). The surface roughness of samples was observed by atomic force microscopy (AFM, NX10 AFM, Korea). The band gap of the sample was obtained from UV-Vis spectroscopy (UH5300, Hitachi, Japan).

Procedure

Copper(II) acetate monohydrate ($\text{Cu}(\text{CH}_3\text{COO})_2 \cdot \text{H}_2\text{O}$) and aluminum acetate ($\text{C}_4\text{H}_7\text{AlO}_5$) was added into the solution to make Cu-doped (CZO) and Al-doped (AZO) ZnO thin film, respectively. The percentage of dopants was calculated according to the molecular weight of the dopants.

Both ZnO and dopant precursor solution has a concentration of 0.5 M with the molar ratio of metal salt and ethanolamine 1:1. Undoped and doped ZnO solution were stirred at a temperature of 60 °C for 1 h with 300 rpm and was left at room temperature for 24 h.

Glass substrates were cleaned using the radio corporation of America (RCA) method, where the substrates were cleaned with ethanol for 10 min and acetone for 5 min using an ultrasonic cleaner to ensure that no organic impurities remained in the sample. The substrates were then rinsed with deionized water.

The solutions were deposited into the substrates using spin-coating (3000 rpm for 50 s) using VTC-100 spin coater to fabricate the thin films. The deposition process was repeated three times, with a pre-heated treatment at a temperature of 110 °C for 10 min. The final heat treatment for the ZnO thin film was done at 400 °C for 1 h.

■ RESULTS AND DISCUSSION

Fig. 1 shows the diffraction pattern of ZnO, AZO, and CZO deposited using sol-gel spin coating. According to ICDD [96-230-0113], all samples have a hexagonal wurtzite structure. Crystal growth and orientation of each sample could be further analyzed using the texture coefficient (TC) obtained from the Harris equation, as shown in Eq. (1).

$$TC = \frac{I_{(hkl)} / I_{0(hkl)}}{\left(\frac{1}{n} \sum I_{(hkl)} / I_{0(hkl)} \right)} \quad (1)$$

where n , $I_{(hkl)}$, and $I_{0(hkl)}$ represent the number of diffraction peaks, peak intensity of a certain plane, and reference intensity. Calculated TC of ZnO, AZO, and CZO, along with the planes associated with diffraction peaks, are presented in Table 1. According to TC calculation, each sample tends to crystallize in a different orientation, as the crystal growth could be attributed to a few particular planes. ZnO tends to crystallize in the direction of (002), (101), and (112) planes. Crystal growth in AZO is dominated by (102), (110), and (112) planes,

while CZO crystallization mostly occurs in (100), (101), (110), and (112) orientations.

The incorporation of Cu and Al also caused the peak intensity of ZnO to decrease, although the decrease is more significant in AZO. This is due to the large difference in ionic radii between Al and Zn, while the ionic radii of Cu and Zn only while the difference in ionic radii for Cu and Zn insignificant. The atomic radii of Al^{3+} , Cu^{2+} , and Zn^{2+} are 0.053, 0.073, and 0.074 nm, respectively. The immense difference between Al and Zn atomic radii would result in a more notable distortion in the ZnO crystal structure, hence the less crystalline structure of AZO [17].

Additionally, other properties are also affected by the doping process, such as lattice parameters (a and c), crystal size (D), lattice strain (ϵ), and dislocation density (ρ). Lattice parameters (a and c) and d -spacing (d) of each

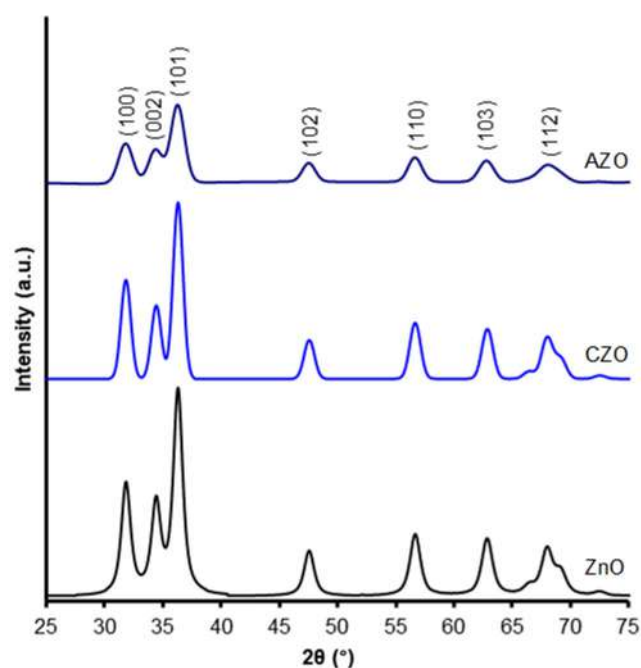


Fig 1. Diffraction pattern of ZnO, AZO, and CZO thin film

Table 1. Texture coefficient (TC) of ZnO, AZO, and CZO thin film

Sample	Texture Coefficient (TC)						
	(100)	(002)	(101)	(102)	(110)	(103)	(112)
ZnO	0.97	1.11	1.01	0.95	0.94	0.97	1.05
CZO	1.00	0.96	1.02	0.97	1.01	0.99	1.06
AZO	0.88	0.98	0.98	1.13	1.02	0.99	1.03

sample could be evaluated using the following relations, according to Eq. (2-4), respectively.

$$a = \frac{\lambda}{\sqrt{3} \sin \theta} \sqrt{h^2 + hk + k^2} \quad (2)$$

$$c = \frac{\lambda}{2 \sin \theta} l \quad (3)$$

$$\frac{1}{d^2} = \frac{4 \sin^2 \theta}{\lambda^2} \quad (4)$$

where λ is the X-ray wavelength (1.5405 Å), θ is the diffraction angle, and $h k l$ are the Miller indices.

Crystal size (D) could be calculated using the Debye-Scherrer formula, as shown in Eq. (5).

$$D = \frac{0.94\lambda}{B \cos \theta} \quad (5)$$

where B represents the full width at half maximum (FWHM) of a particular peak ($h k l$).

Lattice strain (ε), which is a lattice disorder developed during crystallization, could be calculated using the following Eq. (6).

$$\varepsilon = \frac{B}{4 \tan \theta} \quad (6)$$

Dislocation density (ρ) is defined as dislocation-induced imperfection present in a unit volume and could be calculated using the Williamson-Smallman relation (Eq. (7)).

$$\rho = \frac{1}{D^2} \quad (7)$$

Table 2 shows the calculated crystallography parameter such as lattice parameter, crystal size (D), d -spacing (d), lattice strain (ε), and dislocation density (ρ) of ZnO, AZO, and CZO. Al doping resulted in a decrease in lattice constant, while Cu doping increased. The change in lattice parameter is related to the addition of Al and Cu. A similar result has been reported by Jongnavakit et al., where ZnO underwent a decrease in lattice constant

after Cu doping [30]. Al Farsi et al. also reported that Al doping caused the lattice constant of thin film to increase [22].

A shift in lattice constant also indicates an alteration in crystal size (D), where the crystal size of ZnO, AZO, and CZO calculated from the (112) plane are 50.48, 38.38, and 47.96 nm, respectively. This change in crystal size is clearly observed in the broadening of the peak, as shown in Fig. 1, which shows that the addition of Al caused the peak to broaden; thus, the crystallite size decreased compared to ZnO. These changes also show that the doping process was successful, as evidenced by the decrease in crystal size in both doped samples. Moreover, studies by de Lara Andrade et al. and Ali et al. demonstrate that ZnO crystal size decreased along with the increase of Al^{3+} and Cu^{2+} concentrations [23-24]. The ionic radii of the dopants also affect the d -spacing, which represents the distance between parallel planes in the structure. AZO and CZO have lower d -spacing than ZnO, where the calculated values are 1.3772, 1.3781, and 1.3784, respectively. Similar to crystal size, AZO has the lowest d -spacing value as a consequence of the small ionic radius of Al^{3+} .

Furthermore, immense atomic radii differences would consequently cause higher lattice strain in the ZnO structure. Higher lattice strain would result in more dislocation and therefore cause the structure to have a higher dislocation density, as observed in both samples, particularly AZO, which exhibits a significantly higher dislocation density than CZO and ZnO. Additionally, there are published reports that Al and Cu doping increased the lattice strain, which led to an increase in defects in grain boundaries, reinforcing that higher lattice strain is related to higher dislocation in a crystal structure [19,24]. Another suggestion is that the addition of Al and

Table 2. Lattice parameter, crystal size (D), d -spacing (d), lattice strain (ε), and dislocation density (ρ) calculated from plane (112)

Sample	a (Å)	c (Å)	D (Å)	d (Å)	ε (%)	ρ ($\times 10^{-2}$) (line/nm ²)
ZnO	3.2473	5.2111	50.48	1.3784	1.229	3.92
CZO	3.2473	5.2097	47.96	1.3781	1.293	4.34
AZO	3.2503	5.2170	38.38	1.3772	1.615	6.79

Cu could inhibit crystal growth, in which case the lattice distortion is bound to occur [24].

Fig. 2 represents the three-dimensional $2 \times 2 \mu\text{m}$ surface topology of ZnO, AZO, and CZO thin film obtained from AFM analysis. Visually, it could be observed that the addition of Al and Cu to ZnO reshaped its surface topology, as indicated by the relatively more even surface of AZO and CZO. The morphology parameter was further analyzed using Gwyddion software, from which grain size, average surface roughness, and root mean square surface roughness were obtained and presented in Table 3.

The average grain size ranged from 29.95 to 51.95 nm, as shown in Table 3. After being doped with Al, the grain size of the ZnO thin film was reduced from 36.68 to 29.95 nm. Previous studies by Al Farsi et al. and Hsu et al. also found that Al doping resulted in a decrease in grain size and surface roughness [22,25]. The opposite could be

observed in Cu doping, where the grain size increased to 51.95 nm. This result is also in agreement with a study by Istrate et al., who found that the addition of Cu increased the grain size of ZnO thin film [26].

In addition to grain size, the surface topology of each sample is also related to its surface roughness, which was determined by the distribution of its grain. In ZnO, the surface is riddled with elliptical grains of varying sizes, while in AZO and CZO, the grains are more homogenous and evenly distributed. As a result, the average surface roughness of Cu-doped ZnO is slightly lower than that of pristine ZnO, while in Al-doped ZnO, the roughness is reduced to almost a quarter of its initial. On top of that, root mean square (RMS) roughness analysis yields a similar result, which further confirms that the grain of AZO is finer and notably more homogenous than CZO and ZnO.

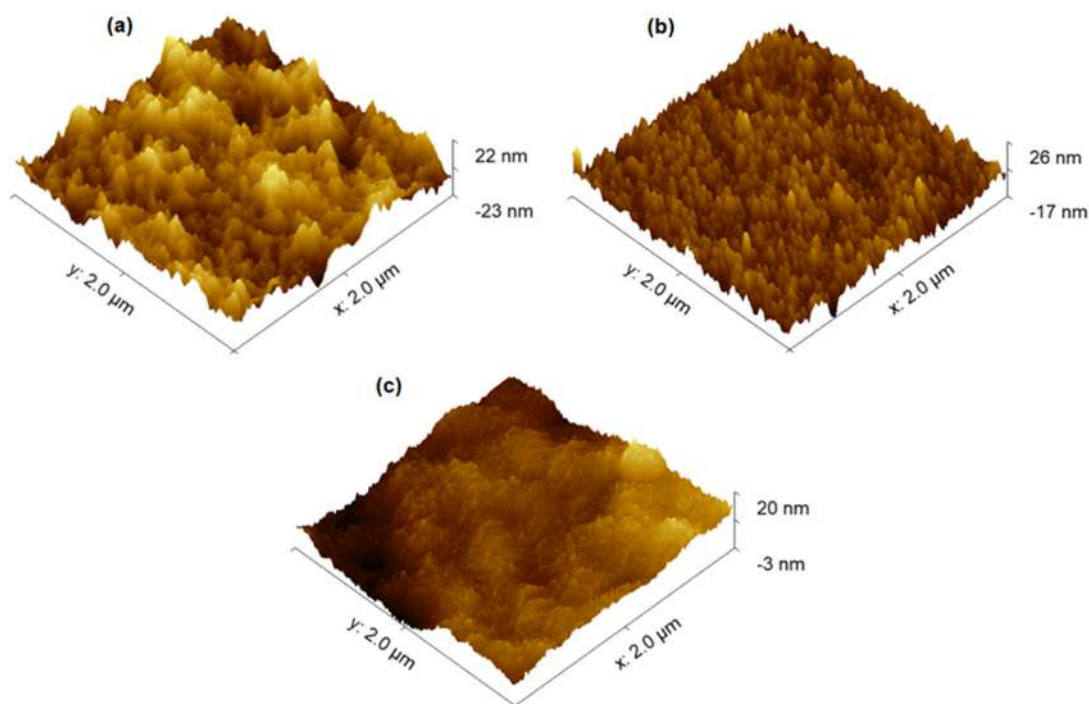


Fig 2. AFM images of (a) ZnO, (b) CZO, and (c) AZO thin film

Table 3. Grain size, average roughness, and RMS roughness of ZnO, AZO, and CZO thin film

Sample	Grain size (nm)	Average roughness (nm)	RMS roughness (nm)
ZnO	36.68	2.02	2.59
CZO	51.95	1.93	2.45
AZO	29.95	0.54	0.69

Fig. 3 shows the optical transmittance of ZnO, AZO, and CZO within the wavelength ranging from 200–1000 nm. Generally, all samples exhibit around 80–90% transmittance in the visible light region. This property is particularly useful for optoelectronics applications such as a transparent electrodes in solar cells. However, the transmittance of AZO and CZO in the visible light region was lower. This could be explained using the structure disorder caused by the incorporation of dopants. After the doping process, ZnO has a higher amount of structural disorder. These defects would increase the optical scattering of ZnO so that the doped samples will have lower transmittance than pristine ZnO. Since structural defects contribute to optical scattering, a higher concentration of defects in a structure indicates poor optical transmittance [18]. This result also agrees with the XRD data, where AZO with the highest amount of disorder in its structure has the lowest transmittance among other samples.

Fig. 3 also reveals the blue shift in both AZO and CZO, where the absorption edge shifted toward a shorter wavelength. After Al doping, the edge shifted from 360 to 300 nm, while Cu doping caused it to shift to 320 nm. This shift would later play a role in determining the bandgap and evaluating the charge carrier concentration. These findings are in agreement with studies related to absorption edge shift in ZnO thin film after Al doping [31] and Cu doping [30].

From transmittance data, the optical band gap could be calculated by using Eq. (8).

$$(\alpha h\nu)^2 = B(h\nu - E_g) \quad (8)$$

where α is the absorption coefficient, B is the edge width parameter, $h\nu$ is the photon energy, and $n = 2$ (for semiconductor band gap). The absorption coefficient (α) of the thin film samples could be obtained by using this relation (9).

$$\alpha = \frac{1}{t} \ln\left(\frac{1}{T}\right) \quad (9)$$

in which t is the thickness of the thin film. Thin-film bandgap could be acquired from the linear extrapolation of $(\alpha h\nu)^2$ with $h\nu$.

As shown in Fig. 4, the optical band gaps of ZnO, AZO, and CZO thin films are 3.26, 3.28, and 3.23 eV. In the thin film, ZnO has a lower band gap than bulk ZnO (3.37 eV). The lower value is due to the heat treatment and the structural defects formed during the fabrication process [19]. For doped samples, Al doping increased the optical band gap of ZnO, while Cu doping lowered the band gap. The shifting of the band gap in ZnO thin film doped with transition metal could be explained by the Burstein-Moss effect. Al^{3+} and Cu^{2+} ions introduced charge carriers into ZnO, which would then modify the band gap.

In AZO, the Al atom, which has more valence electrons than Zn, would introduce more charge carrier concentration in the ZnO thin film. These carriers would

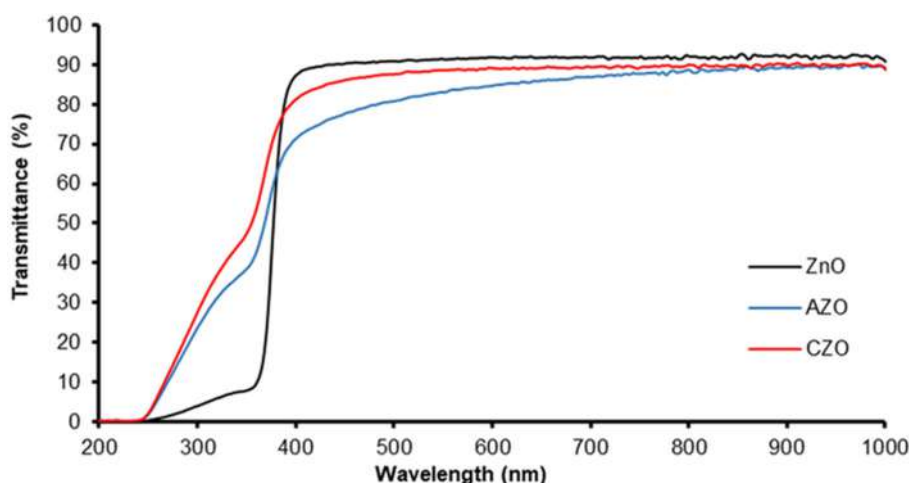


Fig 3. Optical transmittance of ZnO, AZO, and CZO thin film

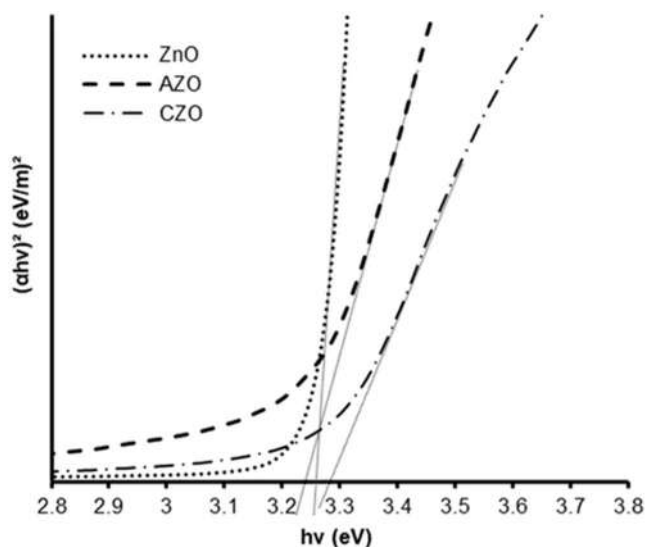


Fig 4. Optical band gap of ZnO, AZO, and CZO

create sites near the conduction band, which would consequently draw the Fermi energy closer to the conduction band, thus increasing the band gap [28]. This also explains the blue shift in absorption edge, where the shift toward a lower wavelength suggests that it would require higher energy to induce a photocatalytic effect in AZO. Likewise, the Cu atom in CZO would create more sites near the valence band and lower the band gap. The band gap shift also proves that the doping process was successful. Additionally, Bakhtiargonbadi et al. suggested that Cu_{Zn}^+ donor-acceptor played a role in lowering the ZnO bandgap, along with $\text{V}_{\text{O}}^{\bullet\bullet}$, $\text{V}_{\text{Zn}}^{\bullet\bullet}$ and $\text{Zn}_i^{\bullet\bullet}$ [29].

■ CONCLUSION

ZnO thin films doped with 1% Al and Cu were fabricated using sol-gel spin coating, and the structure, morphology, and optical properties of the thin films were then analyzed. The diffraction pattern of thin films confirmed the structure of hexagonal wurtzite. Texture coefficient calculation showed that each sample tends to crystallize in a different orientation, particularly during heat treatment. Al and Cu doping resulted in lowered crystal size (D), average surface roughness, and transmittance, as well as heightened lattice strain (ϵ) and dislocation density (ρ). Moreover, shifts in band gaps have been observed according to the type of dopants. ZnO, AZO, and CZO have band gap values of 3.26, 3.28, and 3.23 eV, respectively. In conclusion, the slight

addition of 1 atomic % transition metal (Al and Cu) proved to greatly influence the structure, morphology, and optical properties of ZnO thin film.

■ ACKNOWLEDGMENTS

No funding was used to support this research. We thank Research Center for Advanced Materials-BRIN for the facilities and characterization.

■ AUTHOR CONTRIBUTIONS

Faras Afifah: Writing the original draft and conducted the experiment. Arif Tjahjono: Formal analysis, supervision. Aga Ridhova: Conducted the AFM characterization. Pramitha Yuniar Diah Maulida: Formal analysis. Alfian Noviyanto: formal analysis, visualization, writing - review & editing. Didik Aryanto: Conceptualization, methodology, conducted the experiment, formal analysis, visualization, supervision, writing - review & editing.

■ REFERENCES

- [1] Aryanto, D., Maulana, R.M., Sudiro, T., Masturi, M., Wismogroho, A.S., Sebayang, P., Ginting, M., and Marwoto, P., 2017, Effect of post-thermal annealing on the structural of ZnO thin films deposited using sol-gel spin-coating method, *AIP Conf. Proc.*, 1862, 030045.
- [2] Aryanto, D., Jannah, W.N., Masturi, M., Sudiro, T., Wismogroho, A.S., Sebayang, P., Sugianto, S., and Marwoto, P., 2017, Preparation and structural characterization of ZnO thin films by sol-gel method, *J. Phys.: Conf. Ser.*, 755, 012025.
- [3] Giri, P., and Chakrabarti, P., 2016, Effect of Mg doping in ZnO buffer layer on ZnO thin film devices for electronic applications, *Superlattices Microstruct.*, 93, 248–260.
- [4] Sirelkhatim, A., Mahmud, S., Seeni, A., Mohamad Kaus, N.H., Ann, L.C., Mohd Bakhori, S.K., Hasan, H., and Mohamad, D., 2015, Review on zinc oxide nanoparticles: Antibacterial activity and toxicity mechanism, *Nano-Micro Lett.*, 7 (3), 219–242.
- [5] Aryanto, D., Marwoto, P., Sudiro, T., Wismogroho, A.S., and Sugianto, S., 2019, Growth of a-axis-oriented Al-doped ZnO thin film on glass substrate

- using unbalanced DC magnetron sputtering, *J. Phys.: Conf. Ser.*, 1191, 012031.
- [6] Aryanto, D., Hastuti, E., Taspika, M., Anam, K., Isnaeni, I., Widayatno, W.B., Wismogroho, A.S., Marwoto, P., Nuryadin, B.W., Noviyanto, A., and Sugianto, S., 2020, Characteristics and photocatalytic activity of highly *c*-axis-oriented ZnO thin films, *J. Sol-Gel Sci. Technol.*, 96 (1), 226–235.
- [7] Nulhakim, L., Makino, H., Kishimoto, S., Nomoto, J., and Yamamoto, T., 2017, Enhancement of the hydrogen gas sensitivity by large distribution of *c*-axis preferred orientation in highly Ga-doped ZnO polycrystalline thin films, *Mater. Sci. Semicond. Process.*, 68, 322–326.
- [8] Yathisha, R.O., and Nayaka, Y.A., 2020, Effect of solvents on structural, optical and electrical properties of ZnO nanoparticles synthesized by microwave heating route, *Inorg. Chem. Commun.*, 115, 107877.
- [9] Zhang, W., Gan, J., Li, L., Hu, Z., Shi, L., Xu, N., Sun, J., and Wu, J., 2018, Tailoring of optical and electrical properties of transparent and conductive Al-doped ZnO films by adjustment of Al concentration, *Mater. Sci. Semicond. Process.*, 74, 147–153.
- [10] Sahoo, B., Pradhan, S.K., Mishra, D.K., Sahoo, S.K., Nayak, R.R., and Behera, D., 2021, Mutual effect of solvent and Fe-In codoping on structural, optical and electronic properties of ZnO thin films prepared by spray pyrolysis technique, *Optik*, 228, 166134.
- [11] Ge, Z., Wang, C., Chen, T., Chen, Z., Wang, T., Guo, L., Qi, G., and Liu, J., 2020, Preparation of Cu-doped ZnO nanoparticles via layered double hydroxide and application for dye-sensitized solar cells, *J. Phys. Chem. Solids*, 150, 109833.
- [12] Ou, S.L., Lai, F.M., Yuan, L.W., Cheng, D.L., and Kao, K.S., 2016, Characterization of Al-doped ZnO transparent conducting thin film prepared by off-axis magnetron sputtering, *J. Nanomater.*, 2016, 6250640.
- [13] Nimbalkar, A., and Patil, M., 2017, Synthesis of highly selective and sensitive Cu-doped ZnO thin film sensor for detection of H₂S gas, *Mater. Sci. Semicond. Process.*, 71, 332–341.
- [14] Alatawi, N.M., Saad, L.B., Soltane, L., Moulahi, A., Mjejri, I., and Sediri, F., 2021, Enhanced solar photocatalytic performance of Cu-doped nanosized ZnO, *Polyhedron*, 197, 115022.
- [15] Marwoto, P., Wibowo, E., Suprayogi, D., Sulhadi, S., Aryanto, D., and Sugianto, S., 2016, Properties of ZnO:Ga thin films deposited by dc magnetron sputtering: Influence of Ga-doped concentrations on structural and optical properties, *Am. J. Appl. Sci.*, 13 (12), 1394–1399.
- [16] Aryanto, D., Hastuti, E., Husniya, N., Sudiro, T., and Nuryadin, B.W., 2018, Synthesis, characterization, and photocatalytic properties of nanocrystalline NZO thin films, *J. Phys.: Conf. Ser.*, 985, 012025.
- [17] Koresh, I., and Amouyal, Y., 2017, Effects of microstructure evolution on transport properties of thermoelectric nickel-doped zinc oxide, *J. Eur. Ceram. Soc.*, 37 (11), 3541–3550.
- [18] Asikuzun, E., Ozturk, O., Arda, L., and Terzioglu, C., 2018, Preparation, growth and characterization of nonvacuum Cu-doped ZnO thin films, *J. Mol. Struct.*, 1165, 1–7.
- [19] Ambedkar, A.K., Singh, M., Kumar, V., Kumar, V., Singh, B.P., Kumar, A., and Gautam, Y.K., 2020, Structural, optical and thermoelectric properties of Al-doped ZnO thin films prepared by spray pyrolysis, *Surf. Interfaces*, 19, 100504.
- [20] Kathwate, L.H., Umadevi, G., Kulal, P.M., Nagaraju, P., Dubal, D.P., Nanjundan, A.K., and Mote, V.D., 2020, Ammonia gas sensing properties of Al doped ZnO thin films, *Sens. Actuators, A*, 313, 112193.
- [21] Wang, D., Zhou, J., and Liu, G., 2009, The microstructure and photoluminescence of Cu-doped ZnO nano-crystal thin films prepared by sol-gel method, *J. Alloys Compd.*, 487 (1-2), 545–549.
- [22] Al Farsi, B., Souier, T.M., Al Marzouqi, F., Al Maashani, M., Bououdina, M., Widatallah, H.M., and Al Abri, M., 2021, Structural and optical properties of visible active photocatalytic Al doped ZnO nanostructured thin films prepared by dip coating, *Opt. Mater.*, 113, 110868.

- [23] de Lara Andrade, J., Oliveira, A.G., Mariucci, V.V.G., Bento, A.C., Companhoni, M.V., Nakamura, C.V., Lima, S.M., da Cunha Andrade, L.H., Moraes, J.C.G., Hechenleitner, A.A.W., Pineda, E.A.G., and de Oliveira, D.M.F., 2017, Effects of Al³⁺ concentration on the optical, structural, photocatalytic and cytotoxic properties of Al-doped ZnO, *J. Alloys Compd.*, 729, 978–987.
- [24] Ali, G.A., Emam-Ismail, M., El-Hagary, M., Shaaban, E.R., Moustafa, S.H., Amer, M.I., and Shaban, H., 2021, Optical and microstructural characterization of nanocrystalline Cu doped ZnO diluted magnetic semiconductor thin film for optoelectronic applications, *Opt. Mater.*, 119, 111312.
- [25] Hsu, C.H., Geng, X.P., Huang, P.H., Wu, W.Y., Zhao, M.J., Zhang, X.Y., Huang, Q.H., Su, Z.B., Chen, Z.R., Lien, S.Y., and Zhu, W.Z., 2021, High doping efficiency Al-doped ZnO films prepared by co-injection spatial atomic layer deposition, *J. Alloys Compd.*, 884, 161025.
- [26] Istrate, A.I., Mihalache, I., Romanitan, C., Tutunaru, O., Gavrilă, R., and Dediu, V., 2021, Copper doping effect on the properties in ZnO films deposited by sol-gel, *J. Mater. Sci.: Mater. Electron.*, 32 (4), 4021–4033.
- [27] Hong, M.H., Choi, H., Shim, D.I., Cho, H.H., Kim, J., and Park, H.H., 2018, Study of the effect of stress/strain of mesoporous Al-doped ZnO thin films on thermoelectric properties, *Solid State Sci.*, 82, 84–91.
- [28] Mondal, S., Bhattacharyya, S.R., and Mitra, P., 2013, Effect of Al doping on microstructure and optical band gap of ZnO thin film synthesized by successive ion layer adsorption and reaction, *Pramana*, 80 (2), 315–326.
- [29] Bakhtiargonbadi, F., Esfahani, H., Moakhar, R.S., and Dabir, F., 2020, Fabrication of novel electrospun Al and Cu doped ZnO thin films and evaluation of photoelectrical and sunlight-driven photoelectrochemical properties, *Mater. Chem. Phys.*, 252, 123270.
- [30] Jongnavakit, P., Amornpitoksuk, P., Suwanboon, S., and Ndiege, N., 2012, Preparation and photocatalytic activity of Cu-doped ZnO thin films prepared by the sol-gel method, *Appl. Surf. Sci.*, 258 (20), 8192–8198.
- [31] Yang, S., Gu, H., and Huang, A., 2021, Effect of oxygen partial pressure on microstructure, optical and electrical property of C-Al co-doped ZnO films, *Mater. Sci. Semicond. Process.*, 133, 105946.

Carbon Paste Electrode Modified by Dibenzo-18-crown-6 for the Determination of Paracetamol Using Differential Pulse Voltammetry Technique

Irdhawati Irdhawati*, Ni Ketut Shinta Mas Methaninditya, and Anak Agung Bawa Putra

Department of Chemistry, Faculty of Mathematics and Natural Sciences, Udayana University,
Kampus Bukit Jimbaran, Kuta Selatan, Badung 80361, Bali, Indonesia

* Corresponding author:

email: irdhawati@unud.ac.id

Received: April 27, 2022

Accepted: November 17, 2022

DOI: 10.22146/ijc.74393

Abstract: The fabrication, optimization and validation of measurement using a modified carbon paste electrode (CPE) with dibenzo-18-crown-6 were carried out for the determination of paracetamol in commercial products. The pH, dibenzo-18-crown-6 concentration in carbon paste, and scan rate parameters were optimized. Validation of the measurement was observed from linear concentration range, LoD, LoQ, precision, and percentage of the recovery. The result showed that the optimum pH was at 2, the optimum concentration of dibenzo-18-crown-6 in carbon paste was 0.6%, optimum scan rates were 35 mV/s for CPE, and increased to 50 mV/s using modified CPE. The linear concentration range for CPE was obtained at 10-300 μM with LoD and LoQ of 28.88 and 96.28 μM , respectively. Meanwhile, CPE modified with dibenzo-18-crown-6 gave wider linear concentration range at 1-700 μM with LoD and LoQ of 52.36 and 174.53 μM , respectively. The CPE and modified CPE had good precision, with Horwitz ratio values of less than two. The percentage of recovery for two samples with three replicates measurements was obtained $(89.81 \pm 1.38)\%$ and $(108.02 \pm 0.42)\%$ for samples A and B, respectively. Dibenzo-18-crown-6 modified CPE was used for the determination of paracetamol in both samples yielding 97-98% compared with the paracetamol composition on its labels.

Keywords: carbon paste electrode; dibenzo-18-crown-6; differential pulse voltammetry; paracetamol

■ INTRODUCTION

The methods used in drug analysis are very diverse. Various methods for determination of drugs in biological samples (urine, blood, and sweat) and pharmaceutical formulations that can be used include UV spectrophotometry, High-Performance Thin Layer Chromatography (HPTLC) Spectrophotodensitometry, High-Performance Liquid Chromatography (HPLC), Liquid Chromatography-Mass Spectrometry (LC-MS), Fourier Transform Infra-Red (FTIR), and voltammetry methods [1-6]. Voltammetry is a method in electroanalytical chemistry based on the oxidation-reduction reaction of electroactive species on the surface of the electrode. The resulting current response is proportional to the concentration of the analyte in the solution [7]. Various techniques of the voltammetry

method can be used to determine drugs' content in a sample, including differential pulse voltammetry (DPV).

The performance of the voltammetry method is greatly influenced by the working electrode materials. The most used electrode materials are mercury (Hg), carbon (C), or precious metals such as platinum (Pt) and gold (Au). Carbon-based electrodes are currently widely developed in the electroanalysis field because they have several advantages, i.e., wide potential range, low background current, cheap, inert, and suitably used in various sensors. One type of carbon-based electrode is the carbon paste electrode. The electrode is easily made at a low cost, easy occur exchanges electrons on its surface and can be modified with various kinds of materials [8]. The previous research showed many compounds could be used as a modifier in carbon paste

electrodes in the determination of drugs, including anthraquinone, nanoparticles ferrocene, poly-*L*-leucine, zirconium oxide (ZrO_2), and crown ether [9-13]. The use of crown ether in the modification of carbon paste can speed up the electron transfer rate due to the adsorption process or form of complex compounds. Crown ether is one of the macrocyclic whose oxygen atoms as donor electrons in the formation of complex compounds. Crown ether can form a stable complex compound with alkali metal ions and protonated amine in the gas and solution phase [14]. It shows crown ether is widely used as a modifier in the determination of drugs in pharmaceutical formulations, including paracetamol.

Determination of paracetamol can be carried out by the voltammetry method because paracetamol can be oxidized through the transfer process of two electrons and two protons to form an unstable oxidized product of *N*-acetyl-*p*-quinone imine (NAPQI) [15]. The oxidation process of paracetamol is affected by pH, where the oxidation reaction of paracetamol produces an H^+ ion. If the amount of H^+ formed increase, then the pH of the solution decrease and the product of the reaction will turn back and becomes reactant. Therefore, a buffer solution is needed to retain the reaction product.

This method shall be optimized and validated to determine the performance of the modified working electrode in the identification of the analyte. The validation method gives proof to the measured parameters by testing objectively in a laboratory and has fulfilled requirements that have been determined according to the intended use [16]. In this research, the modification of the carbon paste electrode with crown ether for the determination of paracetamol was carried out by the DPV technique. Carbon paste was modified with crown ether to produce electrodes having high sensitivity or low detection limit in the determination of paracetamol in commercial samples.

■ EXPERIMENTAL SECTION

Materials

All of the reagents were analytical grade without further purification. Paracetamol, KCl, graphite powder (dark grayish black powder, particle size pass 45 μm),

crown ether (dibenzo-18-crown-6), NaOH, and liquid paraffin were purchased from Wako. $K_3Fe(CN)_6$, $K_4Fe(CN)_6 \cdot 3H_2O$, acetone, H_3PO_4 85%, CH_3COOH 100%, and H_3BO_3 were obtained from Merck. On the other hand, HCl 37% was produced from Mallinckrodt while filter paper and double distilled water were purchased from Otsuka. Samples A and B were commercial paracetamol tablets of different brands, bought from a chemist.

Instrumentation

Potentiostat Ingsens 1030, 12 V DC adapter, Ag/AgCl reference electrode (0.1 M KCl), and platinum coil electrode with a diameter 0.5 mm (Nilaco) were used as the counter electrode. Besides, analytical balance (Ohaus PX224), magnetic stirrer (Thermoline), copper wire diameter 1.0 mm (Nilaco), Teflon tube with inner diameter 2.0 mm, pH meter (WalkLAB HP900), agate mortar, and laboratory glass equipment were used in this work.

Procedure

Several conditions can affect the electrochemical currents, such as pH, and the concentration of the modifier. All the measurements were recorded using a potentiostat Ingsens 1030 with three electrodes system by DPV technique at room temperature.

pH optimization

Copper wire (Cu) 7 cm in length was inserted into the Teflon tube as a working electrode body, with around ± 5 mm space at the bottom of the tube for inserting carbon paste. A 100 mg graphite and 35 μL liquid paraffin were mixed gently in an agate mortar until a homogeneous carbon paste formed. Carbon paste was inserted into the space at the bottom of the working electrode (CPE). The surface of CPE was smoothed by polishing on wax paper. Determination of optimum pH was carried out by measuring the current of paracetamol standard solution 1.0 mM, dissolved in Britton Robinson buffer solution in various pH. The pH of 0.1 M Britton Robinson buffer solution was adjusted to 1.0; 1.5; 2.0; 2.5; 3.0; 4.0; 5.0; 6.0; 7.0; and 8.0 by adding HCl 0.1 M or NaOH 0.1 M. Measurement current for each solution

was conducted using a potentiostat with three electrodes system, i.e., CPE as working electrode, Ag/AgCl as reference electrode, and Pt coil as a counter electrode by differential pulse voltammetry technique.

Crown ether concentration optimization

Graphite powder and liquid paraffin were mixed with various concentrations of crown ether (dibenzo-18-crown-6), i.e., 0.0, 0.2, 0.4, 0.5, 0.6, 0.7, 0.8, 1.2, 1.6, and 2.2% from the total mass of graphite and dibenzo-18-crown-6. The modified carbon paste was inserted into the working electrode body, and the surface was smoothed. CPE modified by dibenzo-18-crown-6 was dipped in a voltammeter cell containing 10.0 mL of paracetamol 1.0 mM at optimum pH, then connected to a potentiostat for measuring peak current at a potential range of 0.0–1.2 V with scan rate 50 mV/s.

Scan rate optimization

The peak current of a standard solution of paracetamol 1.0 mM was measured with various scan rates, starting from 20, 25, 30, 35, 40, 45, 50, 55, to 60 mV/s at potential windows between 0.0–1.2 V. Measurement peak current using CPE and modified CPE with dibenzo-18-crown-6 was conducted at optimum concentration.

Determination of linear concentration range

The stock solution of paracetamol was diluted in the range concentration of 1–950 μM and then the electrochemical current was measured using CPE and modified CPE with dibenzo-18-crown-6 at pH and scan rate optimum with three repetitions. The current measured on the y-axis is plotted with the concentration solution on the x-axis, to obtain the linear regression equation $y = a + bx$ with R^2 close to 1.00.

Determination of limit of detection (LoD) and limit of quantitation (LoQ)

LoD and LoQ values were calculated with the following Eq. (1–4):

$$S_{y/x} = \sqrt{\frac{\sum (y_i - \hat{y}_i)^2}{n-2}} \quad (1)$$

$$SB = \frac{S_{y/x}}{\sum (x_i - \bar{x})^2} \quad (2)$$

$$Y \text{ LoD} = Y_B + 3S_B \quad (3)$$

$$Y \text{ LoQ} = Y_B + 10S_B \quad (4)$$

where $S_{y/x}$ = standard deviation to the linear line, S_B = standard deviation of slope, and Y_B = response of blank solution. The values of LoD and LoQ were calculated using Eq. (3) and (4) [16].

Precision

The peak current of paracetamol 1.0 mM was measured using a different modified working electrode in the same composition, with 10 replicates. Measurements were carried out on different days for five days. The standard deviation (SD), relative standard deviation (RSD), and coefficient variance (CV) values were calculated. CV value compared with CV Horwitz to obtain the Horwitz ratio. Precision can be accepted if the Horwitz ratio is less than two [17].

Recovery

The measurements were carried out by measuring the electrochemical current of the sample and adding a known concentration of standard solution into the sample solution as a matrix. The percentage of recovery was calculated by Eq. (5):

$$\%R = \frac{CF - CU}{CA} \times 100 \quad (5)$$

where CF = concentration of sample and standard, CU = concentration of sample without adding standard, and CA = concentration of standard. The acceptable recovery value for analyte measurement with concentrations of g/L is in the range of 80 to 110% [18].

Samples preparation

Three tablets for each sample were weighed and crushed in a mortar, then dissolved with Britton-Robinson buffer at optimum pH. The mixture was filtered through a filter paper into a 50.0 mL flask to eliminate possible interference and diluted until the mark. The standard addition method was used for the analysis of two different samples containing paracetamol. A 2.0 mL was pipetted and transferred into a 10.0 mL flask, added standard paracetamol solution was in various volumes, and then diluted up to 10.0 mL by adding buffer solution. A blank solution was prepared in the same way without a standard solution.

RESULTS AND DISCUSSION

pH Optimization

For the oxidation reaction of paracetamol, DPV was used. The voltammograms were recorded in the potential from 0 to 750 mV. Fig. 1 shows the voltammograms of paracetamol 1 mM at a diverse buffer medium. The most intense anodic peak current was obtained at pH 2.0, while at pH below and above 2.0, the anodic peak current decreased. It indicated that the equilibrium of the reversible redox reaction of paracetamol to *N*-acetyl-*p*-quinone imine occurs at pH 2. The anodic peak potentials were shifted in a negative direction when pH values increased. This study showed that the electron transfer process of paracetamol was dependent on pH. Fig. 2 shows the oxidation reaction of paracetamol occurs in an acidic environment, producing an *N*-acetyl-*p*-quinone imine compound and two protons [19].

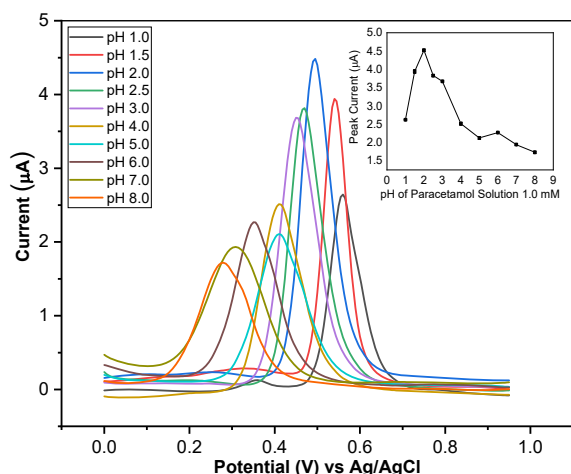


Fig 1. Differential pulse voltammogram of paracetamol 1 mM in various pH, and plot of pH vs its anodic peak current

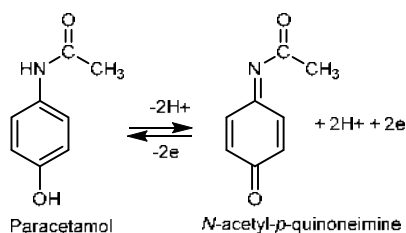


Fig 2. Oxidation reaction of paracetamol in an acidic environment

Crown Ether Concentration Optimization

DPV response of electrochemical oxidation of paracetamol in the presence of modifier dibenzo-18-crown-6 in carbon paste can be seen in Fig. 3. The anodic peak current for carbon paste without a modifier is very low at 1.021 μA . When the modifier was added, the anodic peak current increased up to the concentration of modifier 0.6% at 2.290 μA and then decreased. This shows that the modifier of dibenzo-18-crown-6 can improve the performance of the carbon paste electrode; the rate of electron transfer is faster compared to without the presence of a modifier. All peak currents at different modifier concentrations appeared at the same peak potential around 0.6 V. This is due to two benzene rings in dibenzo-18-crown-6 structure can reduce the polarity of crown ether and easily solvated with paraffin in carbon paste [20]. Dibenzo-18-crown-6 in carbon paste electrode can form a complex compound with a proton in paracetamol with oxygen atoms from the modifier, as shown in Fig. 4.

Scan Rate Optimization

The change in scan rates gives the different anodic peak currents. It was found that the optimum scan rates of paracetamol solution 1.0 mM using CPE were found at 35 mV/s and increased to 50 mV/s using CPE modified by dibenzo-18-crown-6. Moreover, the peak current was

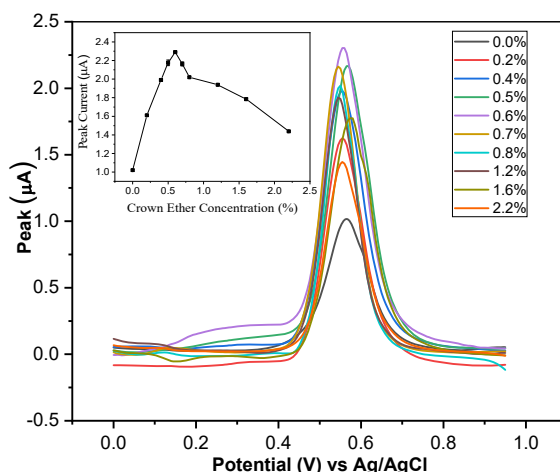


Fig 3. Differential pulse voltammograms in the optimization of dibenzo-18-crown-6 concentration

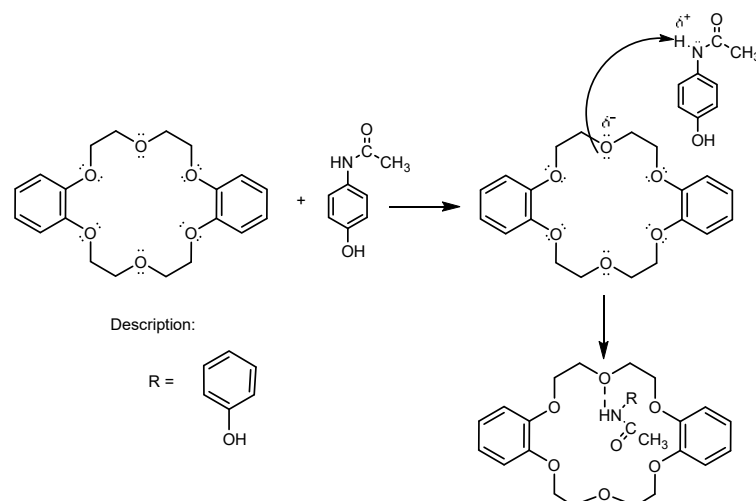


Fig 4. Reaction mechanism of dibenzo-18-crown-6 with paracetamol to form complex compound

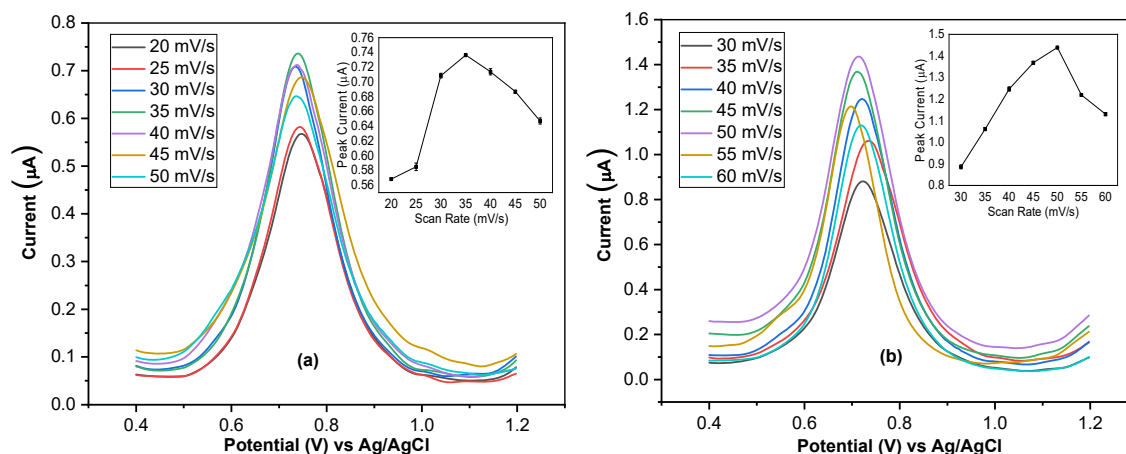


Fig 5. Differential pulse voltammograms of paracetamol 1.0 mM using CPE (a) and CPE modified by dibenzo-18-crown-6 (b) and plot between variation of scan rates and peak current (inset)

obtained at 0.736 μA and went up to 1.4391 μA by CPE and modified CPE, respectively. The result shows the addition of a modifier in carbon paste, the electron transfer rate of paracetamol at the surface of the working electrode becomes faster with a higher anodic peak current. Fig. 5 showed differential pulse voltammograms of paracetamol 1.0 mM in various scan rates.

Linear Concentration Range

Determination of linear concentration ranged using CPE and modified CPE with dibenzo-18-crown-6 in the measurement of anodic peak current was carried out in the concentration range of paracetamol 1–950 μM at optimum scan rate. Fig. 6(a-b) shows the voltammogram of peak current. Fig. 6(c) shows the linear regression

equation on the concentration range of 10–300 μM using CPE was $y = 0.0806 + 0.0051x$ with the correlation coefficient (R^2) value was 0.9947 and the linear regression equation on the concentration range of 1–700 μM using CPE modified by dibenzo-18-crown-6 was $y = 0.1126 + 0.0062x$ with the R^2 value was 0.9951. The result displayed the addition of dibenzo-18-crown-6 in carbon paste increased the anodic peak current response with better linearity and sensitivity.

Detection Limit (LoD) and Quantitation Limit (LoQ)

LoD and LoQ values were determined based on the data from a linear concentration range of 10–300 μM for the measurement using CPE and 1–700 μM for the

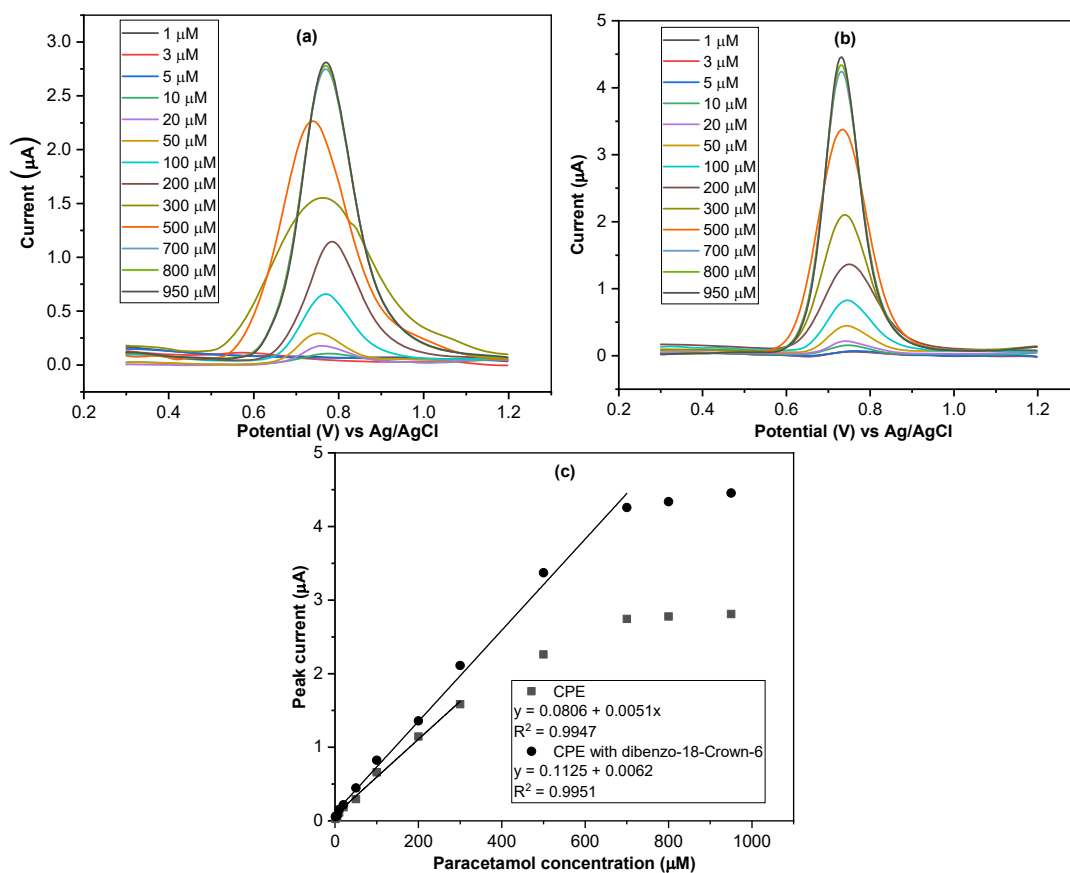


Fig 6. Differential pulse voltammograms of paracetamol with various concentration using CPE (a) and modified CPE with dibenzo-18-crown-6 (b), and linear regression line of paracetamol 10–300 μM by CPE and 1–700 μM by modified CPE with dibenzo-18-crown-6 (c)

measurement using CPE modified by dibenzo-18-crown-6. The values of LoD and LoQ for the measurement paracetamol using CPE were 28.88 and 96.28 μM , respectively, while for modified CPE were 52.36 and 174.53 μM , respectively. Dibenzo-18-crown-6 in carbon paste can increase the sensitivity of the measurement. Although the peak current of modified CPE was larger than CPE at the same concentration, the LoD and LoQ values of modified CPE were higher than CPE. This may be due to the large surface area of the working electrode, about 0.0314 cm^2 . The large surface area causes high noise so the signal and noise ratio becomes larger, and the standard error is large, thereby increasing the LoD and LoQ values.

Precision

The precision can be determined by repeated measurement of the peak current of paracetamol in

different concentrations using the same composition of working electrodes on different days. According to [17], a precise measurement has been established if the Horwitz ratio is less than two. Fig. 7(a) shows the Horwitz ratio value for paracetamol 50 μM by CPE, and CPE modified with dibenzo-18-crown-6 and CPE were 0.3354 and 0.2835, respectively. Fig. 7(b) shows the Horwitz ratio for paracetamol 100 μM was 0.2233 by CPE and 0.2196 by modified CPE. Both concentrations were conducted ten times. The precision of measurement standard paracetamol solution with CPE modified by dibenzo-18-crown-6 is smaller than CPE in paracetamol 50 and 100 μM . It shows the presence of dibenzo-18-crown-6 in carbon paste can increase the precision of the measurement.

Percent of Recovery

Percent of recovery was determined to find out the

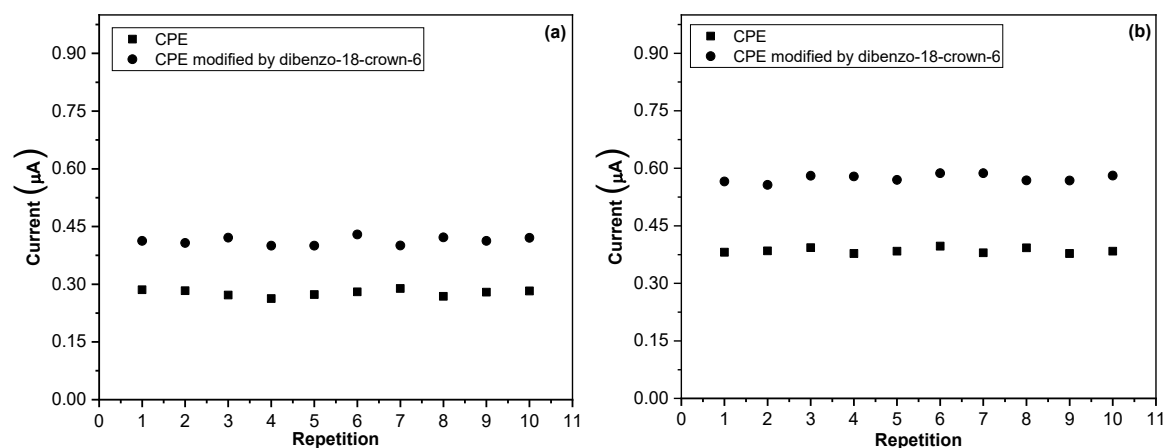


Fig 7. The peak current of ten times paracetamol measurement with concentration of 50 μM (a) and 100 μM (b)

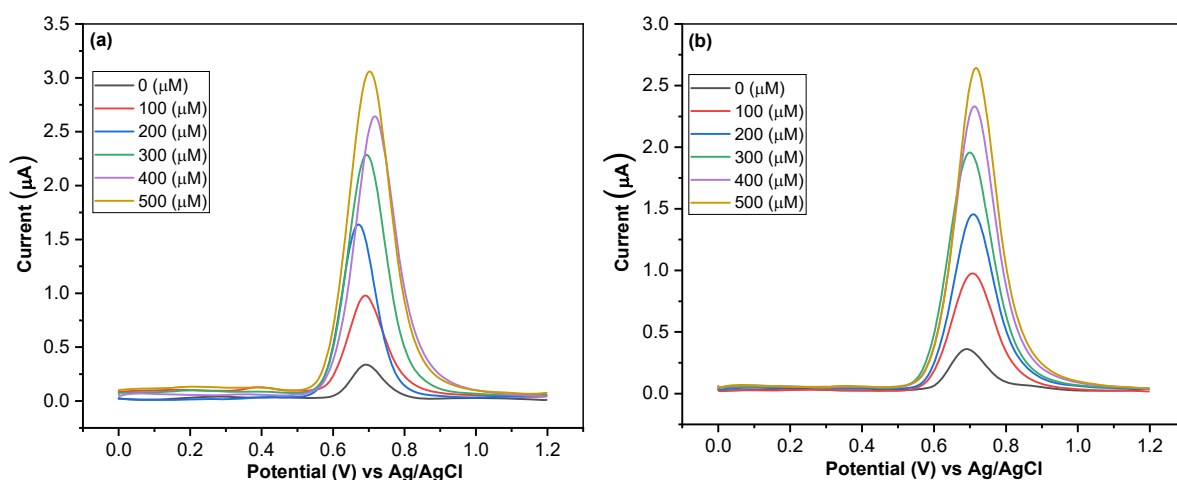
accuracy of measurement. The percent recovery values were $(89.81 \pm 1.38)\%$ in sample A and $(108.02 \pm 0.42)\%$ in sample B. The acceptable recovery is in the range of 80–110% [18]. Based on the results of recovery obtained for samples A and B, measurements have acceptable values by DPV technique using CPE modified by dibenzo-18-crown-6. Sample B has a recovery of more than 100% because the tablet contains paracetamol and caffeine. The presence of caffeine in the solution can produce electrochemical currents that interfere with paracetamol measurement using carbon material as a working electrode due to the overlapping signal with the oxidation of the background medium, resulting in low reproducible analysis.

Determination Paracetamol in Sample

To illustrate the reliability of the results obtained,

two commercial samples (A and B) were prepared, and measurements were conducted by the standard addition method. Sample A contains 500 mg paracetamol, and sample B contains 500 mg paracetamol and 65 mg caffeine. The regression line equations were found at $y = 0.3729 + 0.0063x$ with the value of $R^2 = 0.9962$ for sample A, meanwhile for sample B was obtained regression line equation $y = 0.3232 + 0.0055x$ with a value of $R^2 = 0.9986$. The voltammogram of the paracetamol standard solution and samples and the plot of paracetamol concentration vs its peak current can be seen in Fig. 8.

Paracetamol in sample A and sample B were calculated and found to be 493.2637 and 489.7067 mg/tablet, respectively. Both samples have a good agreement with the labeled value and result of measurement, which are listed in Table 1.



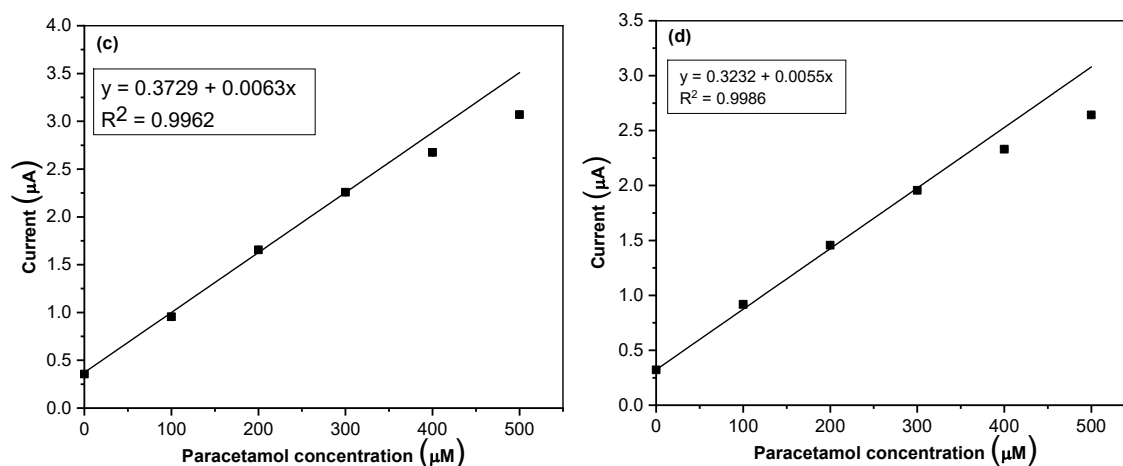


Fig 8. Voltammogram of measurement sample A (a) and sample B (b), and the plot of concentration paracetamol standard in the presence of sample A (c) and sample B (d) using DPV technique with CPE modified by dibenzo-18-crown-6

Table 1. Comparison of paracetamol mass measurement results with paracetamol mass on its labels

Sample	Paracetamol mass on its label (mg/tablet)	Paracetamol mass obtained by proposed method (mg/tablet)	Agreement (%)
A	500	493.3	98.65
B	500	489.7	97.94

■ CONCLUSION

The differential pulse voltammetry technique was applied to the study of paracetamol using CPE modified by dibenzo-18-crown-6. The highest peak current response was found at pH 2 in Britton-Robinson buffer 0.1 M, with 0.6% of modifier in carbon paste. The results of validity measurement were better using modified CPE compared with CPE. The application of CPE modified by dibenzo-18-crown-6 in the determination of paracetamol in commercial samples had a good agreement with its labeled.

■ ACKNOWLEDGMENTS

The authors thank to all members of the electroanalytical research group, Department of Chemistry, Faculty of Mathematics and Natural Sciences, Udayana University, for their help and cooperation.

■ AUTHOR CONTRIBUTIONS

Ni Ketut Shinta Mas Methaninditya conducted the experiment. Irdhawati and Anak Agung Bawa Putra supervised, wrote and revised the manuscript. All authors agreed to the final version of this manuscript.

■ REFERENCES

- [1] Tulandi, G.P., Sri, S., and Widya, A.L., 2015, Validation of analytical methods for determination of paracetamol levels in tablets by ultraviolet spectrophotometry (Indonesian), *Pharmacon*, 4 (4), 168–178.
- [2] Susilawan, I.P.N.A., Siaka, I.M., and Parwata, I.M.O.A., 2018, Validation of chemical analysis methods of paracetamol and phenylbutason in traditional medicinal products with HPTLC-spectrophotodensitometry (Indonesian), *Cakra Kimia*, 7 (1), 1–11.
- [3] Sarmento, Z.L.C., Rangdi, O.S.G., Olivia, S.G.R., Sena, B.M.C.D., and Dewi, K.N.M., 2020, Determination of paracetamol and caffeine levels using high performance liquid chromatography (HPLC) method (Indonesian), *Chakra Kimia*, 8 (2), 99–104.
- [4] Tanuja, S.B., Kumara Swamy, B.E., and Pai, K.V., 2017, Electrochemical determination of paracetamol in presence of folic acid at nevirapine modified carbon paste electrode: A cyclic

- voltammetric study, *J. Electroanal. Chem.*, 798, 17–23.
- [5] Damanik, A.N.T., 2019, Determination of paracetamol levels in tablets with trade names and generics by Fourier transform infra red (FTIR) spectrophotometry (Indonesian), *Thesis*, Pharmacy Study Program, University of North Sumatra, Medan.
- [6] Ayalew, M.E., and Ayitegeb, D.Y., 2021, Differential pulse voltammetric determination of paracetamol using activated glassy carbon electrode, *Am. J. Phys. Chem.*, 10 (2), 16–24.
- [7] Wang, J., 2001, *Analytical Electrochemistry*, 2nd Ed., Wiley-VCH, New York.
- [8] Wachid, M.R., and Setiarso, P., 2014, Preparation of bentonite modified carbon paste electrodes for the analysis of copper (II) metal with lead (II) and mercury (II) interfering ions by cyclic voltammetry stripping (Indonesian), *UJChem*, 3 (3), 93–103.
- [9] Amare, M., and Teklay, W., 2019, Voltammetric determination of paracetamol in pharmaceutical tablet samples using anthraquinone modified carbon paste electrode, *Cogent Chem.*, 5 (1), 1576349.
- [10] Salem, W.M., 2019, Sensitive determination of paracetamol using ferrocene nanoparticles by chitosan-functionalized-modified carbon paste electrode, *Egypt. J. Chem.*, 62 (4), 1079–1090.
- [11] Naik, T.S.S.K., Swamy, B.E.K., Ramamurthy, P.C., and Chetankumar, K., 2020, Poly(L-leucine) modified carbon paste electrode as an electrochemical sensor for the detection of paracetamol in presence of folic acid, *Mater. Sci. Energy Technol.*, 3 (1), 626–632.
- [12] Matt, S.B., Raghavendra, S., Shivanna, M., Sidlinganahalli, M., and Siddalingappa, D.M., 2021, Electrochemical detection of paracetamol by voltammetry techniques using pure zirconium oxide nanoparticle based modified carbon paste electrode, *J. Inorg. Organomet. Polym. Mater.*, 31 (2), 511–519.
- [13] Irdhawati, I., Manurung, M., and Septiawan, K.A., 2015, Voltammetric dopamine detection using crown ether modified carbon paste electrodes (dibenzo-18-crown-6) (Indonesian), *J. Kim. Mulawarman*, 12 (2), 68–74.
- [14] Melson, G.A., 1979, *Coordination Chemistry of Macrocyclic Compounds*, Plenum Press, New York.
- [15] Sadok, I., and Tyszczyk-Rotko, K., 2015, New, simple and sensitive voltammetric procedure for determination of paracetamol in pharmaceutical formulations, *Insights Anal. Electrochem.*, 1, 1.
- [16] Miller, J.N., and Miller, J.C., 2010, *Statistics and Chemometrics for Analytical Chemistry*, 6th Ed., Prentice Hall, Essex, England.
- [17] Horwitz, W., and Albert, R.J., 2006, The Horwitz ratio (HorRat): A useful index of method performance with respect to precision, *J. AOAC Int.*, 89 (4), 1095–1109.
- [18] AOAC International, 1998, *Peer-Verified Methods Program Manual Policies and Procedures*, Association of Official Analytical Chemists, Gaithersburg, MD, USA.
- [19] Mulyasuryani, A., Tjahjanto, R.T., and Andawiyah, R., 2019, Simultaneous voltammetric detection of acetaminophen and caffeine base on cassava starch-Fe₃O₄ nanoparticles modified glassy carbon electrode, *Chemosensors*, 7 (4), 49.
- [20] Irdhawati, I., Manurung, M., and Maulinasari, A., 2015, Modification of carbon paste electrode with crown ether (dibenzo-18-crown-6) for ascorbic acid analysis by differential pulse voltammetry, *ALCHEMY Jurnal Penelitian Kimia*, 11 (2), 175–191.

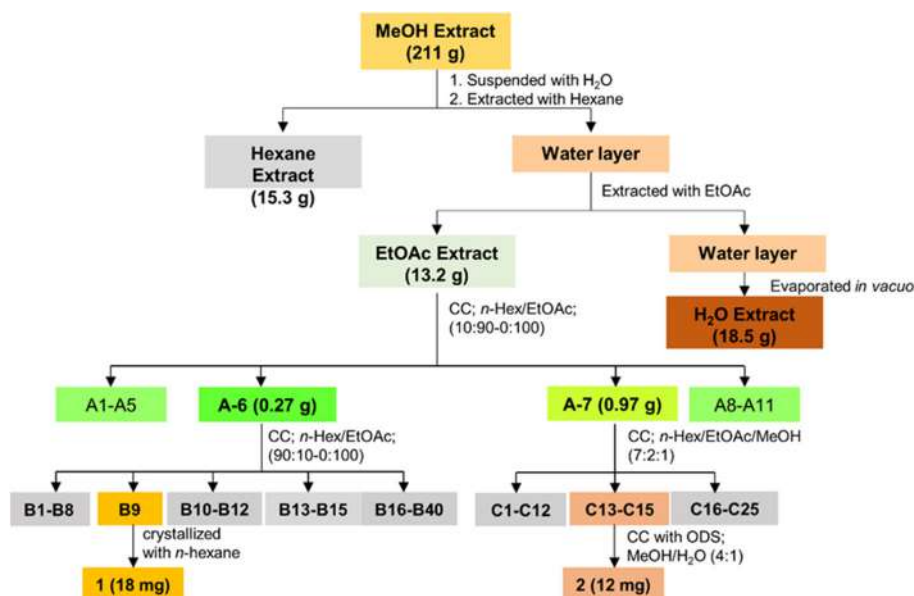
Supplementary Data

This supplementary data is a part of a paper entitled “Evaluation of the Antiplasmodial Properties of *Andrographis paniculata* (Burm.f.) and *Peperomia pellucida* (L.) Kunth”.

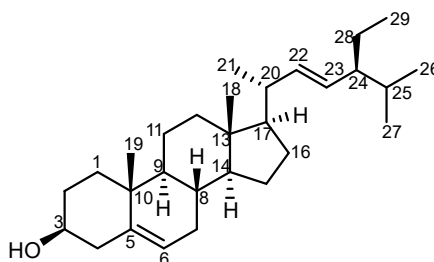
General information

Commercial grade solvents were used unless stated otherwise. Solvents for chromatography were distilled prior to use. Analytical thin layer chromatography (TLC) was performed on Kieselgel 60 F254 glass plates and Octa Desyl Silane (ODS) RP-18 (Merck). Spots were visualized by 10% sulfuric acid in ethanol. Silica column chromatography was performed on silica gel G60 (Merck) (230-400 mesh) and ODS RP-18.

Optical rotations were recorded with an ATAGO AP-300 polarimeter. InfraRed (IR) spectra were measured by using a PerkinElmer spectrum-100 FT-IR spectrometer in KBR. ^1H , ^{13}C and two-dimensional NMR spectra were measured with a JEOL JNM A-500 (500 MHz) spectrometer at 296 K. Chemical shifts (δ) are reported in parts per million (ppm) relative to the respective residual solvent peaks (CD_3OD : δ 4.78 in ^1H -NMR). Chemical shifts (δ) are reported in parts per million (ppm) relative to the respective residual solvent peaks (CDCl_3 : δ 7.26 in ^1H and 77.20 in ^{13}C -NMR; CD_3OD : δ 4.78 in ^1H -NMR and 49.20 in ^{13}C -NMR). The following abbreviations are used to indicate peak multiplicities: s singlet; d doublet; dd doublet of doublets; t triplet; m multiplet. Coupling constants (J) are reported in Hertz (Hz). Mass spectra were recorded using a Waters Xevo QTOF mass spectrometer.

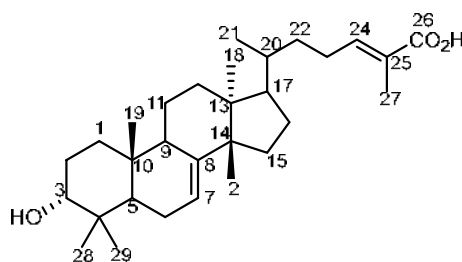


Scheme S1. Isolation procedures of compound 1-2



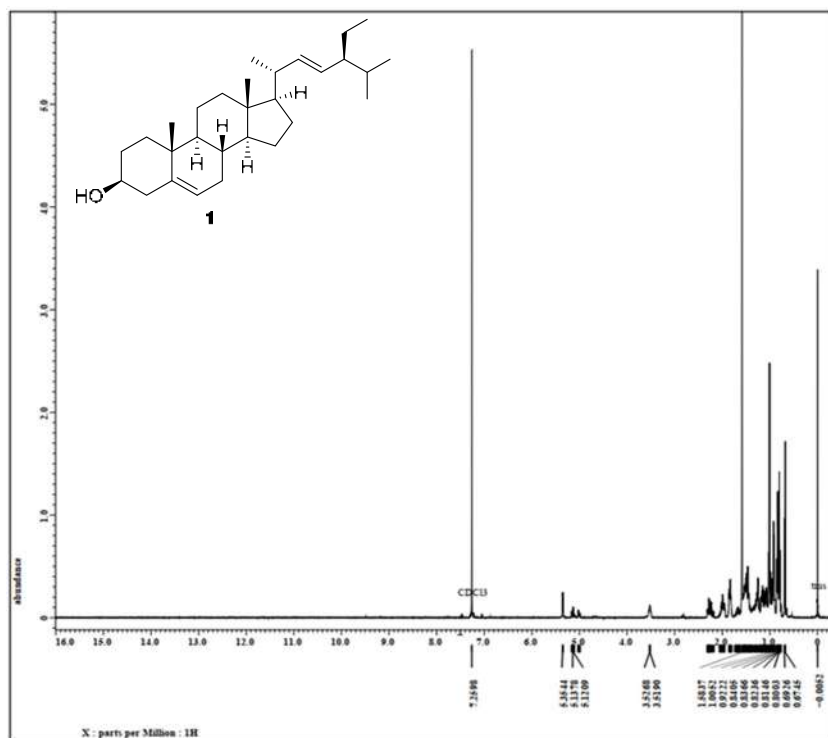
3 β -Hydroxy-24-ethyl-5,22-cholestadiene (1)

A white crystal, m.p 150–152 °C; $[\alpha]_D$ -38.6 (c 0.3, CHCl₃); IR (KBr) V_{\max} 3401, 2861 1457 and 1039 cm⁻¹; ¹H-NMR (500 MHz, Chloroform-d). δ 1.08 (m, 1H, H-1), 1.84 (m, 1H, H-1'), 1.49 (m, 1H, H-2), 1.81 (m, 1H, H-2'), 3.52 (m, 1H, H-3), 2.28 dd, $J = 2.0, 5.2$ Hz, 1H, H-4), 2.30 (dd, $J = 2.0, 5.2$ Hz, 1H, H-4'), 5.35 (d, $J = 5.2$ Hz, 1H, H-6), 1.54 (m, 1H, H-7), 1.96 (m, 1H, H-7'), 1.46 (m, 1H, H-8), 0.94 (m, 1H, H-9), 1.46 (m, 1H, H-11), 1.49 (m, 1H, H-11'), 1.15 (m, 1H, H-12), 1.95 (m, 1H, H-12'), 1.03 (s, 1H, H-14), 1.07 (m, 1H, H-15), 1.56 (m, 1H, H-15'), 1.26 (m, 1H, H-16), 1.67 (m, 1H, H-16'), 1.13 (m, 1H, H-17), 0.67 (s, 3H, H-18), 1.00 (s, 3H, H-19), 2.02 (m, 1H, H-20), 0.92 (d, $J = 9.5$ Hz, 1H, H-21), 5.16 (dd, $J = 8.5, 15.0$ Hz, 1H, H-22), 5.00 (dd, $J = 8.5, 15.0$ Hz, 1H, H-23), 1.53 (m, 1H, H-24), 1.45 (m, 1H, H-25), 0.84 (d, $J = 6.4$ Hz, 3H, H-26), 0.82 (d, $J = 6.1$ Hz, 3H, H-27), 1.15 (t, $J = 3.2$ Hz, 1H, H-28), 0.80 (t, $J = 6.0$ Hz, 1H, H-29); ¹³C-NMR (125 MHz, Chloroform-d). δ 37.4 (C-1), 31.8 (C-2), 72.0 (C-3), 42.5 (C-4), 140.9 (C-5), 121.9 (C-6), 32.1 (C-7), 21.3 (C-8), 50.3 (C-9), 36.7 (C-10), 21.3 (C-11), 39.9 (C-12), 42.5 (C-13), 56.9 (C-14), 24.5 (C-15), 28.4 (C-16), 56.1 (C-17), 12.1 (C-18), 19.5 (C-19), 40.7 (C-20), 21.2 (C-21), 138.5 (C-22), 129.5 (C-23), 51.4 (C-24), 31.8 (C-25), 21.3 (C-26), 19.1 (C-27), 25.6 (C-28), 12.2 (C-29); HR-TOFMS m/z 413.3748 [M+H]⁺, (calculated for C₂₉H₄₈O, m/z 412.3704). In agreement with published data [1].

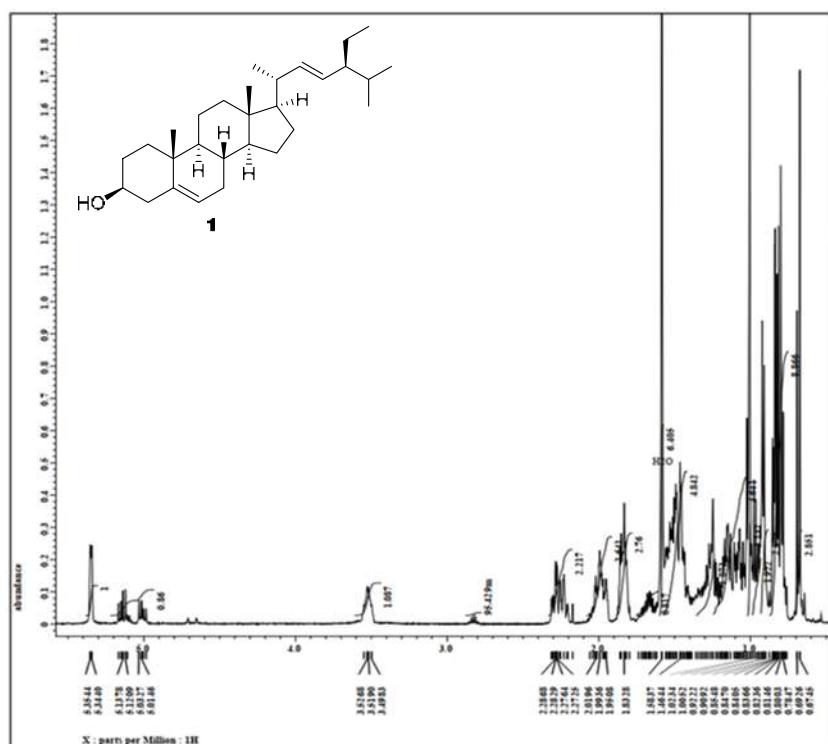
**3 β -hydroxy-9-lanosta-7,24E-dien-26-oic acid (2)**

A white crystal, m.p 162–165 °C; $[\alpha]_D$ +15.6 (c 0.3, EtOH); IR (KBr) V_{\max} 3241, 1701 1633 and 1120 cm⁻¹; ¹H-NMR (500 MHz, Methanol-d). δ 1.54 (m, 2H, H-1), 1.59 (m, 2H, H-2), 3.49 (dd, $J = 4.0, 12.0$ Hz, 1H, H-3), 1.45 (m, 1H, H-5), 1.85 (m, 2H, H-6), 5.26 (dd, $J = 3.0, 6.5$ Hz, 1H, H-7), 2.18 (m, 1H, H-9), 1.40 (m, 2H, H-11), 1.32 (m, 2H, H-12), 1.40 (m, 2H, H-15), 1.96 (m, 2H, H-16), 1.47 (m, 1H, H-17), 0.96 (s, 3H, H-18), 0.89 (s, 3H, H-19), 1.61 (s, 1H, H-20), 0.85 (d, $J = 6.5$ Hz, 3H, H-21), 1.51 (m, 2H, H-22), 2.02 (m, 2H, H-23), 5.98 (t, $J = 7.8$ Hz, 3H, H-24), 2.48 (s, 3H, H-27), 1.08 (s, 3H, H-28), 0.73 (s, 3H, H-29), 1.70 (s, 3H, H-30); ¹³C-NMR (125 MHz, Methanol-d). δ 35.5 (C-1), 28.1 (C-2), 77.1 (C-3), 38.8 (C-4), 48.5 (C-5), 23.1 (C-6), 119.6 (C-7), 147.4 (C-8), 48.4 (C-9), 35.8 (C-10), 22.8 (C-11), 33.4 (C-12), 43.5 (C-13), 52.7 (C-14), 34.7 (C-15), 28.5 (C-16), 53.3 (C-17), 24.7 (C-18), 17.1 (C-19), 35.9 (C-20), 18.4 (C-21), 35.0 (C-22), 25.5 (C-23), 144.3 (C-24), 128.6 (C-25), 171.8 (C-26), 12.6 (C-27), 29.5 (C-28), 23.7 (C-29), 30.8 (C-30); HR-TOFMS m/z 455.3571 [M-H]⁻, (calculated for C₃₀H₄₈O₃, m/z 456.3503). In agreement with published data [2].

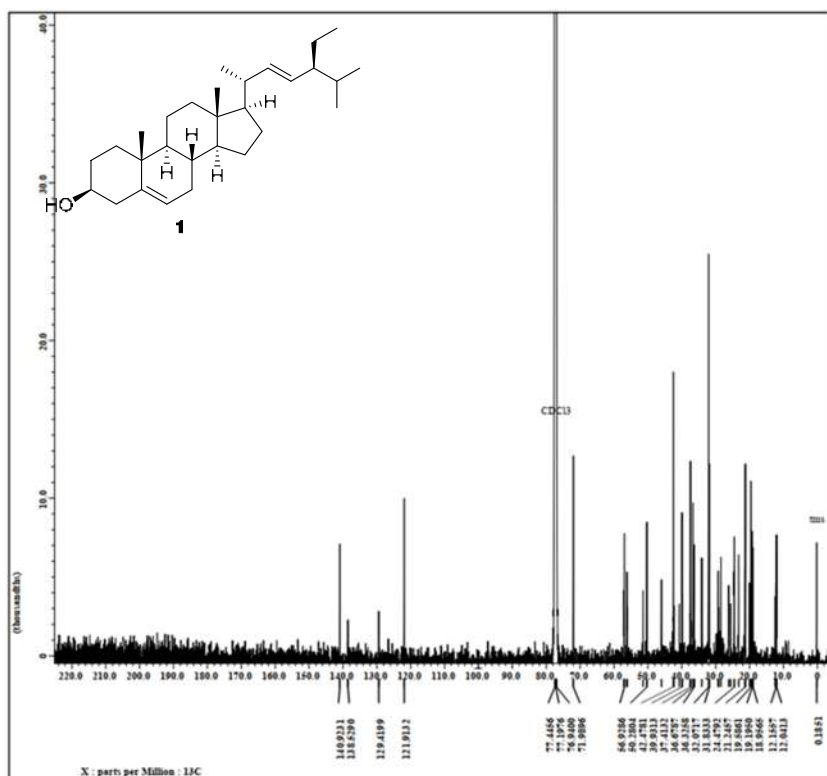
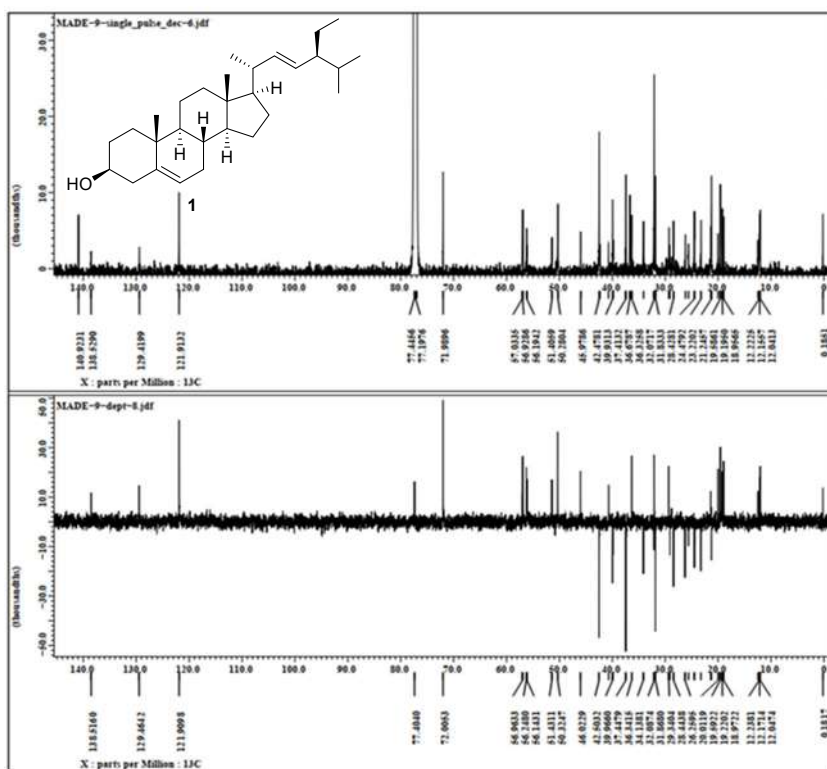
Nuclear Magnetic Resonance (NMR) of Isolated Compound 1-2

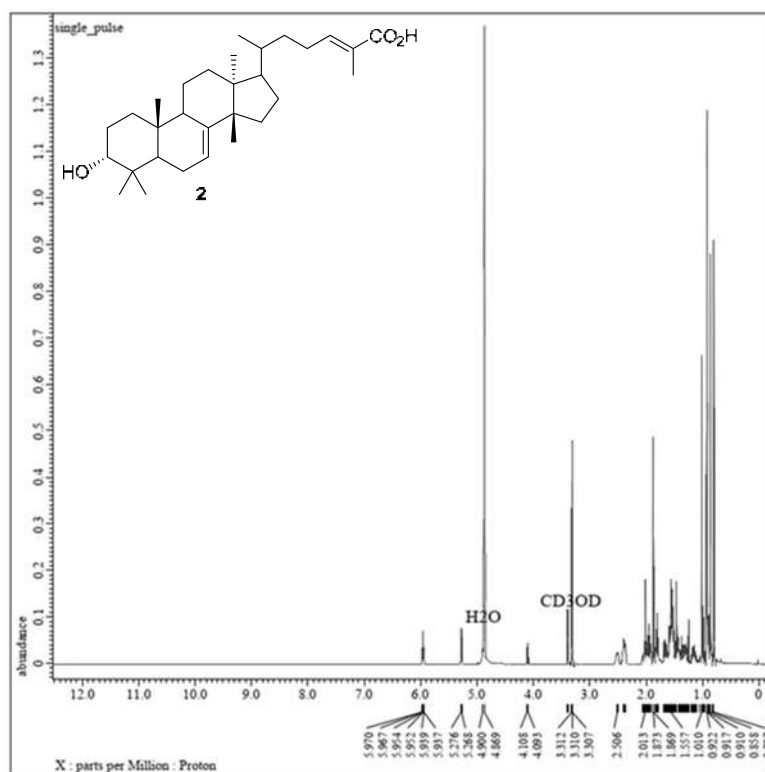


¹H-NMR (CDCl₃, 500 MHz)

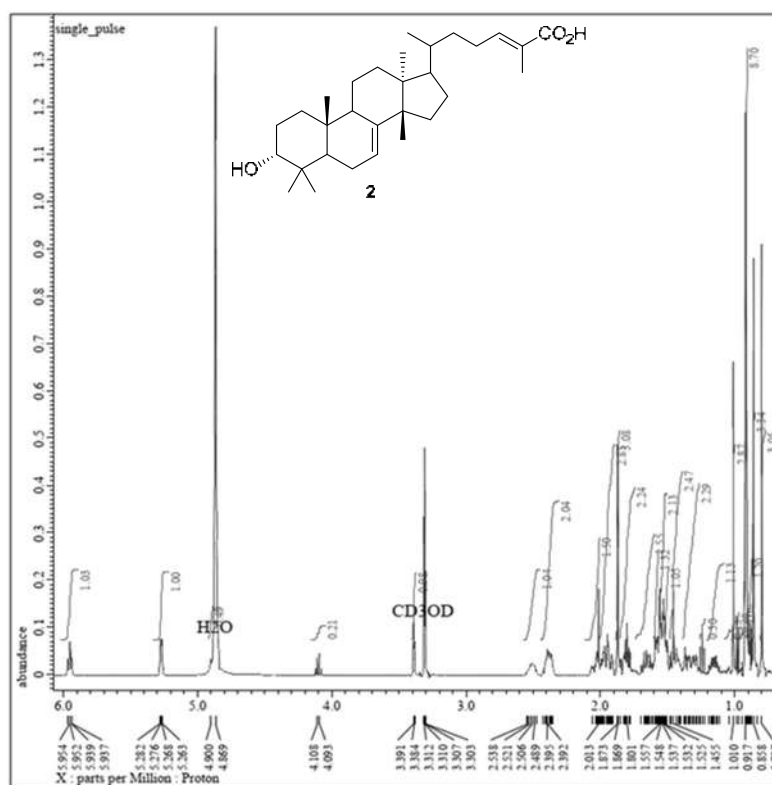


¹H-NMR-Expansion (CDCl₃, 500 MHz)

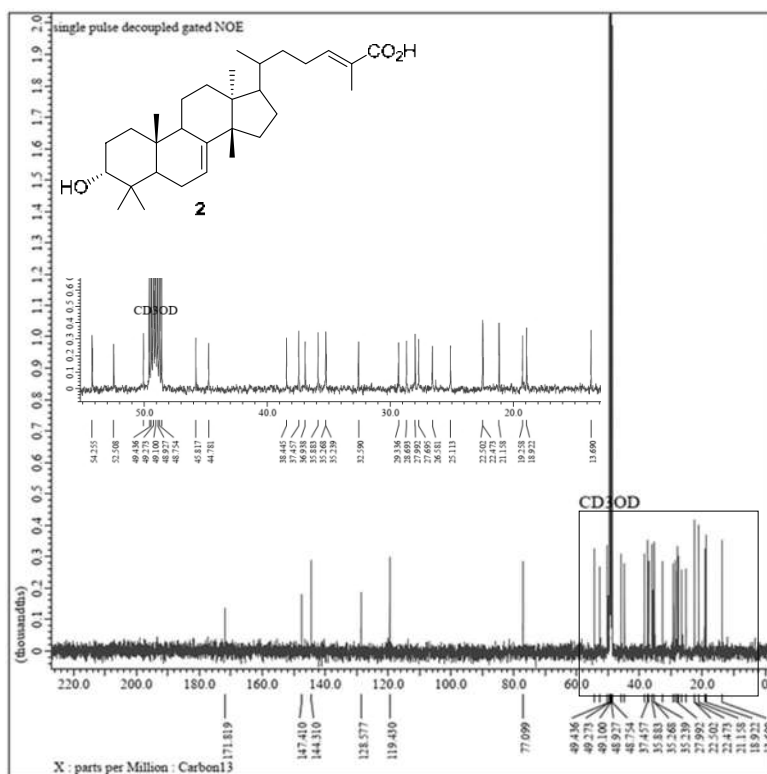
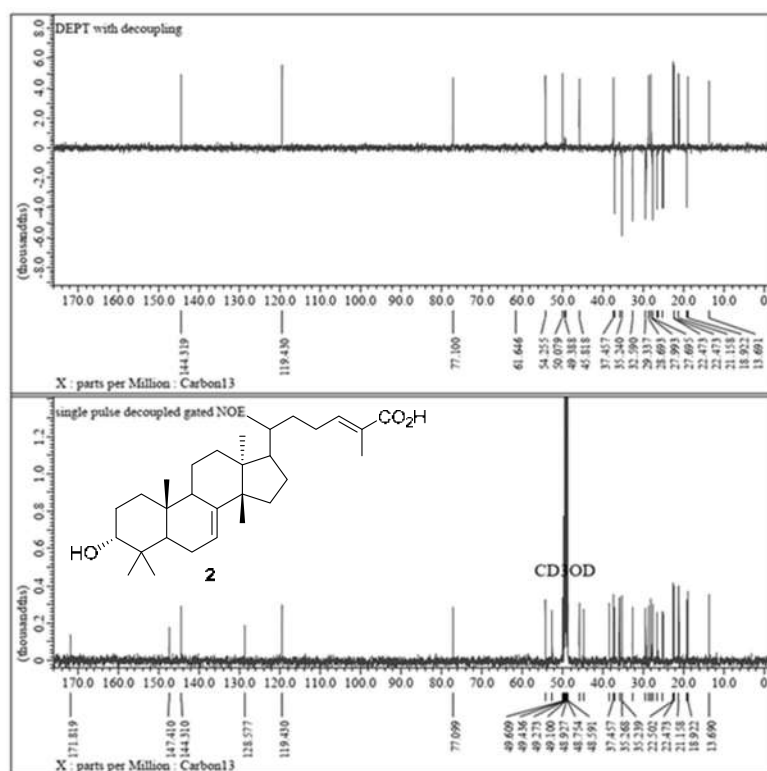
 $^{13}\text{C-NMR}$ (CDCl_3 , 125 MHz) $^{13}\text{C-NMR}$ and DEPT 135 (CDCl_3 , 125 MHz)

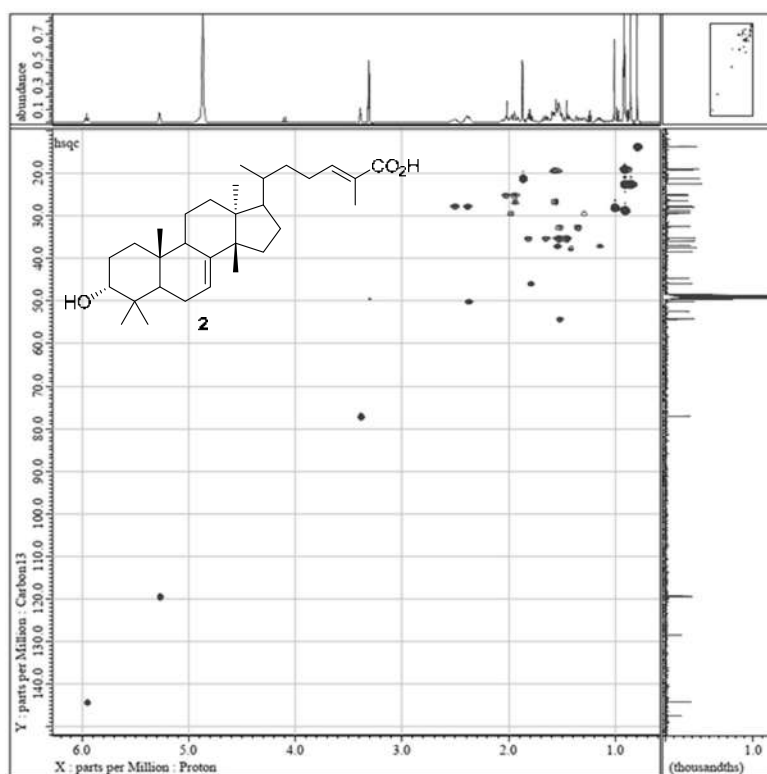


¹H-NMR (CD₃OD, 500 MHz)

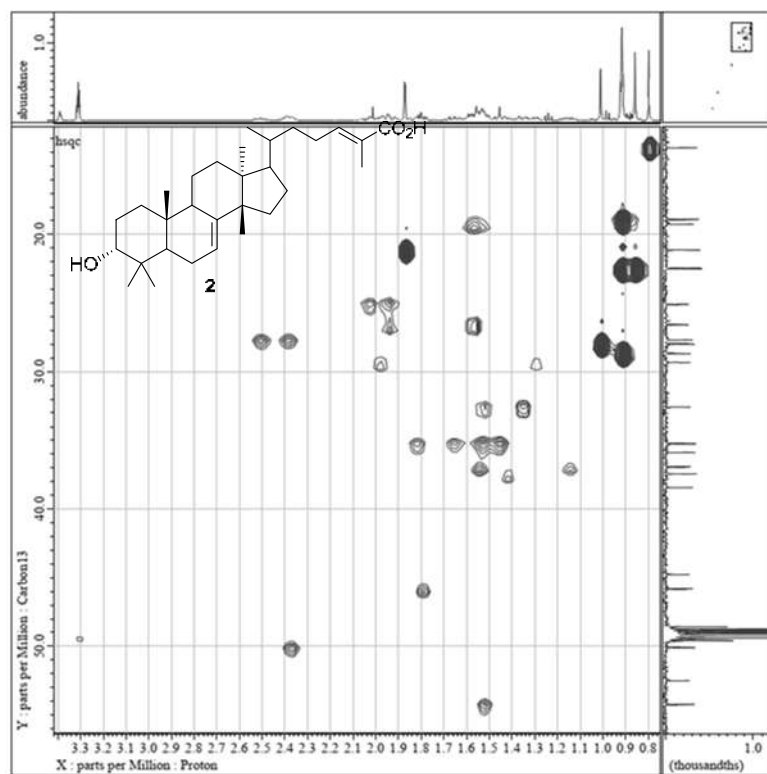


¹H-NMR-Expansion (CD₃OD, 500 MHz)

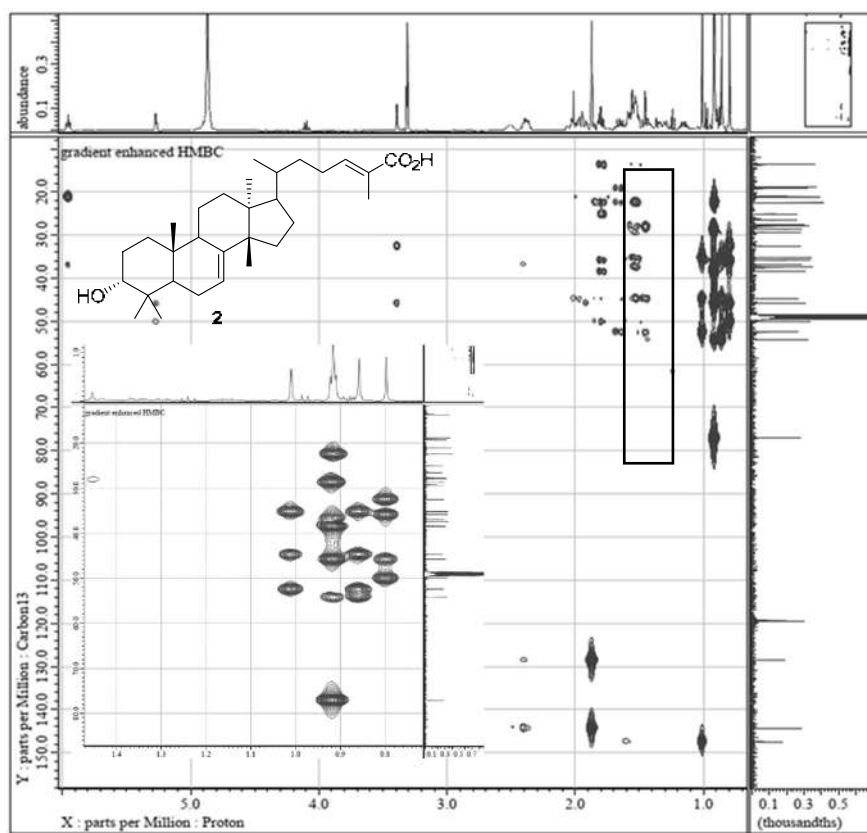
 $^{13}\text{C-NMR}$ (CD_3OD , 125 MHz)DEPT 135 and $^{13}\text{C-NMR}$ (CD_3OD , 125 MHz)



HSQC NMR (CD₃OD, 500 MHz)



HSQC NMR (Expansion, CD₃OD, 500 MHz)

HMBC NMR (CD₃OD, 500 MHz)

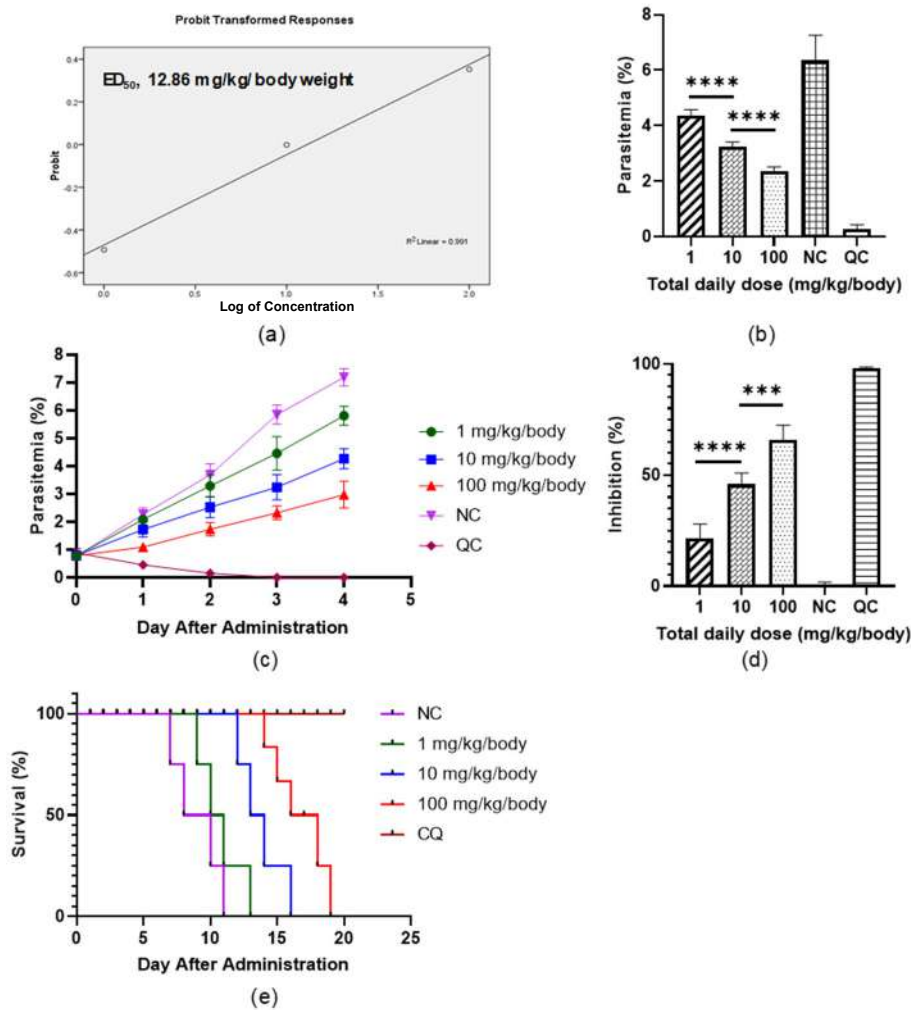


Fig S1. *In vivo* test of the PP extract against malarial parasite *Pb* ANKA strain in BALB/c albino mice. (a) ED₅₀ value of the PP extract in mice. (b) Parasitemia rates after the fourth day of treatment. (c) Chemosuppression of parasitemia from day 0 to day 4. (d) Inhibition rates after the fourth day of treatment. (e) Survival mice treated with 0.5% CMC-Na as a negative control, the PP extract at various doses (1, 10 and 100 mg/kg/body) and chloroquine as a positive control. Bars in Fig. S1(b) and S1(d) indicate the parasitemia and parasite growth inhibition rates treated with 0.5% CMC-Na (NC) (grid), CQ (horizontal) and the PP extract at a daily dose of 1 mg/kg/body (pencil striped), 10 mg/kg/body (herringbone) and 100 mg/kg/body (halftone), while in Fig. S1(c) and S1(e) indicate parasitemia reduction from day 0 to day 4 and survival of mice treated with 0.5% CMC-Na (pink), CQ (carmine) and the PP extract at a daily dose of 1 mg/kg/body (green), 10 mg/kg/body (blue) and 100 mg/kg/body (red). SD is indicated by the error bars. *** $p < 0.001$, **** $p < 0.0001$

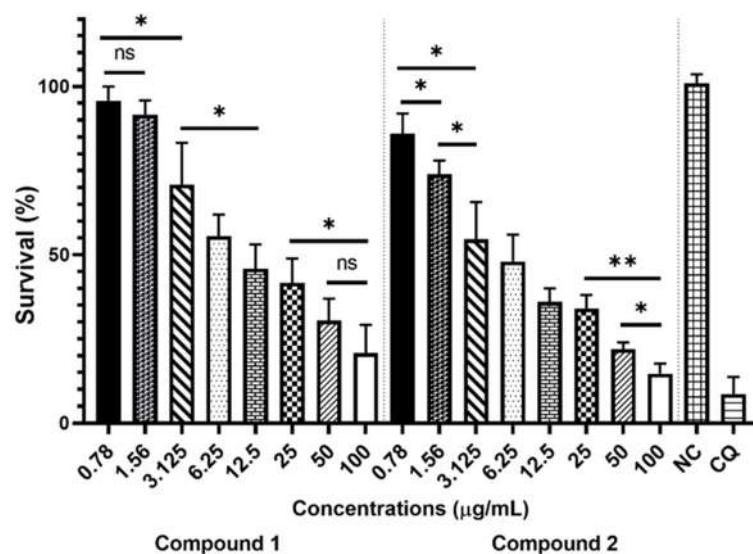


Fig S2. Survival rates of untreated parasites (0.2% DMSO) and parasites treated with compounds 1–2 at a concentration of 0.78 to 100 µg/mL and CQ (1 µM) are shown. Bars indicate parasite survival rates. Untreated parasites (NC - grid), CQ (horizontal) and compounds 1–2 at a concentration of 100 µg/mL (white), 50 µg/mL (small striped), 25 µg/mL (checkerboard), 12.5 µg/mL (brick), 6.25 µg/mL (halftone), 3.125 µg/mL (big striped), 1.56 µg/mL (hexagon) and 0.78 µg/mL (black). All experiments were performed in triplicate ($n = 3$). Standard Deviation (SD) is indicated by the error bars. * $p < 0.05$, ** $p < 0.01$, not significant (ns)

Statistical analysis

Experiments were performed independently in triplicate and average are presented. Statistical analysis was performed by unpaired two-tailed t -test using GraphPad Prism. The statistics were significant when * $p < 0.05$, ** $p < 0.01$ and *** $p < 0.001$

Table S1. *In vitro* Antiplasmodial activity of plant extract against *Plasmodium falciparum* [3]

IC ₅₀ value (µg/mL)	Category of activity
< 10	Promising
10–20	Moderate
20–40	Good
40–70	Marginally potent
> 70	Poor

References

- [1] Greca, M.D., Monaco, P., and Previtara, L., 1990, Stigmasterols from *Typha latifolia*, *J. Nat. Prod.*, 53 (6), 1430–1435.
- [2] Isaka, M., Chinthanom, P., Sappan, M., Supothina, S., Vichai, V., Danwisetkanjana, K., Boonpratuang, T., Hyde, K.D., and Choeyklin, R., 2017, Antitubercular activity of mycelium-associated *Ganoderma* lanostanoids, *J. Nat. Prod.*, 80 (5), 1361–1369.
- [3] Kamaraj, C., Kaushik, N.K., Mohanakrishnan, D., Elango, G., Bagavan, A., Zahir, A.A., Rahuman, A.A., and Sahal, D., 2012, Antiplasmodial potential of medicinal plant extracts from Malaiyur and Javadhu hills of South India, *Parasitol Res.*, 111 (2), 703–715.

Evaluation of the Antiplasmodial Properties of *Andrographis paniculata* (Burm.f.) and *Peperomia pellucida* (L.) Kunth

Nurhayati Bialangi¹, Mohamad Adam Mustapa², Yuszda Salimi¹, Weny Musa¹, Ari Widiyantoro³, Agus Malik Ibrahim⁴, Boima Situmeang^{4*}, and Julinton Sianturi⁵

¹Department of Chemistry, Faculty of Mathematics and Natural Sciences, Universitas Negeri Gorontalo, Gorontalo 96128, Indonesia

²Department of Pharmacy, Faculty of Sport and Health Sciences, Universitas Negeri Gorontalo, Gorontalo 96128, Indonesia

³Department of Chemistry, Faculty of Mathematics and Natural Sciences, Universitas Tanjungpura, Pontianak 78115, Indonesia

⁴Department of Chemistry, Sekolah Tinggi Analisis Kimia Cilegon, Banten, 42411, Indonesia

⁵Max Planck Institute of Colloids and Interfaces, Am Mühlenberg 1, 14424 Potsdam, Germany

* **Corresponding author:**

tel: +62-85262897312

email: boimatumeang@gmail.com

Received: May 4, 2022

Accepted: October 18, 2022

DOI: 10.22146/ijc.74481

Abstract: Plasmodium species are the infectious agents that are responsible for malaria, a disease that claims the lives of approximately 400,000 people annually. The fact that drug resistance against malaria is on the rise suggests that new antimalarial compounds need to be discovered. It is well known that medicinal plants present the best opportunity for the identification of novel antimalaria chemicals. Both the *Andrographis paniculata* (Burm.f.) and *Peperomia pellucida* (L. Kunth) species have been tested for their antiplasmodial ability against the *Plasmodium falciparum* strain. The *P. pellucida* (L. Kunth) species has also been subjected to in vitro and in vivo biological research. *P. pellucida* was used to isolate the steroid known as 3-hydroxy-24-ethyl-5,22-cholestadiene (1) and the triterpenoid known as 3-hydroxy-9-lanosta-7,24E-dien-26-oic acid (2). Both compounds were then tested for their activity in vitro. In the mice model, triterpenoid 2 had a substantial chemo-suppressive impact.

Keywords: *A. paniculata* (Burm.f.); *P. pellucida* L. Kunth; *Plasmodium falciparum*; inhibition; 3 β -hydroxy-9-lanosta-7,24E-dien-26-oic acid

■ INTRODUCTION

Malaria is a significant threat to global public health, as it affects individuals in every region of the world. The disease is brought on by the parasite *Plasmodium*, which is transmitted from female *Anopheles* mosquitoes to human hosts [1]. Since there are not enough preventative measures in place, and because the malaria parasite is becoming more resistant to many antimalarial drugs that are already on the market, such as quinine, chloroquine, and piperazine; this disease continues to be a concern for the health of people all over the world [2-4]. In spite of the devoted research that has been conducted over the

course of several decades, there is still no malaria vaccine that can be bought in stores at this moment. As a result, chemotherapies that make use of combination medications appear to be the best alternative, and novel antimalarial chemicals are an absolute necessity. Regular mining is done on plants that are used for therapeutic purposes with the purpose of determining whether they have the potential to provide novel active chemicals [5]. For instance, Tu [6] created Artemisinin in China in the early 1970s. This medication was derived from *Artemisia annua* L. and was utilized in the treatment of malaria. It is widely known that tropical plants contain a rich reservoir of bioactive compounds. Because of this, there

is the possibility that these plants could serve as sources for the development of novel antimalarial drugs [7].

One of the most common plant families that are farmed in tropical and subtropical regions is Acanthaceae family [8]. Traditional uses for this herb include the treatment of acute diarrhea, coughing, the common cold, inflammation, boils, skin eruptions, and seasonal fever [9]. Other ailments that have been alleviated by using this herb include boils, skin eruptions, and seasonal fever. The investigation of phytochemicals has resulted in the identification of a wide range of secondary metabolites that have significant pharmacological effects. The *Andrographis paniculate* species, more often known as "Sambiloto," which could be found all over Indonesia, is regularly exploited as an element of traditional medical practices [10]. Traditional cultures held the belief that combining this plant with *Peperomia pellucida* could boost the efficacy of antimalarial treatment [11-13]. In spite of the fact that this plant possesses anti-plasmodial activity against many strains of *Plasmodium falciparum*, this is still the case. We investigated the antiplasmodial activity of the *A. paniculata*, and *P. pellucida* isolates against a malarial parasite strain in order to give data in favor of this theory. In addition, we tested the efficacy of these compounds on infected mice and isolated the active compound(s) in an effort to gain a deeper comprehension of the biological role that these compounds play. On the other hand, the investigations regarding the isolated compounds of PP have not been documented in detail. Only one of the studies that we looked at in the literature had isolated chemicals that came from the *P. pellucida* plant.

■ EXPERIMENTAL SECTION

Materials

In June 2016, fresh leaves and stems of *A. paniculata* and *P. pellucida* were harvested in north Gorontalo, Gorontalo Province, Indonesia. The plant was identified at the Herbarium Biology Laboratory, Faculty of Mathematics and Natural Sciences, Universitas Negeri Gorontalo, and voucher specimens (No. 130/H47.B4.Bio.Lab Bio/LL/2016; for *P. pellucida* and No.

131/H48.B4.Bio.Lab Bio/LL/2016; for *A. paniculata*) were deposited to the Herbarium.

Instrumentation

The instruments used in the experiment for molecular determination were Japan Electron Optics Laboratory (JEOL) 125 MHz ^1H -NMR and JEOL 500 MHz ^{13}C -NMR, for the photoelectron analysis the instrument used was JEOL UV-Vis Spectrophotometer, the cell culture was done in ESCO Scientific Laminar Cabinet, and the infrared instrument used was ThermoFisher Scientific Infrared Spectrometer.

Procedure

Plant extraction and isolation

Dried leaves and stems of *P. pellucida* (PP) (2 kg) and *A. paniculata* (AP) (2 kg) were macerated with methanol (12 L) at room temperature for 2 d. After filtrating, the filtrate was evaporated under reduced pressure to yield the PP extract (211 g) and AP extract (278 g). The PP extract was suspended with water (500 mL) and partitioned successively with *n*-hexane and ethyl acetate. Evaporation gave the crude *n*-hexane (15.3 g), ethyl acetate (13.2 g) and aqueous (18.5 g) extracts. The isolation procedures are shown in detail in Scheme S1. The ethyl acetate extract was purified by column chromatography using silica gel G60 (132 g), eluted by *n*-hexane/EtOAc (200 mL) with a linear gradient from 10% to 100% of EtOAc to yield eleven fractions (A1–A11). Fraction A6 (0.27 g) was subjected to silica column chromatography using the isocratic elution mixture of *n*-hexane/EtOAc (90:10-0:100) to yield 40 fractions (B1–B40). Fractions B9 were recrystallized using *n*-hexane and chloroform to afford compound **1** (18 mg) as a needle-shaped crystal. Fraction A7 (0.97 g) was subjected to silica column chromatography (10 g of silica G60) using an isocratic system, eluted by *n*-hexane/EtOAc/MeOH (7:2:1) to yield 25 fractions (B1–B25). Fractions C13–C15 (90 mg) were combined and purified by silica column chromatography on Octa Decyl Silane (ODS), eluted by MeOH/H₂O (4:1) to yield compound **2** (12 mg) as a white powder.

Synchronization and maintenance of parasite strain

The University of Tokyo's chloroquine-sensitive malaria parasite Pf D-10. Parasite Pf D-10 was maintained in fresh O+ human erythrocytes with a hematocrit of 4% in RPMI 1640 culture medium (Gibco) supplemented with 10% (v/v) human serum, 25 mM HEPES (*N*-(2-hydroxyethyl)piperazine-*N'*-2-ethanesulfonic acid, Sigma Aldrich), 45 µg/mL hypoxanthine, 32 mM NaHCO₃, and 50 µg/mL gentamicin, incubated at 37 °C under a gas mixture of 5% O₂ and 5% CO. After 96 h, parasites were microscopically synchronized with 5% sorbitol.

In vivo antiplasmodial activity

The Animal Experimental Development Unit at Universitas Gadjah Mada, Yogyakarta, Indonesia, donated 30 male BALB/c albino mice aged 6–8 weeks weighing 25–28 g for this investigation. At the Universitas Airlangga Institute of Tropical Disease Animal Laboratory, the mice were fed and watered ad libitum. Eijkman Institute for Molecular Biology in Jakarta provided the parasite Pb ANKA strain. At the Institute of Tropical Disease, Universitas Airlangga, male BALB/c mice and cryogenic storage maintained the parasite.

As described by Peter [14], with slight modifications, the sample extract AP/PP (20/80 mg) and isolated chemical (10 mg) were tested in mice infected with Pb ANKA for antiplasmodial activity. Thirty BALB/c albino mice were intraperitoneally infected with Pb ANKA (106 parasitized erythrocytes). The volume of Inoculum used was 200 µL. Five six-mouse groups were formed (three experimental and two control groups). Three groups received the sample at 1, 10, and 100 mg/kg/body in 0.5% CMC-Na (200 µL). A negative control group received 0.5% CMC-Na while a positive control group received chloroquine diphosphate (25 mg/kg/body) intraperitoneally once a day for 4 d. After 4 d, the animals ceased treatment. On the 6th day, thin mouse tail blood smears were made on slides. The slide was stained with 15% Giemsa-dyed solution for 10 min [15-16]. Rinsing and drying at room temperature completed the slide. Giemsa-stained blood smears and microscopy determined parasitemia and growth inhibition. Day 21 post-infection survival was monitored.

Antimalarial assay in vitro

The antimalarial activity of the compounds was tested using the Desjardins method [17]. The test was performed using *P. falciparum* 3D7 strain. The antimalarial examination used 96 wells, each well filled by parasitemia culture 1%. The RPHS media was replaced by a sample containing RPHS media with different sample concentrations. All wells were then stored in the Laminar Airflow cabinets until all solvents were evaporated. Further, we added 50 µL of parasitemia red blood cells into the well and then incubated at 37 °C. After 48 h, slide preparation was stained using Giemsa 20%. The parasite was then swapped with Giemsa-colored blood. The parasitemia percentage was calculated by comparing the number of infected erythrocytes to 500 erythrocytes.

Statistical analysis

The experiments were performed independently in triplicate, and the average data are presented. Statistical analysis was performed by unpaired two-tailed *t*-test using GraphPad Prism. The statistics were significant when **p* < 0.05, ***p* < 0.01 and ****p* < 0.001.

RESULTS AND DISCUSSION

Fresh leaves and stems of species AP and PP were extracted with crude methanolic extracts. A thin blood smear stained with Giemsa was obtained after incubating synchronized *P. falciparum* D-10 strain (Pf D-10) with the AP-PP extract at varied ratios (80:20 to 20:80) in dimethyl sulfoxide (DMSO), chloroquine (CQ) (1 M), and 0.2% DMSO. Microscopically, parasitemia, parasite growth, and inhibition rates were assessed. The chemoprevention of parasitemia against Pf D-10 was investigated. The activity of the AP-PP extract was limited (2.8 to 3.0%) at a ratio of 80:20 to 40:60. However, when the PP extract ratio was increased, the parasitemia rate reduced considerably (Fig. 1(a)). Low suppressions of Pf D-10 were seen at ratios ranging from 80:20 to 40:60, whereas a ratio of 20:80 indicated a 50% inhibitory effect (*p* 0.05). The AP-PP extract's antiplasmodial activity was boosted in a ratio-dependent way (Fig. 1(b)). Furthermore, the IC₅₀ value of AP-PP

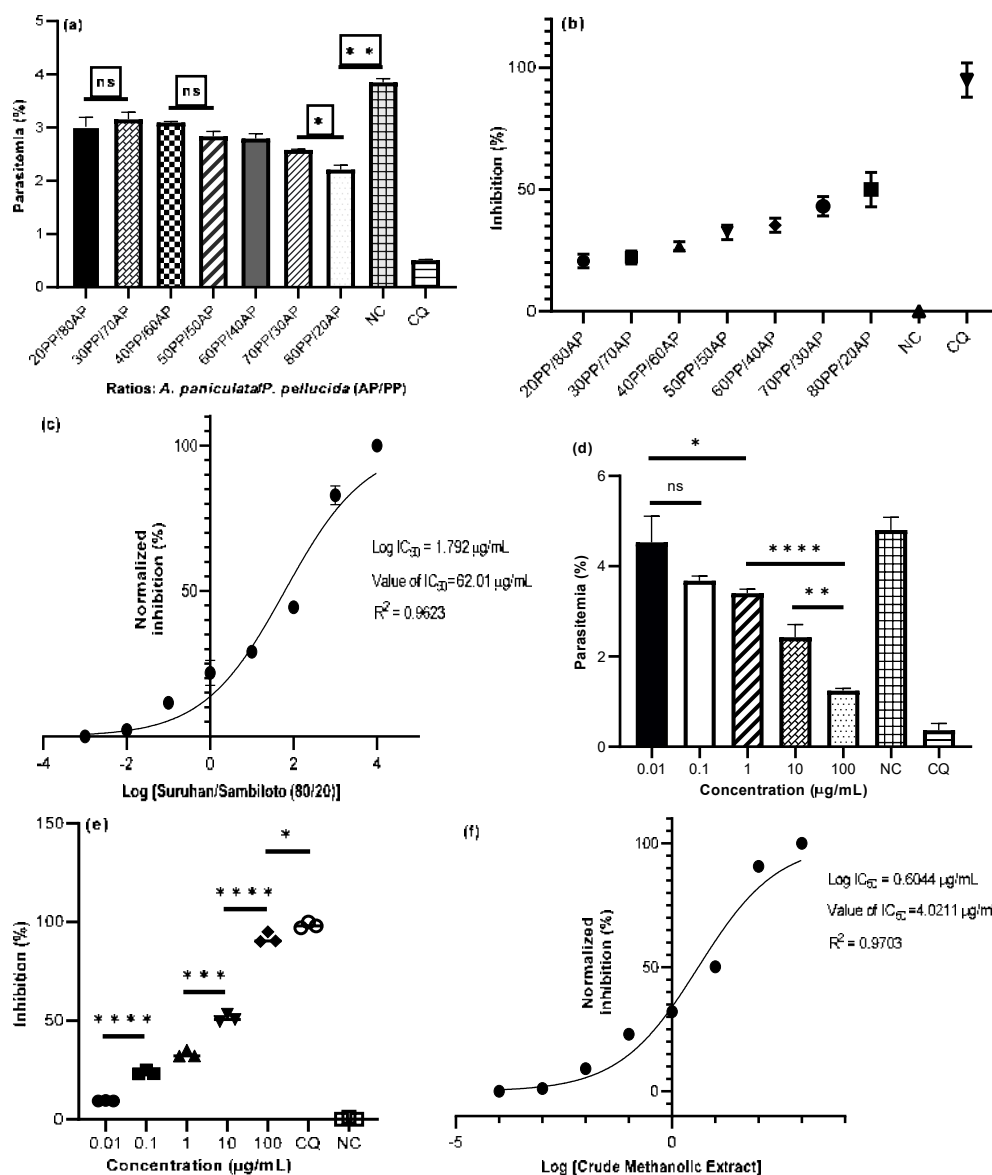


Fig 1. The AP-PP extract was tested *in vitro* against Pf D-10 at a variety of ratios, ranging from 80:20 to 20:80, as well as the PP extract on its own. (a) The level of parasitemia, and (b) the percentage of parasites that were inhibited by treatment with the AP-PP extract, (c) A result of the IC_{50} of the AP-PP extract when it was mixed in a ratio of 20:80. (d) The prevalence of parasitemia, and (e) the percentage of parasites that were inhibited by the PP extract. (f) A value for the IC_{50} of the PP extract. With the use of the GraphPad Prism program, an IC_{50} value was determined. As a negative control, we used parasites that had been treated with 0.2% DMSO, and as a positive control, we employed CQ at a dose of 1 μM . Every experiment was carried out three times, so the total number of participants was three. The standard deviation is represented by the error bars. * $p < 0.05$, ** $p < 0.01$, *** $p < 0.001$, not significant (ns)

extract at a 20:80 ratio was investigated (Fig. 1(c)). The extract was tested at concentrations of 0.01, 0.1, 1, 10, and 100 $\mu\text{g/mL}$ and the inhibition rates were determined after 48 h of incubation. The IC_{50} value was calculated through an examination of inhibition-response curves. Based on

an *in vitro* study with an IC_{50} value of 62.01 $\mu\text{g/mL}$, the AP-PP extract at a 20:80 ratio was rated mildly potent (Table S1) [17].

The PP extract alone must be assessed because its larger ratio had a stronger antiparasitic effect than the

AP extract. *In vitro* concentrations were 0.01 to 100 g/mL. Fig. 1(d) shows that PP extract at 0.1 to 100 g/mL had antiplasmodial potential. The greatest dose of *P. pellucida* extract reduced parasitemia by 1.2% (p 0.01). PP extract was investigated for parasite PfD-10 inhibition (Fig. 1(e)). At 10 and 100 g/mL, 51% (p 0.01) and 92% (p 0.001) inhibition were observed. The PP extract demonstrated promising antiplasmodial activity with an IC_{50} of 4.0 g/mL (Table S1). According to Kwansa-Bentum et al. [17], PP L. Kunth crude methanolic extract had higher antiplasmodial activity than AP (Burm.f.) Nees (IC_{50} , 7.2 g/mL). These results indicate that the PP extract ratio increased antiplasmodial activity.

In addition, we tested the PP extract's efficacy in BALB/c albino mice infected with *Plasmodium berghei* ANKA (Pb ANKA) (Fig. S1). The extract had antiplasmodial action, with a 50% effective dose (ED_{50}) of 12.86 mg/kg/body weight (Fig. S1(a)). A strong chemosuppression of parasitemia (Fig. S1(b)), inhibitory effect (Fig. S1(d)), and chemosuppression of parasitemia from day 0 to day 4 were clearly demonstrated after the fourth day of treatment (Fig. S1(c)). The treatment of the *P. pellucida* extracts intraperitoneally improved the survival of infected mice (Fig. S1(e)).

The crude methanolic extract of PP L. Kunth demonstrated promising antiplasmodial action (Fig. 1(f)),

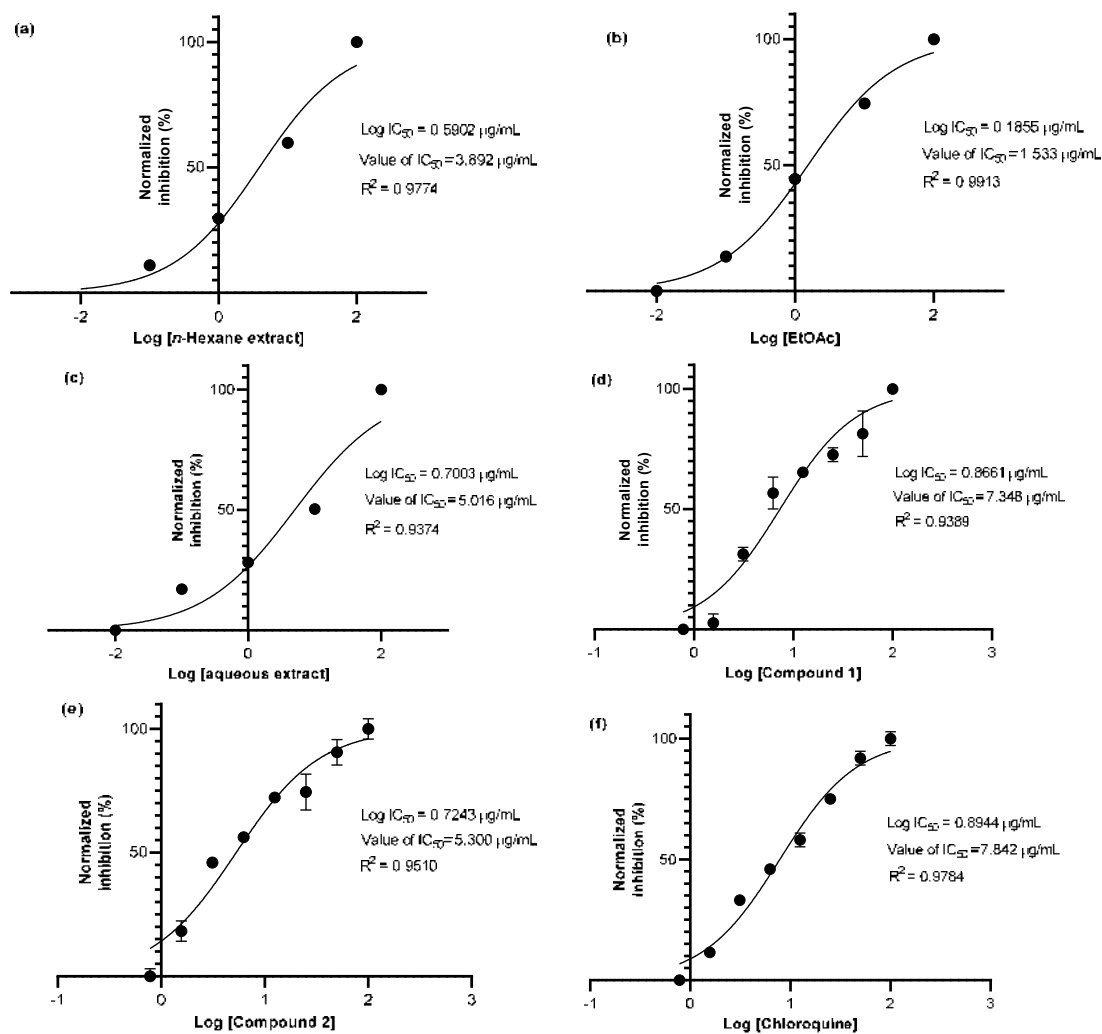


Fig 2. The IC_{50} values for each of the extracts compounds 1-2, and chloroquine, which served as a positive control. To determine the IC_{50} values of the separated compounds, concentrations ranging from 0.78 to 100 g/mL were used in the experiment

indicating the existence of chemicals responsible for this activity [17]. To further understand the mechanism of antiplasmodial activity of the PP extract, the compound(s) must be isolated and identified to assist in finding their biological function and mode of action. The antiplasmodial activity of crude *n*-hexane (E1), ethyl acetate (E2), and aqueous (E3) extracts were first determined. The antiplasmodial activity test shows the EtOAc (Fig. 2(b)) fraction has the most potent antiplasmodial activity due to having the lowest IC₅₀ value of 1.533 µg/mL among the other fraction of *n*-hexane (Fig. 2(a)) with IC₅₀ of 3.892 µg/mL and aqueous extract (Fig. 2(c)) with IC₅₀ value of 5.016 µg/mL.

Because E2 was the most active extract in our investigation, we isolated and identified the compound(s) from it. The E2 was treated to standard, reverse-phase silica column chromatography and recrystallizations, yielding compounds 1–2 (Fig. 3).

The IR spectrum of compound 1 revealed the existence of O-H stretching, C-O bond, C-C, CH₂ vibrations, hydroxyl, and cycloalkane groups at 3373.6, 1247.0, 1641.0, 1457.3, 1381.6, 1038.0, and 881.6 cm⁻¹, respectively. Two methyl singlets, three methyl doublets, and a methyl signal as a triplet was observed in the proton NMR of 1. Characteristic signals were also detected at 4.91, 5.18, and 5.31 ppm, indicating the presence of trisubstituted and disubstituted olefinic groups. The ¹³C-NMR spectrum exhibited the presence of six *sp*³ methyl carbons resonated at δ_C 12.4 (C-29), 18.4 (C-28), 19.3 (C-27), 20.4 (C-26), 12.9 (C-24) and 40.5 (C-18) and four *sp*² carbons resonated at δ_C 140.5, 121.9, 138.7 and 129.4 ppm indicated to a steroid compound related with stigmasterol

[18]. An oxygenated carbon peak at δ_C 71.9 ppm suggested the presence of a hydroxyl group and was usually located at C-3. Furthermore, the correlation of proton and carbon signals of 1 was confirmed by ¹H-¹H COSY and ¹H-¹³C HMBC experiments. Therefore, isolated compound 1 was identified as a 3β-Hydroxy-24-ethyl-5,22-cholestadiene.

Compound 2 was obtained as a white crystal (12 mg), and the IR spectrum displayed absorption peaks for hydroxyl, carboxyl, carbonyl and olefinic groups. The ¹H-NMR spectrum of 2 showed the presence of seven signals of methyl groups as a singlet, resonating at δ_H 0.89–1.70 ppm. An oxymethine protons resonated at δ_H 3.49 (1H, dd, *J* = 4.0 and 12.0 Hz, H-3) indicated as a β isomer [19]. Additional functionalities included the signals of two olefinic protons resonated at δ_H 5.26 (1H, dd, *J* = 6.5 and 3.0 Hz (H-7) and 5.98 (1H, t, *J* = 7.8 Hz, H-24). A total of 30 carbons resonances were observed in the ¹³C-NMR and DEPT 135° spectra. Four *sp*² carbons include two methine carbons and two quaternary carbons resonated at δ_C 119.6 (C-7), 144.3 (C-24), 147.4 (C-8), and 128.6 (C-25), respectively. Seven *sp*³ methyl carbons resonated at δ_C 24.7 (C-18), 17.1 (C-19), 18.4 (C-21), 12.6 (C-27), 29.5 (C-28), 23.7 (C-29), and 30.8 (C-30). Nine methylene carbons resonated at δ_C 35.5 (C-1), 28.1 (C-2), 23.1 (C-6), 22.8 (C-11), 33.4 (C-12), 34.7 (C-15), 28.5 (C-16), 35.0 (C-22), and 25.5 (C-23). Five *sp*³ methines resonated at δ_C 77.1 (C-3), 48.5 (C-5), 48.4 (C-9), 53.5 (C-17), and 35.9 (C-20). Five *sp*³ quaternary carbon signals resonated at δ_C 38.8 (C-4), 35.8 (C-10), 43.5 (C-13), and 52.7 (C-14) while one carbonyl group resonated at δ_C 171.8 (C-26)

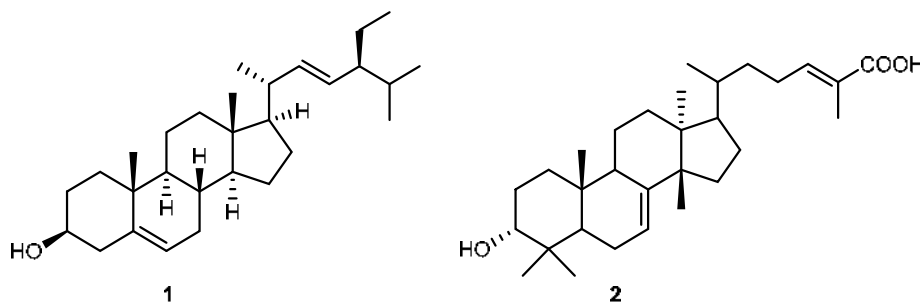


Fig 3. Chemical structure of 3β-hydroxy-24-ethyl-5,22-cholestadiene (1) and 3β-hydroxy-9-lanosta-7,24*E*-dien-26-oic acid (2)

was assigned as a carboxylic acid group. The presence of seven sp^3 methyls, one carboxylic acid group, and nine sp^3 methylene carbons were assigned as a triterpenoid tetracyclic similar to a lanostane derivative skeleton [20-21]. The position of the tetracyclic systems (A, B, C and D) were assigned by the correlation between proton and carbon using HMBC and ^1H - ^1H COSY spectra. The HMBC correlations between six sp^3 methyl carbons (C-18, C-19, C-21, C-27, C-28, C-29, and C-30) and six sp^3 quaternary carbon C-13, C-10, C-20, C-4, C-4, and C-14, respectively, confirmed the tetracyclic systems. The position of the hydroxy group at C-3 was confirmed by the correlation between sp^3 oxygenated methine carbon at δ_{C} 77.1 and sp^3 methyl carbons at δ_{C} 29.5 (C-28) and 23.7 (C-29). The position of an olefin group at C-7/C-8 was confirmed by HMBC correlations between H-5, H-6, H-9 to C-7 and H-6, H-9, H-11 to C-8. Additional correlation between H-24 to C-25 and C-27; H-27 to C-24, C-25, and C-26 (δ_{C} 171.8), suggested that a carboxylic acid group is not located in the tetracyclic systems. Another olefin group was confirmed at C-24/C-25 by HMBC correlations between H-23 to C-24 and H-27 to C-25. The side chain of **2** was further confirmed by a continuous sequence from C-15 to C-24 as deduced from HMBC and ^1H - ^1H COSY and spectra. In addition, the HMBC correlation of H-21 to C-20 indicated the side chain is connected to C-20. Therefore, isolated compound **2** was

identified as a 3β -hydroxy-9-lanosta-7,24*E*-dien-26-oic acid. The isolated compound **2** was first reported from this plant. All compounds were identified, as reported previously [22-23].

Compounds **1-2** were evaluated for their ability to suppress parasitemia and inhibit the parasite growth. The *in vitro* antiplasmodial activity of **1-2** and chloroquine as a positive control are reported in Fig. 2(d-e). Steroid **1** exhibited antiplasmodial activity against Pf D-10 with an IC_{50} value of $7.35 \mu\text{g/mL}$. Interestingly, triterpenoid **2** displayed a more pronounced antiplasmodial activity (IC_{50} , $5.30 \mu\text{g/mL}$) than chloroquine (IC_{50} , $7.84 \mu\text{g/mL}$). The IC_{50} value of chloroquine is in good agreement with Perumal et al. [23].

Next, we take a look at the parasitemia as well as the inhibition rates of **1-2**. In the same way, as was the case with the PP extract, the antiplasmodial activity of compounds **1** and **2** increased in a manner that was dependent on the concentration. For **1**, the prevalence of parasitemia ranged from roughly 4.6 to 1.1%, and for **2**, the prevalence ranged from approximately 3.7 to 0.7% within a range of 0.78 to $100 \mu\text{g/mL}$, respectively (Fig. 4(a)). Fig. 4(b) demonstrates that the growth of the parasite Pf D-10 was stifled as a result of exposure to **1-2**. Under the same conditions, steroid **1** showed a moderate suppression of Pf D-10 at a concentration of

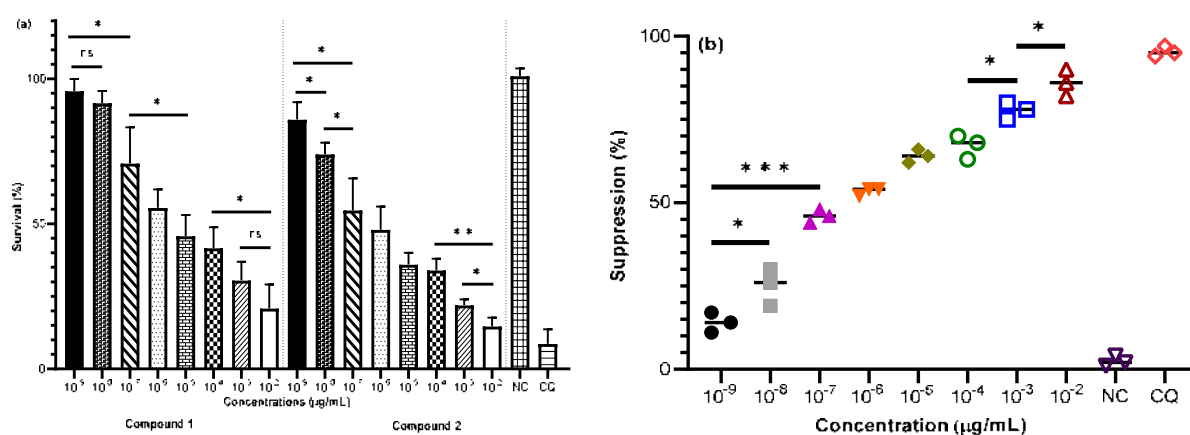


Fig 4. An *in vitro* antiplasmodial activity of steroid **1** and triterpenoid **2**. (a) Parasitemia and (b) inhibition rates of untreated parasites (0.2% DMSO) and parasites treated with compounds **1-2** at a concentration of 0.78 to $100 \mu\text{g/mL}$ and chloroquine ($1 \mu\text{M}$) are shown. All experiments were performed in triplicate ($n = 3$). The standard Deviation (SD) is indicated by the error bars. * $p < 0.05$, ** $p < 0.01$, *** $p < 0.001$ and not significant (ns)

0.78 g/mL (1.7%) and 1.56 g/mL (4.0%), but triterpenoid **2** showed a considerable suppression impact of 14% and 25% ($p < 0.05$). In addition, the ability of compounds **1** and **2** to preserve the life of parasitized red blood cells was investigated. Steroid **1** had a moderate effect (about 96%) when tested at a diluted quantity, whereas triterpenoid **2** demonstrated superior parasite killing at a rate of 86% when tested at the same doses. The survival rates dropped in a manner that was dependent on the concentration of the organisms (Fig. S2).

The substantial response of triterpenoid **2** against Pf D-10 was mediated by a carboxyl functional group, which promoted carboxyl-carboxylate association for the

purpose of providing a stabilizing force in protein interaction [24]. Contrary to compound **2**, a low response of **1** is most likely caused by the compound's cytotoxicity rather than particular action against the parasite itself or being negatively influenced by poor pharmacokinetics [25-27]. This is because compound **1** has poor pharmacokinetics. The antiplasmodial activity of compounds **1-2** supported the hypothesis that the species *Pf L. Kunth* could serve as a possible source of novel antimalarial metabolites. This allowed for the identification of potential antiplasmodial leads derived from *Pf L. Kunth*, which could lead to the discovery of a new anti-malarial candidate.

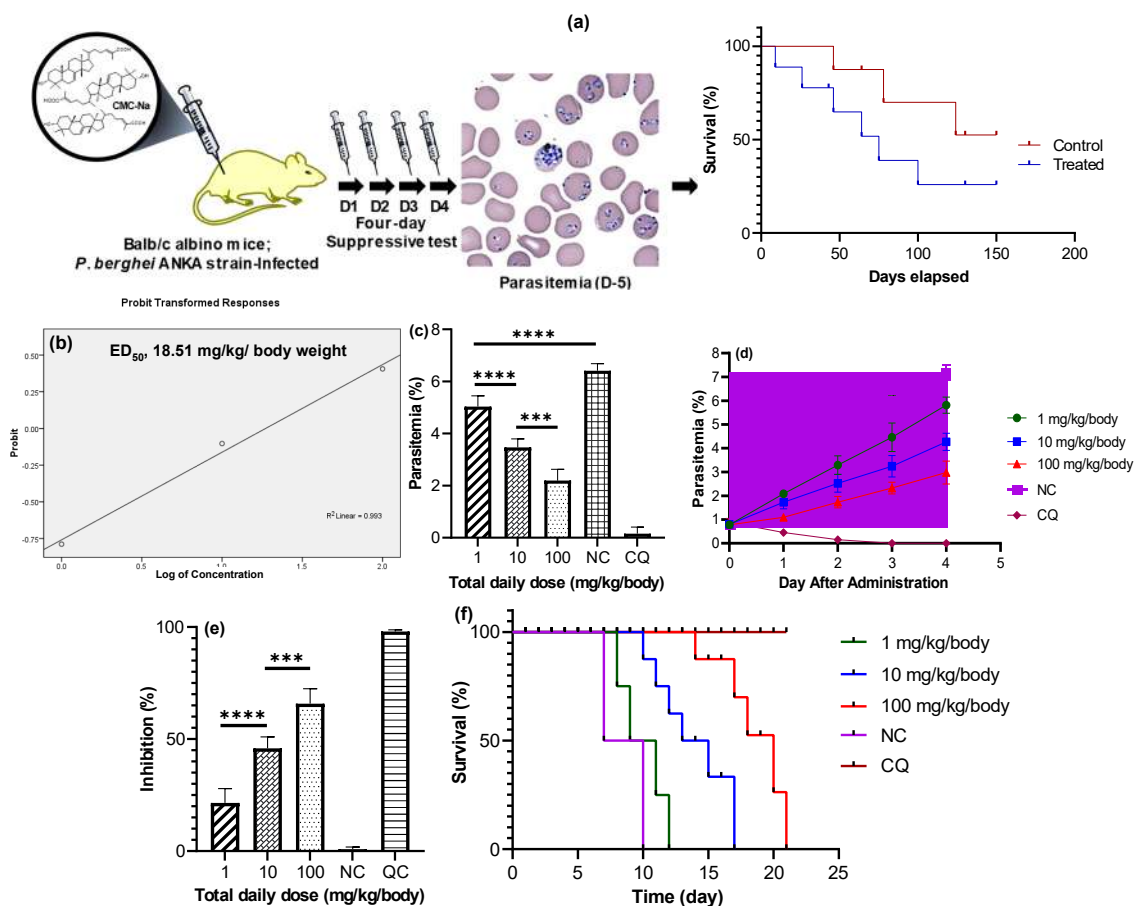


Fig 5. *In vivo* test of triterpenoid **2** in BALB/c albino mice infected with *Pb* ANKA. (a) *In vivo* four-day suppressive test. Infected mice were treated with 0.5% CMC-Na as a negative control (NC), CQ as a positive control (25 mg/kg/body) and triterpenoid **2** at a daily dose of 1, 10 and 100 mg/kg/body. Mice received treatment from day 1 to day 4. On the 5th day, Giemsa-stained blood smears were prepared and analyzed microscopically. (b) ED₅₀ value of triterpenoid **2** in mice. (c) Parasitemia after the fourth day of treatment. (d) Chemo suppression of parasitemia from day 0 to day 4. (e) Suppression rates after the fourth day of treatment. (f) Survival rates of *Pb* ANKA in BALB/c albino mice. SD is indicated by the error bars. *** $p < 0.001$, **** $p < 0.0001$

Triterpenoid **2** proved to be the most powerful antimalarial agent in this investigation, so the next thing we did was test it on mice infected with the malaria parasite Pb ANKA. The method described by Peters et al. [26] was implemented for the purpose of analyzing the *in vivo* test of **2**. Mice of the BALB/c albino strain were given Pb ANKA by the intraperitoneal route. After 4 d of treatment with 0.5% CMC-Na as a negative control, chloroquine diphosphate as a positive control, and triterpenoid **2** at daily doses of 1, 10, and 100 mg/kg/body, thin blood smears stained with Giemsa were obtained for each mouse on the fifth day. This was followed by 4 d of treatment with chloroquine diphosphate as a positive control. On a microscopic level, parasitemia and the reduction of parasite development were observed and measured (Fig. 5(a)). Up until day 21, the survival of mice was carefully monitored and tracked. It was believed that triterpenoid **2** had some biological activity, with an ED₅₀ value of 18.51 mg/kg/body weight (Fig. 5(b)). The drug quinine, which is available for clinical use, has an elimination half-life (ED₅₀) of 34 mg/kg/day and a slow clearance [28]. Triterpenoid **2** was successful in inhibiting the development of parasitemia in mice infected with Pb ANKA, as shown in Fig. 5(c). Even at the lowest dose (1 mg/kg/body), intraperitoneal administration of triterpenoid **2** resulted in a 78% reduction in parasitemia. To be more specific, **2** was successful in killing 22% of the parasites. The incidence of parasitemia fell to lower levels as higher doses of **2** were administered. The rates of parasitemia were reduced to approximately 54 and 34%, respectively when triterpenoid **2** was administered at doses of 10 and 100 mg/kg/body. In addition, the effectiveness of chemotherapy in reducing parasitemia was evaluated from day 0 to day 4 of treatment (Fig. 5(d)). The levels of parasitemia in mice that had not been given any treatment rose consistently after infection, but the number **2** therapy had a significant chemo-suppressive effect that was dose-dependent. Fig. 5(e) shows the suppression of parasite growth that was caused by triterpenoid **2**. This compound had a substantial inhibitory effect against Pb ANKA in mice. Triterpenoid **2** strongly suppressed Pb ANKA, as can be seen in Fig. 5(e), which suggests that it also inhibited the proliferation of parasites

in mice. The suppression rates varied from 66 (at 100 mg/kg/body) to 46 (10 mg/kg/body) to 22% (1 mg/kg/body). These findings made it abundantly evident that factor **2** was responsible for eliminating the parasites. The treatment of **2** also increased the number of ill mice that survived longer. Based on the *in vivo* experiment (Fig. 5(f)) mice that were not given any treatment succumbed to the Pb ANKA infection after 10 d, whereas mice that were given 1, 10, or 100 mg/kg/body of triterpenoid **2** lived until 12, 17, and 21 d, respectively. Positive control groups were given chloroquine diphosphate at a daily dose of 25 mg/kg/body for as long as 21 d, which led researchers to conclude that the Pb ANKA infection was completely eradicated in the mice who participated in the study. These findings are in agreement with those found by Fang et al. [29].

■ CONCLUSION

In this study, the PP extract displayed a more pronounced antiplasmodial activity than the AP extract. Steroid **1** and triterpenoid **2** exhibited promising antiplasmodial activity. This is the first report of 3 β -hydroxy-9-lanosta-7,24*E*-dien-26-oic acid (**2**) as an antiplasmodial agent, and we have shown its promising efficacy in an *in vivo* mouse model. Our results suggest a novel triterpenoid that has the potential for use as an antimalarial agent. Although 3 β -hydroxy-9-lanosta-7,24*E*-dien-26-oic acid may not yet be an ideal drug candidate for treating malaria disease in humans, it may provide a useful lead structure to produce more effective antiplasmodial agents. We plan to do an *in vivo* test with the combination of triterpenoid **2** and antimalarial drug artesunate to improve the efficacy of drug action [30].

■ ACKNOWLEDGMENTS

We thank Dr. Sofa Fajriah in Research Center for Chemistry, Indonesian Science Institute for NMR measurements and Mrs. Hilkatul Ilmi, Institute of Tropical Disease, Universitas Airlangga, Surabaya 60115, Indonesia, for the technical support provided during the *in vivo* studies. We are grateful to Dr. Esther M. Yoo, Mr. Andrew Miller and Dr. Chandradhish

Ghosh at the Max Planck Institute for their helpful discussions.

■ AUTHOR CONTRIBUTIONS

The experiment was conducted by NB with the analysis being conducted by MAM and YS. The NMR and *in vivo* analysis were done by WM and AW. The manuscript was arranged and revised by AMI, BS, and JS. All the authors mentioned have agreed to the final version of this manuscript.

■ REFERENCES

- [1] World Health Organization, 2019, *World malaria report 2019*, World Health Organization, Geneva, <https://apps.who.int/iris/handle/10665/330011>, License: CC BY-NC-SA 3.0 IGO
- [2] Menard, D., and Dondorp, A., 2017, Antimalarial drug resistance: A threat to malaria elimination, *Cold Spring Harbor Perspect. Med.*, 7, a025619.
- [3] Diagana, T.T., 2015, Supporting malaria elimination with 21st century antimalarial agent drug discovery, *Drug Discovery Today*, 20 (10), 1265–1270.
- [4] Cowell, A.N., and Winzeler, E.A., 2019, The genomic architecture of antimalarial drug resistance, *Briefings Funct. Genomics*, 18 (5), 314–328.
- [5] Babatunde, K.A., and Adenuga, O.F., 2022, Neutrophils in malaria: A double edged sword role, *Front. Immunol.*, 13, 922377.
- [6] Tu, Y., 2011, The discovery of artemisinin (*qinghaosu*) and gifts from Chinese medicine, *Nat. Med.*, 17 (10), 1217–1220.
- [7] Gómez-García, A., and Medina-Franco, J.L., 2022, Progress and impact of Latin American natural product databases, *Biomolecules*, 12 (9), 1202.
- [8] Hedrén, M., Chase, M.W., and Olmstead, R.G., 1995, Relationships in the *Acanthaceae* and related families as suggested by cladistic analysis of *rbcL* nucleotide sequences, *Plant Syst. Evol.*, 194 (1), 93–109.
- [9] Dirar, A.I., Adhikari-Devkota, A., Kunwar, R.M., Paudel, K.R., Belwal, T., Gupta, G., Chellapan, D.K., Hansbro, P.M., Dua, K., and Devkota, H.P., 2021, Genus *Blepharis* (Acanthaceae): A review of ethnomedicinally used species, and their phytochemistry and pharmacological activities, *J. Ethnopharmacol.*, 265, 113255.
- [10] Wahidah, B.F., and Husain, F., 2018, Etnobotani tumbuhan obat yang dimanfaatkan oleh masyarakat Desa Samata Kecamatan Somba Opu Kabupaten Gowa Sulawesi Selatan, *Life Sci.*, 7 (2), 39–88.
- [11] Widyawaruyanti, A., Asrory, M., Ekasari, W., Setiawan, D., Radjaram, A., Tumewu, L., and Hafid, A.F., 2014, *In vivo* antimalarial activity of *Andrographis paniculata* tablets, *Procedia Chem.*, 13, 101–104.
- [12] Sari, N., Wahidah, B.F., and Gaffar, N.A., 2017, Etnobotani tumbuhan yang digunakan dalam pengobatan tradisional di Kecamatan Sinjai Selatan Kabupaten Sinjai Sulawesi Selatan, *Pros. Sem. Nas. Biol. Life*, 3 (1), 6–13.
- [13] Dalimartha, S., and Adrian, F., 2013, *Ramuan Herbal Tumpas Penyakit*, Penebar Swadaya, Jakarta, Indonesia.
- [14] Ekasari, W., Fatmawati, D., Khoiriah, S.M., Baquiuddin, W.A., Nisa, H.Q., Maharupini, A., Wahyuni, T.S., Oktarina, R.D., Suhartono, E., and Sahu, R.K., 2022, Antimalarial activity of extract and fractions of *Sauropus androgynus* (L.) Merr, *Scientifica*, 2022, 3552491.
- [15] Giemsa, G., 1902, Färbemethoden für malariaparasiten, *Zentralbl. Bakteriol.*, 31, 429–430.
- [16] McLean, R.C., 1943, Microscopic technique in biology and medicine, *Nature*, 152 (3868), 709.
- [17] Kwansa-Bentum, B., Agyeman, K., Larbi-Akor, J., Anyigba, C., and Appiah-Opong, R., 2019, *In vitro* assessment of antiplasmodial activity and cytotoxicity of *Polyalthia longifolia* leaf extracts on *Plasmodium falciparum* strain NF54, *Malar. Res. Treat.*, 2019, 6976298.
- [18] Kamaraj, C., Kaushik, N.K., Mohanakrishnan, D., Elango, G., Bagavan, A., Zahir, A.A., Rahuman, A.A., and Sahal, D., 2012, Antiplasmodial potential of medicinal plant extracts from Malaiyur and Javadhu hills of South India, *Parasitol. Res.*, 111 (2), 703–715.
- [19] Greca, M.D., Monaco, P., and Previtiera, L., 1990, Stigmasterols from *Typha latifolia*, *J. Nat. Prod.*, 53 (6), 1430–1435.

- [20] Wang, G.W., Lv, C., Yuan, X., Ye, J., Jin, H.Z., Shan, L., Xu, X.K., Shen, Y.H., and Zhang, W.D., 2015, Lanostane-type triterpenoids from *Abies faxoniana* and their DNA topoisomerase inhibitory activities, *Phytochemistry*, 116, 221–229.
- [21] Shen, J., Kai, J., Tang, Y., Zhang, L., Su, S., and Duan, J.A., 2016, The chemical and biological properties of *Euphorbia kansui*, *Am. J. Chin. Med.*, 44 (2), 253–273.
- [22] Isaka, M., Chinthanom, P., Sappan, M., Supothina, S., Vichai, V., Danwisetkanjana, K., Boonpratuang, T., Hyde, K.D., and Choeyklin, R., 2017, Antitubercular activity of mycelium-associated *Ganoderma lanostanoids*, *J. Nat. Prod.*, 80 (5), 1361–1369.
- [23] Perumal, P., Sowmiya, R., Kumar, S.P., Ravikumar, S., Deepak, P., and Balasubramani, G., 2018, Isolation, structural elucidation and antiplasmodial activity of fucosterol compound from brown seaweed, *Sargassum linearifolium* against malarial parasite *Plasmodium falciparum*, *Nat. Prod. Res.*, 32 (11), 1316–1319.
- [24] Workman, S.D., Worrall, L.J., and Strynadka, N.C.J., 2018, Crystal structure of an intramembranal phosphatase central to bacterial cell-wall peptidoglycan biosynthesis and lipid recycling, *Nat. Commun.*, 9 (1), 1159.
- [25] Fu, Y., Ding, Y., Wang, Q., Zhu, F., Tan, Y., Lu, X., Guo, B., Zhang, Q., Cao, Y., Liu, T., Cui, L., and Xu, W., 2020, Blood-stage malaria parasites manipulate host innate immune responses through the induction of sFGL2, *Sci. Adv.*, 6 (9), eaay9269.
- [26] Peters, W., Portus, J.H., and Robinson, B.L., 1975, The chemotherapy of rodent malaria, XXII. The value of drug-resistant strain of *P. berghei* in screening for blood schizontocidal activity, *Ann. Trop. Med. Parasitol.*, 69 (2), 155–171.
- [27] Sianturi, J., Manabe, Y., Li, H.S., Chiu, L.T., Chang, T.C., Tokunaga, K., Kabayama, K., Tanemura, M., Takamatsu, S., Miyoshi, E., Hung, S.C., and Fukase, K., 2019, Development of α -gal-antibody conjugates to increase immune response by recruiting natural antibodies, *Angew. Chem., Int. Ed.*, 58 (14), 4526–4530.
- [28] Jiménez-Díaz, M.B., Viera, S., Ibáñez, J., Mulet, T., Magán-Marchal, N., Garuti, H., Gomez, V., Cortés-Gil, L., Martínez, A., Ferrer, S., Fraile, M.T., Calderón, F., Fernández, E., Shultz, L.D., Leroy, D., Wilson, D.M., García-Bustos, J.F., Gamo, F.J., and Angulo-Barturen, I., 2013, A new *in vivo* screening paradigm to accelerate antimalarial drug discovery, *PLoS One*, 8 (6), e66967.
- [29] Fang, Y., He, X., Zhang, P., Shen, C., Mwangi, J., Xu, C., Mo, G., Lai, R., and Zhang, Z., 2019, *In vitro* and *in vivo* antimalarial activity of LZ1, a peptide derived from snake cathelicidin, *Toxins*, 11 (7), 379.
- [30] Corral, M.G., Leroux, J., Stubbs, K.A., and Mylne, J.S., 2017, Herbicidal properties of antimalarial drugs, *Sci. Rep.*, 7 (1), 45871.

Extraction, Isolation, and Characterization of Nanocrystalline Cellulose from *Barangan* Banana (*Musa acuminata* L.) Peduncles Waste

Ratna Ratna^{1,2}, Nasrul Arahman^{1,3,4,5,6}, Agus Arip Munawar², and Sri Aprilia^{1,3*}

¹Doctoral Program, School of Engineering, Post Graduate Program, Universitas Syiah Kuala, Darussalam, Banda Aceh 23111, Indonesia

²Department of Agricultural Engineering, Universitas Syiah Kuala, Darussalam, Banda Aceh 23111, Indonesia

³Department of Chemical Engineering, Universitas Syiah Kuala, Darussalam, Banda Aceh 23111, Indonesia

⁴Graduate School of Environmental Management, Universitas Syiah Kuala, Darussalam, Banda Aceh 23111, Indonesia

⁵Research Center for Environmental and Natural Resources, Universitas Syiah Kuala, Jl. Hamzah Fansuri No. 4, Darussalam, Banda Aceh 23111, Indonesia

⁶Atsiri Research Center, Universitas Syiah Kuala, Jl. Syeh A. Rauf, Darussalam, Banda Aceh 23111, Indonesia

* **Corresponding author:**

email: sriaprilialia@unsyiah.ac.id

Received: May 18, 2022

Accepted: October 3, 2022

DOI: 10.22146/ijc.74718

Abstract: Microwave-assisted acid hydrolysis has an impact on the characteristics of nanocrystalline cellulose (NCCs). In this study, NCCs was prepared from banana peduncles through hydrolysis of sulfuric acid (concentrations of 1, 2, and 3 M) and hydrolysis time (0.5 and 1.5 h) assisted by microwave and ultrasonic energy to obtain the best NCCs. The characterization of NCCs properties, namely, yield, morphology, functional groups, crystallinity, heat resistance, particle size, and color. The results showed that the yield of NCCs decreased as sulfuric acid concentration and the time length of hydrolysis increased. The FTIR spectra of NCCs showed the most relevant molecular bands, namely O-H, C-H, and C-O, at the wavenumbers range of 3200–4000, 2500–3200, and 500–1500 cm^{-1} , respectively. The TGA test showed that the decomposition of NCCs occurred at a temperature of 275.35–409.40 °C, with a weight loss ranging from 84.00% to 94.09%. Crystallinity index and crystal sizes range from 53.99% to 57.33% and 22.35 to 36.28 nm, respectively. The brightest color of NCCs powder was generated with 1 M sulfuric acid and a hydrolysis time of 0.5 h. In conclusion, barangan banana peduncles waste can be used as raw material for producing NCCs.

Keywords: nanocrystalline cellulose; barangan banana peduncles waste; acid hydrolysis; microwave; ultrasonic

■ INTRODUCTION

Globally, people grow around 5.6 million hectares of bananas, with a production rate of 120 million tons annually. The banana industry is estimated to generate a turnover of 8 billion USD per year [1]. One sector using the most bananas is the food industry [2]. The abundance use of bananas leads to banana waste, including bark, pseudostem, leaves, rejected bananas, peduncles, and fiber [3]. Each banana tree produces one peduncle of bananas, and the tree will become waste after harvesting.

It is estimated that every hectare of banana plantations produces nearly 220 tons of biomass waste [4]. The unused by-product of banana processing is banana peduncles. This by-product is promising because it contains lignocellulose to produce cellulose [5].

Cellulose is widely used as a polymer matrix and has grown rapidly in the last decade [6] because of its advantages, such as being non-toxic, low density, good mechanical properties, environmentally friendly, inexpensive, and biodegradable [7-8]. Cellulose has a linear chain structure of a hydro-glucose monomer unit-

linked via 1-4 β , with amorphous and crystalline regions. The structures, properties, and sizes of cellulose depend on the sources [9]. Cellulose is the largest proportion of lignocellulosic substances; from a structural perspective, cellulose is a polymer formed by β -D glucose units ($C_6H_{12}O_6$) [10-12].

Nanocrystalline cellulose (NCCs) are prominent cellulose derivatives because of their exclusive features and outstanding mechanical properties, high aspect ratio to diameter, several micrometers length, high surface reactivity, and low density [12]. Structurally, NCCs are basic needle-shaped crystals with intact crystal features. NCCs are generally 5–10 nm wide and 500–1000 nm long [13-14]. NCCs are highly crystalline nanocrystals that can be produced from cellulose substances by acids [15-17]. NCCs produced from empty peduncles were previously modified by tannic acid and decyl amine [9]. NCCs have also been successfully extracted from seaweed [18], corn cobs [19-20], oil palm empty fruit peduncles [21-22], ramie fiber [23], waste paper [24], bagasse [25], and kenaf [26].

Cellulose hydrolysis in acid can be done by strong and weak acids at high temperatures and pressures, and by concentrated acid at low temperatures and pressures [27-28]. NCCs can be obtained from various sources using several alkalines or acid hydrolysis [29-30]. The functional properties of substances can be improved by modifying chemical or physical processes, such as acid hydrolysis, oxidation, ultrasonication, and microwave [31]. Microwave energy has been found as an alternative to heating in acid or alkali treatment [32]. Recently, microwave-assisted alkali treatment and microwave-assisted acid hydrolysis before ultrasonication were used to generate higher yields of NCCs [33]. Microwave irradiation can increase the yield of compounds drastically in a short time [34-35]. Mechanical treatment, such as sonication, spreads a stable and uniform suspension of NCCs [36]. Sonication is an alternative for degradation [37] in producing NCCs.

Nanocellulose can be produced from various wastes from agricultural crops [38]. Mocktar et al. has produced nano-cellulose from the kenaf core (*Hibiscus cannabinus*) by chemical method [26]. Produced nanocrystalline

cellulose from eucalyptus was hydrolyzed using sulfuric acid by conventional methods and assisted by thermostable. The nanocrystalline cellulose produced by the thermostable method showed much better thermal stability than hydrolyzed by the conventional method [39]. Kusmono et al. have produced nanocrystalline cellulose made from flax fiber by hydrolysis of sulfuric acid using a conventional method with a hot plate [23]. Rahmawati et al. reported that nanocrystalline cellulose was isolated from *Typha* sp. through conventional acid hydrolysis using a hot plate with a reflux system [40]. There have been many reports on the hydrolysis of nanocrystalline cellulose from plant fibers and agricultural wastes. However, there has been no report on the hydrolysis method and characterization of NCCs from the waste of *barangan* banana (*Musa acuminata* L.) peduncles. Therefore, this study examines the production of NCCs from the waste of *barangan* banana peduncles by studying the alkalizing, bleaching, and hydrolysis treatment of sulfuric acid with variable concentrations of sulfuric acid and hydrolysis time using microwaves-ultrasonics energy on the properties and characteristics of NCCs. The analysis covered the yield and characterization of NCCs properties, namely, morphology, functional groups, crystallinity, heat resistance, particle size, and color.

■ EXPERIMENTAL SECTION

Materials

The waste of *barangan* banana (*Musa acuminata* L.) peduncles was taken from the community around Banda Aceh, Indonesia. The chemicals used were sulfuric acid (Merk Emsure® Germany), NaOH (Merk Emsure® Germany), H_2O_2 35% food-grade, and distilled water.

Procedure

Fiber preparation

The *barangan* banana peduncles were cut into pieces and pressed using a pressing machine to obtain the fiber. The fibers were then dried and ground using a grinder GM-400S1 at a speed of 31000 rpm and sieved using a 40 mesh sieve.

Cellulose extraction

The alkalization process was done by a microwave (Samsung ME731K) with a 1 M NaOH solution (1:15 w/v) at 450 Watt with a temperature of around 90 °C for 1 h. The fiber was then washed to a neutral pH and dried at 60 °C using a hot air sterilizer oven (model: YCO-010, Taiwan). Following the polymerization process, the bleaching process was conducted for one hour using 35% H₂O₂ with a fiber-to-solution ratio of 1:15 (w/v) at 180 W microwave power and a temperature range of 60–65 °C. This process was to remove compounds other than cellulose [41].

Isolation of nanocrystalline cellulose

The isolation of NCCs was conducted by sulfuric acid hydrolysis with the concentrations of 1, 2, and 3 M with a ratio of a sulfuric acid solution of 1:15 (w/v). This process was done by a microwave (Samsung ME731K) at 100 W for 0.5 and 1.5 h, as presented in Fig. 1. Once the hydrolysis process was completed, the sample was washed using distilled water to reach a neutral pH. Next, the samples were centrifuged using a centrifuge (CMC supplied by Phillip Harris INT) at 11000 rpm for 30 min. The water was changed twice, followed by the sonification process using ultrasonics (Branson model 5510, USA) with a frequency of 40 kHz for 4 h. It was centrifuged for 30 min and dried using a hot air sterilizer oven (model

YCO-010, Taiwan) at 60 °C to a maximum moisture content of 12%. Later, it was ground and sieved using a 500 mesh sieve ASTM No: 11. The design of the NCCs isolation treatment is shown in Table 1. The analysis was then conducted for the yield and the characterization of NCCs properties, namely, morphological properties, functional groups, crystallinity properties, heat resistance, particle size, and color.

Characterization of nanocrystalline cellulose

Yield. The yield was calculated as a percentage (%) of the initial weight after hydrolysis. The samples obtained after the treatment were dried and compared to the initial weight. Yield is determined using Eq. (1) [42].

$$\text{Yield}(\%) = \frac{M_a}{M_i} \quad (1)$$

The final (M_a) and initial sample weights (M_i) were measured to calculate the yield.

Table 1. Design of NCCs isolation treatment

Samples	Treatment
SA-1	Sulfuric acid 1 M/0.5 h
SA-2	Sulfuric acid 1 M/1.5 h
SU-1	Sulfuric acid 2 M/0.5 h
SU-2	Sulfuric acid 2 M/1.5 h
SM-1	Sulfuric acid 3 M/0.5 h
SM-2	Sulfuric acid 3 M/1.5 h

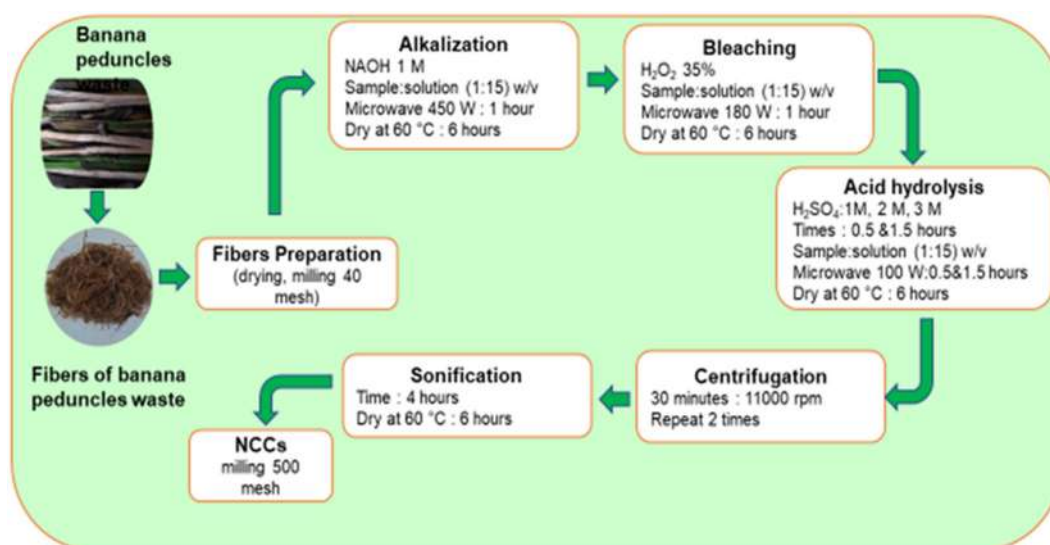


Fig 1. Schematic diagram of the NCCs insulating process

Functional groups. Fourier transform infrared spectroscopy (FTIR, Shimadzu, Japan) was used to determine the functional groups of NCCs products. The NCCs sample was dried in an oven at 60 °C until constant weight to ensure it was free from water content. Then, the NCCs sample was placed on the FTIR panel, and the functional groups were read in the wavenumber of 4000–400 cm^{-1} .

Heat resistance. The heat resistance of gelatin was analyzed using a Thermogravimetric Analyzer (Shimadzu DTG-60, Japan). The sample (10 mg) was put into a platinum pan and then heated to a temperature of 600 °C at a nitrogen atmosphere flow rate of 50 mL/min and a temperature rate of 40 °C/min.

Morphological properties. Morphological studies of samples were done by Scanning Electron Microscopy (SEM, JEOL, JSM-6510LA, Japan) with a resolution of 3.0 nm at 30 kV. To obtain quantitative data on the particle size of NCCs, the SEM images were analyzed using ImageJ software. ImageJ software was used to determine the particle diameter (d) of the NCCs. The particle measurement in the SEM test is based on the sphere's diameter because it cannot be equated with the particle length of the NCCs.

Crystallinity properties. Crystallinity and crystal size were measured using an XRD (Shimadzu-7000, Japan) operated at a voltage of 40 kV and a current of 30 mA, with a scan speed of 2.00 deg/min. The crystallinity index (CI) was calculated based on the deconvolution method, as formulated in Eq. (2).

$$CI = \frac{I_{002} - I_{am}}{I_{002}} \times 100\% \quad (2)$$

where I_{002} is the highest peak intensity for the crystalline region and I_{am} is the minimum peak intensity for the amorphous region. I_{002} represents the crystalline and amorphous regions, while I_{am} only represents the amorphous region of the maximum intensity of the lattice peak diffraction at 22° to 23° and I_{am} is the amorphous part of the material (at the minimum intensity between 18° and 19°) [43-44]. The crystal size was calculated using the Scherrer formula, as given in Eq. (3).

$$t = \frac{K\lambda}{\beta 1/2 \cos\theta} \quad (3)$$

where K (0.91) is the Scherrer constant, λ (1.54060 Å) is the wavelength of the radiation, $\beta 1/2$ is the full width at half maximum (FWHM) of the diffraction peak in radians (2θ), and θ is the Bragg angle [40].

Particle size analyzer. Particle size distribution analysis was performed using a particle size analyzer (HORIBA Scientific SZ-100, Japan) with a scattering angle of 90°, holding temperature of 25.1 °C, and measurement time of 5.12 sec at a rate of 225 kcps. The average particle diameter size of each sample was taken from the average value of three repetitions.

NCCs powder color test. The color of the NCCs was analyzed using the CIE method. CIE is the most comprehensive $L^* a^* b^*$ color space defined by the International Commission on color illumination (French Commission Internationale de l'éclairage, CIELAB). CIELAB can describe all kinds of colors visible to the human eye. This method is often used for color space references [44]. The NCCs image was then analyzed for color using the MVtec Halcon ver.20 software. The sample object was separated by 15 times erosion treatment to get the RGB value. The resulting RGB (Red, Green, Blue) values were converted to the $L^* a^* b^*$ color space.

■ RESULTS AND DISCUSSION

Yield

Yield is the result of the processing activity. The average yield of fiber from the waste of fresh banana peduncles was 5.4%. The alkalization treatment used 1 M NaOH and 35% H_2O_2 for bleaching. The fiber yield produced in the alkalization process and the bleaching process was 39.5%, with a mass loss of 60.5, and 71%, with a mass loss of 29%, respectively. The more stages in the process, the higher the result because most of the lignin and hemicellulose were removed [45]. Alkalization treatment can remove hemicellulose, reducing weight from 33% to 12%. The alkalization process can reduce the lignin and hemicellulose content and enable the fiber to be easily damaged by the hydrolysis media [35]. Also, H_2O_2 can remove more lignin [46]. Alkalization triggers a color change linked to the different pigmentation of the lignin fraction remaining in

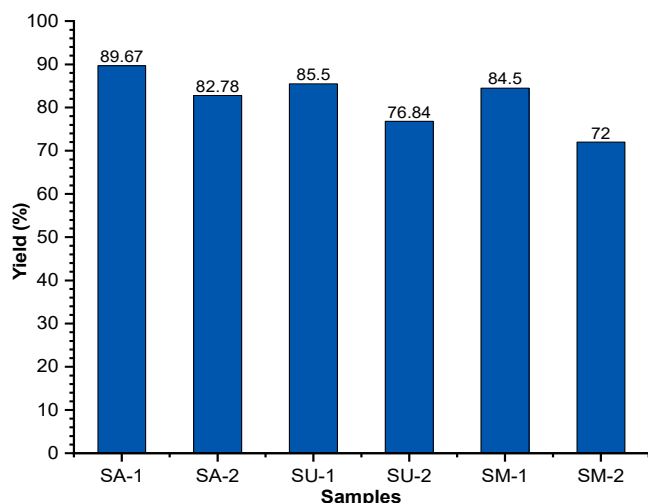


Fig 2. The yield of NCCs isolated from the waste of banana peduncles

the substance [47]. It effectively purifies cellulose fibers, removing non-cellulose components, such as parts of lignin and hemicellulose [13]. The treatment of NaOH solution converts cellulose I to cellulose II with a crystal structure that is much more stable than cellulose I, with stronger hydrophobic interconnections. The hydrolysis yield is shown in Fig. 2.

The yield of NCCs from the treatment variables of different sulfuric acid concentrations and hydrolysis time ranged from 72% to 89.67%, with a mass loss of around 28.00–10.33%. The highest yield was in the treatment of SA-1 (89.67%). Meanwhile, the lowest yield was at the treatment of SM-2 (72%). The yield of NCCs decreased with the increasing sulfuric acid concentration and the hydrolysis time, as shown in Fig. 2. This decrease in yield may be due to the changes in amorphous cellulose or damage to crystalline cellulose [8].

The low yield may result from the gradual disintegration of the amorphous region and degradation of the crystalline moiety during the increasing hydrolysis time. Raja et al. [28] glucose microfibers of cellulose molecules were bonded to form long polymer chains, and the content of lignin and hemicellulose around the cellulose was the main obstacle to hydrolyzing cellulose. Ilyas et al. [8] produce sugar palm cellulose yield in the hydrolysis process using sulfuric acid with a concentration of 60%, which is 82.33%. Seta et al. [6] reported that the yield of NCCs bamboo pulp hydrolyzed using maleic acid

was in the range of 2.8% to 24.5%. In this study, treatment with sulfuric acid concentration and hydrolysis time assisted by microwave and ultrasonic energy was able to produce yields ranging from 72% to 86.67%.

Functional Groups of NCCs

Fig. 3 displays the results of the FTIR spectrum of NCCs from *barangan* banana peduncles using the hydrolysis treatment of sulfuric acid concentration and hydrolysis time. It shows three main absorption spectra, the largest indicated at the absorption region around 3200–4000 cm^{-1} was O-H, 2500–3200 cm^{-1} was C-H, and 500–1500 cm^{-1} was C-O. The increasing concentration of sulfuric acid and the hydrolysis time did not affect the absorption and functional groups of NCCs, showing that the NCCs did not contain functional groups of other compounds, such as lignin and hemicellulose. Acid hydrolysis did not show any absorption region for C=C, C-O-C, and $-\text{CH}_2$ bonds [48]. The C=C and C-O-C bonds are found in lignin. The absorption region around 1420 cm^{-1} showed a deformed $-\text{CH}_2$ bond in cellulose. It showed the crystalline area, where the absorption area increases with the purification process. After hydrolysis, three main absorption regions were found: 3288.08, 1636.43, and 1089.92 cm^{-1} , indicating O-H stretching, O-H deformation, and C-C stretching, respectively. The absorption region that emerged indicates no lignin generated from the acid hydrolysis treatment.

The spectra were identified at the absorption of 3350 cm^{-1} (O-H stretching/intramolecular hydrogen bond stretching for cellulose I), 2900 cm^{-1} (C-H stretching), 1640 cm^{-1} (O-H bending due to adsorbed water), 1510 cm^{-1} (aromatic ring in lignin), 1420 cm^{-1} (due to the scissoring motion of CH_2 in cellulose), 1375 cm^{-1} (C-H bending), 1340 cm^{-1} (O-H in the bending plane), 1311 cm^{-1} (CH_2 wagging), 1250 cm^{-1} (C-O exiting the stretching plane because of the aryl groups in lignin), 1205 cm^{-1} (S=O vibrations, due to the esterification reaction occurred in the hydrolysis), 1159 cm^{-1} (C-C stretching ring), 1109 cm^{-1} (C-O-C glycosidic bond), 1061 cm^{-1} (C-O-C pyranose ring stretching), and 897 cm^{-1} (cellulose glycosidic bonds) [19,50-52]. The vibrational modes of amide I at 1616 cm^{-1}

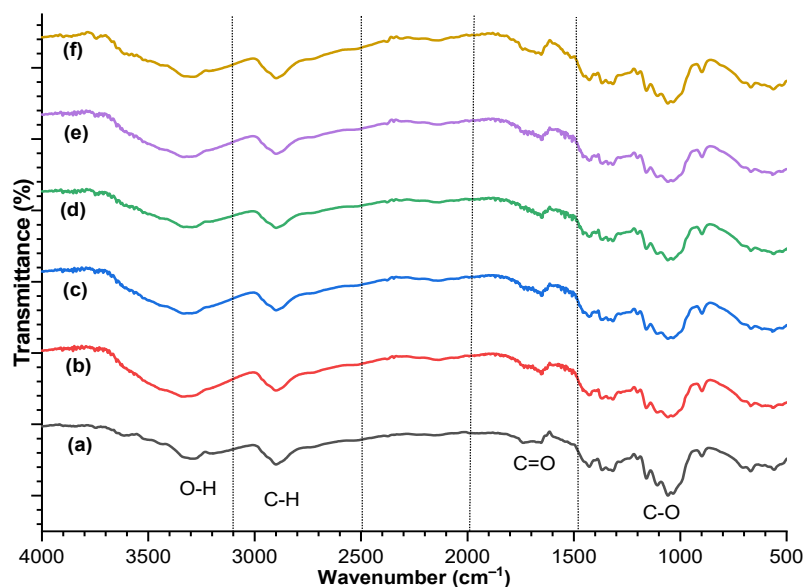


Fig 3. FTIR spectra of NCCs from *barangan* banana peduncles; (a) SA-1; (b) SA-2; (c) SU-1; (d) SU-2; (e) SM-1; and (f) SM-2

and II at 1597 cm^{-1} were observed. The moderate to strong IR absorption band at $1200\text{--}970\text{ cm}^{-1}$ was mainly due to the C–C and C–O stretching of the pyranoid ring [49]. The IR spectra of the NCCs showed a typical absorption band for cellulose substances. The signals at 1429 , 1163 , 1111 , and 897 cm^{-1} indicated the NCCs in cellulose I β [50]. The absorption bands at around 1430 , 1370 , and 2900 cm^{-1} indicated the characteristic of the crystalline region in the polymer, and the absorption band at 890 cm^{-1} showed the type of the amorphous region [51]. Hydrolysis with sulfuric acid did not modify the functional groups of cellulose; instead, discontinuities in the glucose ring only [52].

Heat Resistance of NCCs

The TGA method is a rapid test for measuring a material's thermal stability to predict its real-life and long-term stability. The thermal decomposition process occurred in the compound follows first-order kinetics [53]. The results of the thermogravimetric analysis to examine the thermal stability of NCCs from banana peduncles hydrolyzed with 1, 2, and 3 M sulfuric acid for 0.5 and 1.5 h can be seen in Fig. 4. It shows the initial weight loss of the NCCs was in around region 2 with a temperature range of 95.0 to $180.0\text{ }^{\circ}\text{C}$ because volatile compounds and water molecules evaporated. In regions 3

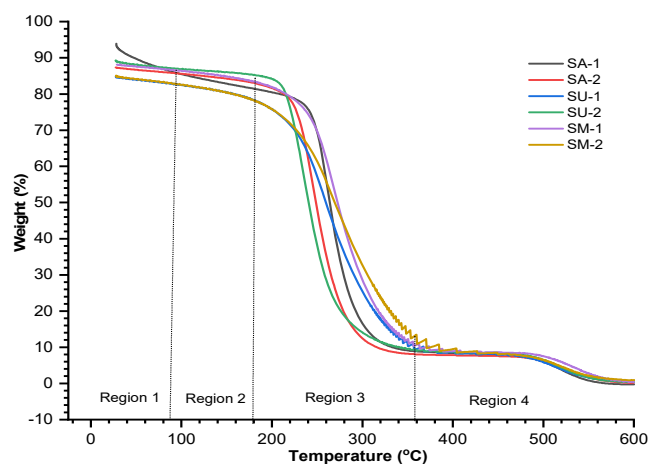


Fig 4. Heat resistance of NCCs from *barangan* banana peduncles

and 4, the NCCs decomposed at a temperature of 275.35 to $409.40\text{ }^{\circ}\text{C}$.

Table 2 shows that the degradation or decomposition of NCCs began to occur in the temperature range of 275.35 to $409.40\text{ }^{\circ}\text{C}$. The greater the concentration of sulfuric acid, the higher the endset temperature (temperature of degradation). Likewise, the hydrolysis time also showed the difference in the decomposition temperature because of hemicellulose and amorphous cellulose, which were more easily degradable than crystalline cellulose. The wider lignin peak covered

Table 2. Thermal degradation, weight loss, and residue of the NCCs from *barangan* banana peduncles

Samples	Cellulose thermal degradation			Weight loss (%)	Residue at 600 °C (%)
	T _{onset} (°C)	T _{mid point} (°C)	T _{endset} (°C)		
SA-1	319.67	348.29	380.83	94.09	5.91
SA-2	340.01	366.69	398.83	87.14	12.86
SU-1	294.10	345.60	405.62	84.10	15.90
SU-2	347.15	373.91	404.08	88.83	11.17
SM-1	314.13	351.22	399.19	87.71	12.29
SM-2	275.35	338.62	409.40	84.00	16.00

the range from 200 to 500 °C, with the maximum at 350 °C. In a nitrogen atmosphere, the main peak appeared at around 360 °C due to the decomposition of α -cellulose [54]. In addition, lignin degradation occurred gradually from 100 to 900 °C, with the disintegration peak occurring after 380 °C. Thus, an additional endothermic peak after 350 °C happened due to the degradation of residual lignin molecules. The presence of foreign material in cellulose samples increased the energy needed for degradation [12]. In the initial temperature region of 70 to 140 °C, the peak endothermic heat energy absorbed was used to evaporate water vapor. Outside of 200 °C, the second and third endotherms were 257.1 and 282.7 °C. This endotherm was related to the decarboxylation and depolymerization of cellulose [13]. The bleaching and alkali processes generated α -cellulose as a crystalline residue. The higher the crystal structure, the higher the degradation temperature [42].

The weight loss due to the treatment of sulfuric acid concentration and hydrolysis time ranged between 84% and 94.09%, with the highest weight loss occurring in the treatment of SA-1 and the lowest in the treatment of SM-2. The treatment of SA, SU, and SM resulted in degradation in the same region, namely region 4. This indicates that the resistance of NCCs to temperature is the same even though the weight loss shows different values. This shows that the resistance characteristics of the NCC samples to temperature are the same. A high weight loss indicates a small residue [13]. The relatively low weight loss indicates a strong cellulose structure to withstand high-temperature conditions. The water loss and the structural hydrophilic nature of the functional groups of each polysaccharide occur between 50 and 100 °C [25].

Hemicellulose loss occurred between 220 and 340 °C, with the main degradation peak around 320 °C. The thermal stability of NCCs with sulfate groups could be improved when the acid sulfate groups were neutralized [39]. Under different conditions, samples of NCCs showed gradual weight loss at around 210 to 378 °C [55].

Morphology of NCCs

Fig. 5 images the morphological microstructure of NCCs from *barangan* banana peduncles treated with sulfuric acid concentrations of 1, 2, and 3 M and hydrolysis times of 0.5 and 1.5 h. Although the sulfuric acid content and hydrolysis time are different, the morphology of the NCCs has the same structure (as displayed in Fig. 5). The size of the resulting NCCs was also the same for all treatments, namely 1 μm . The structure looks like the occurrence of aggregates in the NCCs particles. Wu et al. [38] resulted in the size of the structure of okara nanocellulose (using the method of high-pressure ultrasound or high-pressure homogenization) based on scanning electron microscopy, which was in the range of 2 to 10 μm . Samples of okara nanocellulose also showed the occurrence of aggregation.

Seta et al. [6] convey that the fibers are reduced in size to micro size, and there is a possibility of reaggregation of the fibers of small size. It can be caused by the milling process's activation/interaction of the fiber surface, and the high fiber concentration will increase the friction and shear forces between the fibers. This study resulted in a smaller structure size of NCCs from *barangan* banana peduncles (1 μm) than that produced by Wu et al. [38], which is 2 to 10 μm . The particle diameter (d) of

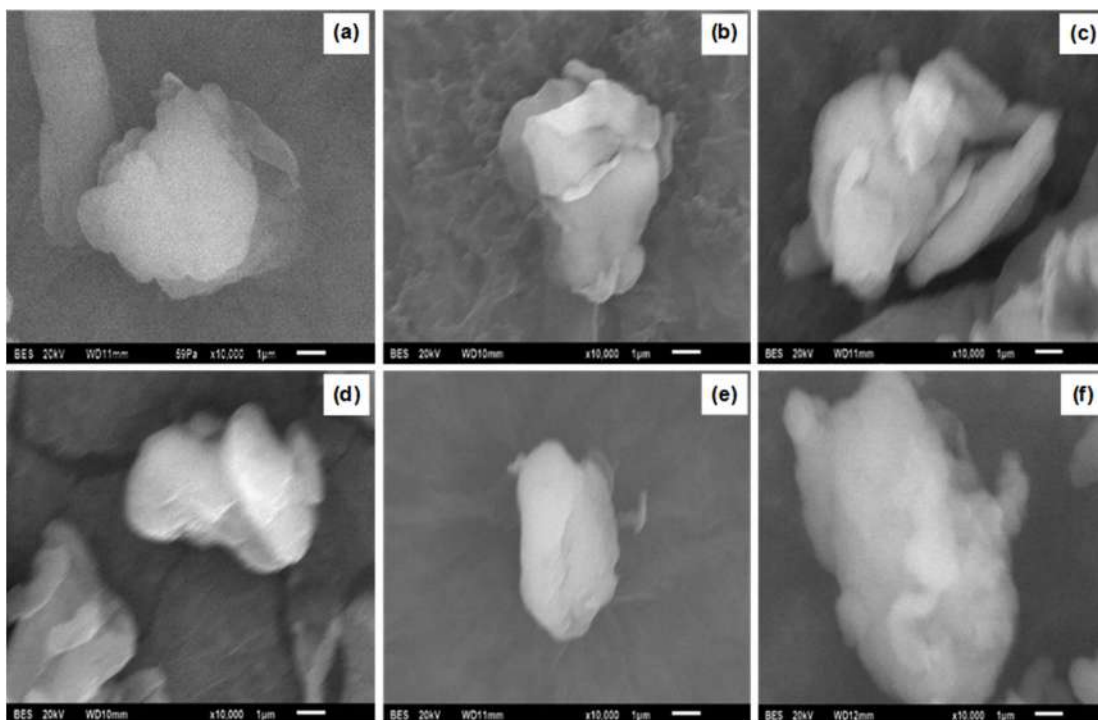
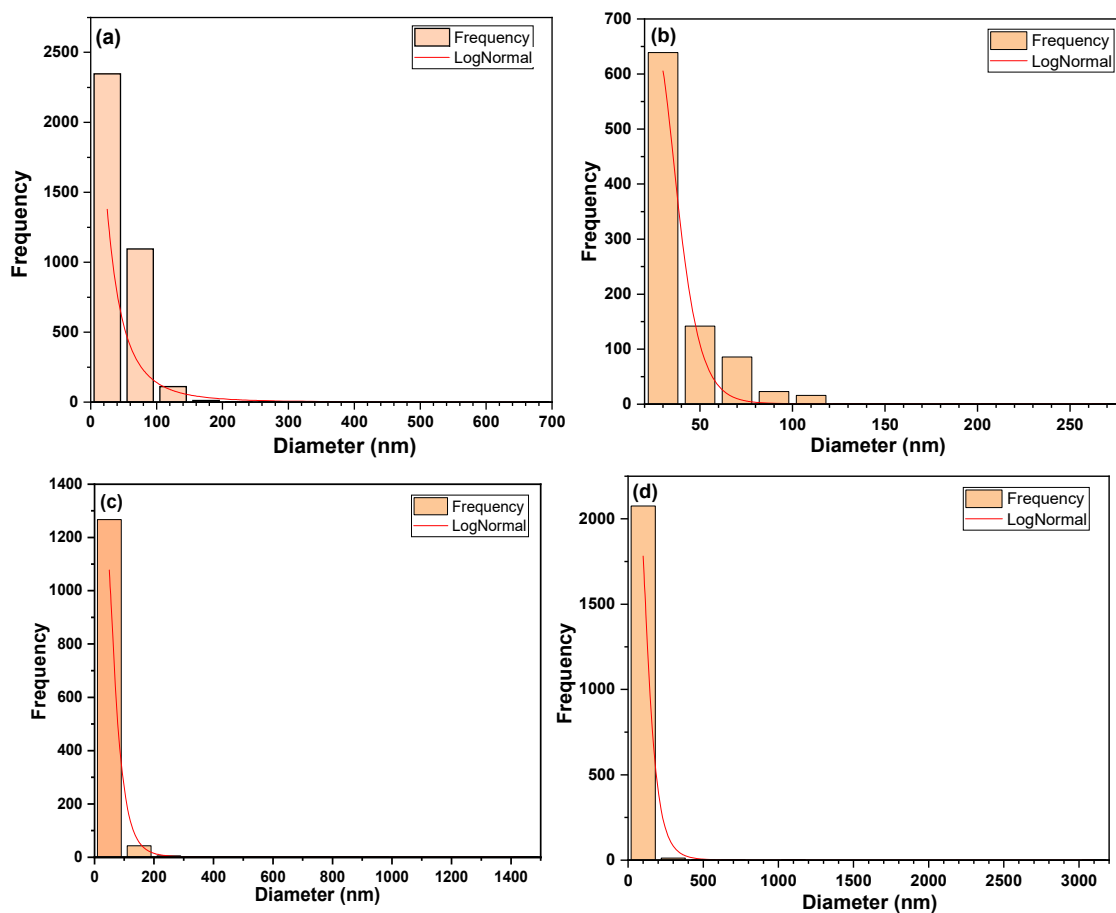


Fig 5. SEM image of NCCs banana peduncles; (a) SA-1, (b) SA-2, (c) SU-1, (d) SU-2, (e) SM-1, and (f) SM-2



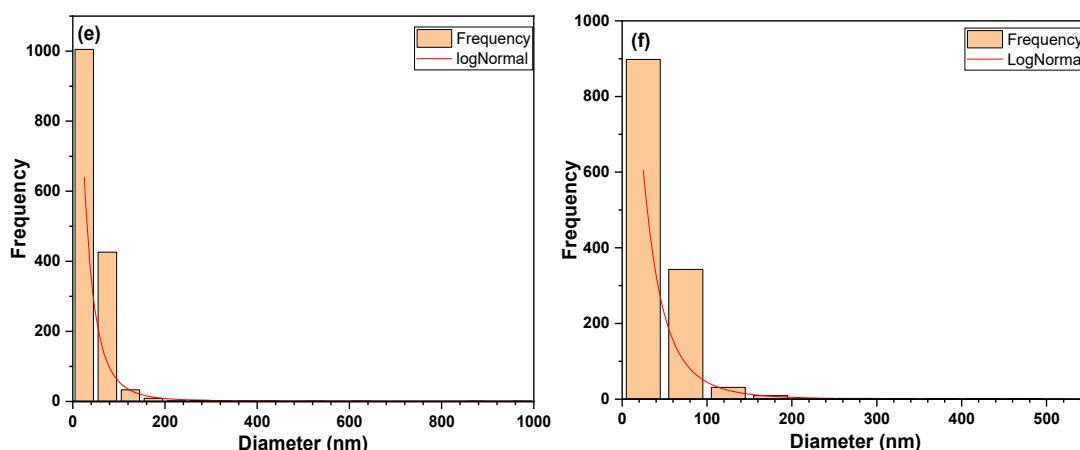


Fig 6. Histogram distribution of NCCs particles from SEM images; (a) SA-1, (b) SA-2, (c) SU-1, (d) SU-2, (e) SM-1, and (f) SM-2

the NCC samples from the SEM test results can be quantitatively analyzed using ImageJ software. Regarding the SEM image analysis using ImageJ software, the histogram of the NCCs particle distribution can be seen in Fig. 6, and the diameter of particles can be seen in Table 3. The particle diameter analysis using ImageJ software of NCCs for all treatments of sulfuric acid concentration and hydrolysis time ranged from 25 to 100 nm.

Crystallinity Properties of NCCs

Enhanced crystallinity can increase the heat resistance and thermal stability of a material. A further decrease in the degradation temperature of NCCs may

correlate with sulfate groups into crystalline cellulose during the hydrolysis of sulfuric acid [56]. Fig. 7 presents the X-ray diffraction pattern of the NCCs from banana peduncles. The diffraction peaks at 2θ for 1, 2, and 3 M sulfuric acids with the hydrolysis times of 0.5 and 1.5 h ranged from 22.19° – 22.41° . All diffraction patterns for all treatments are at the highest peak at 2θ above 22° [9,57-58]. The observed peaks in the XRD pattern of cellulose and NCCs at 2θ of 14.5° and 15.5° correspond to I_{am} planes. The peak of $2\theta = 22.5^\circ$ corresponds to the I_{002} crystallographic plane, indicating that cellulose and nanocellulose had amorphous and crystalline regions and showed the crystal structure of cellulose I.

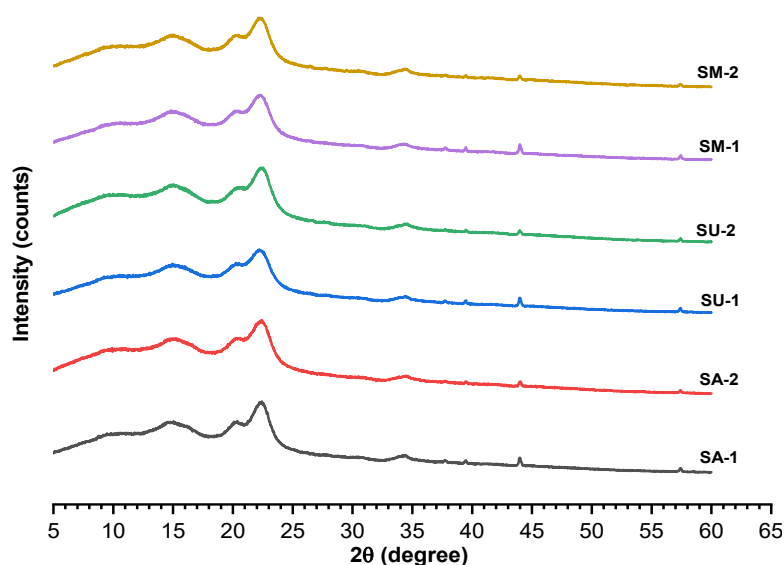


Fig 7. X-ray diffraction pattern of NCCs from *barangan* banana peduncles

Table 3. Crystallinity index (CI), crystal size, and diameter particle (SEM image) of NCCs

Samples	2 θ (am)	2 θ (002)	CI (%)	Crystal size (nm)	ImageJ (SEM image)	
	($^{\circ}$)	($^{\circ}$)			d (nm)	R ²
SA-1	14.82	22.23	57.33	34.38	25	0.72
SA-2	14.75	22.41	56.69	22.35	30	0.98
SU-1	15.04	22.31	54.96	27.94	50	0.98
SU-2	14.98	22.19	55.38	36.28	100	0.98
SM-1	14.99	22.33	53.99	27.43	25	0.78
SM-2	14.81	22.35	55.19	23.67	25	0.81

In the XRD pattern, the absorption peaks tend to have a narrower peak width and higher peaks with high crystallinity. For materials with low crystallinity, the absorption peaks show a wider peak width and lower peak height [59]. Sharp diffraction peaks and flat dispersion curves simultaneously emerge since the composition of the crystalline and amorphous phases of the polymeric material. Structural changes can be due to forces that occur during mechanical processes. The shearing force by a high-pressure homogenizer can remove amorphous cellulose, increasing crystallinity [57]. Ultrasonication hydrolyzes the amorphous regions of cellulose and some parts of the broken cellulose fragments to produce oligo and monosaccharides [30]. Table 3 shows the crystallinity index (CI) of NCCs from the treatment of sulfuric acid concentration and hydrolysis time, ranging from 53.99% to 57.33%. The highest CI value was obtained in the treatment of SA-1 (57.33%), while the lowest CI value was in the treatment of SM-1 (53.99%). The crystal size of NCCs was between 22.35 and 36.28 nm, with the largest size being in the treatment of SU-2 (36.28 nm) and the smallest in the treatment of SA-2 (22.35 nm). Hydrolysis at lower concentrations of sulfuric acid (16% and 40% by weight) reduced the amorphous component of the initial pulp. However, the conditions are insufficient to resynchronize the crystals structurally or reduce the crystal size [58,60].

In addition, the intense cavitation force by ultrasound can remove the amorphous zone and decrease the crystalline zone, ultimately decreasing the crystallinity index [61]. The stronger the strain, the wider the diffraction peaks, increasing the microstrain lattice and decreasing the crystal size [62]. This study resulted in the crystal size of NCCs based on the results of the

crystallinity test and the particle diameter of the NCCs based on the results of the SEM image test using ImageJ software, which was in the 100 nm range.

The Particle Size of NCCs

Particle size analysis is an analysis of the average particle size distribution in a liquid. Fig. 8 shows the average particle size distribution of NCCs treated with sulfuric acid concentrations of 1, 2, and 3 M and hydrolysis times of 0.5 and 1.5 h (Table 4). The particle sizes of NCCs ranged from 250.9 to 4214.6 nm. The most petite particle sizes, 250.9, 257.9, and 259.2 nm, were obtained at concentrations of 1, 2, and 3 M sulfuric acid, respectively, with a hydrolysis duration of 1.5 h. The smaller the particle size of the NCCs produced, the higher the sulfuric acid concentration. Similarly, the longer the hydrolysis period, the smaller the particle size of the formed NCCs. The criteria for determining particle size and distribution depend on various factors, including sample structure, acid concentration, and hydrolysis time. On the other hand, the particle size distribution depends on the degree of aggregation [63]. Dimas et al. [64] reported that the average size of NCCs hydrolyzed with 6, 8, and 10 M HCl were 8334, 3024, and 2086 nm, respectively, as measured by PSA.

Table 4. Particle size distribution of NCCs *barangan* banana peduncles

Sample	Particle size (nm)	PI
SA-1	4214.6	1.025
SA-2	250.9	0.808
SU-1	4157.3	1.062
SU-2	257.9	0.908
SM-1	3267.5	0.965
SM-2	259.2	0.902

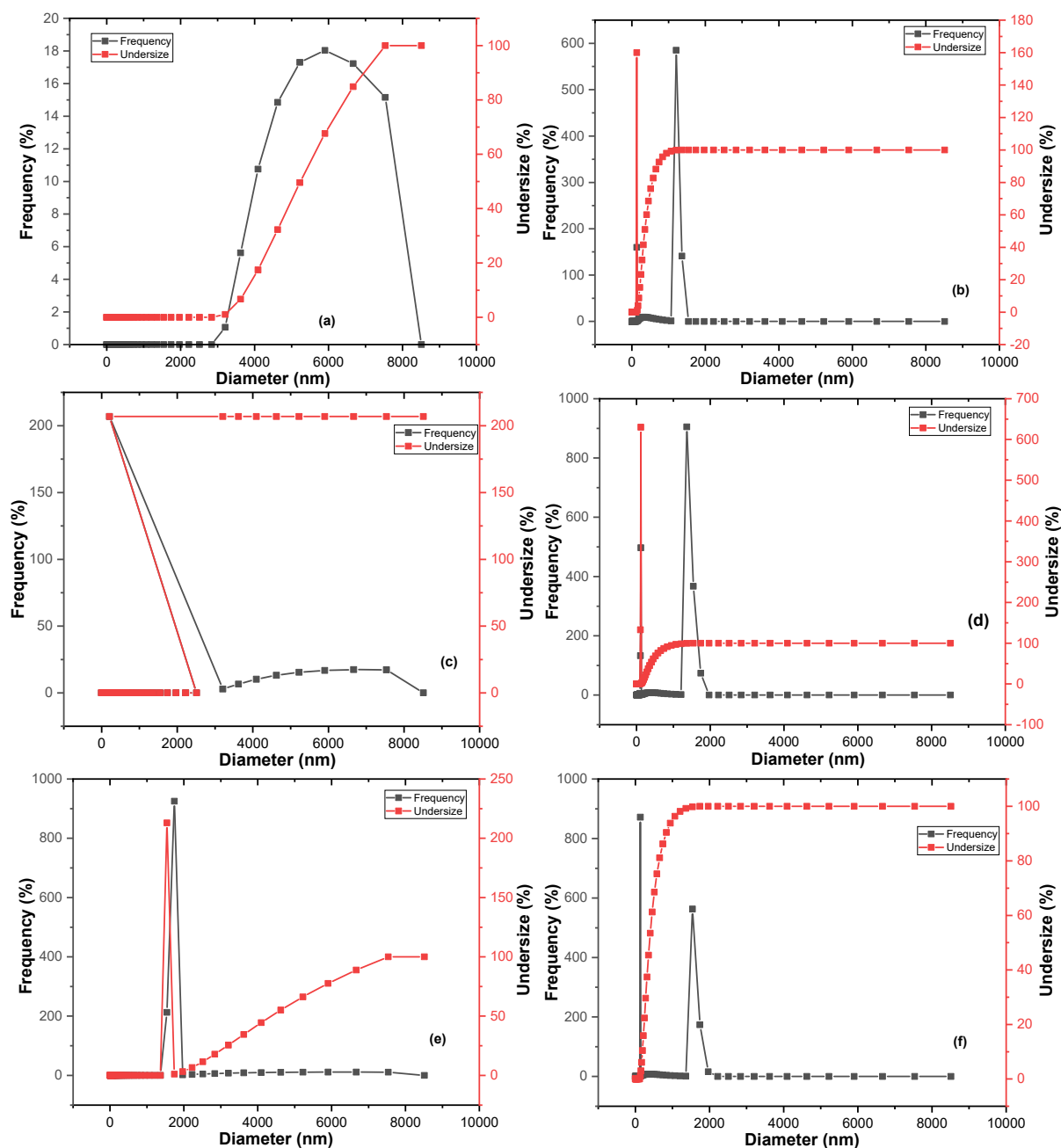


Fig 8. Particle size analyzer of NCCs; (a) SA-1, (b) SA-2, (c) SU-1, (d) SU-2, (e) SM-1, and (f) SM-2

It indicates that NCCs dropped as the concentration of hydrochloric acid increased. After the long fiber amorphous areas were hydrolyzed by acid disintegration to form shorter NCCs particles, the size of the NCCs was reduced. Agglomerates can cause dynamic light scattering, and PSA cannot precisely measure the particle size of single NCCs. In this study, there was a large

agglomeration marked by a significant PI (polydispersity index) value above 0.5. The research of Wu et al. [38] produced a particle size of okara nanocellulose (using the method of high-pressure ultrasound or high-pressure homogenization) based on the PSA test, which was in the range of 233–2430 nm with PI values ranging from 0.22 to 0.91.

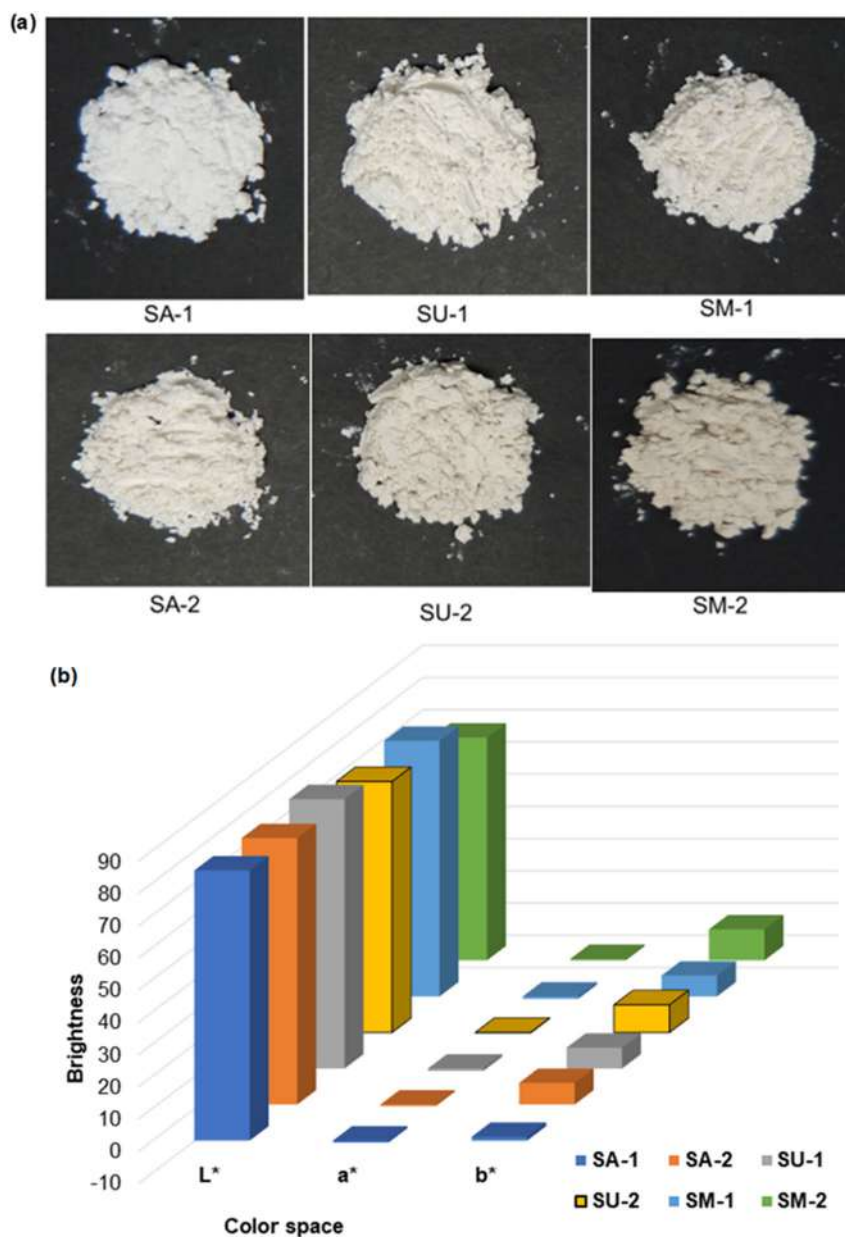


Fig 9. (a) NCCs powder from banana peduncles and (b) CIELAB color space $L^*a^*b^*$ NCCs powder of acid hydrolysis effect

Color of NCCs Powder

Fig. 9(b) describes the brightness of NCCs powder. The L^* value is the brightness value; the higher the L^* , the brighter the NCCs powder. The L^* values range from 69.14 to 83.81. The highest L^* brightness value was found in the treatment of SA-1 (83.81). The lowest was in the treatment of SM-2 (69.14). In contrast, the higher the sulfuric acid concentration and hydrolysis time, the higher the a^* and b^* values. The higher the L^* value, the

lighter (whiter) the color of the NCCs. Brightness is denoted by L^* , ranging from $L^* = 0$ (black) to 100 (white) [65].

The higher the concentration of sulfuric acid and the hydrolysis time, the darker the color of the NCCs powder, as shown in Fig. 9(a). The expected color of the NCCs powder is bright, and thus the best color of NCCs powder was the one that resulted from the treatment of SA-1. The cellulose content in the fiber influences the

fiber absorption of color, resulting in differences in color absorption in each fiber [5]. The increasing amount of polymer will increase light diffusion [65]. Good light reflection is the one directed at the surface of an object. If the surface of an object reflects light in all directions, it will be blunt. The microwave effect is through ionic conduction, which is resistance heating [66]. The collision between the dye molecules and fiber particles depends on the acceleration of the particles through the dye solution.

■ CONCLUSION

Treatment of sulfuric acid concentration and time of hydrolysis assisted by microwave energy resulted in different yields of NCCs. The yield of NCCs decreased with increasing sulfuric acid concentration and hydrolysis time. FTIR test results showed that the concentration of sulfuric acid and hydrolysis time produced NCCs with the same functional groups in the same absorption spectrum zone. TGA test results showed that the decomposition of NCCs occurred at a temperature of 275.35–409.40 °C, with a weight loss ranging from 84% to 94.09%. In addition, the XRD test results revealed that all diffraction patterns for all treatments were at the highest peak of 2θ above 22° , with index crystallinity values ranging from 53.99% to 57.33% and crystal sizes ranging from 22.35 to 36.28 nm. The brightest NCCs powder was obtained from the treatment of 1 M sulfuric acid and 0.5 h of hydrolysis time.

■ ACKNOWLEDGMENTS

This research was supported by Universitas Syiah Kuala, Aceh, Indonesia, through the Institute for Research and Community Service (LPPM) under the Lecturer Research Program [241/UN11.2.1/PT.01.03/PNBP/2021].

■ AUTHOR CONTRIBUTIONS

Ratna: Writing, methodology-data analysis, original draft, conceptualization & investigation. Sri Aprilia: Supervision, writing-methodology, review-editing, conceptualization & investigation. Nasrul Arahman: Supervision, review-editing & conceptualization. Agus Arip Munawar: Supervision & review. All authors agreed to the final version of this manuscript.

■ REFERENCES

- [1] Adsal, K.A., Üçtuğ, F.G., and Arıkan, O.A., 2020, Environmental life cycle assessment of utilizing stem waste for banana production in greenhouses in Turkey, *Sustainable Prod. Consumption*, 22, 110–125.
- [2] Padam, B.S., Tin, H.S., Chye, F.Y., and Abdullah, M.I., 2014, Banana by-products: an under-utilized renewable food biomass with great potential, *J. Food Sci. Technol.*, 51 (12), 3527–3545.
- [3] Gumisiriza, R., Hawumba, J.F., Okure, M., and Hensel, O., 2017, Biomass waste-to-energy valorisation technologies: A review case for banana processing in Uganda, *Biotechnol. Biofuels*, 10 (1), 11.
- [4] Ahmad, T., and Danish, M., 2018, Prospects of banana waste utilization in wastewater treatment: A review, *J. Environ. Manage.*, 206, 330–348.
- [5] Nur, C., and Djati, I.D., 2018, Studi daya serap warna serat tandan pisang dengan pembanding serat abaka dan serat sabut kelapa, *Arena Tekstil*, 33 (1), 19–28.
- [6] Seta, F.T., An, X., Liu, L., Zhang, H., Yang, J., Zhang, W., Nie, S., Yao, S., Cao, H., Xu, Q., Bu, Y., and Liu, H., 2020, Preparation and characterization of high yield cellulose nanocrystals (CNC) derived from ball mill pretreatment and maleic acid hydrolysis, *Carbohydr. Polym.*, 234, 115942.
- [7] Chen, Q., Xiong, J., Chen, G., and Tan, T., 2020, Preparation and characterization of highly transparent hydrophobic nanocellulose film using corn husks as main material, *Int. J. Biol. Macromol.*, 158, 781–789.
- [8] Ilyas, R.A., Sapuan, S.M., Atikah, M.S.N., Asyraf, M.R.M., Ayu Rafiqah, S., Aisyah, H.A., Mohd Nurazzi, N., and Norrrahim, M.N.F., 2021, Effect of hydrolysis time on the morphological, physical, chemical, and thermal behavior of sugar palm nanocrystalline cellulose (*Arenga pinnata* (Wurmb.) Merr), *Text. Res. J.*, 91 (1-2), 152–167.
- [9] Ng, L.Y., Wong, T.J., Ng, C.Y., and Amelia, C.K.M., 2021, A review on cellulose nanocrystals production and characterization methods from *Elaeis guineensis* empty fruit bunches, *Arabian J. Chem.*, 14 (9), 103339.

- [10] Abdul Khalil, H.P.S., Davoudpour, Y., Saurabh, C.K., Hossain, M.S., Adnan, A.S., Dungani, R., Paridah, M.T., Islam Sarker, M.Z., Fazita, M.R.N., Syakir, M.I., and Haafiz, M.K.M., 2016, A review on nanocellulosic fibres as new material for sustainable packaging: Process and applications, *Renewable Sustainable Energy Rev.*, 64, 823–836.
- [11] Flores-Velázquez, V., Córdova-Pérez, G.E., Silahua-Pavón, A.A., Torres-Torres, J.G., Sierra, U., Fernández, S., Godavarthi, S., Ortiz-Chi, F., and Espinosa-González, C.G., 2020, Cellulose obtained from banana plant waste for catalytic production of 5-HMF: Effect of grinding on the cellulose properties, *Fuel*, 265, 116857.
- [12] Harini, K., and Chandra Mohan, C., 2020, Isolation and characterization of micro and nanocrystalline cellulose fibers from the walnut shell, corncob and sugarcane bagasse, *Int. J. Biol. Macromol.*, 163, 1375–1383.
- [13] Kian, L.K., Saba, N., Jawaid, M., Alothman, O.Y., and Fouad, H., 2020, Properties and characteristics of nanocrystalline cellulose isolated from olive fiber, *Carbohydr. Polym.*, 241, 116423.
- [14] Camacho, M., Ureña, Y.R.C., Lopretti, M., Carballo, L.B., Moreno, G., Alfaro, B., and Vega Baudrit, J.R., 2017, Synthesis and characterization of nanocrystalline cellulose derived from Pineapple peel residues, *J. Renewable Mater.*, 5 (5), 271–279.
- [15] Xu, Y., Atrens, A., and Stokes, J.R., 2020, A review of nanocrystalline cellulose suspensions: Rheology, liquid crystal ordering and colloidal phase behaviour, *Adv. Colloid Interface Sci.*, 275, 102076.
- [16] Ghorbani, M., and Roshangar, L., 2021, Construction of collagen/nanocrystalline cellulose based-hydrogel scaffolds: Synthesis, characterization, and mechanical properties evaluation, *Int. J. Polym. Mater. Polym. Biomater.*, 70 (2), 142–148.
- [17] Qi, W., Li, T., Zhang, Z., and Wu, T., 2021, Preparation and characterization of oleogel-in-water pickering emulsions stabilized by cellulose nanocrystals, *Food Hydrocolloids*, 110, 106206.
- [18] Doh, H., Lee, M.H., and Whiteside, W.S., 2020, Physicochemical characteristics of cellulose nanocrystals isolated from seaweed biomass, *Food Hydrocolloids*, 102, 105542.
- [19] Ditzel, F.I., Prestes, E., Carvalho, B.M., Demiate, I.M., and Pinheiro, L.A., 2017, Nanocrystalline cellulose extracted from pine wood and corncob, *Carbohydr. Polym.*, 157, 1577–1585.
- [20] Shao, X., Wang, J., Liu, Z., Hu, N., Liu, M., and Xu, Y., 2020, Preparation and characterization of porous microcrystalline cellulose from corncob, *Ind. Crops Prod.*, 151, 112457.
- [21] Supian, M.A.F., Amin, K.N.M., Jamari, S.S., and Mohamad, S., 2020, Production of cellulose nanofiber (CNF) from empty fruit bunch (EFB) via mechanical method, *J. Environ. Chem. Eng.*, 8 (1), 103024.
- [22] Foo, M.L., Ooi, C.W., Tan, K.W., and Chew, I.M.L., 2020, A step closer to sustainable industrial production: Tailor the properties of nanocrystalline cellulose from oil palm empty fruit bunch, *J. Environ. Chem. Eng.*, 8 (5), 104058.
- [23] Kusmono, K., Listyanda, R.F., Wildan, M.W., and Iلمان, M.N., 2020, Preparation and characterization of cellulose nanocrystal extracted from ramie fibers by sulfuric acid hydrolysis, *Heliyon*, 6 (11), e05486.
- [24] Jiang, Q., Xing, X., Jing, Y., and Han, Y., 2020, Preparation of cellulose nanocrystals based on waste paper via different systems, *Int. J. Biol. Macromol.*, 149, 1318–1322.
- [25] Plengnok, U., and Jarukumjorn, K., 2020, Preparation and characterization of nanocellulose from sugarcane bagasse, *Biointerface Res. Appl. Chem.*, 10 (3), 5675–5678.
- [26] Mocktar, N.A., Abdul Razab, M.K.A., Mohamed Noor, A., and Abdullah, N.H., 2020, Preparation and characterization of kenaf and oil palm nanocellulose by acid hydrolysis method, *Mater. Sci. Forum*, 1010, 495–500.
- [27] Haldar, D., and Purkait, M.K., 2020, Micro and nanocrystalline cellulose derivatives of lignocellulosic biomass: A review on synthesis, applications and advancements, *Carbohydr. Polym.*, 250, 116937.
- [28] Raja, P.M., Rangkuti, I.U.P., Hendra Ginting, M., Giyanto, G., and Siregar, W.F., 2021, Preparation

- and characterization of cellulose microcrystalline made from palm oil midrib, *IOP Conf. Ser.: Earth Environ. Sci.*, 819, 012002.
- [29] Mohd Ishak, N.A., Khalil, I., Abdullah, F.Z., and Muhd Julkapli, N., 2020, A correlation on ultrasonication with nanocrystalline cellulose characteristics, *Carbohydr. Polym.*, 246, 116553.
- [30] Abdul Khalil, H.P.S., Davoudpour, Y., Sri Aprilia, N.A., Mustapha, A., Hossain, M.S., Islam, M.N., and Dungani, R., 2014, "Nanocellulose-Based Polymer Nanocomposite: Isolation, Characterization and Applications" in *Nanocellulose Polymer Nanocomposites*, Eds. Thakur, V.K., Scrivener Publishing LLC, Wiley, Massachusetts, 273–309.
- [31] Villalobos, K., Rojas, H., González-Paz, R., Granados, D.B., González-Masís, J., Baudrit, J.V., and Corrales-Ureña, Y.R., 2017, Production of starch films using propolis nanoparticles as novel bioplasticizer, *J. Renewable Mater.*, 5 (3-4), 189–198.
- [32] Tiwari, G., Sharma, A., Kumar, A., and Sharma, S., 2019, Assessment of microwave-assisted alkali pretreatment for the production of sugars from banana fruit peel waste, *Biofuels*, 10 (1), 3–10.
- [33] Abdul Khalil, H.P.S., Chong, E.W.N., Owolabi, F.A.T., Asniza, M., Tye, Y.Y., Rizal, S., Nurul Fazita, M.R., Mohamad Haafiz, M.K., Nurmiati, Z., and Paridah, M.T., 2019, Enhancement of basic properties of polysaccharide-based composites with organic and inorganic fillers: A review, *J. Appl. Polym. Sci.*, 136, 47251.
- [34] Chavan, R.R., and Hosamani, K.M., 2018, Microwave-assisted synthesis, computational studies and antibacterial/anti-inflammatory activities of compounds based on coumarin-pyrazole hybrid, *R. Soc. Open Sci.*, 5 (5), 172435.
- [35] Chowdhury, Z.Z., and Abd Hamid, S.B., 2016, Preparation and characterization of nanocrystalline cellulose using ultrasonication combined with a microwave-assisted pretreatment process, *BioResources*, 11 (2), 3397–3415.
- [36] Ilyas, R.A., Sapuan, S.M., Sanyang, M.L., Ishak, M.R., and Zainuddin, E.S., 2018, Nanocrystalline cellulose as reinforcement for polymeric matrix nanocomposites and its potential applications: A review, *Curr. Anal. Chem.*, 14 (3), 203–225.
- [37] Silva-Castro, I., Martín-Ramos, P., Matei, P.M., Fernandes-Correa, M., Hernández-Navarro, S., and Martín-Gil, J., 2017, "Eco-Friendly Nanocomposites of Chitosan with Natural Extracts, Antimicrobial Agents, and Nanometals" in *Handbook of Composites from Renewable Materials*, Eds. Thakur, V.K., Thakur, M.K., and Kessler, M.R., Scrivener Publishing LLC, Wiley, Massachusetts, 35–60.
- [38] Wu, C., McClements, D.J., He, M., Zheng, L., Tian, T., Teng, F., and Li, Y., 2021, Preparation and characterization of okara nanocellulose fabricated using sonication or high-pressure homogenization treatments, *Carbohydr. Polym.*, 255, 117364.
- [39] Wang, H., Xie, H., Du, H., Wang, X., Liu, W., Duan, Y., Zhang, X., Sun, L., Zhang, X., and Si, C., 2020, Highly efficient preparation of functional and thermostable cellulose nanocrystals via H₂SO₄ intensified acetic acid hydrolysis, *Carbohydr. Polym.*, 239, 116233.
- [40] Rahmawati, C., Aprilia, S., Saidi, T., Aulia, T.B., and Ahmad, I., 2021, Preparation and characterization of cellulose nanocrystals from *Typha* sp. as a reinforcing agent, *J. Nat. Fibers*, 00, 1–14.
- [41] Ratna, R., Aprilia, S., Arahman, N., and Munawar, A.A., 2021, Characterization of cellulose nanocrystalline isolated from banana peduncles using acid hydrolysis, *IOP Conf. Ser.: Earth Environ. Sci.*, 922, 012072.
- [42] Ilyas, R.A., Sapuan, S.M., and Ishak, M.R., 2018, Isolation and characterization of nanocrystalline cellulose from sugar palm fibres (*Arenga pinnata*), *Carbohydr. Polym.*, 181, 1038–1051.
- [43] Gan, P.G., Sam, S.T., Bin Abdullah, M.F., Bin Zulkepli, N.N., and Yeong, Y.F., 2017, Characterization of nanocrystalline cellulose isolated from empty fruit bunch using acid hydrolysis, *Solid State Phenom.*, 264, 9–12.
- [44] Rulaningtyas, R., Suksmono, A.B., Mengko, T.L.R., and Putri Saptawati, G.A., 2015, Segmentasi citra berwarna dengan menggunakan metode clustering berbasis patch untuk identifikasi mycobacterium

- tuberculosis, *Jurnal Biosains Pascasarjana*, 17 (1), 19–25.
- [45] Johar, N., Ahmad, I., and Dufresne, A., 2012, Extraction, preparation and characterization of cellulose fibres and nanocrystals from rice husk, *Ind. Crops Prod.*, 37 (1), 93–99.
- [46] Pereira, P.H.F., Waldron, K.W., Wilson, D.R., Cunha, A.P., de Brito, E.S., Rodrigues, T.H.S., Rosa, M.F., and Azeredo, H.M.C., 2017, Wheat straw hemicelluloses added with cellulose nanocrystals and citric acid. Effect on film physical properties, *Carbohydr. Polym.*, 164, 317–324.
- [47] Collazo-Bigliardi, S., Ortega-Toro, R., and Chiralt Boix, A., 2018, Isolation and characterisation of microcrystalline cellulose and cellulose nanocrystals from coffee husk and comparative study with rice husk, *Carbohydr. Polym.*, 191, 205–215.
- [48] Aditama, A.G., and Ardhyanta, H., 2017, Isolasi selulosa dari serat tandan kosong kelapa sawit untuk nano filler komposit absorpsi suara: Analisis FTIR, *Jurnal Teknik ITS*, 6 (2), 228–231.
- [49] Ghazy, M.B., El-Hai, F.A., El-Zawawy, W.K., and Owda, M.E., 2017, Morphology and mechanical properties of nanocrystalline cellulose reinforced chitosan based nanocomposite, *Global J. Chem.*, 3 (1), 125–135.
- [50] Leung, A.C.W., Hrapovic, S., Lam, E., Liu, Y., Male, K.B., Mahmoud, K.A., and Luong, J.H.T., 2011, Characteristics and properties of carboxylated cellulose nanocrystals prepared from a novel one-step procedure, *Small*, 7 (3), 302–305.
- [51] Alves, L., Medronho, B., Antunes, F.E., Fernández-García, M.P., Ventura, J., Araújo, J.P., Romano, A., and Lindman, B., 2015, Unusual extraction and characterization of nanocrystalline cellulose from cellulose derivatives, *J. Mol. Liq.*, 210, 106–112.
- [52] Putri, E., and Gea, S., 2018, Isolasi dan karakterisasi nanokristal selulosa dari tandan sawit (*Elaeis guineensis* Jack), *Elkawanie*, 4, 13–22.
- [53] Tritt-Goc, J., Lindner, Ł., Bielejewski, M., Markiewicz, E., and Pankiewicz, R., 2020, Synthesis, thermal properties, conductivity and lifetime of proton conductors based on nanocrystalline cellulose surface-functionalized with triazole and imidazole, *Int. J. Hydrogen Energy*, 45 (24), 13365–13375.
- [54] Ludueña, L., Fasce, D., Alvarez, V.A., and Stefani, P.M., 2011, Nanocellulose from rice husk following alkaline treatment to remove silica, *BioResources*, 6 (2), 1440–1453.
- [55] Wang, H., Pudukudy, M., Ni, Y., Zhi, Y., Zhang, H., Wang, Z., Jia, Q., and Shan, S., 2020, Synthesis of nanocrystalline cellulose via ammonium persulfate-assisted swelling followed by oxidation and their chiral self-assembly, *Cellulose*, 27 (2), 657–676.
- [56] Evans, S.K., Wesley, O.N., Nathan, O., and Moloto, M.J., 2019, Chemically purified cellulose and its nanocrystals from sugarcane bagasse: Isolation and characterization, *Heliyon*, 5 (10), e02635.
- [57] Sun, Q., Zhao, X., Wang, D., Dong, J., She, D., and Peng, P., 2018, Preparation and characterization of nanocrystalline cellulose/*Eucommia ulmoides* gum nanocomposite film, *Carbohydr. Polym.*, 181, 825–832.
- [58] Hamad, W.Y., and Hu, T.Q., 2010, Structure-process-yield interrelations in nanocrystalline cellulose extraction, *Can. J. Chem. Eng.*, 88 (3), 392–402.
- [59] Qian, Y., Bian, L., Wang, K., Chia, W.Y., Khoo, K.S., Zhang, C., and Chew, K.W., 2021, Preparation and characterization of curdlan/nanocellulose blended film and its application to chilled meat preservation, *Chemosphere*, 266, 128948.
- [60] Liu, Z., Li, X., Xie, W., and Deng, H., 2017, Extraction, isolation and characterization of nanocrystalline cellulose from industrial kelp (*Laminaria japonica*) waste, *Carbohydr. Polym.*, 173, 353–359.
- [61] Costa, A.L.R., Gomes, A., Tibolla, H., Menegalli, F.C., and Cunha, R.L., 2018, Cellulose nanofibers from banana peels as a Pickering emulsifier: High-energy emulsification processes, *Carbohydr. Polym.*, 194, 122–131.
- [62] Sumadiyah, M., and Manuaba, I.B.S., 2018, Penentuan ukuran kristal menggunakan formula Scherrer, Williamson-Hull plot, dan ukuran partikel dengan SEM, *Buletin Fisika*, 19, 28–35.

- [63] Sri Aprilia, N.A., Davoudpour, Y., Zulqarnain, W., Abdul Khalil, H.P.S., Che Mohamad Hazwan, C.I., Hossain, M.S., Dungani, R., Fizree, H.M., Zaidon, A., and Mohamad Haafiz, M.K., 2016, Physicochemical characterization of microcrystalline cellulose extracted from kenaf bast, *BioResources*, 11, 3875–3889.
- [64] Akbar, D.A., Kusmono, K., Wildan, M.W., and Ilman, M.N., 2020, Extraction and characterization of nanocrystalline cellulose (NCC) from ramie fiber by hydrochloric acid hydrolysis, *Key Eng. Mater.*, 867, 109–116.
- [65] Maruddin, F., Malaka, R., Baba, S., Amqam, H., Taufik, M., and Sabil, S., 2020, Brightness, elongation and thickness of edible film with caseinate sodium using a type of plasticizer, *IOP Conf. Ser.: Earth Environ. Sci.*, 492, 012043.
- [66] Atalla, S.M.M., EL Gamal, N.G., Awad, H.M., and Ali, N.F., 2019, Production of pectin lyase from agricultural wastes by isolated marine *Penicillium expansum* RSW_SEP1 as dye wool fiber, *Helikon*, 5 (8), e02302.

Effects of Various Parameters on the Antioxidant Activities of the Synthesized Heterocyclic Pyrimidinium Betaines

Fatiha Malki¹, Ali Alouache^{2*}, and Soumia Krimat¹

¹Laboratoire de Recherche sur les Produits Bioactifs et Valorisation de la Biomasse (LPBVB), Ecole Normale Supérieure Kouba, Bp 92 16006 Alger, Algeria

²Laboratoire de Biologie des Systèmes Microbiens (LBSM), Ecole Normale Supérieure Kouba, Bp 92 16006 Alger, Algeria

* **Corresponding author:**

tel: +213-0550801704

email: ali.alouache@g.ens-kouba.dz

Received: May 21, 2022

Accepted: September 23, 2022

DOI: 10.22146/ijc.74803

Abstract: Betaine derivatives are widely used in cosmetic, industrial uses, biology and other scientific fields. Pyrimidinium betaine is a special class of bioactive heterocyclics. They have interesting antioxidant and free radical scavenging activities. This work aims to examine the influence of some parameters on the antioxidant activity of some synthesized betaines containing pyrimidine ring. Four pyrimidinium betaines: monocyclic, bicyclics, and one with a fatty alkyl chain were synthesized from condensation of 2-aminopyrimidine or amidine derivatives with malonic esters, and their antioxidant capacity was evaluated. The effects of concentration, reaction time and temperature on their antioxidant activities were investigated by three common methods: 2,2-diphenyl-1-picrylhydrazyl (DPPH) free radical scavenging, ferric reducing antioxidant power (FRAP) and β -carotene bleaching. The results showed that all pyrimidinium betaines exhibited antioxidant activities in different assays. In the DPPH and reducing power assays, antioxidant activity increased with concentration, whereas in the β -carotene/linoleic acid system, it increased with temperature. On the other hand, the DPPH assay showed an increase in antioxidant capacity over time, while the β -carotene bleaching assay showed a decrease. These results indicate that the antioxidant activity differs depending on the method used and that the various factors affect the antioxidant activity in a different order.

Keywords: antioxidant activity; DPPH; FRAP; β -carotene bleaching assay; pyrimidinium betaines

■ INTRODUCTION

Molecules or molecular fragments with an unpaired electron are classified as free radicals. They are typically reactive and can have negative consequences [1]. Free radicals are one of the principal byproducts of lipid oxidation and have been linked to over a hundred disorders, including cancer, atherosclerosis, and arthritis [2]. Excessive free radical production leads to oxidative stress, which is thought to be a crucial factor in a variety of human diseases such as neurological, inflammatory, carcinogenesis, and psychiatric disorders [3].

Antioxidants are substances that can delay or prevent the oxidation process of free radicals [4]. Excess free radicals are neutralized by dietary antioxidants that

transform them into non-radical products and/or scavenge the intermediates [5]. Due to their ability to scavenge reactive free radicals, antioxidants can protect the human body from free radicals and the consequences of reactive oxygen species (ROS). They slow the evolution of several chronic diseases while also lipid peroxidation [6-7]. A variety of antioxidant molecules have been added to foods to preserve their quality, and a variety of antioxidant molecules have been provided to humans and animals as food additives or pharmaceuticals [6]. Antioxidants have proven effective in treating many health problems, including neurodegeneration, systemic, and infectious [8]. Recently, many researchers have focused on research on

substances that can act as a free radical scavenger, and there is an increasing interest in substances that present antioxidant capacities. Concurrently, several methods for evaluating the antioxidant activity of natural and synthetic compounds have been developed [9-11].

Betaine is an interesting group of zwitterionic surfactants. The term betaine refers to the glycine betaine (*N,N,N*-trimethylglycine), as well as its derivatives and any organic compound with quaternary nitrogen [12]. Betaine is found in a variety of plants, animals, and microorganisms as it aids in the resistance to osmotic stress in these organisms. This molecule is a human nutrient and is used to treat a variety of ailments [13].

Betaine derivative is a class of compounds that are becoming increasingly important in cosmetic, domestic, and industrial uses [14]. They have a variety of applications in biological research, medicine, pharmacy, and other scientific fields [15]. Pyrimidine derivatives have been reported to have a wide spectrum of biological activity since the pyrimidine ring is a critical nucleus in DNA and RNA [16]. Betaines containing a pyrimidine ring have generated a lot of interest among synthetic chemists for their chemical stability [17]. These materials are strongly stabilized by π electron and charge delocalization [18]. Pyrimidine betaines continue to be an important group of bioactive heterocyclics [19] due to the presence of a biologically active pyrimidine ring [16] in their structure.

However, there are very few reports on the antioxidant activities of pyrimidinium betaines [20], and to our knowledge, no information is available on the antioxidant potency of pyrimidinium betaines having a fatty alkyl chain. For this reason, we decided in a recent study to evaluate the *in vitro* antioxidant capacity of various betaines containing a pyrimidine ring in their structure, including one with a long chain, as a type of alkyl pyrimidinium betaines used as amphoteric surfactants. The results showed that the tested compounds have variable and interesting antioxidant properties and free radical scavenging activities compared to the standard antioxidants [20-22]. However, without considering many factors that could affect the results, the

measurement of antioxidant activities cannot be evaluated satisfactorily by a simple antioxidant test [23].

The goal of this study was to investigate how different factors affected the antioxidant activity of some synthesized pyrimidinium betaines. We used three distinct methods: DPPH free radical scavenging, ferric reducing antioxidant power (FRAP) and β -carotene bleaching, to examine the effect of concentration, reaction time, and temperature on the antioxidant activity of these compounds and on some conventional antioxidants, such as butylated hydroxytoluene (BHT), butylated hydroxyanisole (BHA), and ascorbic acid (vitamin C).

■ EXPERIMENTAL SECTION

Materials

Chemicals and solvents were analytical grade and purchased from Sigma-Aldrich, Merck (Germany). They were supplied in purities ≥ 99 . Triethylamine ($(C_2H_5)_3N$) was purified by distillation before use.

Instrumentation

Melting points were determined by using a Buchi 512 oil bath. UV-Visible absorption spectra were carried out using a Shimadzu 160 double-beam spectrophotometer. FTIR spectra were recorded as KBr pellets on a JASCO System 4100. 1H -NMR and ^{13}C -NMR spectra were acquired on a Bruker AC 200 instrument at 300 and 75 MHz, respectively, using TMS as the internal standard. Electron impact mass spectra (EIMS) were performed on a Nermag R10-10 type apparatus.

Procedure

Synthesis

The selected pyrimidinium betaines: monocyclic BT1, bicyclics BT2, BT3 and one with fatty alkyl chain having 12 carbon atoms BT12 (Fig. 1), were synthesized from condensation of 2-aminopyrimidine or amidines derivatives with malonic acid derivatives according to the methods reported in previous publications [24-26]. Their structures were confirmed by spectroscopic analyses, including UV-visible, IR, 1H -NMR, ^{13}C -NMR and MS.

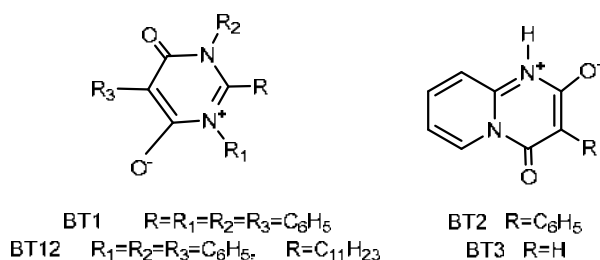


Fig 1. Chemical structure of studied pyrimidinium betaines

General procedure for the synthesis of bicyclic Betaines BT2, BT3. The bicyclic betaine BT3 was synthesized according to the method reported by Tschitschibabin [24] by condensation of 2-aminopyrimidine **C** with an excess of diethyl malonate **B** through heating the reaction mixture at 160–200 °C for 3 h with a continuous distillation of the resulting alcohol (Fig. 2). The corresponding betaine was obtained in 81% yield as an orange solid.

The bicyclic betaine BT2 was prepared according to the method reported by Dvortsák et al. [25] by condensation of 2-aminopyrimidine **C** with the bis pentachlorophenyl ester of phenyl malonic acid **A** (Fig. 2). The reaction was performed in acetone at room temperature in the presence of triethylamine. In a few minutes, the product precipitated and was isolated by filtration with a yield of 72%.

General procedure for the synthesis of monocyclic Betaines BT1 and fatty chain betaine BT12. Monocyclic betaine BT1 was prepared by condensation of *N,N'*-diphenyl benzamidine **D** instead of α -aminopyrimidine **C** with the bis pentachlorophenyl ester of phenyl malonic acid **A** in diethyl ether at room temperature [25-26] in the presence of triethylamine (Fig. 3). The product was isolated by filtration, purified by extraction or column procedure [27-28] and then

obtained as yellow crystals in a yield of 66%.

Under the identical protocol, the fatty chain pyrimidinium betaine BT12 was prepared by reacting fatty *N,N'*-diphenyldodecamidine **E** with the same ester **A** in diethyl ether at room temperature [26] in the presence of triethylamine (Fig. 3). Due to the chemical reactivity of malonic ester **A**, the fatty betaine BT12 precipitated within minutes. The precipitate was then purified [29-30] and obtained as a white solid with a 37% yield.

Characterization of synthesized compounds

Pyrimidinium betaines, BT3, BT2, BT1, and BT12 were characterized by common spectroscopic analyses, including UV-visible, IR, 1H -NMR, ^{13}C -NMR and MS [29-30]. Their physical and spectroscopic data are as follows:

BT3 (6-oxo-4H-pyrido[1,2-a]pyrimidin-3-ium-4-olate). Chemical formula: $C_8H_6N_2O_2$; Orange solid; Mol. Mass. 162 g/mol, m.p.: 306–317 °C (decomposed), UV-Visible (dioxane) λ_{max} : 268 nm; IR (KBr) cm^{-1} : 3093 (C-H, Ar.), 2553 (NH); 1693 (C=O); 1519 (C=C Ar.); 1H -NMR (300 MHz, DMSO- d_6): insoluble; ^{13}C -NMR (75 MHz, DMSO- d_6): insoluble; EI-Mass m/z : 163 [M+1] $^+$.

BT2 (6-oxo-5-phenyl-4H-pyrido[1,2-a]pyrimidin-3-ium-4-olate). Chemical formula: $C_{14}H_{10}N_2O_2$; Yellow crystals; Mol. Mass. 238 g/mol, m.p.: 310–312 °C (decomposed); UV-Visible (dioxane) λ_{max} : 355 nm; IR (KBr) cm^{-1} : 3112 (C-H Ar), 2657 (NH), 1678 (C=O),

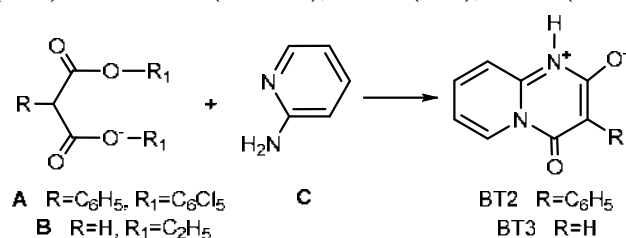


Fig 2. Synthetic pathway of bicyclic betaines BT2 and BT3

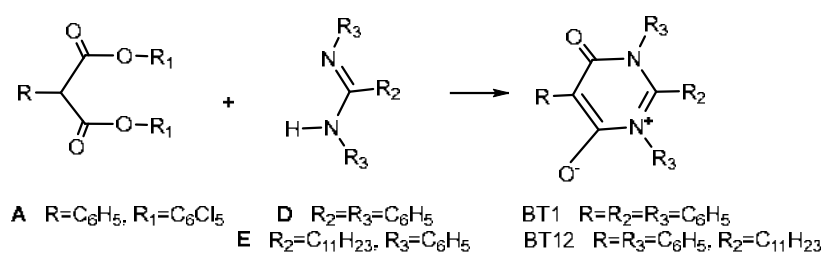


Fig 3. Synthetic pathway of bicyclic betaines BT1 and BT12

1527 (C=C, Ar.); ¹H-NMR (300 MHz, DMSO-*d*₆): δ 12.42–12.27 (s, 1H, NH), 9.05–9.03 (d, 1H, 7), 8.14–8.10 (m, 1H, 9), 7.72–7.66 (d, 2H, 8, 10), 7.46–7.13 (m, 5H, Ar.); ¹³C-NMR (DMSO-*d*₆): δ 160 (C-4, C-6), 155.15 (C-2); 146–135 (C-7, C-8, C-9, C-10), 130–125.69 (C, Ar.) 116 (C-5); EI-Mass *m/z*: 238.0742 [M]⁺.

BT1 (6-oxo-1,2,3,5-tetraphenyl-1,6-dihydropyrimidin-3-ium-4-olate). Chemical formula: C₂₈H₂₀N₂O₂, Yellow crystals; Mol. Mass. 416 g/mol, m.p.: 317–319 (decomposed); UV-Visible (dioxane) λ_{max}: 357 nm; IR (KBr) cm⁻¹: 3051 (C-H, Ar.); 1651 (C=O), 1593 (C=C, Ar.); ¹H-NMR (300 MHz, DMSO-*d*₆): δ 7.82–6.98 (m, 20H, Ar.); ¹³C-NMR (75 MHz, DMSO-*d*₆): δ 159.87 (C-4, C-6), 159.35 (C-2), 137.77 (C-7, C-19), 135.76–130.58 (C-13, C-16), 129.91/128.77 (C-8,12,20,24, C-9,11,21,23, C-10,22), 127.65/125.36 (C-14,18, C-15,17), 96.03 (C-5); EI-Mass *m/z*: 416.1527 [M].

BT12 (6-oxo-2-dodecyl,1,3,5-triphenyl-1,6-dihydropyrimidin-3-ium-4-olate). Chemical formula: C₃₃H₃₈N₂O₂; White solid; Mol. Mass. 494 g/mol; m.p.: 124–128; UV-Visible (dioxane) λ_{max}: 352 nm; IR (KBr) cm⁻¹: 3055 (C-H, Ar.), 1647 (C=O); 1597 (C=C, Ar.); ¹H-NMR (300 MHz, CDCl₃): δ 7.91–7.14 (15H, Ar.), 2.41–0.78 (23H, aliph.), ¹³C-NMR (75 MHz, CDCl₃): δ 161.42 (C-14,16), 159.00 (C-12), 136.27–125.76 (C, Ar.) 32.77–14.11 (C, aliph.), EI-Mass *m/z*: 495.2 [M+1]⁺.

Antioxidant activity

There are still no standardized procedures for determining a sample's antioxidant potential [31]. Since various trends in antioxidant activity assays have been noticed, it is useful to estimate and compare the antioxidant potential of synthetic compounds using several assays [32]. To assess the effects of concentration, temperature, and reaction time on the antioxidant activity of the pyrimidinium betaines under investigation, we used three methods: DPPH assay, reducing power measurement and β-carotene bleaching procedure. In parallel tests, the effects of parameters on the antioxidant activity of conventional antioxidants (BHT, BHA and ascorbic acid (vitamin C)) used for comparison have been studied. All samples were assayed in triplicate.

DPPH radical scavenging assay

The DPPH method is commonly used to evaluate antioxidants' ability to scavenge free radicals [27]. The reduction of an alcoholic solution of DPPH in the presence of a hydrogen or electron donor antioxidant is the basis of this method. The ability of the related compounds to donate a hydrogen atom or an electron was determined spectrophotometrically by bleaching the purple methanolic solution of DPPH [28]. In this study, the capacities of pyrimidinium betaines to quench the DPPH radical were measured according to the method of Blois [10] and Brand-Williams et al. [11] with some modifications.

A 0.004% DPPH solution in methanol was prepared, and 1 mL of this solution was mixed with 1 mL of various concentrations of betaines solution in ethanol. The reaction mixture was carefully agitated and then kept at room temperature in the dark. The absorbance was measured spectrophotometrically at 517 nm in comparison to a negative control containing only DPPH solution.

The radical scavenging activity of DPPH was calculated as a percentage inhibition using the following formula (Eq. (1)):

$$\text{DPPH inhibition (\%)} = \frac{A_c - A_s}{A_c} \times 100 \quad (1)$$

where A_c denotes the absorbance of the control reaction (DPPH solution devoid of the substance to be tested) and A_s indicates the absorbance of the test sample.

Reducing power assay

The reducing power of a substance is a measure of its antioxidant ability, and it is evaluated by converting Fe(III) to Fe(II) in the presence of the sample extract [6]. Singh et al. [33] ascribe the capacity to reduce Fe(III) to the hydrogen-donating ability of phenolic compounds. The yellow color of the test solution in this assay changes to green and blue depending on the reducing power of the test material. Based on the absorbance at 700 nm after incubation, the oxidant's ability to decrease the ferric ferricyanide complex to the ferrous one was measured. The greater absorbance indicates a greater

reducing power [34]. The Oyaizu method was used to evaluate the reducing power of the synthesized compounds [35].

Different concentrations of betaines in 1 mL of ethanol were combined with 2.5 mL of phosphate buffer (0.2 M, pH 6.6) and 2.5 mL of potassium ferricyanide [$K_3Fe(CN)_6$] (1%) before incubating at 50 °C for 20 min. Following that, 2.5 mL of trichloroacetic acid (10%) was added to the mixture, which was then centrifuged at 1000 rpm for 10 min. Finally, 2.5 mL of the top layer solution was combined with 2.5 mL of distilled water and 0.5 mL of $FeCl_3$ (0.1%), and absorbance at 700 nm was recorded.

β -Carotene bleaching assay

This method is based on the fact that linoleic acid generates a free radical, which β -carotene reduces. The inclusion of an antioxidant allows for a delay in the kinetics of β -carotene discoloration [36]. Several researchers [37] found the test of inhibition of linoleic acid oxidation in combination with β -carotene to be highly useful as a model of lipid peroxidation in biological.

β -Carotene bleaching assay was conducted by using the method suggested by Tepe and Moure [38-39] with some modifications. The absorbance of the samples was measured at 470 nm at regular time intervals using a spectrophotometer. The same procedure was followed with the positive controls, BHT, BHA, and vitamin C, as well as a blank. The following formula (Eq. (2)) was used to compute the Relative Antioxidant Activity (RAA) as a percentage:

$$RAA (\%) = \frac{A_s}{A_c} \times 100 \quad (2)$$

where A_s is the absorbance of the sample) and A_c , the absorbance of BHT used as the positive control.

Statistical analysis

Data were analyzed with the statistical software statistica. Values were expressed as means \pm standard deviations (SD). Differences were considered significant at $p < 0.05$.

RESULTS AND DISCUSSION

Pyrimidinium betaines were synthesized, as reported earlier [24-26]. The effects of various parameters

(concentration, reaction time, and temperature) on their antioxidant activities were investigated using DPPH assay, ferric ions reducing antioxidant power (FRAP), and β -carotene bleaching procedure as three separate tests.

Concentration Effect

The antioxidant properties of the examined substances were studied *in vitro*, and the effect of the concentration on their antioxidant activity was examined by DPPH radical scavenging capacity and FRAP in the concentration range of 0–500 g/mL.

DPPH radical scavenging assay

Fig. 4 presents the inhibition percentage of the DPPH free radical in the presence of betaines at various concentrations for 180 min. As shown in Fig. 4, all betaines exhibited potent activity in a concentration-dependent manner. This activity can be attributed to the conjugate systems with nitrogen atoms in these molecules, which are known to stabilize free radicals [20]. The findings of this study show that the compounds examined have variable rates of scavenging DPPH radicals.

On the basis of the statistical analysis of our data, we noted that at low concentrations (0–100 μ g/mL), bicyclic betaine BT3 exhibited a higher DPPH radical scavenging rate than the remaining betaines, whereas at high concentrations (200–500 μ g/mL) both monocyclic BT1 and fatty betaine BT12 showed the highest DPPH radical scavenging rate, and that monocyclic betaine BT1 is more active than fatty betaine BT12 and betaine BT3, while the bicyclic betaine BT2 has the lowest radical

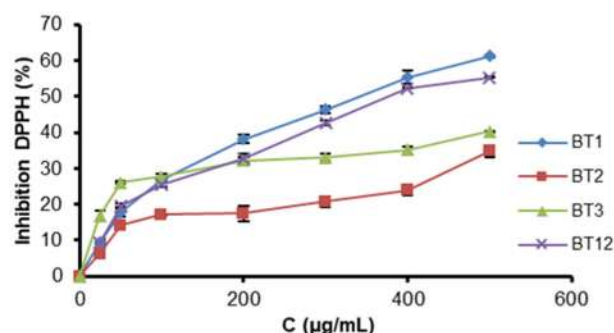


Fig 4. Inhibition of DPPH free radical in the presence of pyrimidinium betaines

scavenging activity over the entire concentrations range (0–500 $\mu\text{g/mL}$). Fig. 5 shows the impact of concentration on betaines' antioxidant activity, using different concentrations (25, 100, 500 $\mu\text{g/mL}$) as an example, maintaining the reaction time constant for 180 min.

Fig. 5 indicated that the antioxidant's efficiency increased as the concentration of the tested betaines increased. At 25 $\mu\text{g/mL}$, the antiradical activity of the betaines was very weak, and the percentages of inhibition of DPPH radical by the compounds BT1, BT2, and BT12 were very close and lower than that of BT3. At 100 $\mu\text{g/mL}$, their antioxidant capacity was moderate. At the maximum value (500 $\mu\text{g/mL}$), the antioxidant's power had increased, and monocyclic betaine BT1 had the highest activity that was comparable to long-chain betaine BT12 ($p < 0.05$).

Betaines' DPPH radical scavenging activity could be due to their reducing action by electron donation, converting a free radical to a nonreactive species [20]. The nitrogen-atom conjugated systems that are more abundant in monocyclic betaine BT1 and fatty betaine BT12 than in bicyclic betaines BT2 and BT3 may be responsible for the antioxidant activity of these two molecules. In betaines BT1 and BT12, the radical formed is strongly stabilized by resonance through the phenyl and carbonyl groups [22].

Reducing power assay

The reducing properties of tested betaines at 700 nm are illustrated in Fig. 6. As shown in Fig. 6, all betaines displayed potent reducing power in a concentration-dependent manner. With increasing concentrations, the reducing power of the tested betaines increased, reaching a plateau further than 200 $\mu\text{g/mL}$.

To investigate the effect of concentration on betaines' reducing power, we used as an example three different concentrations (20, 100, 500 $\mu\text{g/mL}$), as shown in Fig. 7. By examining the results, we observed that the reducing power of each betaine examined increased somewhat with increasing concentration and that on the three proposed concentrations, monocyclic betaine BT1 exhibited the highest reducing power, while long chain betaine BT12 revealed the lowest one. Decreased reducing

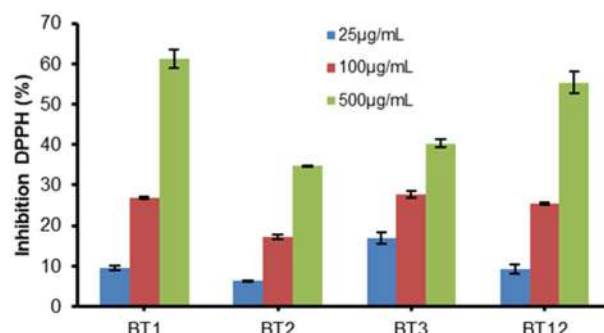


Fig 5. Effect of concentration on the antioxidant activity of tested betaines

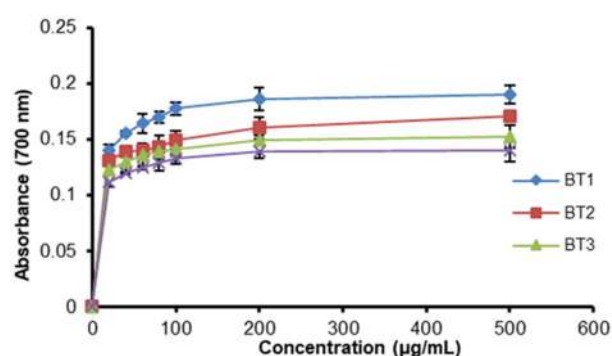


Fig 6. Reducing powers of pyrimidinium betaines

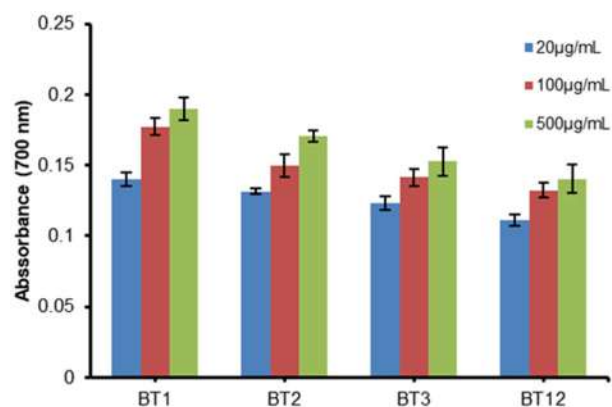


Fig 7. Effect of concentration on reducing the power of pyridinium betaines

power of BT12 appears to be related to a steric effect [22]. The presence of a long alkyl chain in fatty betaine could provide steric hindrance, which would decrease the contact with the Fe^{3+} ions. Based on the previous findings, we conclude that in both tests (DPPH and reducing power), the antioxidant efficiency of betaines increases with increasing concentration and that monocyclic betaine BT1 has the highest antioxidant activity.

The results of the effect of concentration on the reducing power of betaines and reference antioxidants (BHA and vitamin C) are shown in Fig. 8. As shown in Fig. 8, the evaluated betaines were less active than the reference antioxidants BHA, BHT, and Vitamin C ($p < 0.05$). The latter is strongly influenced by the concentration and showed the highest activity. With regard to the molecular structures, the reference antioxidants' higher reducing power could be due to the presence of hydroxyl groups in their structure [31], while the pyridinium betaines' lower reactivity was mainly due to steric hindrance in these molecules.

Effect of Time

We used two methods to study the effect of time on the antioxidant activity of selected betaines: the DPPH radical scavenging assay and the β -carotene bleaching assay.

Test for DPPH radical scavenging

To assess the scavenging activity as a function of time, kinetic studies of the DPPH-betaines reaction were conducted while keeping their concentration constant at 300 $\mu\text{g/mL}$. The percentages of inhibition of the DPPH radical as a function of time are represented in Fig. 9.

Fig. 9 illustrated that the antioxidant activity of the betaines increased as the reaction time increased. The results revealed that specific activity of the compounds was obtained depending on the reaction time used: during the 0–60 min period, bicyclic betaines BT2 and BT3 had low activity, as did monocyclic BT1 and fatty chain betaine BT12, which were more active. As the reaction time increased, the antioxidant activity of the betaines increased as well. They reached their highest activity at the maximum time of 240 min, at which monocyclic betaine BT1 showed the highest activity compared to other compounds ($p < 0.05$).

Fig. 10 depicts the influence of time on the antioxidant activity of studied betaines for 30, 120, and 240 min. As can be seen, the antioxidant activity was significantly improved from 30 to 240 min ($p < 0.05$). The results showed that the studied betaines were more effective at 240 min compared to 30 and 120 min. At 240 min, monocyclic betaine BT1 had the highest antioxidant activity, while bicyclic BT2 had the lowest one.

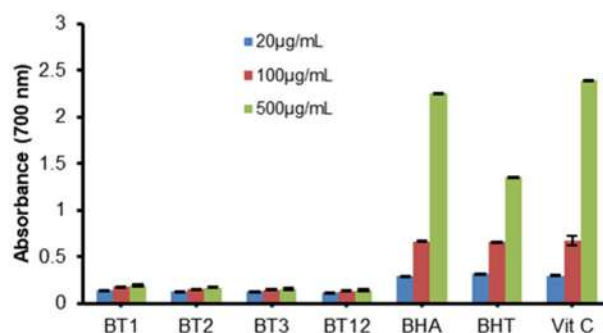


Fig 8. Effect of concentration on the reducing power of betaines and reference antioxidants

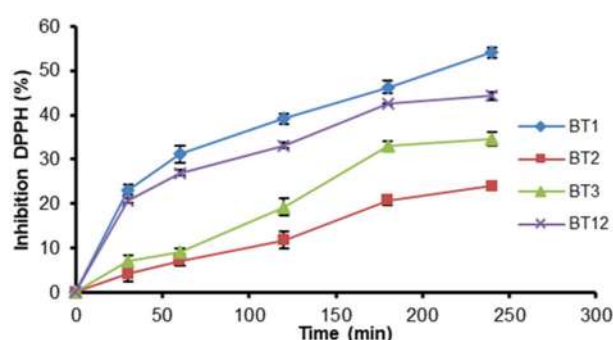


Fig 9. Betaines' DPPH radical scavenging activity as a function of time

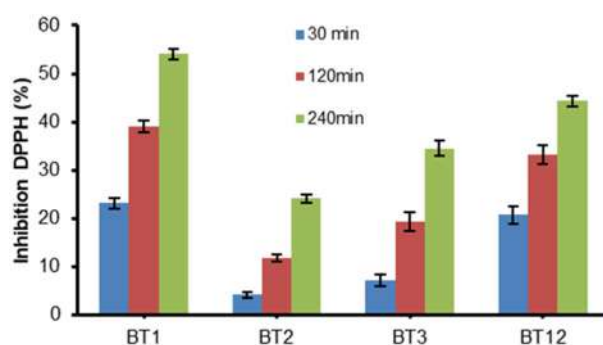


Fig 10. Effect of time on the antioxidant activity of betaines

From the above findings, we conclude that in the DPPH assay, the antioxidant activity of betaines is profoundly influenced by reaction time: the longer the reaction time, the greater the antioxidant activity.

β -Carotene bleaching test

Fig. 11 represents the bleaching kinetics of β -carotene in the presence of synthesized betaines and the reference antioxidant BHT as a positive control. It was obvious that all betaines efficiently inhibited linoleic acid

oxidation and prevented β -carotene bleaching. The findings demonstrated that betaine activity was reduced with increasing time. The relative rate of reduction in antioxidant activity with increasing time was not the same for all betaines investigated. Indeed, as compared to other betaines, bicyclic BT3 demonstrated a slower reduction in antioxidant activity with increasing time.

We calculated the antioxidant activities of betaines relative to that of positive control (BHT) for 2, 24, and 48 h. The results are shown in Fig. 12. According to the results, the highest oxidation inhibitory action of linoleic acid in the presence of tested betaines is observed at 2 h, and the effectiveness of the monocyclic BT1 and bicyclic BT2 reduced significantly with increasing time ($p < 0.05$). At 48 h, the highest activities were found for BT3 (RAA = $90.02 \pm 1.01\%$) and BT12 (RAA = $76.22 \pm 1.08\%$), whereas the activity of BT1 (RAA = $45.57 \pm 0.47\%$) was lower than that of BT2 (RAA = $63.25 \pm 1.9\%$).

A decrease in antioxidant activity with increasing reaction time could be caused by a decrease in the ability of antioxidants to react with free radicals (particularly with peroxy radicals of fatty acids) and, consequently, a discoloration of β -carotene by radicals produced by fatty acid oxidation, since the assay is carried out in an aqueous emulsion of linoleic acid and β -carotene. Through the results above, we noted that bicyclic betaine BT3 exhibited the highest inhibition of linoleic acid oxidation at all times when compared to BHT. In contrast, long-chain betaine BT12 showed higher antioxidant activity in comparison to monocyclic BT1, especially at 24 and 48 h ($p < 0.05$). Increasing lipophilicity appears to have resulted in an increase in antioxidant activity. In the β -carotene discoloration test, steric effects can be very important. Indeed, the presence of four phenyl groups in monocyclic betaine BT1 may cause steric hindrance, resulting in low reactivity. The greater reactivity of bicyclic betaine BT3 may, on the other hand, can be attributed to its smaller molecule size when compared to the other betaines.

The results of the antioxidant activities of betaines and reference compounds (BHA and vitamin C) relative to that of the BHT at 2, 24, and 48 h are shown in Fig. 13. Compared to the tested compounds, BT3 and the reference antioxidant BHA exhibited the highest

inhibition of linoleic acid oxidation at all times relative to BHT. Although the activity of BT1 was the lowest among the other betaines, it was much higher than that of ascorbic acid (Vitamin C) used as a positive control ($p < 0.05$), which was very poor in activity.

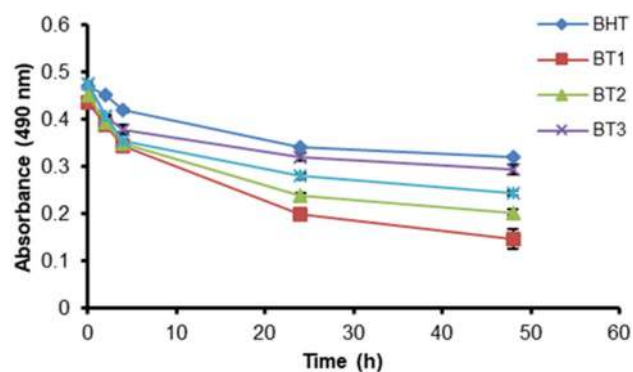


Fig 11. Antioxidant capacity of synthesized betaines in linoleic acid/ β -carotene system

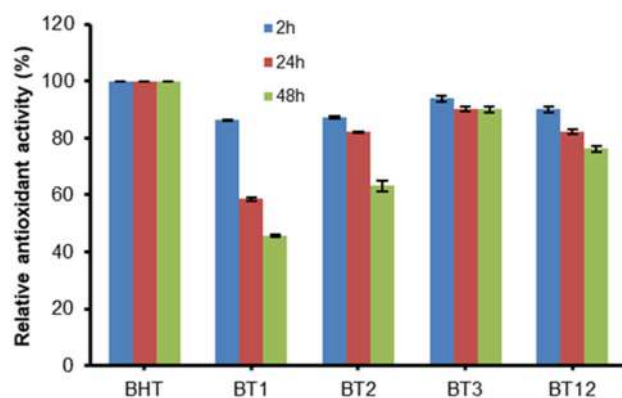


Fig 12. Effect of time on the antioxidant activity of betaines in β -carotene/linoleic acid system

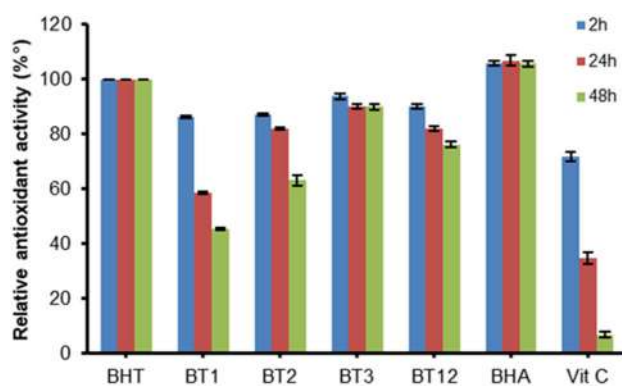


Fig 13. Effect of time on the antioxidant activity of betaines and reference antioxidants in β -carotene/linoleic acid system

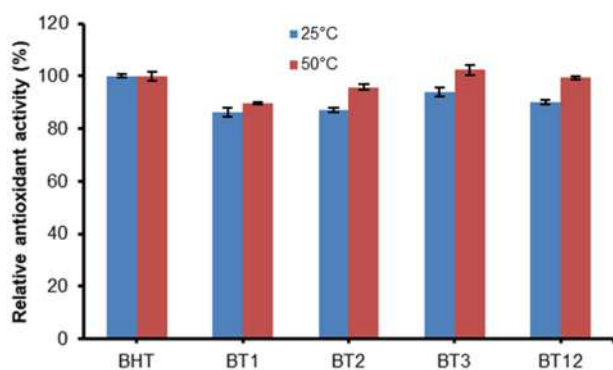


Fig 14. Effect of temperature on the antioxidant activity of betaines at 25 and 50 °C

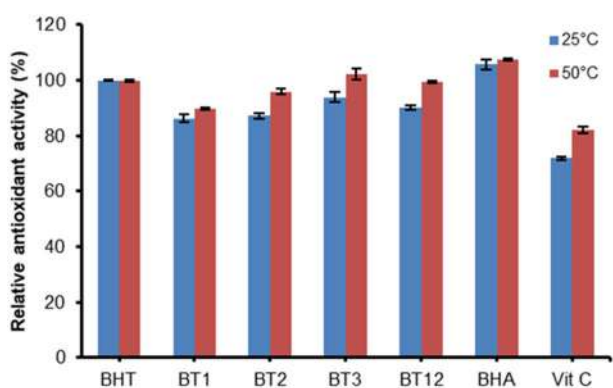


Fig 15. Effect of temperature on the antioxidant activity of betaines and reference antioxidants

Effect of Temperature

Temperature is one of the most significant factors influencing antioxidant activity [40]. The effect of temperature on the antioxidant power of betaines was investigated using a β -carotene assay. Fig. 14 represents the antioxidant activity of the betaines tested and BHT in the β -carotene/linoleic acid system at 25 and 50 °C, after 2 h of inhibition of the oxidation of linoleic acid. As can be seen, the antioxidant activity in the β -carotene/linoleic acid system increased as a function of temperature; increasing temperature caused an increase in antioxidant activity, indicating a high dependence of the antioxidant activity on the temperature.

According to the findings, heating betaines and reference antioxidants to 50 °C was found to be more effective, and as Fig. 15 showed, the pyrimidinium betaines exhibited considerable antioxidant activities compared to those of the reference antioxidants. The

above revealed that the temperature has a favorable effect on the inhibition of the oxidation of linoleic acid.

CONCLUSION

In this study, four pyrimidinium betaines were evaluated for their antioxidant capacities by three methods, and the effects of some factors such as concentration, reaction time and temperature on their antioxidant activity were investigated. The results revealed that all the betaines tested had potent antioxidant and free radical scavenging properties in various assays. The findings indicated that, in both the DPPH and the reducing power assays, antioxidant activity increased as the concentration increased; however, increasing the temperature caused an increase in antioxidant activity in the β -carotene/linoleic acid system. On the other hand, as time increased, the antioxidant capacity increased in the DPPH assay, but it decreased in the β -carotene bleaching assay. By comparing the results obtained according to the three methods, it can be seen that the antioxidant activity varies depending on the method used and that the different factors affect the antioxidant activity in a different order. This could be due to differences in reaction conditions, molecular interactions in the reaction medium, specific free radicals being used as a reactant and radical kinetics. *In vitro* antioxidant assays suggest that pyrimidinium betaines may be important sources of synthetic antioxidants that could be helpful in preventing the progression of various oxidative stresses and could have significant and wide applications in the pharmaceutical and food industries.

ACKNOWLEDGMENTS

The authors are thankful to the Laboratory for Research on Bioactive Products and the Valorization of Biomass, Ecole Normale Supérieure, Kouba - Algiers, Algeria, for providing us with the facilities required to perform this work. We are also grateful to Doctor Michel Baltas for the NMR and mass spectra performed in the Laboratory of Synthesis and Physicochemistry of Molecules of Biological Interest, UMR 5068, University Paul Sabatier Toulouse, France.

■ REFERENCES

- [1] Sharifi-Rad, J., Hoseini-Alfatemi, S.M., Miri, A., Sharifi-Rad, M., Soufi, L., Sharifi-Rad, M., Setzer, W.N., Hoseini, M., Sharifi-Rad, M., and Rokni, M., 2015, Phytochemical analysis, antioxidant and antibacterial activities of various extracts from leaves and stems of *Chrozaphora tinctoria*, *Environ. Exp. Biol.*, 13, 169–175.
- [2] Papuc, C., Goran, G.V., Predescu, C.N., and Nicorescu, V., 2016, Mechanisms of oxidative processes in meat and toxicity induced by postprandial degradation products: A review, *Compr. Rev. Food Sci. Food Saf.*, 16 (1), 96–123.
- [3] Alkadi, H., 2020, A review on free radicals and antioxidants, *Infect. Disord.: Drug Targets*, 20 (1), 16–26.
- [4] Marinova, E., Georgiev, L., Totseva, I., Seizova, K., and Milk, T., 2013, Antioxidant activity and mechanism of action of some synthesised phenolic acid amides of aromatic amines, *Czech J. Food Sci.*, 31, 5–13.
- [5] Alam, M.N., Bristi, N.J., and Rafiquzzaman, M., 2013, Review on *in vivo* and *in vitro* methods evaluation of antioxidant activity, *Saudi Pharm. J.*, 21 (2), 143–152.
- [6] Gulcin, İ., 2020, Antioxidants and antioxidant methods: An updated overview, *Arch. Toxicol.*, 94 (3), 651–715.
- [7] Parcheta, M., Świsłocka, R., Orzechowska, S., Akimowicz, M., Choińska, R., and Lewandowski, W., 2021, Recent developments in effective antioxidants: The structure and antioxidant properties, *Materials*, 14 (8), 1984.
- [8] Pisoschi, A.M., Pop, A., Iordache, F., Stanca, L., Predoi, G., and Serban, A.I., 2021, Oxidative stress mitigation by antioxidants - An overview on their chemistry and influences on health status, *Eur. J. Med. Chem.*, 209, 112891.
- [9] Jaman, M.S., Alam, M.S., Rezwani, M.S., Husna, A.U., Islam, M.R., and Sayeed, M.A., 2017, Comparison of total antioxidant activity between fresh and commercial mango juices available in Bangladesh, *GSC Biol. Pharm. Sci.*, 1 (2), 26–33.
- [10] Blois, M.S., 1958, Antioxidant determinations by the use of stable free radical, *Nature*, 181 (4617), 1199–1200.
- [11] Brand-Williams, W., Cuvelier, M.E., and Berset, C., 1995, Use of a free radical method to evaluate antioxidant activity, *LWT-Food Sci. Technol.*, 28 (1), 25–30.
- [12] Nsimba, Z.F., Paquot, M., Mvumbi, L.G., and Deleu, M., 2010, Les dérivés tensioactifs de la glycine bêtaïne: Méthodes de synthèse et potentialités d'utilisation, *Biotechnol., Agron., Soc. Environ.*, 14 (4), 737–748.
- [13] Zakanda, F.N., Laurent, P., Paquot, M., Lelo, G.M., and Deleu, M., 2011, Alkylbetainate chlorides: Synthesis and behavior of monolayers at the air-water interface, *Thin Solid Films*, 520 (1), 344–350.
- [14] Breslawec, T.E., and Gottschalck, H., 2012, *International Cosmetic Ingredient Dictionary and Handbook: INCI name monographs I-S*, Volume 2, 14th Ed., Personal Care Products Council, Washington DC.
- [15] Birnie, C.R., Malamud, D., and Schnaare, R.L., 2000, Antimicrobial evaluation of *N*-alkyl betaines and *N*-alkyl-*N,N*-dimethylamine oxides with variations in chain length, *Antimicrob. Agents Chemother.*, 44 (9), 2514–2517.
- [16] Sharma, V., Chitranshi, N., and Agarwal, A.K., 2014, Significance and biological importance of pyrimidine in the microbial world, *Int. J. Med. Chem.*, 2014, 202784.
- [17] Malki, F., Touati, A., and Moulay, S., 2015, Stability of mesoionic pyrimidinium betaines in aqueous media, *Chem. J.*, 5 (6), 123–126.
- [18] Koch, A., Jonas, U., Ritter, H., and Spiess, H.W., 2004, Extended mesoionic systems: Synthesis and characterization of monocyclic, polycyclic and macrocyclic pyrimidinium-olate derivatives and their photochemical behavior, *Tetrahedron*, 60 (44), 10011–10018.
- [19] Munteanu, I.G., and Apetrei, C., 2021, Analytical methods used in determining antioxidant activity: A review, *Int. J. Mol. Sci.*, 22 (7), 3380.

- [20] Malki, F., Touati, A., and Moulay, S., 2013, Antioxidant activity of two mesomeric heterocyclic betaines containing a pyrimidine moiety, *Pertanika J. Trop. Agric. Sci.*, 36 (4), 393–402.
- [21] Malki, F., and Touati, A., 2019, Study of antioxidant activity of pyrimidinium betaines by DPPH radical scavenging method, *J. Anal. Pharm. Res.*, 8 (2), 33–36.
- [22] Malki, F., Touati, A., Moulay, S., and Baltas, M., 2016, Evaluation of antioxidant activity of some mesoionic pyrimidinium betaines by three different methods, *Int. J. Chem. Eng. Appl.*, 7 (6), 373–377.
- [23] Antolovich, M., Prenzler, P.D., Patsalides, E., McDonald, S., and Robards, K., 2002, Methods for testing antioxidant activity, *Analyst*, 127 (1), 183–198.
- [24] Tschitschibabin, A.E., 1924, Tautomerie des α -amino-pyridins, II: Über die bildung von bicyclischen derivaten des α -amino-pyridins, *Ber. Dtsch. Chem. Ges.*, 57 (7), 1168–1172.
- [25] Dvortsák, P., Resofszki, G., Huhn, M., Zalántai, L., and Kiss, A.I., 1976, Reactions of pentachlorophenyl esters of malonic acid derivatives—II: Preparation and investigation of pyrimidine betaines, *Tetrahedron*, 32 (17), 2117–2120.
- [26] Malki, F., Touati, A., Rahal, S., and Moulay, S., 2011, Total synthesis of monocyclic pyrimidinium betaines with fatty alkyl chain, *Asian J. Chem.*, 23 (3), 961–967.
- [27] Malki, F., Touati, A., and Moulay, S., 2017, Comparative study of antioxidant activity of some amides, *J. Anal. Pharm. Res.*, 5 (3), 00143.
- [28] Baliyan, S., 2022, Determination of antioxidants by DPPH radical scavenging activity and quantitative phytochemical analysis of *Ficus religiosa*, *Molecules*, 27 (4), 1326.
- [29] Malki, F., Touati, A., and Moulay, S., 2014, Extraction and recrystallization of mesoionic pyrimidinium betaines, *Int. J. Chem. Eng. Appl.*, 5 (2), 151–154.
- [30] Malki, F., Touati, A., and Moulay, S., 2015, Use of column chromatography for quantitative isolation of mesoionic pyrimidinium betaines, *Int. J. Res. Chem. Metall. Civ. Eng.*, 2 (1), 29–32.
- [31] Arró-Díaz, D.J., Castelnaux-Ochoa, N., Ochoa-Pacheco, A., and Do-Nascimento, Y.M., 2021, Antioxidant activity of bioactive compounds isolated from leaves and bark of *Gymnanthes lucida* Sw, *Rev. Cubana Quim.*, 33 (1), 22–39.
- [32] Sun, H., Yuan, X., Zhang, Z., Su, X., and Shi, M., 2018, Thermal processing effects on the chemical constituent and antioxidant activity of okara extracts using subcritical water extraction, *J. Chem.*, 2018, 6823789.
- [33] Singh, R., Shushni, M.A.M., and Belkheir, A., 2015, Antibacterial and antioxidant activities of *Mentha piperita* L., *Arabian J. Chem.*, 8 (3), 322–328.
- [34] Gülçin, İ., 2012, Antioxidant activity of food constituents: An overview, *Arch. Toxicol.*, 86 (3), 345–391.
- [35] Mitic, V., Jovanovic, V.S., Dimitrijevic, M., Cvetkovic, J., and Stojanovic, G., 2013, Effect of food preparation technique on antioxidant activity and plant pigment content in some vegetables species, *J. Food Nutr. Res.*, 1 (6), 121–127.
- [36] Sharma, K.D., Karki, S., and Thakur, N.S., 2012, Chemical composition, functional properties and processing of carrot—A review, *J. Food Sci. Technol.*, 49 (1), 22–32.
- [37] Fuentealba, C., Gálvez, L., Cobos, A., Olaeta, J.A., Defilippi, B.G., Chirinos, R., Campos, D., and Pedreschi, R., 2016, Characterization of main primary and secondary metabolites and *in vitro* antioxidant and antihyperglycemic properties in the mesocarp of three biotypes of *Pouteria lucuma*, *Food Chem.*, 190, 403–411.
- [38] Tepe, B., Sokmen, M., Akpulat, H.A., and Sokmen, A., 2006, Screening of the antioxidant potentials of six *Salvia* species from Turkey, *Food Chem.*, 95 (2), 200–204.
- [39] Moure, A., Franco, D., Sineiro, J., Dominguez, H., Nunez, M.J., and Lema, J.M., 2000, Evaluation of extracts from *Gevuina avellana* hulls as antioxidants, *J. Agric. Food Chem.*, 48 (9), 3890–3897.
- [40] Réblová, Z., 2012, Effect of temperature on the antioxidant activity of phenolic acids, *Czech J. Food Sci.*, 30 (2), 171–177.

Adsorption of Fe(II) by Layered Double Hydroxide Composite with Carbon-Based Material (Biochar and Graphite): Reusability and Thermodynamic Properties

Neza Rahayu Palapa¹, Alfian Wijaya², Patimah Mega Syah Bahar Nur Siregar², Amri Amri², Nur Ahmad², Tarmizi Taher³, and Aldes Lesbani^{2,4*}

¹Department of Chemistry, Faculty of Mathematics and Natural Sciences, Sriwijaya University, Jl. Palembang-Prabumulih, Km. 90-32, Ogan Ilir 30862, South Sumatra, Indonesia

²Research Center of Inorganic Materials and Complexes, Faculty of Mathematics and Natural Sciences, Sriwijaya University, Jl. Padang Selasa Bukit Besar, Palembang 30139, South Sumatra, Indonesia

³Department of Environmental Engineering, Institut Teknologi Sumatera, Jl. Terusan Ryacudu, Way Hui, Lampung Selatan 35365, Indonesia

⁴Graduate School, Faculty of Mathematics and Natural Sciences, Sriwijaya University, Jl. Palembang-Prabumulih, Km. 90-32, Ogan Ilir 30862, South Sumatra, Indonesia

* Corresponding author:

email: aldeslesbani@pps.unsri.ac.id

Received: June 10, 2022

Accepted: December 25, 2022

DOI: 10.22146/ijc.75307

Abstract: Layered double hydroxide (LDH) of Ni/Al was synthesized by coprecipitation method at pH 10 followed by the formation of composite with carbon-based material i.e., biochar (B) and graphite (G) to form Ni/Al-B and Ni/Al-G. Materials were characterized by XRD powder, FTIR, BET surface area, thermal analyses, and SEM analysis. The regeneration process and adsorption evaluated the performance of materials toward iron(II) [Fe(II)] from an aqueous solution. The results showed that the surface area of Ni/Al-B (428.94 m²/g) was increased mainly up to twenty-nine-fold than Ni/Al LDH (15.11 m²/g), while Ni/Al-G (21.59 m²/g) had slightly increased than pristine LDH. Composite of Ni/Al-B had reusability properties for Fe(II) adsorption up to five cycles and showed higher structural stability. The adsorption capacity of Ni/Al-B was 104.167 mg/g and can be a potential adsorbent to remove Fe(II) from an aqueous solution.

Keywords: layered double hydroxide; graphite; biochar; Ni/Al; structural stability

■ INTRODUCTION

Adsorption is suitable for removing various wastewater pollutants such as organic molecules, heavy metals, and dyes [1-2]. This method offers several advantages: fast process, easy to conduct, and high efficiency. The successful adsorption process depends on the properties of the adsorbent. The adsorbent can be categorized as inorganic and organic adsorbents [3-5]. Each type of adsorbent has advantages and disadvantages depending on the pollutants and properties of adsorbents [6]. Organic adsorbents such as chitin, chitosan, cellulose, lignin, and algae have various functional groups, which can be used as active sites for the adsorption process [5,7-9]. The organic adsorbents are easily decomposed by temperature. On the other hand, inorganic adsorbents

such as zeolite, clay, metal oxide, bentonite, kaolinite, and layered double hydroxide have pores and layers as active sites for adsorption [10-13]. Inorganic adsorbents are temperature resistant. Based on the advantages and disadvantages of organic-inorganic adsorbents, modification of adsorbents based on organic-inorganic materials is an interesting topic to explore, in regards to obtain novel properties of adsorbents for the removal of pollutants.

Layered double hydroxide (LDH) is an inorganic layered material consisting of divalent and trivalent metal ions with the general formula $[M^{2+}_x M^{3+}_x (OH)_2]^{x+} (A^{n-})_{x/n} \cdot nH_2O$, where M is divalent and trivalent metal ions and Aⁿ⁻ is interlayer anions with valence n [14]. The merit of this material is that it can be

easily modified using various supports by intercalation, impregnation, and support matrix to improve the stability, the interlayer space, and also the thermal/physical properties of the material. LDH is widely used as an adsorbent to remove pollutants from aqueous solution, as reported by Bessaies et al. [15] in which the Ca/Al and Zn/Al LDH have been studied as arsenic removal. The adsorption capacity was obtained at 10.31 and 30.13 mg/g for Ca/Al and Zn/Al LDH, respectively. Rahmadan et al. [16] reported that ZnAl was prepared for the adsorption of cadmium from an aqueous solution and the adsorption capacity was 22.727 mg/g. In another research, LDH was also widely prepared to remove dyes. According to Starukh and Levytska [17], ZnAl LDH was studied for indigo carmine removal at 298 K and obtained an adsorption capacity of 47 mg/g. Mg–Al–Cu–Fe–CO₃ LDH was prepared to remove acid red in adsorption with pH 6.8 at 298 K. The adsorption results showed that the adsorption capacity reached 66.19 mg/g from an initial concentration of 66.1 mg/L. Unfortunately, the adsorption process of LDH still has limitations and has become challenging for researchers. Furthermore, the modification of LDH using several techniques has been explored.

The modification of LDH by intercalation and impregnation is also conducted to increase the interlayer space and stability of materials such as polyoxometalate, organic compounds, and also carbon-based materials. According to Palapa et al. [18], the unique adsorption process of malachite green was obtained by CuAl LDH intercalated using polyoxometalate. The adsorption capacity showed equal data with increasing surface area properties of the material before and after intercalation. The adsorption capacity CuAl LDH intercalated using polyoxometalate is 149.253 mg/g, higher than 55.866 mg/g from CuAl LDH pristine. Siregar et al. [19] showed that the composites of Mg/Al-AH and Mg/Al-HC had a higher adsorption capacity for Cr(VI) (32.017 and 208.333 mg/g, respectively) than pristine Zn/Cr LDHs (30.211 mg/g). Choong et al. [20] had reported the study of polyacrylamide polyvinyl alcohol. LDH results in higher efficiency for As(V) and As(III) removal with maximum adsorption capacities of 22.8 and 14.1 mg/g, respectively,

higher than that of pristine LDH with adsorption capacities of 7.9 and 7.1 mg/g, respectively. Lv et al. [21] also reported that as-prepared ternary (Fe@LDH/rGO) had good efficiency and capacity for Cr(VI) oxyanions. The adsorption capacity increased after modification, from 5.94 to 14.68 mg/g.

Based on the mentioned literature, it is shown that the development of LDH by impregnation to form carbon-based composite is intriguing research. In the current study, LDH Ni/Al will be composited with carbon-based materials i.e., biochar (B) and graphite (G), to form Ni/Al-B and Ni/Al-G composites. B and G are carbon-rich materials and can stabilize the formation of LDH composites. Ni/Al-B and Ni/Al-G composites will be used as adsorbents for iron(II) from an aqueous solution. The reusability of composites will be investigated first to evaluate the structural stability of composites followed by the adsorption thermodynamics of iron(II).

■ EXPERIMENTAL SECTION

Materials

Chemicals such as nickel(II) nitrate, aluminum (III) nitrate, sodium hydroxide, iron(II) nitrate, sodium carbonate, and graphite were supplied from Merck and used directly after being purchased. Biochar was obtained from Bukata Organic Java, Indonesia, by pyrolysis of Indonesian Java rice husk. Water was purified several times by Purite® water resin ion exchange method.

Instrumentation

Characterization of materials was performed by powder XRD Rigaku Miniflex-600 by scanning at 1°/min. Functional groups were analyzed by FTIR Shimadzu Prestige-21 using the KBr method. BET analysis was conducted using Quantachrome Micrometric 2020, and the sample was degassed under liquid N₂ prior to analysis. Thermal analysis was conducted using TG-DTA Shimadzu analyzer using N₂ flow. SEM analysis was conducted using Scanning Electron Microscopes (SEM) analyzer SU800 Series. The concentration of Fe(II) was analyzed by UV-Visible Bio-

Base BK-UV 1800 PC spectrophotometer after complexation using 1,10-phenanthroline as a ligand at 510 nm.

Procedure

Synthesis of Ni/Al LDH

Ni/Al LDH was synthesized by the coprecipitation method at pH 10. As much as 100 mL of nickel(II) nitrate and aluminum(III) nitrate mixture was made with a concentration ratio of 3:1. The mixture was constantly stirred at room temperature, and sodium carbonate (0.3 M) was added. The pH mixture was adjusted to 10 by the addition of sodium hydroxide solution. The reaction was kept at 80 °C for 24 h. The solid material was filtered, washed and dried at 110 °C.

Preparation of Ni/Al-G and Ni/Al-B

Preparation of Ni/Al-G and Ni/Al-B was conducted by the coprecipitation method. As much as 100 mL of nickel(II) nitrate and aluminum(III) nitrate mixture with the concentration ratio molar of 3:1 was stirred for 60 min. G was added to the mixture by constant stirring followed by the addition of sodium hydroxide (2 M). The pH of the mixture was adjusted with a solution of sodium hydroxide up to pH 10. The reaction mixture was constantly stirred for 72 h. The solid material of Ni/Al-G was formed, washed, and dried at 110 °C for 3 days. The preparation of Ni/Al-B was similar to Ni/Al-G but by changing G to B to form Ni/Al-B.

Structural stability of materials toward re-adsorption

Structural stability of Ni/Al-G, Ni/Al-B, Ni/Al LDH, G, and B was evaluated by Fe(II) re-adsorption process after desorption using an ultrasonic system. After Fe(II) adsorption, the adsorbent was desorbed by an ultrasonic system equipped with a water chamber and then the adsorbent was dried at 110 °C for 3 h. The adsorbent was then reused for Fe(II) adsorption. Re-adsorption was performed until five cycles.

Adsorption isotherm

Adsorption of Fe(II) on composite and pristine materials was conducted by the batch system. Adsorption isotherm was studied by variation of the Fe(II) initial concentration and temperature. The concentration of Fe(II) was adjusted to 10, 20, 30, 40, and 50 mg/L and

adsorption temperature was set to 30, 40, 50, and 60 °C. The concentration of Fe(II) after adsorption on the filtrate was analyzed at 510 nm using a UV-Visible spectrophotometer.

RESULTS AND DISCUSSION

The XRD powder patterns of the composite based on B and G and also the pristine materials are presented in Fig. 1. Ni/Al LDH had diffraction patterns at 11.63° (003); 23.00° (006); 35.16° (012); 39.56° (015); 47.4° (018) and 61.59° (110) [22]. These patterns show the formation of well-known layer structures at 11.63° (003) and 61.59° (110). The diffraction pattern of Ni/Al LDH shows the high crystallinity of the material, which was different from B, as shown in Fig. 1(b). B had a broad diffraction pattern and had one maximum diffraction peak at around 22.30° (002). The diffraction at (002) was attributed to the high carbon content of B from rice husk [23]. On the other hand, the diffraction peak of G was one sharp peak at 26.5° (002) and one small peak at 54° (004). These diffraction peaks were reflected from polyarene structures [24]. The formation of composite based on the carbon material i.e., Ni/Al-B and Ni/Al-G, is shown in Fig. 1(d) and 1(e). Ni/Al-B had a broad diffraction peak, which was similar to B at 22.3° (002). Other diffraction peaks were detected at 11.63° (003) and 36° (012) that come from Ni/Al LDH. Thus, the formation of the composite was based on the starting

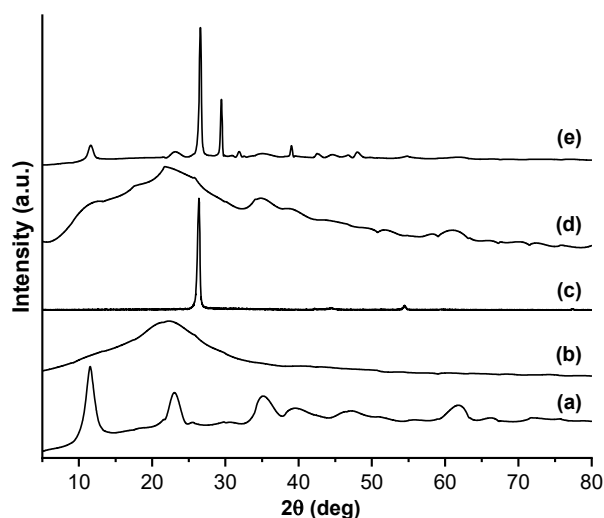


Fig 1. XRD patterns of Ni/AL LDH (a), B (b), G (c), Ni/Al-B (d), and Ni/Al-G (e)

materials. These phenomena were also found for the composite based on G. Ni/Al-G had higher crystallinity than Ni/Al-B. The diffraction of Ni/Al-G was detected at 11.63° , 26.5° (middle intensity), 29° (high intensity), and low intensity at 32° , 41° , 44° and 48° . All diffractions were contributed to LDH and G. Thus, the formation of a composite based on carbon materials was successfully conducted.

The functional groups of the composite and pristine materials were detected by FTIR spectra, as shown in Fig. 2. Ni/Al LDH had main vibration peaks at 3448 cm^{-1} (ν O-H stretching), 1635 cm^{-1} (ν O-H bending), and 1381 cm^{-1} (ν N-O, nitrate, stretching). B had an organic compound and the main vibration appeared at 3448 cm^{-1} (ν O-H stretching), 1635 cm^{-1} (ν O-H bending, and 1095 cm^{-1} (ν C-O stretching). The C-H vibration was also found at 2368 cm^{-1} on B. Similar vibration with B was detected on G at 3448 , 2368 , 1635 , and 1381 cm^{-1} [25]. Composites Ni/Al-B and Ni/Al-G consisted of LDH, B, and G thus, all vibrations of LDH-B and LDH-G should have appeared with almost similar vibrations, as shown in Fig. 2(d) and 2(e).

The nitrogen isotherm adsorption-desorption of composite and starting materials is shown in Fig. 3. All materials have a hysteresis loop due to the adsorption step being different from the desorption step. The materials also had type IV adsorption-desorption curves in which the distribution size of the materials was ununiform [26]. Mesoporous size type was mixed with microporous size in this case. The data of the adsorption-desorption isotherm in Fig. 3 was then calculated using Brunauer-Emmett-Teller (BET) method to obtain the value of the surface area, pore size, and pore distribution, as shown in Table 1.

The BET data in Table 1 shows that Ni/Al-B had a

higher surface area properties compared to the Ni/Al-G composite. The increased surface area properties of Ni/Al-B are almost twenty-nine-fold that of Ni/Al LDH.

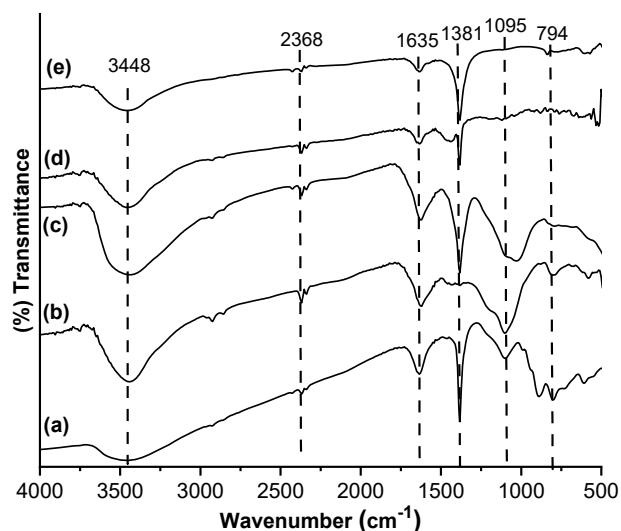


Fig 2. FTIR spectrum of Ni/Al LDH (a), B (b), G (c), Ni/Al-B (d), and Ni/Al-G (e)

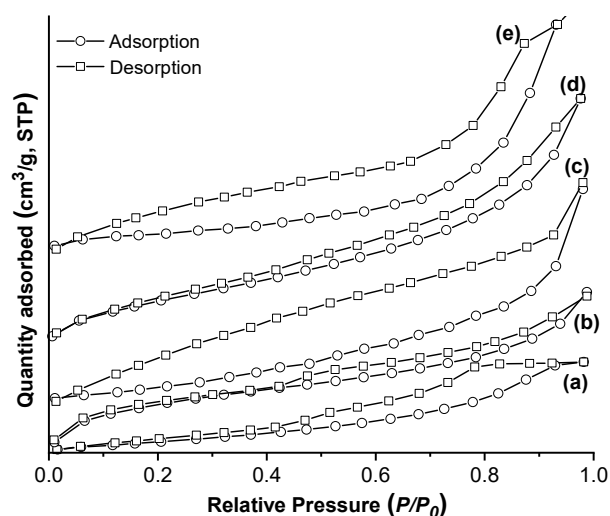


Fig 3. N₂ adsorption-desorption profile of Ni/Al LDH (a), B (b), G (c), Ni/Al-B (d), and Ni/Al-G (e)

Table 1. BET data of materials

Materials	Surface area (m ² /g)	Pore size (nm), BJH	Pore volume (cm ³ /g) _{BJH}
Ni/Al LDH	15.11	2.90	0.04
B	50.94	12.09	0.02
G	11.56	3.17	0.03
Ni/Al-B	438.94	12.30	0.002
Ni/Al-G	21.59	3.15	0.03

On the other hand, the surface area and pore size of Ni/Al-G were slightly higher than Ni/Al-B. The lower surface area of Ni/Al-G compared to Ni/Al-G was because G covered the surface sites of LDH by polyarene. The active site of Ni/Al-G was dominated by G, which was collated with a composite of high crystallinity, similar to G.

Fig. 4 shows the thermal properties of the

composites and starting materials. Ni/Al LDH is an inorganic layer material that had three endothermic peaks, as shown in Fig. 4(a). The endothermic peaks were identified at 100 °C (loss of water on surface material), 220 °C (loss of water of crystallization), and 320 °C (decomposition of anion on the interlayer). On the other hand, B, which is an organic material had one

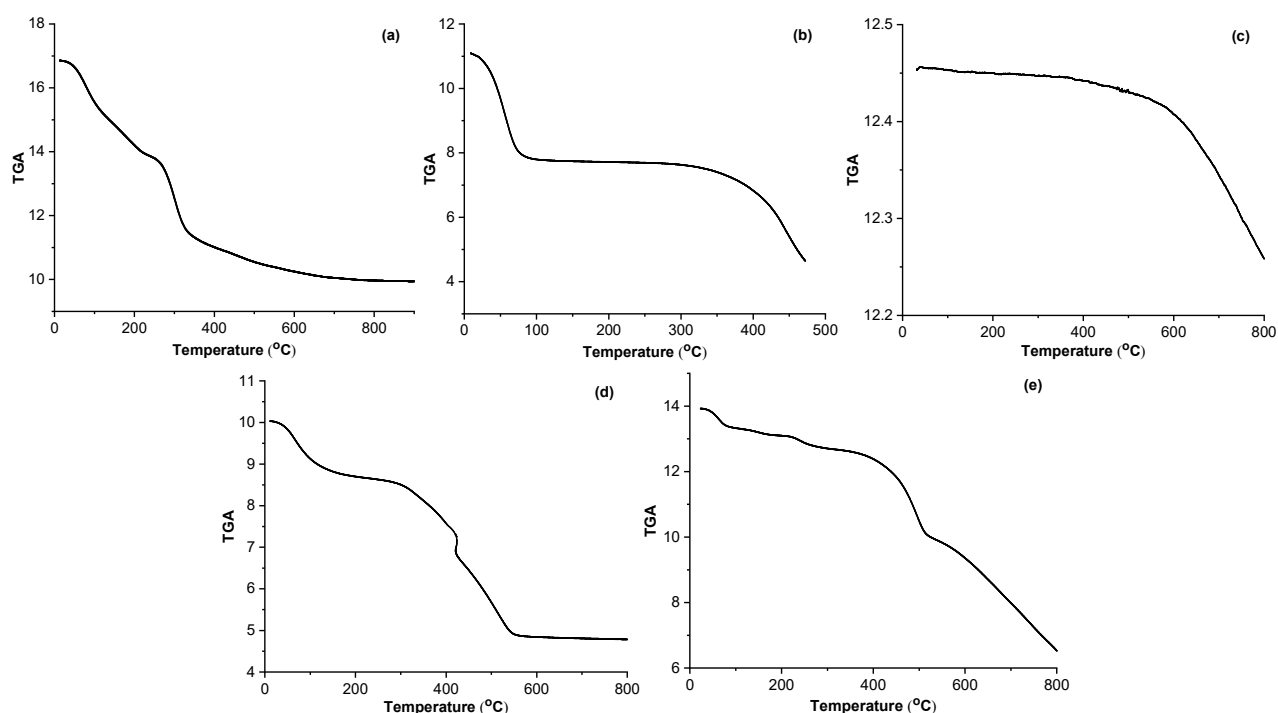


Fig 4. TGA profile of Ni/Al LDH (a), B (b), G (c), Ni/Al-B (d), and Ni/Al-G (e)

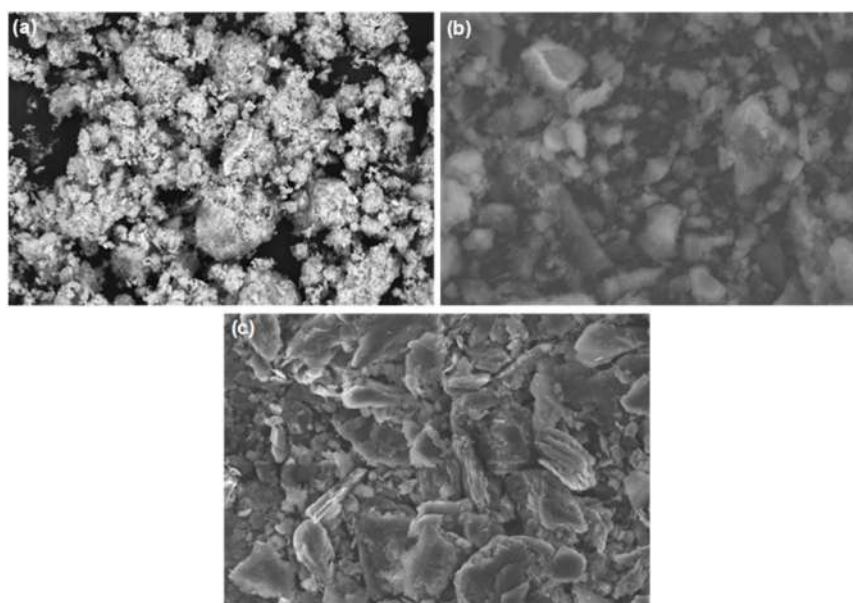


Fig 5. SEM images of Ni/Al LDH (a), Ni/Al-B (b), and Ni/Al-G (c)

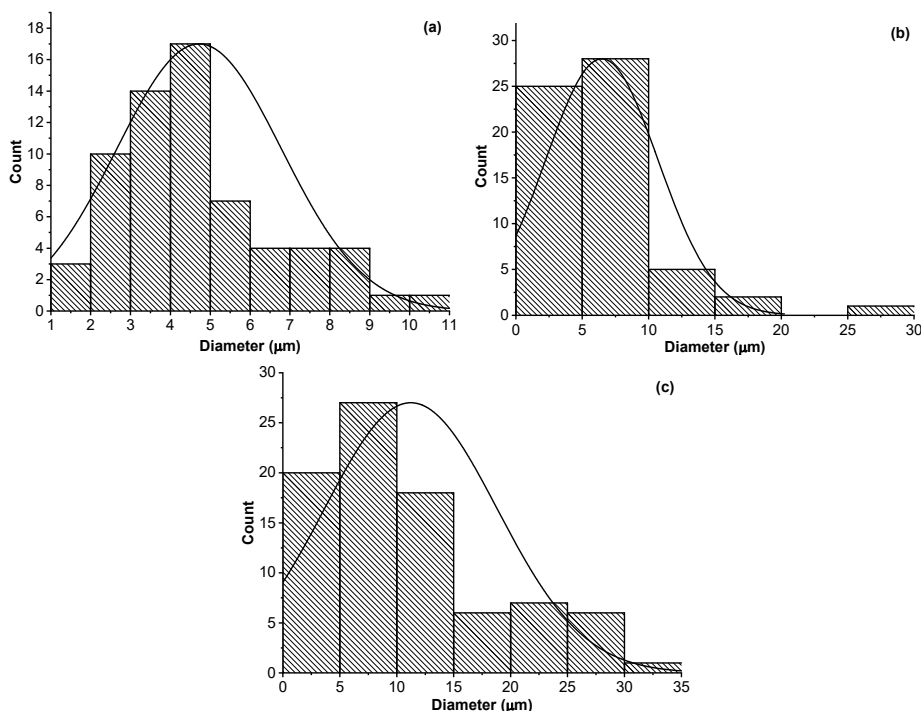


Fig 6. The particle size of Ni/Al LDH (a), Ni/Al-B (b), and Ni/Al-G (c)

endothermic peak and one exothermic peak. The endothermic peak at 95 °C was attributed to the loss of water on surface B. The exothermic peak at 490 °C was identified as the oxidation of an organic compound on B. The G material had one endothermic peak at 795 °C due to the decomposition of the G layer [27]. Composites Ni/Al-B and Ni/Al-G had both endothermic and exothermic peaks, which was related to the decomposition of inorganic substances and oxidation of organic molecules on the composite, as shown in Fig. 4(d) and 4(e).

The SEM images and particle size of Ni/Al LDH, Ni/Al-B, and Ni/Al-G are shown in Fig. 5 and 6. Based on Fig. 5, it is indicated that the morphology of Ni/Al LDH, Ni/Al-B, and Ni/Al-G materials form aggregates and tends to be heterogeneous. From the data of particle sizes in Fig. 6, it can be seen that the mean particle size of Ni/Al LDH, Ni/Al-B, and Ni/Al-G are 4.787, 6.568, and 11.328 μm, respectively.

To evaluate the ability of a composite as an adsorbent with high stability structure toward the adsorption of Fe(II), the regeneration and re-adsorption of the adsorbent was performed until five cycles as shown in Fig. 7. FTIR analysis was carried out on the adsorbent

after the re-adsorption process (Fig. 8) which showed no change in the material structure characterized by insignificant wavenumber shifts and vibrations that appeared the same as the initial material.

The composite of Ni/Al-B had a higher adsorption capacity than Ni/Al-G. As mentioned in the previous results, the surface area of Ni/Al-B was higher than Ni/Al-G and Ni/Al LDH, thus giving the highest adsorption

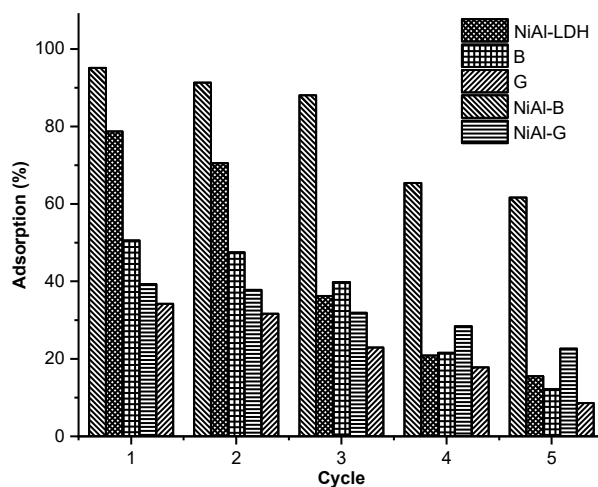


Fig 7. Reusability of adsorbent until five cycles re-adsorption process

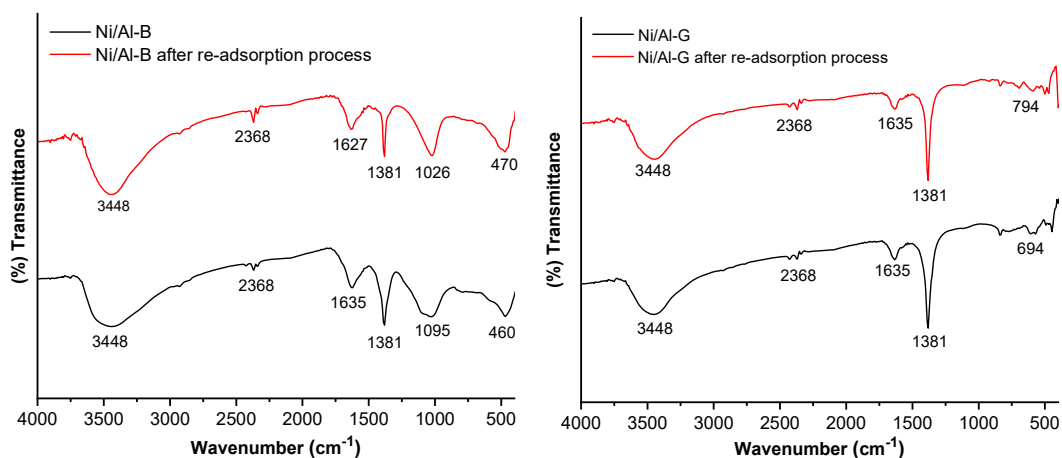
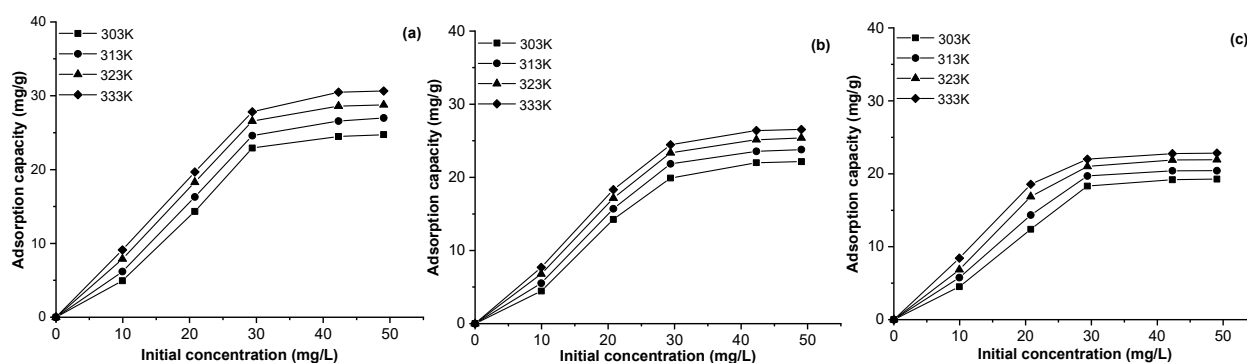


Fig 8. FTIR spectrum of Ni/Al-B and Ni/Al-G after the re-adsorption process

capacity toward Fe(II). Adsorption of Fe(II) on B was higher than on G. The reusability of the Ni/Al-B adsorbent until five re-adsorption processes gave a relatively stable structure toward Fe(II) adsorption compared to the other adsorbents. The Fe(II) adsorption on Ni/Al-B at five re-adsorption processes reached more than 70%. These phenomena showed that the active site of Ni/Al-B was relatively retained, although it had adsorption-desorption cycles [27-28]. The composite of Ni/Al-G also showed similar phenomena to Ni/Al-B. Although the adsorption capacity of Fe(II) in Ni/Al-G is low, the re-adsorption process resulted in almost the same adsorption capacity, in the range of 39–32%, up to five cycles. The pristine material of Ni/Al LDH had decreasing adsorption capacity at the third re-adsorption cycle due to the exfoliation of the LDH structure. The adsorption capacity of B and G was also decreased sharply due to unstable organic materials toward the desorption process. Thus, the formation of composite by carbon-based materials can increase the structural stability of Ni/Al LDH.

Adsorption of Fe(II) on the aqueous solution by pristine materials and composites is shown in Fig. 9. Adsorption of Fe(II) gradually increased by increasing the Fe(II) initial concentration and reached equilibrium at almost 40 mg/L for all adsorbents. Adsorption of Fe(II) was increased with increasing adsorption temperature from 303 K to 333 K. The data in Fig. 9 was then calculated using Langmuir and Freundlich isotherm models to obtain the adsorption isotherm model of Fe(II). Furthermore, the adsorption thermodynamic was obtained by the calculation of ΔH , ΔG , and ΔS . The isotherm data and adsorption thermodynamics are presented in Tables 2 and 3.

Adsorption isotherm Langmuir and Freundlich models were applied to obtain adsorption isotherm of Fe(II) on composites and starting materials. The isotherm for each adsorbent followed different types of models. Starting materials of G, B, and Ni/Al LDH almost follows the Langmuir model more than the Freundlich model. Layered materials such as Ni/AL LDH



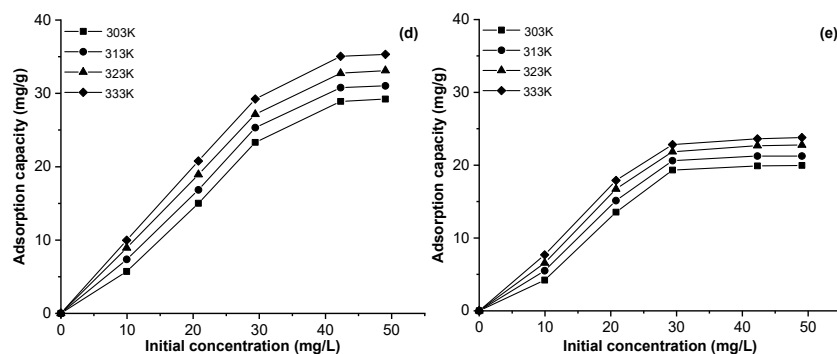


Fig 9. Effect of Fe(II) adsorption by variation of Fe(II) initial concentration and temperature on Ni/Al LDH (a), B (b), G (c), Ni/Al-B (d), and Ni/Al-G (e)

Table 2. Isotherm model for Fe(II) adsorption on LDH, B, G, and composites

Adsorbent	Adsorption isotherm	Adsorption constant	T (K)			
			303	313	323	333
G	Langmuir	Q_{\max}	22.936	20.523	22.936	23.310
		k_L	0.199	0.387	0.906	1.977
		R^2	0.9678	0.9913	0.9993	0.999
	Freundlich	n	0.498	27.855	25.575	32.468
		k_F	6.411	18.180	19.355	20.711
		R^2	0.9849	0.9538	0.9616	0.9809
B	Langmuir	Q_{\max}	25.974	26.455	27.248	31.250
		k_L	0.241	0.393	0.633	0.295
		R^2	0.9869	0.993	0.9974	0.9436
	Freundlich	n	0.148	1.2	1.647	2.398
		k_F	2.718	4.061	7.852	12.578
		R^2	0.999	0.999	0.999	0.999
Ni/Al LDH	Langmuir	Q_{\max}	29.412	27.701	30.395	31.447
		k_L	0.999	1.597	0.997	2.356
		R^2	0.9486	0.999	0.9964	0.9995
	Freundlich	n	16.949	0.174	0.225	24.272
		k_F	20.554	3.284	2.116	2.734
		R^2	0.9906	0.9993	0.9934	0.9845
Ni/Al-G	Langmuir	Q_{\max}	42.373	31.056	28.653	26.954
		k_L	0.138	0.366	0.650	1.111
		R^2	0.9618	0.9997	0.9983	0.970
	Freundlich	n	31.250	35.587	28.902	31.746
		k_F	17.968	19.422	20.384	21.513
		R^2	0.9762	0.9465	0.9834	0.9959
Ni/Al-B	Langmuir	Q_{\max}	104.167	48.309	42.017	42.017
		k_L	0.137	0.593	1.478	1.831
		R^2	0.997	0.725	0.932	0.999
	Freundlich	n	0.275	0.413	0.723	2.257
		k_F	1.422	1.382	1.239	1.035
		R^2	0.9663	0.9276	0.9907	0.9905

Table 3. Adsorption thermodynamic of Fe(II) on LDH, B, G, and composites

Adsorbents	T (K)	Q _e (mg/g)	ΔH (kJ/mol)	ΔS (kJ/mol)	ΔG (kJ/mol)
G	303	19.268	9.056	0.035	-1.408
	313	20.428			-1.753
	323	21.929			-2.099
	333	22.849			-2.444
B	303	22.149	1.022	0.032	-8.666
	313	23.79			-8.985
	323	25.39			-9.305
	333	26.551			-9.625
Ni/Al LDH	303	24.730	13.562	0.045	-0.052
	313	26.991			-0.501
	323	28.772			-0.950
	333	30.643			-1.400
Ni/Al-G	303	19.968	9.449	0.036	-1.561
	313	21.248			-1.924
	323	22.769			-2.288
	333	23.790			-2.651
Ni/Al-B	303	29.218	13.943	0.049	-0.958
	313	31.027			-1.450
	323	33.108			-1.942
	333	35.317			-2.433

Table 4. Comparison of Fe(II) adsorption capacity on several adsorbents

Adsorbent	Adsorbate	Adsorption capacity (mg/g)	Reference
Co/Mo LDH		10	[31]
Ca/Al LDH		11.16	[32]
Zn/Cr-POM		76.923	[19]
Banana peel		33.79	[33]
Intercalated Ca/Al LDH		11.93	[32]
Bentonite		7.09	[34]
Chitosan		64.10	[35]
Sawdust		6.54	[36]
Rice husk ask		6.211	[37]
Pomegranate peel carbon	Fe(II)	18.52	[38]
Zn/Cr LDH		50	[19]
Intercalated Co/Mo LDH with carbonate		77.9	[39]
Ni/Al LDH intercalated with keggion ion		36.496	[22]
Rice husk ask			
Ni/Al LDH		31.447	This Work
B		31.250	This Work
G		23.310	This Work
Ni/Al-B		104.167	This Work
Ni/Al-G		42.373	This Work

and G follow the Langmuir isotherm model, while B follows the Freundlich model. On the other hand, Ni/Al-G and Ni/Al-B follow Freundlich and Langmuir isotherm models, where the R-value was close to one [29]. Adsorption temperature gave an effect on the isotherm of Fe(II) on composites such as Ni/Al-G at low temperatures following the Langmuir isotherm model, but Ni/Al-B follows the Freundlich isotherm model. The adsorption thermodynamic of Fe(II) on composites and starting materials shows negative ΔG for all temperature adsorption due to the spontaneity of the adsorption process. The negative value of ΔG increased by increasing the temperature. The opposite result was found for ΔS , which had a positive value due to growing randomness of the adsorption process between adsorbent and adsorbate.

The value of ΔH was also positive. The value of ΔH for G, B, and Ni/Al LDH was 9.056–43.540, 1.022–40.655, and 13.562–54.939 kJ/mol, respectively. On the other hand, the value of ΔH for composites was higher than the starting materials namely in the range of 9.449–75.800 kJ/mol. All value of ΔH was less than 100 kJ/mol, and that was categorized as physical adsorption [30]. Although the involvement of chemical interaction occurred in the adsorption, their contribution was low. Thus adsorption of Fe(II) on the starting materials and composite was classified as physical adsorption.

Table 4 shows that various adsorbents had been tested to remove Fe(II) from an aqueous solution ranging from organic to inorganic adsorbents. The composite of Ni/Al-B in this research shows the highest adsorption capacity among the other adsorbents. On the other hand, Ni/Al-G had a middle adsorption capacity, only up to 42.373 mg/g and slightly higher than the starting materials. Thus Ni/Al-B was a potential composite for the removal of Fe(II) from an aqueous solution.

■ CONCLUSION

Composites Ni/Al-G and Ni/Al-B were successfully prepared and had different adsorption properties toward Fe(II) on the aqueous solution. The surface area of Ni/Al-B (438.942 m²/g) was largely higher than Ni/Al-G (21.595 m²/g). Adsorption of Fe(II) on the composite was higher than on the starting material. The adsorption

capacity of Ni/Al-G and Ni/Al-B was up to 42.373 and 104.167 mg/g, respectively. The adsorption energy was less than 100 kJ/mol for both starting materials, and composites indicated that the adsorption of Fe(II) on G, B, Ni/Al LDH, Ni/Al-G, and Ni/Al-B was physical adsorption. Ni/Al-B can be reused up to five cycles of re-adsorption and shows the structural stability toward the adsorption of Fe(II).

■ ACKNOWLEDGMENTS

The authors thank the Research Center of Inorganic Materials and Coordination Complexes FMIPA Universitas Sriwijaya for instrumental and lab analysis.

■ REFERENCES

- [1] Zubair, M., Daud, M., McKay, G., Shehzad, F., and Al-Harhi, M.A., 2017, Recent progress in layered double hydroxides (LDH)-containing hybrids as adsorbents for water remediation, *Appl. Clay Sci.*, 143, 279–292.
- [2] Esan, O.S., Kolawole, A.O., and Olumuyiwa, A.C., 2019, The removal of single and binary basic dyes from synthetic wastewater using bentonite clay adsorbent, *Am. J. Polym. Sci. Technol.*, 5 (1), 16–28.
- [3] Ouassif, H., Moujahid, E.M., Lahkale, R., Sadik, R., Bouragba, F.Z., Sabbar, E., and Diouri, M., 2020, Zinc-aluminum layered double hydroxide: High efficient removal by adsorption of tartrazine dye from aqueous solution. *Surf. Interfaces*, 18, 100401.
- [4] Jitianu, M., Gunness, D.C., Aboagye, D.E., Zaharescu, M., and Jitianu, A., 2013, Nanosized Ni–Al layered double hydroxides—Structural characterization, *Mater. Res. Bull.*, 48 (5), 1864–1873.
- [5] Cheng, S.Y., Show, P.L., Lau, B.F., Chang, J.S., and Ling, T.C., 2019, New prospects for modified algae in heavy metal adsorption, *Trends Biotechnol.*, 37 (11), 1255–1268.
- [6] Yagub, M.T., Sen, T.K., Afroze, S., and Ang, H.M., 2014, Dye and its removal from aqueous solution by adsorption: A review, *Adv. Colloid Interface Sci.*, 209, 172–184.

- [7] Boulaiche, W., Hamdi, B., and Trari, M., 2019, Removal of heavy metals by chitin: Equilibrium, kinetic and thermodynamic studies, *Appl. Water Sci.*, 9 (2), 39.
- [8] Okon, A.N., Udoh, F.D., and Bassey, P.G., 2014, Evaluation of Rice Husk as Fluid Loss Control Additive in Water-Based Drilling Mud, *SPE Nigeria Annual International Conference and Exhibition*, August 5–7, 2014, Lagos, Nigeria.
- [9] Patil, N.P., Bholay, A.D., Kapadnis, B.P., and Gaikwad, V.B., 2016, Biodegradation of model azo dye methyl red and other textile dyes by isolate *Bacillus circulans* NPP1, *J. Pure Appl. Microbiol.*, 10 (4), 2793–2800.
- [10] Vimonses, V., Lei, S., Jin, B., Chow, C.W.K., and Saint, C., 2009, Kinetic study and equilibrium isotherm analysis of Congo Red adsorption by clay materials, *Chem. Eng. J.*, 148 (2-3), 354–364.
- [11] Ravi, R., and Pandey, L.M., 2019, Enhanced adsorption capacity of designed bentonite and alginate beads for the effective removal of methylene blue, *Appl. Clay Sci.*, 169, 102–111.
- [12] Taher, T., Rohendi, D., Mohadi, R., and Lesbani, A., 2019, Congo red dye removal from aqueous solution by acid-activated bentonite from sarolangun: kinetic, equilibrium, and thermodynamic studies, *Arab J. Basic Appl. Sci.*, 26 (1), 125–136.
- [13] Palapa, N.R., Taher, T., Rahayu, B.R., Mohadi, R., Rachmat, A., and Lesbani, A., 2020, CuAl LDH/rice husk biochar composite for enhanced adsorptive removal of cationic dye from aqueous solution, *Bull. Chem. React. Eng. Catal.*, 15 (2), 525–537.
- [14] Chakraborty, C., Dana, K., and Malik, S., 2011, Intercalation of perylene diimide dye into LDH clays: Enhancement of photostability, *J. Phys. Chem. C*, 115 (5), 1996–2004.
- [15] Bessaies, H., Iftekhar, S., Doshi, B., Kheriji, J., Ncibi, M.C., Srivastava, V., Sillanpää, M., and Hamrouni, B., 2020, Synthesis of novel adsorbent by intercalation of biopolymer in LDH for the Removal of arsenic from synthetic and natural water, *J. Environ. Sci.*, 91, 246–261.
- [16] Rahmadan, J., Parhusip, V., Palapa, N.R., Taher, T., Mohadi, R., and Lesbani, A., 2021, ZnAl-humic acid composite as adsorbent of cadmium(II) from aqueous solution, *Sci. Technol. Indones.*, 6 (4), 247–255.
- [17] Starukh, H., and Levytska, S., 2019, The simultaneous anionic and cationic dyes removal with Zn–Al layered double hydroxides, *Appl. Clay Sci.*, 180, 105183.
- [18] Palapa, N.R., Juleanti, N., Normah, N., Taher, T., and Lesbani, A., 2020, Unique adsorption properties of malachite green on interlayer space of Cu-Al and Cu-Al-SiW₁₂O₄₀ layered double hydroxides, *Bull. Chem. React. Eng. Catal.*, 15 (3), 653–661.
- [19] Siregar, P.M.S.B.N., Wijaya, A., Amri, A., Nduru, J.P., Hidayati, N., Lesbani, A., and Mohadi, R., 2022, Layered double hydroxide/C (C=humic acid;hydrochar) as adsorbents of Cr(VI), *Sci. Technol. Indones.*, 7 (1), 41–48.
- [20] Choong, C.E., Wong, K.T., Jang, S.B., Saravanan, P., Park, C., Kim, S.H., Jeon, B.H., Choi, J., Yoon, Y., and Jang, M., 2021, Granular Mg-Fe layered double hydroxide prepared using dual polymers: Insights into synergistic removal of As(III) and As(V), *J. Hazard. Mater.*, 403, 123883.
- [21] Lv, X., Qin, X., Wang, K., Peng, Y., Wang, P., and Jiang, G., 2019, Nanoscale zero valent iron supported on MgAl-LDH-decorated reduced graphene oxide: Enhanced performance in Cr(VI) removal, mechanism and regeneration, *J. Hazard. Mater.*, 373 (6), 176–186.
- [22] Lesbani, A., Normah, N., Palapa, N.R., Taher, T., Andreas, R., and Mohadi, R., 2020, Removal of iron(II) using Ni/Al layered double hydroxide intercalated with Keggin ion, *Molekul*, 15 (3), 149–157.
- [23] Palapa, N.R., Juleanti, N., Mohadi, R., Taher, T., and Rachmat, A., 2020, Copper aluminum layered double hydroxide modified by biochar and its application as an adsorbent for procion red, *J. Water Environ. Technol.*, 18 (6), 359–371.

- [24] Zhu, X., Liu, Y., Qian, F., Zhou, C., Zhang, S., and Chen, J., 2014, Preparation of magnetic porous carbon from waste hydrochar by simultaneous activation and magnetization for tetracycline removal, *Bioresour. Technol.*, 154, 209–214.
- [25] Li, R., Wang, J.J., Zhou, B., Awasthi, M.K., Ali, A., Zhang, Z., Gaston, L.A., Lahori, A.H., and Mahar, A., 2016, Enhancing phosphate adsorption by Mg/Al layered double hydroxide functionalized biochar with different Mg/Al ratios, *Sci. Total Environ.*, 559, 121–129.
- [26] Modwi, A., Abbo, M.A., Hassan, E.A., Al-Duaij, O.K., and Houas, A., 2017, Adsorption kinetics and photocatalytic degradation of malachite green (MG) via Cu/ZnO nanocomposites, *J. Environ. Chem. Eng.*, 5 (6), 5954–5960.
- [27] Luo, X., Wang, C., Wang, L., Deng, F., Luo, S., Tu, X., and Au, C., 2013, Nanocomposites of graphene oxide-hydrated zirconium oxide for simultaneous removal of As(III) and As(V) from water, *Chem. Eng. J.*, 220, 98–106.
- [28] Ribas, M.C., de Franco, M.A.E., Adebayo, M.A., Lima, E.C., Parkes, G.M.B., and Feris, L.A., 2020, Adsorption of Procion Red MX-5B dye from aqueous solution using homemade peach and commercial activated carbons, *Appl. Water Sci.*, 10 (6), 154.
- [29] Hu, F., Wang, M., Peng, X., Qiu, F., Zhang, T., Dai, H., Liu, Z., and Cao, Z., 2018, High-efficient adsorption of phosphates from water by hierarchical CuAl/biomass carbon fiber layered double hydroxide, *Colloids Surf., A*, 555, 314–323.
- [30] Sharifpour, E., Alipanahpour Dil, E., Asfaram, A., Ghaedi, M., and Goudarzi, A., 2019, Optimizing adsorptive removal of malachite green and methyl orange dyes from simulated wastewater by Mn-doped CuO-nanoparticles loaded on activated carbon using CCD-RSM: Mechanism, regeneration, isotherm, kinetic, and thermodynamic studies, *Appl. Organomet. Chem.*, 33 (3), e4768.
- [31] Mostafa, M.S., Bakr, A.A., Eshaq, G., and Kamel, M.M., 2015, Novel Co/Mo layered double hydroxide: Synthesis and uptake of Fe(II) from aqueous solutions (Part 1), *Desalin. Water Treat.*, 56 (1), 239–247.
- [32] Taher, T., Christina, M.M., Said, M., Hidayati, N., Ferlinahayati, F., and Lesbani, A., 2019, Removal of iron(II) using intercalated Ca/Al layered double hydroxides with $[\alpha\text{-SiW}_{12}\text{O}_{40}]^{4-}$, *Bull. Chem. React. Eng. Catal.*, 14 (2), 260–267.
- [33] Shrestha, S.L., 2018, Study of the adsorption kinetics of iron ion from wastewater using banana peel, *Int. J. Adv. Res. Chem. Sci.*, 5 (3), 1–8.
- [34] Ain, Q.U., Zhang, H., Yaseen, M., Rasheed, U., Liu, K., Subhan, S., and Tong, Z., 2020, Facile fabrication of hydroxyapatite-magnetite-bentonite composite for efficient adsorption of Pb(II), Cd(II), and crystal violet from aqueous solution, *J. Cleaner Prod.*, 247, 119088.
- [35] Wan Ngah, W.S., Ab Ghani, S., and Kamari, A., 2005, Adsorption behaviour of Fe(II) and Fe(III) ions in aqueous solution on chitosan and cross-linked chitosan beads, *Bioresour. Technol.*, 96 (4), 443–450.
- [36] El-Sherif, I.Y., Fathy, N.A., and Hanna, A.A., 2013, Removal of Mn(II) and Fe(II) ions from aqueous solution using precipitation and adsorption methods, *J. Appl. Sci. Res.*, 9 (1), 233–239.
- [37] Zhang, Y., Zhao, J., Jiang, Z., Shan, D., and Lu, Y., 2014, Biosorption of Fe(II) and Mn(II) ions from aqueous solution by rice husk ash, *Biomed Res. Int.*, 2014, 973095.
- [38] Moghadam, M.R., Nasirizadeh, N., Dashti, Z., and Babanezhad, E., 2013, Removal of Fe(II) from aqueous solution using pomegranate peel carbon: Equilibrium and kinetic studies, *Int. J. Ind. Chem.*, 4 (1), 19.
- [39] Bakr, A.A., Mostafa, M.S., Eshaq, G., and Kamel, M.M., 2015, Kinetics of uptake of Fe(II) from aqueous solutions by Co/Mo layered double hydroxide (Part 2), *Desalin. Water Treat.*, 56 (1), 248–255.

Characterization of Poly(vinylidene Fluoride) Nanofiber-Based Electrolyte and Its Application to Dye-Sensitized Solar Cell with Natural Dyes

Nita Kusumawati^{1*}, Pirim Setiarso¹, Agus Budi Santoso², Supari Muslim², Qurrota A'yun¹, and Marinda Mayliansarisyah Putri¹

¹Department of Chemistry, Faculty of Mathematics and Natural Sciences, Universitas Negeri Surabaya, Jl. Ketintang, Surabaya 60231, Indonesia

²Department of Electrical Engineering, Faculty of Engineering, Universitas Negeri Surabaya, Jl. Ketintang, Surabaya 60231, Indonesia

* **Corresponding author:**

email: nitakusumawati@unesa.ac.id

Received: June 12, 2022

Accepted: October 17, 2022

DOI: 10.22146/ijc.75357

Abstract: The potential of dye-sensitized solar cells (DSSC) as an alternative to depleting fossil fuels has been investigated. To optimize performance and efficiency, the effectiveness of PVDF and PVDF nanofiber (NF) membrane-based electrolytes in suppressing solvent leakage and evaporation in liquid electrolyte systems was evaluated. SEM results for PVDF NF membranes showed the formation of a network with a three-dimensional structure with a diameter of 100–300 nm and an average thickness of 0.14 μm . The Infrared (IR) spectrum shows the electrolyte and polymer-PVDF interactions. Differential Scanning Calorimetry (DSC) curve shows the melting transition of PVDF NF 7.66% lower than PVDF. Efficiency and resistance of DSSC based on natural dyes as measured by multimeter and Electrochemical Impedance Spectroscopy (EIS) at a solar intensity of 100 mW/cm^2 showed the highest efficiency of anthocyanin-based DSSC from telang (*Clitoria ternatea L.*) flower extract. Its use as a photosensitizer in an electrolyte system based on PVDF NF membranes resulted in an efficiency that was not significantly different from that of liquid electrolytes (1.69%).

Keywords: DSSC; natural dye; electrolyte; PVDF; PVDF NF

■ INTRODUCTION

Energy, especially electrical energy, is one of the main drivers of a country [1-2]. Despite being one of the main needs of the community, the availability of electrical energy still depends on petroleum, natural gas, and various sources of fossil fuels which are getting depleted [3]. As an alternative, the use of solar cell technology is very promising [4]. The sensitization capability of wide band gap semiconductors by photosensitizer enables solar cell technology to convert solar energy into electrical energy [5]. High energy conversion efficiency and low electricity production costs compared to silicon solar cells make DSSC attracts a lot of research interest [6]. DSSC consists of two conductive glasses with three important components: a wide band gap semiconductor porous film with a dye molecule as a photosensitizer, a platinum (Pt)

counter electrode, and a redox electrolyte [7-9]. In the DSSC system, photo-excitation of the dye produces electrons which are then injected into the titanium dioxide (TiO_2) semiconductor conduction band, while the redox reaction occurring at the interface of electrons is transferred to the counter electrode by an external circuit will result in regeneration of the oxidized photosensitizer dye [1].

The dye is one of the determining factors for the performance of DSSC, where its efficiency is influenced by the absorption spectrum and the loss of dye on the TiO_2 surface. Excellent conversion efficiency, chemical stability, and intense charge transfer absorption across the ultraviolet-visible (UV-Vis) light spectrum make ruthenium polypyrrrole complexes one of the most effective photosensitizers. However, the metal content, which is not only relatively expensive but also harmful

to the environment, is the main weakness of this photosensitizer. Natural organic dyes from various plant species, such as chlorophyll, have been widely developed as an inexpensive alternative to ruthenium [5]. Chlorophyll from spinach leaves and *Sambucus ebulus* was reported to produce an electrical efficiency value of 1.15% in the DSSC system [10]. The presence of many chromophores in their molecular structure makes anthocyanins, betaxanthin, and braziline potential natural photosensitizer candidates for further development. Therefore, in this study, standardization of the use of anthocyanins from *telang* flower extract, betaxanthin from turmeric extract, and braziline from sappan wood bark extract as a natural photosensitizer for DSSC.

On the other hand, an electrolyte is one of the determining factors for DSSC stability. In DSSCs with liquid electrolytes, stability limits their wide commercialization [11-12]. Although it provides higher efficiency than gel and solid electrolytes, problems such as leakage, evaporation of volatile solutions, and iodine sublimation make liquid electrolytes have short-term stability [13]. To improve the DSSC stability, several studies were carried out for the polymer electrolytes development. High ionic conductivity, solvent-free, and flexibility are the advantages of this electrolyte. With a network capable of producing an ionic conductivity nearly as high as that of a liquid electrolyte and a solid structure with high mechanical resistance, the utilization of this electrolyte has the potential to reduce evaporation and leakage, thus, providing physical stability to the DSSC [14].

Poly(vinylidene fluoride) (PVDF) is a polymer with high electrochemical resistance and mechanical strength compared to other polymers, such as poly(vinyl chloride), polyacrylonitrile, and poly(methyl methacrylate). Sahito et al. reported the use of PVDF membrane-based electrolytes that is promising in the future because even though they have a 1.9% decrease in efficiency compared to liquid electrolytes, they have much better stability [15]. However, its hydrophobic nature reduces the I^-/I_3^- ionic mobility in the PVDF. To increase mobility, the use of PVDF NF membrane made by the electrospinning

method is an ideal choice [16]. Increasing the mobility of ions in the membrane can increase the stability and electrical efficiency of the DDSC circuit. The dominance of amorphous structures in PVDF NF membranes has the potential to produce higher ionic conductivity than in PVDF membranes. By combining the use of PVDF and PVDF NF membrane-based electrolytes as an effective electrolyte trap and the use of anthocyanins, betaxanthin, and braziline as natural photosensitizers, the DSSC system is not only expected to be able to minimize leakage and produce better performance and efficiency but also be more eco-friendly than the previous DSSC system.

■ EXPERIMENTAL SECTION

Materials

Several materials with specifications that were used in this study were ethylene carbonate (EC) anhydrous (99%) and propylene carbonate (PC) anhydrous (99.7%), both obtained from Sigma Aldrich (USA); Iodine (I_2) ($\geq 99.8\%$), nitric acid (HNO_3) ($\geq 99.9\%$), Poly(vinylidene fluoride) powder ($M_w \sim 534,000$), acetone ($\geq 99.5\%$) from Sigma Aldrich (Singapore); potassium iodide (KI) ($\geq 99\%$) and *N,N*-Dimethylacetamide (DMAc) ($\geq 99\%$) from Merck (Belgium); Titanium dioxide (TiO_2) nanopowder (21 nm; 99.5%) from Sigma Aldrich (China); polyethylene glycol (PEG-1000) (M_w 1000) from Merck (Germany); Tween-80 from PT. Brataco Chemika (Indonesia); and Fluorine-doped Tin Oxide (FTO) glass (resistivity 10Ω) were obtained from Changchun Yutai Optics Co., Ltd. (China).

Instrumentation

The instruments included a rotary evaporator (Buchi R-300), magnetic stirrer (NESCO LAB MS-H280-Pro), UV-Vis spectrophotometer (Shimadzu UV-1800), Fourier Transform Infrared (FTIR) spectrophotometer (Perkin Elmer Spectrum Two), Scanning Electron Microscope (SEM) (Zeiss EVO MA-10), Differential Scanning Calorimetry (DSC) (Linseis STA PT-1000), Voltammetry (797 VA Computrace Metrohm), Multimeter (Krisbow KW08-267).

Procedure

Natural photosensitizer

Natural photosensitizer was prepared by the maceration method. Natural dye material is immersed in a solvent in a ratio of 1:6. The maceration results were evaporated using a Buchi R-300 rotary evaporator. The natural dye concentrate is then stored at a temperature of 20–25 °C and ready to be used as a natural photosensitizer for DSSC.

Electrolyte solution

A total of 9.2 mg I₂; 0.06 g KI; 0.4 g EC; and 0.4 g PC; were mixed and stirred using NESCO LAB MS-H280-Pro magnetic stirrer (100 rpm; 30 min) to prepare an electrolyte solution.

Electrolyte polymer

PVDF membranes are made by a phase separation method followed by a casting knife and electrospinning casting techniques. As much as 18% (w/v) of PVDF has dissolved in DMAc and acetone (3:2) mixture by stirring for 12 h (65 °C; 270 rpm). The solution was cast on a glass plate with a thickness of 0.4 mm at 30 °C for 5 min pre-immersion, then immersed in 1000 mL aquadest for 30 min. The solid PVDF membrane was washed and dried for 24 h. Specifically, the electrospinning casting method was run at a voltage of 15 kV, the injector and drum collector distance of 15 cm, and a flow rate of 1 mL/h for 5 h.

Making of TiO₂ paste

A mixture of 0.2 g TiO₂, 0.4 mL 0.1 M HNO₃, 0.08 g

PEG-1000, and 0.05 mL Tween-80 were stirred at 100 rpm for 30 min to produce a TiO₂ paste.

Fabrication of DSSC

The DSSC consists of two glasses: an FTO anode and an FTO cathode. The FTO anode glass has an active surface area of 3 cm². The TiO₂ paste was coated on the glass by the doctor blade method, then sintered for 1 h at 450 °C. The TiO₂ photoanode was cooled and then immersed in 10 mL of natural dye for 24 h. PVDF and PVDF NF membranes immersed in 1 mL of electrolyte for 1 h were coated on a carbon-coated cathode FTO glass. Thus, the FTO/TiO₂/PVDF/Pt/FTO system is formed (see Fig. 1).

Characterization

The absorption spectrum of the natural UV photosensitizer was analyzed using Shimadzu UV-1800 UV-Vis Spectrophotometry. The infrared spectra of liquid electrolytes and PVDF and PVDF-NF membrane-based electrolytes were analyzed using Perkin Elmer Spectrum Two FTIR spectrometer with Attenuated Total Reflection (ATR) mode at 30 °C. Meanwhile, membrane morphology was analyzed by Zeiss EVO MA-10 Scanning Electron Microscopy. The electrolyte thermal stability was evaluated using Linseis STA PT-1000 Differential Scanning Calorimetry (DSC) at 70–170 °C with a 10 °C/min heating rate [1]. Band gap natural photosensitizers were analyzed based on the reduction and oxidation currents using 797 VA Computrace Metrohm Voltammetry. The sample solution was a mixture of 20 mL of a natural photosensitizer with 5 mL

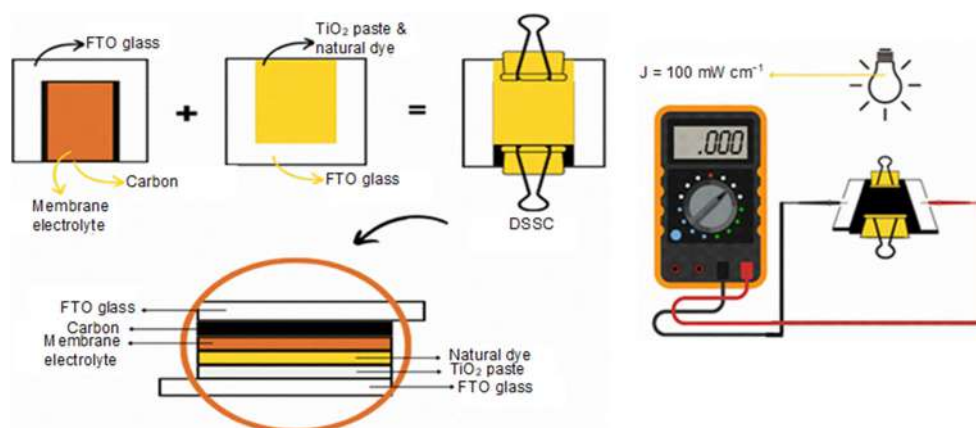


Fig 1. Schematic illustration of the DSSC fabrication

of potassium chloride (KCl) 0.3%. The efficiency of the DSSC circuit was analyzed based on the current and voltage obtained from measurements using a Krisbow KW08-267 Multimeter at 200 k Ω resistance and 200 mV voltage, while to get the effect of ionic conductivity on the J_{sc} value, an electron transport analysis was carried out, especially the interface resistance in the electrochemical system of the DSSC circuit using Gamry Reference 3000 Electrochemical Impedance Spectroscopy (EIS).

■ RESULTS AND DISCUSSION

Making Electrolyte Polymer

PVDF membranes are known for their good thermal and chemical stability. The low mass transfer resistance presented by its asymmetrical structure minimizes the fouling potential [17-19]. A phase inversion method is a promising option in this structure preparation due to its simple process and flexible production scale [20]. The selection of the right solvent is an absolute requirement to prevent particle aggregation in this preparation method. The minimum difference in solubility parameters indicates a high degree of compatibility with the solvent [21]. The solubility parameter values of PVDF, DMAc, and acetone are shown in Table 1.

The phase inversion step is induced using a non-solvent, namely water [22]. The high difference in the solubility parameters of PVDF-water (15.88 MPa^{1/2}), DMAc-water (25.23 MPa^{1/2}), and acetone-water (28.3 MPa^{1/2}) has caused PVDF-DMAc and PVDF-acetone systems thermodynamic equilibrium disturbances thus triggering phase separation. Diffusion of non-solvent in the casting solution produces a solid PVDF membrane [23].

Despite having various advantages, PVDF membranes are known to have crystallinity that has the potential to inhibit the movement of ions, resulting in low

efficiency. Therefore, in this study, the effectiveness and efficiency of using electrolytes based on PVDF membranes with lower crystallinity will also be evaluated. PVDF NF has secondary structures such as a cavity and a core-shell [24]. PVDF NF can be made by various methods, one of which is electrospinning, which can produce hollow fibers and porous polymers [25]. The formation of NF is influenced by several factors, namely polymer concentration, preparation conditions (temperature, time, and stirring speed), solvent, and aging time [26-27]. With the method used, NF with perfect fibers has been obtained without beads and fiber defects. The addition of acetone can accelerate solvent evaporation and reduce the concentration of the casting solution to prevent further bead formation and conglutination [28].

Natural Dye Absorption

Anthocyanins, betaxanthins, carotenoids, chlorophyll, and flavonoids are some of the pigments that have a high potential to be used as natural photosensitizers in DSSC [29]. Natural dyes are one of the main components supporting the DSSC performance, known as low-cost solar cell technology [30]. Natural dyes are also known for their eco-friendly properties. When applied as a natural photosensitizer, each natural dye has a different sensitivity [31].

The classification of endemic plants spread and easily found throughout Indonesia makes turmeric (*Curcuma longa*) one of the sources of natural photosensitizer providers for DSSC. Turmeric is a natural dye containing betaxanthin pigment, which produces a yellowish orange [32]. To optimize the betaxanthin extraction, the suitability degree of 3 solvents with different polarities was investigated, namely

Table 1. Hansen solubility parameter

No	Material	δ_d (MPa ^{1/2})	δ_p (MPa ^{1/2})	δ_h (MPa ^{1/2})	δ_t (MPa ^{1/2})
1	PVDF	16	14.3	23.9	32.12
2	DMAc	16.8	11.5	10.2	22.77
3	Acetone	13.0	9.8	11.0	19.7
4	Water	12.2	22.8	40.4	48.0

distilled water, methanol, and ethanol. The maceration results show a yellow appearance in distilled water and orange in methanol as well as in ethanol [33].

Turmeric extract with distilled water showed absorbance at 502.3 nm (0.523), while 484.3 nm (0.744) and 462.3 nm (0.735) were indicated by methanol and ethanol, respectively. A higher absorbance value at 484.3 nm indicates a higher level of pigment solubility in methanol than in distilled water and ethanol. These findings are in line with publications reporting the maximum absorption of turmeric at 480 nm [34].

Braziline is a pigment that produces a red color [35]. With the abundant presence of this bark, braziline is also very potential to be used as a natural photosensitizer in DSSC. In this study, the water extract of sappan wood showed a red color, while the methanol and ethanol extract both showed a brick red color. The UV-Vis absorption spectrum of the sappan wood bark extract showed absorption peaks at 532.0 nm (0.223) for distilled water, 449.3 nm (0.506) for methanol, and 447.3 nm (0.539) for ethanol. In contrast to turmeric, the highest absorbance of the sappan bark extract was shown by ethanol. The dominant non-polar functional group in the sappan bark resulted in a higher degree of solubility of the braziline pigment in ethanol.

Telang flower is known to have high anthocyanin content. Anthocyanins are natural colorants from the flavonoid group, which give red, purple, and blue colors to vegetables, fruits, and wheat grains, almost tasteless and odorless [36-37]. Maceration of *telang* flower with aquadest produces a purple color, while maceration with methanol and ethanol both produce a bluish-green color. This bluish-green color is predicted to appear due to the combination of anthocyanin and chlorophyll pigments. However, the higher intensity of the green color indicates the dominant chlorophyll pigment in the methanol and ethanol extracts. Identification of the UV absorption of the *telang* flower extract showed an absorbance value of 0.176 at 574.3 nm; 0.164 at 621.9 nm; and 0.146 at 663.2 nm. The highest UV absorption at a wavelength of 574.3 nm indicates the good solubility of anthocyanins from *telang* flowers in distilled water. The polar nature of anthocyanins

causes good solubility in aquadest, which has the highest level of polarity compared to methanol and ethanol [38].

Specifically, the spectrum of the *telang* flower dye extract in methanol showed the appearance of 2 absorbance peaks at 663.2 and 621.9 nm. This result is corroborated by the publication of Jeyaram and Geethakrishna, who reported the maximum absorption of anthocyanins at 629 nm. This spectral region belongs to the anthocyanin resonance wavelength range, 520–700 nm. The more π -conjugated the anthocyanin structure, the stronger the color and the higher the absorption wavelength [39].

Hardeli et al. reported that anthocyanins are dyes that have a lot of π -conjugated. The more conjugate bonds, the more electrons are excited when exposed to light. Thus, the natural photosensitizer from the *telang* flower extract has the potential to produce high-efficiency DSSCs [40]. Furthermore, Ndeze et al. reported the ability of the carbonyl and hydroxyl groups of anthocyanins to retain color on the surface of TiO₂ and facilitate HOMO to LUMO electron transfer of dyes which were then transferred to the TiO₂ conduction band [41].

Band-Gap Energy of Natural Dye

Natural dyes must have a narrower band gap energy than the semiconductor energy (TiO₂; 3.2 eV for anatase and 3.0 eV for rutile phase) to be a photosensitizer so that the efficiency of the resulting DSSC is high. In the DSSC, there is a charge separation process [42]. Thus, it is important to determine the band gap energy value of the dye. The determination of the dye band gap energy follows the equation:

$$E_{\text{HOMO}} = -(E_{\text{ox}} + 4.4) \quad (1)$$

$$E_{\text{LUMO}} = -(E_{\text{red}} + 4.4) \quad (2)$$

$$\Delta E = \text{LUMO} - \text{HOMO} \quad (3)$$

The results are shown in Table 2.

The dye with the narrowest band gap energy has electrons with higher excitation potential. Thus, light sensitivity is also increased [43]. Anthocyanin pigments become dyes with many conjugate bonds. The more conjugated chains, the longer the electron resonance that occurs from the donor structure to the acceptor,

Table 2. Dyes band gap energy

Dye	Volta		Bandgap
	HOMO	LUMO	
Ethanol-sappanwood	-4.274	-2.934	1.379
Methanol-turmeric	-4.298	-2.907	1.395
Aquadest-turmeric	-4.299	-2.905	1.395
Aquadest- <i>telang</i> flower	-4.895	-3.713	1.182
Methanol- <i>telang</i> flower	-5.396	-3.357	2.038

resulting in a narrower band gap energy. Thus, making anthocyanin pigments have the highest potential for improving DSSC performance [44]. Table 5 shows the energy values for the widest band gap produced by the *telang* flower extract in methanol (2.038 eV) and the narrowest obtained by the *telang* flower extract in distilled water (1.182 eV).

Scanning Electron Microscopy (SEM)

Fig. 2 shows the PVDF and PVDF NF (d 100–300 nm) polymer electrolyte surface morphology. In the manufacture of PVDF NF polymer by electrospinning method, parameters such as voltage, tip distance from a collector, and polymer concentration are parameters that build surface morphology and fiber diameter on nanofiber membranes. Significant differences between PVDF and PVDF NF polymer electrolytes are shown in Fig. 2(a) and 2(b). Differences were observed in the

formation of nanofiber fibers, larger pore size, higher porosity, and lower particle density of PVDF NF compared to PVDF. The SEM images also provide information on the formation of fine NF without beads at 18% by weight of the composition. This is in line with that published by Prasad et al. [45].

To obtain high mechanical strength and stability, the presence of cross-links in the nanofiber network is the most promising option because the increase in the density of the electrolyte-trapping polymer particles poses a significant obstacle to the electron flow rate in the DSSC system. Therefore, polymer electrolytes based on PVDF NF has better application potential in DSSC circuit systems than PVDF [1].

Photovoltaic Studies

As shown in Table 3, the performance of natural photosensitizer-based DSSC was determined by analysis

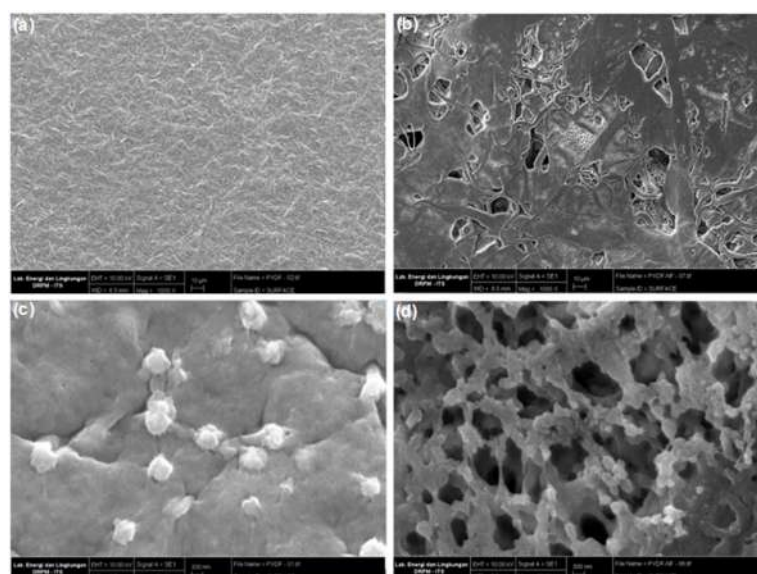


Fig 2. Electrolyte polymer surface morphology of the (a) PVDF 10,000×; (b) PVDF NF 10,000×; (c) PVDF 30,000×; (d) PVDF NF 30,000×

of open circuit voltage (V_{oc}), short circuit current density (J_{sc}), fill factor (FF), and efficiency (η) based on previously published equations [46]. Furthermore, the effect of using a combination of dyes and various electrolytes on the performance of natural photosensitizer-based DSSC can be seen from the photocurrent-voltage curve presented in Fig. 3.

The photovoltaic parameters showed a higher ionic conductivity of the liquid electrolyte than the electrolyte trapped in the polymer. The presence of a polymer electrolyte in the charge transport system causes a decrease in the Pt/electrolyte interface recombination reaction, thereby reducing the short-circuit current [47].

Among the five types of dye variations used, the order of efficiency is T-A > S-E > T-M > T_u-M > T_u-A.

Telang flower produced the highest efficiency, with 1.69% for liquid electrolyte, 1.6% for PVDF NF polymer electrolyte, and 1.23% for PVDF polymer electrolyte. The overall efficiency value is much higher compared to the DSSC system based on a braziline photosensitizer and liquid electrolyte with the highest efficiency of 0.034% published by Zulenda et al., a chlorophyll photosensitizer from pandan leaf extract and liquid electrolyte with an efficiency of 0.1% published by Al Alwani et al., a chlorophyll photosensitizer from spinach leaf extract and liquid electrolyte with an efficiency of 0.398% published by Kabir et al. [2,5-6]. High efficiency is generally determined by the pigment content and band gap value. Specifically, anthocyanin pigments contain chromophore and auxochrome ($-\text{COOH}$; $-\text{OH}$),

Table 3. Photovoltaic parameters of DSSC

No	Dye	J_{sc} (10^{-3} mA cm $^{-2}$)			V_{oc} (mV)			FF (10^{-2} %)			η (%)		
		L	NF	P	L	NF	P	L	NF	P	L	NF	P
1	T _u -A	3.5	2.3	1.4	344	340	321	40.5	27.6	23.5	1.21	0.79	0.45
2	T _u -M	3.3	3.2	2.2	401	393	354	46.9	36.6	29.5	1.32	1.28	0.77
3	T-A	3.6	3.4	2.9	475	463	424	25.3	23.8	21.3	1.69	1.6	1.23
4	T-M	3.3	3.1	2.8	416	389	383	42.5	38.2	32.8	1.36	1.21	1.06
5	S-E	3.6	3.2	2.8	434	416	363	19.4	17.1	13.4	1.56	1.35	1.03

Notes. T_u: turmeric; T: *telang* flower; S: sappanwood; A: aquadest; M: methanol; E: ethanol; L: liquid electrolyte; NF: PVDF NF electrolyte; P: PVDF electrolyte

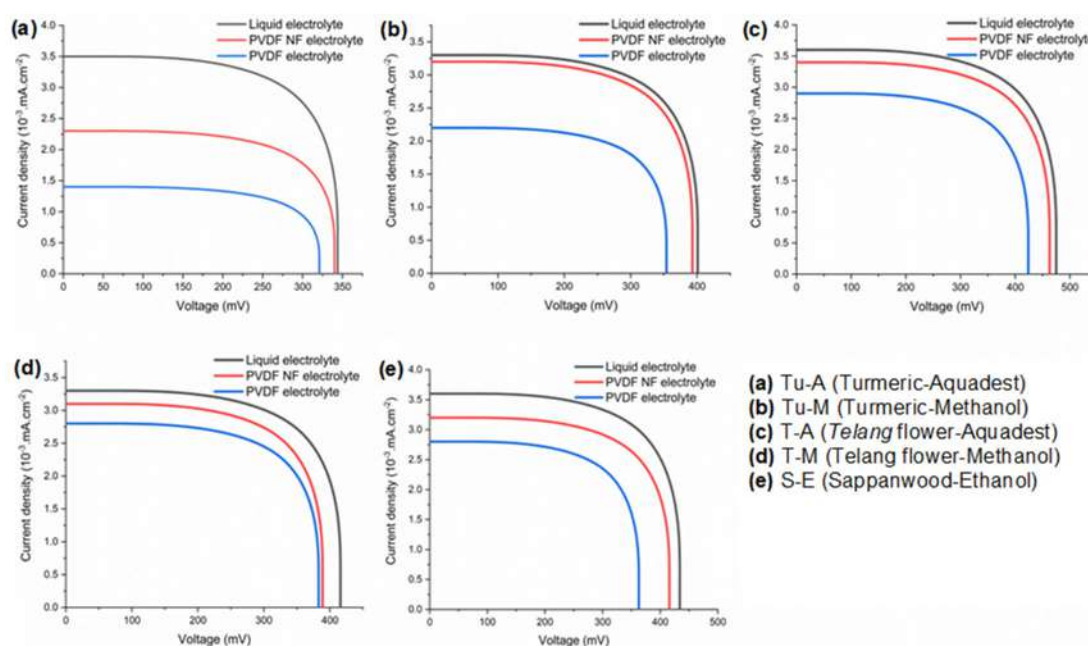


Fig 3. Photocurrent–voltage curve for DSSC sensitized by various extracts and electrolytes

which can absorb light in the energy range of UV visible light. Chromophores and auxochromes can attach to Ti(IV) sites on the TiO₂ surface, which supports electron transfer from anthocyanins to the TiO₂ conduction band [48]. In addition, the high number of conjugated chains in anthocyanins has triggered the electron resonance from the donor to acceptor to be longer, resulting in a narrow band gap value [1].

Electrochemical Impedance Spectroscopy

To get the effect of ionic conductivity on the J_{sc} value, an electron transport analysis was carried out by measuring the interface resistance in the electrochemical system of the DSSC circuit using EIS [49]. Injection of small amplitude in the form of voltage into the DSSC circuit is carried out to obtain voltage and current at a certain angle frequency in the form of a Nyquist plot [24-25].

EIS measurements resulted in the parameters R_s , R_{CT1} , and R_{CT2} of the FTO/TiO₂/dye/electrolyte/Pt/FTO configuration. R_s is the series resistance, R_{CT1} is the Pt/electrolyte interface charge transfer resistance, and R_{CT2} is the TiO₂/electrolyte interface charge transfer resistance [50].

$$Z_{DSSC} = R_s + \frac{R_{pT}}{1 + (j\omega)^{n_{PT}} R_{pT} CPE_{pT}} + \frac{R_{CT}}{1 + (j\omega)^{n_{CT}} R_{CT} CPE_{CT}} + R_D \sqrt{\frac{D_{Is} - J\delta^2}{j\omega}} \tanh \sqrt{\frac{j\omega}{D_{Is} - J\delta^2}} \quad (4)$$

where n_{PT} is the constant phase element (CPE) referring to the counter electrode/electrolyte, n_{CT} represents the photoanode/electrolyte interface, R_D is the Warburg diffusion resistance, and δ represents the effective diffusion length [51]. Table 4 shows the impedance measurement parameters of the DSSC circuit with

electrolyte variations.

The impedance parameter values in Table 4 show the values of R_s , R_{CT1} , and R_{CT2} following the order of liquid electrolyte < PVDF NF-based electrolyte < PVDF based electrolytes. The high polymer content tends to create a 2D network, increasing the resistance for recombination reactions at the Pt/electrolyte and TiO₂/electrolyte interfaces. The polymer density of PVDF and PVDF NF can also effectively suppress the increased adhesion of the electrolyte to the counter electrode [52].

Charge transport kinetics in all three DSSC electrolytes can be used to predict the TiO₂ electron life by referring to Eq. (5).

$$\tau_r = \frac{1}{\omega_{max}} = \frac{1}{2\pi f_{max}} \tau_r \quad (5)$$

where ω_{max} is the angular frequency and f_{max} is the peak frequency. It was found that DSSC with a liquid electrolyte had a short electron life, whereas a PVDF and PVDF NF membrane electrolyte had a longer electron life. The results show that the excited electrons in liquid electrolyte-based cells recombine with I_3^- in electrolytes faster than in PVDF and PVDF NF membrane-based cells [53]. Thus, the photoelectron's lifetime (T) on the photoelectrode follows the order of the liquid < PVDF NF < PVDF membrane-based electrolyte. This result is in contrast to the electron recombination rate of the photoelectrode/electrolyte interface, which follows the order of liquid > PVDF NF > PVDF membrane-based electrolyte.

FTIR

To study the interactions of ions/polymers/solvents and electrolytes, chemical bonds and structures were analyzed using Fourier Transform Infrared (FTIR) Spectroscopy [54]. The PVDF and PVDF NF membrane IR spectra were compared in Fig. 4.

Table 4. Impedance parameters of DSSC

Electrolyte	R_s/Ω	R_{CT1}/Ω	R_{CT2}/Ω	T/ms	$\eta/\%$
Liquid electrolyte	5.5	2.0	8.8	2.54	1.69
PVDF NF-based electrolyte	6.2	2.5	9.2	3.37	1.60
PVDF-based electrolyte	7.4	5.4	9.4	3.87	1.23

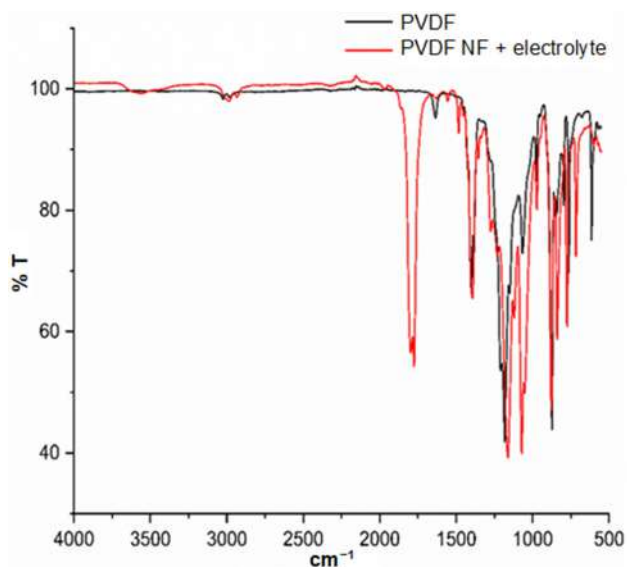


Fig 4. Infra-red spectra comparison of the PVDF and PVDF NF

PVDF is a semicrystalline thermoplastic polymer that has four crystalline phases, namely α , β , γ , and δ [55]. Bandara et al. publish the location of the α -phase and β -phase of pure PVDF [1]. Based on the publications of Saha et al., which report a typical peak of pure PVDF, the appearance of a peak of 841.15 cm^{-1} in the current work indicates CF_2 asymmetric stretching, while a peak at 873.09 cm^{-1} indicates the combined CF stretching, CF_2 stretching vibration, and CH_2 bending [56]. Peak appearance at 613.88 cm^{-1} indicates CF_2 bending and CCC skeletal vibrations in mixed mode. Respectively, the peak at 762.71 cm^{-1} indicates CH_2 rocking, while 795.97 cm^{-1} indicates CF_3 stretching vibration. The CF stretching at 975.61 and 1182.17 cm^{-1} also became the most significant peak marker for the PVDF crystal phase. Three peaks remain, namely at 1066.92 ; 1402.30 ; and 2984.09 cm^{-1} , showing CH bending, CH_2 wagging, and CH_2 asymmetric stretching, respectively. Several peaks indicating the amorphous phase of PVDF are also shown in Fig. 5.

By comparing the two, PVDF and PVDF NF, a slight shift in peak position was detected. For example, the appearance of a peak at 841.15 cm^{-1} , which is a marker of CF_2 asymmetric stretching in PVDF, shifted to 838.81 cm^{-1} in PVDF NF. Furthermore, a slight shift in the peak was also detected from 873.09 cm^{-1} to

875.84 cm^{-1} , which indicates a combination of CF stretching, CF_2 stretching vibration, and CH_2 bending in PVDF. The process of electrospinning on PVDF NF provides a lower level of crystalline as the cause of several shifts in peaks of the PVDF NF infra-red spectra.

Vibration bands of PVDF and PVDF NF amorphous phase were observed at certain wave numbers, although they did not seem clear. This condition is related to the interaction between the chains in the polymer. When mixed with the electrolyte, the polymers, in their interactions, are replaced by solvent-polymers. Because of that, the IR peaks associated with the amorphous phases of PVDF and PVDF NF appear insignificant for these electrolytes.

DSC Analysis

The large potential of DSSC utilization causes the analysis of the DSSC maximum operating temperature to be urgent to be carried out. Fig. 6 shows the DSC curves of EC, PC, PVDF membrane, PVDF, and PVDF NF membrane-based electrolyte at $60\text{--}170\text{ }^\circ\text{C}$. The results show the melting temperature of EC at $38.21\text{ }^\circ\text{C}$ and PC above $170\text{ }^\circ\text{C}$. The low melting temperature of EC is one of the causes of high solvent evaporation in the electrolyte system, which triggers the low shelf life of the liquid electrolyte-based DSSC system [57-58].

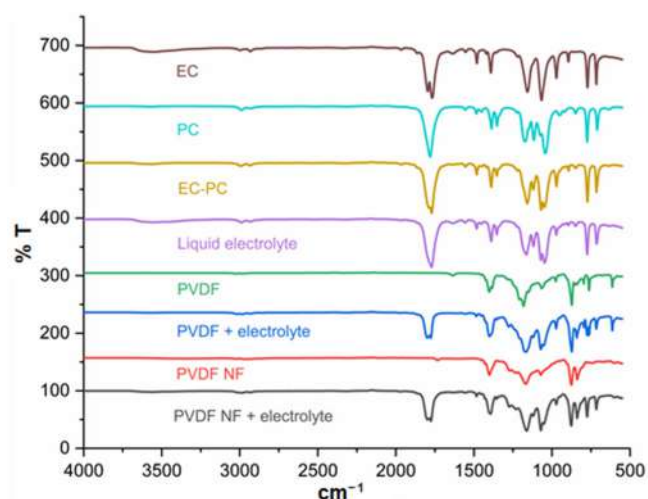
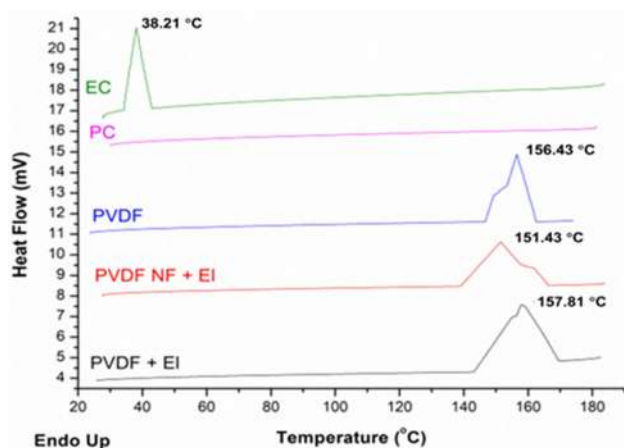


Fig 5. Infra-red spectra of PVDF and PVDF NF membrane, liquid electrolyte, PVDF and PVDF NF membrane-based electrolyte, EC-PC mixture, EC, PC ($400\text{--}4000\text{ cm}^{-1}$)

Table 5. Melting enthalpy of PVDF and PVDF NF membrane electrolytes

Electrolyte	Peak area (mJ)	Weight (mg)	ΔH_m (Jg^{-1})	Relative crystallinity (%)
PVDF	57.18	23.04	2.48	2.31
PVDF NF	38.76	16.89	2.29	2.19

**Fig 6.** DSC thermograms (25–180 °C) of the EC, PC, PVDF membrane, PVDF, and PVDF NF membrane-based electrolyte

To determine the DSSC shelf life, the thermal stability of the PVDF and PVDF NF membrane-based electrolytes was investigated. The effectiveness of both types of membranes in producing a higher DSSC shelf life can be seen in the presence of liquid electrolytes in both membranes, even at temperatures above 100 °C. By comparing the DSC curve of the PVDF membrane with the PVDF and PVDF NF membranes-based electrolytes, it is found that the presence of liquid electrolytes in the membranes at temperature 157.81 °C on the PVDF membrane electrolyte system and 151.43 °C on the PVDF NF membrane electrolyte.

The broad endothermic peak at 130–160 °C indicates the melting of the polymer components in the electrolyte. This is in line with that published by previous researchers [59]. Specifically, the melting peak of PVDF was observed at a temperature of 157.81 °C, while that of PVDF NF was at 151.43 °C. The effect of nano-size was predicted as the cause of the lower melting temperature of PVDF NF compared to PVDF. In general, neither electrolyte shows a significant thermal transition up to 100 °C. Thus, the PVDF and PVDF NF electrolytes have

thermal stability over the temperature range in which the solar cell operates.

Determination of relative crystallinity is done by calculating the melting enthalpy of PVDF and PVDF NF based on the peak area. The PVDF and PVDF NF melting enthalpies are 2.48 and 2.29 Jg^{-1} , respectively. This value shows a 5.19% decrease in PVDF NF crystallinity compared to PVDF. PVDF with 100% crystallinity can be assumed to have a melting enthalpy of 107.4 Jg^{-1} . Table 5 shows the relative crystallinity of each polymer electrolyte.

■ CONCLUSION

To make DSSC more environmentally friendly, in this work, the use of three natural pigment variants was evaluated, namely betaxanthin (484.3–502.3 nm), braziline (447.3 nm), and anthocyanin (574.3–621.9 nm). DSSCs with three types of electrolytes (liquid NF membrane-based electrolytes, PVDF, and PVDF NF) and natural photosensitizers were further characterized by measuring V_{OC} , J_{SC} , and FF, and EIS, the results were compared. The interaction of EC with cations in the three electrolytes showed the lowest prevalence of solvation (I^- by K^+) in the PVDF NF membrane-based electrolyte. This result is in line with the band shift of the polymer combination of 876 cm^{-1} in the FTIR spectra, which indicates a decrease in inter-chain interactions in the PVDF NF membrane-based electrolyte. The DSC thermogram showed that the melting peak of PVDF NF (151.43 °C) was lower than that of PVDF (157.81 °C). Nevertheless, in general, no significant thermal transitions were detected in the PVDF and PVDF NF electrolytes at the temperature at which the solar cells operate. Thus, the trapping of liquid electrolytes in the PVDF and PVDF NF membrane structures can be expected to suppress solvent leakage and evaporation, thereby potentially extending the shelf life of DSSC.

PVDF NF electrolyte-based DSSC and natural photosensitizer from *telang* flower extract offer the highest energy conversion efficiency (1.69%), with V_{OC} and J_{SC} values comparable to liquid electrolytes under the AM 1.5 solar irradiation standard. However, the impedance parameter values indicate that the high polymer content tends to create a 2D network, increasing the resistance for recombination reactions at the Pt/electrolyte and TiO_2 /electrolyte interfaces. Decreasing the crystallinity of the PVDF NF membrane is expected to be a solution for this, while the simultaneous use of natural photosensitizers with varying absorption areas in the UV-Vis region is expected to increase light harvesting, which can further improve DSSC performance and efficiency.

■ ACKNOWLEDGMENTS

The author would like to thank the Indonesia Ministry of Education and Culture, Research and Technology of the Republic of Indonesia for providing financial support through national competitive research grants and the Department of Chemistry, Faculty of Mathematics and Natural Sciences Universitas Negeri Surabaya for providing research facilities support.

■ REFERENCES

- [1] Bandara, T.M.W.J., Weerasinghe, A.M.J.S., Dissanayake, M.A.K.L., Senadeera, G.K.R., Furlani, M., Albinsson, I., and Mellander, B.E., 2018, Characterization of poly (vinylidene fluoride-co-hexafluoropropylene) (PVdF-HFP) nanofiber membrane based quasi solid electrolytes and their application in a dye sensitized solar cell, *Electrochim. Acta*, 266, 276–283.
- [2] Zulenda, Z., Naselia, U.A., Gustian, N., Zaharah, T.A., and Rahmalia, W., 2018, Sintesis dan karakterisasi kompleks brazilin dari ekstrak kayu secang (*Caesalpinia sappan* Linn) serta aplikasinya dalam Dye Sensitized Solar Cells (DSSC), *J. Kim. Valensi*, 5 (1), 8–14.
- [3] Roslan, N., Ya'acob, M., Radzi, M.A.M., Hashimoto, Y., Jamaludin, D., and Chen, G., 2018, Dye Sensitized Solar Cell (DSSC) greenhouse shading: New insights for solar radiation manipulation, *Renewable Sustainable Energy Rev.*, 92, 171–186.
- [4] Sonker, R.K., Rahul, R., and Sabhajeet, S.R., 2018, ZnO nanoneedle structure-based dye-sensitized solar cell utilizing solid polymer electrolyte, *Mater. Lett.*, 223, 133–136.
- [5] Al-Alwani, M.A.M., Mohammad, A.B., Kadhum, A.A.H., Ludin, N.A., Safie, N.E., Razali, M.Z., Ismail, M., and Sopian, K., 2017, Natural dye extracted from *Pandanus amaryllifolius* leaves as sensitizer in fabrication of dye-sensitized solar cells, *Int. J. Electrochem. Sci.*, 12, 747–761.
- [6] Kabir, F., Sakib, S.N., and Matin, N., 2019, Stability study of natural green dye based DSSC, *Optik*, 181, 458–464.
- [7] Kusumawati, N., Setiarso, P., and Muslim, S., 2018, Polysulfone/polyvinylidene fluoride composite membrane: Effect of coating dope composition on membrane characteristics and performance, *Rasayan J. Chem.*, 11 (3), 1034–1041.
- [8] Önen, T., Karakuş, M.Ö., Coşkun, R., and Çetin, H., 2019, Reaching stability at DSSCs with new type gel electrolytes, *J. Photochem. Photobiol., A*, 385, 112082.
- [9] Tan, C.Y., Farhana, N.K., Saidi, N.M., Ramesh, S., and Ramesh, K., 2018, Conductivity, dielectric studies and structural properties of P(VA-co-PE) and its application in dye-sensitized solar cell, *Org. Electron.*, 56, 116–124.
- [10] Ahliha, A.H., Nurosyid, F., Supriyanto, A., and Kusumaningsih, T., 2018, Optical properties of anthocyanin dyes on TiO_2 as photosensitizers for application of dye-sensitized solar cell (DSSC), *IOP Conf. Ser.: Mater. Sci. Eng.*, 333, 012018.
- [11] Pavithra, N., Velayutham, D., Sorrentino, A., and Anandan, S., 2017, Thiourea incorporated poly(ethylene oxide) as transparent gel polymer electrolyte for dye-sensitized solar cell applications, *J. Power Sources*, 353, 245–253.
- [12] Dissanayake, M.A.K.L., Jaseetharan, T., Senadeera, G.K.R., Mellander, B.E., Albinsson, I., Furlani, M., and Kumari, J.M.K.W., 2021, Solid-state solar cells co-sensitized with PbS/CdS quantum dots and N719 dye and based on solid polymer electrolyte

- with binary cations and nanofillers, *J. Photochem. Photobiol., A*, 405, 112915.
- [13] Sundaramoorthy, K., Muthu, S.P., and Perumalsamy, R., 2018, Enhanced performance of 4,4'-bipyridine-doped PVDF/KI/I₂ based solid state polymer electrolyte for dye-sensitized solar cell applications, *J. Mater. Sci.: Mater. Electron.*, 29 (21), 18074–18081.
- [14] Dissanayake, M.A.K.L., Divarathne, H.K.D.W.M.N.R., Thotawatthage, C.A., Dissanayake, C.B., Senadeera, G.K.R., and Bandara, B.M.R., 2014, Dye-sensitized solar cells based on electrospun polyacrylonitrile (PAN) nanofiber membrane gel electrolyte, *Electrochim. Acta*, 130, 76–81.
- [15] Sahito, I.A., Sun, K.C., Arbab, A.A., and Jeong, S.H., Synergistic effect of thermal and chemical reduction of graphene oxide at the counter electrode on the performance of dye-sensitized solar cells, *Sol. Energy*, 190, 112–118.
- [16] Sahito, I.A., Ahmed, F., Khatri, Z., Sun, K.C., and Jeong, S.H., 2017, Enhanced ionic mobility and increased efficiency of dye-sensitized solar cell by adding lithium chloride in poly(vinylidene fluoride) nanofiber as electrolyte medium, *J. Mater. Sci.*, 52 (24), 13920–13929.
- [17] Ahmad, N.A., Goh, P.S., Yogarathinam, L.T., Zulhairun, A.K., and Ismail, A.F., 2020, Current advances in membrane technologies for produced water desalination, *Desalination*, 493, 114643.
- [18] Kusumawati, N., Wijastuti, A., and Santoso, A.B., 2015, Manufacture of PVDF-Kitosan composite membrane and its utilization in batik industrial wastewater treatment, *Res. J. Pharm., Biol. Chem. Sci.*, 6 (2), 495–503.
- [19] Kusumawati, N., Setiarso, P., Sianita, M.M., and Muslim, S., 2018, Transport properties, mechanical behavior, thermal and chemical resistance of asymmetric flat sheet membrane prepared from PSf/PVDF blended membrane on gauze supporting layer, *Indones. J. Chem.*, 18 (2), 257–264.
- [20] Maharani, K.D.A., and Kusumawati, N., 2016, The effect of casting solution and non-solvent composition on the performance of polysulfone membranes against chromium (VI), *Res. J. Pharm., Biol. Chem. Sci.*, 7 (2), 495–504.
- [21] Ningrum, R.D.C., and Kusumawati, N., 2016, Development and characterization of polysulfone/polyvinylidene fluoride blend membrane induced by delayed liquid-liquid demixing, *Int. J. Adv. Sci. Eng. Inf. Technol.*, 6 (5), 716–722.
- [22] Kusumawati, N., Setiarso, P., Muslim, S., and Purwidiani, N., 2018, Synergistic ability of PSf and PVDF to develop high-performance PSf/PVDF coated membrane for water treatment, *Rasayan J. Chem.*, 11 (1), 260–279.
- [23] Guilen, G.R., Pan, Y., Li, M., and Hoek, E.M.V., 2011, Preparation and characterization of membranes formed by non-solvent induced phase separation: A review, *Ind. Eng. Chem. Res.*, 50 (7), 3798–3817.
- [24] Mousavi, S.M., Zarei, M., Hashemi, S.A., Babapoor, A., and Amani, A.M., 2019, A conceptual review of rhodanine: Current applications of antiviral drugs, anticancer and antimicrobial activities, *Artif. Cells, Nanomed., Biotechnol.*, 47 (1), 1132–1148.
- [25] Zhu, H., Wang, H., Wang, F., Guo, Y., Zhang, H., and Chen, J., 2013, Preparation and properties of PTFE hollow fiber membranes for desalination through vacuum membrane distillation, *J. Membr. Sci.*, 446, 145–153.
- [26] Mousavi, S.M., Zarei, M., Hashemi, S.A., Ramakrishna, S., Chiang, W.H., Lai, C.W., Gholami, A., Omidifar, N., and Shokripour, M., 2020, Asymmetric membranes: A potential scaffold for wound healing applications, *Symmetry*, 12 (7), 1100.
- [27] Ahmadi, S., 2020, Nanoparticles induced oxidative stress and related effects especially under exposure to electromagnetic radiations, *Adv. Appl. NanoBio-Technol.*, 1 (4), 91–98.
- [28] Moshfeghian, M., Azimi, H., Mahkam, M., Kalae, M.R., Mazinani, S., and Mosafer, H., 2021, Effect of solution properties on electrospinning of polymer nanofibers: A study on fabrication of PVDF nanofiber by electrospinning in DMAC and

- (DMAC/Acetone) solvents, *Adv. Appl. NanoBio-Technol.*, 2 (2), 53–58.
- [29] Ammar, M., Mohamed, H.S.H., Yousef, M.M.K., Abdel-Hafez, G.M., Hassanien, A.S., and Khalil, A.S.G., 2019, Dye-sensitized solar cells (DSSCs) based on extracted natural dyes, *J. Nanomater.*, 2019, 1867271.
- [30] Enciso, P., Decoppet, J.D., Grätzel, M., Wörner, M., Cabrerizo, F.M., and Cerdá, M.F., 2017, A cockspur for the DSS cells: *Erythrina crista-galli* sensitizers, *Spectrochim. Acta, Part A*, 176, 91–98.
- [31] Valaa, M., Krajčovič, J., Luňák, S., Ouzzane, I., Bouillon, J.P., and Weiter, M., 2014, HOMO and LUMO energy levels of *N,N'*-dinitrophenyl-substituted polar diketopyrrolopyrroles (DPPs), *Dyes Pigm.*, 106, 136–142.
- [32] Sinha, D., De, D., and Ayaz, A., 2018, Performance and stability analysis of curcumin dye as a photosensitizer used in nanostructured ZnO based DSSC, *Spectrochim. Acta, Part A*, 193, 467–474.
- [33] Choi, M., Noh, Y., Kim, K., and Song, O., 2016, Properties of dye sensitized solar cells with porous TiO₂ layers using polymethyl-methacrylate nano beads, *Korean J. Mater. Res.*, 26 (4), 194–199.
- [34] Syafinar, R., Gomesh, N., Irwanto, M., Fareq, M., and Irwan, Y.M., 2015, Potential of purple cabbage, coffee, blueberry and turmeric as natural dyes for dye sensitive solar cells (DSSC), *Energy Procedia*, 79, 799–807.
- [35] Nilesh, P.N., Rajput, M.S., Prasad, R.G.S.V., and Ahmad, M., 2015, Brazilin from *Caesalpinia sappan* heartwood and its pharmacological activities: A review, *Asian Pac. J. Trop. Med.*, 8 (6), 421–430.
- [36] Martín, J., Navas, M.J., Jiménez-Moreno, A.M., and Asuero, A.G., 2017, “Anthocyanin Pigments: Importance, Sample Preparation and Extraction” in *Phenolic Compounds - Natural Sources, Importance and Applications*, Eds. Soto-Hernandez, Palma-Tenango, M., and Garcia-Mateos, R., IntechOpen, Rijeka, Croatia.
- [37] Priska, M., Peni, N., Carvallo, L., and Ngapa, Y.D., 2018, Review: Antosianin dan pemanfaatannya, *Chakra Kimia*, 6 (2), 79–97.
- [38] Hutagalung, R.A., Victor, V., Karjadidjaja, M., Prasasty, V.D., and Mulyono, N., 2014, Extraction and characterization of bioactive compounds from cultured and natural sponge, *Haliclona molitba* and *Stylotella aurantium* origin of Indonesia, *Int. J. Biosci., Biochem. Bioinf.*, 4 (1), 14–18.
- [39] Jeyaram, S., and Geethakrishna, T., 2020, Vibrational spectroscopic, linear and nonlinear optical characteristics of *Anthocyanins* extracted from blueberry, *Results Opt.*, 1, 100010.
- [40] Hardeli, H., Suwardani, S., Riky, R., Fernando, T., Maulidis, M., and Ridwan, S., 2013, Dye sensitized solar cells (DSSC) berbasis nanopori TiO₂ menggunakan antosianin dari berbagai sumber alami, *Proceedings of the Semirata FMIPA*, University of Lampung, 155–161.
- [41] Ndeze, U.I., Aidan, J., Ezike, S.C., and Wansah, J.F., 2021, Comparative performances of nature-based dyes extracted from Baobab and Shea leaves photosensitizers for dye-sensitized solar cells (DSSCs), *Curr. Res. Green Sustainable Chem.*, 4, 100105.
- [42] Dahlan, D., Leng, T.S., and Aziz, H., 2016, Dye-sensitized solar cells (DSSC) dengan sensitizer dye alami daun pandan, akar kunyit dan biji beras merah (black rice), *Jurnal Ilmu Fisika*, 8 (1), 1–8.
- [43] Imelda, I., and Putri, R.A., 2020, Optimalisasi struktur π -konjugasi pada zat warna organik tipe D- π -A, *J. Res. Educ. Chem.*, 2 (2), 61–72.
- [44] Maynez-Rojas, M.A., Casanova-González, E., and Ruvalcaba-Sil, J.L., 2017, Identification of natural red and purple dyes on textiles by Fiber-optics Reflectance Spectroscopy, *Spectrochim. Acta, Part A*, 178, 239–250.
- [45] Prasad, G., Liang, J.W., Zhao, W., Yao, Y., Tao, T., Liang, B., and Lu, S.G., 2021, Enhancement of solvent uptake in porous PVDF nanofibers derived by a water-mediated electrospinning technique, *J. Materiomics*, 7 (2), 244–253.
- [46] Sarker, S., Seo, H.W., and Kim, D.M., 2014, Calculating current density-voltage curves of dye-sensitized solar cells: A straight-forward approach, *J. Power Sources*, 248, 739–744.

- [47] Kutlu, N., 2020, Investigation of electrical values of low-efficiency dye-sensitized solar cells (DSSCs), *Energy*, 199, 117222.
- [48] Tractz, G.T., Viomar, A., Dias, B.V., de Lima, C.A., Banczek, E.P., da Cunha, M.T., Antunes, S.R.M., and Rodrigues, P.R.P., 2019, Recombination study of dye sensitized solar cells with natural extracts, *J. Braz. Chem. Soc.*, 30 (2), 371–378.
- [49] Omar, A., Ali, M.S., and Abd Rahim, N., 2020, Electron transport properties analysis of titanium dioxide dye-sensitized solar cells (TiO₂-DSSCs) based natural dyes using electrochemical impedance spectroscopy concept: A review, *Sol. Energy*, 207, 1088–1121.
- [50] Kim, K.H., Lee, S.M., Seo, M.H., Cho, S.E., Hwang, W.P., Park, S.H., Kim, Y.K., Lee, J.K., and Kim, M.R., 2012, Syntheses of organic dyes based on phenothiazine as photosensitizers and effects of their π -conjugated bridges on the photovoltaic performances of dye-sensitized solar cells, *Macromol. Res.*, 20 (2), 128–137.
- [51] Bakri, A.S., Sahdan, M.Z., Adriyanto, F., Raship, N.A., Said, N.D.M., Abdullah, S.A., and Rahim, M.S., 2017, Effect of annealing temperature of titanium dioxide thin films on structural and electrical properties, *AIP Conf. Proc.*, 1778, 030030.
- [52] Shah, S., Noor, I.M., Pitawala, J., Albinson, I., Bandara, T.M.W.J., Mellander, B.E., and Arof, A.K., 2017, Plasmonic effects of quantum size metal nanoparticles on dye-sensitized solar cell, *Opt. Mater. Express*, 7 (6), 2069–2083.
- [53] Selvanathan, V., Yahya, R., Alharbi, H.F., Alharthi, N.H., Alharthi, Y.S., Ruslan, M.H., Amin, N., and Akhtaruzzaman, M., 2020, Organosoluble starch derivative as quasi-solid electrolytes in DSSC: Unravelling the synergy between electrolyte rheology and photovoltaic properties, *Sol. Energy*, 197, 144–153.
- [54] Mokhtari, F., Latifi, M., and Shamshirsaz, M., 2015, Electrospinning/electrospray of polyvinylidene fluoride (PVDF): Piezoelectric nanofibers, *J. Text. Inst.*, 107 (8), 1037–1055.
- [55] Osman, Z., and Arof, A.K., 2003, FTIR studies of chitosan acetate-based polymer electrolytes, *Electrochim. Acta*, 48 (8), 993–999.
- [56] Saha, S., Yauvana, V., Chakraborty, S., and Sanyal, D., 2019 Synthesis and characterization of polyvinylidene-fluoride (PVDF) nanofiber for application as piezoelectric force sensor, *Mater. Today: Proc.*, 18, 1450–1458.
- [57] Duh, Y.S., Lee, C.Y., Chen, Y.L., and Kao, C.S., 2016, Characterization on the exothermic behaviors of cathode materials reacted with ethylene carbonate in lithium-ion battery studied by differential scanning calorimeter (DSC), *Thermochim. Acta*, 642, 88–94.
- [58] Hofmann, A., Wang, Z., Bautista, S.P., Weil, M., Müller, F., Löwe, R., Schneider, L., Mohsin, I.U., and Hanemann, T., 2022, Dataset of propylene carbonate based liquid electrolyte mixture for sodium-ion cells, *Data Brief*, 40, 107775.
- [59] Shalu, S., Singh, V.K., and Singh, R.K., 2015, Development of ion conducting electrolyte membranes based on polymer PVdF-HFP, BMIMTFSI ionic liquid and the Li-salt with improved electrical, thermal and structural properties, *J. Matter. Chem. C*, 3 (28), 7305–7318.

Degradable Bioplastic Developed from Pine-Wood Nanocellulose as a Filler Combined with Orange Peel Extract

Alyaa Farrah Dibha, Masruri Masruri*, and Arie Srihardyastutie

Department of Chemistry, Brawijaya University, Jl. Veteran, Malang 65145, East Java, Indonesia

* **Corresponding author:**

tel: +62-82142017342

email: masruri@ub.ac.id

Received: June 17, 2022

Accepted: September 21, 2022

DOI: 10.22146/ijc.75520

Abstract: This research presents the degradable bioplastics developed from pinewood nanocellulose as a filler in PVA matrices. The steps involve the isolation and characterization of cellulose and nanocellulose. Meanwhile, the manufacturing of degradable bioplastic involves the combination of PVA, nanocellulose, and with or without orange peel extract. The effect of bioplastics without the addition of citric acid and orange peel extract is also reported as a comparison. It is found that orange peel extract improves the tensile strength (1708.54 kPa), elastic modulus (42.71 kPa), elongation (40%), and degradability (78.44% in 2 weeks) compared to bioplastic without the orange peel extract. These results indicate that orange peel extract acts as a reinforcing agent in PVA-nanocellulose bioplastic.

Keywords: pinewood-nanocellulose; degradable-bioplastic; orange peel extract

■ INTRODUCTION

Plastic waste has reached 6.9 billion tons on a global scale, and every year 34 million tons of plastic waste are produced, with up to 93% of that waste ending up in a landfill or the ocean [1-2]. Fan et al. predicted in the year 2040, it is estimated that 710 Mt of plastic waste will be disposed of and pollute the surface and groundwater sources [3]. Java Island produces 189,349 tons per month of plastic waste, and the Malang regions generate 4,829.77 tons per month [4]. Plastic waste takes nearly a million years to naturally decompose in the environment due to the non-degradable characteristic of plastic materials [5-6]. Thus, it severely threatens the environment and living matters, such as sewage blocking up and animal and human health problems [7]. As an alternative strategy, degradable bioplastics must be developed to replace the petroleum-based plastic used in packaging.

Generally, bioplastics can be made from several components, such as reinforcing agents, crosslinkers, and additives components. According to references, cellulose and nanocellulose can be used as reinforcing agents [8-9], combining with polyhydroxyalkanoate (PHA), polyvinyl alcohol (PVA), or polylactic acid (PLA) [10-11]. The cellulose or nanocellulose can be isolated from forest and

agricultural wastes. In addition, the other component reported as a linker, i.e., citric acid, sorbitol, glyoxal, dicarboxylic acid, and organic acid reagents like maleic acid and ascorbic acid [12-14]. Meanwhile, additive materials are generally added to improve the degradability characteristic and/or appearance of bioplastic [15]. The natural plant extract has been reported previously to increase the strength of bioplastic [16-17]. Nasihin et al. used pine flower waste cellulose combined with starch, PVA, and turmeric extract. The resulting bioplastic has a gradation color from yellow to colorless with the decreasing turmeric extract concentration [18]. However, the strength and elasticity of bioplastic are lower.

According to the report from the Ministry of Industry of the Republic of Indonesia, the number of wood industries in Indonesia has increased by 62.7%. As an outcome, a large amount of biomass contained-cellulosic material such as sawdust, tree bark, and other forest by-product is wasted [19-20], and only 40% of waste from the wood industry or agriculture is processed [21]. Similar data also reported that pine forests in East Java (a total area of about 800 kha) also provide biomass as waste. The pine flower waste still composes its important volatile terpenoid compounds [22], including

cellulosic material (22.22%) [23]. Meanwhile, pine wood contains 54.9% of cellulose, hemicellulose (14%), lignin (24.3%), ash (1.1%), and silica (0.2%) [24]. The treatment process of the pine wood by using acid hydrolysis and bleaching produces pure cellulose. The step removes polyphenolic and lignin from the matrix [25]. This step generally provides cellulose in micrometric size. Further hydrolysis process to produce cellulose in nano-size is performed by cutting the β -glycosidic bonds of cellulose polymer [26]. The resulting nanocellulose can form fiber or crystalline nanocellulose, which depends on the original source of cellulose and the strategy to hydrolyze it [27]. For example, nanocrystalline cellulose can be isolated after acidic hydrolysis using citric acid, sulfuric acid, and hydrochloric acid [18,28]. Enzymatic hydrolysis of cellulose also produces crystalline nanocellulose [25]. Meanwhile, oxidation following hydrolysis generally provides amorphous nanocellulose [29]. Besides that, nanocrystalline cellulose is also produced through hydrolysis under mechanical and ultrasonication-assisted hydrolysis [30]. According to Agustin et al. applying nanocellulose as a filler for bioplastic affect the physical performance of bioplastics, such as tensile strength and modulus value [31]. Another paper reported an increase in the transparency of bioplastic [32].

On the other side, Indonesia is also the main producer of orange fruits. It is sold and consumed directly as fresh fruit or converted into packaging juice. The global waste of orange peel is projected to be 15×10^6 tons annually [33]. Meanwhile, Indonesia produces 6.8×10^8 tons of orange peel waste [34]. Hassan et al. reported that orange peel contains ascorbic acid of around 59 mg/100 g (w/w) [35]. Ascorbic acid is an organic acid containing polyhydroxy and ester functional groups. This substituent is predicted to be applied as a linker to bind with nanocellulose and PVA [12-13]. Thus, it could improve the binding inter-molecular component of bioplastic. This paper reports the contribution of orange extract containing ascorbic acid to improve the performance of degradable bioplastic developed with nanocellulose from pinewood as a filler.

■ EXPERIMENTAL SECTION

Materials

Pinewood (*Pinus merkusii*) waste was used as a natural source of cellulose taken from the Brawijaya University Forest, and the pinewood waste was ground into powder. The chemical reagents used in this research were sodium hypochlorite (99% purity Merck, Germany), acetic acid (99% purity SMART LAB, Indonesia), sodium hydroxide (99% purity Merck, Germany), hydrogen peroxide (30% purity SMART LAB, Indonesia), hydrochloric acid (37% purity Merck, Germany), polyvinyl alcohol (99% purity Merck, Germany), glycerin (85% purity Merck, Germany), and citric acid (99% purity Merck, Germany).

Instrumentation

Instruments used for research include ultrasonicator (DELTA D150H, 48 kHz, 220-240 volt), Fourier Transform Infrared (Shimadzu FTIR-8400S), X-ray Diffractometer (XRD PANanalytical- type X'pert Pro), Scanning Electron Microscope (FEI SEM Inspect-S50), Tensile Strength Apparatus (ZP-50 N).

Procedure

Preparation of cellulose

The procedure to produce cellulose followed the reference [36] with minor modifications. Pinewood waste was washed under running water to remove the impurity from the pinewood waste and dried under the sunlight for 2–3 days. Then, the clean pinewood waste was ground into powder. The powder was weighed to 50 g and put into a 1000 mL beaker glass. Then, the delignification process continued with the addition of sodium hypochlorite 6% and acetic acid 1% solution with a ratio of powder to solution was 1:10 (w/v). The mixture was stirred and heated at 70 °C for 1 h. After that, the alkaline bleaching process was done with the addition of sodium hydroxide 4% and hydrogen peroxide 24% (1:1 v/v) with the ratio of powder to the mixture was 1:10 (w/v). The mixing under stirring was conducted for 2 h at 50 °C, and this process was repeated up to 3 times until the

white cellulose was obtained. Then, it was neutralized and dried in an oven at 50 °C for 24 h. Characterization was undergone by means of FTIR, XRD, and SEM.

Preparation of nanocellulose

The isolated cellulose from the previous step was further hydrolyzed following reference [28] with modification. The modification procedure in this step involves hydrolysis assisted by ultrasonication. The detailed procedure is reported elsewhere separately. The drying process was undertaken in an oven at 50 °C for 1 h. Nano cellulose was produced as a white-fine powder after separation under centrifugation, and further characterization was taken place using FTIR, XRD, and SEM.

Preparation of orange peel waste extract

Orange peel waste samples were obtained from the industrial waste of orange juice production in Malang, East Java, Indonesia. Samples were washed and cut into small sizes. Then, it was dried in an oven at 50 °C for 48 h. The dried peel was ground to get a powder. Then, orange peel powder was extracted with ethanol 50%, using a powder-to-solvent ratio of 1:2 (w/v) [37]. The extraction process was assisted by ultrasonication (ultrasonicator D150H and 220–240 V power and 48 kHz) for 1 h at room temperature. The extract was filtered using a Buchner funnel, and the resulting filtrate was evaporated under reduced pressure using a rotary evaporator to yield crude extract.

Fabrication of bioplastics

The procedure to fabricate bioplastics was done following Hussein et al. [38] with some modifications. The composition ratio of each component of bioplastic is displayed in Table 1. The steps to fabricate bioplastic involves the mixing of 10% PVA solution with 1.5% nanocellulose in a 50-mL Erlenmeyer. This mixture was

stirred for 1 h at 90 °C, then 2% citric acid solution or 2% orange peel extract was added to the mixture. The mixture was further stirred for 1 h at the same temperature. One mL of glycerin was added to the mixture until a viscous solution was formed. Then, it was poured into a molding glass (20 × 20 cm²) and left in an oven at 50 °C for 24 h.

Characterization

Fourier transform infrared (FTIR) spectroscopy analysis. Fourier Transform Infrared Spectroscopy (FTIR) analysis of nanocellulose and bioplastic was done to determine the absorption bands of functional groups composed in the nanocellulose and bioplastic. The measurement was performed by scanning in a range of 400–4000 cm⁻¹.

X-ray diffraction (XRD) analysis. The crystallinity of cellulose and nanocellulose was measured from the crystallinity index (CI) value. It was conducted using PanAnalytical type X'pert Pro with a range of 2θ = 10–90° and a scan rate of 2°/min. The CI was calculated following the equation [39].

$$CI = \frac{I_{002} - I_{amorph}}{I_{002}} \times 100\% \quad (1)$$

Scanning electron microscope (SEM) analysis. Scanning Electron Microscope (SEM) was used to observe morphological surface cellulose, nanocellulose, and bioplastic. The samples were put into a specimen holder and analyzed using field emission scanning electron microscope (FEI SEM) Inspect-S50.

Mechanical properties analysis. The mechanical properties of bioplastic were determined using the Tensile Strength apparatus model: ZP-50N. The tensile strength, elongation break, and elastic modulus parameters were measured following the ASTM-D1708-18 standard method (ASTM, 2018). The bioplastic was

Table 1. The composition of PVA, nanocellulose, citric acid, and orange peel waste extract

Sample code	PVA 10% (mL)	Nanocellulose 1.5% (mL)	Citric acid (g)	Orange peel waste extract (g)	Glycerin (mL)	Total volume (mL)
PVA/NC/Orange peel waste extract	8	2	-	0.2	1	11
PVA/NC/citric acid	8	2	0.2	-	1	11
PVA/NC	8	2	-	-	1	11

cut into 2.2×0.5 cm of width sizes, each side of the bioplastic was made wider. The wider part was placed into the grip part of the tensile strength tools. Then, the tensile strength tools stretched the bioplastic. The time began when the bioplastic was stretched, and the time ended when the sample was broken.

Bioplastic degradation test. A degradation test of manufactured bioplastic was performed following the procedure of soil burial test [17]. The bioplastic was cut into 2×2 cm² sizes and weighed. Then, it was buried in the soil at a 5 cm depth. The soil was watered every 3–4 days for 15 days to keep the humidity of the soil. Then, the bioplastic was taken from the soil, washed, and dried in an oven at 50 °C until dry. Then, it was weighted until a constant value resulted. The percentage of degradation was calculated following Eq. (2):

$$\text{Degradation (\%)} = \frac{M_i - M_a}{M_i} \times 100\% \quad (2)$$

while M_i was the initial mass of the bioplastic before the degradation test, and M_a was the final mass of the bioplastic after the biodegradation test.

■ RESULTS AND DISCUSSION

Cellulose and Nanocellulose Pinewood

The extraction of cellulose from pinewood waste was done by the acid pre-treatment and alkaline process. The acid pre-treatment process provides 97.16% of dark brown powder. This step eliminates hemicellulose and non-cellulosic components such as wax, chlorophyll, and other acidic soluble compounds. Additionally, it is also used to increase the surface area of cellulose [40].

Meanwhile, the alkaline process is the step to delignification, i.e., removing lignin from cellulose. The delignification process uses sodium hydroxide and hydrogen peroxide as reagents to accelerate the breaking down of the bonds between lignin and cellulose [25]. The yield from this step was 61.86%, and white powder was isolated (Fig. 1). Fig. 1(a) and 1(b) show the appearance of pine wood waste before and after turning. An acid pre-treatment process was carried out by reacting pinewood powder with sodium hypochlorite and acetic acid. This step changes the color of pinewood powder to dark brown (Fig. 1(c)). The delignification process was completed by stirring the pinewood resulting from acid pre-treatment with sodium hydroxide and hydrogen peroxide. This process produces white cellulose (Fig. 1(d)). Further acid hydrolysis of cellulose with hydrochloric acid 10% assisted by ultrasonication provide a white nanocellulose. It has a softer form (Fig. 1(e)). Previous research stated that nanocrystalline cellulose could be obtained by an acid hydrolysis process using hydrochloric acid [28]. Cheng et al. stated that after 30 min of ultrasonication for nanocellulose extraction, the cellulose particles break into smaller fibrils and produce fibrils with a dimension of 100 nm [41]. Nanocellulose was reported to have functional properties such as high degradability, low toxicity, biocompatibility, and excellent mechanical strength. It was also easily adapted into polymeric matrices and blended easily, thus producing cost-effective and durable materials [32,42]. A further study stated that

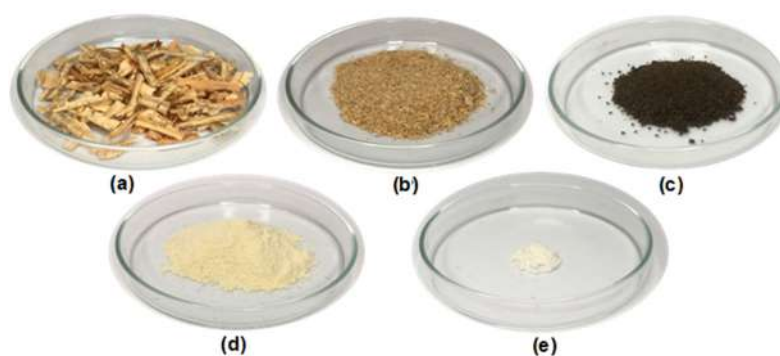


Fig 1. Pictures: (a) Pinewood waste, (b) Pinewood waste powder, (c) Acid pre-treatment result, (d) Cellulose, (e) Nanocellulose

nanocellulose could be used as a reinforcing filler in bioplastic fabrication and improve the tensile strength and elastic modulus of a bioplastic produced [31].

Fourier Transform Infrared (FTIR) Analysis of Cellulose and Nanocellulose

The FTIR spectra of pinewood, cellulose, and nanocellulose were measured to examine the changes in the functional groups composed in the sample. The FTIR result of pinewood waste, cellulose, and nanocellulose was explained in Table 2. From Table 2, there was the absorption of O–H stretching at a wavenumber of 3387.25, 3398.66, and 3345.89 cm^{-1} in pinewood waste, cellulose, and nanocellulose. Then, the absorption of C–H stretching vibration was found at 2898.06, 2900.91, and 2899.49 cm^{-1} . However, the absorption of C=O stretching and vibration of C=C were only found in pinewood waste at a wavenumber of 1732.85 and 1510.36 cm^{-1} , which were assigned as hemicellulose and lignin. Similar findings were also reported by Popescu et al. and Sukmawan et al. that C=O and C=C groups assigned as hemicellulose and lignin could be found at a wavenumber at 1700 and 1510 cm^{-1} [43-44].

X-Ray Diffraction (XRD) Analysis of Cellulose and Nanocellulose

X-Ray Diffraction (XRD) is a technique used to assess the degree of crystallinity in various materials. Among the wood components, only cellulose has a crystallinity phase,

and the other polymer has a non-crystalline phase [43]. The X-Ray diffractogram is explained in Fig. 2. The XRD analysis of cellulose and nanocellulose was recorded at $2\theta = 22.5^\circ$ and the peaks for cellulose and nanocellulose characteristics with grid plane 200 [45].

Table 3 describes the crystallinity index of cellulose and nanocellulose, resulting in a crystallinity index of 58.49% for cellulose and 60.32% for nanocellulose at 2θ degrees of 22.59° and 22.62° . The crystallinity of nanocellulose is higher than cellulose, which implies that the acid hydrolysis process on cellulose reduces the amorphous phase of cellulose and increases the crystalline phase [46].

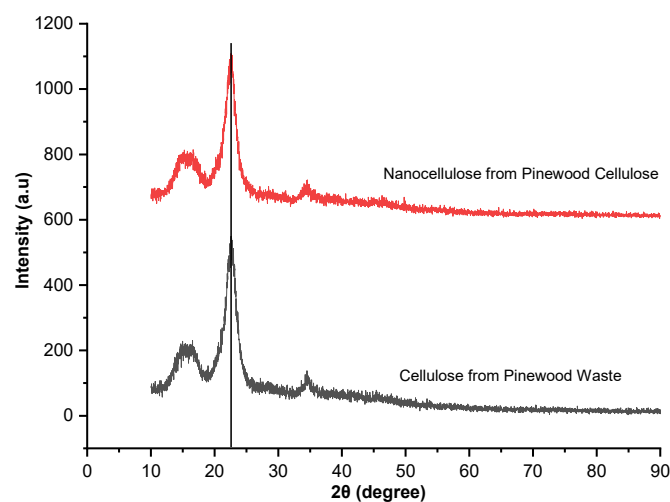


Fig 2. X-Ray diffractograms pattern of cellulose and nanocellulose from pinewood waste

Table 2. The FTIR result of pinewood waste, cellulose, and nanocellulose

Wavenumber (cm^{-1})			Functional group
Pinewood	Cellulose	Nanocellulose	
3387.25	3398.66	3345.89	O–H stretching
2898.06	2900.91	2899.49	C–H stretching
1732.85	-	-	Hemicellulose, C=O stretching
1640.14	1644.42	1647.27	Water absorption, O–H bonding
1510.36	-	-	Lignin, C=C
-	1427.64	1429.06	CH_2 bending from carboxylate
1374.87	1372.02	1372.02	C–O–C cellulose amorph and crystalline
1317.82	1317.82	1319.25	Cellulose, C–O–C
1059.68	1062.53	1062.53	C–O stretching in glycoside bond
897.09	898.51	898.51	C–O stretching

Table 3. Crystallinity index of cellulose and nanocellulose

	Cellulose	Nanocellulose
Peak (2 θ)	22.59°	22.62°
Crystallinity index (%)	58.49	60.32

Scanning Electron Microscope (SEM) of Cellulose and Nanocellulose

SEM is an important instrument for determining the morphological behavior of the bioplastic surface [17]. The surface morphological images of cellulose and nanocellulose are shown in Fig. 3. The result indicates that both cellulose and nanocellulose have a crystalline shape. Both are different in size. The diameter and length of cellulose and nanocellulose were calculated with ImageJ software [47]. The cellulose has a larger size than the nanocellulose (Fig. 3). The diameter and length of cellulose were 101.65 and 173.21 nm (Table 4), respectively. Meanwhile, nanocellulose has a diameter and a length of 16.36 and 29.44 nm, respectively. The

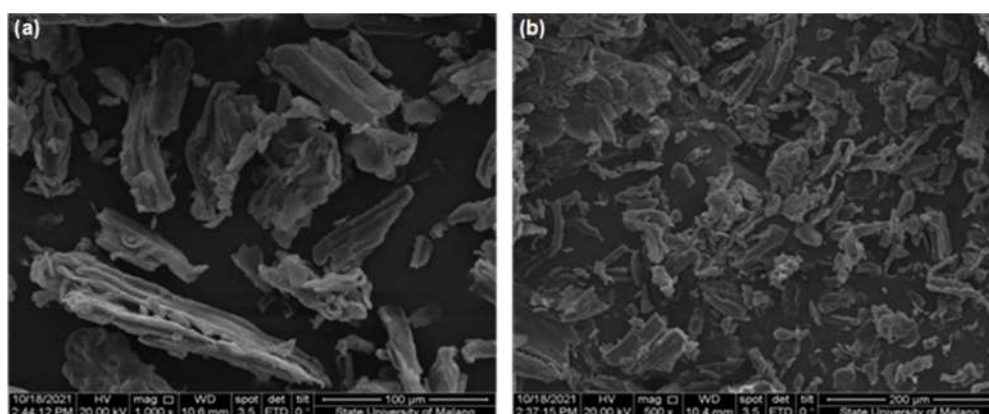
breakdown process of a polymeric chain of cellulose by acidic hydrolysis combined with an ultrasonication strategy forms the cellulose into a smaller size. Some research also reported an increase in the surface area of cellulose [47-48].

Bioplastic Film's Appearance

The bioplastic made from orange peel waste extract had a slightly yellow color, while the bioplastic made with the addition of citric acid gave a transparent and glossy surface (Fig. 4). Meanwhile, the appearance of bioplastic produced without the addition of citric acid or orange peel waste extract has a transparent and doff surface.

Table 4. The particle size of cellulose and nanocellulose

Sample	Dimension	
	Diameter (nm)	Length (nm)
Cellulose	101.65	173.21
Nanocellulose	16.36	29.44

**Fig 3.** Morphological of (a) Cellulose (1000 \times), (b) Nanocellulose (500 \times)**Fig 4.** Degradable bioplastics

Fourier Transform Infrared (FTIR) Analysis of Bioplastics

The result of FTIR analysis shows that stretching vibration of the hydroxyl (O–H) group of bioplastics with the addition of citric acid and orange peel waste extract gives absorption band at 3274.58 and 3271.73 cm^{-1} , whereas bioplastic without the addition of both has a hydroxyl group (O–H) stretching band at 3271.73 cm^{-1} . Meanwhile, the bending vibration H–O–CO composed of bioplastic prepared with the addition of citric acid and orange peel waste extract appears at 1650.13 and 1645.85 cm^{-1} , respectively. The shift of bending vibration to a lower value implies that bioplastic with citric acid and orange peel waste extract has a new atmosphere. And it is predicted that this shifting (from 1651.55 to 1650.13 cm^{-1} and 1645.85 cm^{-1}) indicates a hydrogen bond interaction between functional groups in each component [49]. Furthermore, the C–O group stretching vibration in C–O–H from all bioplastics showed a peak of 1036.86 cm^{-1} .

The only peak that comes from C=O stretching vibration (1712.88 cm^{-1}) was given from bioplastic with the addition of citric acid. It indicates a free carbonyl group in the bioplastic does not interact (Fig. 5).

Additionally, bioplastic without the addition of citric acid and orange peel extract changes the intensity of hydroxyl group stretching vibration. It is detected at wave number 3271.73 cm^{-1} . Besides, C–H stretching vibration from the alkyl group was recorded at 2939.42 cm^{-1} . This finding has similar results to Hussein et al. and Popescu et al. [38,43]. The illustration of the interaction between nanocellulose and citric acid is described in Fig. 6(a), and the illustration reaction between nanocellulose and orange peel extract is described in Fig. 6(b).

Scanning Electron Microscope (SEM) Analysis of Bioplastics

The surface morphology and internal microstructure of the films are revealed by SEM analysis [50]. Fig. 7(a) shows the smooth surfaces of bioplastic with citric acid. However, there is a part of nanocellulose that does not blend perfectly. While in Fig. 7(b), the surfaces of bioplastic with the addition of orange peel extract seem smoother than those using citric acid, and the cross-section SEM analysis (a1) looks more pore than the bioplastic with the addition of orange peel extract (b1). It is proven by another paper report that the

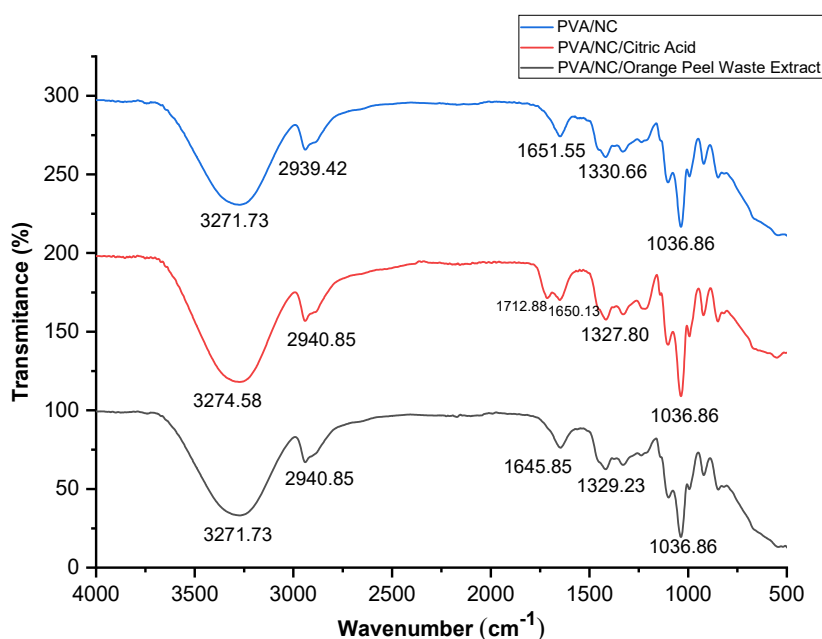


Fig 5. FTIR spectra of biodegradable plastics pinewood nanocellulose based, bioplastic without citric acid and orange peel waste extract (blue line), bioplastic with citric acid (red line), bioplastic with orange peel waste extract (black line)

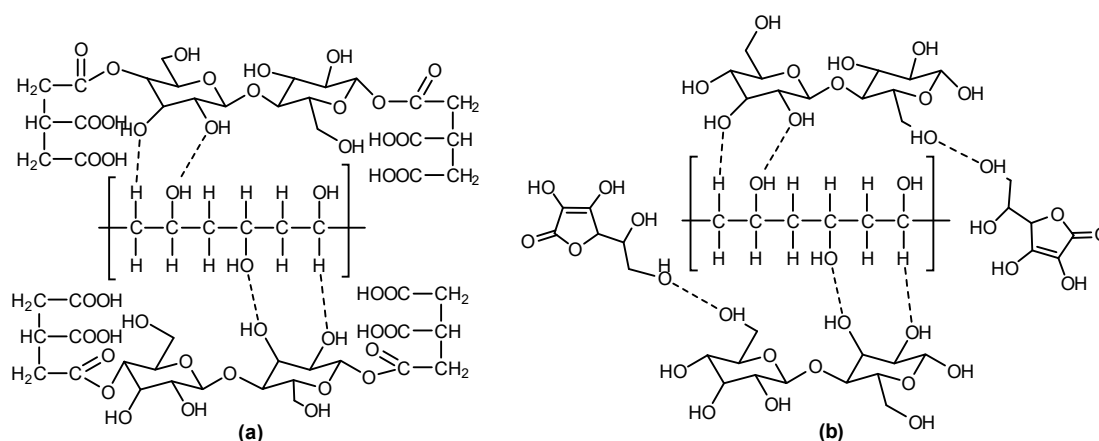


Fig 6. The illustration reaction of bioplastic pinewood nanocellulose based using citric acid (a) and orange peel waste extract (b)

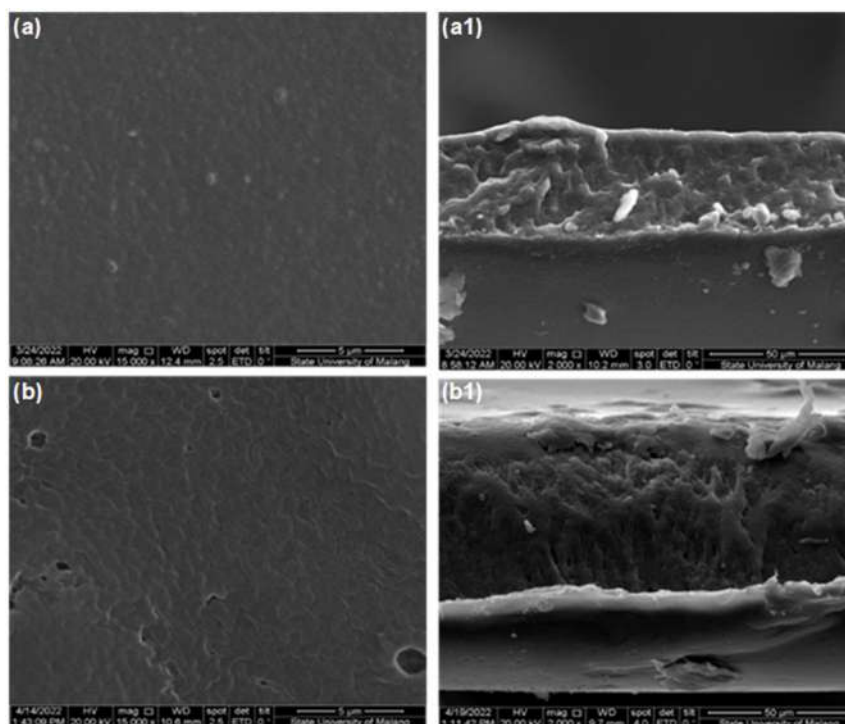


Fig 7. (a) Bioplastic with citric acid (15000 \times), (a1) Cross-section of bioplastic with citric acid (2000 \times), (b) Bioplastic with orange peel extract (15000 \times), (b1) Cross-section of bioplastic with orange peel extract (2000 \times)

addition of plant extract showed a smoother surface of bioplastic. Furthermore, this smoother surface is indicated by the strong hydrogen between the other components [17,51].

Mechanical Properties Analysis of Bioplastics

The mechanical properties studied were elastic modulus, tensile strength, and percentage elongation at

break. The material stiffness is defined by EM or elastic modulus, the resistance to elongation at break is represented by tensile strength, and the capacity for stretching is represented by ϵ [52]. From Table 5, the elastic modulus of bioplastic without the addition of citric acid and orange peel waste extract is lower than bioplastic that fabricates with citric acid and orange peel waste extract. The tensile strength and elastic modulus of

Table 5. Elastic modulus (EM), tensile strength (TS), percentage of elongation at break (EB) of bioplastic

Samples	EM (kPa)	TS (kPa)	% ϵ
PVA/NC/Orange peel waste extract	42.71	1708.54	40.00
PVA/NC/Citric acid	36.12	1203.85	33.33
PVA/NC	31.71	317.11	10.00

bioplastic with the addition of orange peel waste extract have the highest value at 1708.54 and 40.86 kPa. The elongation at break of bioplastics with the addition of citric acid and orange peel extract was 33.33% and 42.71%, respectively. It proved that orange peel extract makes bioplastic stiffer than when it uses citric acid. A similar finding was reported by Marsi et al. that the addition of orange peel powder increases the mechanical properties of bioplastic [15]. Another report on the use of plant extract also increases the mechanical properties and provides a smooth surface morphology of bioplastic. It is due to the amount of hydrogen bonding interaction between the components [17].

Fig. 8 shows the tensile strength curve of the bioplastic with and without the addition of citric acid and orange peel waste extract. From the tensile strength curve, the fabrication of bioplastics without the addition of citric acid and orange peel waste extract had the lowest tensile strength values and the lowest breaking time for the resulting bioplastics. Furthermore, the fabrication of bioplastics with the addition of orange peel waste extract has a higher tensile strength value and the highest breaking time.

Degradability Test Result of Bioplastics

The degradability studies of bioplastics were obtained from the biodegradability test using the soil burial method. The soil-buried bioplastics were collected at 15 days to measure the degradation. After the bioplastic was taken out from the soil, bioplastics were washed with

water to remove the soil residue and dried in an oven at 50 °C for 2 h. The results showed a weight loss of the bioplastics in 15 days. Fig. 9 shows the biodegradability analysis of bioplastic without citric acid and orange peel waste extract, bioplastic with citric acid, and bioplastic with orange peel waste extract, and it shows bioplastic can degrade well in soil. From Table 6, the degradation result of bioplastic without citric acid and orange peel waste extract had the highest result at 86.27%. Furthermore, the degradation result of bioplastic with citric acid at 77.27%, and the degradation result of bioplastic with orange peel waste extract at 78.44%.

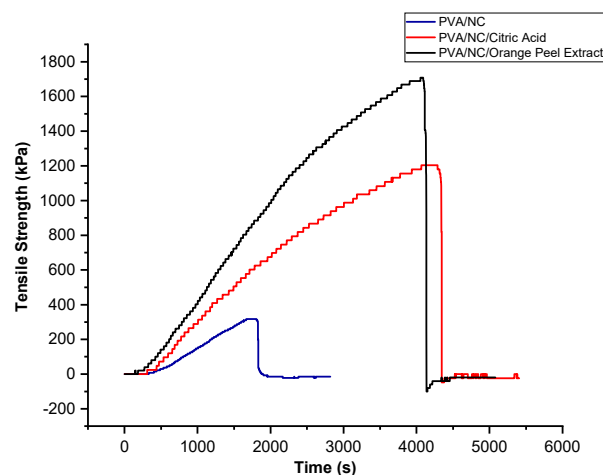


Fig 8. Tensile strength curves of bioplastic without the addition of citric acid and orange peel waste extract (blue line), bioplastic with citric acid (red line), and bioplastic with orange peel waste extract (black line)

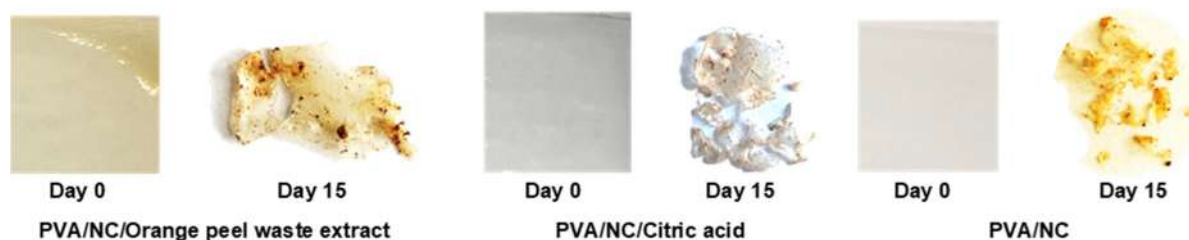


Fig 9. Biodegradation analysis on days 0 and 15

Table 6. Degradation percentage of bioplastic

Sample	% Degradation after 15 days
PVA/NC/Orange peel waste extract	78.44
PVA/NC/Citric acid	77.27
PVA/NC	86.27

The results of the degradation analysis of bioplastics without the addition of citric acid and orange peel waste extract had the highest degradation results, while bioplastics without the addition of citric acid and orange peel waste extract had a large rate of degradation analysis of the PVA and nanocellulose by the water is due to the leaching process of PVA and nanocellulose by the water. It caused the hydroxyl groups in PVA to have higher water sorption and solubility in water [49]. Furthermore, the bioplastic with the addition of citric acid and extract had a slower degradability result due to the antimicrobial effect of citric acid and extract [53]. The results of the analysis of the degradation of bioplastics with citric acid and orange peel extract had a lower value than the degradation analysis of bioplastics without the addition of citric acid and orange peel waste extract. The degradation of bioplastic with orange peel extract had a higher result than the bioplastic with citric acid. It is because the orange peel waste extract act as a biodegradation component that can give a higher oxygen permeability to microorganism [15].

■ CONCLUSION

Pinewood waste has an important application. Cellulose and nanocellulose can be extracted from it and used as an environmentally friendly bioplastic material. In this study, pinewood waste was bleached using the alkaline bleaching method to obtain cellulose, and nanocellulose was isolated after hydrolysis assisted by ultrasonication. Nanocellulose is used as a filler material with PVA to produce bioplastics. The integration of PVA, nanocellulose, and orange peel waste extract increases the tensile strength, modulus of elasticity, and elongation at the break of bioplastics compared to bioplastics without the addition of citric acid and orange peel waste extract. Tensile strength, modulus of elasticity, and elongation at break prove that bioplastic with the addition of orange peel extract has the highest performance. The addition of

orange peel waste extract also creates the degradability of bioplastics slower than that without the addition of it.

■ REFERENCES

- [1] Duhan, S.S., Khyalia, P., and Laura, J.S., 2022, "Plastic Waste Management in Rural Areas Around the World" in *Plastic Waste Management: Turning Challenges into Opportunities*, Eds. Pandey, S., and Manuja, S., Bharti Publications, New Delhi, India, 99–106.
- [2] Pathak, S., Sneha, C.L.R., and Mathew, B.B., 2014, Bioplastics: Its timeline based scenario & challenges, *J. Polym. Biopolym. Phys. Chem.*, 2 (4), 84–90.
- [3] Fan, Y.V., Jiang, P., Tan, R.R., Aviso, K.B., You, F., Zhao, X., Lee, C.T., and Klemeš, J.J., 2022, Forecasting plastic waste generation and interventions for environmental hazard mitigation, *J. Hazard. Mater.*, 424, 127330.
- [4] Darus, N., Tamimi, M., Tirawaty, S., Muchtazar, M., Trisyanti, D., Akib, R., Condorini, D., and Ranggi, K., 2020, An overview of plastic waste recycling in the urban areas of Java Island in Indonesia, *J. Environ. Sci. Sustainable Dev.*, 3 (2), 402–415.
- [5] Chamas, A., Moon, H., Zheng, J., Qiu, Y., Tabassum, T., Jang, J.H., Abu-Omar, M., Scott, S.L., and Suh, S., 2020, Degradation rates of plastics in the environment, *ACS Sustainable Chem. Eng.*, 8 (9), 3494–3511.
- [6] Razali, M.N., Mohd Isa, S.N.E., Md Salehan, N.A., Musa, M., Abd Aziz, M.A., Nour, A.H., and Mohd Yunus, R., 2020, Formulation of emulsified modification bitumen from industrial wastes, *Indones. J. Chem.*, 20 (1), 96–104.
- [7] Panda, A.K., Singh, R.K., and Mishra, D.K., 2010, Thermolysis of waste plastics to liquid fuel: A suitable method for plastic waste management and manufacture of value added products—A world prospective, *Renewable Sustainable Energy Rev.*, 14 (1), 233–248.
- [8] Gan, P.G., Sam, S.T., bin Abdullah, M.F., and Omar, M.F., 2020, Thermal properties of nanocellulose-reinforced composites: A review, *J. Appl. Polym. Sci.*, 137 (11), 48544.

- [9] Kargarzadeh, H., Mariano, M., Huang, J., Lin, N., Ahmad, I., Dufresne, A., and Thomas, S., 2017, Recent developments on nanocellulose reinforced polymer nanocomposites: A review, *Polymer*, 132, 368–393.
- [10] Ilyas, R.A., Sapuan, S.M., Norrahim, M.N.F., Tengku Yasim-Anuar, T.A., Kadier, A., Kalil, M.S., Atikah, M.S.N., Ibrahim, R., Asrofi, M., Abral, H., Nazrin, A., Syafiq, R., Aisyah, H.A., and Asyraf, M.R.M., 2020, "Nanocellulose/Starch Biopolymer Nanocomposites: Processing, Manufacturing, and Applications" in *Advanced Processing, Properties, and Applications of Starch and Other Bio-Based Polymers*, Elsevier, Cambridge, US, 65–88.
- [11] Kalia, S., Kaith, B.S., and Kaur, I., 2011, *Cellulose Fibers: Bio- and Nano-Polymer Composites: Green Chemistry and Technology*, Springer, Heidelberg, Berlin.
- [12] Awadhiya, A., Kumar, D., and Verma, V., 2016, Crosslinking of agarose bioplastic using citric acid, *Carbohydr. Polym.*, 151, 60–67.
- [13] Yoon, S.D., 2014, Cross-linked potato starch-based blend films using ascorbic acid as a plasticizer, *J. Agric. Food Chem.*, 62 (8), 1755–1764.
- [14] Tanjung, D.A., Jamarun, N., Arief, S., Aziz, H., Ritonga, A.H., and Isfa, B., 2022, Influence of LLDPE-g-MA on mechanical properties, degradation performance and water absorption of thermoplastic sago starch blends, *Indones. J. Chem.*, 22 (1), 171–178.
- [15] Marsi, N., Huzaisham, N.A., Hamzah, A.A., Zainudin, A.Z., Mohd Rus, A.Z., Leman, A.M., Rahmad, R., Mahmood, S., Abdul Rashid, A.H., Mohd Harun, D., and Darlis, N., 2019, Biodegradable plastic based on orange peel for packaging application, *JDSE*, 1 (2), 1–6.
- [16] Medina Jaramillo, C., Gutiérrez, T.J., Goyanes, S., Bernal, C., and Famá, L., 2016, Biodegradability and plasticizing effect of yerba mate extract on cassava starch edible films, *Carbohydr. Polym.*, 151, 150–159.
- [17] Hiremani, V.D., Goudar, N., Gasti, T., Khanapure, S., Vanjeri, V.N., Sataraddi, S., D'souza, O.J., Vootla, S.K., Masti, S.P., Malabadi, R.B., and Chougale, R.B., 2022, Exploration of multifunctional properties of *Piper betel* leaves extract incorporated polyvinyl alcohol-oxidized maize starch blend films for active packaging applications, *J. Polym. Environ.*, 30 (4), 1314–1329.
- [18] Nasihin, Z.D., Masruri, M., Warsito, W., and Srihardyastutie, A., 2020, Preparation of nanocellulose bioplastic with a gradation color of red and yellow, *IOP Conf. Ser.: Mater. Sci. Eng.*, 833, 012078.
- [19] Astuti, R., Deoranto, P., and Aula, M.M., 2019, Productivity and environmental performance: An empirical evidence from a furniture factory in Malang City, Indonesia, *IOP Conf. Ser.: Earth Environ. Sci.*, 230, 012064.
- [20] Shaheen, T.I., and Emam, H.E., 2018, Sonochemical synthesis of cellulose nanocrystals from wood sawdust using acid hydrolysis, *Int. J. Biol. Macromol.*, 107, 1599–1606.
- [21] Sari, R.M., Torres, F.G., Troncoso, O.P., De-la-Torre, G.E., and Gea, S., 2021, Analysis and availability of lignocellulosic wastes: Assessments for Indonesia and Peru, *Environ. Qual. Manage.*, 30 (4), 71–82.
- [22] Masruri, M., Pangestin, D.N., Ulfa, S.M., Riyanto, S., Srihardyastutie, A., and Rahman, M.F., 2018, A potent *Staphylococcus aureus* growth inhibitor of a dried flower extract of *Pinus merkusii* Jungh & De Vriese and copper nanoparticle, *IOP Conf. Ser.: Mater. Sci. Eng.*, 299, 012072.
- [23] Lusiana, S.E., Srihardyastutie, A., and Masruri, M., 2019, Cellulose nanocrystal (CNC) produced from the sulphuric acid hydrolysis of the pine cone flower waste (*Pinus merkusii* Jungh Et De Vriese), *J. Phys.: Conf. Ser.*, 1374, 012023.
- [24] Hadi, Y.S., Herliyana, E.N., Mulyosari, D., Abdillah, I.B., Pari, R., and Hiziroglu, S., 2020, Termite resistance of furfuryl alcohol and imidacloprid treated fast-growing tropical wood species as function of field test, *Appl. Sci.*, 10 (17), 6101.
- [25] Bauli, C.R., Rocha, D.B., de Oliveira, S.A., and Rosa, D.S., 2019, Cellulose nanostructures from wood waste with low input consumption, *J. Cleaner Prod.*, 211, 408–416.

- [26] Pradhan, D., Jaiswal, A.K., and Jaiswal, S., 2022, Emerging technologies for the production of nanocellulose from lignocellulosic biomass, *Carbohydr. Polym.*, 285, 119258.
- [27] Trache, D., Tarchoun, A.F., Derradji, M., Hamidon, T.S., Masruchin, N., Brosse, N., and Hussin, M.H., 2020, Nanocellulose: From fundamentals to advanced applications, *Front. Chem.*, 8, 392.
- [28] Hastuti, N., Kanomata, K., and Kitaoka, T., 2018, Hydrochloric acid hydrolysis of pulps from oil palm empty fruit bunches to produce cellulose nanocrystals, *J. Polym. Environ.*, 26 (9), 3698–3709.
- [29] Ioelovich, M., 2008, Cellulose as a nanostructured polymer: A short review, *BioResources*, 3 (4), 1403–1418.
- [30] Seta, F.T., An, X., Liu, L., Zhang, H., Yang, J., Zhang, W., Nie, S., Yao, S., Cao, H., Xu, Q., Bu, Y., and Liu, H., 2020, Preparation and characterization of high yield cellulose nanocrystals (CNC) derived from ball mill pretreatment and maleic acid hydrolysis, *Carbohydr. Polym.*, 234, 115942.
- [31] Agustin, M.B., Ahmmad, B., Alonzo, S.M.M., and Patriana, F.M., 2014, Bioplastic based on starch and cellulose nanocrystals from rice straw, *J. Reinf. Plast. Compos.*, 33 (24), 2205–2213.
- [32] Phanthong, P., Reubroycharoen, P., Hao, X., Xu, G., Abudula, A., and Guan, G., 2018, Nanocellulose: Extraction and application, *Carbon Resour. Convers.*, 1 (1), 32–43.
- [33] M'Hiri, N., Ioannou, I., Ghoul, M., and Boudhrioua, M., 2015, Proximate chemical composition of orange peel and variation of phenols and antioxidant activity during convective air drying, *J. New Sci.*, 9, 881-890.
- [34] Yufinanda, A.R., Nur Laila, A.N., Nurusalam, A.M.R., and Fajar, Y., 2019, Utilization of orange peel waste (*Citrus nobilis* Lour.) as biogas for electricity source in isolated areas, *Asia Young Scholar Summit (AYSS)*, Tianjin, China, May 17-18, 2019.
- [35] Hassan, F.A., Elkassas, N., Salim, I., El-Medany, S., Aboelenin, S.M., Shukry, M., Taha, A.E., Peris, S., Soliman, M., and Mahrose, K., 2021, Impacts of dietary supplementations of orange peel and tomato pomace extracts as natural sources for ascorbic acid on growth performance, carcass characteristics, plasma biochemicals and antioxidant status of growing rabbits, *Animals*, 11 (6), 1688.
- [36] Suhartini, M., Ernawati, E.E., Roshanova, A., Haryono, H., and Mellawati, J., 2020, Cellulose acetate of rice husk blend membranes: Preparation, morphology and application, *Indones. J. Chem.*, 20 (5), 1061–1069.
- [37] Mehmood, T., Khan, M.R., Shabbir, M.A., and Zia, M.A., 2018, Phytochemical profiling and HPLC quantification of citrus peel from different varieties, *Prog. Nutr.*, 20 (Suppl. 1), 279–288.
- [38] Hussein, Y., Loutfy, S.A., Kamoun, E.A., El-Moslamy, S.H., Radwan, E.M., and Elbehairi, S.E.I., 2021, Enhanced anti-cancer activity by localized delivery of curcumin form PVA/CNCs hydrogel membranes: Preparation and *in vitro* bioevaluation, *Int. J. Biol. Macromol.*, 170, 107–122.
- [39] Segal, L., Creely, J.J., Martin, A.E., and Conrad, C.M., 1959, An empirical method for estimating the degree of crystallinity of native cellulose using the X-ray diffractometer, *Text. Res. J.*, 29 (10), 786–794.
- [40] Bali, G., Meng, X., Deneff, J.I., Sun, Q., and Ragauskas, A.J., 2015, The effect of alkaline pretreatment methods on cellulose structure and accessibility, *ChemSusChem*, 8 (2), 275–279.
- [41] Cheng, Q., Wang, S., and Han, Q., 2009, Novel process for isolating fibrils from cellulose fibers by high-intensity ultrasonication. II. Fibril characterization, *J. Appl. Polym. Sci.*, 115 (5), 2756–2762.
- [42] Abitbol, T., Rivkin, A., Cao, Y., Nevo, Y., Abraham, E., Ben-Shalom, T., Lapidot, S., and Shoseyov, O., 2016, Nanocellulose, a tiny fiber with huge applications, *Curr. Opin. Biotechnol.*, 39, 76–88.
- [43] Popescu, M.C., Popescu, C.M., Lisa, G., and Sakata, Y., 2011, Evaluation of morphological and chemical aspects of different wood species by spectroscopy and thermal methods, *J. Mol. Struct.*, 988 (1-3), 65–72.
- [44] Sukmawan, R., Saputri, L.H., Rochmadi, R., and Rochardjo, H.S.B., 2019, The effects of the blending condition on the morphology, crystallinity, and

- thermal stability of cellulose microfibrils obtained from bagasse, *Indones. J. Chem.*, 19 (1), 166–175.
- [45] Bano, S., and Negi, Y.S., 2017, Studies on cellulose nanocrystals isolated from groundnut shells, *Carbohydr. Polym.*, 157, 1041–1049.
- [46] Tafflick, T., Schwendler, L.A., Rosa, S.M.L., Bica, C.I.D., and Nachtigall, S.M.B., 2017, Cellulose nanocrystals from acacia bark–Influence of solvent extraction, *Int. J. Biol. Macromol.*, 101, 553–561.
- [47] Gond, R.K., Gupta, M.K., and Jawaid, M., 2021, Extraction of nanocellulose from sugarcane bagasse and its characterization for potential applications, *Polym. Compos.*, 42 (10), 5400–5412.
- [48] Obele, C.M., Ejimofor, M.I., Atuanya, C.U., and Ibenta, M.E., 2021, Cassava stem cellulose (CSC) Nanocrystal for optimal methylene Blue Bio sorption with response surface design, *Curr. Res. Green Sustainable Chem.*, 4, 100067.
- [49] Ejara, T.M., Balakrishnan, S., and Kim, J.C., 2021, Nanocomposites of PVA/cellulose nanocrystals: Comparative and stretch drawn properties, *SPE Polym.*, 2 (4), 288–296.
- [50] Salleh, E., Muhamad, I.I., and Khairuddin, N., 2009, Structural characterization and physical properties of antimicrobial (AM) starch-based films, *World Acad. Sci. Eng. Technol.*, 55, 432–440.
- [51] Guimarães, M., Botaro, V.R., Novack, K.M., Teixeira, F.G., and Tonoli, G.H.D., 2015, Starch/PVA-based nanocomposites reinforced with bamboo nanofibrils, *Ind. Crops Prod.*, 70, 72–83.
- [52] Cano, A.I., Cháfer, M., Chiralt, A., and González-Martínez, C., 2015, Physical and microstructural properties of biodegradable films based on pea starch and PVA, *J. Food Eng.*, 167, 59–64.
- [53] Hernández-García, E., Vargas, M., González-Martínez, C., and Chiralt, A., 2021, Biodegradable antimicrobial films for food packaging: Effect of antimicrobials on degradation, *Foods*, 10 (6), 1256.

Electronic Structures of Graphene/MoS₂ Heterostructure: Effects of Stacking Orientation, Element Substitution, and Interlayer Distance

Dian Putri Hastuti^{*}, Kenji Nawa^{1,2}, and Kohji Nakamura¹

¹Graduate School of Engineering, Mie University, 1577 Kurimamachiya-cho, Tsu city, Mie 514-8507, Japan

²Research Center for Magnetic and Spintronic Materials, National Institute for Materials Science, 1-2-1 Sengen, Tsukuba, Ibaraki 305-0047, Japan

*** Corresponding author:**

tel: +81-8065026351
email: 420DE01@m.mie-u.ac.jp

Received: June 17, 2022
Accepted: October 20, 2022

DOI: 10.22146/ijc.75538

Abstract: Effects of stacking orientation, element substitution, and interlayer distance on electronic structures of graphene/MoS₂ heterostructures were investigated using first-principles calculations. The results predicted that the stacking orientation does not take a crucial role in changing the electronic structures in contrast to element substitution, which converts the system from semiconductor to metallic. A bandgap opening originating in a Dirac band of graphene is found to be governed by the interface distance between graphene and MoS₂ layers.

Keywords: graphene; transition-metal dichalcogenide; heterostructure; electronic structure; first-principles calculations

■ INTRODUCTION

Graphene, a stable two-dimensional (2D) material with a honeycomb structure [1-2], has attracted significant attention both in experimental and theoretical studies for decades [3]. Graphene has excellent properties in ultra-high intrinsic mobility and large electrical conductivity [4], making graphene have many potential applications in electronic devices, transparent electrodes, and spintronics devices [1,5]. The low intrinsic spin-orbit coupling (SOC) strength in graphene further provides an advantage in spin transports [6]. However, the absence of bandgap in graphene limits graphene usage in electronics due to its poor on/off ratio [7]. Although many efforts on the bandgap opening have been carried out previously in various ways, such as doping [8-10], creating multilayer graphene [11], and constructing bilayer graphene that demonstrates an electrically gate-controlled, continuously tunable bandgap of up to 250 meV [12], applying an electric field [5], and forming heterostructures [7,13-16], the understanding of the electronic structure of graphene, e.g., focusing the bandgap opening, is crucial for making graphene applicable in a broader area.

Transition-metal dichalcogenide (TMD) is a desired group of materials due to their outstanding properties in potential utilization, such as for electronic devices, optoelectronic devices [17], gas sensing [18] and energy storage [19]. MoS₂, as a member of TMD, shows intriguing mechanical and electrical properties [20]. Unlike graphene, two-dimensional MoS₂ is an excellent semiconductor with a 1.8 eV bandgap. Meanwhile, the bulk system has a 1.2 eV indirect bandgap [21-22]. It further notes that TMD possesses a strong intrinsic SOC of tens of meV compared to graphene [23]. A direct bandgap in two-dimensional MoS₂ could be a solution for bandgap opening on graphene and become the motivation to combine both materials as a heterostructure.

For years, keen interest has been given to heterostructure materials [15,24-27]. A number of the previous studies show exemplary implementations for a heterostructure of graphene and TMD, for example, graphene/MoS₂, applied to supercapacitors, gas sensors, spintronic devices, and electrochemical detectors of Morin [28-29]. Heterostructures of the others, graphene/MoSe₂ and graphene/WTe₂, are potential materials in the optoelectronic field [30-31],

graphene/MoTe₂ and graphene/WSe₂ are also beneficial in photodetector devices [32-33], and graphene/WS₂ is a prospective material for nanoelectronics and optoelectronic devices [34-35].

In the present work, we have systematically performed density functional theory (DFT) calculations to clarify the effects of the electronic structure of graphene/MoS₂ on stacking, element substitution, and interlayer distance. We find that stacking orientation is not significantly affecting the electronic structures, which contrasts with how element substitution and interlayer distance successfully tune the electronic structures. The findings are essential to navigating the tuning of electronic properties of graphene/MoS₂ heterostructure since they directly impact practical applications.

■ COMPUTATIONAL DETAILS

First-principles calculations using the full-potential linearized augmented plane-wave (FLAPW) method that treats a single slab geometry [36-37] were carried out to investigate the electronic structures of graphene/MoS₂. Generalized gradient approximation (GGA) was employed as exchange correlation [38] and to account for long-range dispersion correction, and the DFT-D2 method was introduced [39]. The core states were treated fully relativistically, and the valence states were treated semi-relativistically, where spin-orbit coupling was incorporated using the second variational method [40]. The LAPW basis with a cutoff of $|\mathbf{k}+\mathbf{G}| \leq 5.0$ Bohr⁻¹ and muffin-tin (MT) sphere radii of 2.6 Bohr for Mo, 1.9 Bohr for S, Se, and Te, and 1.2 Bohr for C were used, and lattice harmonics with angular momenta up to $l = 8$ for Mo and S, and 6 for C were employed to expand the charge density, potential, and wavefunctions. A 15×15 k-point mesh was used for self-consistent field (SCF) calculations. Atomic force calculations fully optimized all the heterostructures.

As for models, graphene/MoS₂ heterostructures with two different later-stacking orientations, namely, C_s stacking for C atoms stacked on the top of S atoms and C_{Mo} stacking for C atoms stacked on the top of Mo atoms, as illustrated in Fig. 1. These stacking orientations were considered based on the previous study which analyzed

the most stable stacking for bilayer MoS₂ [41]. The structural periodicity in graphene and MoS₂ layers sets with two ratios, 1:1 and 4:3, i.e., the 1:1 heterostructure consists of 1×1 cell of both graphene and MoS₂ while the 4:3 heterostructure is 4×4 of graphene and 3×3 of MoS₂. For the element substitution, then, three graphene/TMD heterostructures, consisting of graphene/MoS₂, graphene/MoSe₂, and graphene/MoTe₂, respectively, were considered. Finally, the dependence of interlayer distance between graphene and MoS₂ in the heterostructure was analyzed by varying the distance from 2.6 to 3.6 Å.

■ RESULTS AND DISCUSSION

Effect of Stacking Orientation

We first confirmed that the calculated lattice constants of single monolayers of graphene and MoS₂ are 3.16 and 2.46 Å, respectively, which agree with the previous works [42]. Fig. 1 displays the optimized 1:1 and 4:3 heterostructures of graphene/MoS₂ for the C_s and C_{Mo} stackings. In the 1:1 heterostructure, for both C_s and C_{Mo} stackings, the bond lengths of C-C in the graphene layer and Mo-Mo atoms in the MoS₂ layer are 1.73 and 3.09 Å, respectively, and the interlayer distances between graphene and MoS₂ layers are 3.38 Å. Even in the 4:3 heterostructure, the interlayer distances in the C_s

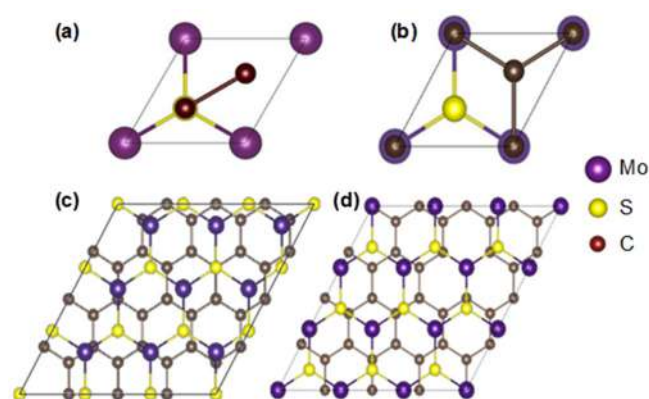


Fig 1. Top view of arrangements of graphene/MoS₂ heterostructure: (a) 1:1 heterostructure with C_s stacking, (b) 1:1 heterostructure with C_{Mo} stacking, (c) 4:3 heterostructure with C_s stacking, and (d) 4:3 heterostructure with C_{Mo} stacking. Purple, yellow, and brown balls represent Mo, S, and C atoms, respectively

and C_{M_0} stackings are 4.47 and 3.50 Å, respectively, and the present results correspond to the previous works [43-44]. Despite the change in the stacking orientations, the structural properties remain the same.

Fig. 2 shows the calculated band structures and densities of states (DOSs) of the 1:1 and 4:3 heterostructures in the C_S and C_{M_0} stackings. The identical feature of the Dirac cone in the band structures and DOSs can be seen in each heterostructure regardless of the stackings. The bandgap at K in both stackings is distinguishable, as shown in the figure, where the bandgaps of the C_S and C_{M_0} stackings are 19 and 8.5 meV. The total energy in the C_{M_0} stacking for the 1:1 heterostructure is slightly lower than that in the C_S one by only 0.872 meV/cell. It occurs in the 4:3 heterostructure, where the total energy of C_{M_0} stacking is lower than that on the C_S by 0.54 meV/cell.

Fig. 3 shows the charge density plot for C_{M_0} and C_S stacking orientation for an optimized 1:1 structure. To identify the presence of charge transfer between layers, we calculated the total charge for each atom for MoS_2 and graphene as a unit cell and the total charge for MoS_2 -graphene as a heterostructure and compared the values,

which later showed no differences.

The physical origin of the bandgap that emerged in the graphene/ MoS_2 is due to the hybridization between the graphene and MoS_2 layers, where weak interaction bonds the layers, proven by no charge transfer between both layers. Thus, the stacking orientation does not affect their electronic structures qualitatively, as both have identical band structure and does not change the character of the material. However, stacking orientation changes the band structure quantitatively as the band gap differs from each other. This result also corresponds to the previous study, which studied the 5:4 and 4:4 heterostructures [45].

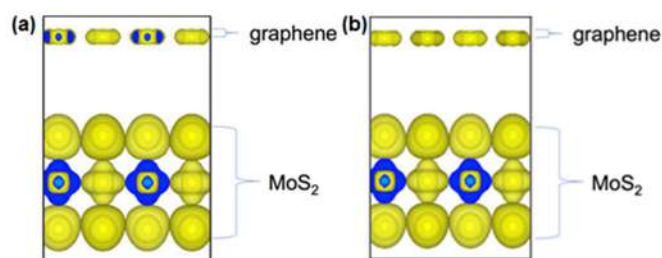


Fig 2. Charge density for optimized 1:1 structure (a) C_{M_0} stacking orientation and (b) C_S stacking orientation. The yellow color shows positive charges

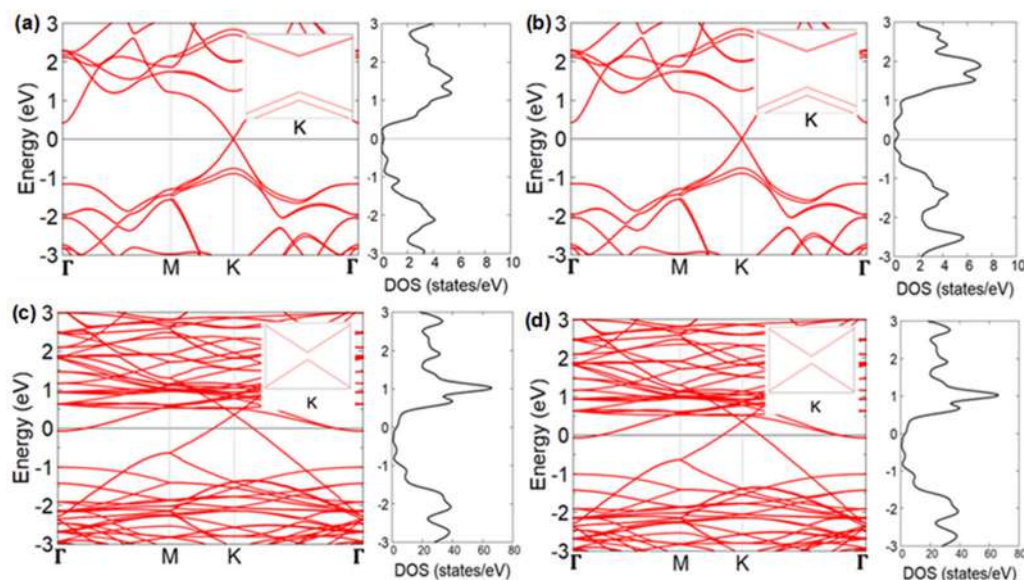


Fig 3. Calculated band structures and DOSs of graphene/ MoS_2 heterostructures under different structure arrangements: (a) 1:1 structure with C_S stacking orientation, (b) 1:1 heterostructure with C_{M_0} stacking orientation, (c) 4:3 structure with C_S stacking orientation, and (d) 4:3 structure with C_{M_0} stacking orientation. The insets show a bandgap at K in each structure

Effect of Element Substitution

We next present the results for three different heterostructures, graphene/MoS₂, graphene/MoSe₂, and graphene/MoTe₂, to examine the effect of element substitution. As for the graphene/MoS₂, we chose the C_{Mo} stacking with the lowest total energy. The calculated interlayer distances and bandgaps for the three heterostructures are given in Table 1, and the band structures are shown in Fig. 4. From the calculated band structures, we observe that the bandgap in the Dirac cone at K of each system varies in nominal values. The graphene/MoTe₂ show a metallic characteristic. Enlarged pictures along the G-M-K-G direction show that the Dirac cone for the graphene/MoTe₂ is shifting toward the valence bands.

The calculated optimized interlayer distances for the three heterostructures are given in Table 1. The three heterostructures have different values of the optimized interlayer distances, where the graphene/MoS₂ has the most significant distance of 3.38 Å compared to those in the graphene/MoSe₂ (3.28 Å) and graphene/MoTe₂ (3.19 Å). Alongside the optimized interlayer distance, the calculated bandgaps located on the Dirac cone in graphene are also given in Table 1. Meanwhile, the graphene/MoS₂ has the lowest bandgap of 8.5 meV, while graphene/MoSe₂ increases to 15 meV due to the interlayer reduction. For the graphene/MoTe₂, where the interlayer

distance further decreases, the system becomes metallic, and the energy state of the Dirac cone shifts to 0.8 eV below the Fermi level.

For further analysis, we calculated the projected density of states (PDOS) as shown in Fig. 5. Based on these graphs, we can see that the orbitals which have significant contributions to valence and conduction bands are d orbitals attributed in Mo.

Table 1. Calculated interlayer distance (d) and bandgap (ΔE) of optimized graphene/MoS₂, graphene/MoSe₂, and graphene/MoTe₂ heterostructure

Elements	d (Å)	ΔE (meV)
graphene/MoS ₂	3.38	8.5
graphene/MoSe ₂	3.28	15

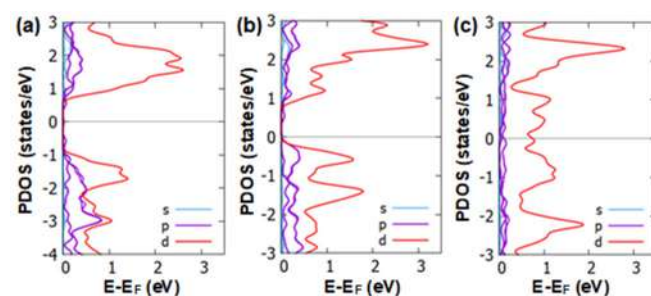


Fig 4. Calculated PDOS of (a) graphene/MoS₂, (b) graphene/MoSe₂, and (c) graphene/MoTe₂. Different color of plotting shows different orbital. Blue and purple represent the s and p orbital for C, S, Se and Te atoms, and red represents the d orbital for Mo atoms

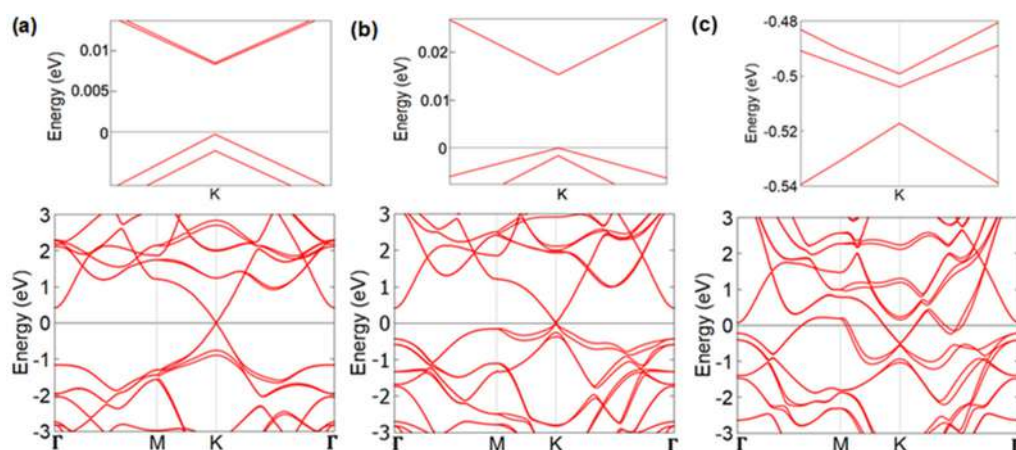


Fig 5. Calculated electronic structures of graphene/TMD heterostructures: (a) graphene/MoS₂, (b) graphene/MoSe₂, and (c) graphene/MoTe₂. Enlarged figures of Dirac bands are shown at the top of the figures. Zero energy sets to the top of the valence band in (a) and (b), and that in (c) sets to Fermi level

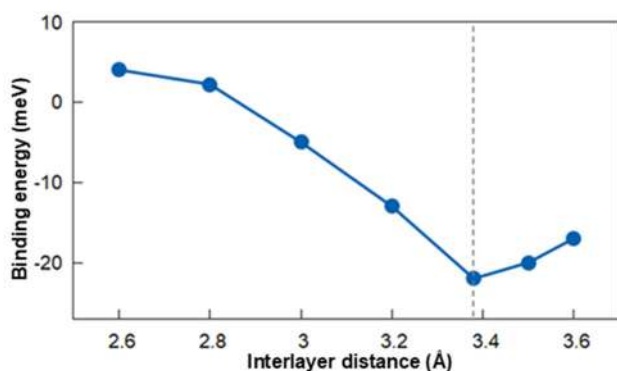


Fig 6. Binding energy (E_B) variation for 1:1 graphene/MoS₂ heterostructure concerning the interlayer distance. The dashed grey vertical line indicates the optimized interlayer distance with the lowest binding energy of -22 meV

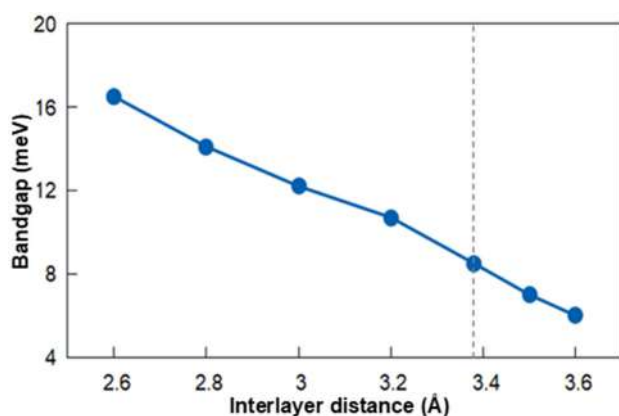


Fig 7. The calculated band gap of 1:1 graphene/MoS₂ heterostructure as a function of interlayer distance. The dashed grey vertical line portrays the optimized interlayer distance of the system at 3.38 Å with a band gap of 8.5 meV

Effect of Interlayer Distance

In a comprehensive analysis of interlayer distance, binding energy (E_B) between the graphene and MoS₂ layers was calculated by $E_B = E_{M/G} - (E_M + E_G)$, where $E_{M/G}$, E_M , and E_G are the total energies for the graphene/MoS₂, monolayer MoS₂, and monolayer graphene, respectively. The results are shown in Fig. 6. At an optimized interlayer distance of 3.38 Å, the calculated E_B reaches its lowest value of -22 meV, which corresponds with the previous work [46].

The dependence of interlayer distance on the bandgap at the K point in the graphene/MoS₂ is shown in

Fig. 7, where the interlayer distance varies from 2.6 to 3.6 Å. As seen in the figure, at the optimum state of 3.38 Å of interlayer distance, the bandgap is 8.5 meV. The band gap is found to decrease when the interlayer distance increases gradually. Thus, widening interlayer distance between graphene and MoS₂ layers diminishes the orbital hybridization between the layers, leading to a pure graphene-like electronic structure with no bandgap.

CONCLUSION

We performed a first-principles calculation to investigate the effects of the electronic structures of graphene/MoS₂ heterostructure on stacking orientation, element substitution, and interlayer distance bonded through weak van der Waals interaction. We find that the electronic structures of graphene/MoS₂ are unlikely to be affected by stacking orientation. On the other hand, element substitution modifies the electronic properties, transforming the system to a metal characteristic. At last, the bandgap opening originating from the Dirac band in the graphene/MoS₂ may be tuned by the interlayer distance modification.

ACKNOWLEDGMENTS

This work is partly supported by Grants-in-Aid for Scientific Research (Grants numbers JP21K03444, JP21H04562, JP19K03716, and JP22K14290); the Tatematsu Foundation; the Okasan-Kato Foundation; the Research Foundation for the Electrotechnology of Chubu; the Data-Science Research Center for Material, Quantum, and Measurement Technologies, Mie University; and the Center for Spintronics Research Network, Osaka University. Numerical calculations were partially performed using computational facilities at Research Institute for Information Technology, Kyushu University and NIMS.

REFERENCES

- [1] Novoselov, K.S., Geim, A.K., Morozov, S.V., Jiang, D., Katsnelson, M.I., Grigorieva, I.V., Dubonos, S.V., and Firsov, A.A., 2005, Two-dimensional gas of massless Dirac fermions in graphene, *Nature*, 438 (7065), 197–200.

- [2] Novoselov, K.S., Geim, A.K., Morozov, S.V., Jiang, D., Zhang, Y., Dubonos, S.V., Grigorieva, I.V., and Firsov, A.A., 2004, Electric field effect in atomically thin carbon films, *Science*, 306 (5696), 666–669.
- [3] Chung, C., Kim, Y.K., Shin, D., Ryoo, S.R., Hong, B.H., and Min, D.H., 2013, Biomedical applications of graphene and graphene oxide, *Acc. Chem. Res.*, 46 (10), 2211–2224.
- [4] Zhang, W., Chuu, C.P., Huang, J.K., Chen, C.H., Tsai, M.L., Chang, Y.H., Liang, C.T., Chen, Y.Z., Chueh, Y.L., He, J.H., Chou, M.Y., and Li, L.J., 2015, Ultrahigh-gain photodetectors based on atomically thin graphene-MoS₂ heterostructures, *Sci. Rep.*, 4, 3826.
- [5] Castro, E.V., Novoselov, K.S., Morozov, S.V., Peres, N.M.R., dos Santos, J.M.B.L., Nilsson, J., Guinea, F., Geim, A.K., and Castro Neto, A.H., 2007, Biased bilayer graphene: Semiconductor with a gap tunable by the electric field effect, *Phys. Rev. Lett.*, 99 (21), 216802.
- [6] Avsar, A., Tan, J.Y., Taychatanapat, T., Balakrishnan, J., Koon, G.K.W., Yeo, Y., Lahiri, J., Carvalho, A., Rodin, A.S., O'Farrell, E.C.T., Eda, G., Castro Neto, A.H., and Özyilmaz, B., 2014, Spin-orbit proximity effect in graphene, *Nat. Commun.*, 5 (1), 4875.
- [7] Fu, S., Wang, D., Ma, Z., Liu, G., Zhu, X., Yan, M., and Fu, Y., 2021, The first-principles study on the halogen-doped graphene/MoS₂ heterojunction, *Solid State Commun.*, 334-335, 114366.
- [8] Tang, S., Wu, W., Xie, X., Li, X., and Gu, J., 2017, Band gap opening of bilayer graphene by graphene oxide support doping, *RSC Adv.*, 7 (16), 9862–9871.
- [9] Tayyab, M., Hussain, A., Adil, W., Nabi, S., and Asif, Q.A., 2020, Band-gap engineering of graphene by Al doping and adsorption of Be and Br on impurity: A computational study, *Comput. Condens. Matter*, 23, e00463.
- [10] Matis, B.R., Burgess, J.S., Bulat, F.A., Friedman, A.L., Houston, B.H., and Baldwin, J.W., 2012, Surface doping and band gap tunability in hydrogenated graphene, *ACS Nano*, 6 (1), 17–22.
- [11] Hirahara, T., Ebisuoka, R., Oka, T., Nakasuga, T., Tajima, S., Watanabe, K., Taniguchi, T., and Yagi, R., 2018, Multilayer graphene shows intrinsic resistance peaks in the carrier density dependence, *Sci. Rep.*, 8 (1), 13992.
- [12] Zhang, Y., Tang, T.T., Girit, C., Hao, Z., Martin, M.C., Zettl, A., Crommie, M.F., Shen, Y.R., and Wang, F., 2009, Direct observation of a widely tunable bandgap in bilayer graphene, *Nature*, 459 (7248), 820–823.
- [13] Cao, X., Shi, J.J., Zhang, M., Jiang, X.H., Zhong, H.X., Huang, P., Ding, Y.M., and Wu, M., 2016, Band gap opening of graphene by forming heterojunctions with the 2D carbonitrides nitrogenated holey graphene, g-C₃N₄, and g-CN: Electric field effect, *J. Phys. Chem. C*, 120 (20), 11299–11305.
- [14] Gmitra, M., and Fabian, J., 2017, Proximity effects in bilayer graphene on monolayer WSe₂: Field-effect spin valley locking, spin-orbit valve, and spin transistor, *Phys. Rev. Lett.*, 119 (14), 146401.
- [15] Singh, S., Espejo, C., and Romero, A.H., 2018, Structural, electronic, vibrational, and elastic properties of graphene/MoS₂ bilayer heterostructures, *Phys. Rev. B*, 98 (15), 155309.
- [16] Yu, X., Zhao, G., Gong, S., Liu, C., Wu, C., Lyu, P., Maurin, G., and Zhang, N., 2020, Design of MoS₂/Graphene van der Waals heterostructure as highly efficient and stable electrocatalyst for hydrogen evolution in acidic and alkaline media, *ACS Appl. Mater. Interfaces*, 12 (22), 24777–24785.
- [17] Yin, Z., Li, H., Li, H., Jiang, L., Shi, Y., Sun, Y., Lu, G., Zhang, Q., Chen, X., and Zhang, H., 2012, Single-layer MoS₂ phototransistors, *ACS Nano*, 6 (1), 74–80.
- [18] Lee, E., Yoon, Y.S., and Kim, D.J., 2018, Two-dimensional transition metal dichalcogenides and metal oxide hybrids for gas sensing, *ACS Sens.*, 3 (10), 2045–2060.
- [19] Peng, Q., and De, S., 2013, Outstanding mechanical properties of monolayer MoS₂ and its application in elastic energy storage, *Phys. Chem. Chem. Phys.*, 15 (44), 19427–19437.
- [20] Han, S.A., Bhatia, R., and Kim, S.W., 2015, Synthesis, properties and potential applications of

- two-dimensional transition metal dichalcogenides, *Nano Convergence*, 2 (1), 17.
- [21] Splendiani, A., Sun, L., Zhang, Y., Li, T., Kim, J., Chim, C.Y., Galli, G., and Wang, F., 2010, Emerging photoluminescence in monolayer MoS₂, *Nano Lett.*, 10 (4), 1271–1275.
- [22] Zhang, Z.Y., Si, M.S., Wang, Y.H., Gao, X.P., Sung, D., Hong, S., and He, J., 2014, Indirect-direct band gap transition through electric tuning in bilayer MoS₂, *J. Chem. Phys.*, 140 (17), 174707.
- [23] Nevalaita, J., and Koskinen, P., 2018, Atlas for the properties of elemental two-dimensional metals, *Phys. Rev. B*, 97 (3), 035411.
- [24] Baik, S.S., Im, S., and Choi, H.J., 2017, Work function tuning in two-dimensional MoS₂ field-effect-transistors with graphene and titanium source-drain contacts, *Sci. Rep.*, 7 (1), 45546.
- [25] Zhang, F., Li, W., Ma, Y., Tang, Y., and Dai, X., 2017, Tuning the Schottky contacts at the graphene/WS₂ interface by electric field, *RSC Adv.*, 7 (47), 29350–29356.
- [26] Roy, K., Padmanabhan, M., Goswami, S., Sai, T.P., Ramalingam, G., Raghavan, S., and Ghosh, A., 2013, Graphene-MoS₂ hybrid structures for multifunctional photoresponsive memory devices, *Nat. Nanotechnol.*, 8 (11), 826–830.
- [27] Han, S.W., Kwon, H., Kim, S.K., Ryu, S., Yun, W.S., Kim, D.H., Hwang, J.H., Kang, J.S., Baik, J., Shin, H.J., and Hong, S.C., 2011, Band-gap transition induced by interlayer van der Waals interaction in MoS₂, *Phys. Rev. B*, 84 (4), 045409.
- [28] Gmitra, M., Kochan, D., Högl, P., and Fabian, J., 2016, Trivial and inverted Dirac bands and the emergence of quantum spin Hall states in graphene on transition-metal dichalcogenides, *Phys. Rev. B*, 93 (15), 155104.
- [29] Lee, C.S., and Kim, T.H., 2021, Large-scale preparation of MoS₂/graphene composites for electrochemical detection of morin, *ACS Appl. Nano Mater.*, 4 (7), 6668–6677.
- [30] Wen, X., Chen, H., Wu, T., Yu, Z., Yang, Q., Deng, J., Liu, Z., Guo, X., Guan, J., Zhang, X., Gong, Y., Yuan, J., Zhang, Z., Yi, C., Guo, X., Ajayan, P.M., Zhuang, W., Liu, Z., Lou, J., and Zheng, J., 2018, Ultrafast probes of electron-hole transitions between two atomic layers, *Nat. Commun.*, 9 (1), 1859.
- [31] Liu, Y., Liu, C., Wang, X., He, L., Wan, X., Xu, Y., Shi, Y., Zhang, R., and Wang, F., 2018, Photoresponsivity of an all-semimetal heterostructure based on graphene and WTe₂, *Sci. Rep.*, 8 (1), 12840.
- [32] Zhang, K., Fang, X., Wang, Y., Wan, Y., Song, Q., Zhai, W., Li, Y., Ran, G., Ye, Y., and Dai, L., 2017, Ultrasensitive near-infrared photodetectors based on a graphene-MoTe₂-graphene vertical van der Waals heterostructure, *ACS Appl. Mater. Interfaces*, 9 (6), 5392–5398.
- [33] Gao, A., Liu, E., Long, M., Zhou, W., Wang, Y., Xia, T., Hu, W., Wang, B., and Miao, F., 2016, Gate-tunable rectification inversion and photovoltaic detection in graphene/WSe₂ heterostructures, *Appl. Phys. Lett.*, 108 (22), 223501.
- [34] Akinwande, D., Petrone, N., and Hone, J., 2014, Two-dimensional flexible nanoelectronics, *Nat. Commun.*, 5 (1), 5678.
- [35] Huo, N., Wei, Z., Meng, X., Kang, J., Wu, F., Li, S.S., Wei, S.H., and Li, J., 2015, Interlayer coupling and optoelectronic properties of ultrathin two-dimensional heterostructures based on graphene, MoS₂ and WS₂, *J. Mater. Chem. C*, 3 (21), 5467–5473.
- [36] Wimmer, E., Krakauer, H., Weinert, M., and Freeman, A.J., 1981, Full-potential self-consistent linearized-augmented-plane-wave method for calculating the electronic structure of molecules and surfaces: O₂ molecule, *Phys. Rev. B*, 24 (2), 864.
- [37] Weinert, M., Wimmer, E., and Freeman, A.J., 1982, Total-energy all-electron density functional method for bulk solids and surfaces, *Phys. Rev. B*, 26 (8), 4571–4578.
- [38] Perdew, J.P., Burke, K., and Ernzerhof, M., 1996, Generalized gradient approximation made simple, *Phys. Rev. Lett.*, 77 (18), 3865–3868.
- [39] Bučko, T., Hafner, J., Lebègue, S., and Ángyán, J.G., 2010, Improved description of the structure of molecular and layered crystals: Ab initio DFT

- calculations with van der Waals corrections, *J. Phys. Chem. A*, 114 (43), 11814–11824.
- [40] Nakamura, K., Ito, T., Freeman, A.J., Zhong, L., and Fernandez-de-Castro, J., 2003, Enhancement of magnetocrystalline anisotropy in ferromagnetic Fe films by intra-atomic noncollinear magnetism, *Phys. Rev. B*, 67 (1), 014420.
- [41] Tao, P., Guo, H.H., Yang, T., and Zhang, Z.D., 2014, Stacking stability of MoS₂ bilayer: An ab initio study, *Chin. Phys. B*, 23 (10), 106801.
- [42] Rasmussen, F.A., and Thygesen, K.S., 2015, Computational 2D materials database: Electronic structure of transition-metal dichalcogenides and oxides, *J. Phys. Chem. C*, 119 (23), 13169–13183.
- [43] Sachs, B., Britnell, L., Wehling, T.O., Eckmann, A., Jalil, R., Belle, B.D., Lichtenstein, A.I., Katsnelson, M.I., and Novoselov, K.S., 2013, Doping mechanisms in graphene-MoS₂ hybrids, *Appl. Phys. Lett.*, 103 (25), 251607.
- [44] Singh, A.K., Kumar, P., Late, D.J., Kumar, A., Patel, S., and Singh, J., 2018, 2D layered transition metal dichalcogenides (MoS₂): Synthesis, applications and theoretical aspects, *Appl. Mater. Today*, 13, 242–270.
- [45] Ebnonnasir, A., Narayanan, B., Kodambaka, S., and Ciobanu, C.V., 2014, Tunable MoS₂ bandgap in MoS₂-graphene heterostructures, *Appl. Phys. Lett.*, 105 (3), 031603.
- [46] Liu, B., Wu, L.J., Zhao, Y.Q., Wang, L.Z., and Cai, M.Q., 2016, First-principles investigation of the Schottky contact for the two-dimensional MoS₂ and graphene heterostructure, *RSC Adv.*, 6 (65), 60271–60276.

Supplementary Data

This supplementary data is a part of a paper entitled “Synthesis, Characterization, and Theoretical Study of a New Organotellurium Ligands Containing Amino Group”.

The spectra details (FT-IR and MS) of the prepared organotellurium compounds

(4-Amino-[1,1'-biphenyl]-3-yl)mercury(II) chloride (A): -

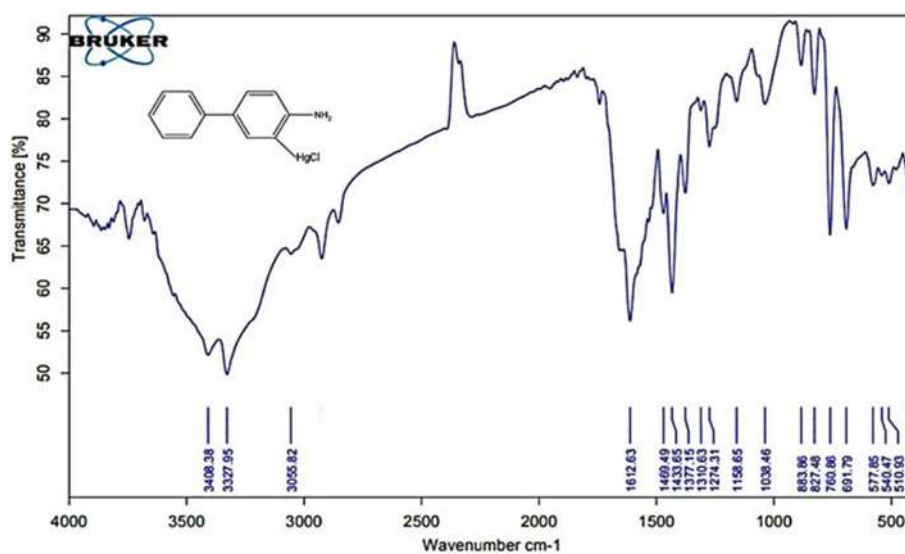


Fig S1. Infrared spectrum of the compound A

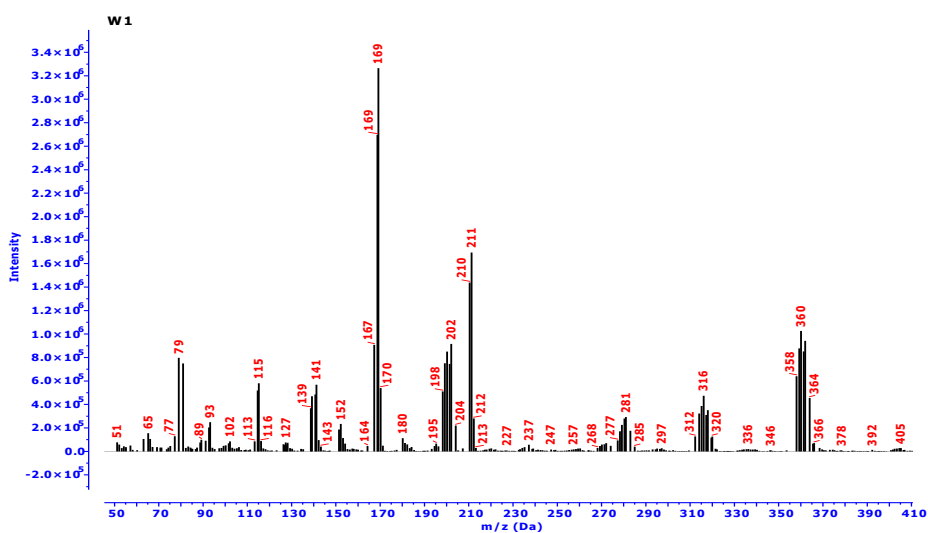


Fig S2. The mass spectrum of the compound A

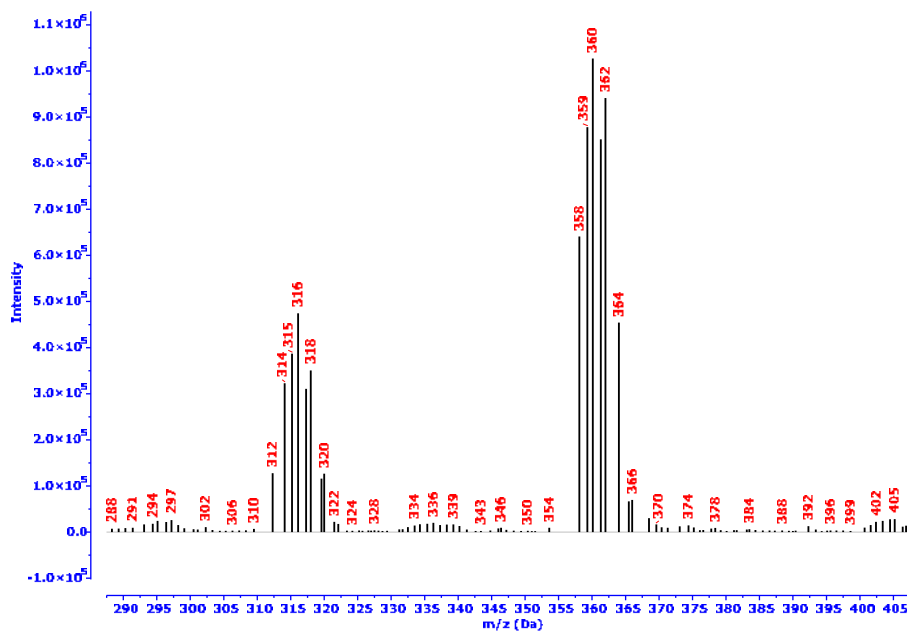
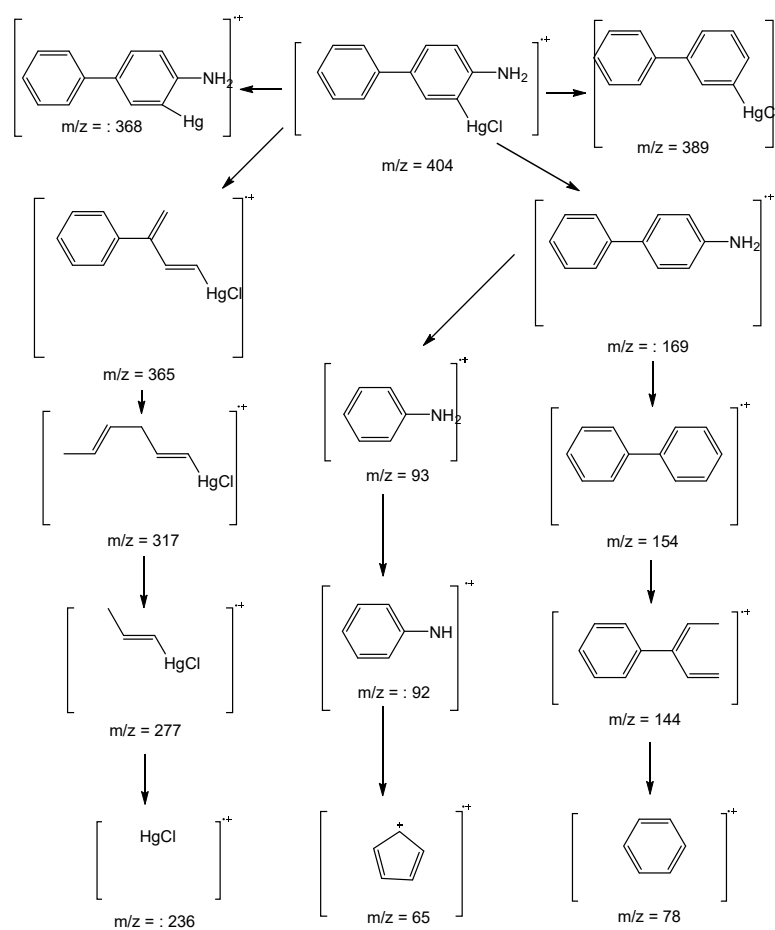


Fig S3. Expanded mass spectrum of the compound A



Scheme S1. Mechanical fragmentation of the compound A

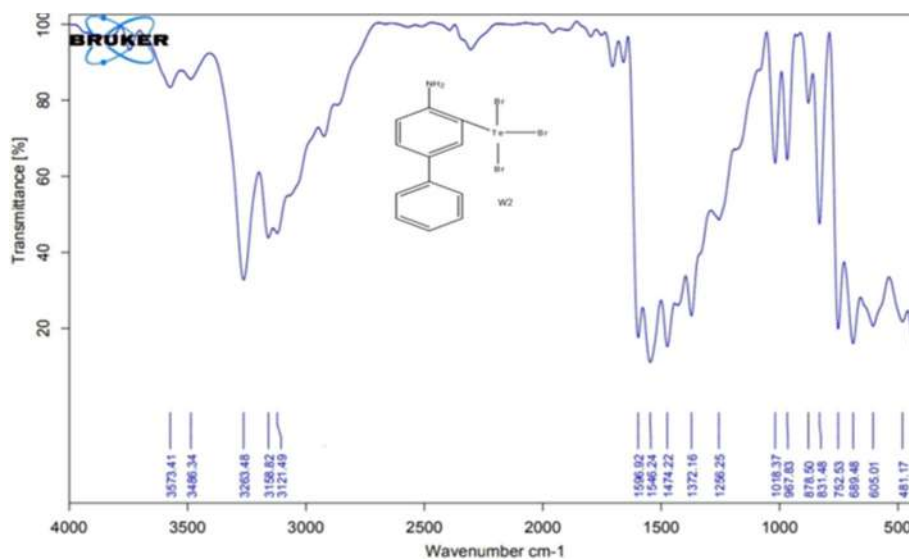
3-(Tribromo- λ^4 -tellanyl)-[1,1'-biphenyl]-4-amine (B): -

Fig S4. Infrared spectrum of the compound B

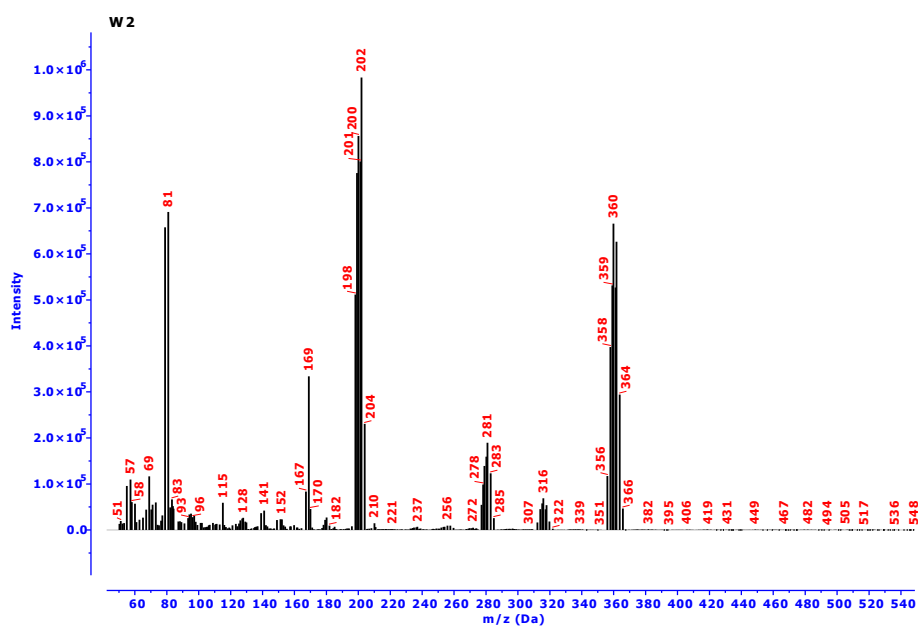


Fig S5. The mass spectrum of the compound B

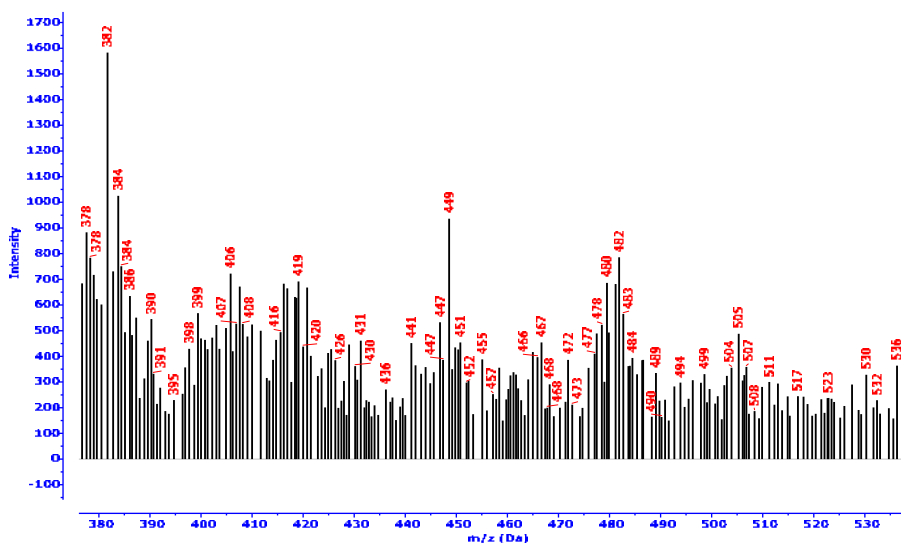
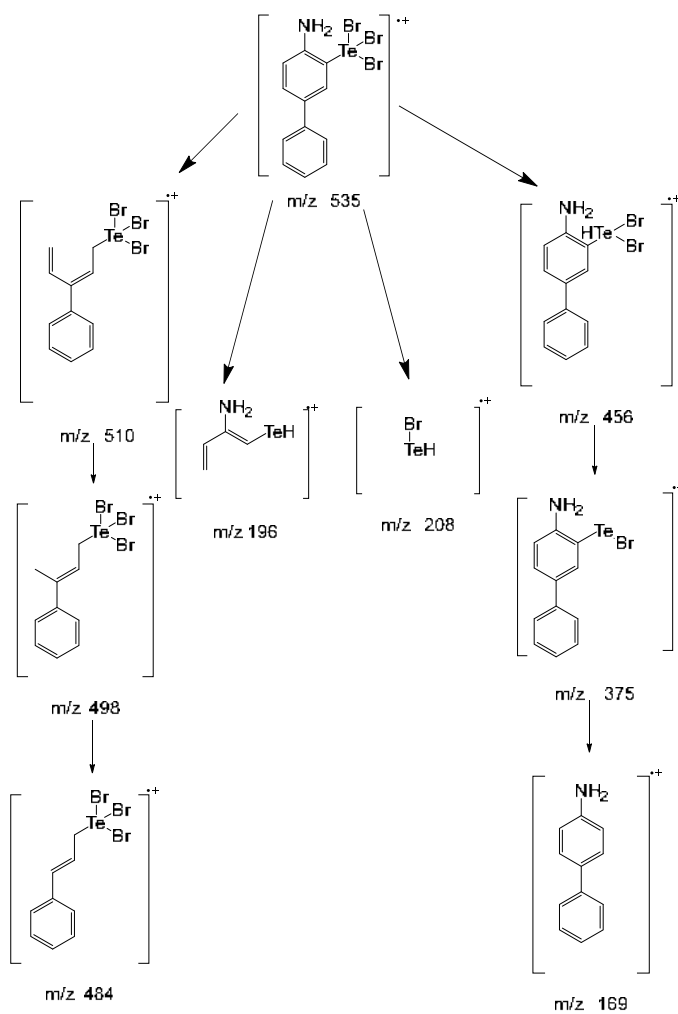


Fig S6. Expanded mass spectrum of the compound B



Scheme S2. Mechanical fragmentation of the compound B

3,3'-(Dibromo- λ^4 -tellanediyl)bis([1,1'-biphenyl]-4-amine) (C): -

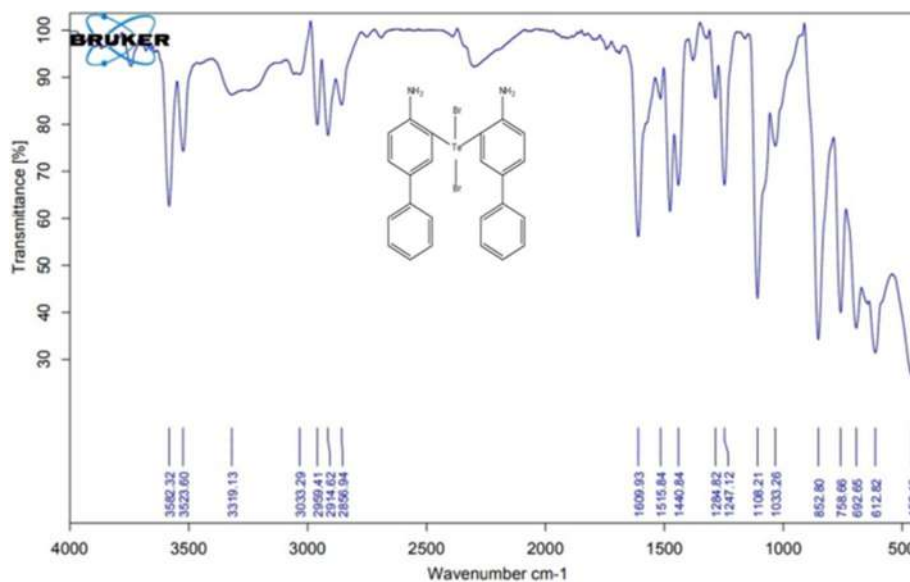


Fig S7. Infrared spectrum of the compound C

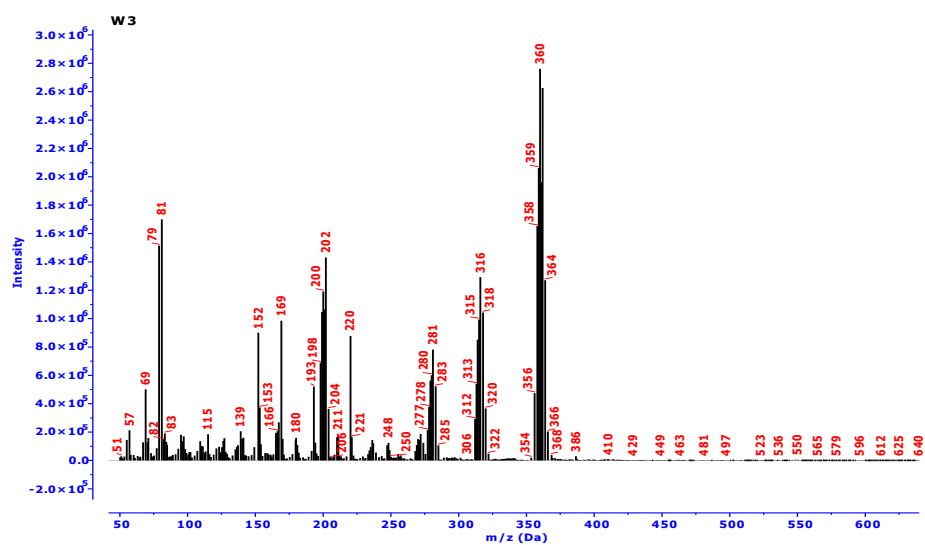


Fig S8. The mass spectrum of the compound C

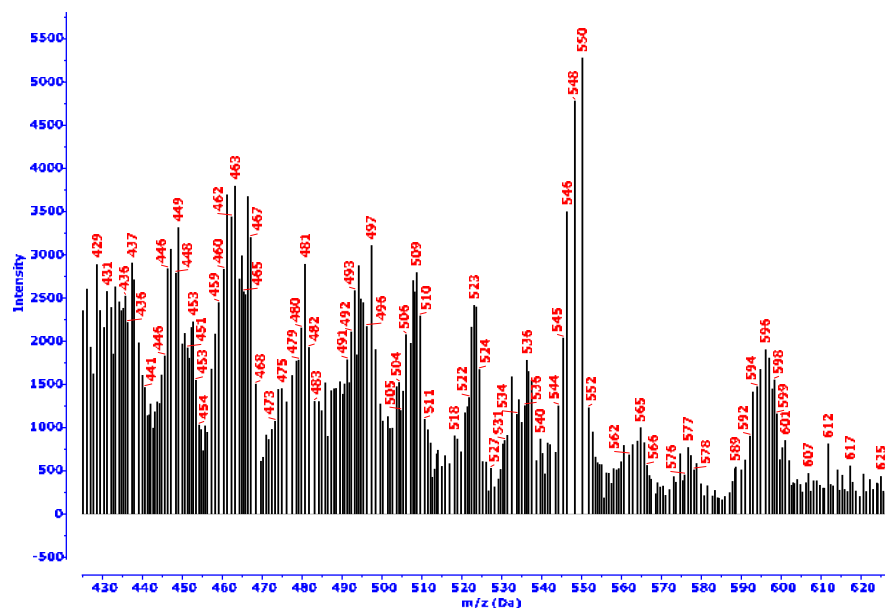
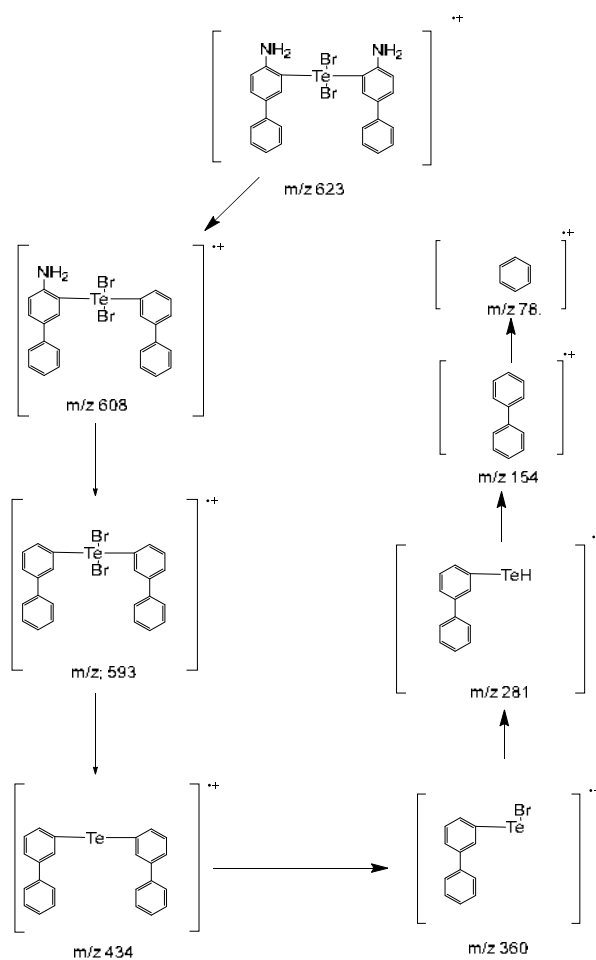


Fig S9. Expanded mass spectrum of the compound C



Scheme S3. Mechanical fragmentation of the compound C

3,3''-tellurobis([1,1'-biphenyl]-4-amine) (D): -

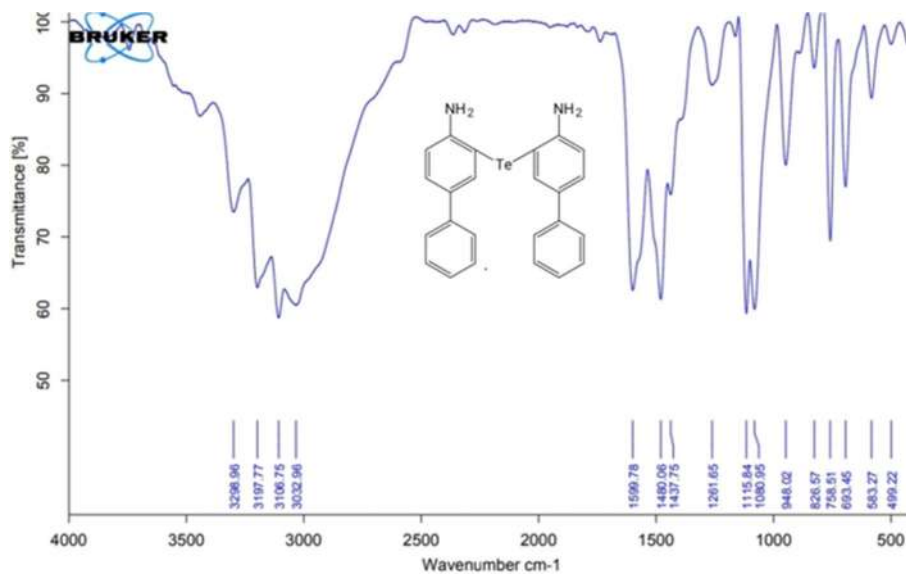


Fig S10. Infrared spectrum of the compound D

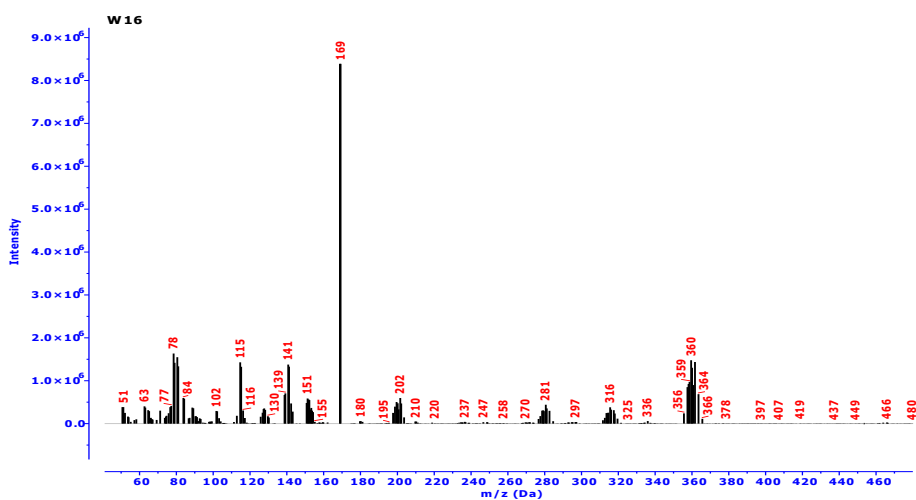


Fig S11. The mass spectrum of the compound D

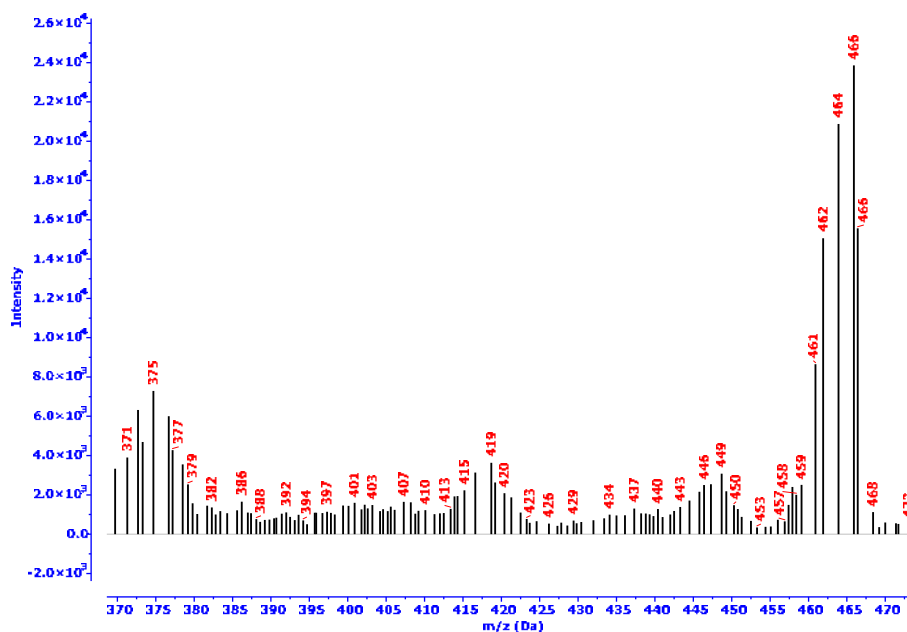
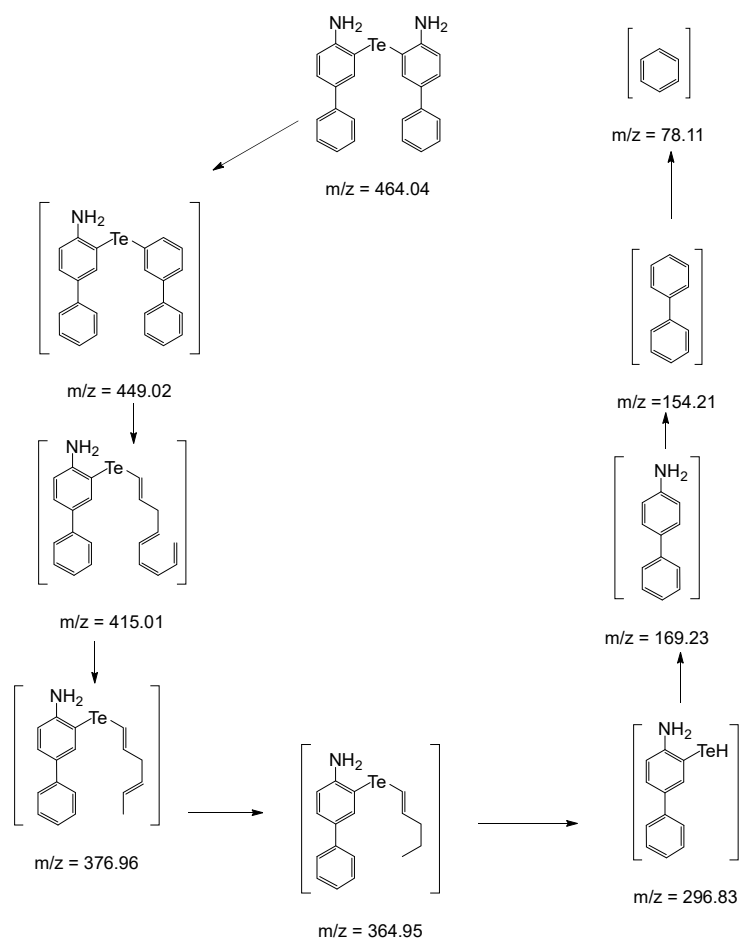


Fig S12. Expanded mass spectrum of the compound D



Scheme S4. Mechanical fragmentation of the compound D

3,3''-ditellanediyl bis([1,1'-biphenyl]-4-amine) (E): -

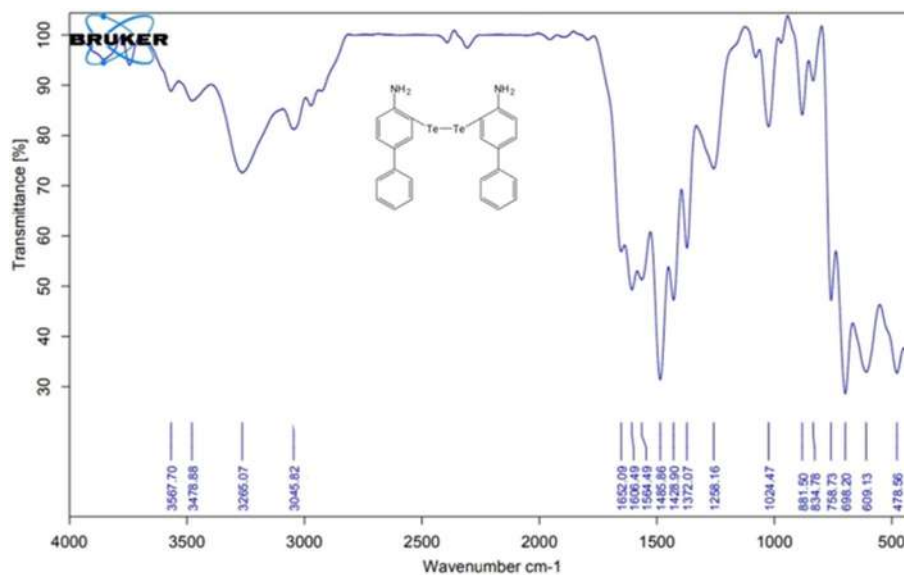


Fig S13. Infrared spectrum of the compound E

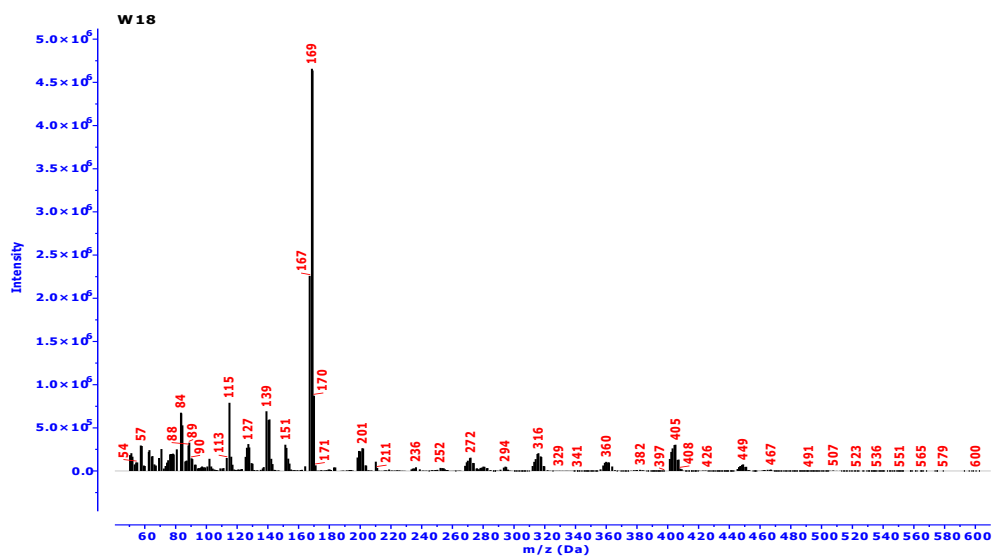


Fig S14. The mass spectrum of the compound E

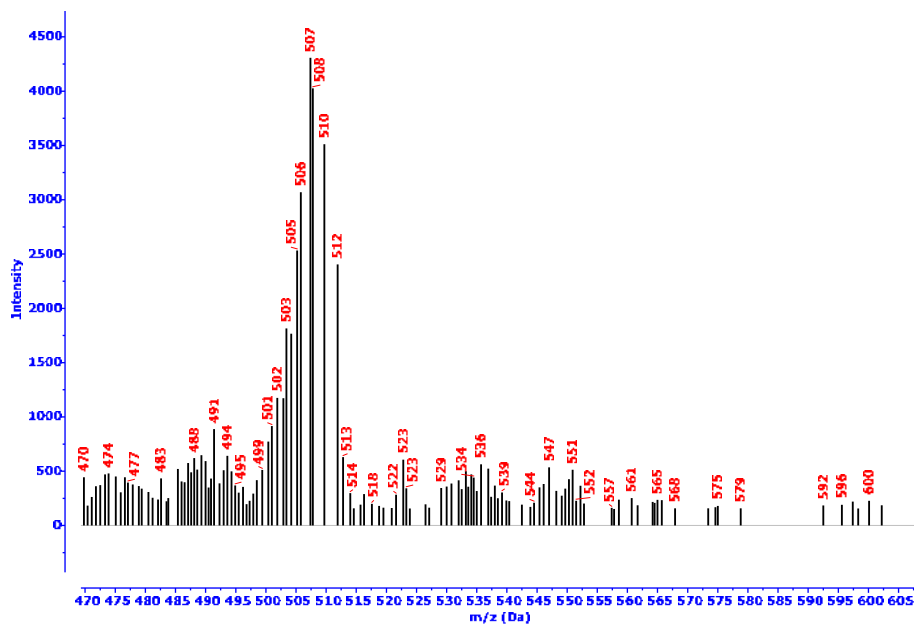
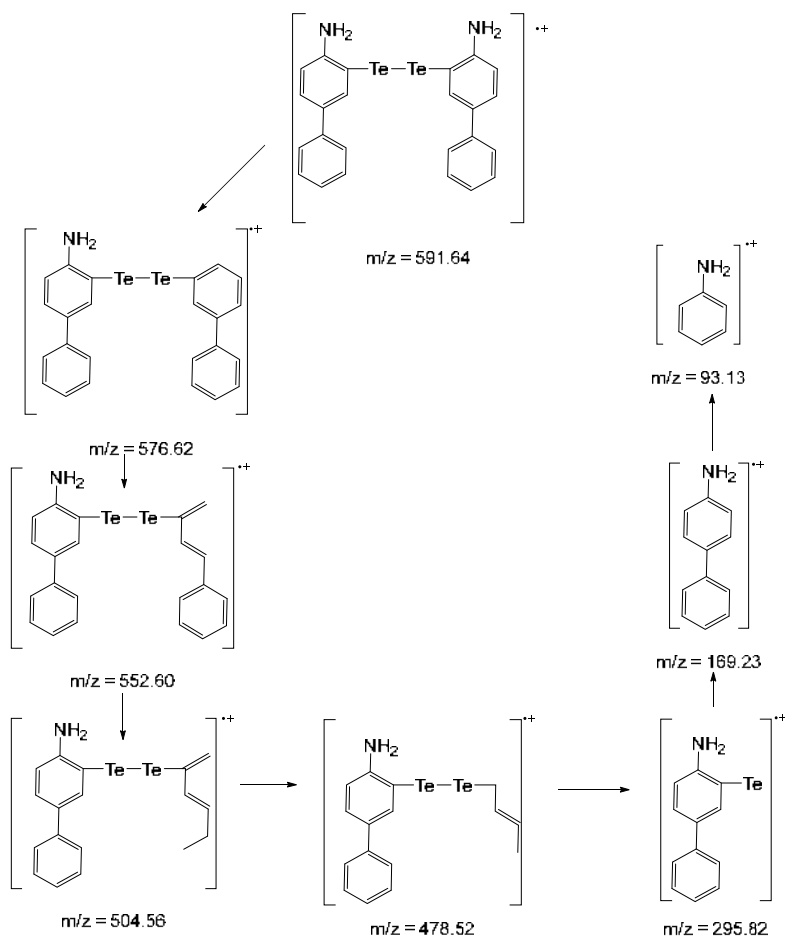


Fig S15. Expanded mass spectrum of the compound E



Scheme S5. Mechanical fragmentation of the compound E

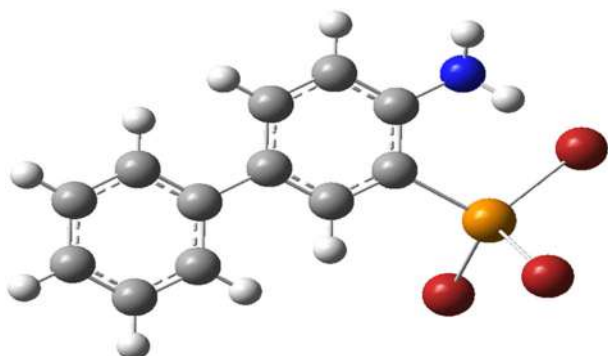


Fig S16. Molecular structure of compound B

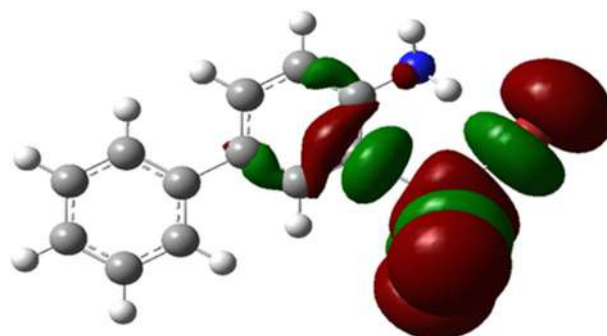


Fig S17. Molecular orbital (HOMO) of compound B

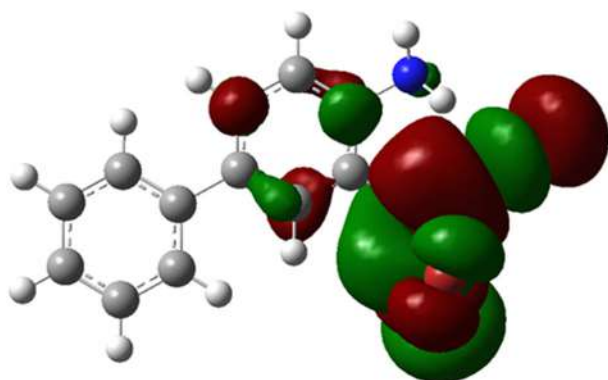


Fig S18. Molecular orbital (LUMO) of compound C

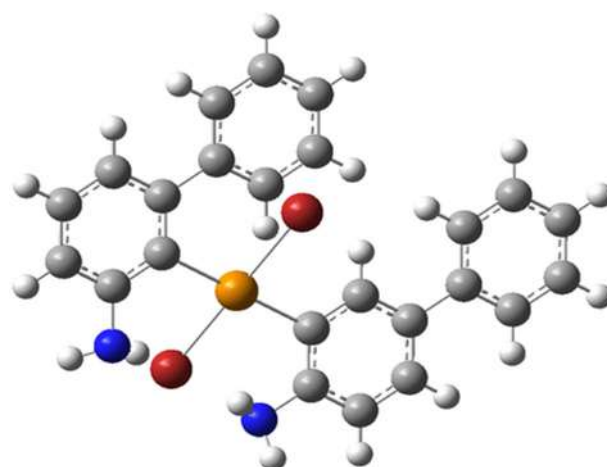


Fig S19. Molecular structure of compound C

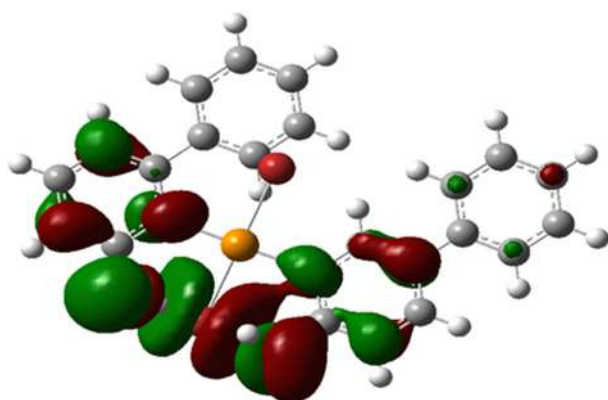


Fig S20. Molecular orbital (HOMO) of compound C

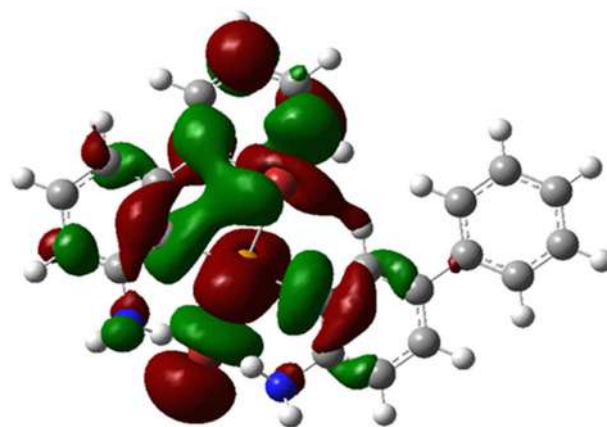


Fig S21. Molecular orbital (LUMO) of compound C

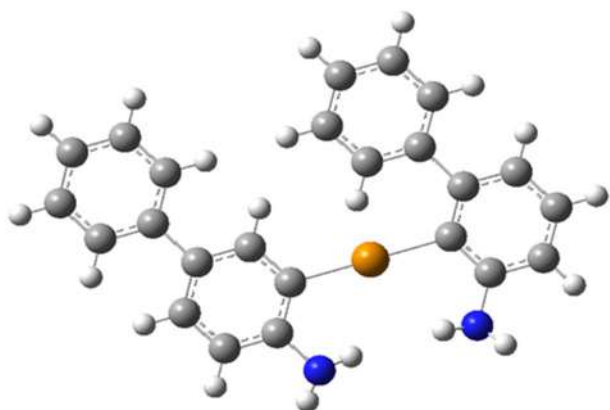


Fig S22. Molecular structure of compound D

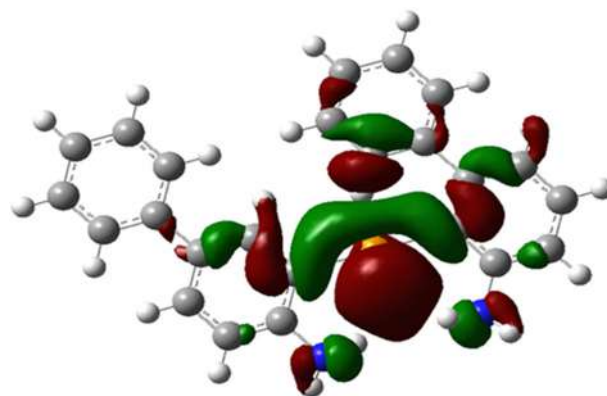


Fig S23. Molecular orbital (HOMO) of compound D

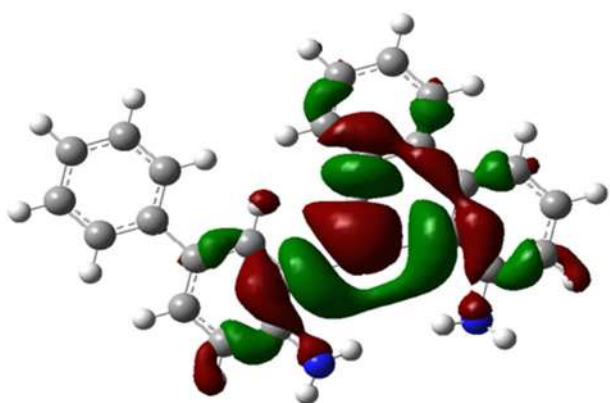


Fig S24. Molecular orbital (LUMO) of compound D

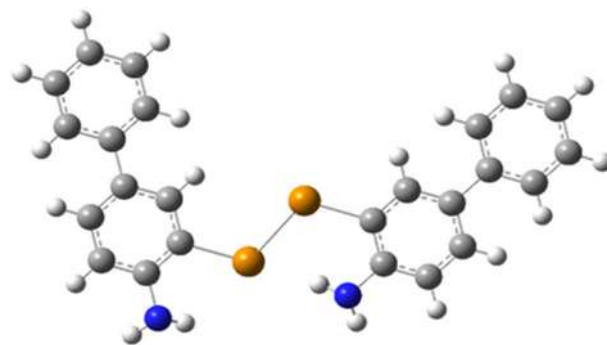


Fig S25. Molecular structure of compound E

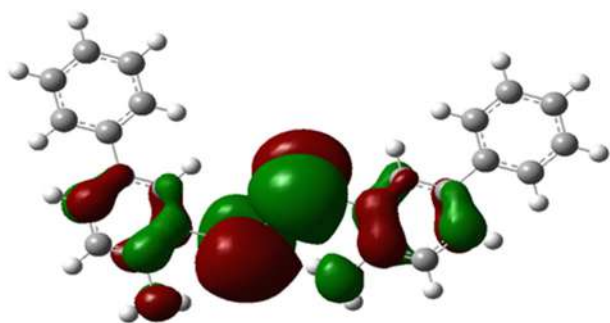


Fig 26. Molecular orbital (HOMO) of compound E

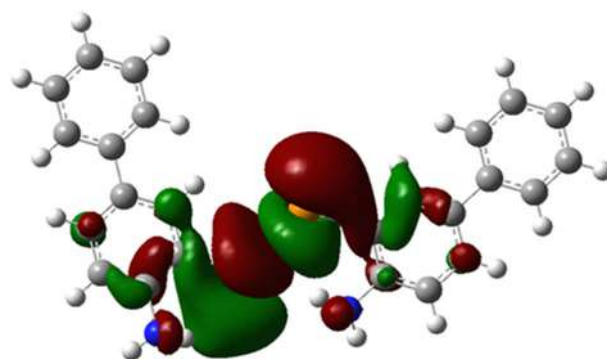


Fig S27. Molecular orbital (LUMO) of compound E

Table S1. The most important fissions of the compound A

Molecular ion	<i>m/z</i>	Molecular ion	<i>m/z</i>
[C ₁₂ H ₁₀ NHgCl] ⁺	404	[C ₆ H ₉ HgCl] ⁺	317
[C ₁₂ H ₁₁ N] ⁺	169	[C ₁₂ H ₁₀] ⁺	154
[C ₁₀ H ₉ HgCl] ⁺	365	[C ₃ H ₅ HgCl] ⁺	277

Table S2. The most important fissions of the compound **B**

Molecular ion	<i>m/z</i>	Molecular ion	<i>m/z</i>
[C ₁₂ H ₁₀ Br ₃ NTe] ⁺	535	[C ₄ H ₇ NTe] ⁺	196
[TeHBr] ⁺	202	[C ₁₂ H ₁₁ Br ₂ NTe] ⁺	456
[C ₁₁ H ₁₁ Br ₃ Te] ⁺	510	[C ₁₂ H ₁₁ N] ⁺	169

Table S3. The most important fissions of the compound **C**

Molecular ion	<i>m/z</i>	Molecular ion	<i>m/z</i>
[C ₂₄ H ₂₀ N ₂ Br ₂ Te] ⁺	623	[C ₂₄ H ₁₈ Br ₂ Te] ⁺	593
[C ₁₂ H ₉ BrTe] ⁺	360	[C ₂₄ H ₁₈ Te] ⁺	434
[C ₂₄ H ₁₉ Br ₂ NTe] ⁺	608	[C ₁₂ H ₁₀ Te] ⁺	281

Table S4. The most important fissions of the compound **D**

Molecular ion	<i>m/z</i>	Molecular ion	<i>m/z</i>
[C ₂₄ H ₂₀ N ₂ Te] ⁺	464	[C ₂₁ H ₂₁ NTe] ⁺	415
[C ₁₂ H ₁₁ N] ⁺	169	[C ₁₇ H ₁₉ NTe] ⁺	364
[C ₂₄ H ₁₉ NTe] ⁺	449	[C ₆ H ₆] ⁺	77

Table S5. The most important fissions of the compound **E**

Molecular ion	<i>m/z</i>	Molecular ion	<i>m/z</i>
[C ₂₄ H ₂₀ N ₂ Te ₂] ⁺	591	[C ₂₂ H ₁₉ NTe ₂] ⁺	552
[C ₁₂ H ₁₁ N] ⁺	169	[C ₁₂ H ₁₀ NTe] ⁺	296
[C ₂₄ H ₁₉ NTe ₂] ⁺	576	[C ₆ H ₇ N] ⁺	93

Synthesis, Characterization, and Theoretical Study of a New Organotellurium Ligands Containing Amino Group

Gofran Safi Mokhtar¹ and Nuha Hussain Al-Saadawy^{2*}

¹Faculty of Archaeology, University of Thi-Qar, Thi-Qar, 64001, Iraq

²Department of Chemistry, College of Science, University of Thi-Qar, Thi-Qar, 64001, Iraq

* Corresponding author:

email: nuh.hussain@sci.utq.edu.iq

Received: June 20, 2022

Accepted: August 2, 2022

DOI: 10.22146/ijc.75583

Abstract: The aim of the current study is to prepare organomercury and organotellurium compounds containing amino groups such as [1,1'-biphenyl]-4-amine and their derivatives by a mercuriation reaction. The research includes the preparation of a new organotellurium compound based on [1,1'-biphenyl]-4-amine. $C_{12}H_{10}NHgCl$ (A) was obtained by mercuriation reaction to [1,1'-biphenyl]-4-amine by mercuric acetate and lithium chloride. $C_{12}H_{10}Br_3NTe$ (B), $C_{24}H_{20}N_2Br_2Te$ (C), $C_{24}H_{20}N_2Te$ (D), and $C_{24}H_{20}N_2Te_2$ (E) were prepared by different reactions to get the corresponding compounds. All the prepared ligands were characterized by using infrared spectroscopy and mass spectroscopy. DFT has been obtained by the basis set 3-21G to investigate the molecular structure of the new prepared organotellurium compounds. HOMO and LUMO surfaces, geometrical structure, and energy gap have been obtained throughout the geometry optimization. Finally, the electron affinity, electronegativity, electrophilicity, ionization potential, and lower case of organotellurium compounds have been calculated and discussed. The result of the chemical analysis showed that it agreed with the proposed chemical structures, and a theoretical study using DFT has concluded that more stability of the prepared organotellurium compounds.

Keywords: organotellurium; 4-amino biphenyl; ditelluride; organyl tellurium dibromide

■ INTRODUCTION

Tellurium belongs to the family of chalcogens in the sixth group of the periodic table, which is the oxygen group itself. It is a metalloid with atomic number 52 and has five known oxidation states -1, -2, +2, +4, and +6 [1]. Tellurium is a toxic element, but it has existed in the human diet, where it is used in some side metabolic processes [2]. The low natural abundance of the element tellurium has partly been reflected in the scant interest attached to it. Based on old studies, the structures and reactions of tellurium compounds can be extrapolated by studying the behavior of analogs of other lighter chalcogens such as Sulfur and Selenium. In fact, recent results and well-established observations clearly show that this assumption or concept is invalid; the emerging importance of the unique properties of tellurium compounds from a variety of their known and potential

applications in both inorganic and organic chemistry [3-4]. Tellurium is derived from the Latin word *tellus*, which means earth, and was discovered by the scientist, Reichenstein, in 1782 from ores extracted from the gold regions of Transylvania [5-6]. For the element tellurium, there are a number of stable isotopes, of which there are eight stable isotopes (Te-120, Te-122, Te-123, Te-124, Te-125, Te-126, Te-128, and Te-130) in addition to twenty-one synthetic isotopes that take the cluster shape in their structures [7-8]. Despite the relative abundance of tellurium in the human body, nevertheless, the diverse activities of tellurium agents in both cancerous and normal cells are important, though highly complex [2,9]. The element tellurium is similar to selenium in terms of its structural formula, but it has a more distinct metallic character than selenium. It has an anisotropic crystalline structure consisting of long helical chains of atoms

arranged symmetrically, each atom having four bonds with its nearest neighbors in adjacent chains [10]. Tellurium is a great significant element for research purposes in the modern era of its entry into the manufacture of nano-devices [11-12]. Tellurium compounds are also used in the field of the plastics and rubber industry to add hardness to electronic industries, optics, and the ceramics industry. Also, it is utilized in petroleum refining and petrochemical industries. Other uses of tellurium are in the manufacture of crackers and fireworks as an explosive material [13-15].

In this work, we synthesized a new organometallic compound type organomercury and organotellurium namely (4-amino-[1,1'-biphenyl]-3-yl)mercury(II) chloride hereinafter referred to as compound **A**, 3-(tribromo- λ^4 -tellanyl)-[1,1'-biphenyl]-4-amine hereinafter referred to as compound **B**, 3,3'-(dibromo- λ^4 -tellanediyl)bis([1,1'-biphenyl]-4-amine) hereinafter referred to as compound **C**, 3,3''-tellurobis([1,1'-biphenyl]-4-amine) hereinafter referred to as compound **D**, and 3,3''-ditellanediyl bis([1,1'-biphenyl]-4-amine) hereinafter referred to as compound **E**, then the molecular structure of organotellurium compound (**B-E**) has been investigated theoretically by the DFT with a good agreement of theoretical results.

■ EXPERIMENTAL SECTION

Materials

The chemicals used in this study included ethanol absolute, bromine, sodium metal, lithium chloride (Sigma-Aldrich), glacial acetic acid, mercuric acetate, hydrazine hydrate, dioxane (Fluka), chloroform, potassium hydroxide, tellurium powder (BDH), hydrochloric acid (HGB).

Instrumentation

Infra-red spectra were recorded with KBr disks utilizing an FTIR spectrophotometer Shimadzu model 8400 S in reach $4000-250\text{ cm}^{-1}$. The mass spectra were performed using a HAT-8200 analyzer at the ionizing potential of 70 eV (Central Laboratory, University of Tehran, Iran). The melting point was measured using the Melting point SMP 31 model.

Procedure

Synthesis of (4-amino-[1,1'-biphenyl]-3-yl)mercury(II) chloride (A)

Firstly, 8.3 g (0.05 mol) of 4-amino biphenyl was dissolved in 50 mL of absolute ethanol, then added to it 15.7 g (0.05 mol) of mercury acetate dissolved in 50 mL of absolute ethanol, and the mixture was refluxed for 12 h with the follow-up of the reaction via thin-layer chromatography TLC. After the reaction was completed, 2.5 g (0.06 mol) of lithium chloride was added, and the reaction was continued again for 1 h then the solution was filtered. White crystals were formed on the filter paper and then washed via hot ethanol several times to get rid of the remains of unwanted materials. The weight of produced compound was 15.3 g, the yield was 77%, and the melting point of the compound was measured after completely drying was $170-172\text{ }^\circ\text{C}$.

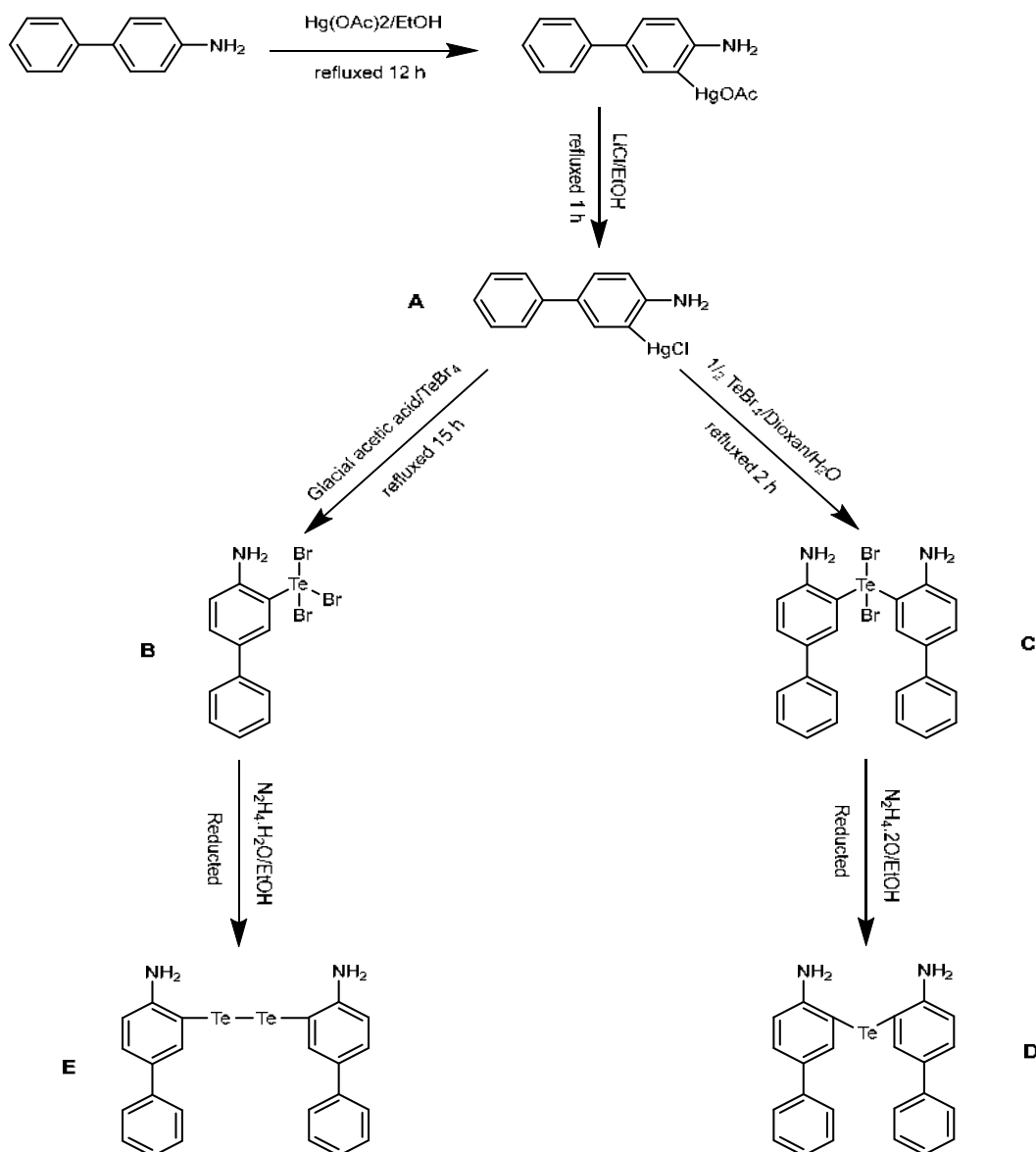
FT-IR using KBr: $\nu(\text{C-H})$ Aromatic = 3055 cm^{-1} , $\nu(\text{C-N})$ Aromatic = 1310 cm^{-1} , $\nu(\text{C=C})$ Aromatic = 1612 cm^{-1} , $\nu(\text{NH}_2)$ = (3327 cm^{-1} , 3408 cm^{-1}).

Mass spectra: The MS calculated for **A** $\text{C}_{12}\text{H}_{10}\text{NHgCl}$ (404.26) was found to be as follows: $\text{M}^+ + 1$ (405); MS/MS (m/z): 365, 317, 277, 236, 169, 154, 144, 78.

These data were shown in Scheme 1 and S1, Table 1, 2 and S1, Fig. S1, S2 and S3.

Synthesis of 3-(tribromo- λ^4 -tellanyl)-[1,1'-biphenyl]-4-amine (B)

Add 16 g of compound **A** with 18 g (0.04 mol) of TeBr_4 and both materials in their solid state after grinding them well (the reaction here was at a ratio of 1:1 mole, then add 400 mL of glacial acetic acid. The mixture was refluxed for 15 h, and the reaction progress was followed up by TLC to assure the completion of the reaction. In the first hours of the reaction, the color of the solution turns brown, and after the end of the heating period, we filter the solution under hot conditions. The filtered mixture then has left to cool down, where we notice the formation of dark brown crystals that are the compound 3-(tribromo- λ^4 -tellanyl)-[1,1'-biphenyl]-4-amine to be prepared; separated by normal filtration. The precipitate was washed on a filter paper with hot ethanol, and the precipitate was dried and collected. The weight of produced compound was 13 g,



Scheme 1. Synthesis of organotellurium compounds A-E

and the yield was 60%. The dissociation of the compound was at a degree 161–163 °C.

FT-IR using KBr: $\nu(\text{C-H})$ Aromatic = 3121 cm^{-1} , $\nu(\text{C-N})$ Aromatic = 1256 cm^{-1} , $\nu(\text{C=C})$ Aromatic = 1596 cm^{-1} , $\nu(\text{NH}_2)$ = (3486 cm^{-1} , 3576 cm^{-1}), $\nu(\text{C-Te})$ = 481 cm^{-1} , $\nu(\text{Br-Te})$ = 689 cm^{-1} .

Mass spectra: The MS calculated for **B** $\text{C}_{12}\text{H}_{10}\text{Br}_3\text{NTe}$ (535.53) was found to be as follows: $M^+ + 1$ (536); MS/MS (m/z): 510, 456, 484, 375, 202, 196, 169.

These data were shown in Scheme 1 and S2, Table 1, 2 and S2, Fig. S4, S5 and S6.

Synthesis of 3,3'-(dibromo- λ^4 -tellanediyl)bis([1,1'-biphenyl]-4-amine) (C)

Five grams (0.013 mol) of **A** with 2.7 g (0.006 mol) of TeBr_4 were mixed, and both materials in their solid state after grinding them well (the reaction here is 2:1 mole). Then 50 mL of dry dioxane was added, and after the process of re-escalation for 2 h, we filtered the mixture while it was hot and left the filtrate to cool down to room temperature. It has noticed the separation of white crystals resembling glass fragments which is the complex (HgClBr.dioxan), and we get rid of them by

Table 1. Physical data for organotellurium compounds

Compound	Molecular formula	M.Wt	Color	m.p. (°C)	Yield (%)
A	C ₁₂ H ₁₀ ClHgN	404.26	white	170–172	77
B	C ₁₂ H ₁₀ Br ₃ NTe	535.53	dark brown	161–163	60
C	C ₂₄ H ₂₀ Br ₂ N ₂ Te	623.85	pale yellow	182–184	50
D	C ₂₄ H ₂₀ N ₂ Te	464.04	pale green	208–210	42
E	C ₂₄ H ₂₀ N ₂ Te	591.64	orange	214–216	32

Table 2. Main absorption bands in the infrared spectra of the prepared compounds

Compound	C-H aromatic (cm ⁻¹)	C=C (cm ⁻¹)	N-H ₂ (cm ⁻¹)	Te-Br (cm ⁻¹)	C-N (cm ⁻¹)	Te-c (cm ⁻¹)
A	3055	1612	3408, 3327	-	1310	-
B	3121	1596	3486, 3573	689	1256	481
C	3033	1609	3582, 3523	692	1284	455
D	3032	1480	3298, 3442	-	1261	499
E	3045	1564	3478, 3567	-	1258	478

normal filtration, then adding the filtrate in batches to 300 mL of ice-distilled water in a beaker with continuous stirring, where we have crystals with the pale color yellow is isolated by filtering. The precipitate was washed on the filter paper with distilled water several times, and the precipitate was dried; the resulting weight is 4 g, and the yield was 50%. The dissociation of the compound at a degree 182–184 °C.

FT-IR using KBr: $\nu(\text{C-H})$ Aromatic = 3033 cm⁻¹, $\nu(\text{C-N})$ = 1284 cm⁻¹, $\nu(\text{C=C})$ Aromatic = 1609 cm⁻¹, $\nu(\text{NH}_2)$ = (3582 cm⁻¹, 3523 cm⁻¹), $\nu(\text{C-Te})$ = 455 cm⁻¹, $\nu(\text{Br-Te})$ = 692 cm⁻¹.

Mass spectra: The MS calculated for **C** C₂₄H₂₀N₂Br₂Te (623.85) was found to be as follows: M⁺+2 (625); MS/MS (*m/z*): 608, 593, 484, 434, 360, 281, 154.

These data were shown in Scheme 1 and S3, Table 1, 2, and S3, Fig. S7, S8 and S9.

Synthesis of 3,3''-tellurobis([1,1'-biphenyl]-4-amine) (D)

From the previously prepared composite, compound **C**, 1 g was dissolved in a beaker and then added 20 mL of ethanol, then some drops of (0.1 mol, 5 mL) of aqueous hydrazine diluted in 5 mL of ethanol were added until the vapors disappear. Pale green crystals were formed and isolated by filtration. The precipitate is washed with hot ethanol on the filter paper and dried, where the resulting weight was 0.3 g, and the yield was 46%. The dissociation of the compound at a degree 208–210 °C.

FT-IR using KBr: $\nu(\text{C-H})$ Aromatic = 3032 cm⁻¹, $\nu(\text{C-N})$ Aromatic = 1261 cm⁻¹, $\nu(\text{C=C})$ Aromatic = 1480 cm⁻¹, $\nu(\text{NH}_2)$ = (3298 cm⁻¹, 3442 cm⁻¹), $\nu(\text{C-Te})$ = 499 cm⁻¹.

Mass spectra: The MS calculated for **D** C₂₄H₂₀N₂Te (464.02) was found to be as follows: M⁺+2 (466); MS/MS (*m/z*): 449, 415, 364, 296, 169, 154, 78.

These data were shown in Scheme 1 and S4, Table 1, 2 and S4, Fig. S10, S11 and S12.

Synthesis of 3,3''-ditellanediy bis([1,1'-biphenyl]-4-amine) (E)

From the previously prepared composite, compound **B**, 1 g was put in a beaker, then added 20 mL of ethanol until got completely dissolved in the solvent after heating. Some drop 5 mL (0.1 mol) of aqueous hydrazine diluted in 5 mL of ethanol were added until the fumes disappeared where orange crystals are formed that are isolated by filtration. The precipitate was washed with hot ethanol on a filter paper. The resulting weight was 0.32 g, and the yield was 32%. The dissociation of the compound was at a degree 214–216 °C.

FT-IR using KBr: $\nu(\text{C-H})$ Aromatic = 3045 cm⁻¹, $\nu(\text{C-N})$ = 1258 cm⁻¹, $\nu(\text{C=C})$ Aromatic = 1564 cm⁻¹, $\nu(\text{NH}_2)$ = (3478 cm⁻¹, 3567 cm⁻¹), $\nu(\text{C-Te})$ = 478 cm⁻¹.

Mass spectra: The MS calculated for **E** C₂₄H₂₀N₂Te₂ (591.64) was found to be as follows: M⁺+1 (592); MS/MS (*m/z*): 576, 552, 504, 478, 296, 169, 93.

These data were shown in Scheme 1 and S5, Table 1, 2 and S5, Fig. S13, S14 and S15.

■ RESULTS AND DISCUSSION

This current study included the preparation of the organic tellurium compounds such as ArTeBr_3 , Ar_2TeBr_2 , Ar_2Te , and Ar_2Te_2 , where Ar is the organic compound (4-amino biphenyl), which represents the organic part in the prepared organic tellurium compounds, Scheme 1.

IR spectra of the compounds under study displayed standard features in specific regions and characteristic bands in the other areas explained in Table 2. In all the compounds under study, the aromatic C–H bond appeared in the range $3032\text{--}3121\text{ cm}^{-1}$ [16-21]. The clear band in the range of $1480\text{--}1612\text{ cm}^{-1}$ was attributed to the aliphatic bond C=C [16-21]. A clear double package also appeared in all the compounds prepared, belonging to the NH_2 group within the range $3298\text{--}3573\text{ cm}^{-1}$ [16-20]. The appearance of a weak to medium intensity band in the fingerprint area for the two compounds **B** and **C** are 689 and 691 cm^{-1} straight, belonging to the Br-Te bond [17,22-25]. All compounds except **A** showed a weak to medium intensity band within the range $481\text{--}499\text{ cm}^{-1}$ belonging to the Te-C bond [17-21], while those spectra which showed bands at $1256\text{--}1310\text{ cm}^{-1}$ are due to the amplitude oscillation of the C–N bond [26-27].

The mass spectrum gives clear evidence about the formula of the proposed compounds by noting the value of the molecular ion, the parent band, which refers to the total molecular weight of the compound, in addition to the baseband with high abundance, which indicates the high stability of the fragmented molecule, and that the presence of other bands gives us an idea of the structural formula and the possibility of ions that depend on the rules of fragmentation [28-32]. (Explained in Table 2 and S1–S5, Scheme S1–S5, and Fig. S1–S15).

Computational Study

The molecular structure for the organotellurium compounds was investigated using optimization plus frequency at the ground state level. In addition, density functional theory has been applied to optimize the organotellurium compounds with Gaussian 09 software program [33-39].

Density Functional Theory (DFT)

It is one of the methods used in the study of molecular structures, electronic properties, and lines the circumference and surfaces of individual atoms and molecules, and this method is widely used in science materials and Solid-State Physics. DFT theory deals with electron density rather than the wave function. That is, the electron density depends only on the spatial coordinates without regard to how it is located electrons in the system [32]. DFT is one of the most important methods; it is used in theoretical physics and chemistry, and with it, we can determine the properties of multiple system particles (total system energy, electron density of orbitals, physical, and optical parameters for matter), which is one of the most widely used methods in quantitative calculations because of the possibility of it applied to a variety of systems at a low cost and high speed [34-35].

Electronic Properties

HOMO and LUMO are terms used to refer to the position of molecular orbitals in terms of it is occupied with electrons, as HOMO is the highest molecular orbital occupied by electrons, and LUMO represents the lowest unoccupied molecular orbital with electrons (see Fig. S16–S27). Uses the energy difference between these two boundary orbits in knowing the stability and stability of the elements in addition to the color that they show in solutions (energy gap). The energy gap is the amount of energy needed for an electron to move from its valence level to its conductivity level through this value (energy gap). We can know what elements or materials are if it is a conductor, an insulator, or a semiconductor, where the energy gap can be calculated by difference. The energy between the lowest energy level and the highest energy level [36-37], represents the energy difference between the lower virtual energy and the higher total energy levels (see Table 3).

$$E_g = E_{\text{LUMO}} - E_{\text{HOMO}} \quad [38] \quad (1)$$

The HOMO and LUMO energies are explained in Table 3. The HOMO energy of prepared compounds

Table 3. The electronic states of the organotellurium compounds

Compound	E _{HOMO} (eV)	E _{LUMO} (eV)	E _g (eV)
RTeBr ₃ (B)	5.4011	2.9767	2.4244
R ₂ TeBr ₂ (C)	4.3454	2.6230	1.7224
R ₂ Te (D)	4.4814	3.3876	1.0938
R ₂ Te ₂ (E)	4.9821	2.5522	2.4299

were arranged [34-38] as follows:

C > D > E > B

while the LUMO energies were arranged as the following [34-38]:

E > C > B > D

Therefore, the highest energy gap was observed by compound **E**, while the lowest value was observed by compound **D** (see Table 3).

Electronegativity and Electrophilicity

Electronegativity is defined as the ability of an atom to attract electrons towards itself in a chemical compound, where fluorine is the most negative electrolyte element. Electronegativity increases with increasing numbers of atomic elements. In addition, electronic affinity can be defined as the susceptibility of a neutral atom. In the gaseous state, it can gain one electron and release energy; the atomic number becomes more difficult to add an electron. Electronegativity and electronic affinity can be calculated respectively from the two relationships (2) and (3) [38-39] as shown in Table 4.

$$X = \frac{E_{\text{HOMO}} + E_{\text{LUMO}}}{2} \quad (2)$$

$$W = \frac{X^2}{2\eta} \quad (3)$$

In Table 4, the electronegativity of organotellurium compounds under study was arranged as the following:

D > B > C > E

but compound **E** had the greatest electrophilicity, whereas compound **D** had the least such as the following arrangement:

E > C > B > D

Ionization potential and electron affinity ionization energy are defined as the amount of energy required to remove an electron from an atom of a particular element. It is neutral in its gaseous state; for example, a hydrogen

atom has one ionization energy in the outer shell because it has one electron, while atoms that contain more than an electron in their last shell have ionization energy for each electron, while electronic affinity can be defined as it is the amount of energy released when an atom gains an electron equal to the energy required to remove an electron from a negative ion. For example, atoms have seven electrons in the outer shell. It has a strong electronegativity, and it is opposite, if the atoms have a closed shell, then they have an attraction weak electronic, and according to Koopman's theory, the following Eq. (4) and (5) [18,28,37-38] can express the ionization potential and electron affinity, as shown in Table 5.

$$\text{I.P} = -E_{\text{HOMO}} \quad (4)$$

$$\text{E.A} = E_{\text{LUMO}} \quad (5)$$

The information in Table 5 shows the ionization potentials and electron affinity values in (eV) for compounds **B**, **C**, **D**, and **E**. According to Koopman's theory, the results of ionization potentials and electron affinity, in turn, depend on the energies in the valence band and conduction distance preserver; accordingly, the prepared tellurium compounds can be arranged as the following (according to the increase in their ionization potential) [18,37]:

D > B > C > E

Table 4. Electronegativity and electrophilicity of the organotellurium compounds

Compound	Electronegativity (X) (eV)	Electrophilicity (W) (eV)
RTeBr ₃ (B)	4.1889	7.2209
R ₂ TeBr ₂ (C)	3.4842	7.0538
R ₂ Te (D)	3.9345	14.0730
R ₂ Te ₂ (E)	3.7671	5.8399

Table 5. Ionization potential and electron affinity of the organotellurium compounds

Compound	Ionization potential (I.P) (eV)	Electron affinity (E.A) (eV)
RTeBr ₃ (B)	5.40	2.97
R ₂ TeBr ₂ (C)	4.34	2.62
R ₂ Te (D)	4.48	3.38
R ₂ Te ₂ (E)	4.98	2.55

Hardness Softness Acid Base

Chemical hardness is a very useful concept in chemistry and physics, knowing the resistance or deformation of atoms, molecules, or ions [40]. Based on this concept, Lewis acids and bases were both hard and soft, and this principle was described by Pearson. A base can be defined as soft is the donor atom that is highly polarizable and has a low negative electronegativity. It is easily oxidized and bound to empty lower orbitals. As for the solid base, the donor atom is low polarizability, has high negative electronegativity, is easily oxidized, and is associated with empty orbitals with high energy, soft acid can be defined as the accepting atom with a positive charge. It is low, large, and polarizable. As for the solid acid, the receiving atom is the same high positive charge, small size, and non-polarizable. This principle includes a description of the behavior of molecules or atoms as acids and bases in chemistry. The soft base and the hard base represent the donors, but the soft acid the solid acid represents the acceptors. The following Eq. (6) and (7) can express the hardness and softness.

$$\eta = \frac{I.P - W.P}{2} \quad (6)$$

$$\sigma = \frac{1}{2\eta} \quad (7)$$

η refers to chemical hardness, and σ refers to chemical softness, from Table 6. The compound **D** was harder than compounds **B**, **C**, and **E**, respectively, indicating that compound **D** will behave as a hard base [40-42].

D > C > E > B

In addition, and from the information provided in Table 6, compound **D** appears softer than other compounds, while compound **B** behaves as a soft base. Therefore, organo-tellurium compounds are classified as donors or acceptors.

Table 6. Chemical hardness and chemical softness of the organotellurium compounds

Compound	Chemical hardness (η)	Chemical softness (σ)
R ₂ TeBr ₃ (B)	1.215	0.4115
R ₂ TeBr ₂ (C)	0.86	0.581
R ₂ Te (D)	0.55	0.9090
R ₂ Te ₂ (E)	1.216	0.4116

CONCLUSION

In the present study, compounds **A**, **B**, **C**, **D**, and **E** were obtained in a 32–77% yield. All the prepared compounds were characterized by the mass spectrum and FTIR. Findings from this study were in concordance with previous research findings, confirming the correctness of the proposed structures for all the prepared compounds.

As for the theoretical study, it can be obtained that the DFT used in this study is an interest method, and the B3LYP functional is suitable for studying the electronic properties of these structures. The density functional theory method has been used for geometry optimization and the electronic properties of all prepared compounds by using B3LYP functional.

The total energies of the donor-acceptor system show that this structure is more stable. The results obtained in this work may help to select a type of bridge to interact with the donor and acceptor to calculate the physical properties of the donor-bridge-acceptor.

REFERENCES

- [1] Liang, X., Perez, M.A.M.J., Nwoko, K.C., Egbers, P., Feldmann, J., Csetenyi, L., and Gadd, G.M., 2019, Fungal formation of selenium and tellurium nanoparticles, *Appl. Microbiol. Biotechnol.*, 103 (17), 7241–7259.
- [2] Irfan, M., Rehman, R., Razali, M.R., Ur Rehman, S., Ur Rehman, A., and Iqbal, M.A., 2020, Organotellurium compounds: An overview of synthetic methodologies, *Rev. Inorg. Chem.*, 40 (4), 193–232.
- [3] Chivers, T., and Laitinen, R.S., 2015, Tellurium: A maverick among the chalcogens, *Chem. Soc. Rev.*, 44 (7), 1725–1739.
- [4] Pop, A., Silvestru, C., and Silvestru, A., 2019, Organoselenium and organotellurium compounds containing chalcogen-oxygen bonds in organic synthesis or related processes, *Phys. Sci. Rev.*, 4 (5), 20180061.
- [5] Vaigankar, D.C., Dubey, S.K., Mujawar, S.Y., D'Costa, A., and Shyama, S.K., 2018, Tellurite biotransformation and detoxification by *Shewanella*

- baltica* with simultaneous synthesis of tellurium nanorods exhibiting photo-catalytic and anti-biofilm activity, *Ecotoxicol. Environ. Saf.*, 165, 516–526.
- [6] Missen, O.P., Ram, R., Mills, S.J., Etschmann, B., Reith, F., Shuster, J., Smith, D.J., and Brugger, J., 2020, Love is in the earth: A review of tellurium (bio)geochemistry in surface environments, *Earth-Sci. Rev.*, 204, 103150.
- [7] Alduino, C., Alfonso, K., Artusa, D.R., Avignone, F.T., Azzolini, O., Banks, T.I., Bari, G., Beeman, J.W., Bellini, F., Bersani, A., Biassoni, M., Brofferio, C., Bucci, C., Camacho, A., Caminata, A., Canonica, L., Cao, X.G., Capelli, S., Cappelli, L., Carbone, L., Cardani, L., Carniti, P., Casali, N., Cassina, L., Chiesa, D., Chott, N., Clemenza, M., Copello, S., Cosmelli, C., Cremonesi, O., Creswick, R.J., Cushman, J.S., D'Addabbo, A., Dafinei, I., Davis, C.J., Dell'Oro, S., Deninno, M.M., Di Domizio, S., Di Vacri, M.L., Drobizhev, A., Fang, D.Q., Faverzani, M., Feintzeig, J., Fernandes, G., Ferri, E., Ferroni, F., Fiorini, E., Franceschi, M.A., Freedman, S.J., Fujikawa, B.K., Giachero, A., Gironi, L., Giuliani, A., Gladstone, L., Gorla, P., Gotti, C., Gutierrez, T.D., Haller, E.E., Han, K., Hansen, E., Heeger, K.M., Hennings-Yeomans, R., Hickerson, K.P., Huang, H.Z., Kadel, R., Keppel, G., Kolomensky, Y.G., Leder, A., Ligi, C., Lim, K.E., Liu, X., Ma, Y.G., Maino, M., Marini, L., Martinez, M., Maruyama, R.H., Mei, Y., Moggi, N., Morganti, S., Mosteiro, P.J., Napolitano, T., Nones, C., Norman, E.B., Nucciotti, A., O'Donnell, T., Orio, F., Ouellet, J.L., Pagliarone, C.E., Pallavicini, M., Palmieri, V., Pattavina, L., Pavan, M., Pessina, G., Pettinacci, V., Piperno, G., Pira, C., Pirro, S., Pozzi, S., Previtali, E., Rosenfeld, C., Rusconi, C., Sangiorgio, S., Santone, D., Scielzo, N.D., Singh, V., Sisti, M., Smith, A.R., Taffarello, L., Tenconi, M., Terranova, F., Tomei, C., Trentalange, S., Vignati, M., Wagaarachchi, S.L., Wang, B.S., Wang, H.W., Wilson, J., Winslow, L.A., Wise, T., Woodcraft, A., Zanotti, L., Zhang, G.Q., Zhu, B.X., Zimmermann, S., and Zucchelli, S., 2017, Measurement of the two-neutrino double beta decay half-life of ^{130}Te with the CUORE-o experiment, *Eur. Phys. J. C*, 77 (1), 13.
- [8] Clark, R.A., McNamara, B.K., Barinaga, C.J., Peterson, J.M., Govind, N., Andersen, A., Abrecht, D.G., Schwantes, J.M., and Ballou, N.E., 2015, Electron ionization mass spectrum of tellurium hexafluoride, *Inorg. Chem.*, 54 (10), 4821–4826.
- [9] Sredni, B., 2012, Immunomodulating tellurium compounds as anti-cancer agents, *Semin. Cancer Biol.*, 22 (1), 60–69.
- [10] Perron, J.C., 1967, Electrical and thermoelectrical properties of selenium-tellurium liquid alloys, *Adv. Phys.*, 16 (64), 657–666.
- [11] Yin, Y., Cao, R., Guo, J., Liu, C., Li, J., Feng, X., Wang, H., Du, W., Qadir, A., Zhang, H., Ma, Y., Gao, S., Xu, Y., Shi, Y., Tong, L., and Dai, D., 2019, High-speed and high-responsivity hybrid silicon/black-phosphorus waveguide photodetectors at 2 μm , *Laser Photonics Rev.*, 13 (6), 1900032.
- [12] Yamago, S., 2021, Practical synthesis of dendritic hyperbranched polymers by reversible deactivation radical polymerization, *Polym. J.*, 53 (8), 847–864.
- [13] Kavlak, G., and Graedel, T.E., 2013, Global anthropogenic tellurium cycles for 1940–2010, *Resour., Conserv. Recycl.*, 76, 21–26.
- [14] Filella, M., Reimann, C., Biver, M., Rodushkin, I., and Rodushkina, K., 2019, Tellurium in the environment: Current knowledge and identification of gaps, *Environ. Chem.*, 16 (4), 215–228.
- [15] Aziz, F.K., Gazar, S.H., and Al-Saadawy, N.H., 2020, Simple, selective, and sensitive spectrophotometric method for determination of trace amounts of lead(II), cadmium(II), cobalt(II) with organomercury compounds, *J. Global Pharma Technol.*, 12 (6), 248–255.
- [16] Al-Fregi, A.A., Al-Asfoor, A.F., and Jabar, S.F., 2015, Synthesis and characterization of some new series of 2-(4-hydroxynaphthylazo)-5-substituted phenyltellurium tribromides and ditellurides compounds, *Int. J. Sci. Eng. Res.*, 6 (3), 274–281.
- [17] Silverstein, R.M., and Bassler, G.C., 1962, Spectrometric identification of organic compounds, *J. Chem. Educ.*, 39 (11), 546.
- [18] Oliveira, G.P., Barboza, B.H., and Batagin-Neto A., 2022, Polyaniline-based gas sensors: DFT study on

- the effect of side groups, *Comput. Theor. Chem.*, 1207, 113526.
- [19] Ahmed, W.M., Al-Saadawy, N.H., and Abowd, M.I., 2021, Synthesis and characterization of a new organoselenium and organotellurium compounds depending on 9-chloro-10-nitro-9,10-dihydroanthracene, *Ann. Romanian Soc. Cell Biol.*, 25 (4), 11035–11043.
- [20] Anand, D., He, Y., Li, L., and Zhou, L., 2019, A photocatalytic sp^3 C–S, C–Se and C–B bond formation through C–C bond cleavage of cycloketone oxime esters, *Org. Biomol. Chem.*, 17 (3), 533–540.
- [21] Pavia, D.L., Lampman, G.M., Kriz, G.S., and Vyvyan, J.A., 2014, *Introduction to Spectroscopy*, Cengage Learning, Boston, US.
- [22] Al-Saadawy, N.H., 2022, New organotellurium compounds based on camphor, aniline and *p*-toluidine: Preparation, characterization and theoretical study, *Egypt. J. Chem.*, 65 (2), 19–27.
- [23] Abbas, S.H., Al-Fregi, A.A., and Al-Yaseen, A.A., 2021, Synthesis of some new organotellurium compounds based on 1-substituted tetrazole, *J. Phys.: Conf. Ser.*, 1853, 012034.
- [24] McWhinnie, W.R., and Thavorniyutikarn, P., 1972, A spectroscopic examination of phenyltellurium trihalides, *J. Chem. Soc., Dalton Trans.*, 4, 551–554.
- [25] Boursas, F., Berrah, F., Kanagathara, N., Anbalagan, G., and Bouacida, S., 2019, XRD, FT-IR, FT-Raman spectrum and ab initio HF vibrational analysis of bis (5-amino-3-carboxy-1*H*-1,2,4-triazol-4-ium) selenate dihydrate, *J. Mol. Struct.*, 1180, 532–541.
- [26] Khanage, S.G., 2014, Synthesis and biological evaluation of new triazole derivatives, *Dissertation*, Vinayaka Missions University, Tamil Nadu, India.
- [27] Abdul-Nabi, A.S., and Jasim, E.Q., 2014, Synthesis, characterization and study of some tetrazole compounds as new corrosion inhibitors for C-steel in 0.5 M HCl solution, *Int. J. Eng. Res.*, 3 (10), 613–617.
- [28] Scheinmann, F., 2013, *An Introduction to Spectroscopic Methods for the Identification of Organic Compounds: Mass Spectrometry, Ultraviolet Spectroscopy, Electron Spin Resonance Spectroscopy, Nuclear Magnetic Resonance Spectroscopy (Recent Developments), Use of Various Spectral Methods Together, and Documentation of Molecular Spectra*, Elsevier Science, Amsterdam, Netherlands.
- [29] Al-Rubaie, A.Z., and Yousif, L.Z., 2020, Synthesis and reaction of 2-acetylamino-2'-tellurocyanato-1,1'-binaphthyl, *IOP Conf. Ser.: Mater. Sci. Eng.*, 928, 52035.
- [30] Achouba, A., Dumas, P., Ouellet, N., Little, M., Lemire, M., and Ayotte, P., 2019, Selenoneine is a major selenium species in beluga skin and red blood cells of Inuit from Nunavik, *Chemosphere*, 229, 549–558.
- [31] Frogley, B.J., Genet, T.L., Hill, A.F., and Onn, C.S., 2019, Alkynylselenolatoalkylidynes ($L_nM\equiv C-Se-C\equiv CR$) as building blocks for mixed metal/main-group extended frameworks, *Dalton Trans.*, 48 (22), 7632–7643.
- [32] Al-Asadi, R.H., 2019, Synthesis, DFT calculation and biological activity of some organotellurium compounds containing azomethine group, *Orbital: Electron. J. Chem.*, 11 (7), 402–410.
- [33] Gusakova, J., Wang, X., Shiao, L.L., Krivosheeva, A., Shaposhnikov, V., Borisenko, V., Gusakov, V., and Tay, B.K., 2017, Electronic properties of bulk and monolayer TMDs: Theoretical study within DFT framework (GVJ-2e method), *Phys. Status Solidi A*, 214 (12), 1700218.
- [34] Bagayoko, D., 2014, Understanding density functional theory (DFT) and completing it in practice, *AIP Adv.*, 4 (12), 127104.
- [35] Koch, W., and Holthausen, M.C., 2015, *A Chemist's Guide to Density Functional Theory*, Wiley-VCH, Weinheim, Germany.
- [36] Ali, A.M., 2009, Investigations of some antioxidant materials by using density functional and semiempirical theories, *Dissertation*, College of Science, University of Basrah, Iraq.
- [37] Sheela, N.R., Muthu, S., and Sampathkrishnan, S., 2014, Molecular orbital studies (hardness, chemical potential, and electrophilicity), vibrational investigation and theoretical NBO analysis of 4-4'-(1*H*-1,2,4-triazol-1-yl methylene) dibenzonitrile

- based on *ab initio* and DFT methods, *Spectrochim. Acta, Part A*, 120, 237–251.
- [38] Arivazhagan, M., Manivel, S., Jeyavijayan, S., and Meenakshi, R., 2015, Vibrational spectroscopic (FTIR and FT-Raman), first-order hyperpolarizability, HOMO, LUMO, NBO, Mulliken charge analyses of 2-ethylimidazole based on Hartree–Fock and DFT calculations, *Spectrochim. Acta, Part A*, 134, 493–501.
- [39] Al-Saadawy, N.H., 2022, Synthesis, characterization, and theoretical study of some new organotellurium compounds derived from camphor, *Indones. J. Chem.*, 22 (2), 437–448.
- [40] Abood, H.I., 2014, Density functional theory calculations of di-amino naphthalene, *J. Univ. Babylon Pure Appl. Sci.*, 22 (3), 1132–1145.
- [41] Vikramaditya, T., and Lin, S.T., 2017, Assessing the role of Hartree Fock exchange, correlation energy and long range corrections in evaluating ionization potential, and electron affinity in density functional theory, *J. Comput. Chem.*, 38 (21), 1844–1852.
- [42] Kaya, S., Kariper, S.E., Ungördü, A., and Kaya, C., 2014, Effect of some electron donor and electron acceptor groups on stability of complexes according to the principle of HSAB, *J New Results Sci.*, 4, 82–89.
- [43] Vennila, P., Govindaraju, M., Venkatesh, G., and Kamal, C., 2016, Molecular structure, vibrational spectral assignments (FT-IR and FT-RAMAN), NMR, NBO, HOMO-LUMO and NLO properties of O-methoxybenzaldehyde based on DFT calculations, *J. Mol. Struct.*, 1111, 151–156.

Photocatalytic Degradation of Metronidazole Using Zinc Oxide Nanoparticles Supported on Acha Waste

Olushola Sunday Ayanda^{1*}, Blessing Oluwatobi Adeleye¹, Omolola Helen Aremu¹, Folasade Busayo Ojobola², Olayide Samuel Lawal¹, Olusola Solomon Amodu³, Oyedele Oyebamiji Oketayo⁴, Michael John Klink⁵, and Simphiwe Maurice Nelana⁵

¹Nanoscience Research Unit, Department of Industrial Chemistry, Federal University Oye Ekiti, P.M.B. 373, Oye Ekiti, Ekiti State, Nigeria

²Department of Science Education, Federal University Oye Ekiti, P.M.B. 373, Oye Ekiti, Nigeria

³Department of Chemical Engineering, Lagos State Polytechnic, P.M.B. 21606, Ikorodu, Lagos, Nigeria

⁴Department of Physics, Federal University Oye Ekiti, P.M.B. 373, Oye Ekiti, Nigeria

⁵Department of Chemistry, Vaal University of Technology, Vanderbijlpark 1900, South Africa

* **Corresponding author:**

email: osayanda@gmail.com

Received: June 20, 2022

Accepted: September 15, 2022

DOI: 10.22146/ijc.75585

Abstract: The presence of emerging pollutants like pharmaceutical compounds in the environment is currently an issue of concern. Pharmaceutical compounds often escape conventional treatment systems and are persistent in the receiving environment; thus, the advanced oxidation processes could complement existing treatment methods to completely remove pharmaceuticals from contaminated water bodies. This work investigated the removal of metronidazole by ultra-violet light catalyzed by zinc oxide nanoparticles supported on acha waste. The synthesized zinc oxide nanoparticles, acha waste, and zinc oxide nanoparticles/acha waste composite were characterized by electron microscopy (SEM and TEM), Fourier transforms infrared spectrometry (FTIR) and X-ray diffractometry (XRD). Experimental results revealed that the UV light combined with zinc oxide nanoparticles and/or acha waste was more effective for metronidazole removal in combination than UV alone. The degradation of the metronidazole by UV light only, UV/nano-ZnO, and UV/nano-ZnO/acha waste systems follow the pseudo-first-order kinetic model. The addition of a catalyst to the UV reactor enhanced the degradation of metronidazole (5 mg/L) from 41.0 up to 86.1%. The outcome of this research showed that UV light in the presence of nanometal oxides and composites is an efficient technique for the removal of pharmaceuticals from an aqueous solution.

Keywords: metronidazole; zinc oxide nanoparticles; acha waste; UV light; photocatalysis

■ INTRODUCTION

Pharmaceutical industries are major sectors that contribute to an increase in the presence of toxic pollutants and hazardous chemicals in the environment [1-2]. Due to the high production of pharmaceuticals resulting from its growing demand, there is an increase in the generation of pharmaceutical wastewater (PWW). PWW, when not properly regulated and treated before disposal into the environment, can cause adverse effects

on plants, animals, soil, groundwater resources, aquatic organisms, and humans present in the environment. The degree of toxicity depends on the type of pharmaceutical product involved. PWW contains a high amount of various organic pollutants, COD, BOD, and suspended solids with varying colors [3]. PWW can be formed through i) improper treatment of waste obtained from the production process of the pharmaceuticals, ii) hospital effluents because of the numerous pharmaceuticals used in the treatment of patients, iii)

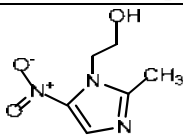
human and animal excretions when treated with pharmaceutical products, and iv) unused drugs disposed into the environment. Metronidazole (MNZ), a common synthetic pharmaceutical antibiotic, is used in destroying or inhibiting the growth of bacteria caused by microorganisms such as *Giardia lamblia*, *Trichomonas vaginalis*, *Entamoeba histolytica*, and *Clostridium difficile* [4]. MNZ is used majorly in treating vagina infections, gastrointestinal infections, pelvic inflammatory disease, rosacea, and pneumonia [5]. The use of MNZ can cause certain side effects such as diarrhea, nausea, abdominal pain [5], vomiting, constipation, loss of appetite, and rashes [6]. Most times, these side effects occur when MNZ is taken alongside alcohol or food whose constituents can agitate the effects [7]. MNZ is usually administered orally through the mouth, intravenously by the use of injection into the vein and is also available for use in the form of cream [8]. Due to its non-biodegradability, MNZ can bioaccumulate in the environment, survive in the aquatic environment for longer periods [9] and can therefore result in the presence of antibiotic resistant bacteria in the environment [10]. The chemical structure and some important properties of MNZ are presented in Table 1.

Various conventional methods, which include the physical (sedimentation, coagulation, flocculation, and filtration), biological (use of microorganisms in degrading pollutants) and chemical (disinfection, neutralization, adsorption, ion exchange) methods, have been used in the removal of MNZ from wastewater. However, they are not efficient enough since PWW

contains a high concentration of toxic, organic and hazardous pollutants. A more convenient, effective and efficient method for PWW treatment is the advanced oxidation processes (AOPs). AOP, a promising technique sometimes referred to as the tertiary treatment of wastewater, involves reactions of pollutants with hydroxyl radicals to remove organic and inorganic pollutants in wastewater [11].

The treatment of wastewater via photocatalysis allows the creation of electron-hole pairs by the catalyst, which leads to the generation of free radicals. The hydroxyl radical generated helps in converting toxicants pollutants present in the wastewater to non-dangerous and less harmful substances [12]; the organic pollutants present are converted into CO₂ and H₂O. Farzadkia et al. [13] studied the degradation of MNZ in an aqueous solution by nano-ZnO/UV photocatalytic process. In their study, the effects of some operational parameters such as pH, time, nano-dosage, and power of radiation on the degradation efficiency of MNZ wastewater using zinc oxide nanoparticles as a photocatalyst were investigated. Results showed that the removal of MNZ and chemical oxygen demand (COD) has a direct correlation with the power of the UV-A lamp and irradiation time. Also, in the experiment carried out, 96.55% degradation was achieved. Fang et al. [14] researched the effective removal of MNZ from water by nanoscale zero-valent iron (nZVI) particles. In their study, it was reported that the removal of MNZ by nZVI followed pseudo-first order kinetics, and the removal is

Table 1. Chemical structure and properties of metronidazole

Chemical structure	
IUPAC name	(2-methyl-5-nitroimidazole-1-ethanol)
Molar mass	171.156 g/mol
Melting point	159 to 163 °C
Color	yellow, white
Solubility	Soluble in water (10 mg/mL at 20 °C); ethanol (5 mg/mL); methanol, chloroform, and ether (< 0.5 mg/mL); DMSO (34 mg/mL at 25 °C); and dilute acids
Synonym	Flagyl

influenced by several factors such as nZVI dosage, initial MNZ concentration and initial solution pH. The authors reported that the MNZ solution at 80 mg/L was removed rapidly by nZVI in 5 min, at an initial solution of pH 5.60 and catalyst dosage of 0.1 g/L. Farzadkia et al. [15] investigated the degradation of aqueous MNZ with illuminated TiO₂-NP_s at different catalyst dosages, time, pH, initial MNZ concentration, and light intensity. In their study, it was observed that maximum removal of MNZ occurs at near neutral pH, the rate of removal decreases by dosage increase, and increase in initial MNZ concentration. Moreover, the authors reported that the reaction rate constant (k_{obs}) decreased from 0.0513 to 0.0072 min⁻¹, and the value of electrical energy per order (E_{EO}) increased from 93.57 to 666.67 (kWh/m³) with an increasing initial MNZ concentration from 40 to 120 mg/L.

Acha, commonly referred to as “fonio” is a species of the grass family and one of the ancient African crops [16]. It has other common names such as “hungry rice” (English), “fonyo” (Fulani), and “fini” (Bambara). Acha is mainly of two species, white fonio (*Digitaria exilis*) and black fonio (*Digitaria iburua*). Of the two species, the white fonio is commonly used and is grown particularly on the upland Plateau of Central Nigeria as well as its neighboring regions, with the black specie limited to the Jos-Bauchi Plateau of Nigeria [17]. The acha grains serve as a great source of food as they are used as rice, made into porridge and couscous, for bread and beer making process. Moreover, acha has great usefulness as a source of starch after it has undergone various processes, with acha chaff as waste resulting from acha processing. The use of acha waste in environmental remediation will provide a better means of utilizing the waste than disposing it into the environment, thereby reducing pollution, which can cause damage to the ecosystem. It also reduces cost when compared to the high cost of other chemicals used in wastewater treatment, and it helps in improving economic stability by use of other simpler methods in effecting a change in the environment.

The objective of this study is to investigate the removal of MNZ from an aqueous solution using ultra-violet (UV) light in the presence of catalysts (zinc oxide nanoparticles, acha waste (agricultural waste), and zinc

oxide nanoparticles/acha waste composite). Operating parameters such as the effect of time, catalyst dosage, initial MNZ concentration and solution pH were considered in the course of the investigation.

■ EXPERIMENTAL SECTION

Materials

Winnowed acha grains were collected from a local market in Jos, Plateau State. MNZ and sodium hydroxide pellets (98% pure) were purchased from Sigma Aldrich, whereas zinc chloride (97% pure) was purchased from Loba Chemie Pvt. Ltd., India. The stock solution of MNZ was prepared by dissolving a suitable amount of MNZ in 1 L of deionized water in a standard volumetric flask. Serial dilution of the stock was used to prepare the working solutions.

Instrumentation

The surface morphological study of zinc oxide nanoparticles and zinc oxide nanoparticles/acha waste composite was carried out using TESCAN MIRA3 and JSM-7600F SEM, respectively. The sample was observed at 7000–9000× magnification with an accelerating voltage of 15 Kv [19]. TEM analysis of the zinc oxide nanoparticles was by Tecnai G2 20, and the FTIR spectra of the nanoparticles and composite were obtained using Universal Attenuated Total Reflectance (UATR) Infrared spectrometer Perkin Elmer Spectrum 2 recorded over 400–4000 cm⁻¹ range. To capture the diffraction patterns of the samples, an X-ray diffractometer (D8 Advance, BRUCER AXS, Karlsruhe, Germany) operating at Bragg angle (2θ) in the range of (3–40 °C) with scan step (0.035°), step time (0.5 s), and generator settings (40 Kv, 40 mA) was used [20].

Procedure

Extraction of acha starch and separation of chaff

The winnowed acha grain was stepped into water for 6 h, after which the solution was discarded. The swollen grain was washed with water and blended using a domestic milling machine. The slurry (a mixture of starch and chaff) obtained was suspended in water (5 L) and was adjusted to pH 8 using NaOH (0.1 M). The starch slurry was sieved until the starch had been

separated from the chaff. Thereafter, the chaff (acha waste) was air-dried for 24 h and further dried in the oven for 48 h at 100 °C.

Preparation of nano zinc oxide/acha waste composite

The method by Ayanda et al. [18] was used in the synthesis of zinc oxide nanoparticles (Fig. 1) and to prepare the composite, 0.5 g of zinc oxide nanoparticles was mixed thoroughly with 5 g of the acha chaff before the material was air and oven dried at 100 °C.

Photolysis

During this experiment, photolytic treatment (ultra-violet light only) of aqueous MNZ was observed under the effect of time, pH and concentration. For the effect of time on the degradation of MNZ, aqueous MNZ (20 mL) was placed in a beaker, and a UV lamp with a wavelength of 254 nm was placed above the reactor containing the solution, 14 cm is the distance between the UV lamp and the aqueous MNZ. The time intervals investigated were 10, 20, 30, 40, and 60 min. To investigate the effect of pH, varying pH range (2–10) was used. MNZ concentrations of 5, 2.5, 1.25, 0.625, and 0.3125 mg/L at pH 2 and time of 60 min were utilized during the investigation of the effect of initial MNZ concentration.

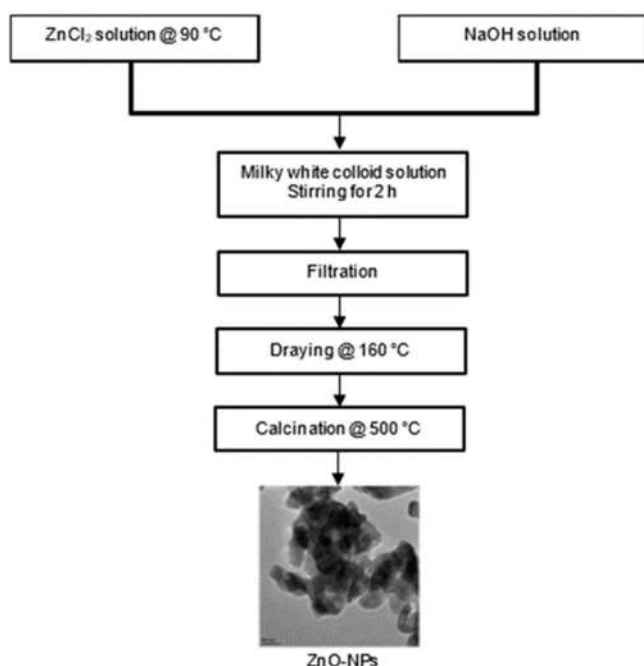


Fig 1. Flowchart for the synthesis of zinc oxide nanoparticles

Photocatalysis

Photocatalysis was also considered at a wavelength of 254 nm; moreover, the effect of time, catalyst dosage, pH, and concentration were examined. Zinc oxide nanoparticles and zinc oxide nanoparticles/acha waste composite were used as catalysts. For the effect of time, 20 mL of aqueous MNZ containing catalyst (0.02 g) was placed in a beaker, and the UV lamp was placed above the reactor containing the solution. The time intervals investigated were between 10–60 min. The effect of the amount of catalyst dosage on the degradation of MNZ was achieved by placing 20 mL of aqueous MNZ in a beaker containing 0.02–0.1 g of the catalyst for 60 min. To investigate the effect of pH, the experiment was conducted by varying the pH from 2 to 10. Lastly, the effect of initial MNZ concentration on the photocatalytic degradation of MNZ was achieved using MNZ at concentrations of 5, 2.5, 1.25, 0.625, and 0.3125 mg/L, the pH of the solution was kept at 2 and a contact time of 60 min.

After the completion of each experiment, samples were taken (filtered in the case of photocatalysis) and analyzed using a BIOBASE BK-UV1900BC spectrophotometer at a wavelength of 320 nm [21]. The percentage degradation was calculated using Eq. (1).

$$\% \text{ Degradation} = \frac{\text{MNZ}_0 - \text{MNZ}_f}{\text{MNZ}_0} \times 100 \quad (1)$$

where MNZ_0 and MNZ_f are the initial and final concentrations of MNZ (mg/L), respectively.

RESULTS AND DISCUSSION

The Results of FTIR and XRD

The FTIR bands observed in the spectra of zinc oxide nanoparticles and zinc oxide nanoparticles/acha waste composite are presented in Table 2. The peaks observed at 469.11 and 460.84 cm^{-1} correspond to the Zn-O group [22]. A strong and broad band observed at 3448.94 cm^{-1} corresponds to the O-H stretching mode of hydroxyl groups [23], and this indicates the contribution of water molecules. The FTIR band at 2927 cm^{-1} could be assigned to aliphatic νCH_2 symmetric frequency and may be due to the presence of ethanol in the acha waste. The band at 1644.13 cm^{-1} may be due to

Table 2. Absorption bands of zinc oxide nanoparticles, acha waste and zinc oxide nanoparticles/acha waste composite

S/N	Zinc oxide nanoparticles (cm ⁻¹)	Acha waste	Zinc oxide nanoparticles/acha waste composite (cm ⁻¹)
1	469.11	3448.94	3448.94
2	460.84	2927.70	2927.70
3		1644.13	1644.13
4		1155.57	1155.57
5		1080.35	1080.35
6		1019.76	1019.76
7		713.86	713.86
8			469.11

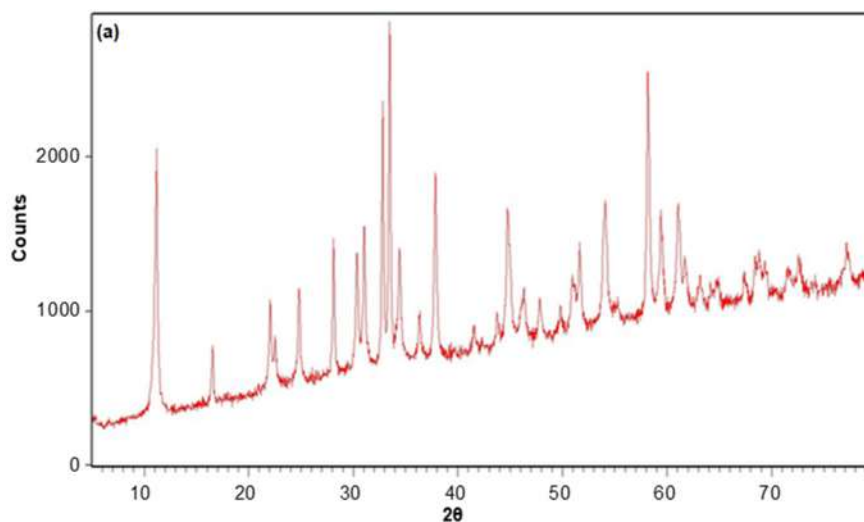
the double bonds ($-C=C-$), carbonyl bonds ($-C=O$) groups stretching vibration and may be related to the aromatic ring deformation associated with polyphenol compounds. The FTIR bands at 1155.57, 1080.35, and 1019.76 cm^{-1} may be linked to sugar moiety attached to polyphenols; moreover, they may be related to the aromatic $-OH$ group vibration and symmetry stretching of $-C-C-$. The band at 713.86 cm^{-1} may be related to aromatic ring vibration [24]. The presence of all the FTIR bands associated with zinc oxide nanoparticles and acha waste in the zinc oxide nanoparticles/acha waste composite indicated that the two precursors interacted.

The XRD patterns provided having 2θ values with strong diffraction peaks appear at 10.9°, 15.2°, 24.3°, 37.8°, and 57.6° (Fig. 2(a)) and 10.8°, 27.9°, 22.2°, 33°, 37.8°, and 57.6° (Fig. 2(b)). The XRD pattern indicated that the zinc oxide nanoparticles are crystalline, having a wurtzite

crystalline structure with a hexagonal phase, and no characteristic diffraction peaks other than zinc oxide nanoparticles were observed [25]. The zinc oxide nanoparticles/acha waste composite tends to be amorphous after the addition of zinc oxide nanoparticles and acha waste, as depicted in Fig. 2(b).

The SEM and TEM Results

The SEM and TEM of zinc oxide nanoparticles in Fig. 3(a) and 3(b) showed that the zinc oxide nanoparticles are agglomerated, and there's no complete separation between them. The TEM micrograph also confirmed the presence of multiple hexagonal structures in mass. This result may be due to weak physical force holding the particles together [26]. Fig. 3(c) shows that the composite material has an irregular, non-smooth surface with more large size pores [20].



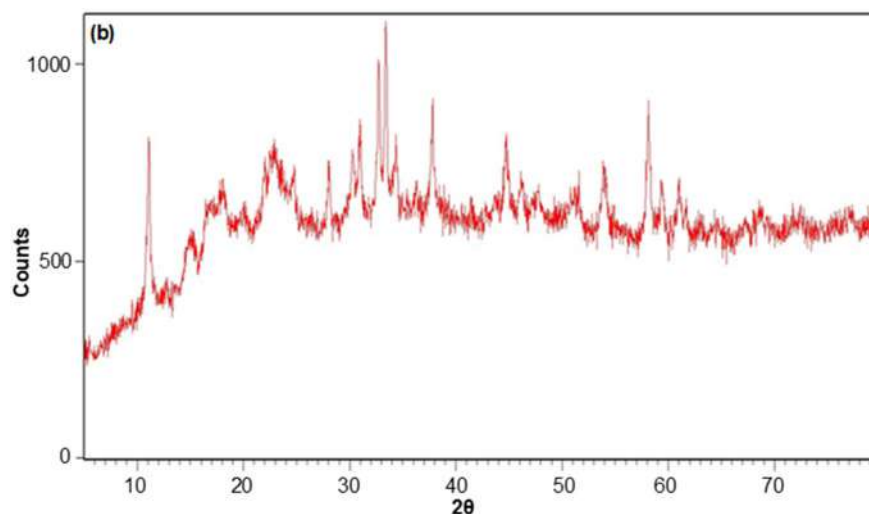


Fig 2. XRD patterns of zinc oxide nanoparticles (a) and zinc oxide nanoparticles/acha waste composite (b)

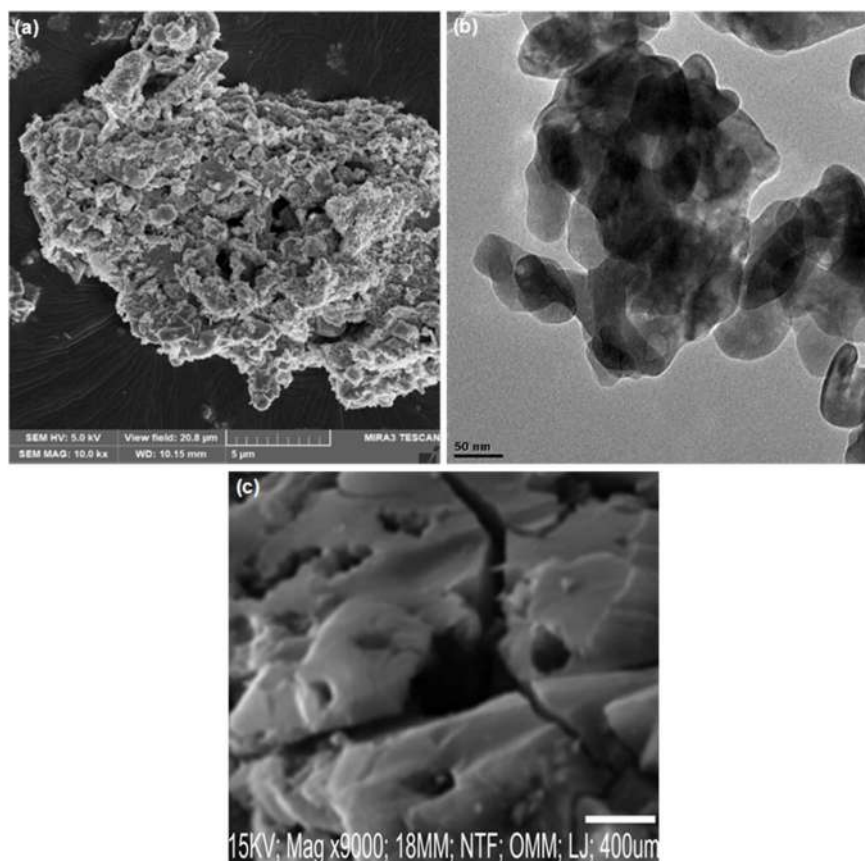


Fig 3. SEM (a) and TEM (b) micrographs of zinc oxide nanoparticles, and SEM of zinc oxide nanoparticles/acha waste composite (c)

Degradation of Aqueous Metronidazole

Effect of time of exposure

Fig. 4 shows the effect of time on the degradation of the MNZ solution. The figure indicated that the

percentage degradation increases and improves with time. For the photolysis (UV only), the percentage degradation increases from 30.2 ± 0.2 to $64.0 \pm 0.2\%$. The UV/nano-ZnO and UV/nano-ZnO/acha waste systems

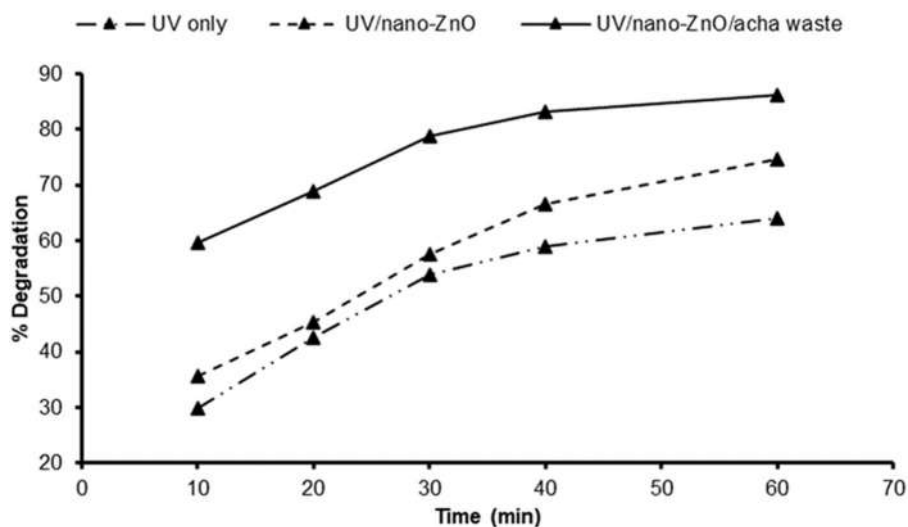


Fig 4. Effect of contact time on the degradation of metronidazole using UV, UV/nano-ZnO and UV/nano-ZnO/acha waste systems

resulted in 35.7 ± 0.3 to $74.7 \pm 0.3\%$ and 59.7 ± 0.2 to $86.1 \pm 0.2\%$, respectively. The highest degradation efficiency with photocatalysis (UV/nano-ZnO and UV/nano-ZnO/acha waste), when compared to UV light only, might be due to the synergistic effect between the UV light, zinc oxide nanoparticles and acha waste. The result obtained is similar to previous studies on the degradation of amoxicillin, ampicillin and cloxacillin antibiotics by Moradmand Jalali and Dezhampannah [27].

Effect of initial MNZ concentration

The effect of initial MNZ concentration on the

photolytic and photocatalytic degradation of MNZ solution is presented in Fig. 5. The figure showed that the percentage degradation of MNZ decreases as the initial concentration of MNZ increases from 0.3125 to 5.0 mg/L. For UV only, $3.47 \pm 0.2\%$ of MNZ was degraded at 5.0 mg/L MNZ initial concentration, whereas an MNZ solution of 0.3125 mg/L resulted in $74.1 \pm 0.2\%$ degradation. The UV/nano-ZnO and UV/nano-ZnO/acha waste systems resulted in $54.7 \pm 0.1 - 81.4 \pm 0.1\%$ and 73.9 ± 0.2 to $98.9 \pm 0.2\%$, respectively, when the concentration of MNZ was varied from 5.0 to 0.3125 mg/L.

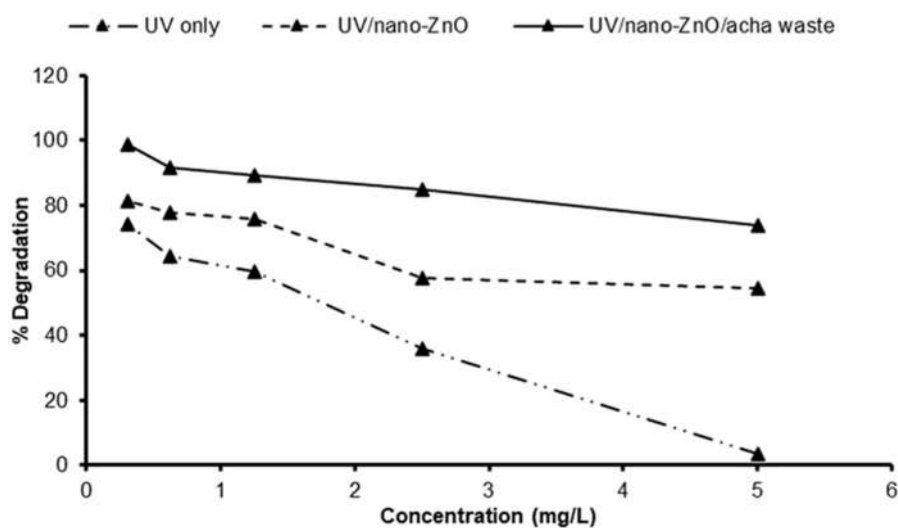


Fig 5. Effect of initial concentration on the degradation of metronidazole using UV, UV/nano-ZnO and UV/nano-ZnO/acha waste systems

The results obtained are similar to the work reported by Farzadkia et al. [15]. The authors reported that the photocatalytic degradation of MNZ with illuminated TiO₂ nanoparticles decreased with increasing initial MNZ concentration. The reason for this observation was presumed to be i) the surface of the catalyst might be occupied by MNZ as the initial MNZ concentration increases, ii) more degradation intermediates can be accumulated on the catalyst surface, causing a negative effect in the utilization of hydroxyl radicals or positive holes in the valence band of the catalyst surface, and iii) inner filtration effect which causes a decrease of photon reaching the catalyst surface.

Effect of solution pH

Fig. 6 shows the effect of pH on the degradation of the MNZ solution. The percentage degradation of MNZ by UV light increases from $1.33 \pm 0.1\%$ in the basic medium to $76.27 \pm 0.1\%$ in the acidic medium. Therefore, the degradation of the MNZ solution could be said to be favored in the acidic medium over the basic medium. The point of zero charges (pH_{pzc}) of zinc oxide nanoparticles was estimated at about 8.3–9.0 [28–29]. This implies that at pH values below the pH_{pzc} , the surface of zinc oxide nanoparticles has a net positive charge, whereas, at pH greater than the pH_{pzc} , the surface of zinc oxide nanoparticles has a net negative charge. Thus, at low pH value, the surfaces of zinc oxide nanoparticles were highly

protonated and became positively charged so that the MNZ anion was electrostatically attracted towards the catalyst surface.

Similarly, the same trends were observed for the UV/nano-ZnO and UV/nano-ZnO/acha waste systems. The percent degradation decreased from 70.9 ± 0.2 to $10.9 \pm 0.2\%$ as the pH of the solution was increased from 2 to 10 during UV/nano-ZnO degradation of 5 mg/L MNZ solution. The UV/nano-ZnO/acha waste MNZ treatment system resulted to a reduction in the percent degradation from 76.9 ± 0.2 to $18.4 \pm 0.2\%$ as the pH of the solution was increased from pH 2 to 10. Farzadkia et al. [15] obtained the highest degradation efficiency of MNZ at neutral pH (pH 7) with the lowest degradation at pH 11; moreover, the removal efficiency of MNZ by Asgharzadeh et al. [30] increased as the pH increased from 3 to 7; nevertheless, the efficiency decreased with further increase in pH value from 9 to 11. Thus, the trend observed in this study could be explained by the variation of charges on MNZ ($pK_a = 2.55$) as well as on the surface of the catalyst at different solution pH.

Effect of catalyst dosages

Fig. 7 shows the effect of catalyst dosages (0.02–0.1 g) on the photocatalytic degradation of MNZ at a pH of 2, observed for 60 min. The degradation efficiency decreased as the nano dosage increased from 0.02–0.1 g. The decrease in the degradation efficiencies of MNZ might

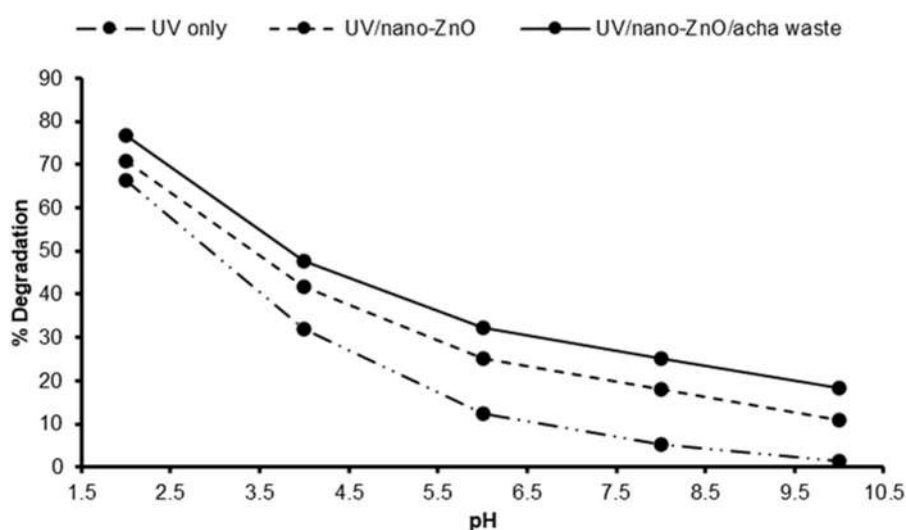


Fig 6. Effect of pH on the degradation of metronidazole using UV, UV/nano-ZnO and UV/nano-ZnO/acha waste systems

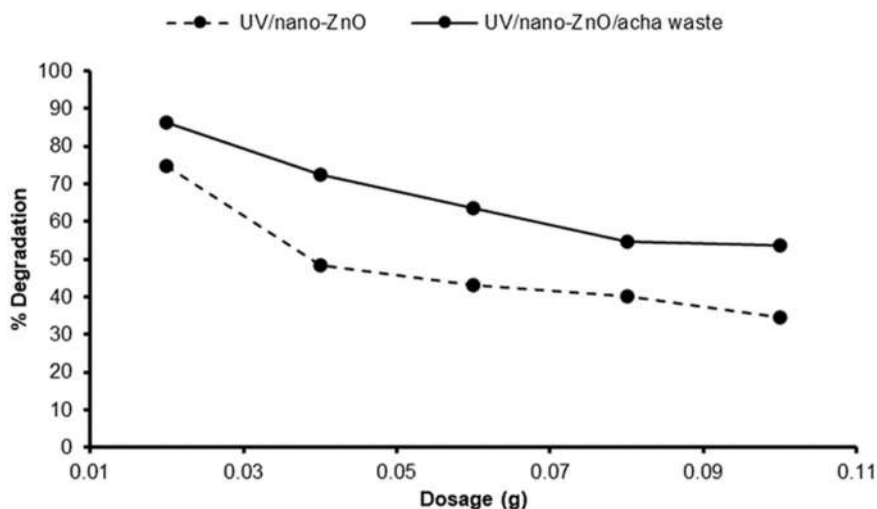


Fig 7. Effect of catalyst dosages on the degradation of metronidazole using UV/nano-ZnO and UV/nano-ZnO/acha waste systems

have resulted from increased blockage of the incident UV light with increasing catalyst dosages. Sheikhsamany et al. [31] and Farzadkia et al. [15] observed similar results.

Kinetics of Degradation

Applying the data of the effect of time of exposure, the degradation of MNZ solution by UV light only, UV/nano-ZnO, and UV/nano-ZnO/acha waste treatment systems follow the pseudo-first-order kinetics with respect to the concentration of MNZ in the solution (Eq. (2)). The integration of Eq. (2) gives Eq. (3).

$$r = \frac{d\text{MNZ}}{d_t} = k\text{MNZ} \quad (2)$$

$$\ln\left(\frac{\text{MNZ}_0}{\text{MNZ}_t}\right) = kt \quad (3)$$

where, MNZ_0 is the initial MNZ concentration of the solution in mg/L and MNZ_t is the concentration of MNZ at time t , the rate constant (k) was obtained from the slope of the plot of $\ln \text{MNZ}_0/\text{MNZ}_t$ versus time (t).

According to Fig. 8, the rate constant (k) and the R^2 values for MNZ degradation are presented in Table 3. The high R^2 values obtained for the three treatment methods are an indication that the degradation of MNZ conforms to the pseudo-first-order kinetic model. The rate constants showed that the UV treatment system is not

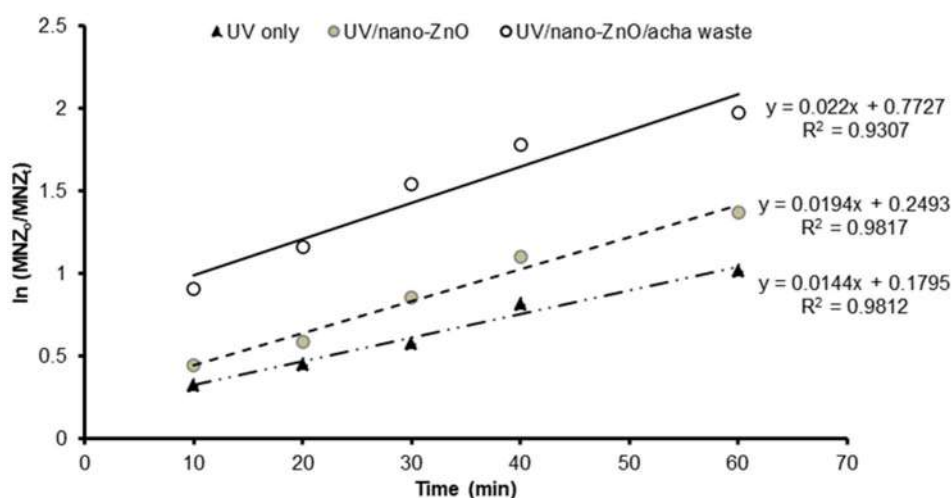


Fig 8. The kinetic plot of the degradation of metronidazole in UV, UV/nano-ZnO and UV/nano-ZnO/acha waste systems

Table 3. Metronidazole degradation kinetic constants

Treatment technique	Kinetic constant (min ⁻¹)	R ²
UV only	0.0144	0.9812
UV/nano-ZnO	0.0194	0.9817
UV/nano-ZnO/acha waste system	0.0220	0.9307

Table 4. Comparison of the photocatalytic degradation of metronidazole

Photocatalytic methods	Efficiency (%)	References
UV/TiO ₂	99.5	[15]
UV/TiO ₂	86.1	[32]
UV/ZnO	60.3	[32]
UV/Fe ₃ O ₄ /TiO ₂ /biochar	80.0	[29]
UV/nanoCoFe ₂ O ₄ @methycellulose	85.3	[33]
UV/ Ag-ZnO/graphite	88.5	[34]
Solar/ Ag-ZnO/graphite	97.3	[34]
UV/TiO ₂ -P25 + PbS	95.0	[35]
UV	64.0	[35]
UV/nano-ZnO	74.7	Present study
UV/nano-ZnO/acha waste	86.1	Present study

as effective as the treatment systems involving the catalysts. The UV treatment catalyzed with zinc oxide nanoparticles is 1.3 times faster in comparison to UV only, whereas the use of nano-ZnO/acha waste is 1.5 times faster. The fast reaction rate with nano-ZnO/acha waste highlights its excellent removal of the MNZ from aqueous solution, owing to a synergistic influence of UV, zinc oxide nanoparticles and acha waste. The removal efficiency of MNZ in the present study compared with other photocatalytic treatment methods is presented in Table 4. The table indicated that the photocatalytic degradation of MNZ by zinc oxide nanoparticles supported on acha waste shows satisfactory performance.

■ CONCLUSION

This study employs the use of UV light, a promising technique in the field of AOPs, to degrade MNZ using zinc oxide nanoparticles and nano-ZnO/acha waste composite as photocatalysts. The percentage degradation of MNZ obtained using UV light combined with nano-ZnO is approximately 2 times faster when compared to the use of UV light only, whereas, the introduction of the nano-ZnO/acha waste composite also enhanced the photocatalytic ability, thereby allowing more degradation of MNZ wastewater to occur. Generally, experimental results have

proven that the UV/nano-ZnO and UV/nano-ZnO/acha waste treatment systems had better performance for the degradation of MNZ wastewater than UV alone.

■ AUTHOR CONTRIBUTIONS

Olushola Sunday Ayanda conceived and designed the experiments. Blessing Oluwatobi Adeleye and Omolola Helen Aremu performed the experiment. Folasade Busayo Ojobola, Michael John Klink and Simphiwe Maurice Nelana contributed to the characterization of the materials. Olusola Solomon Amodu and Oyedele Oyebamiji Oketayo analyzed and interpreted the data, Olushola Sunday Ayanda wrote the paper, and Olayide Samuel Lawal revised the manuscript. All authors agreed to the final version of this manuscript.

■ REFERENCES

- [1] Kapoor, D., 2015, Impact of pharmaceutical industries on environment, health and safety, *J. Crit. Rev.*, 2 (4), 25–30.
- [2] Manasa, R.L., and Mehta, A., 2020, “Wastewater: Sources of Pollutants and Its Remediation” in *Environmental Biotechnology*, Vol. 2, Eds. Gothandam, K.M., Ranjan, S., Dasgupta, N., and Lichtfouse, E., Springer, Cham, 197–219.

- [3] Chen, J.Q., Shang, C., and Cai, X.L., 2013, Application of cyclonic floatation integrated technology in low oil content sewage treatment, *China Pet. Mach.*, 41 (9), 62–66.
- [4] Hemphill, A., Müller, N., and Müller, J., 2019, Comparative pathobiology of the intestinal protozoan parasites *Giardia lamblia*, *Entamoeba histolytica*, and *Cryptosporidium parvum*, *Pathogens*, 8 (3), 116.
- [5] Ceruelos, A.H., Romero-Quezada, L.C., Ruvalcaba Ledezma, J.C., and López Contreras, L., 2019, Therapeutic uses of metronidazole and its side effects: An update, *Eur. Rev. Med. Pharmacol. Sci.*, 23 (1), 397–401.
- [6] Kannigadu, C., and N'Da, D.D., 2020, Recent advances in the synthesis and development of nitroaromatics as anti-infective drugs, *Curr. Pharm. Des.*, 26 (36), 4658–4674.
- [7] Edwards, D.I., 1993, Nitroimidazole drugs-action and resistance mechanisms I. Mechanism of action, *J. Antimicrob. Chemother.*, 31 (1), 9–20.
- [8] Nunn, A.J., 2021, “Routes of Administration and Formulations” in *Paediatric Clinical Pharmacology*, Eds. Jacqz-Aigrain, E., and Choonara, I., CRC Press, Boca Raton, Florida, 219–233.
- [9] Arslan-Alaton, I., and Dogruel, S., 2004, Pre-treatment of penicillin formulation effluent by advanced oxidation processes, *J. Hazard. Mater.*, 112 (1-2), 105–113.
- [10] Rozas, O., Contreras, D., Mondaca, M.A., Pérez-Moya, M., and Mansilla, H.D., 2010, Experimental design of Fenton and photo-Fenton reactions for the treatment of ampicillin solutions, *J. Hazard. Mater.*, 177 (1-3), 1025–1030.
- [11] Ayanda, O.S., Nelana, S.M., Petrik, L.F., and Naidoo, E.B., 2018, Kinetic study of ultrasound degradation of 2,2-bis(4-hydroxyphenyl)propane assisted by nFe/TiO₂ composite, *J. Adv. Oxid. Technol.*, 21 (1), 170–177.
- [12] Deng, Y., and Zhao, R., 2015, Advanced oxidation processes (AOPs) in wastewater treatment, *Curr. Pollut. Rep.*, 1 (3), 167–176.
- [13] Farzadkia, M., Esrafil, A., Baghapour, M.A., Shahamat, Y.D., and Okhovat, N., 2014, Degradation of metronidazole in aqueous solution by nano-ZnO/UV photocatalytic process, *Desalin. Water Treat.*, 52 (25-27), 4947–4952.
- [14] Fang, Z., Chen, J., Qiu, X., Qiu, X., Cheng, W., and Zhu, L., 2011, Effective removal of antibiotic metronidazole from water by nanoscale zero-valent iron particles, *Desalination*, 268 (1-3), 60–67.
- [15] Farzadkia, M., Bazrafshan, E., Esrafil, A., Yang, J.K., and Shirzad-Siboni, M., 2015, Photocatalytic degradation of metronidazole with illuminated TiO₂ nanoparticles, *J. Environ. Health Sci. Eng.*, 13 (1), 35.
- [16] Garí, J.A., 2002, “Review of the African Millet Diversity” in *International Workshop on Fonio, Food Security and Livelihood Among the Rural Poor in West Africa*, November 19-22, 2001, Bamako, Mali.
- [17] Cruz, J.F., Béavogui, F., and Dramé, D., 2011, *Le Fonio, Une Céréale Africaine*, Agricultures tropicales en poche, Quae Editions, Presses Agronomiques de Gembloux, Belgium.
- [18] Ayanda, O.S., Aremu, O.H., Akintayo, C.O., Sodeinde, K.O., Igboama, W.N., Oseghe, E.O., and Nelana, S.M., 2011, Sonocatalytic degradation of amoxicillin from aquaculture effluent by zinc oxide nanoparticles, *Environ. Nanotechnol. Monit. Manage.*, 16, 100513.
- [19] Awe, A.A., Opeolu, B.O., Fatoki, O.S., Ayanda, O.S., Jackson, V.A., and Snyman, R., 2020, Preparation and characterisation of activated carbon from *Vitis vinifera* leaf litter and its adsorption performance for aqueous phenanthrene, *Appl. Biol. Chem.*, 63 (1), 12.
- [20] Alimi, B.A., Workneh, T.S., and Femi, F.A., 2021, Fabrication and characterization of edible films from acha (*Digitalia exilis*) and iburu (*Digitalia iburua*) starches, *CyTA-J. Food*, 19 (1), 493–500.
- [21] Alibeigi, A.N., Javid, N., Amiri Gharaghani, M., Honarmandrad, Z., and Parsaie, F., 2021, Synthesis, characteristics, and photocatalytic activity of zinc oxide nanoparticles stabilized on the stone surface for degradation of metronidazole from aqueous

- solution, *Environ. Health Eng. Manage. J.*, 8 (1), 55–63.
- [22] Jan, H., Shah, M., Usman, H., Khan, A., Zia, M., Hano, C., and Abbasi, B.H., 2020, Biogenic synthesis and characterization of antimicrobial and anti-parasitic zinc oxide (ZnO) nanoparticles using aqueous extracts of the Himalayan columbine (*Aquilegia pubiflora*), *Front. Mater.*, 7, 00249.
- [23] Wei, C., Ge, Y., Liu, D., Zhao, S., Wei, M., Jiliu, J., Hu, X., Quan, Z., Wu, Y., Su, Y., Wang, Y., and Cao, L., 2022, Effects of high-temperature, high-pressure, and ultrasonic treatment on the physicochemical properties and structure of soluble dietary fibers of millet bran, *Front. Nutr.*, 8, 820715.
- [24] Bello, O.M., Ogbesejana, A.B., Balkisu, A., Osibemhe, M., Musa, B., and Oguntoye, S.O., 2022, Polyphenolic fractions from three millet types (Fonio, Finger millet, and Pearl millet): Their characterization and biological importance, *Clin. Complementary Med. Pharmacol.*, 2 (1), 100020.
- [25] Al-Kordy, H.M.H., Sabry, S.A., and Mabrouk, M.E.M., 2021, Statistical optimization of experimental parameters for extracellular synthesis of zinc oxide nanoparticles by a novel haloaliphilic *Alkalibacillus* sp. W7, *Sci. Rep.*, 11 (1), 10924.
- [26] Mohan, A.C., and Renjanadevi, B., 2016, Preparation of zinc oxide nanoparticles and its characterization using scanning electron microscopy (SEM) and X-ray diffraction (XRD), *Procedia Technol.*, 24, 761–766.
- [27] Moradmand Jalali, H., and Dezhampannah, H., 2021, Kinetic investigation of photo-degradation of amoxicillin, ampicillin, and cloxacillin by semiconductors using Monte Carlo simulation, *Chem. Eng. Commun.*, 208 (2), 159–165.
- [28] Khezrianjoo, S., and Revanasiddappa, H.D., 2013, Photocatalytic degradation of acid yellow 36 using zinc oxide photocatalyst in aqueous media, *J. Catal.*, 2013, 582058.
- [29] Isai, K.A., and Shrivastava, V.S., 2019, Photocatalytic degradation of methylene blue using ZnO and 2% Fe–ZnO semiconductor nanomaterials synthesized by sol–gel method: A comparative study, *SN Appl. Sci.*, 1 (10), 1247.
- [30] Asgharzadeh, F., Gholami, M., Jafari, A.J., Kermani, M., Asgharnia, H., and Kalantary, R.R., 2019, Heterogeneous photocatalytic degradation of metronidazole from aqueous solutions using Fe₃O₄/TiO₂ supported on biochar, *Desalin. Water Treat.*, 175, 304–315.
- [31] Sheikhsamany, R., Faghihian, H., and Fazaeli, R., 2022, Synthesis of novel HKUST-1-based SnO₂ porous nanocomposite with the photocatalytic capability for degradation of metronidazole, *Mater. Sci. Semicond. Process.*, 138, 106310.
- [32] Tran, M.L., Fu, C.C., and Juang, R.S., 2018, Removal of metronidazole by TiO₂ and ZnO photocatalysis: A comprehensive comparison of process optimization and transformation products, *Environ. Sci. Pollut. Res.*, 25 (28), 28285–28295.
- [33] Nasiri, A., Tamaddon, F., Mosslemin, M.H., Gharaghani, M.A., and Asadipour, A., 2019, New magnetic nanobiocomposite CoFe₂O₄@methycellulose: Facile synthesis, characterization, and photocatalytic degradation of metronidazole, *J. Mater. Sci.: Mater. Electron.*, 30 (9), 8595–8610.
- [34] Tran, M.L., Nguyen, C.H., Fu, C.C., and Juang, R.S., 2019, Hybridizing Ag-Doped ZnO nanoparticles with graphite as potential photocatalysts for enhanced removal of metronidazole antibiotic from water, *J. Environ. Manage.*, 252, 109611.
- [35] Stando, K., Kasprzyk, P., Felis, E., and Bajkacz, S., 2021, Heterogeneous photocatalysis of metronidazole in aquatic samples, *Molecules*, 26 (24), 7612.
- [36] Taoufik, N., Boumya, W., Achak, M., Sillanpää, M., and Barka, N., 2021, Comparative overview of advanced oxidation processes and biological approaches for the removal pharmaceuticals, *J. Environ. Manage.*, 288, 112404.

Adsorption Kinetics and Isotherm of Crystal Violet by Carbon Modified with Magnetite (Fe₃O₄) and Triethoxyphenylsilane (TEPS) from Rubber Fruit Shell

Nadya Syarifatul Fajriyah¹, Buhani Buhani^{2*}, and Suharso Suharso²

¹Postgraduate Student of Master Program in Chemistry, Department of Chemistry, University of Lampung, Jl. Sumantri Brojonegoro No 1, Bandar Lampung 35145, Indonesia

²Department of Chemistry, Faculty of Mathematics and Natural Sciences, University of Lampung, Jl. Sumantri Brojonegoro No. 1, Bandar Lampung 35145, Indonesia

* **Corresponding author:**

tel: +62-81278152368

email: buhani_s@yahoo.co.id

Received: July 13, 2022

Accepted: September 30, 2022

DOI: 10.22146/ijc.76201

Abstract: Rubber fruit shells-derived carbon (RC) modified with magnetite (MRC) and triethoxyphenylsilane (TEPS) (SRC) made from rubber fruit shells were used to adsorb crystal violet (CV) dye effectively. The RC was successfully modified by magnetite and TEPS, according to the characterization of the adsorbent utilizing Fourier transform infrared (FTIR) spectroscopy, X-ray diffraction (XRD), and scanning electron microscopy-energy-dispersive X-ray (SEM-EDX) showed that the RC was successfully modified by magnetite and TEPS. Several adsorption process parameters were investigated, and the ideal results were obtained with an adsorbent dose of 0.1 g, pH 10, contact time of 15 min, and initial concentration of CV 250 mg L⁻¹. The MRC and SRC adsorption capacities are 71.43 and 69.93 mg g⁻¹, respectively. The adsorption kinetics followed a pseudo-second-order model with MRC and SRC rate constants of 3.40 and 0.83 g mg⁻¹ min⁻¹, respectively. The Freundlich adsorption isotherm is suitable for CV dye adsorption using MRC and SRC with K_F values are 1.36 and 1.76 mg g⁻¹ L mg⁻¹ which gives R² 0.943 and 0.932, respectively. These findings showed that the modified RC with magnetite and TEPS effectively removes the CV dye solution through the adsorption process.

Keywords: magnetite rubber fruit shells-derived carbon; silane rubber fruit shells-derived carbon; adsorption; crystal violet; rubber fruit shells

■ INTRODUCTION

Environmental issues, especially in Indonesia, are still a problem that needs attention. Various residual pollutants from human activities interfere with the life processes of living things, especially water pollution. Water is said to be polluted when it cannot be used according to its function. Water pollution commonly found can be in the form of dyes, herbicides, heavy metals, and other contaminants that accumulate in the environment [1].

One of the most common industrial pollutants is the textile industry. The textile industry produces a lot of dye waste in the environment. Dyes used in the textile industry are classified into three categories, namely cationic, anionic, and non-ionic dyes [2-3]. Cationic dyes are hazardous compared to others and are most widely

used in the textile industry. Crystal violet (CV) is triphenylmethane and one of the cationic dyes used in various industries, such as pharmaceuticals, paper, textiles, and printer inks [4]. CV, if getting in the water even with just a minor concentration of 1 ppm, can reduce the penetration of sunlight and interfere with the photosynthesis process [5]. If CV enters the human body a certain amount, it can cause various diseases such as respiratory problems, eye, and skin irritation, increased heart rate, blindness, and mutagenesis [6]. Considering the impact caused by the presence of CV dye can be harmful to humans, several steps to reduce or even eliminate CV dye waste have been carried out, such as chemical degradation, adsorption, coagulation, filtration membrane, ion exchange, and photocatalysis [6-11].

Adsorption is the cheapest method, easy to do, and proven effective in removing various contaminants, such as dyes, in the aquatic environment [12]. Several adsorbents used to remove CV dyes include organoclay (bentonite-alginate), agricultural waste (pine bark), organic polymers (chitosan composite), biomass (algae), and carbon materials [13-16]. The carbon material is one of the most commonly used adsorbents for the process of adsorption because of its abundant source, good stability, and wide application [17]. In this study, the carbon used came from rubber fruit shells. The rubber fruit shells-derived carbon (RC) was modified using magnetite to overcome the lack of effectiveness of RC. The scientific community has keenly interested in magnetite nanoparticles because of their unique features. Since magnetite has a large surface area and many active surface sites, it has a high capacity for adsorption [18]. The benefit of using magnetic particles is that they may be retrieved by an external magnetic field relatively fast and reused without losing the active site [19-20]. The magnetite-coated material is environmentally safe because it does not produce contaminated substances such as suspended solids. In addition, it enhances the process of removing dyes from the solution [21-22].

The rubber fruit shells-derived carbon magnetite (MRC) has magnetic properties and a more significant molecular weight than ordinary RC, so the filtration process runs more effectively. It is recyclable and doesn't contribute to further environmental issues [23]. Besides, it was modified using magnetite, and modification of RC was also carried out using a triethoxyphenylsilane (TEPS) coupling agent [24]. Silane coupling agent, a silicon-based substance, can improve chemical bonding at the interface of organic and inorganic materials. The silane coupling agent has an R-Si-X₃ structure, where R is an organofunctional group and X is an alkoxy. TEPS is one of the coupling agents that can be applied as a coating to the surface of solid materials because it has two distinct active groups that are linked to silica atoms in the molecule TEPS has a phenyl group that can bind organic materials and an ethoxy group that can bind inorganic materials, which increases the potential of CV dyes to adsorb [24-25].

Therefore, MRC will interact with CV dyes because it has an active group from Fe₃O₄ other than the pores of the RC. The rubber fruit shells-derived carbon silane (SRC) will interact with CV dyes by the phenyl and hydroxyl groups that SRC has. MRC and SRC adsorbents obtained were tested for their ability to CV, covering several parameters, including adsorbent dose, the influence of pH, the influence of contact time, and the concentration of adsorbate. The adsorption kinetics was calculated by converting the data from the contact time parameters into pseudo-first-order and pseudo-second-order equations. The Langmuir and Freundlich equations were used to determine the adsorption isotherm.

■ EXPERIMENTAL SECTION

Materials

Some materials used in this study were CV, FeSO₄·7H₂O, FeCl₃·6H₂O, NaNO₃, HCl, NaOH, ethanol, triethoxyphenylsilane (TEPS) and buffer solution from Merck (Darmstadt Germany). Rubber fruit shells were obtained from East Lampung Regency.

Instrumentation

The adsorbent material was characterized by X-ray diffraction (XRD) (LabX XRD-6000 Shimadzu) to recognize the magnetite's phase after modification, scanning electron microscope-energy-dispersive X-ray (SEM-EDX) (Zeiss EVO MA 10) to discover the surface structure of adsorbents, and FTIR (IRPrestige-21) is used to determine the functional groups of adsorbents. The CV concentration in the solution was determined using UV-Vis Spectrophotometer (Agilent Cary 100).

Procedure

Preparation of RC

Eleven kilograms of rubber fruit shells were cleaned and dried in the sun. Furthermore, it is burned in a drum made of an iron plate with a diameter ± 58 cm and height of 93 cm for approximately 6 h to obtain an RC weighing 3 kg. The RC obtained from carbonization is then pulverized by grinding and sifted through a 100-mesh sieve.

Modification of RC using magnetite coating

The MRC was obtained by putting 6.5 g of RC in 300 mL of distilled water and heating it to 70 °C. Then, iron salt consisting of 7.6 g FeCl₃·6H₂O and 3.9 g FeSO₄·7H₂O was diffused in 300 mL of distilled water. The mixture was then stirred for 30 min while adding 100 mL of 5 M NaOH dropwise. The obtained residue was separated and neutralized to pH 6. Afterward, it was dried at 100 °C for 3 h [26].

Modification of RC using silane agent TEPS

A total of 4 g of RC was mixed with 200 mL of ethanol. Next, 0.4 mL of triethoxyphenylsilane (TEPS) was put into the mixture and hereafter stirred using a magnetic stirrer for 7 h at 70 °C in a water bath. The resulting SRC was separated and cleansed using ethanol and dried at 60 °C for 1 h [24].

A total of 0.1 g MRC and SRC were put into 20 mL 0.1 M NaNO₃, respectively. A pH range of 3 to 12 was used for the initial pH. The pH was adjusted by adding 0.1 M HCl and NaOH. Then, the pH was maintained by the addition of a buffer solution. The mixture was stirred using a shaker for 24 h. After that, the final pH was observed and measured using a pH meter [27].

Adsorption experiment

CV adsorption by MRC and SRC was carried out by batch method using several parameters such as adsorbent dose (0.1–0.5 g), solution pH (3–12), contact time (15–120 min), and CV dye concentration (10–250 mg L⁻¹). For each experiment, a certain amount of MRC and SRC were added to 20 mL CV solution with an initial concentration at the appropriate pH value. 0.1 M NaOH and HCl were

used to alter the initial pH solution. At a steady speed of 100 rpm, the mixture was agitated in an orbital shaker. CV residues were analyzed on λ_{max} 590 nm using Spectrophotometer UV-Vis. The CV dye adsorption percentage and adsorption capacity were calculated by Eq. (1) and (2), respectively:

$$\text{Adsorption(\%)} = \frac{C_o - C_e}{C_o} \times 100 \quad (1)$$

$$q = \frac{(C_o - C_e)v}{w} \quad (2)$$

where w (g) is the amount of adsorbent, v (L) is the volume of the solution, q (mg g⁻¹) is the amount of CV dye adsorbed per unit mass, C_o and C_e (mg L⁻¹) are the initial CV concentration and CV concentration after the adsorption, respectively.

RESULTS AND DISCUSSION

Adsorbent Characterization

The MRC modification was carried out through a magnetite coating process using FeCl₃·6H₂O, and FeSO₄·7H₂O mixed to form Fe₃O₄, which then coats the RC surface. The SRC modification was carried out through the silanization process using a silane coupling agent, namely TEPS. TEPS has two active groups, namely the phenyl group, which can bind organic materials and ethoxy to bind inorganic materials [24].

FTIR characterized the obtained MRC and SRC adsorbents to identify the functional groups, XRD to identify magnetite crystals and SEM-EDX to recognize the RC surface pattern and analyze its constituent elements. Fig. 2 shows a hydroxyl group (OH) as seen by

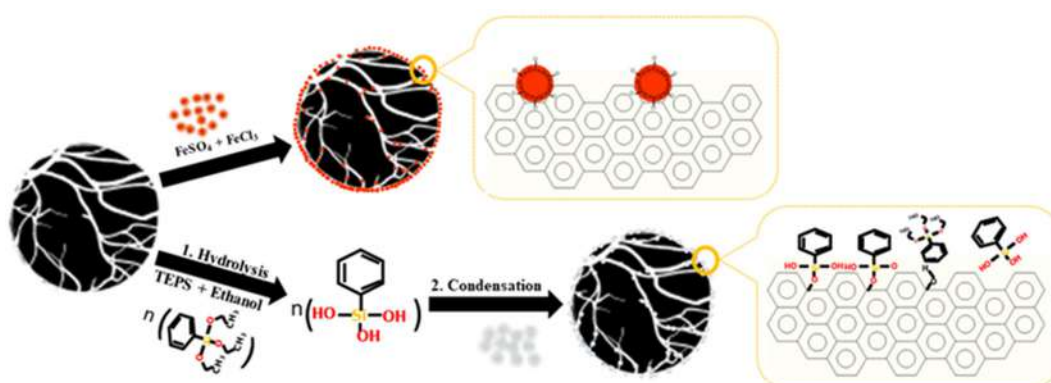


Fig 1. Scheme of RC surface modification using magnetite and silane agent

the peaks at wavenumber 3433 cm^{-1} , and Fe-O is indicated by absorption at wavenumber 586 cm^{-1} which indicates that Fe_3O_4 has coated RC [24].

Peaks at 2368 , 1620 and 1604 cm^{-1} correspond to C-H vibration and the C=C group. Peaks at 1435 and 1527 cm^{-1} correspond to an aromatic C=C group [28-30]. In addition, the presence of Si-O-Si is indicated by the absorption at wavenumber 1049 cm^{-1} which indicates the RC has been coated with TEPS [13].

The XRD pattern (Fig. 3) on the RC shows a broad asymmetric peak at 2θ $20\text{--}45^\circ$, which is characteristic of amorphous carbon. Based on Fig. 3, MRC shows sharp

peaks compared to RC at 2θ 35.46 , 43.04 , 57.22 , and 62.58° [31]. The asymmetrical RC peaks turn into sharp peaks in the XRD MRC pattern, indicating that RC has been coated with magnetite so that the peaks appear with sharp intensity. The SRC diffraction pattern at 2θ $20\text{--}30^\circ$ showed broad peaks, indicating the presence of amorphous silica formed on RC's surface. Amorphous silica was obtained by hydrolysis of TEPS [24].

The morphology of MRC can be seen in Fig. 4(b). The MRC surface looks rougher than the RC surface. Magnetite grains have entirely coated the RC surface. EDX data support this. The elemental compositions of

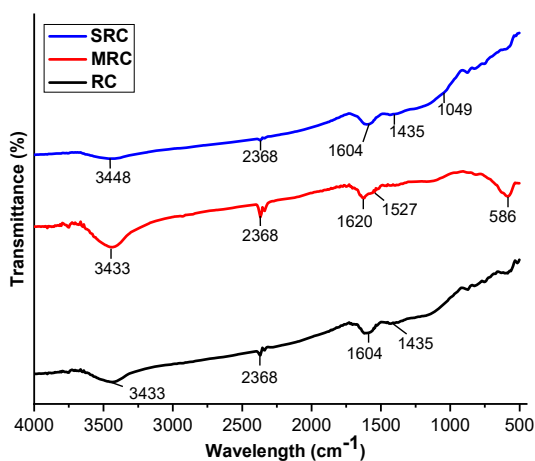


Fig 2. FTIR spectra of RC, MRC, and SRC

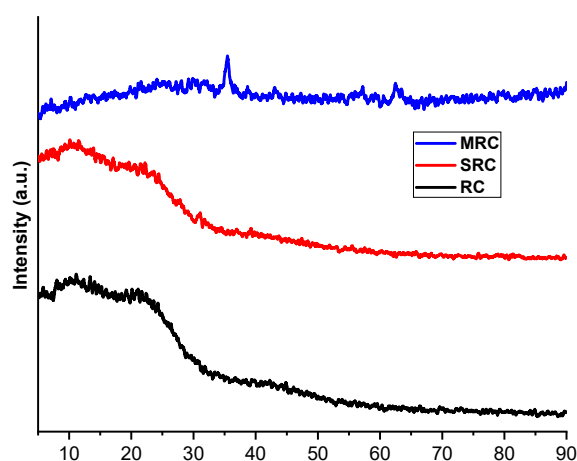


Fig 3. Diffractogram of RC, MRC and SRC

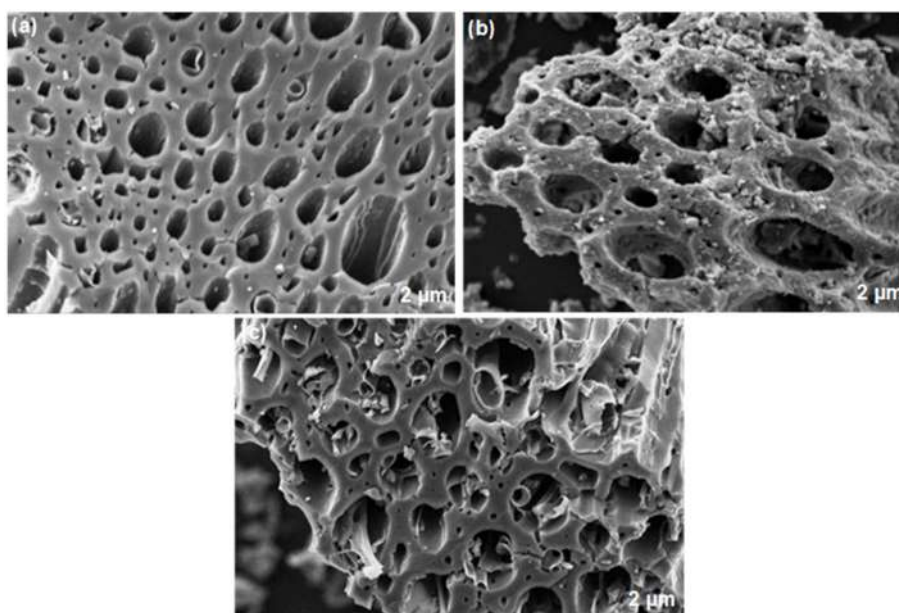


Fig 4. Micrographs of (a) RC, (b) MRC, and (c) SRC

C, O, and Fe are 65.97, 30.95, and 3.08%, respectively.

In addition, the pore diameter of MRC is around 2.05–6.45 μm , smaller than the diameter of RC, which has a pore diameter of around 3.52–9.38 μm . This finding indicates that Fe_3O_4 has been perfectly attached to the RC surface. The particles of Fe_3O_4 coat the entire carbon surface, including the carbon pores, so the carbon pores become narrower, resulting in a smaller carbon pore diameter.

The surface morphology of SRC in Fig. 4(c) shows the presence of small white particles of silica from TEPS modification and stick to the RC pores. Because of the lack of oxygenated surface from RC, TEPS does not

entirely cover the RC pores. The results of the EDX analysis (Fig. 5) showed the elemental compositions of C, O, and Si were 90.43, 9.45, and 0.13%, respectively. From the EDX data, it can be seen that TEPS has coated the RC surface.

Adsorption Study

Adsorbent dosage

The adsorbent dose can affect the adsorption ability. Fig. 7(a) shows the adsorption percentage depending on the adsorbent dose. Based on Fig. 7(a), the adsorption efficiency decreased while the adsorbent dose increased. This phenomenon is because adsorption

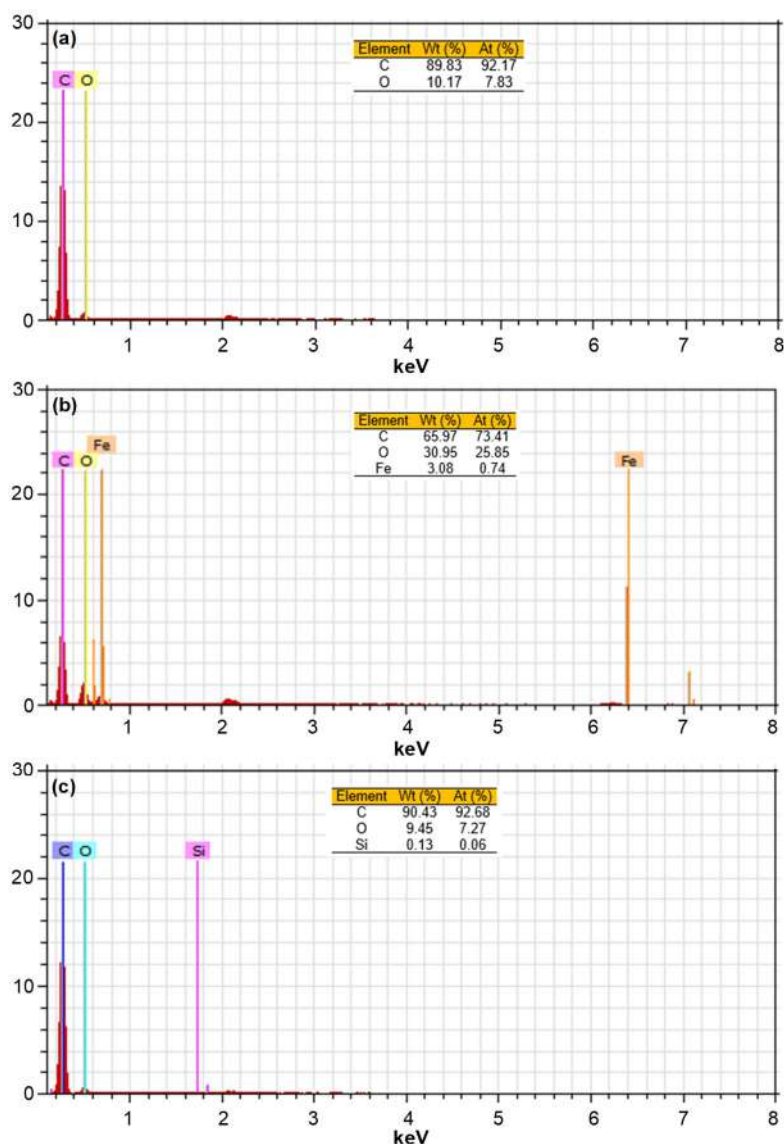


Fig 5. EDX Spectra of (a) RC, (b) MRC and (c) SRC

will occur more quickly as the adsorbent's mass increases. Because of the superficial adsorption, the contact between the adsorbent and adsorbate happens quickly on the adsorbent's surface [32]. The decrease in adsorption efficiency can be due to a decrease in the surface area of the adsorbent so that the adsorbent has reached saturation on its surface. In addition, it can also be caused by overlapping and agglomeration of the large number of adsorbents contained in the adsorbate solution [33]. The optimum mass of the adsorbent in absorbing the CV solution was 0.1 g, with a percent absorption of 92.10% against MRC and 89.59% against SRC.

Influence of pH

The influence of pH depends on the surface charge of the adsorbent and the pH of the adsorbate solution. To determine the surface charge on the adsorbent can be determined by pH_{pzc} . pH_{pzc} is obtained from the difference between the initial pH and the final pH. The surface charge of the adsorbent whose value is close to zero is the optimum zeta potential value of the adsorbent. The surface charge of the adsorbent will be positive if the pH

is below pH_{pzc} and negative if the pH is above pH_{pzc} . The higher the adsorbent surface charge, the lower the pH_{pzc} value or close to zero [34]. The pH_{pzc} values obtained on the MRC and SRC adsorbents were optimum at pH 8 and had a negative surface charge, so they would be good at absorbing positively charged adsorbates (Fig. 6).

As shown in Fig. 7(b), the effect of pH on the CV is insignificant; from pH 4 to 12, the efficiency tends to fluctuate pH 12 at MRC gave the highest adsorption percentage, but the CV solution became saturated. Thus, the optimum pH obtained is pH 10 for both MRC and

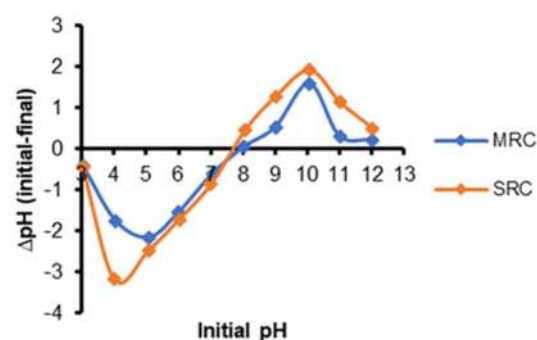


Fig 6. pH_{pzc} curve of MRC and SRC adsorbent

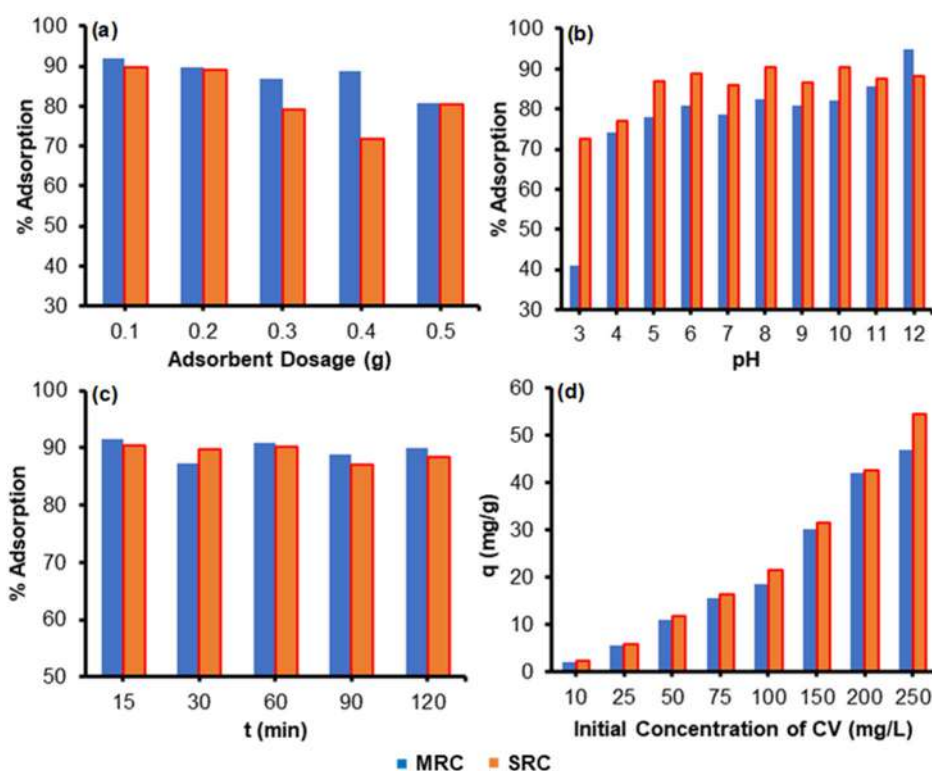


Fig 7. Influence of (a) adsorbent dosage, (b) pH solution, (c) contact time, and (d) initial concentration CV adsorbed by MRC and SRC

SRC, with absorption percentages of 82.15 and 90.37%, respectively. The adsorption percentage obtained indicates that the pH of the solution affects the CV adsorption process, where the results obtained from the SRC adsorbent are better than MRC. This result can occur due to the presence of two active groups in the SRC, which in alkaline conditions gives a more optimal contribution.

At pH 10, the adsorption process worked because it followed the previously obtained pH_{pzc} at pH 8, and the adsorbent had a negative surface charge so that it could interact with a CV which is a cationic dye. Due to competition between CV molecules and H^+ ions on the surface of the adsorbent at $pH < 7$, the adsorption process is not ideal, and a repulsion reaction will occur between the adsorbate and adsorbent [12].

The amount of H^+ ions on the adsorbent's surface will decrease in alkaline conditions ($pH > 7$) so that the adsorbent effectively adsorbs the adsorbate. The more negative the surface charge on the adsorbent, the more electrostatic interactions between the adsorbent and adsorbate will increase. At an increasingly alkaline pH ($pH > 10$), there is an increase in the concentration of OH^- , which will cause precipitation in the solution, and the adsorption ability will be inhibited [35].

Influence of contact time and the kinetic studies

The effect of contact time is essential for defining the appropriate duration for the interaction between adsorbent and adsorbate so that the highest adsorption efficiency may be achieved. Contact time varies from 15 to 120 min. Based on Fig. 7(c), the highest adsorption percentages obtained by MRC and SRC were 91.51 and 90.36%, respectively. Where the results obtained were more remarkable than CV adsorption carried out using Raw *Parthenium hysterophorus* and Raw *Saccharum munja*, which gave the respective adsorption percentages of 84.2 and 86% [36]. The percentage result of adsorption using MRC adsorbent is slightly larger than SRC adsorbent, but the difference is not too significant.

The contact time of 15 min gave the highest efficiency for MRC and SRC adsorbents, which means the adsorption process is faster. This result can occur because of the empty and available part of the surface (active site)

from the adsorbent that can interact with CV dyes. The brief contact time suggests that MRC or SRC with a CV is a physical interaction [37]. The decrease in adsorption efficiency if the contact time is longer can be due to the unavailability or limited availability of active sites on the adsorbent [38]. Thus, the influence of contact time gives a result of 15 min for MRC and SRC to adsorb the CV solution with high efficiency.

The kinetics throughout the adsorption process was computed utilizing the contact time data gathered for this study. Pseudo-first-order and pseudo-second-order kinetics are determined using Eq. (3) and (4), respectively:

$$\ln(q_e - q_t) = \ln(q_e) - k_1 t \quad (3)$$

$$\frac{t}{q_t} = \frac{1}{k_2 q_e^2} + \frac{1}{q_e} t \quad (4)$$

where q_t and q_e ($mg\ g^{-1}$) represent the total adsorption capacity of CV at time t and equilibrium k_1 , and k_2 represent the first-order and second-order rate constants of adsorption, respectively.

The Eq. (3) for pseudo-first-order kinetics is plotted on a graph of $\ln(q_e - q_t)$ versus time (t) as shown in Fig. 8(a), a straight line is formed with a direction tangent of k_1 and an intersection point on the y axis of $\ln(q_e)$. The value of k_1 can be determined using linear regression. While Eq. (4) is represented in the t/q_t versus t graph as shown in Fig. 8(b), a straight line is produced with a direction tangent of $1/q_e$ and an intersection point on the y-axis of $1/k_2 q_e^2$. As a result, it is possible to determine the value of the constant k_2 .

In Table 1, kinetic information, adsorption rate constants, and regression coefficients are shown. The results demonstrated that CV adsorption by MRC and SRC had a pseudo-second-order kinetic model because the correlation coefficient (R^2) value was closer to 1, as we can see in Table 1. R^2 value on MRC 0.991 and SRC 0.982 [35]. The kinetic model obtained in this study is the same as several studies using carbon material as an adsorbent in the adsorption of CV [12,38-39].

If it is seen from the rate constant on the adsorbent, SRC is faster than MRC, inversely proportional to the percentage of adsorption obtained. These different rates

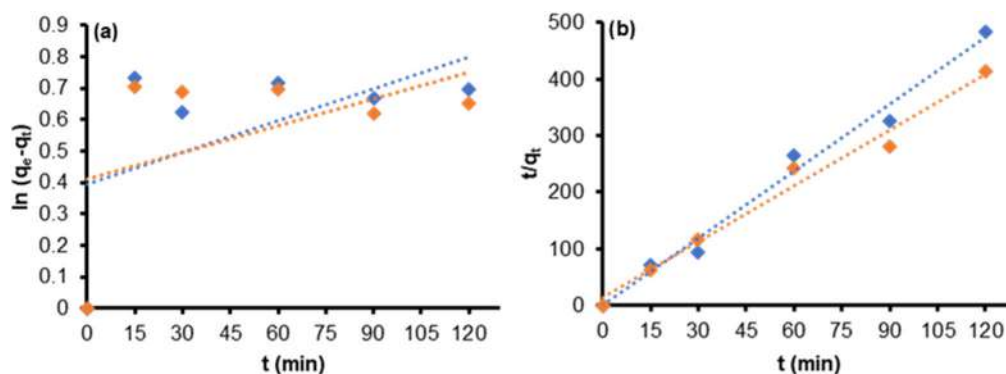


Fig 8. (a) Pseudo-first-order and (b) pseudo-second-order kinetics for adsorption of CV dye on MRC and SRC

Table 1. Kinetic parameters for CV adsorption on MRC and SRC

Adsorbents	Pseudo-first-order		Pseudo-second-order	
	k_1 (min^{-1}) (10^{-1})	R^2	k_2 ($\text{g mg}^{-1} \text{min}^{-1}$)	R^2
MRC	0.034	0.301	3.403	0.991
SRC	0.029	0.230	0.827	0.982

can be due to the presence of two active groups in SRC, namely (-OH) hydroxyl and (-C₆H₅) phenyl, so that it can carry out the adsorption process faster than MRC, which has an active group (-OH) in interacting with the active part of the dye, (N⁺) and the benzene ring. The fast adsorption time that lasts can affect the percentage of CV adsorption by the adsorbent.

Influence of Concentration and Adsorption Isotherm

The influence of CV adsorption concentration by MRC and SRC was carried out with various concentrations of 10, 25, 50, 75, 100, 150, 200, and 250 mg L⁻¹. The initial concentration used is plotted against the adsorption capacity (q) obtained, which can be seen in Fig. 7(d). The increase in initial concentration enhances the adsorption capacity of CV from 2.14 to 47.01 mg g⁻¹ for MRC adsorbent and from 2.27 to 54.63 mg g⁻¹ for SRC adsorbent. This increment is due to the adsorbent's high affinity, which enables the active site to adsorb the adsorbate better [12].

According to the statistics on adsorption capacity, MRC has a smaller adsorption capacity than SRC adsorbent. This fact can be explained due to the narrowing of the pores of the magnetite coating so that the surface's active site of the RC becomes slightly

reduced. MRC and SRC adsorbents can remove the CV dyes in the solution.

The result data of the influence of concentration were then analyzed using the Langmuir Eq. (5) and Freundlich adsorption isotherm pattern Eq. (6).

$$\frac{1}{q_e} = \frac{1}{q_m K_L C_e} + \frac{1}{q_m} \quad (5)$$

$$\log q_e = \log K_F + \frac{1}{n} \log C_e \quad (6)$$

where C_e (mg L⁻¹) is the equilibrium concentration of CV in solution, q_e (mg g⁻¹) is the equilibrium adsorption capacity, q_m is the adsorption capacity of a single layer, K_L (L mg⁻¹) is the equilibrium constant incorporating the binding site affinity, K_F ((mg g⁻¹)(L mg⁻¹)^{1/n}) is the adsorption capacity factor, and n is the adsorption intensity factor which has a value between 1 to 10 [35].

The linear plot equation C/m against C_e yields a straight line with $1/q_m K_L$ as the slope and $1/q_m$ as the intercept, which can be seen in Fig. 9(a). Hence, it may be used to determine K_L and q_m from the Langmuir equation. The linear plot of $\log q_e$ versus $\log C_e$ yields a straight line with $1/n$ as a slope and $\log K_F$ as an intercept, shown in Fig. 9(b). Therefore, the value of n and K_F can be determined.

The Langmuir isotherm model assumes that there are a certain number of active sites on the adsorbent's

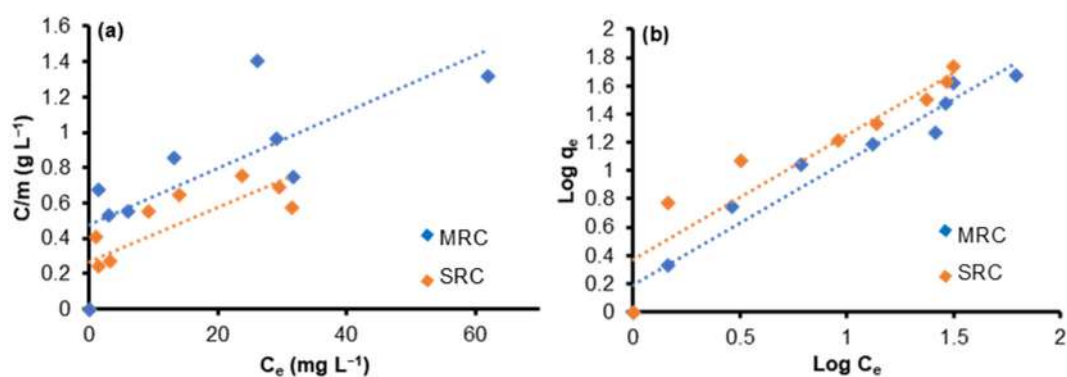


Fig 9. Adsorption isotherm of CV dye on MRC and SRC based on (a) Langmuir and (b) Freundlich

surface that are proportional to the surface area, the adsorbent surface is uniform, and the adsorption process is monolayer [40-41]. When the active site of a surface has been filled with adsorbate, there will be no additional adsorption at that site [42]. Thus, the maximum saturation point of adsorption on the adsorbent surface will be reached [43]. As a result, the occurrence of the adsorption process is known as monolayer adsorption. Freundlich's isotherm model is an empirical formula that is used to illustrate a heterogeneous system which is conveyed through Eq. (6) [44].

The Freundlich isotherm pattern tends to be followed in the adsorption of CV by MRC and SRC, as shown in Table 2. The Freundlich isotherm pattern of the adsorbent has a higher R^2 value than the Langmuir isotherm pattern, which is closer to 1. This fact

demonstrates that the adsorption occurs on a CV because not all of the adsorbent's active surfaces can do so; as a result, the adsorption that takes place is heterogeneous. The development of a multilayer on the surface of the adsorbent distinguishes the heterogeneous adsorption process [45].

The formation of layers on the surface of the adsorbent is caused by physical interactions that occur in the ongoing adsorption process [12]. Physical interactions that occur in CV adsorption by MRC and SRC can be in the form of electrostatic interactions between the hydroxyl group from Fe_3O_4 on MRC (Fig. 10(a)) and the hydroxyl group on SRC to the (N^+) group on the CV as well as π - π bond interactions between phenyl group on SRC to benzene ring on CV (Fig. 10(b)) [46-47].

Table 2. Isotherm parameters for adsorption of CV onto MRC and SRC

Adsorbents	Langmuir			Freundlich		
	q_m (mg g^{-1})	K_L (L mg^{-1})	R^2	n	K_F (mg g^{-1})(L mg^{-1}) $^{1/n}$)	R^2
MRC	71.429	0.025	0.428	1.093	1.362	0.943
SRC	69.930	0.049	0.549	1.026	1.761	0.932

Table 3. Comparison of MRC and SRC with other adsorbents used in CV removal

Adsorbent	q_m (mg g^{-1})	References
Rice husk activated carbon	11.18	[48]
AC- Fe_2O_3 .NPLs	16.50	[49]
ACL/ Fe_3O_4 magnetic nanocomposite	35.31	[39]
AC (Common Reed)	38.50	[50]
AC derived from Golbasi lignite	60.8–65.8	[51]
Chitosan AC	12.50	[16]
rGO/ Fe_3O_4 NCs	62.00	[52]
MRC (Rubber Fruit shell)	71.43	This Work
SRC (Rubber Fruit shell)	69.93	This Work

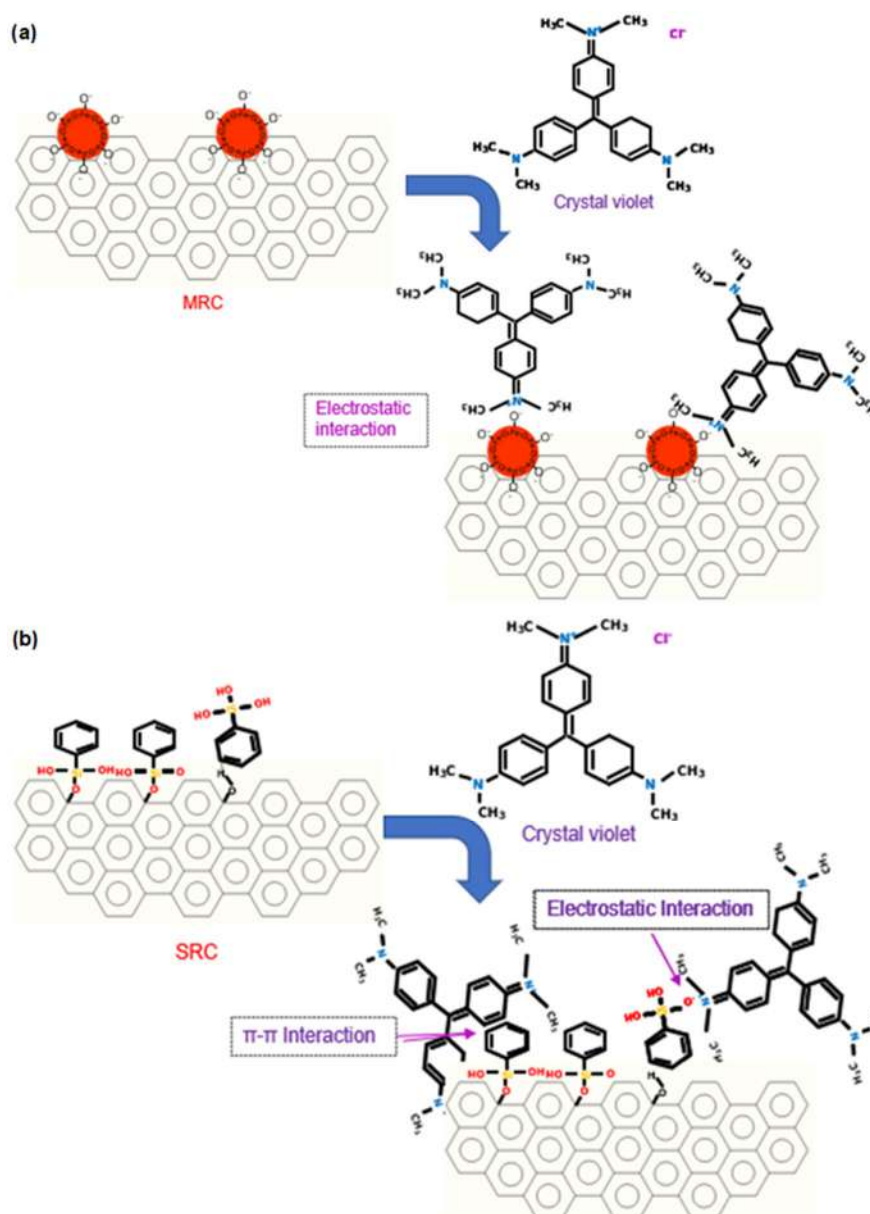


Fig 10. Mechanism adsorption of CV dye by (a) MRC and (b) SRC

If the adsorption capacity of the modified RC with magnetite and silane agents is compared with several adsorbents used to remove CV in solution (Table 3), it can be stated that MRC and SRC are effective adsorbents in absorbing CV. Thus, it can be stated that RC modification with magnetite coating and silane agent has increased the number of active adsorption sites on MRC and SRC. Our results align with the research reported by Alizadeh et al. [53], who used Azolla. Fig leaves modified magnetite nanoparticles as adsorbents in absorbing CV, and Jiao et

al. [54] used a hydrophobic clinoptilolite-modified silane coupling agent as a CV adsorption adsorbent.

CONCLUSION

In this research, modified RC with magnetite (MRC) and TEPS coupling agent (SRC) has been made, which is used as an effective and inexpensive adsorbent for CV dye solution. The adsorption capacity of MRC and SRC is influenced by several parameters, including adsorbent dose (0.1 g), pH (10), contact time (15 min),

and initial CV concentration (250 mg L^{-1}), with excellent results. The adsorption capacity obtained at MRC was 71.43, and SRC was 69.93 mg g^{-1} . The rate of adsorption kinetics tends to follow pseudo-second-order kinetics. The Freundlich isotherm is suitable for this adsorption compared to the Langmuir model, indicating that the adsorption that occurs is multilayer with physical interactions. MRC and SRC can be effective adsorbents to remove CV dye solution.

■ ACKNOWLEDGMENTS

The authors are grateful to the Research and Community Service Institute of the University of Lampung (LPPM Universitas Lampung) has funded this project with contract number: 819/UN26.21/PN/2022, and the Ministry of Education, Culture, Research, and Technology, Republic of Indonesia (Kemendikbud-Ristek) for the support of this research.

■ AUTHOR CONTRIBUTIONS

Nadya Syarifatul Fajriyah experimented. Nadya Syarifatul Fajriyah wrote the manuscript with the support and supervision of Buhani and Suharso. All authors approved the final version of the manuscript.

■ REFERENCES

- [1] Yahaya Sanda, B., and Ibrahim, I., 2020, Causes, categories and control of water pollution, *IJSES*, 4 (9), 84–90.
- [2] Foroutan, R., Peighambardoust, S.J., Aghdasinia, H., Mohammadi, R., and Ramavandi, B., 2020, Modification of bio-hydroxyapatite generated from waste poultry bone with MgO for purifying methyl violet-laden liquids, *Environ. Sci. Pollut. Res.*, 27 (35), 44218–44229.
- [3] Peighambardoust, S.J., Aghamohammadi-Bavil, O., Foroutan, R., and Arsalani, N., 2020, Removal of malachite green using carboxymethyl cellulose-g-polyacrylamide/montmorillonite nanocomposite hydrogel, *Int. J. Biol. Macromol.*, 159, 1122–1131.
- [4] Pashaei-Fakhri, S., Peighambardoust, S.J., Foroutan, R., Arsalani, N., and Ramavandi, B., 2021, Crystal violet dye sorption over acrylamide/graphene oxide bonded sodium alginate nanocomposite hydrogel, *Chemosphere*, 270, 129419.
- [5] Mittal, H., Al Alili, A., Morajkar, P.P., and Alhassan, S.M., 2021, Graphene oxide crosslinked hydrogel nanocomposites of xanthan gum for the adsorption of crystal violet dye, *J. Mol. Liq.*, 323, 115034.
- [6] Abdi, M., Balagabri, M., Karimi, H., Hossini, H., and Rastegar, S.O., 2020, Degradation of crystal violet (CV) from aqueous solutions using ozone, peroxone, electroperoxone, and electrolysis processes: A comparison study, *Appl. Water Sci.*, 10 (7), 168.
- [7] Thuong, N.T., Nhi, N.T.T., Nhung, V.T.C., Bich, H.N., Quynh, B.T.P., Bach, L.G., and Nguyen, T.D., 2019, A fixed-bed column study for removal of organic dyes from aqueous solution by pre-treated durian peel waste, *Indones. J. Chem.*, 19 (2), 486–494.
- [8] Thattil, P.P., and Rose, A.L., 2020, Enhanced removal of crystal violet dye using zinc oxide nanorods and air oxidation under sunlight radiation, *Rasayan J. Chem.*, 13 (2), 1166–1173.
- [9] Shi, B., Li, G., Wang, D., Feng, C., and Tang, H., 2007, Removal of direct dyes by coagulation: The performance of preformed polymeric aluminum species, *J. Hazard. Mater.*, 143 (1-2), 567–574.
- [10] Liu, H., Zhang, J., Lu, M., Liang, L., Zhang, H., and Wei, J., 2020, Biosynthesis based membrane filtration coupled with iron nanoparticles reduction process in removal of dyes, *Chem. Eng. J.*, 387, 124202.
- [11] Wu, J., Gao, H., Yao, S., Chen, L., Gao, Y., and Zhang, H., 2015, Degradation of crystal violet by catalytic ozonation using Fe/activated carbon catalyst, *Sep. Purif. Technol.*, 147, 179–185.
- [12] Buhani, B., Suharso, S., Luziana, F., Rilyanti, M., and Sumadi, S., 2019, Production of adsorbent from activated carbon of palm oil shells coated by Fe_3O_4 particle to remove crystal violet in water, *Desalin. Water Treat.*, 171, 281–293.
- [13] Permatasari, D., Buhani, B., Rilyanti, M., and

- Suharso, S., 2021, Adsorption kinetic and isotherm of solution pair of methylene blue and crystal violet by algae-silica-magnetite hybrid adsorbent on *Porphyridium* sp. algae, *J. Phys.: Conf. Ser.*, 1751, 012084.
- [14] Fabryanty, R., Valencia, C., Soetaredjo, F.E., Putro, J.N., Santoso, S.P., Kurniawan, A., Ju, Y.H., and Ismadji, S., 2017, Removal of crystal violet dye by adsorption using bentonite – alginate composite, *J. Environ. Chem. Eng.*, 5 (6), 5677–5687.
- [15] Ahmad, R., 2009, Studies on adsorption of crystal violet dye from aqueous solution onto coniferous pinus bark powder (CPBP), *J. Hazard. Mater.*, 171 (1-3), 767–773.
- [16] Jayasanthi Kumari, H., Krishnamoorthy, P., Arumugam, T.K., Radhakrishnan, S., and Vasudevan, D., 2017, An efficient removal of crystal violet dye from waste water by adsorption onto TLAC/Chitosan composite: A novel low cost adsorbent, *Int. J. Biol. Macromol.*, 96, 324–333.
- [17] Li, H., Qi, H., Yin, M., Chen, Y., Deng, Q., and Wang, S., 2021, Carbon tubes from biomass with prominent adsorption performance for paraquat, *Chemosphere*, 262, 127797.
- [18] Sebastian, A., Nangia, A., and Prasad, M.N.V., 2018, A green synthetic route to phenolics fabricated magnetite nanoparticles from coconut husk extract: Implications to treat metal contaminated water and heavy metal stress in *Oryza sativa* L., *J. Cleaner Prod.*, 174, 355–366.
- [19] Buhani, B., Hariyanti, F., Suharso, S., Rinawati, R., and Sumadi, S., 2019, Magnetized algae-silica hybrid from *Porphyridium* sp. biomass with Fe₃O₄ particle and its application as adsorbent for the removal of methylene blue from aqueous solution, *Desalin. Water Treat.*, 142, 331–340.
- [20] Singh, K.P., Gupta, S., Singh, A.K., and Sinha, S., 2011, Optimizing adsorption of crystal violet dye from water by magnetic nanocomposite using response surface modeling approach, *J. Hazard. Mater.*, 186 (2-3), 1462–1473.
- [21] Mohmood, I., Lopes, C.B., Lopes, I., Tavares, D.S., Soares, A.M.V.M., Duarte, A.C., Trindade, T., Ahmad, I., and Pereira, E., 2016, Remediation of mercury contaminated saltwater with functionalized silica coated magnetite nanoparticles, *Sci. Total Environ.*, 557-558, 712–721.
- [22] Buhani, B., Herasari, D., Suharso, S., and Yuwono, S.D., 2017, Correlation of ionic imprinting cavity sites on the amino-silica hybrid adsorbent with adsorption rate and capacity of Cd²⁺ ion in solution, *Orient. J. Chem.*, 33 (1), 418–429.
- [23] Zulaicha, A.S., Buhani, B., and Suharso, S., 2021, Modification of activated carbon from *Elaeis guineensis* Jacq shell with magnetite (Fe₃O₄) particles and study adsorption-desorption on Ni(II) ions in solution, *J. Phys.: Conf. Ser.*, 1751, 012086.
- [24] Wong, K.T., Yoon, Y., Snyder, S.A., and Jang, M., 2016, Phenyl-functionalized magnetic palm-based powdered activated carbon for the effective removal of selected pharmaceutical and endocrine-disruptive compounds, *Chemosphere*, 152, 71–80.
- [25] Kausar, R.A., Buhani, B., and Suharso, S., 2020, Methylene blue adsorption isotherm on *Spirulina* sp. microalgae biomass coated by silica-magnetite, *IOP Conf. Ser.: Mater. Sci. Eng.*, 857, 012019.
- [26] Buhani, B., Suharso, S., Rilyanti, M., Sari, M., and Sumadi, S., 2021, Removal of Cd(II) ions in solution by activated carbon from palm oil shells modified with magnetite, *Desalin. Water Treat.*, 218, 352–362.
- [27] Buhani, B., Suharso, S., Miftahza, N., Permatasari, D., and Sumadi, S., 2021, Improved adsorption capacity of *Nannochloropsis* sp. through modification with cetyltrimethylammonium bromide on the removal of methyl orange in solution, *Adsorpt. Sci. Technol.*, 2021, 1641074.
- [28] Yamaura, M., Camilo, R.L., Sampaio, L.C., Macêdo, M.A., Nakamura, M., and Toma, H.E., 2004, Preparation and characterization of (3-aminopropyl)triethoxysilane-coated magnetite nanoparticles, *J. Magn. Magn. Mater.*, 279 (2-3), 210–217.
- [29] Dalali, N., Habibzadeh, M., Rostamzadeh, K., and Nakisa, S., 2014, Synthesis of magnetite multi-

- walled carbon nanotubes composite and its application for removal of basic dyes from aqueous solutions, *Asia-Pac. J. Chem. Eng.*, 9 (4), 552–561.
- [30] Romanos, J., Beckner, M., Stalla, D., Tekeei, A., Suppes, G., Jalisatgi, S., Lee, M., Hawthorne, F., Robertson, J.D., Firlej, L., Kuchta, B., Wexler, C., Yu, P., and Pfeifer, P., 2013, Infrared study of boron-carbon chemical bonds in boron-doped activated carbon, *Carbon*, 54, 208–214.
- [31] Harimu, L., Wahyuni, S., Nasrudin, N., Baari, M.J., and Permana, D., 2022, Fabrication of chitosan/Fe₃O₄ nanocomposite as adsorbent for reduction methylene blue contents, *Indones. J. Chem.*, 22 (3), 878–886.
- [32] Khuluk, R.H., Rahmat, A., Buhani, B., and Suharso, S., 2019, Removal of methylene blue by adsorption onto activated carbon from coconut shell (*Cococus nucifera* L.), *Indones. J. Sci. Technol.*, 4 (2), 229–240.
- [33] Gundogdu, A., Duran, C., Senturk, H.B., Soylak, M., Ozdes, D., Serencam, H., and Imamoglu, M., 2012, Adsorption of phenol from aqueous solution on a low-cost activated carbon produced from tea industry waste: Equilibrium, kinetic, and thermodynamic study, *J. Chem. Eng. Data*, 57 (10), 2733–2743.
- [34] Mohan, D., Sarswat, A., Singh, V.K., Alexandre-Franco, M., and Pittman, C.U., 2011, Development of magnetic activated carbon from almond shells for trinitrophenol removal from water, *Chem. Eng. J.*, 172 (2-3), 1111–1125.
- [35] Buhani, B., Halimah, S.N., Suharso, S., and Sumadi, S., 2022, Utilization of activated carbon from candlenut shells (*Aleurites moluccana*) as methylene blue adsorbent, *Rasayan J. Chem.*, 15 (1), 124–131.
- [36] Singh, A., Kumar, S., Panghal, V., Arya, S.S., and Kumar, S., 2019, Utilization of unwanted terrestrial weeds for removal of dyes, *Rasayan J. Chem.*, 12 (4), 1956–1963.
- [37] Kakavandi, B., Jonidi Jafari, A., Rezaei Kalantary, R., Nasser, S., Esrafil, A., Gholizadeh, A., and Azari, A., 2016, Simultaneous adsorption of lead and aniline onto magnetically recoverable carbon: Optimization, modeling and mechanism, *J. Chem. Technol. Biotechnol.*, 91 (12), 3000–3010.
- [38] Abdel-Salam, A.H., Ewais, H.A., and Basaleh, A.S., 2017, Silver nanoparticles immobilised on the activated carbon as efficient adsorbent for removal of crystal violet dye from aqueous solutions. A kinetic study, *J. Mol. Liq.*, 248, 833–841.
- [39] Foroutan, R., Peighambar, S.J., Peighambar, S.H., Pateiro, M., and Lorenzo, J.M., 2021, Adsorption of crystal violet dye using activated carbon of lemon wood and activated carbon/Fe₃O₄ magnetic nanocomposite from aqueous solutions: A kinetic, equilibrium and thermodynamic study, *Molecules*, 26 (8), 2241.
- [40] Toan, N.C., Binh, Q.A., Tungtakanpoung, D., and Kajitvichyanukul, P., 2020, Kinetic, isotherm and mechanism in paraquat removal by adsorption processes using different biochars, *Lowl. Technol. Int.*, 22 (2), 304–317.
- [41] Iryani, A., Nur, H., Santoso, M., and Hartanto, D., 2020, Adsorption study of rhodamine B and methylene blue dyes with ZSM-5 directly synthesized from Bangka kaolin without organic template, *Indones. J. Chem.*, 20 (1), 130–140.
- [42] Damiyine, B., Guenbour, A., and Boussem, R., 2020, Comparative study on adsorption of cationic dye onto expanded perlite and natural clay, *Rasayan J. Chem.*, 13 (1), 448–463.
- [43] Pranoto, P., Purnawan, C., and Utami, T., 2018, Application of Bekonang clay and andisol soil composites as copper(II) metal ion adsorbent in metal crafts wastewater, *Rasayan J. Chem.*, 11 (1), 23–31.
- [44] Shao, Y., Zhou, L., Bao, C., Ma, J., Liu, M., and Wang, F., 2016, Magnetic responsive metal-organic frameworks nanosphere with core-shell structure for highly efficient removal of methylene blue, *Chem. Eng. J.*, 283, 1127–1136.
- [45] Buhani, B., Narsito, N., Nuryono, N., Kunarti, E.S., and Suharso, S., 2015, Adsorption competition of Cu(II) ion in ionic pair and multi-metal solution by ionic imprinted amino-silica hybrid adsorbent, *Desalin. Water Treat.*, 55 (5), 1240–1252.
- [46] Wong, K.T., Eu, N.C., Ibrahim, S., Kim, H., Yoon,

- Y., and Jang, M., 2016, Recyclable magnetite-loaded palm shell-waste based activated carbon for the effective removal of methylene blue from aqueous solution, *J. Cleaner Prod.*, 115, 337–342.
- [47] Abbas, M., Harrache, Z., and Trari, M., 2020, Mass-transfer processes in the adsorption of crystal violet by activated carbon derived from pomegranate peels: Kinetics and thermodynamic studies, *J. Eng. Fibers Fabr.*, 15, 1558925020919847.
- [48] Mohanty, K., Naidu, J.T., Meikap, B.C., and Biswas, M.N., 2006, Removal of crystal violet from wastewater by activated carbons prepared from rice husk, *Ind. Eng. Chem. Res.*, 45 (14), 5165–5171.
- [49] Hamidzadeh, S., Torabbeigi, M., and Shahtaheri, S.J., 2015, Removal of crystal violet from water by magnetically modified activated carbon and nanomagnetic iron oxide, *J. Environ. Health Sci. Eng.*, 13 (1), 8.
- [50] Shouman, M.A., and Rashwan, W.E., 2012, Studies on adsorption of basic dyes on activated carbon derived from *Phragmites australis* (common reed), *Univers. J. Environ. Res. Technol.*, 2 (3), 119–134.
- [51] Depci, T., Kul, A.R., Onal, Y., Disli, E., Alkan, S., and Turkmenoglu, Z.F., 2012, Adsorption of crystal violet from aqueous solution on activated carbon derived from Gölbaşı lignite, *Physicochem. Probl. Miner. Process.*, 48 (1), 253–270.
- [52] Kahsay, M.H., Belachew, N., Tadesse, A., and Basavaiah, K., 2020, Magnetite nanoparticle decorated reduced graphene oxide for adsorptive removal of crystal violet and antifungal activities, *RSC Adv.*, 10 (57), 34916–34927.
- [53] Alizadeh, N., Shariati, S., and Besharati, N., 2017, Adsorption of crystal violet and methylene blue on azolla and fig leaves modified with magnetite iron oxide nanoparticles, *Int. J. Environ. Res.*, 11 (2), 197–206.
- [54] Jiao, J., Sun, J., Ullah, R., Bai, S., and Zhai, C., 2020, One-step synthesis of hydrophobic clinoptilolite modified by silanization for the degradation of crystal violet dye in aqueous solution, *RSC Adv.*, 10 (38), 22809–22818.

Synthesis of Zeolite/NPK Coated with Cu-Alginate-PVA-Glutaraldehyde as a Slow-Release Fertilizer

Ratna Betriani*, Sutarno Sutarno, Indriana Kartini, and Jolang Budiarta

Department of Chemistry, Faculty of Mathematics and Natural Sciences, Universitas Gadjah Mada, Sekip Utara, Yogyakarta 55281, Indonesia

* **Corresponding author:**

email: ratnabetriani@mail.ugm.ac.id

Received: July 12, 2022

Accepted: October 17, 2022

DOI: 10.22146/ijc.76205

Abstract: The objectives of this study were to synthesize zeolite/NPK coated with Cu-alginate-PVA-glutaraldehyde as a material for slow-release fertilizers and to study the effect of various Cu concentrations in the coating material on the resistance of the zeolite/NPK fertilizer and to study the release rate reaction in citric acid. The study began with the synthesis of the zeolite/NPK fertilizer and the Cu-alginate-PVA-glutaraldehyde coating materials with variations of Cu concentration of 0.0; 0.2; 0.4; 0.6; 0.8; and 1.0 M. The Zeolite/NPK fertilizer and the coated NPK fertilizer were characterized by XRD and FTIR. The determination of the released N and P was conducted using a UV-Visible spectrophotometer, while released K and Cu was analyzed using AAS. XRD showed that the composite had a crystalline structure. The FTIR spectra showed characteristic cross-linking interactions between PVA-glutaraldehyde and Cu-alginate. A study of the release kinetics of zeolite/NPK coated with Cu-alginate-PVA-glutaraldehyde showed that increasing Cu concentration to 0.4 M decreased the amount of nutrition released, and the release process followed the pseudo-second-order kinetics. The release rate constants of N,P,K and Cu in the citric acid medium on zeolite/NPK coated with Cu 0.4 M were 8.49×10^{-3} , 17.48×10^{-3} , 21.73×10^{-3} , and $8.57 \times 10^{-3} \text{ mg g}^{-1} \text{ h}^{-1}$, respectively.

Keywords: alginate; cross-link; Cu; glutaraldehyde; PVA

■ INTRODUCTION

Plants need an adequate amount of nutrition to grow. There are two kinds of nutrients for plants: macronutrients and micronutrients. The former are those which are required in relatively large amounts: carbon, hydrogen, oxygen, nitrogen, phosphorus, calcium, sulfur, potassium and magnesium. The micronutrients are those required in small amounts, such as chlorine, iron, manganese, boron, zinc, copper, molybdenum, sodium and selenium [1]. Even though micronutrients are not necessarily needed in a huge amount, they have an equal role in the growth of plants. Copper (Cu) is a type of micronutrient that is crucially needed though in a small amount. One of the functions of Cu is to activate some of the enzymes involved in lignin synthesis. Cu is also very crucial for photosynthesis, respiration, and also helps the metabolism of carbohydrates and protein. Lack of Cu in plants can cause withered-looking young leaves, which

will die eventually, and it can also cause the branches to turn brown and eventually die [2].

Nutrients needed by plants can be fulfilled by providing fertilizers, an important material in plant growth. Commercial NPK (Nitrogen Phosphorus Kalium) fertilizers in the market have a disadvantage, in that they are easily soluble in water, so they can pollute the environment. Besides that, commercial fertilizers have reduced efficiency and need to be frequently applied to optimize nutrient intake [3]. Zeolite is used as an additive in slow-release fertilizers. Zeolites added to fertilizers give double results when applied to soil: provide long lasting action of the fertilizer (prolongation effect) and prevent nutrient leaching [4]. One of the methods to reduce the rate of release of nutrients in fertilizers is by using slow-release or controlled fertilizers. Slow-release fertilizers are fertilizers that have low solubility and can provide a gradual supply of

nutrients over a long period of time, thereby increasing the efficiency of nutrient uptake by plants and reducing their loss due to the leaching process [5-7]. One type of slow-release fertilizer is coated fertilizers [8].

The constituent materials in slow-release fertilizers consist of two components, namely carrier material or support material and minerals needed by plants [9]. Zeolite is a support material used in agriculture because it is environmentally friendly, relatively stable to acids and easy to obtain. In the manufacture of fertilizers, zeolite is often used as carrier material and ballast or filler material. Sustainable development of agricultural products could also be assisted by zeolite as a slow-release fertilizer and to control pests [10]. NPK is a nutrient needed by plants to grow and can be mixed with zeolite with the help of starch as an adhesive material. The interaction between zeolite and NPK is a physical interaction that can cause NPK to be easily released by water, so zeolite/NPK fertilizers require coating materials to control or slow down the nutrient release rate from the fertilizers [11].

The synthesis of slow-release fertilizers has undergone many developments. Sodium alginate can be used as a coating material for fertilizers to produce slow-release fertilizers. The alginate-gelatin hydrogel can be a slow-release nutrient to plant an environmentally friendly fertilizer [12]. Sodium alginate can be cross-linked with divalent and trivalent metals such as Ca(II), and Fe(III) [13-14]. Alginate and Cu(II) as a divalent metal ion create intermolecular bonds forming a nonplanar geometry [15]. These cross-links can decrease the solubility of alginate membranes in water [16]. The CuSO_4 solution was also used as a cross-linking agent because Cu(II) ions belong to the group of essential micronutrients [17]. In the presence of divalent metal cations such as Cu^{2+} , alginates can form gels where cross-linking occurs due to the presence of chelating complexes between divalent ions and carboxylate anions of the G-G block. The cross-link interaction between alginate and Cu metal will increase the binding strength and stability of the fertilizer composite [18]. The CMC/PVA blend film may be a potential coating material for the application in the control-release fertilizer [19]. In addition to alginate, polyvinyl alcohol (PVA) can also form cross-links with

glutaraldehyde so that it can release K slowly from chitosan/PVA composites [20]. These studies show that the fertilizers synthesized using a single cross-linker have good resistance and are able to release nutrients slowly.

Based on the previous research, a study was conducted on slow-release fertilizers that have better resistance by using a double cross-linker. In this research, the synthesis of Cu-alginate-PVA-glutaraldehyde-coated zeolite/NPK was carried out as a slow-release fertilizer material, where Cu and glutaraldehyde act as cross-linkers.

■ EXPERIMENTAL SECTION

Materials

Natural zeolite was taken from Klaten, and technical-grade sodium alginate was obtained from Sigma-Aldrich. Urea (commercial quality), SP36 (commercial quality), KCl (commercial quality), technical-grade PVA, glutaraldehyde, copper sulfate pentahydrate ($\text{CuSO}_4 \cdot 5\text{H}_2\text{O}$), ethanol 95%, *p*-dimethylamino benzaldehyde (PDAB), vanadic acid, ammonium molybdate, concentrated HNO_3 , and citric acid were purchased from Sigma-Aldrich. Other materials include filter paper, double distilled water, and distilled water.

Instrumentation

The release of K and Cu nutrients test was carried out using atomic absorption spectroscopy (Perkin Elmer 3110), and the release of N and P nutrients was carried out using a UV-Vis spectrophotometer (Thermo Scientific Evolution 201). The samples were characterized using an infrared spectrophotometer (Shimadzu FTIR Prestige 21) and an X-ray diffractometer (PANalytical X'pert Pro).

Procedure

Preparation of zeolite/NPK fertilizer

The Zeolite/NPK fertilizer was made by mixing 316 g of previously sieved natural zeolite (200 mesh) with 100 g urea, 30 g KCl, and 30 g SP36. As much as 10 g of starch was weighed, dissolved in 100 mL of hot water, and stirred until thickened. The starch solution

prepared was mixed in the previous mixture, then the mixture was stirred until evenly distributed, and the resulting mixture was formed into granules with a mass that is made as similar in size as possible. The zeolite/NPK granules were then dried.

Preparation of Cu-alginate-PVA-glutaraldehyde coating solution with variations in Cu concentration

A total of 10 mL of 5% w/v PVA solution (5 mixed systems) was mixed with 10 mL of 2% w/v alginate solution (5 mixed systems), then stirred until homogeneous. The five mixed systems were then added with 10 mL of 1.25 v/v glutaraldehyde and stirred until homogeneous. Furthermore, 10 mL of CuSO₄ solution were added into five mixed systems with a concentration of 0.00; 0.20; 0.40; 0.60; 0.80; and 1.00 M. The dried zeolite/NPK fertilizer was then soaked in the five mixed systems for 30 min. Furthermore, the zeolite/NPK fertilizer which had been coated with a mixture of alginate-PVA-glutaraldehyde with various concentrations of CuSO₄, was dried at room temperature.

Characterization of zeolite/NPK and zeolite/NPK fertilizers coated with Cu-alginate-PVA-glutaraldehyde

The composite sample to be analyzed was first grounded to form a powder. Characterization was carried out using FTIR and XRD with the powder sample method.

Swelling test on the release of NPK and Cu from the zeolite/NPK fertilizer coated with Cu-alginate-PVA-glutaraldehyde in citric acid media

Each composite sample in a dry state was weighed and put in a container and was then added with 20 mL of 0.33 M citric acid solution. The citric acid solution was used because it has similar pH as the soil. On the 7th day, each sample that was soaked in citric acid was taken and weighed again. The swelling percentage can be obtained by calculating the difference (Eq. (1)) between the mass of the composite in a wet state (W_w) and the mass of the composite in a dry state (W_0) and then dividing it by the mass of the composite in a dry state.

$$Q_w = \frac{W_w - W_0}{W_0} \quad (1)$$

Test of the release of NPK and Cu from zeolite/NPK fertilizer coated with Cu-alginate-PVA-glutaraldehyde in citric acid media

A total of 0.20 g of each composite sample was put in a container and added with 20 mL of 0.33 M citric acid solution. The fertilizer immersion in the solution was allowed to sit, and 1 mL was taken for analysis of N, P, K, and Cu at intervals 3, 6, 12, 24, 48, 72, 96, 120, 144, 168, 192, 216, 240, 264, 288, 312, and 336 h. The filtrate containing N and P was then diluted, and a complexified solution was added and analyzed using a UV-Vis spectrophotometer, while the filtrate containing K and Cu was then diluted and analyzed using atomic absorption spectroscopy (AAS). The filtrate containing P was complexed with molybdovanadate and measured using a UV-Vis spectrophotometer at 400 nm, while the filtrate containing N was complexed with PDAB and measured using a UV-Vis spectrophotometer at 410 nm.

RESULTS AND DISCUSSION

XRD Spectroscopy

Zeolite/NPK fertilizers, alginate-PVA-glutaraldehyde-coated zeolite/NPK fertilizers, and Cu-alginate-PVA-glutaraldehyde-coated zeolite/NPK fertilizers were characterized using XRD and FTIR spectroscopy. Characterization using XRD spectroscopy was carried out to obtain information related to the crystallinity of zeolite/NPK fertilizer coated with Cu-alginate-PVA-glutaraldehyde as a result of the synthesis and the minerals contained in it. The crystallinity of a material indicates the regularity of the bonds in it. Crystallinity increases along with the increasing bond regularity. The sharper (pointer) diffraction peaks indicate the more crystalline the material, meaning that the regularity of the bonds within the material is also getting higher.

Fig. 1 shows the comparison of X-ray diffractograms between natural zeolite, Na-alginate, PVA, zeolite/NPK, zeolite/NPK alginate-PVA-glutaraldehyde, and zeolite/NPK Cu-alginate-PVA-glutaraldehyde with a Cu concentration of 0.4 M. The choice of X-ray diffractogram with variations in Cu concentration of 0.4 M was made

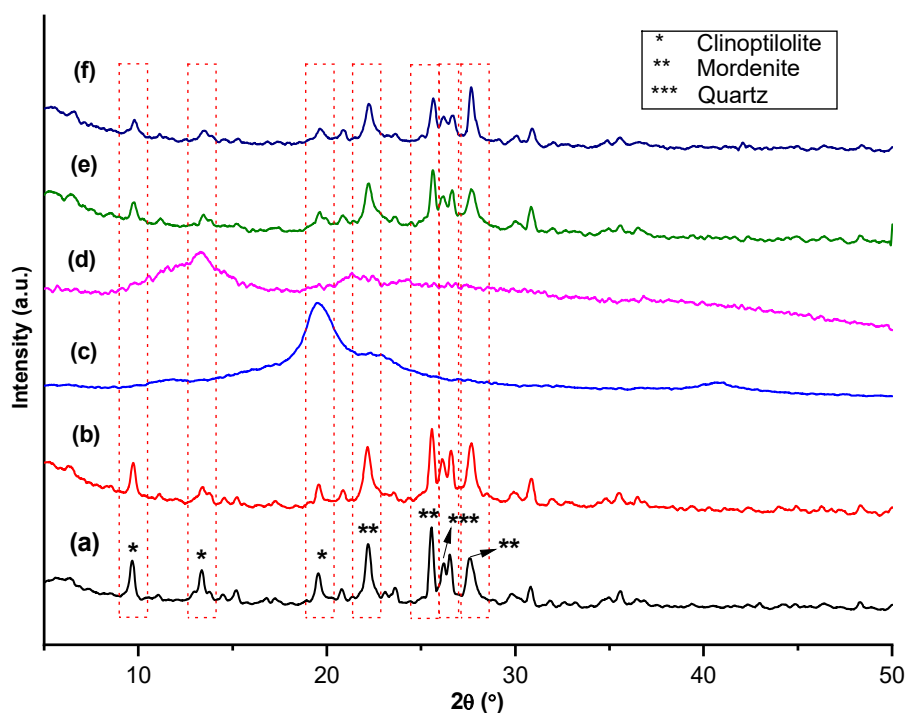


Fig 1. XRD diffractogram (a) natural zeolite, (b) zeolite/NPK, (c) PVA, (d) alginate, (e) zeolite/NPK alginate-PVA-glutaraldehyde, and (f) zeolite/NPK Cu (0.4 M)-alginate-PVA-glutaraldehyde

because at that concentration, the nutrient release was best, it had the slowest nutrient release compared to other concentration variations and also the smallest development value. This will be explained in detail in the next sub-chapter. It was expected that the Cu concentration of 0.4 M might be able to represent all samples using other variations of Cu.

The results of characterization using X-ray diffraction of natural zeolite-based material showed several sharp peaks at $2\theta = 26.5^\circ$, which identified the presence of quartz minerals according to JCPDS 05-0490, sharp peaks at $2\theta = 9.676$; 13.02 ; and 20.6° indicate the presence of clinoptilolite minerals according to JCPDS 25-1349, and sharp peaks at $2\theta = 15.17$; 22.15 ; 26.21 ; 27.57 ; and 30.67° indicate the presence of mineral mordenite in accordance with JCPDS 11-0155. The results of the characterization of the alginate base material showed that there were three peaks of alginate characteristics at $2\theta = 19.06$; 28.93 ; and 32.08° . The three peaks have a high intensity which indicates the formation of very strong hydrogen bond interactions in the guluronate and mannuronic units in alginate through

intermolecular interactions. The hydrogen bonds formed between the carboxyl and hydroxyl groups in the alginate structure. The results of the comparison of the zeolite/NPK fertilizer composite diffractogram with the natural zeolite diffractogram provide information that the same peak appears as the zeolite peak at $2\theta = 25.68$; 28.60 ; and 27.73° which indicates the presence of the mineral mordenite. Overall, zeolite/NPK fertilizer produced sharp diffractogram peaks, indicating that the zeolite/NPK fertilizer was crystalline.

The results of the comparison of the diffractogram of zeolite/NPK alginate-PVA-glutaraldehyde fertilizer with the diffractogram of natural zeolite and alginate provide information on peaks at $2\theta = 25.84^\circ$ and 27.87° that indicate the presence of mordenite minerals from zeolite, and there is a low-intensity peak at $2\theta = 32.12^\circ$ which is the typical peak of alginate. The presence of more zeolite in the composite material allows the zeolite to cover the alginate so that the crystalline peaks of the alginate mineral are not clearly visible. Polyvinyl alcohol is an amorphous material, but in this composite, the presence of amorphous PVA did not reduce the

crystallinity of the fertilizer. It is possible because there is a cross-link between PVA and glutaraldehyde which can improve the chemical properties of the material so that the fertilizer material remains crystalline. The diffractogram of alginate-PVA-glutaraldehyde-coated zeolite/NPK fertilizer showed sharp peaks, which indicates that the addition of coating material in the form of alginate-PVA-glutaraldehyde to zeolite/NPK fertilizer did not change the crystalline nature of the fertilizer.

Furthermore, the diffractogram of zeolite/NPK alginate-PVA-glutaraldehyde fertilizer was compared with that of zeolite/NPK Cu-alginate-PVA-glutaraldehyde fertilizer with variations in Cu concentration of 0.4 M. It can be seen that the diffractograms of the two composites were relatively the same, indicating that the addition of Cu in the composite did not decrease the crystallinity of the fertilizer which means that the regularity of the bonds in the material did not decrease due to the addition of Cu. This can happen because Cu itself has crystalline properties, so the addition of Cu in the composite does not damage the crystallinity of zeolite/NPK fertilizers.

Fig. 2 shows the comparison of the zeolite/NPK diffractogram of Cu-alginate-PVA-glutaraldehyde with

variations in Cu concentration 0.2; 0.4; 0.6; 0.8; and 1.0 M. Increasing the concentration of Cu in the coating material did not change the crystallinity of the fertilizer material even though Cu was crystalline. This is because the Cu in the composite acts as an alginate cross-linker in the coating material and does not directly interact with the zeolite/NPK fertilizers, so the crystallinity of the fertilizer does not increase significantly. In addition, the addition of a relatively small concentration of Cu in the composite system also resulted in the intensity of the diffractogram tending to remain constant even though Cu with varying concentrations was added.

FTIR Spectroscopy

The goal of the characterization using FTIR spectroscopy is to determine the presence of functional groups contained in the starting material, which includes natural zeolite, PVA, and alginate, as well as interactions/bonds between polymer chains of PVA, alginate and glutaraldehyde in the coating material for zeolite/NPK fertilizers which are interpreted into absorption peaks in the FTIR spectra. The absorption peak that indicates the interaction between PVA and

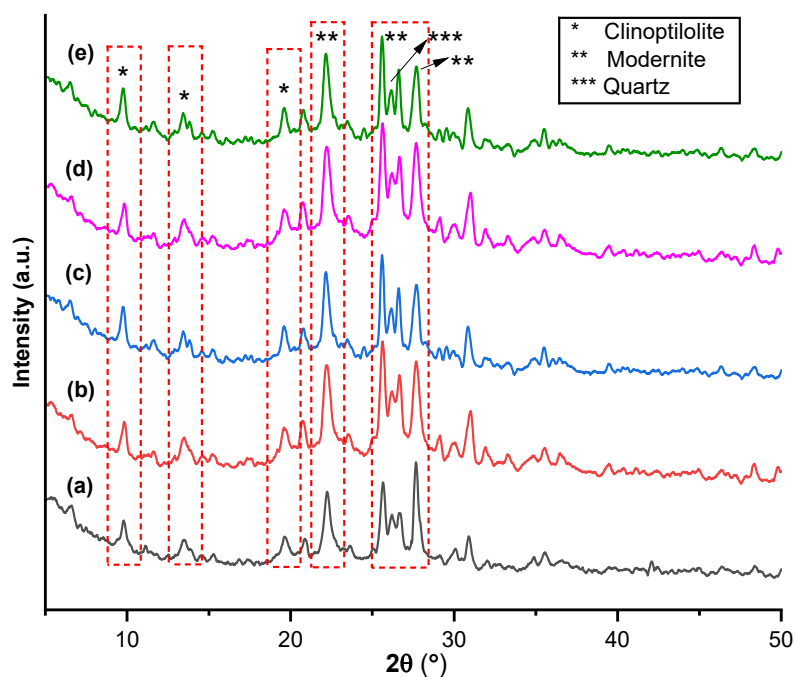


Fig 2. XRD diffractogram of zeolite/NPK Cu-alginate-PVA-glutaraldehyde with various concentrations of Cu; (a) 0.20 M, (b) 0.4 M, (c) 0.6 M, (d) 0.8 M, and (e) 1.0 M

glutaraldehyde is visible, as well as the absorption peak that indicates the interaction between Cu and alginate, in which this interaction indicates that the double cross-linking process had been successful.

Fig. 3 shows the FTIR spectra of natural zeolite, showing a wide absorption at 3448 cm^{-1} , indicating the presence of hydrogen bonds from water [21]. The peak at the wavenumber of 1435 cm^{-1} indicates the presence of H-O-H bending vibrations. The peak characteristic of the zeolite is shown at the wavenumber of 1049 cm^{-1} , which is a characteristic of the asymmetric stretching vibration of Si-O-Al, and 462 cm^{-1} , which is the bending vibration of Si-O/Al-O.

The FTIR spectra of alginate showed strong absorption at the wavenumber of 1620 cm^{-1} , which is a characteristic of the asymmetric stretching vibration of the COO^- group and a weak absorption peak at 1419 cm^{-1} , which is an indication of the COO^- symmetric stretching vibration. The FTIR spectra of PVA showed that there were several peaks that appeared at wavenumbers of 1435 , 1635 , and 3448 cm^{-1} . The absorption peak at wavenumber 3448 cm^{-1} is considered as the stretching vibration of the

hydroxyl group (OH^-) originating from the hydroxyl group of the PVA chain and the hydroxyl group from water. The FTIR spectra of the zeolite/NPK fertilizer showed an absorption peak at wavenumber 3371 cm^{-1} which indicated the presence of N-H stretching vibrations in urea. At wavenumber 1666 cm^{-1} , there is a peak indicating the presence of C=O bonds in urea, and at wavenumber 1458 cm^{-1} , there is a peak indicating the presence of C-N vibrations from urea. An absorption peak is also formed at 786 cm^{-1} , which is a characteristic of the P-O symmetric stretching vibration. The peak that shows the characteristics of the zeolite is still visible at the wavenumber of 1165 cm^{-1} , which is the asymmetry range of Si-O-Si/Al-O-Al. The absorption peak at wavenumber 3448 cm^{-1} indicates the presence of hydroxyl groups from PVA and water that are also still visible.

In the FTIR spectra of the alginate-PVA-glutaraldehyde-coated zeolite/NPK fertilizer, there is a sharp absorption peak at wavenumber 1049 cm^{-1} . This indicates that there are other vibrations besides the asymmetric stretching vibration of Si-O(Si) or Si-O(Al);

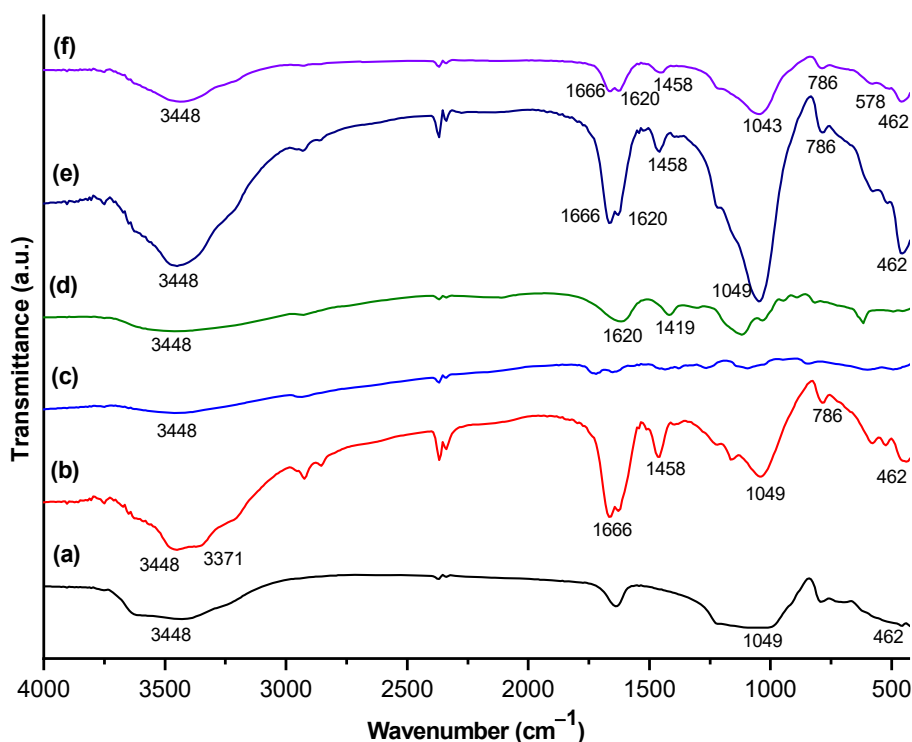


Fig 3. FTIR spectra (a) natural zeolite, (b) zeolite/NPK, (c) PVA, (d) alginate, (e) zeolite/NPK alginate-PVA-glutaraldehyde, and (f) zeolite/NPK Cu (0.4 M)-alginate-PVA-glutaraldehyde

it is the presence of C-O ether bonds produced by the cross-linking process of PVA and glutaraldehyde so that at this wavenumber, it produces a sharper peak than the peak in the zeolite/NPK fertilizer without alginate-PVA-glutaraldehyde coating. The appearance of a sharp peak at the wavenumber of 1049 cm^{-1} also indicates that the cross-linking process occurred in the zeolite/NPK fertilizer coating. In addition, the characteristic peaks of the zeolite/NPK fertilizer were also clearly visible in the alginate-PVA glutaraldehyde-coated zeolite/NPK fertilizer, which indicated that the cross-linking process in the coating material did not interfere with the interaction of compounds in the initial composite.

Furthermore, the FTIR spectra of zeolite/NPK fertilizer coated with alginate-PVA-glutaraldehyde were compared with the FTIR spectra of zeolite/NPK fertilizer coated with Cu-alginate-PVA-glutaraldehyde with a Cu concentration of 0.4 M. Spectra from the sample with the addition of 0.4 M Cu concentration was selected because it was the best composite which has a late release of nutrients proven by the nutrient release test. Overall, it can be seen that there is a new absorption peak due to the

addition of Cu at wavenumber 579 cm^{-1} . The absorption peak indicates the formation of Cu-O bonds from cross-linking between Cu and alginate. The characteristic peaks of the alginate-PVA-glutaraldehyde-coated zeolite/NPK fertilizer were also seen in the composites with the addition of Cu.

Fig. 4 shows that the addition of Cu will decrease the peak intensity of the characteristic C=O in urea at a wavenumber of 1666 cm^{-1} and the peak characteristic of COO^- belonging to alginate at a wavenumber of 1620 cm^{-1} . This is possible because Cu, which has a positive charge, will interact with the carbonyl group of urea and the carboxyl group of alginate. The interaction between Cu and the two groups will increase the bond length between the groups themselves. The elongation of the bond that occurs has an impact on the weakening of the bonds in both C=O in urea and COO^- in alginate. When more Cu is added, the number of C=O bonds in urea and COO^- in alginate will decrease because they have formed new bonds with Cu. This causes a decrease in the intensity of the absorption peak as seen in the FTIR spectra above.

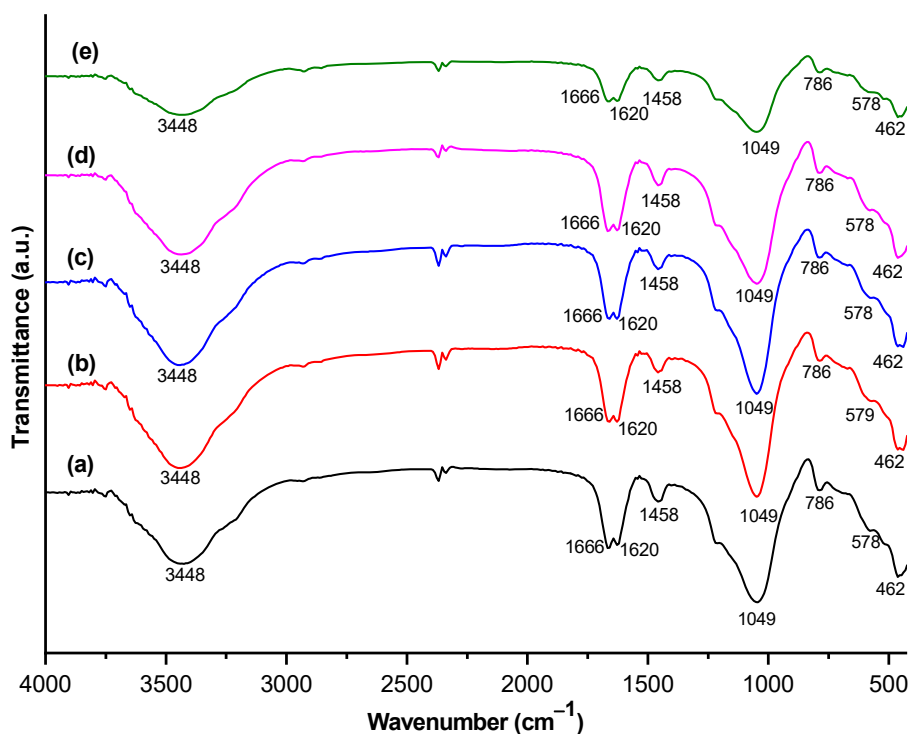


Fig 4. FTIR spectra of zeolite/NPK Cu-alginate-PVA-glutaraldehyde with various concentrations of Cu; (a) 0.20 M, (b) 0.4 M, (c) 0.6 M, (d) 0.8 M, and (e) 1.0 M

Determination of the optimum conditions for the Cu-alginate-PVA-glutaraldehyde-coated zeolite/NPK composite with a Cu concentration of 0.4 M was based on the results of the minimum data release occurring at that particular concentration. In addition, it can be seen that under these optimum conditions, there is a characteristic wavenumber belonging to the Cu-O cross-link bond in the Cu-alginate, which initially shifted from 578 to 579 cm^{-1} . The shift in the wavenumber towards a larger direction indicates that the bond distance was getting shorter, resulting in a stronger Cu-O bond. When the addition of Cu is above 0.4 M, the Cu-O absorption peak reappears at the wavenumber of 578 cm^{-1} . From the data obtained, it can be concluded that the strongest alginate-Cu cross-linked bond occurred at the addition of 0.4 M Cu.

Swelling Properties

In this study, some of the active sites of alginate bind to PVA and some are cross-linked by Cu. PVA and alginate form hydrogen bonds, while alginate and Cu form cross-links in the form of an egg box, making it stronger than alginate-PVA. The higher the concentration of Cu added, the more cross-linked alginate will form. This causes the bond between PVA and alginate to be reduced. The reduced interaction between PVA and alginate will also disrupt the PVA-glutaraldehyde cross-link bond, which causes the composite system to not be

optimally protected, causing water from the environment to enter the composite easily. In this sub-chapter, the effect of variations in Cu concentration on the swelling of the zeolite/NPK fertilizer composites is discussed. The swelling test was carried out by measuring the change in mass of the Cu-alginate-PVA-glutaraldehyde-coated zeolite/NPK fertilizer in a dry state and after experiencing swelling for a certain time. The swelling test was carried out on zeolite/NPK fertilizer coated with Cu-alginate-PVA-glutaraldehyde with variations of Cu 0.00; 0.20; 0.40; 0.60; 0.80; and 1.00 M. Swelling measurements were carried out on the 7th day of immersion of the fertilizer in 0.33 M citric acid. The results of swelling measurements are presented in Fig. 5.

Fig. 5 shows that the increase in Cu concentration reduces the swelling rate of the zeolite/NPK fertilizer composite up to the Cu concentration of 0.40 M. At Cu concentrations of 0.00; 0.20; and 0.40 there was a decrease in the swelling rate. Furthermore, when more Cu was added to the composite, the swelling increased, as seen in Cu concentration of 0.60; 0.80; and 1.00 M; in which the swelling number rose consecutively. This indicates that the bond between Cu-alginate-PVA-glutaraldehyde is optimum when the Cu concentration was 0.40 M. Cu concentration of above 0.40 M caused the bond between Cu and alginate to increase, thereby

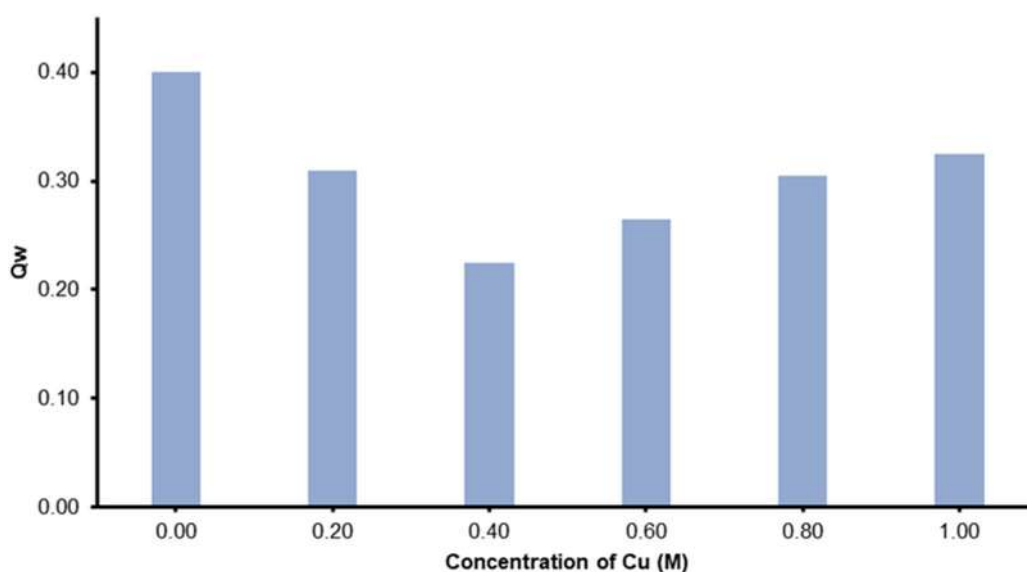


Fig 5. Effect of variations in glutaraldehyde concentration on swelling of zeolite/NPK fertilizer composites on day 7

reducing the interaction between PVA and alginate, which causes the bond between PVA-glutaraldehyde to the composite to also weaken, increasing the swelling value. Greater swelling allows water to enter the composite more easily and will accelerate the rate of release of the NPK and Cu nutrients in zeolite/NPK fertilizers. Thus, the addition of Cu above 0.40 M will make the application of the double cross-linker not optimum in which the aqueous solution from the environment will enter the composite system more easily.

Study of the Effect of Variations in Cu Concentration in Cu-Alginate-PVA-Glutaraldehyde Coating Materials on N Release from Zeolite/NPK Fertilizers

Fig. 6 shows the release of N from the Cu-alginate-PVA-glutaraldehyde-coated zeolite/NPK composite in the citric acid system through two mechanisms: the fast mechanism and the slow mechanism, according to the results of Sukma's research [22]. The slow mechanism is shown in the relatively gentle slope of the graph from the 6th to the 144th h. Meanwhile, the fast mechanism is shown on the fairly steep slope from the 144th to the 336th h. This indicates that the release of N from the composite after 144 h experienced a significant increase which could be

caused by the weakening of the cross-link system in the coating material. The weak cross-linking between PVA-glutaraldehyde and Cu-alginate can cause a decrease in the density of the composite so that the release of the nutrients in it also increases.

Variations in Cu concentration affect the amount of N released in the composite. Zeolite/NPK fertilizer without coating material released 15.04 mg/0.20 g of N fertilizer at the 3rd h, then the N release was constant at the 12th h by releasing 16.02 mg/0.20 g of N fertilizer. The zeolite/NPK fertilizer coated with alginate-PVA-glutaraldehyde released 15.95 mg/0.20 g of N fertilizer after 120 h and afterwards remained constant. In zeolite/NPK coated with Cu-alginate-PVA-glutaraldehyde with a Cu concentration of 0.2 M, the release of N at 312 h was 15.67 mg/0.20 g of fertilizer. In zeolite/NPK coated with Cu-alginate-PVA-glutaraldehyde with a Cu concentration of 0.4 M, the release of N at 336 h was 12.98 mg/0.20 g of fertilizer. In zeolite/NPK coated with Cu-alginate-PVA-glutaraldehyde with the Cu concentration of 0.6 M, the release of N at 336 h was 15.50 mg/0.20 g of fertilizer. The Cu-alginate-PVA-glutaraldehyde-coated zeolite/NPK with a Cu concentration of 0.8 M at 336 h released 15.95 mg/0.20 g

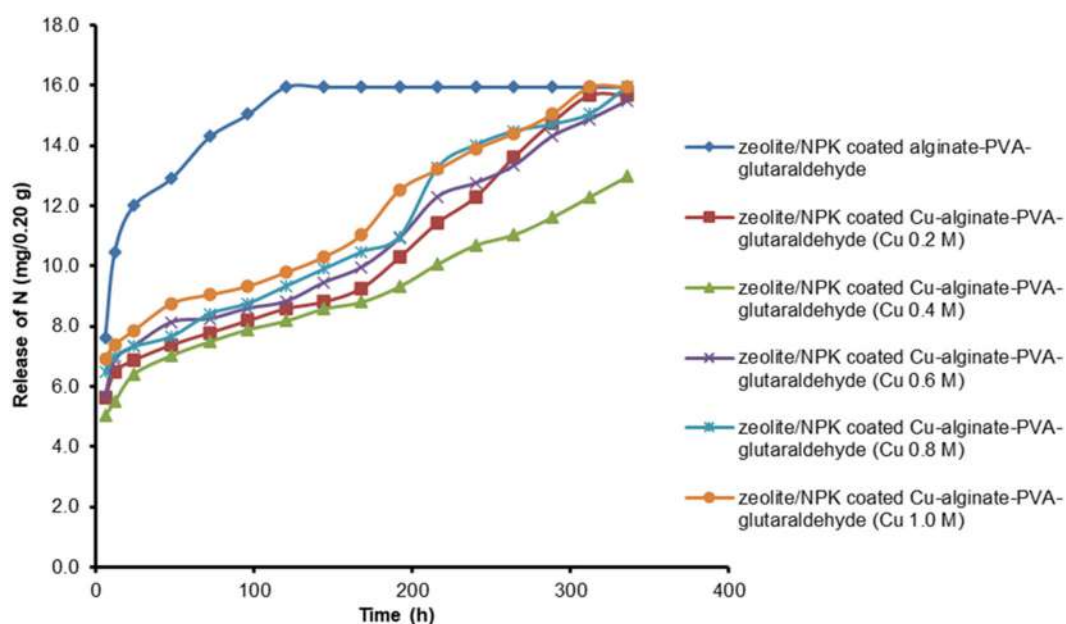


Fig 6. Graph of effect of Cu concentration on N release in zeolite/NPK fertilizer coated with Cu-alginate-PVA-glutaraldehyde in 0.33 M citric acid system for 14 d

of N fertilizer. Furthermore, in Cu-alginate-PVA-glutaraldehyde-coated zeolite/NPK with a Cu concentration of 1.0 M, the release of N at 312 h was 15.95 mg/0.20 g of N fertilizer, and afterwards remained constant. From the data obtained, it can be deduced that the minimum N release occurred in the composite with the addition of 0.4 M Cu. This indicated that the cross-link bond in the composite was strongest at the addition of 0.4 M Cu.

The N release kinetics followed the pseudo-second-order reaction kinetics with a value of R^2 closest to 1 (Table 1). Meanwhile, the results of the calculation of the N release rate constant from the composite are shown in Table 2. Based on the rate constant data (k) in Table 2, it is shown that the N release rate slows down with the addition of Cu concentration of 0.4 M, then the N release rate increased again at Cu concentrations above 0.4 M, causing the double cross-link system not to run optimally so that the release of nutrients will also increase. This indicates that the interaction between Cu-alginate-PVA-glutaraldehyde was optimum at the addition of 0.4 M Cu to produce a slow-release of nutrients. In addition, at the Cu concentration of 0.4 M, the application of double

cross-linker went well so that a strong and tight composite system was obtained, which can be seen from the low swelling value and the lowest release rate, causing the release of nutrients in fertilizers to run slowly at this concentration.

Study of the Effect of Variations in Cu Concentration in Cu-Alginate-PVA-Glutaraldehyde Coating Materials on P Release from Zeolite/NPK Fertilizers

The graph of P release from zeolite/NPK fertilizer coated with Cu-alginate-PVA-glutaraldehyde is shown in Fig. 7. The Cu concentration of 0.4 M in the coating material increased the cross-linking between Cu and alginate without reducing the interaction between alginate-PVA, resulting in a zeolite/NPK coating material which has optimum coating resistance and strength. The Cu concentration above 0.4 M in the Cu-alginate-PVA-glutaraldehyde coating material caused the Cu-alginate interaction to increase, and the interaction between PVA and alginate to decrease. The reduced interaction between PVA and alginate caused the PVA-glutaraldehyde cross-link bond to also be disrupted

Table 1. The results of the calculation of the value of R^2 on the kinetics of N release from zeolite/NPK fertilizer composites coated with Cu-alginate-PVA-glutaraldehyde variations in Cu content

Cu concentration (M)	R^2				
	First-order	Second-order	Third-order	Pseudo-first-order	Pseudo-second-order
0.0	0.91	0.75	0.53	0.95	0.99
0.2	0.96	0.98	0.79	0.93	0.99
0.4	0.95	0.97	0.98	0.95	0.99
0.6	0.93	0.95	0.95	0.93	0.99
0.8	0.99	0.98	0.98	0.99	0.99
1.0	0.98	0.97	0.94	0.98	0.99

Table 2. The value of the N release rate constant with variations in Cu concentration from Cu-alginate-PVA-glutaraldehyde-coated zeolite/NPK composites

Cu concentration (M)	Pseudo-second-order	
	R^2	k ($\text{mg g}^{-1} \text{h}^{-1}$)
0.0	0.99	21.73×10^{-3}
0.2	0.99	11.75×10^{-3}
0.4	0.99	8.49×10^{-3}
0.6	0.99	9.27×10^{-3}
0.8	0.99	9.45×10^{-3}
1.0	0.99	10.86×10^{-3}

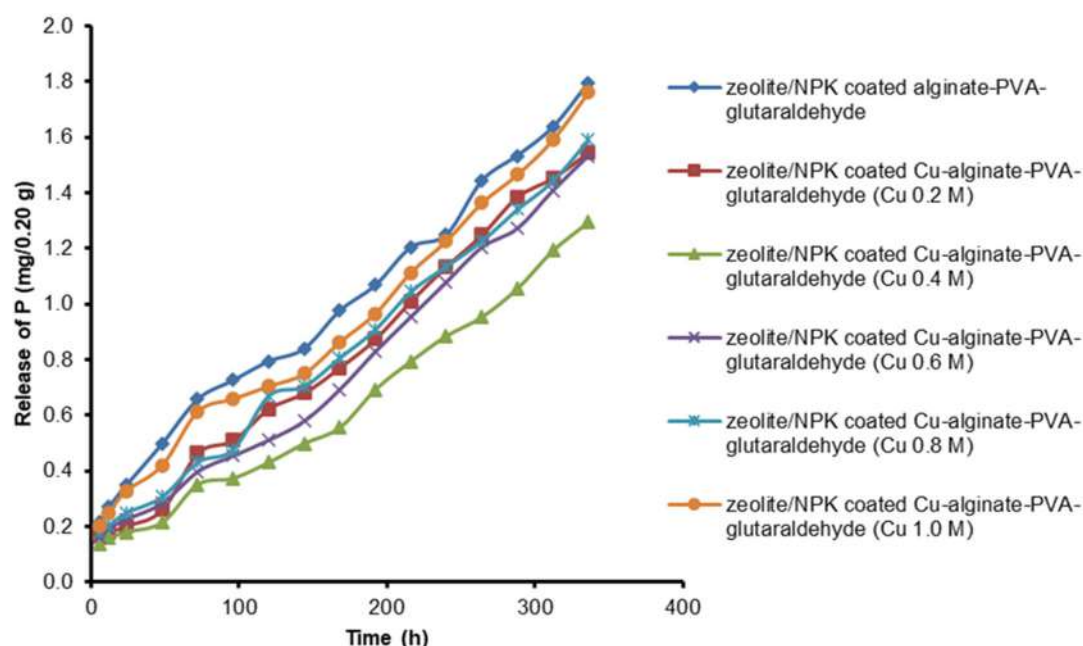


Fig 7. Graph of effect of Cu concentration on P release in zeolite/NPK fertilizer coated with Cu-alginate-PVA-glutaraldehyde in 0.33 M citric acid system for 14 d

so the double cross-linker composite system is not optimal. The non-optimal double cross-linker system will certainly have an impact on the faster release of nutrients compared to the optimum double cross-linker composite. Disruption of the bond between PVA-glutaraldehyde causes solutions from the environment to enter the system more easily so that the P nutrients in the zeolite/NPK fertilizer will diffuse out more easily, and the release of nutrients will be faster.

From Fig. 7, it is shown that variations in Cu concentration affect the amount of P released in the composite. The lowest P release occurred in the zeolite/NPK fertilizer coated with Cu-alginate-PVA-glutaraldehyde with a Cu concentration of 0.4 M. This

indicates that the cross-linking process is optimum when adding 0.4 M Cu to the zeolite/NPK coating material, both for the cross-links between PVA and glutaraldehyde and the cross-links between Cu and alginate. Further observations can be made by calculating the kinetics of P release from Cu-alginate-PVA-glutaraldehyde-coated zeolite/NPK fertilizers.

The P release kinetics followed the pseudo-second-order reaction kinetics with R^2 values closest to 1 (Table 3). Table 4 shows the results of the calculation of the P release rate constant from the composite.

Based on the constant rate data (k) in Table 4, it is shown that with the increasing Cu concentration in the coating material, the value of the P release constant rate

Table 3. Calculation of the value of R^2 on the kinetics of P release from zeolite/NPK fertilizer composites coated with Cu-alginate-PVA-glutaraldehyde variations in Cu content

Cu concentration (M)	R^2				
	First-order	Second-order	Third-order	Pseudo-first-order	Pseudo-second-order
0.0	0.97	0.98	0.95	0.93	0.99
0.2	0.91	0.98	0.96	0.94	0.99
0.4	0.99	0.99	0.96	0.95	0.99
0.6	0.99	0.95	0.94	0.92	0.99
0.8	0.98	0.98	0.96	0.94	0.99
1.0	0.96	0.97	0.95	0.93	0.99

Table 4. P release constant rate value with the variation of Cu concentration from Cu-alginate-PVA-glutaraldehyde-coated zeolite/NPK composite

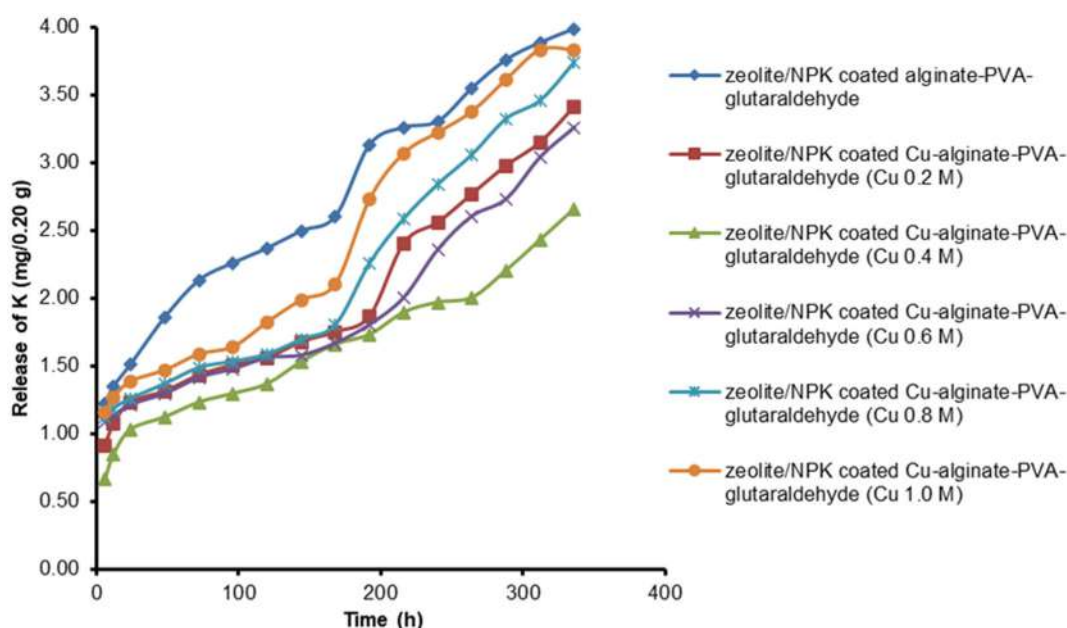
Cu concentration (M)	Pseudo-second-order	
	R ²	k (mg g ⁻¹ h ⁻¹)
0.0	0.99	29.08 × 10 ⁻³
0.2	0.99	22.34 × 10 ⁻³
0.4	0.99	17.48 × 10 ⁻³
0.6	0.99	49.62 × 10 ⁻³
0.8	0.99	29.04 × 10 ⁻³
1.0	0.99	33.21 × 10 ⁻³

in the composite fluctuates, starting with a decrease in the rate and followed by an increase. Overall, the P release rate was minimum when Cu with a concentration of 0.4 M was added. From the data obtained, it can be concluded that the lowest P release rate was found in the addition of 0.4 M Cu, which indicates that the double cross-link bond between PVA-glutaraldehyde and Cu-alginate was optimum at the Cu concentration of 0.4 M, meaning it had the best ability to withstand the release of P compared to the other Cu concentrations.

Study of the Effect of Variations in Cu Concentration in Cu-Alginate-PVA Glutaraldehyde Coating Material on K Release from Zeolite/NPK Fertilizers

The graph of K release from alginate-PVA-

glutaraldehyde-coated zeolite/NPK fertilizer is shown in Fig. 8. Fig. 8 shows that variations in Cu concentration affect the amount of K released in the composite. With the addition of variations of Cu concentrations of up to 0.4 M, the release of K experienced a slowdown. In the Cu concentration of 0.6 M, K release increased again to 1.08 mg/0.20 g fertilizer at the 6th h and 3.26 mg/0.20 g fertilizer on the 14th d. At Cu concentrations of 0.8 and 1.0 M, the release of K increased again by 1.12 and 1.16 mg/0.20 g at the 6th h, and 3.74 and 3.83 mg/0.20 g of fertilizer on the 14th d or 336th h. The slowest release of K occurred at Cu concentration of 0.4 M, where the double cross-link interaction between PVA-glutaraldehyde Cu-alginate was optimum, resulting in a composite with the

**Fig 8.** Graph of effect of Cu concentration on K release in zeolite/NPK fertilizer coated with Cu-alginate-PVA-glutaraldehyde in 0.33 M citric acid system for 14 d

best coating material, which caused the release of K to be minimum. Further observations were made by calculating K release kinetics and K release efficiency from the zeolite/NPK fertilizer coated with Cu-alginate-PVA-glutaraldehyde.

Based on the results of the plot of concentration data in a certain time set, it was discovered that the rate of K release follows the pseudo-second-order reaction kinetics with the R^2 value closest to 1 (Table 5). The results of the calculation of the K release of the constant rate from the composite are shown in Table 6.

Based on the constant rate data (k) in Table 5, it is shown that the addition of 0.4 M Cu had the lowest K release rate compared to the other Cu concentrations. This indicates that the interaction between Cu-alginate-PVA-glutaraldehyde is optimum at the addition of Cu 0.4 M, resulting in a slow-release of nutrients.

The release of N, P, and K, in general, shows a similar trend with the optimum condition represented by Cu 0.4 M. This can be proven by the FTIR spectra, in which the double-cross-linker bond between PVA-glutaraldehyde and Cu-alginate was optimum at 0.4 M.

Cu-alginate was optimal with a shift in wavenumber indicating a stronger bond, along with the PVA-glutaraldehyde bond which was still good. The addition of a higher concentration of Cu weakened the PVA-alginate bond causing the PVA-glutaraldehyde cross-link bond to also decrease, and the double cross-linker system to not be optimal and release more nutrients.

Study of the Effect of Variations in Cu Concentration in Cu-Alginate-PVA-Glutaraldehyde Coating Materials on Cu Release from Zeolite/NPK Fertilizers

Fig. 9 shows that the Cu released from the composite decreased along with the increasing Cu concentration up to a concentration of 0.4 M. Afterwards, the Cu release increased again with the addition of Cu 0.6, 0.8, and 1.0 M.

The slow mechanism is shown in the relatively gentle slope of the graph from the 6th to the 144th h. Meanwhile, the fast mechanism is shown in the steeper slope of the graph from the 144th to the 336th h. This indicates that the release of Cu from the composite after 144 h experienced a significant increase which could be

Table 5. Calculation of the value of R^2 on the kinetics of K release from zeolite/NPK fertilizer composites coated with Cu-alginate-PVA-glutaraldehyde variations in Cu content

Cu concentration (M)	R^2				
	First-order	Second-order	Third-order	Pseudo-first-order	Pseudo-second-order
0.0	0.97	0.99	0.99	0.97	0.99
0.2	0.94	0.96	0.97	0.94	0.99
0.4	0.72	0.78	0.84	0.72	0.99
0.6	0.98	0.96	0.98	0.97	0.99
0.8	0.99	0.99	0.99	0.99	0.99
1.0	0.99	0.99	0.99	0.99	0.99

Table 6. K release constant rate value with the variation of Cu concentration from alginate-PVA-glutaraldehyde-coated zeolite/NPK composite

Cu concentration (M)	Pseudo-second-order	
	R^2	k ($\text{mg g}^{-1} \text{h}^{-1}$)
0.0	0.99	46.52×10^{-3}
0.2	0.99	36.24×10^{-3}
0.4	0.99	21.73×10^{-3}
0.6	0.99	63.63×10^{-3}
0.8	0.99	54.79×10^{-3}
1.0	0.99	51.43×10^{-3}

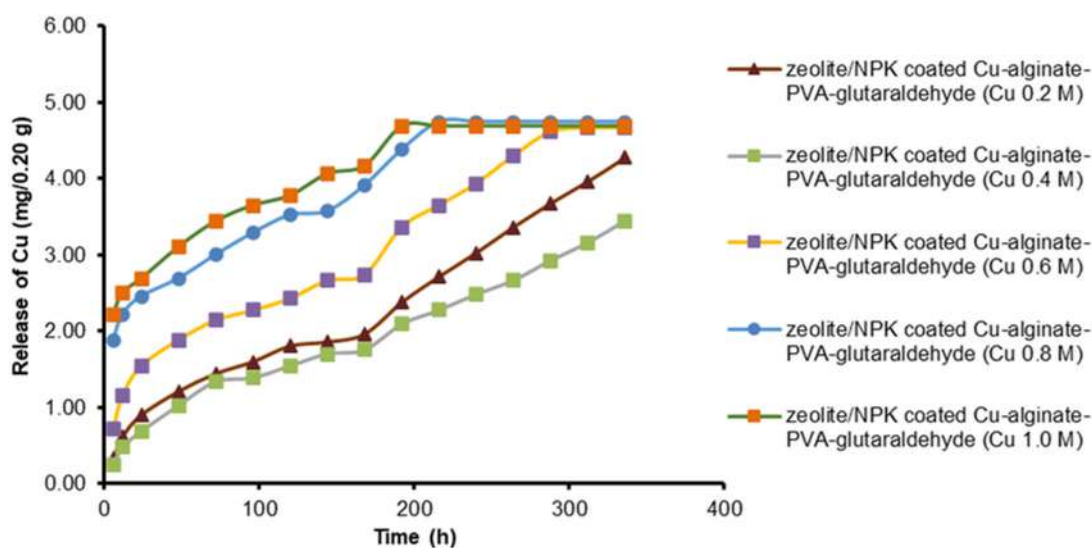


Fig 9. Graph of effect of Cu concentration on Cu release in zeolite/NPK fertilizer coated with Cu-alginate-PVA-glutaraldehyde in 0.33 M citric acid system for 14 d

caused by the weakening of the cross-linking system in the coating material. From the data obtained, it can be deduced that the minimum Cu release occurred in the composite with the addition of Cu 0.4 M. This indicated that the cross-link bond in the composite was strongest at the addition of Cu 0.4 M. Further observations were made by calculating the release kinetics of Cu and efficiency of Cu release from the zeolite/NPK fertilizer coated with Cu-

alginate-PVA-glutaraldehyde.

The kinetics of Cu release followed the pseudo-second-order reaction kinetics with the R^2 value closest to 1 (Table 7). In contrast, the results of the calculation of the Cu release rate constant from the composite are shown in Table 8.

Based on the rate constant data (k) in Table 8, it is shown that the Cu release rate slows down with the

Table 7. Calculation of the value of R^2 on the kinetics of Cu release from zeolite/NPK fertilizer composites coated with Cu-alginate-PVA-glutaraldehyde variations in Cu content

Cu concentration (M)	R^2				
	First-order	Second-order	Third-order	Pseudo-first-order	Pseudo-second-order
0.2	0.94	0.96	0.98	0.94	0.99
0.4	0.77	0.97	0.98	0.95	0.99
0.6	0.94	0.98	0.99	0.94	0.99
0.8	0.97	0.99	0.98	0.97	0.99
1.0	0.99	0.96	0.87	0.99	0.99

Table 8. The value of Cu constant release rate with the variation of Cu concentration from Cu-alginate-PVA-glutaraldehyde-coated zeolite/NPK composite

Cu concentration (M)	Pseudo-second-order	
	R^2	k ($\text{mg g}^{-1} \text{h}^{-1}$)
0.2	0.99	10.33×10^{-3}
0.4	0.99	8.57×10^{-3}
0.6	0.99	13.61×10^{-3}
0.8	0.99	17.44×10^{-3}
1.0	0.99	19.72×10^{-3}

addition of 0.4 M Cu, then the Cu release rate increases again at Cu concentrations above 0.4 M. This indicates that the interaction between Cu-alginate-PVA-glutaraldehyde was optimum at the addition of 0.4 M Cu resulting in a slow-release of nutrients. In addition, at the concentration of Cu 0.4 M, the application of a double cross-linker went well so a strong and tight composite system was obtained, which caused the release of nutrients in the fertilizer to run slowly. The addition of Cu concentration above 0.4 M increased the interaction between Cu and alginate, reducing the number of PVA and alginate bonds which resulted in the disruption of the PVA-glutaraldehyde cross-link bond. The addition of Cu above 0.4 M will make the double cross-linker system unable to run optimally so the release of N, P, K, and Cu nutrients in the fertilizer will also increase.

■ CONCLUSION

Zeolite/NPK coated with Cu-alginate-PVA-glutaraldehyde as a double cross-linker slow-release fertilizer has been successfully synthesized by the coating method. The addition of Cu concentration up to 0.4 M in the coating material increased the resistance in citric acid and decreased the amount of N, P, K, and Cu released. The release process of N, P, K, and Cu follows pseudo-second-order release kinetics. The release rate constants of N, P, K, and Cu were 8.49×10^{-3} , 17.48×10^{-3} , 21.73×10^{-3} , and $8.57 \times 10^{-3} \text{ mg g}^{-1} \text{ h}^{-1}$, respectively.

■ REFERENCES

- [1] Raviv, M., and Lieth, J.H., 2007, *Soilless Culture: Theory and Practice*, Elsevier Science, Amsterdam.
- [2] Yruela, I., 2009, Copper in plants acquisition transport and interactions, *Funct. Plant Biol.*, 36 (5), 409–430.
- [3] Lehman, J., and Schroth, G., 2003, “Nutrient Leaching” in *Trees, Crops and Soil Fertility*, Eds. Schroth, G., and Sinclair, F.L., CAB International, Wallingford, UK, 151–166.
- [4] Soltys, L., Myronyuk, I., Tatarchuk, T., and Tsinurchyn, V., 2020, Zeolite-based composites as slow-release fertilizers (Review), *Phys. Chem. Solid State*, 21 (1), 89–104.
- [5] Preetha, P.S., Subramanian, K.S., and Rahale, C.S., 2014, Sorption characteristics of nano zeolite based slow release sulphur fertilizer, *Int. J. Dev. Res.*, 4, 225–228.
- [6] Hendrawan, H., Khoerunnisa, F., Sonjaya, Y., and Chotimah, N., 2014, Physical and chemical characteristics of alginate-poly(vinyl alcohol) based control released hydrogel, *J. Environ. Chem. Eng.*, 4 (4, Part B), 4863–4869.
- [7] Kenawy, E., Kamoun, E.A., Mohy Eldin, M.S., and El-Meligy, M.A., 2014, Physically crosslinked poly(vinyl alcohol)-hydroxyethyl starch blend hydrogel membranes: Synthesis and characterization for biomedical applications, *Arabian J. Chem.*, 7 (3), 372–380.
- [8] Rashidzadeh, A., and Olad, A., 2014, Slow-released NPK fertilizer encapsulated by NaAlg-g-poly(AA-co-AAm)/MMT superabsorbent nanocomposite, *Carbohydr. Polym.*, 114, 269–278.
- [9] Trankel, M., 2010, *Slow-and-controller-release and stabilized fertilizer: an option for enhancing nutrient use efficiency in agriculture*, International Fertilizer Industry Association (IFA), Paris.
- [10] Kurniawan, T., Nuryoto, N., and Firdaus, M.A., 2019, Zeolite for agriculture intensification and catalyst in agroindustry, *World Chem. Eng. J.*, 3 (1), 14–23.
- [11] Himmah, N.I.F., Djajakirana, G., and Darmawan, D., 2018, Nutrient release performance of starch coated NPK fertilizers and their effect on corn growth, *STJSSA*, 15 (2), 104–114.
- [12] Hnoosong, W., Rungcharoenthong, P., and Sangjan, S., 2021, Preparation and properties of urea slow-release fertilizer hydrogel by sodium alginate-gelatin biopolymer, *Key Eng. Mater.*, 889, 98–103.
- [13] Ngafif, A., Ikasari, E.D., and Ariani, L.W., 2020, Optimasi kombinasi natrium alginat dan kalsium klorida (CaCl_2) sebagai agen sambung silang nanopartikel ekstrak etanol daun katuk (*Sauropus androgynus* (L.) Merr) (Indonesian), *BIMFI*, 7 (2), 13–23.
- [14] Roquero, D.M., Othman, A., Melman, A., and Katz, E., 2022, Iron(III)-cross-linked alginate hydrogels: A critical review, *Mater. Adv.*, 3 (4), 1849–1873.
- [15] Zaafarany, I.A., 2010, Non-isothermal decomposition of Al, Cr, and Fe cross-linked

- trivalent metal-alginate complexes, *JKAU: Sci.*, 22 (1), 193–202.
- [16] Kamoun, E.A., Kanewy, E.S., Tamer, T.M., El-Meligy, M.A., and Mohy Eldin, M.S., 2015, Poly(vinyl alcohol)-alginate physically crosslinked hydrogel membranes for wound dressing applications: Characterization and bio-evaluation, *Arabian J. Chem.*, 8 (1), 38–47.
- [17] Mikula, K., Skrzypczak, D., Ligas, B., and Witek-Krowiak, A., 2019, Preparation of hydrogel composites using Ca^{2+} and Cu^{2+} ions as crosslinking agents, *SN Appl. Sci.*, 1 (6), 643.
- [18] Wikanta, T., and Erizal, E., 2013, Properties of sodium alginate-polyvinyl alcohol hydrogel irradiated by gamma ray for wound dressing materials, *Squalen*, 8 (1), 1–12.
- [19] Zhang, L., Zhang, G., Lu, J., and Liang, H., 2013, Preparation and characterization of carboxymethyl cellulose/polyvinyl alcohol blend film as a potential coating material, *Polym.-Plast. Technol. Eng.*, 52 (2), 163–167.
- [20] Campos, E., Coimbra, P., and Gill, M.H., 2013, An improved method for preparing glutaraldehyde cross-linked chitosan-poly(vinyl alcohol) microparticles, *Polym. Bull.*, 70 (2), 549–561.
- [21] Pritamawati, R.N., Nurlina, N., and Shofiyani, A., 2018, Penentuan permselektivitas ion Cd(II) pada membran komposit kitosan-zeolit (Indonesian), *Jurnal Kimia Khatulistiwa*, 7 (3), 56–65.
- [22] Sukma, N.S., Arryanto, Y., and Sutarno, S., 2016, Characterization and study of iron(III)-released from alginate/zeolite/Fe composite (Indonesian), *Eksakta: Jurnal Ilmu-Ilmu MIPA*, 16 (2), 80–93.

Supplementary Data

This supplementary data is a part of a paper entitled “Steroids from *Atactodea striata* and Their Cytotoxic Activity against MCF-7 Breast Cancer Cell Lines”.

Contents of Supporting Information

Table of Contents	Page
Fig S1. HRTOF-MS Spectra of 1	4
Fig S2. FTIR Spectra of 1	5
Fig S3. ¹ H-NMR Spectra of 1 (500 MHz in CDCl ₃)	6
Fig S4. ¹³ C-NMR Spectrum of 1 (125 MHz in CDCl ₃)	7
Fig S5. DEPT-135° Spectrum of 1 (125 MHz in CDCl ₃)	8
Fig S6. HMQC Spectrum of 1	9
Fig S7. HMBC Spectrum of 1	10
Fig S8. ¹ H- ¹ H-COSY Spectra of 1	11
Fig S9. HRTOF-MS Spectra of 2	12
Fig S10. FTIR Spectra of 2	13
Fig S11. ¹ H-NMR Spectra of 2 (500 MHz in CDCl ₃)	14
Fig S12. ¹³ C-NMR Spectrum of 2 (125 MHz in CDCl ₃)	15
Fig S13. DEPT-135° Spectrum of 2 (125 MHz in CDCl ₃)	16
Fig S14. HMQC Spectrum of 2	17
Fig S15. HMBC Spectrum of 2	18
Fig S16. ¹ H- ¹ H-COSY Spectra of 2	19
Fig S17. HRTOF-MS Spectra of 3	20
Fig S18. FTIR Spectra of 3	21
Fig S19. ¹ H-NMR Spectra of 3 (500 MHz in CDCl ₃)	22
Fig S20. ¹³ C-NMR Spectrum of 3 (125 MHz in CDCl ₃)	23
Fig S21. DEPT-135° Spectrum of 3 (125 MHz in CDCl ₃)	24
Fig S22. HRTOF-MS Spectra of 4	25
Fig S23. FTIR Spectra of 4	26
Fig S24. ¹ H-NMR Spectra of 4 (500 MHz in CDCl ₃)	27
Fig S25. ¹³ C-NMR Spectrum of 4 (125 MHz in CDCl ₃)	28
Fig S26. HRTOF-MS Spectra of 5	29
Fig S27. FTIR Spectra of 5	30
Fig S28. ¹ H-NMR Spectra of 5 (500 MHz in CDCl ₃)	31
Fig S29. ¹³ C-NMR Spectrum of 5 (125 MHz in CDCl ₃)	32
Fig S30. DEPT-135° Spectrum of 5 (125 MHz in CDCl ₃)	33
Fig S31. HRTOF-MS Spectra of 6	34
Fig S32. FTIR Spectra of 6	35
Fig S33. ¹ H-NMR Spectra of 6 (500 MHz in CDCl ₃)	36
Fig S34. ¹³ C-NMR Spectrum of 6 (125 MHz in CDCl ₃)	37
Fig S35. DEPT-135° Spectrum of 6 (125 MHz in CDCl ₃)	38
Fig S36. HRTOF-MS Spectra of 7	39
Fig S37. FTIR Spectra of 7	40
Fig S38. ¹ H-NMR Spectra of 7 (500 MHz in CDCl ₃)	41
Fig S39. ¹³ C-NMR Spectrum of 7 (125 MHz in CDCl ₃)	42
Fig S40. DEPT-135° Spectrum of 7 (125 MHz in CDCl ₃)	43

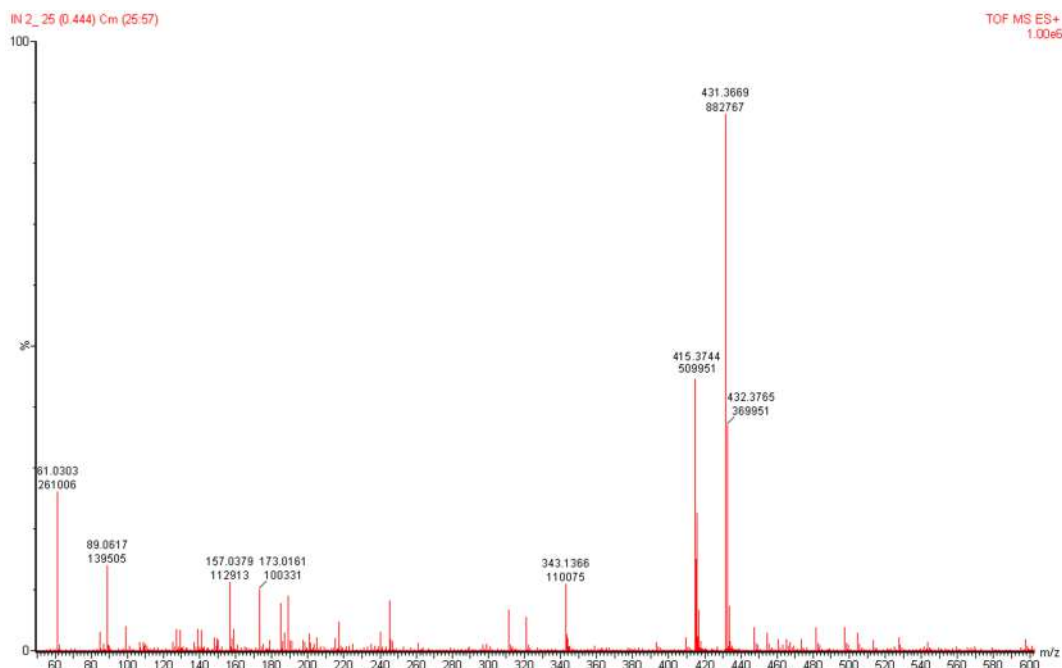


Fig S1. HRTOF-MS spectra of 1

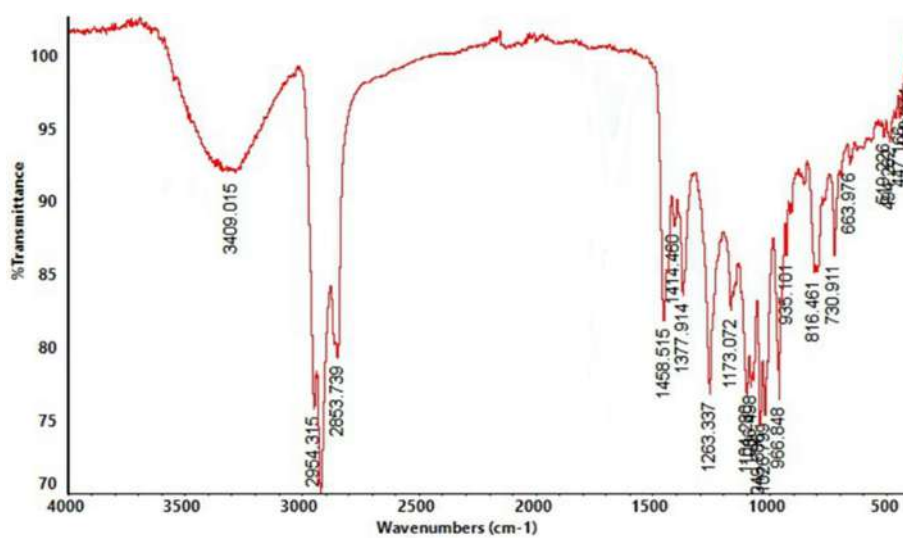
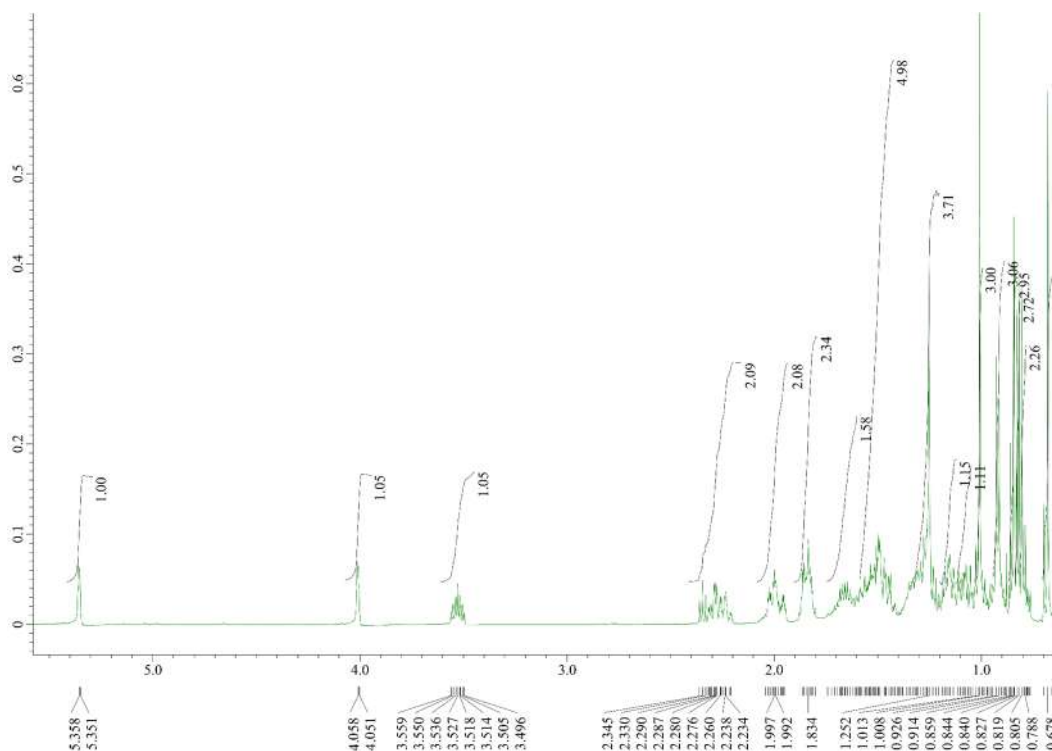
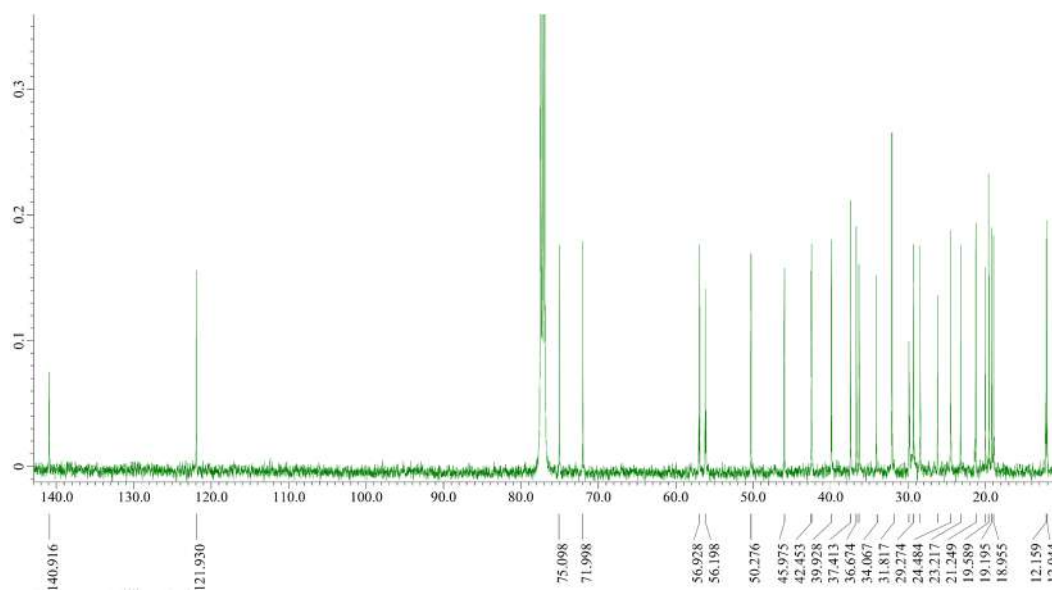
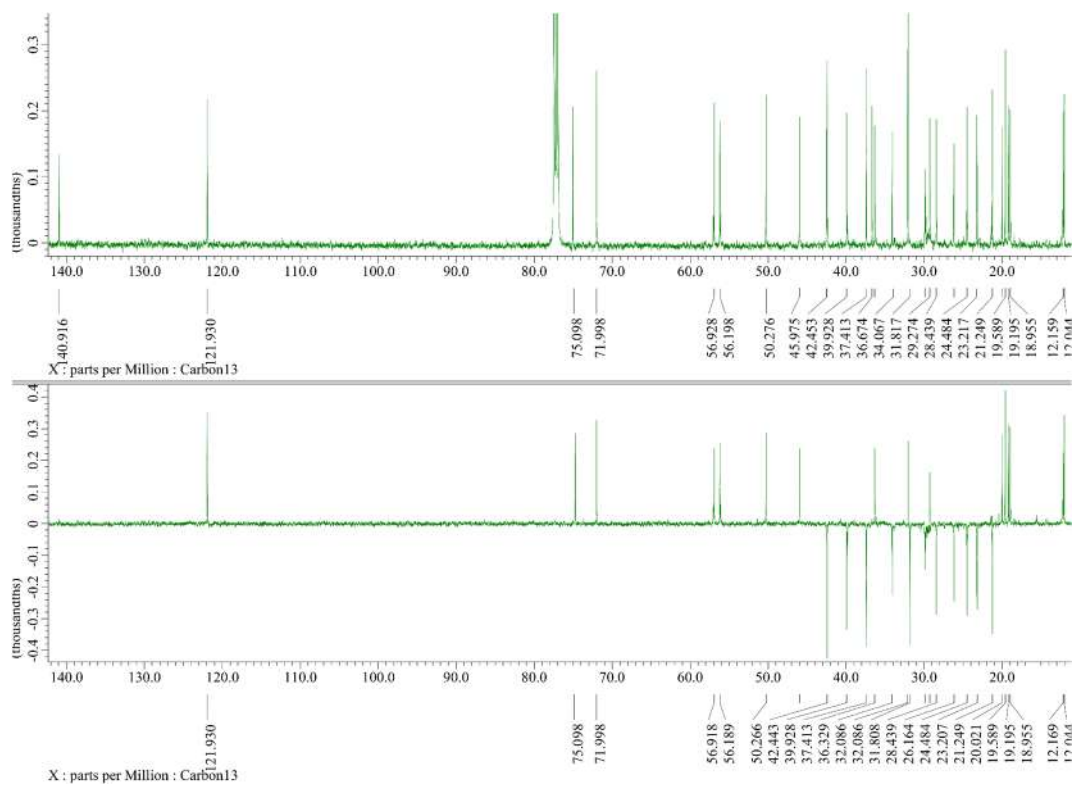
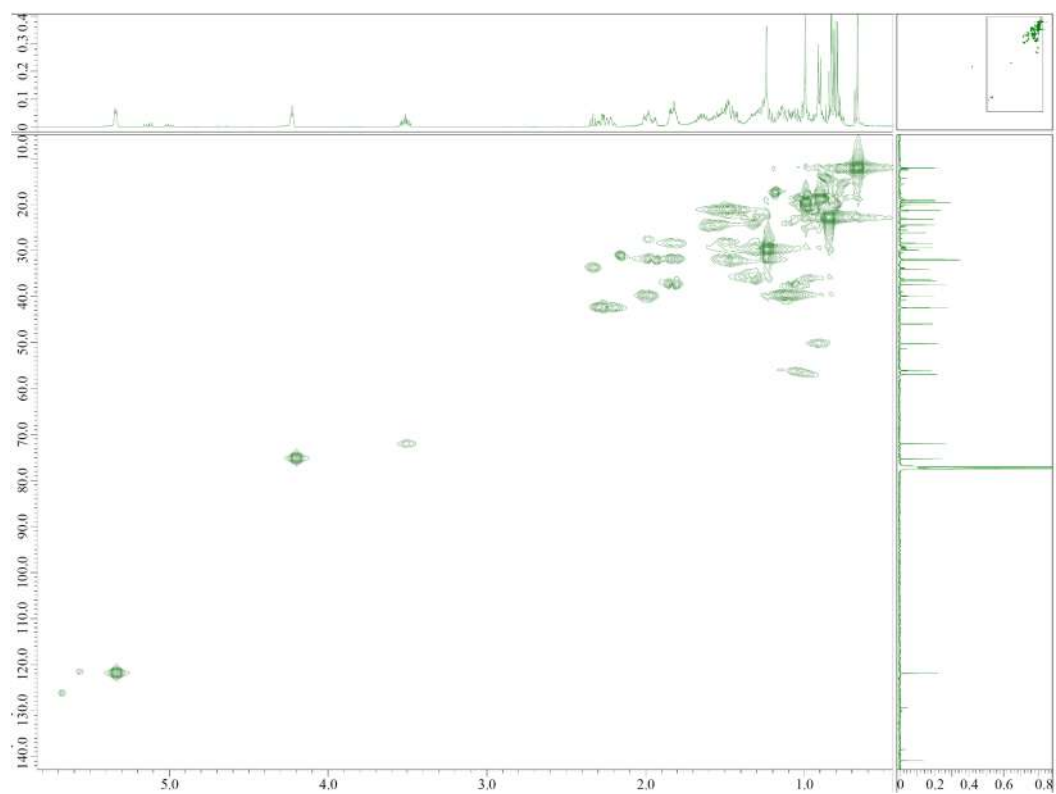


Fig S2. FTIR spectra of 1

Fig S3. ^1H -NMR spectra of **1** (500 MHz in CDCl_3)Fig S4. ^{13}C -NMR spectrum of **1** (125 MHz in CDCl_3)

Fig S5. DEPT-135° spectrum of **1** (125 MHz in CDCl₃)Fig S6. HMQC spectrum of **1**

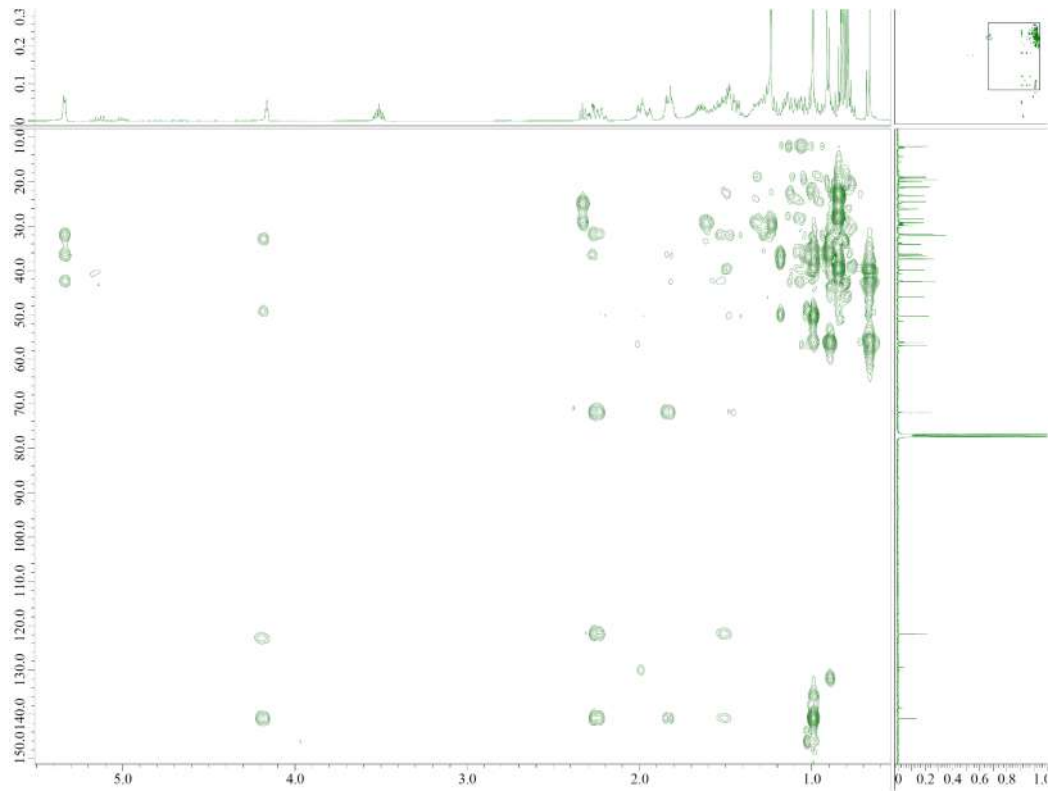


Fig S7. HMBC spectrum of **1**

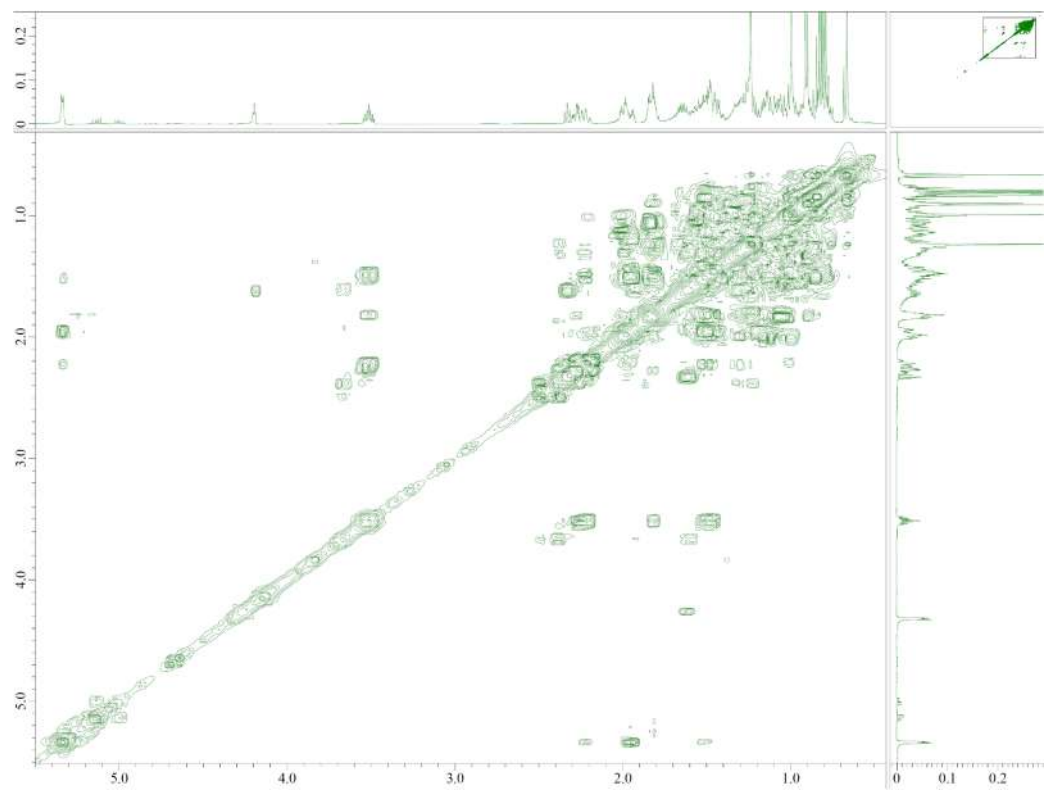


Fig S8. ^1H - ^1H -COSY spectra of **1**

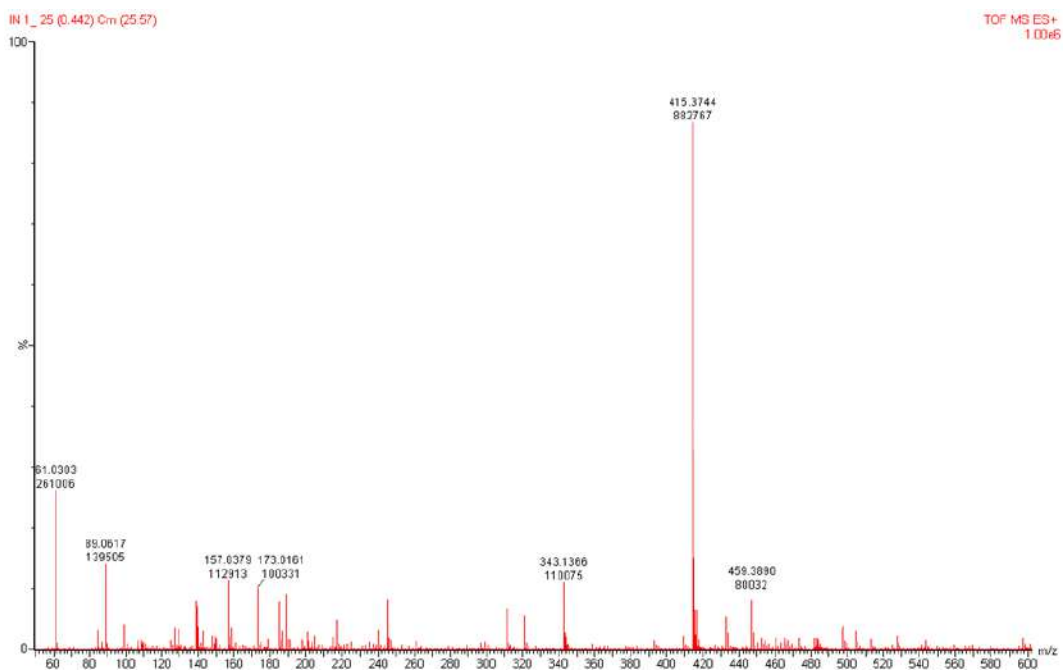


Fig S9. HRTOF-MS spectra of 2

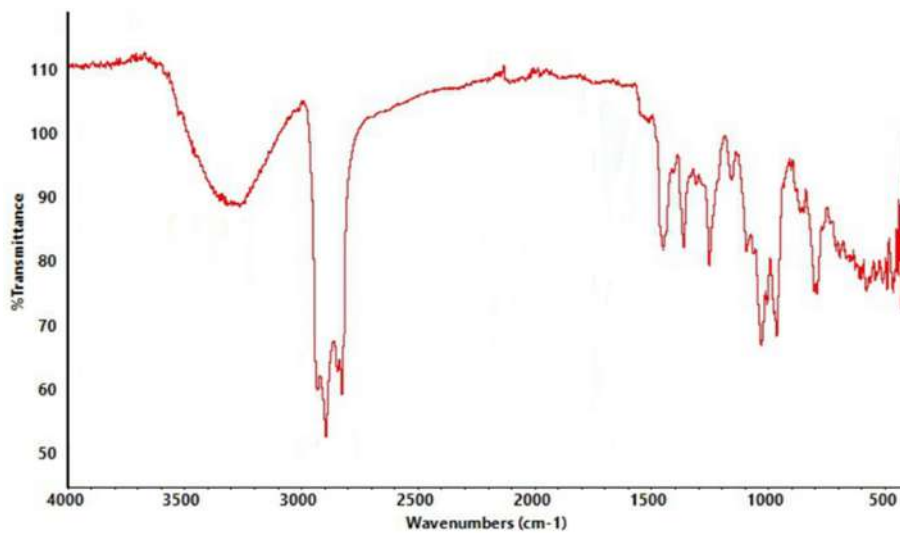
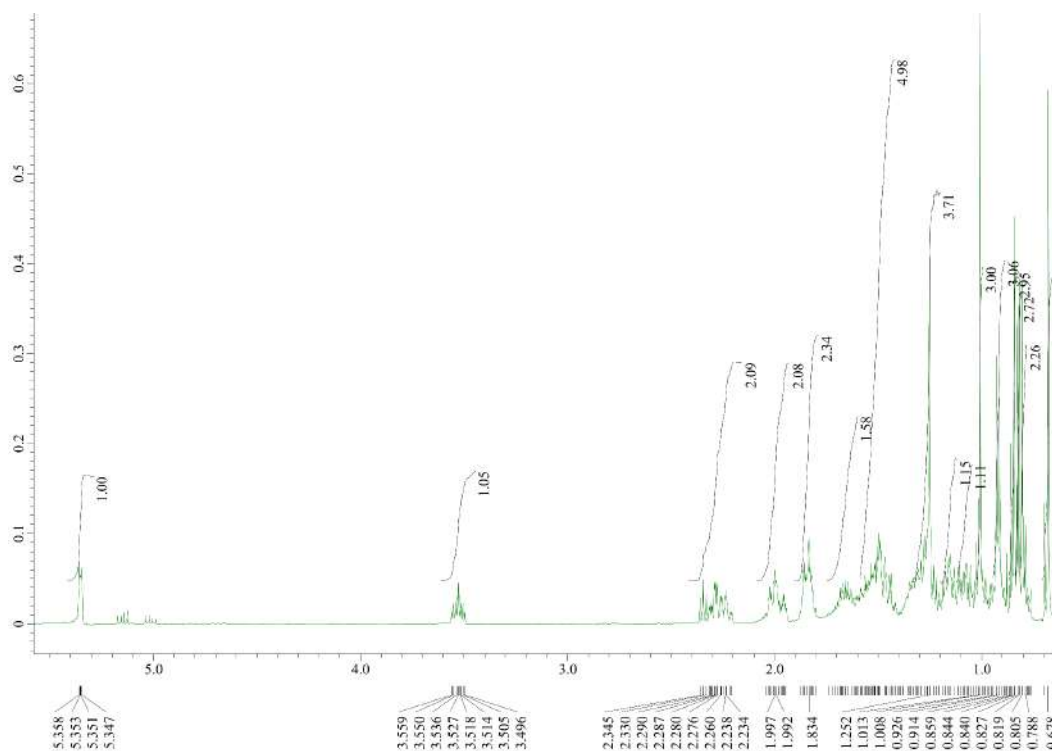
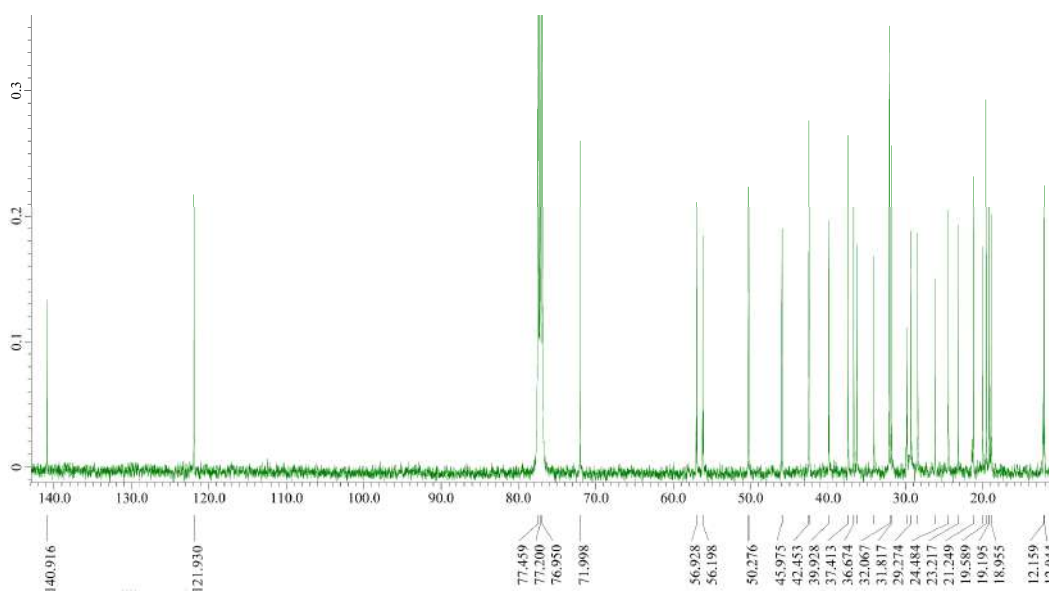


Fig S10. FT-IR spectra of 2

Fig S11. ^1H -NMR spectra of **2** (500 MHz in CDCl_3)Fig S12. ^{13}C -NMR spectrum of **2** (125 MHz in CDCl_3)

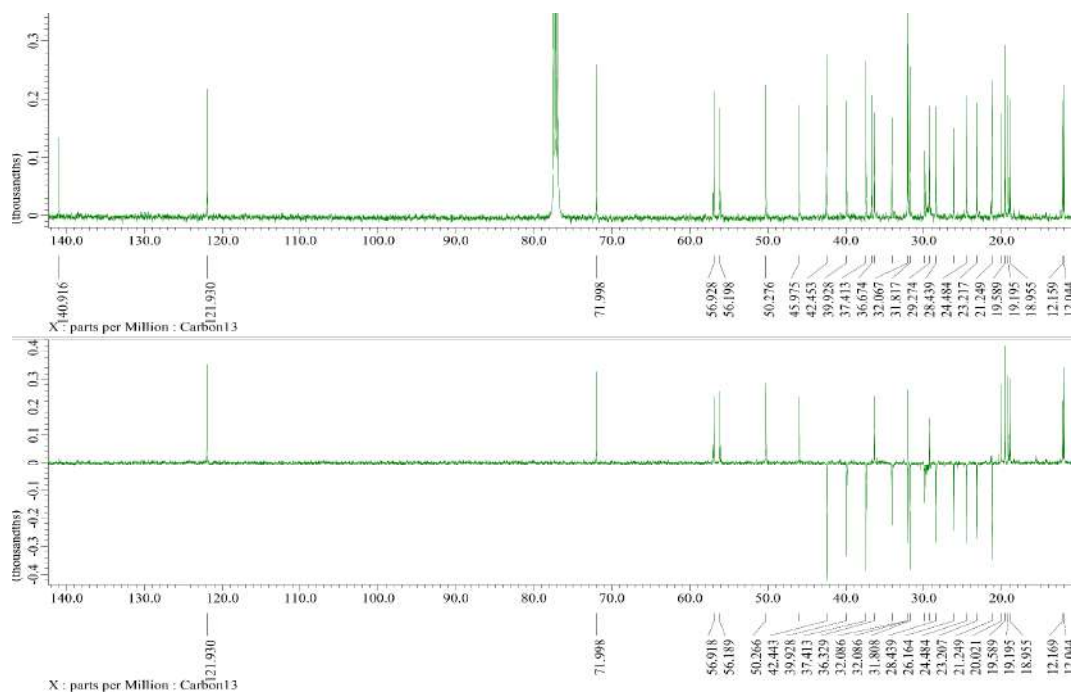
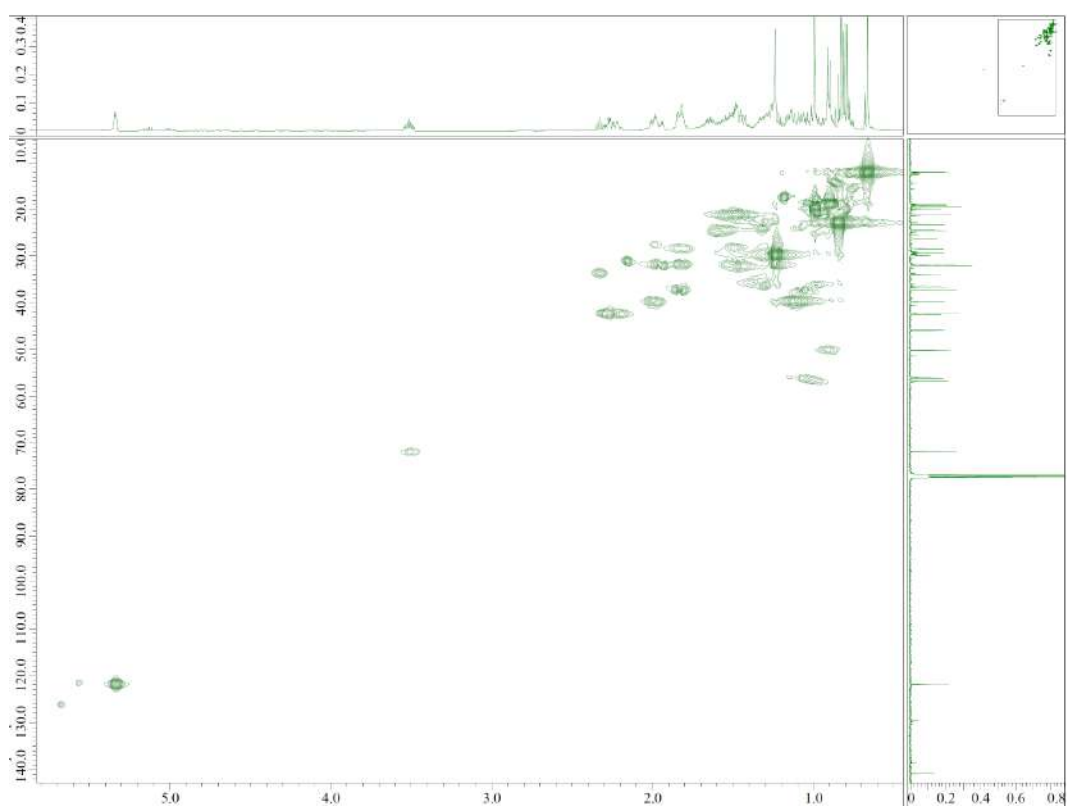
Fig S13. DEPT-135° spectrum of 2 (125 MHz in CDCl₃)

Fig S14. HMQC spectrum of 2

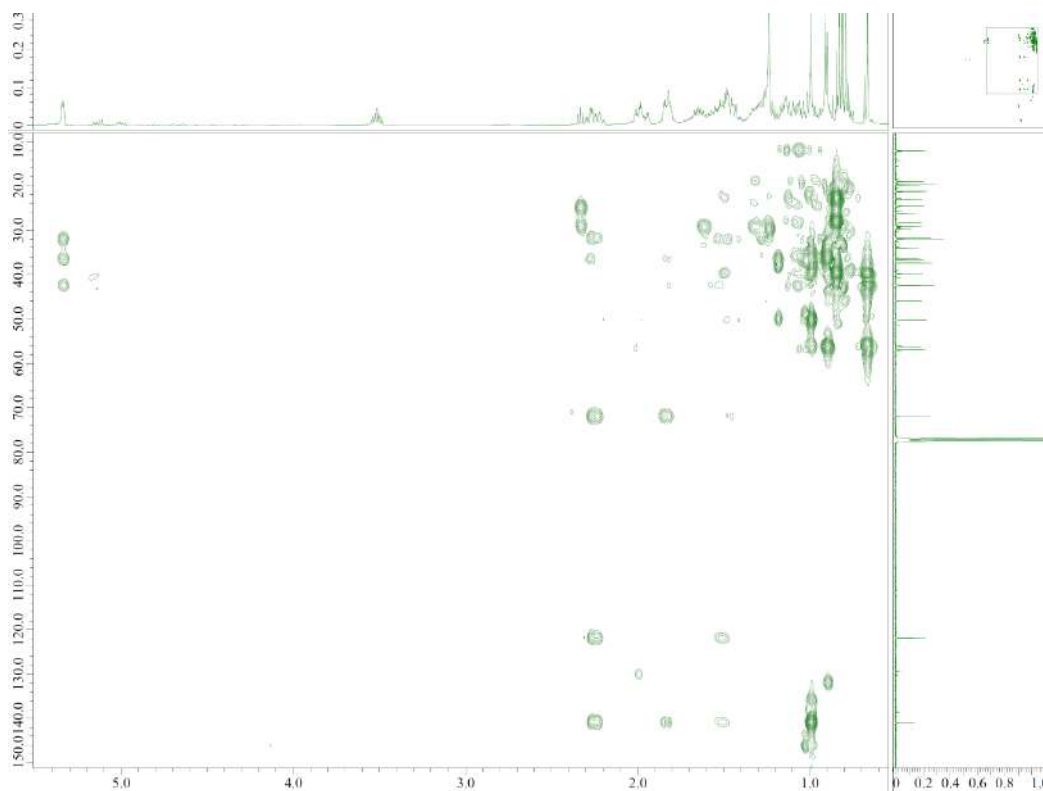


Fig S15. HMBC spectrum of 2

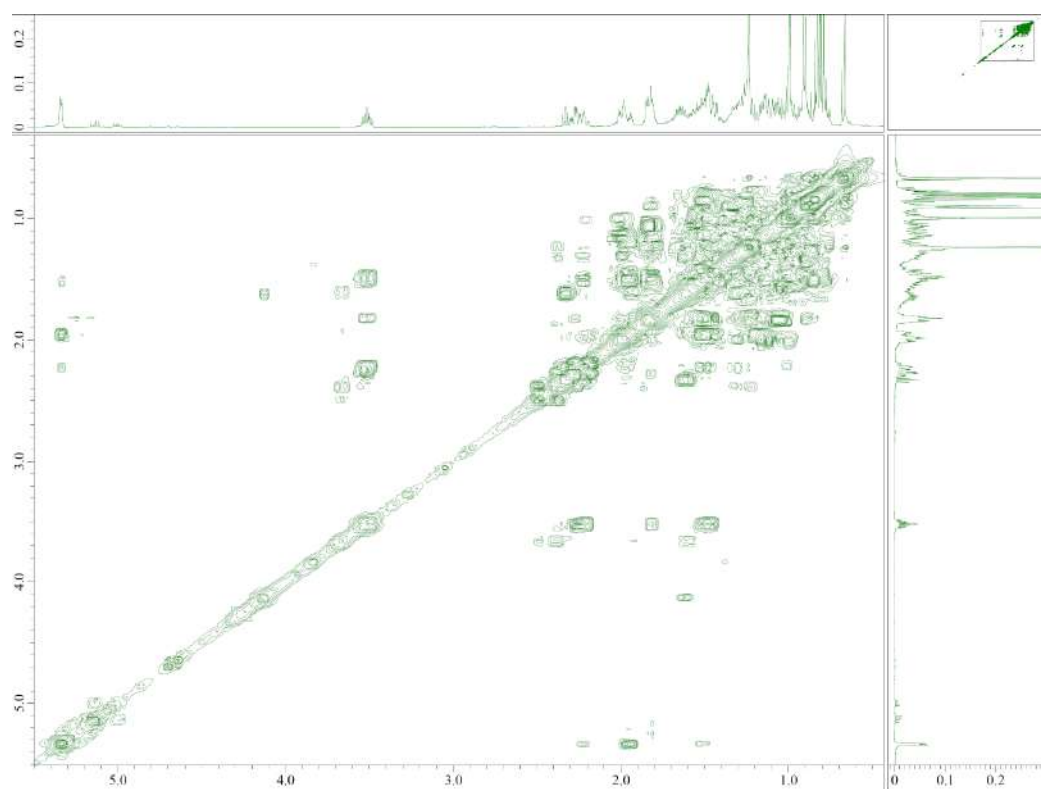


Fig S16. ^1H - ^1H -COSY spectra of 2

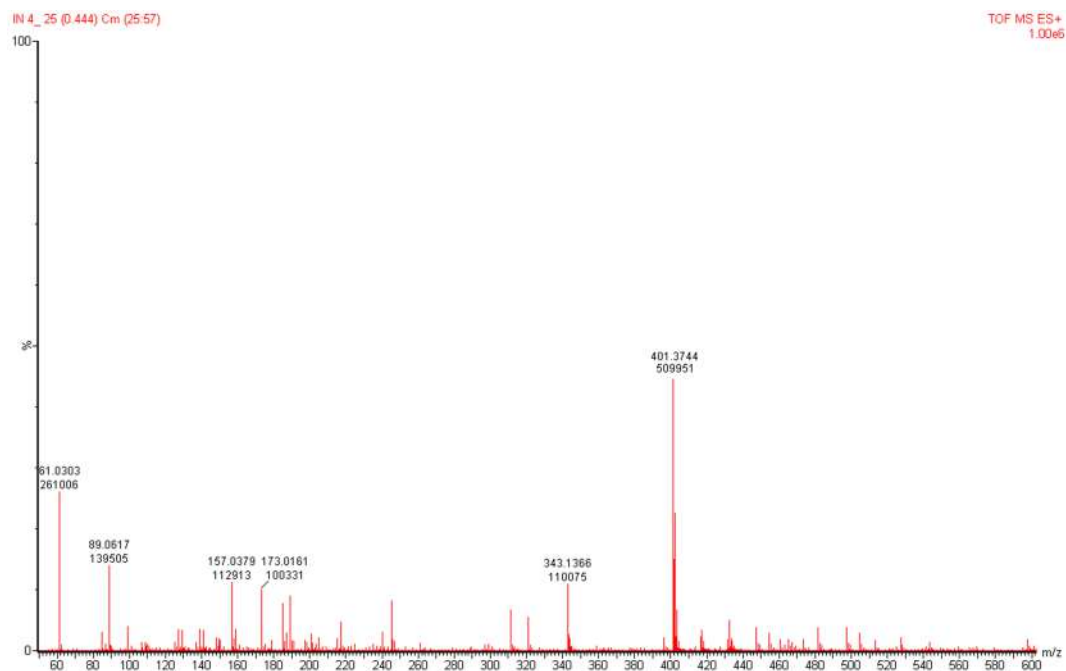


Fig S17. HRTOF-MS spectra of 3

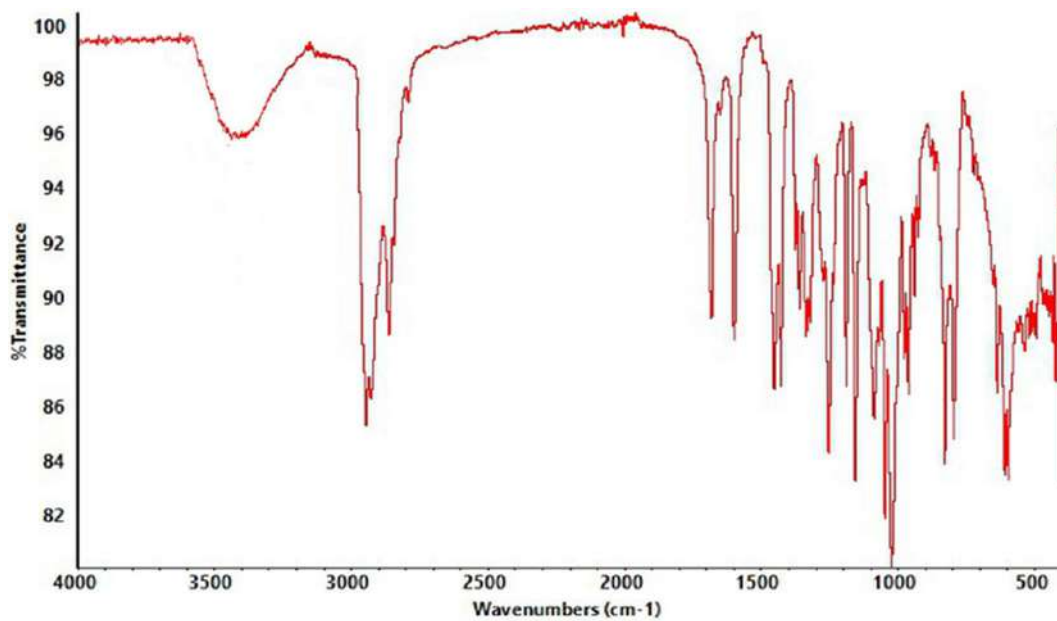


Fig S18. FT-IR spectra of 3

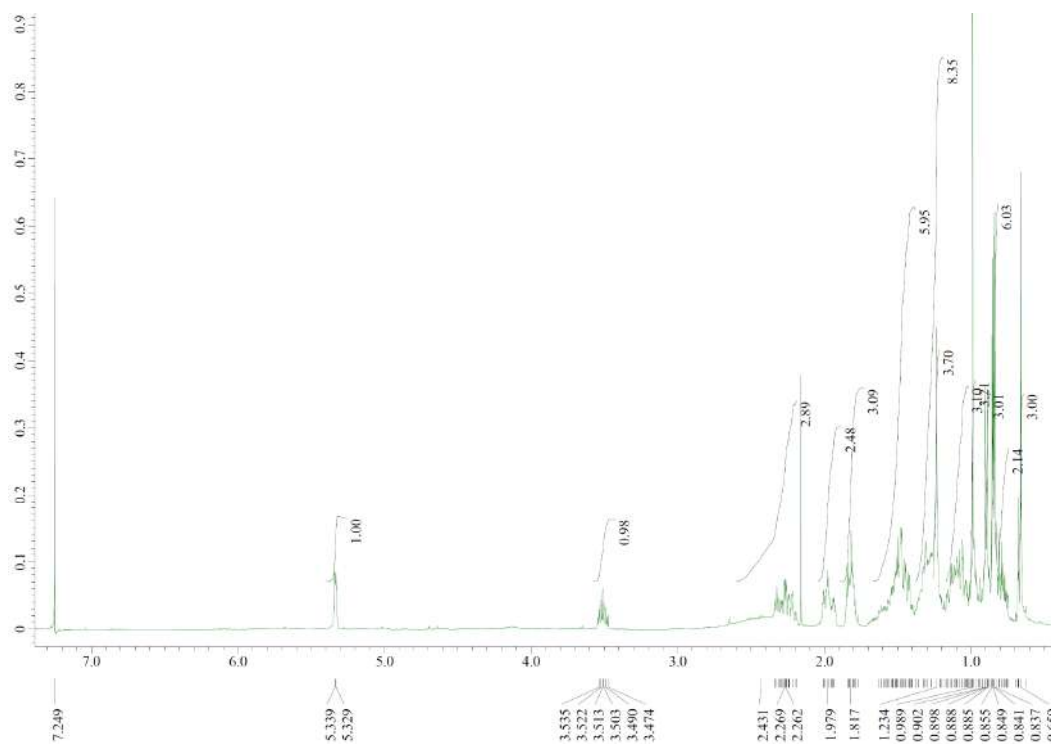


Fig S19. ¹H-NMR spectra of 3 (500 MHz in CDCl₃)

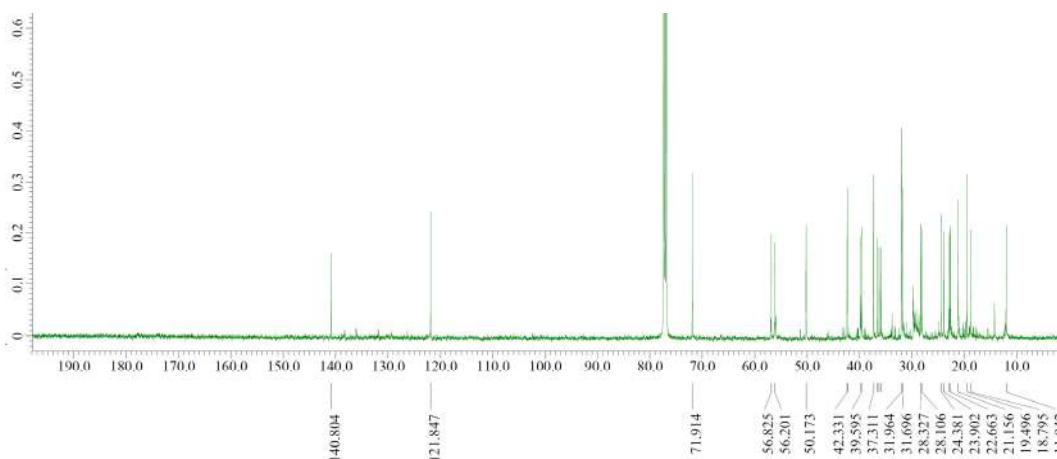


Fig S20. ¹³C-NMR spectrum of 3 (125 MHz in CDCl₃)

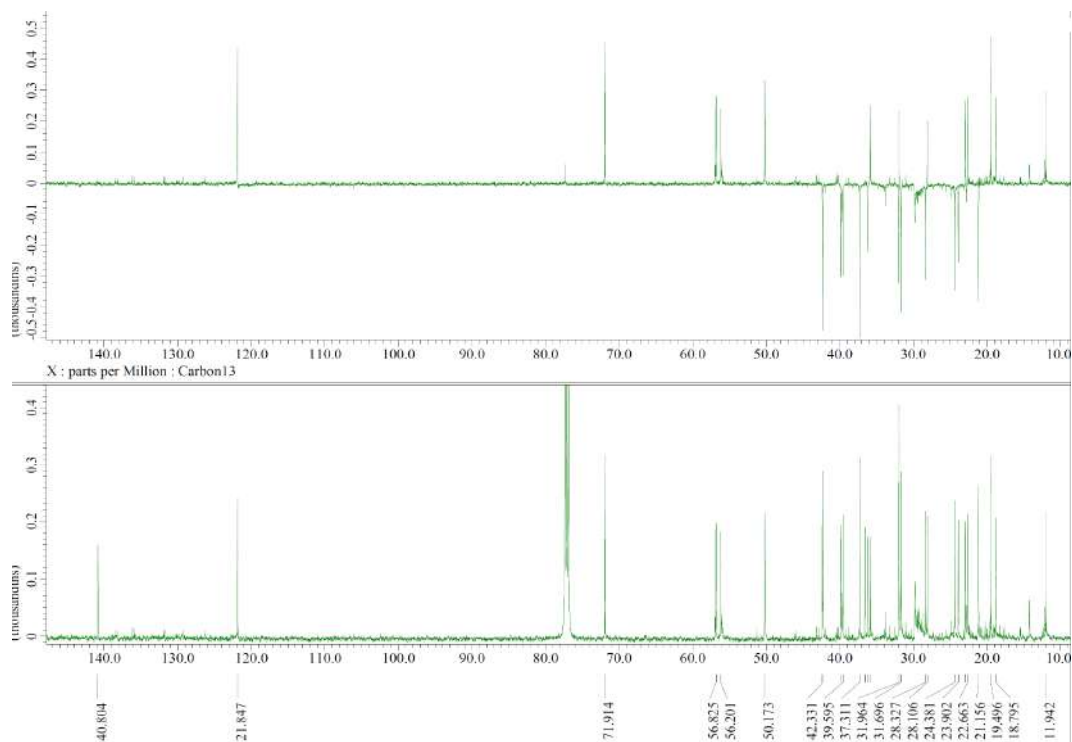


Fig S21. DEPT-135° spectrum of 3 (125 MHz in CDCl₃)

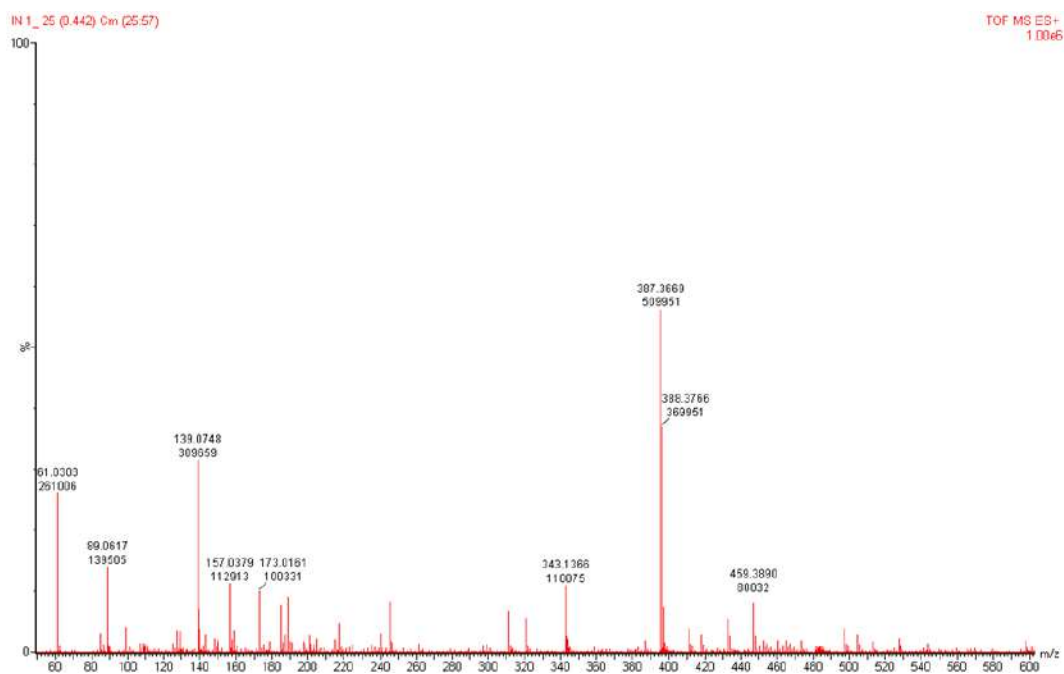


Fig S22. HRTOF-MS spectra of 4

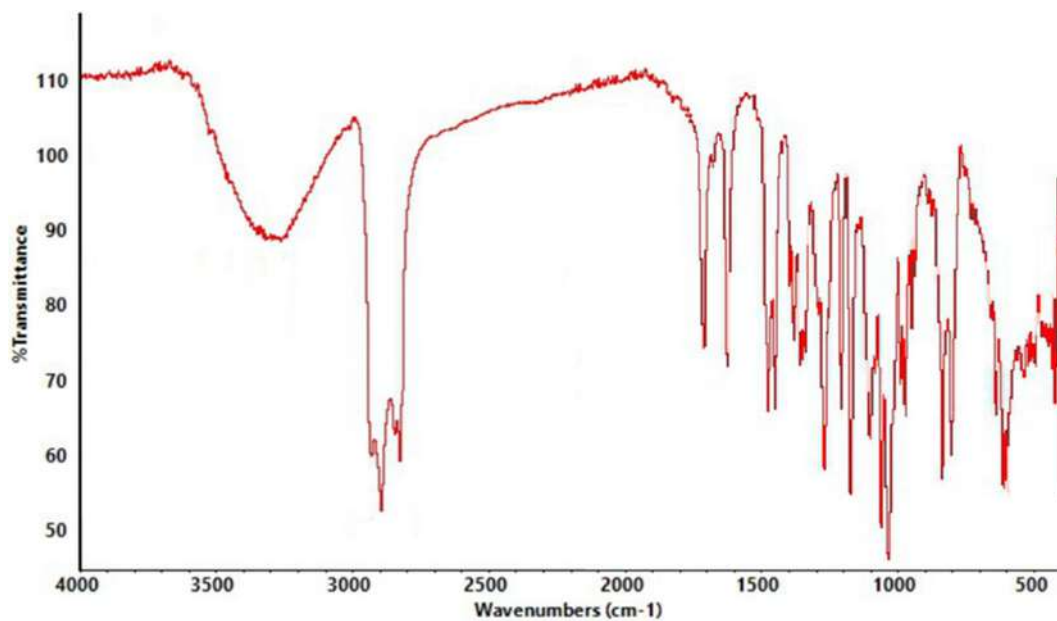


Fig S23. FTIR spectra of 4

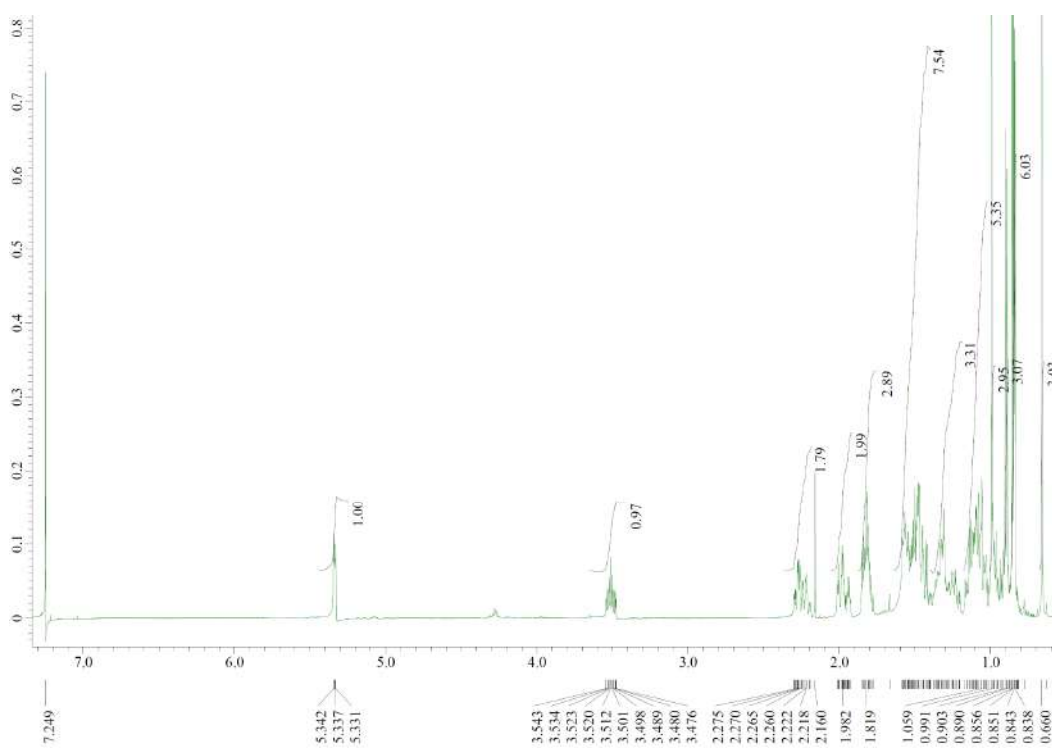


Fig S24. ¹H-NMR spectra of 4 (500 MHz in CDCl₃)

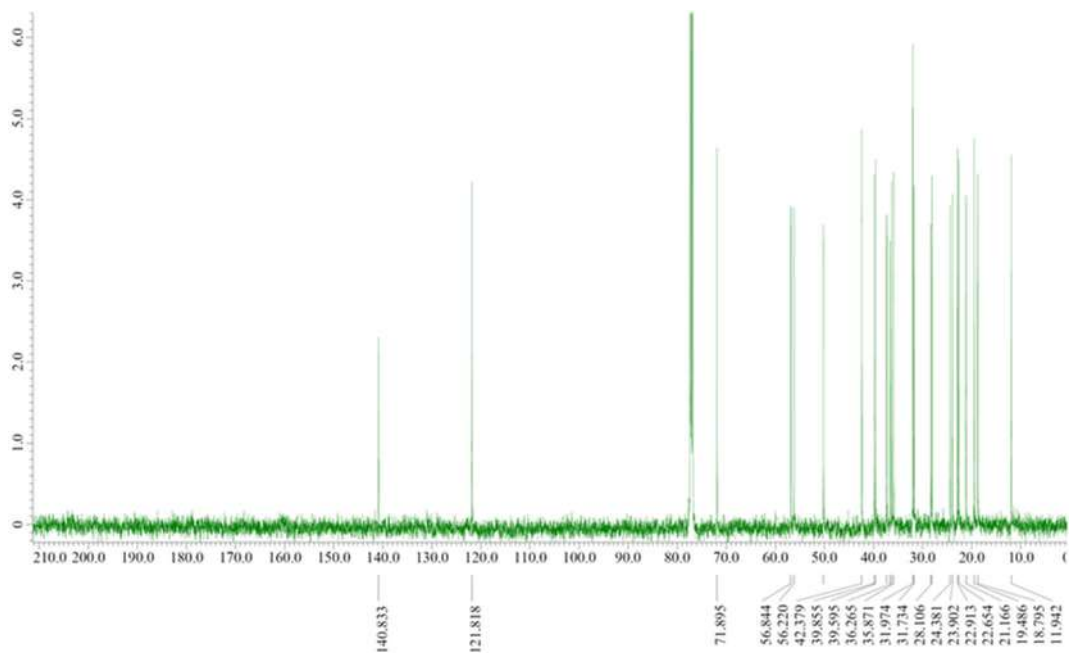
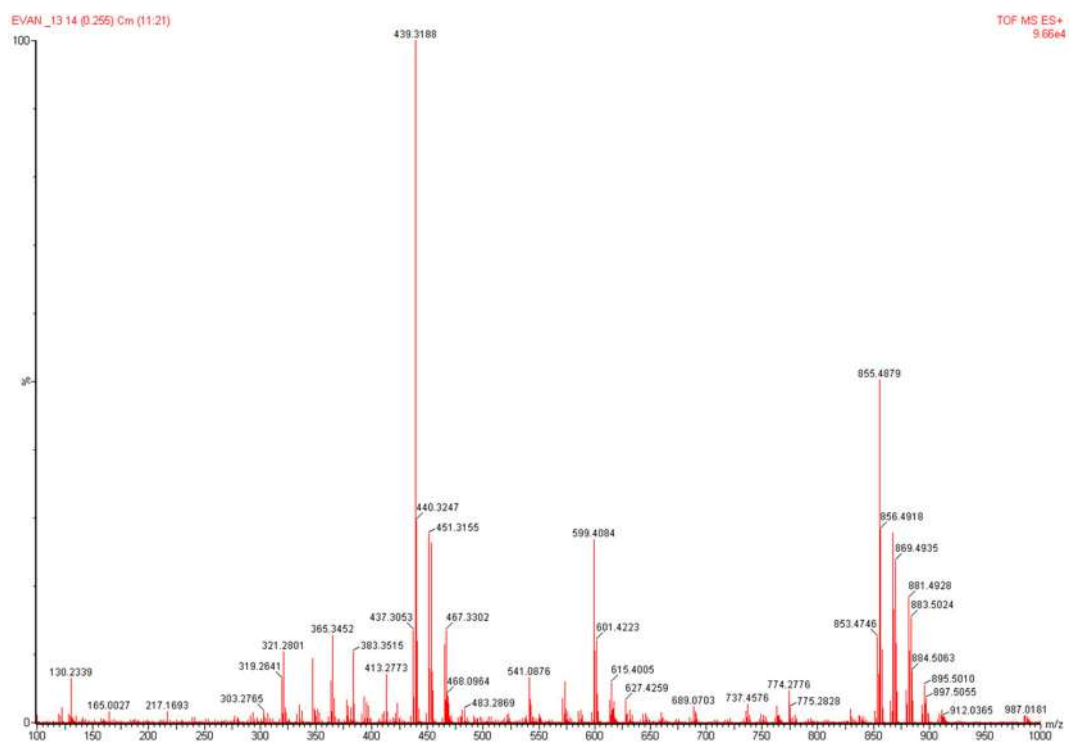
Fig S25. ^{13}C -NMR spectrum of 4 (125 MHz in CDCl_3)

Fig S26. HRTOF-MS spectra of 5

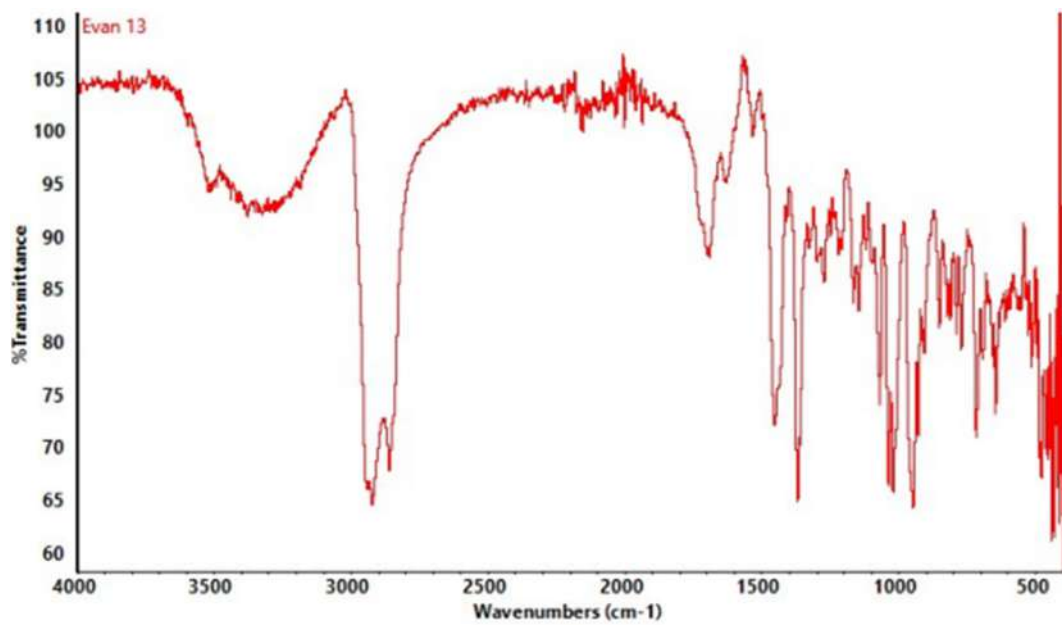
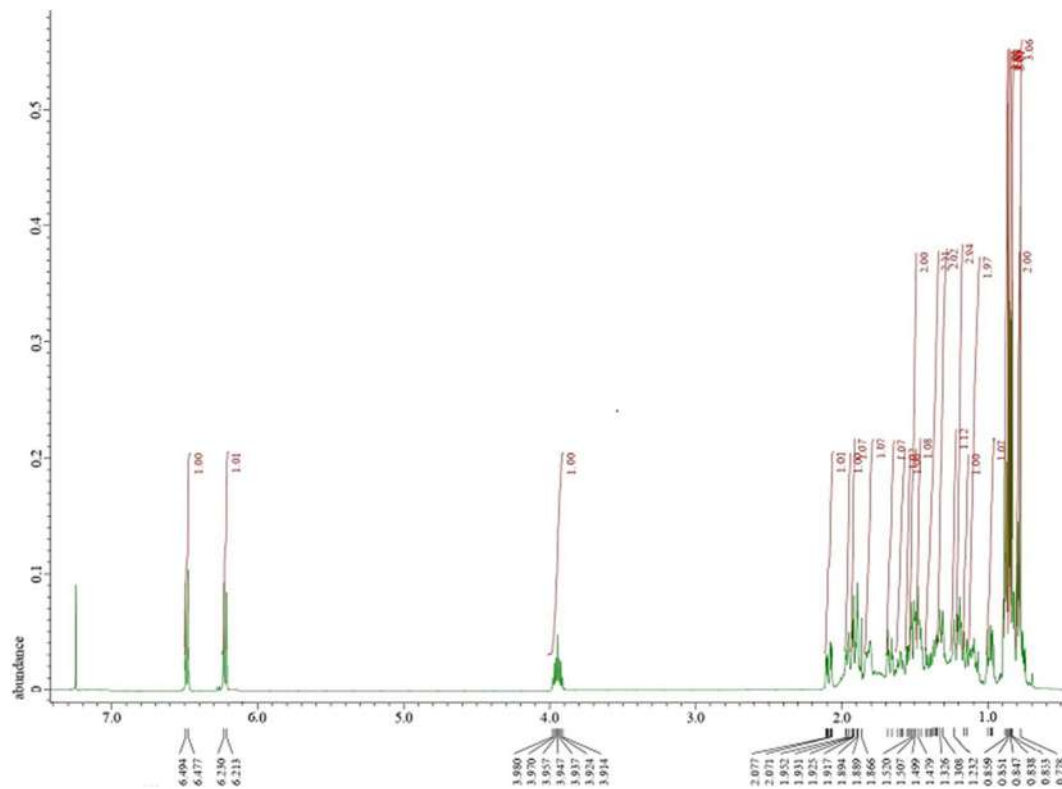
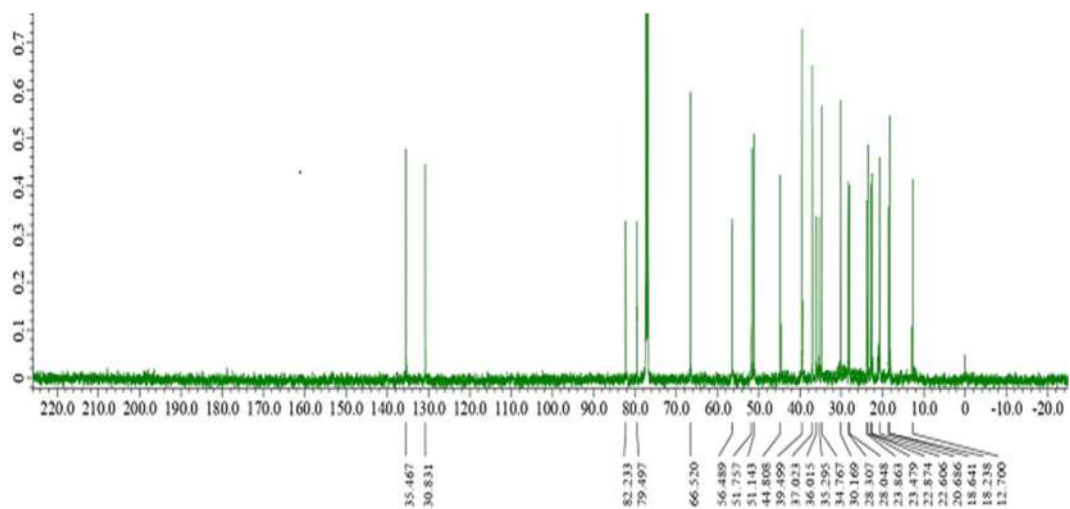
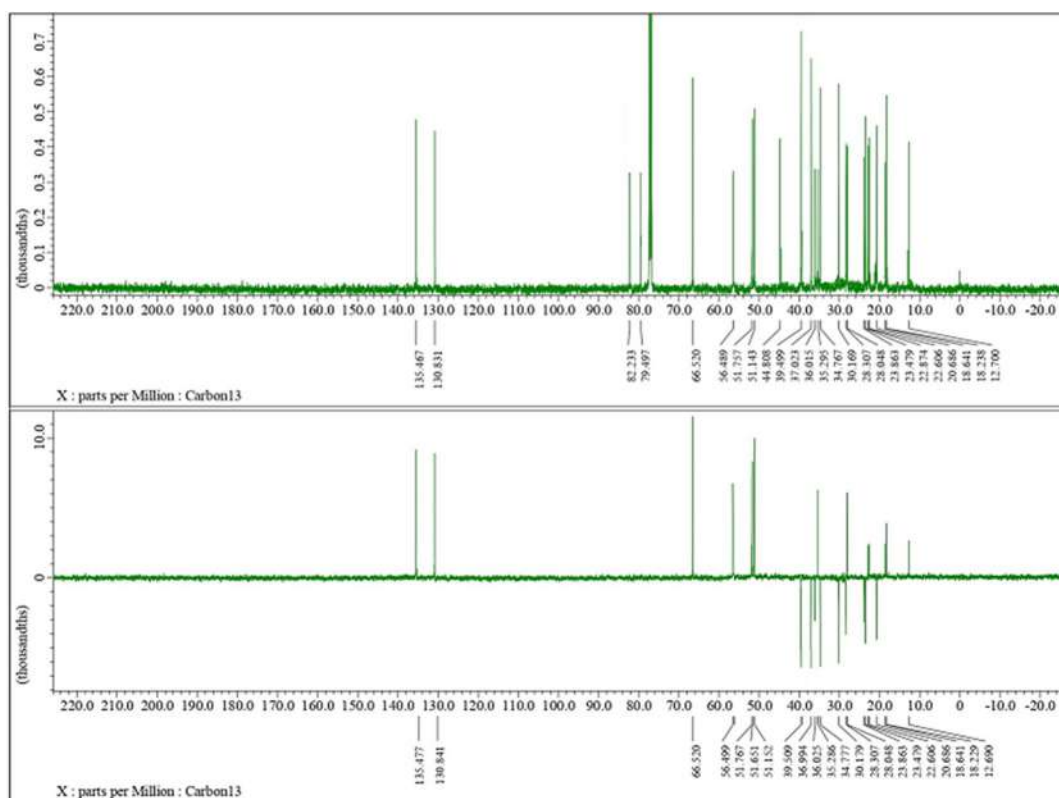


Fig S27. FTIR spectra of 5

Fig S28. ¹H-NMR spectra of 5 (500 MHz in CDCl₃)

Fig S29. ^{13}C -NMR spectrum of 5 (125 MHz in CDCl_3)Fig S30. DEPT- 135° spectrum of 5 (125 MHz in CDCl_3)

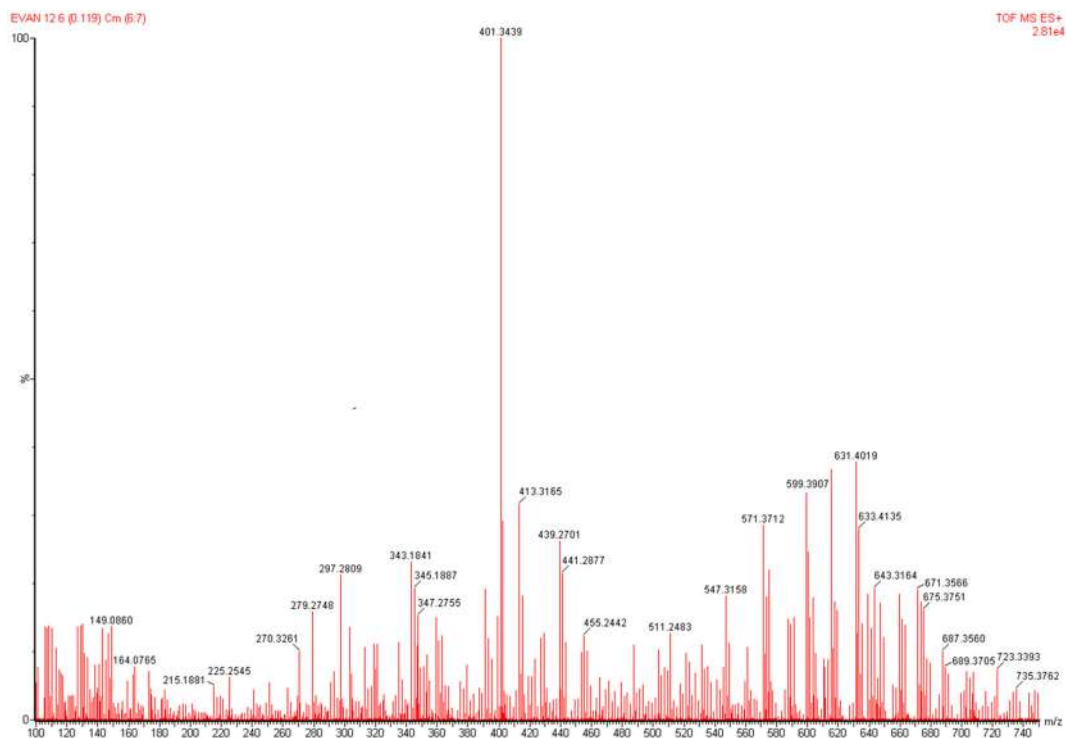


Fig S31. HRTOF-MS spectra of 6

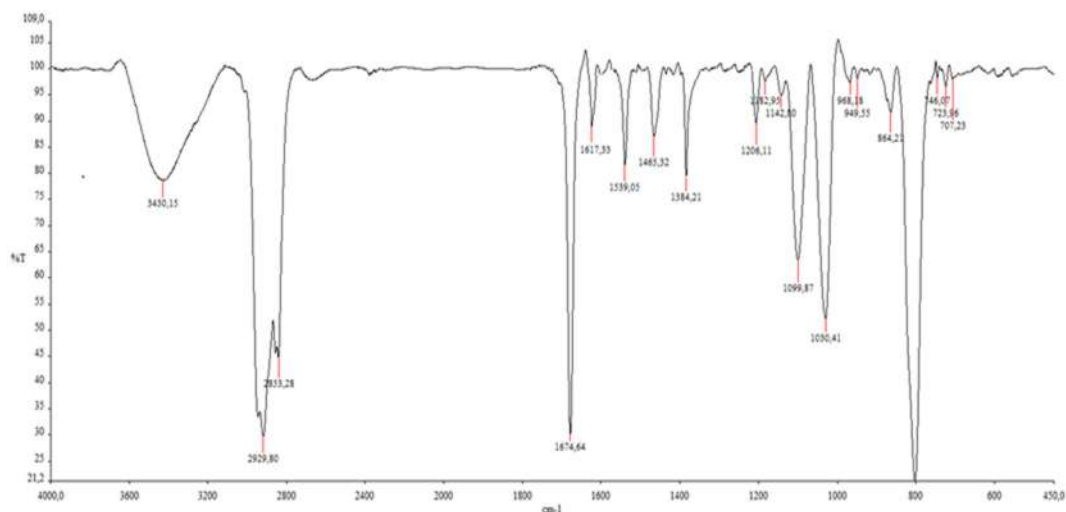


Fig S32. FTIR Spectra of 6

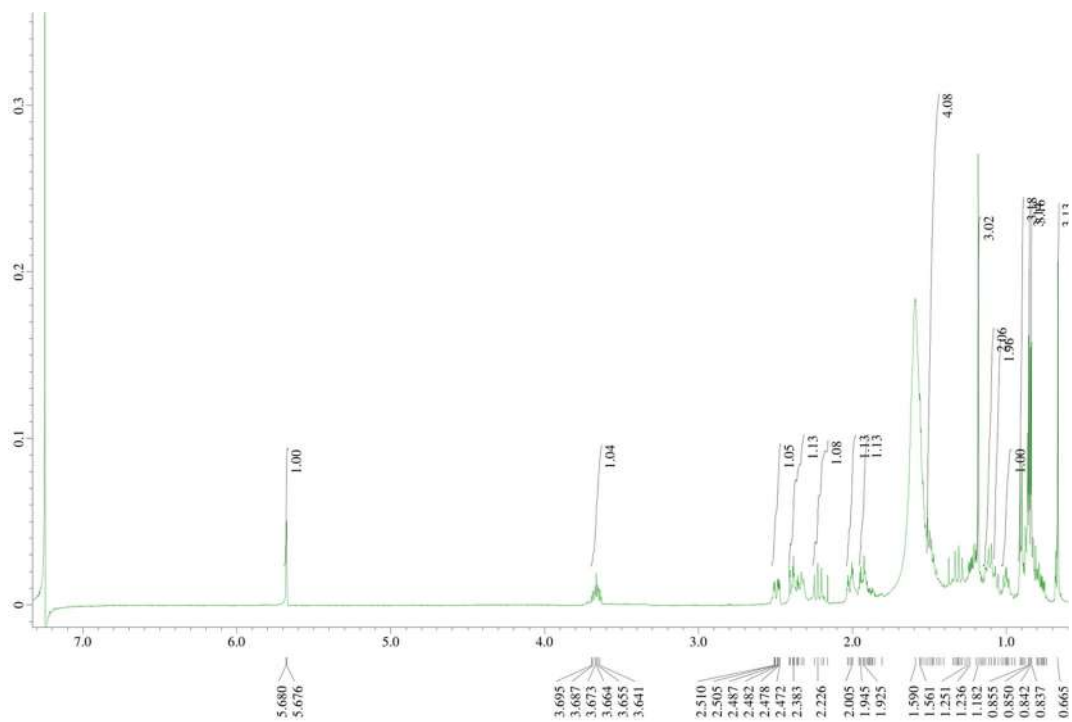


Fig S33. ^1H -NMR Spectra of **6** (500 MHz in CDCl_3)

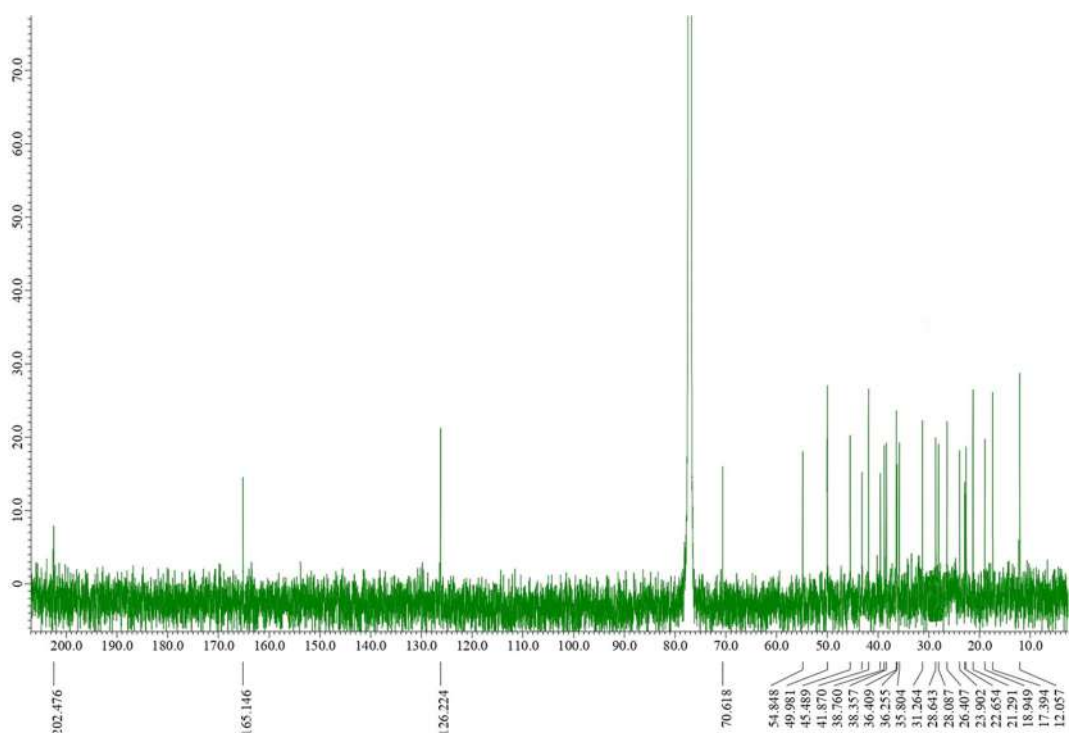


Fig S34. ^{13}C -NMR spectrum of **6** (125 MHz in CDCl_3)

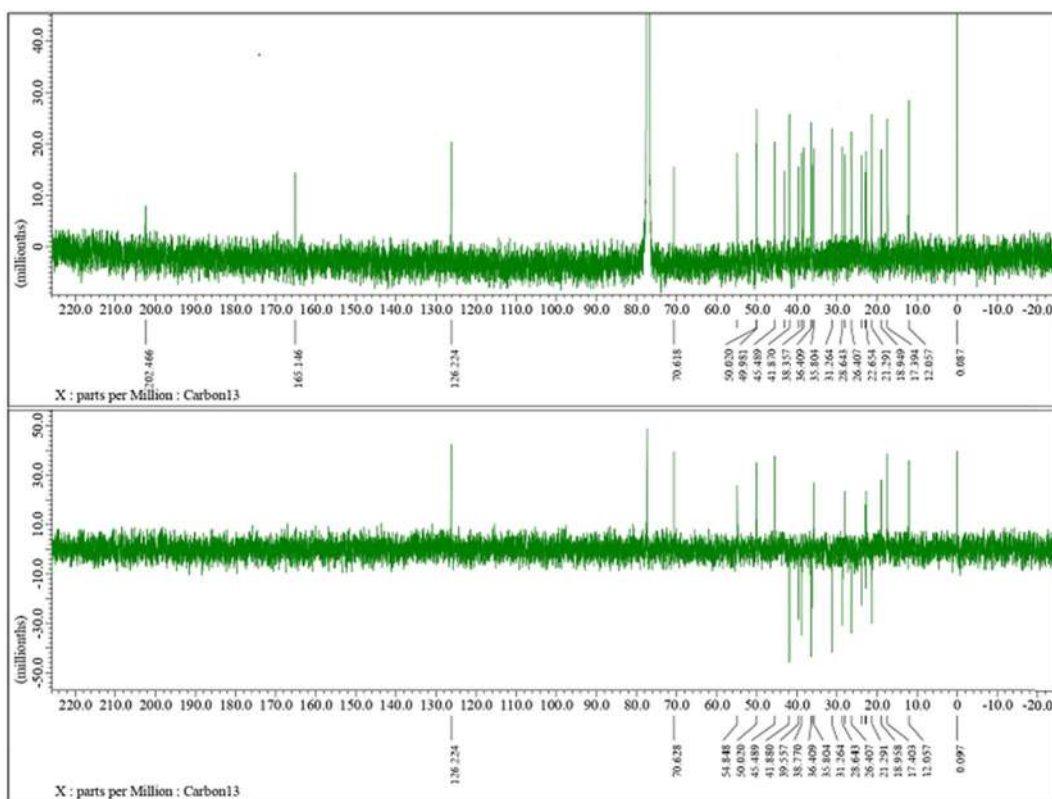


Fig S35. DEPT-135° spectrum of **6** (125 MHz in CDCl₃)

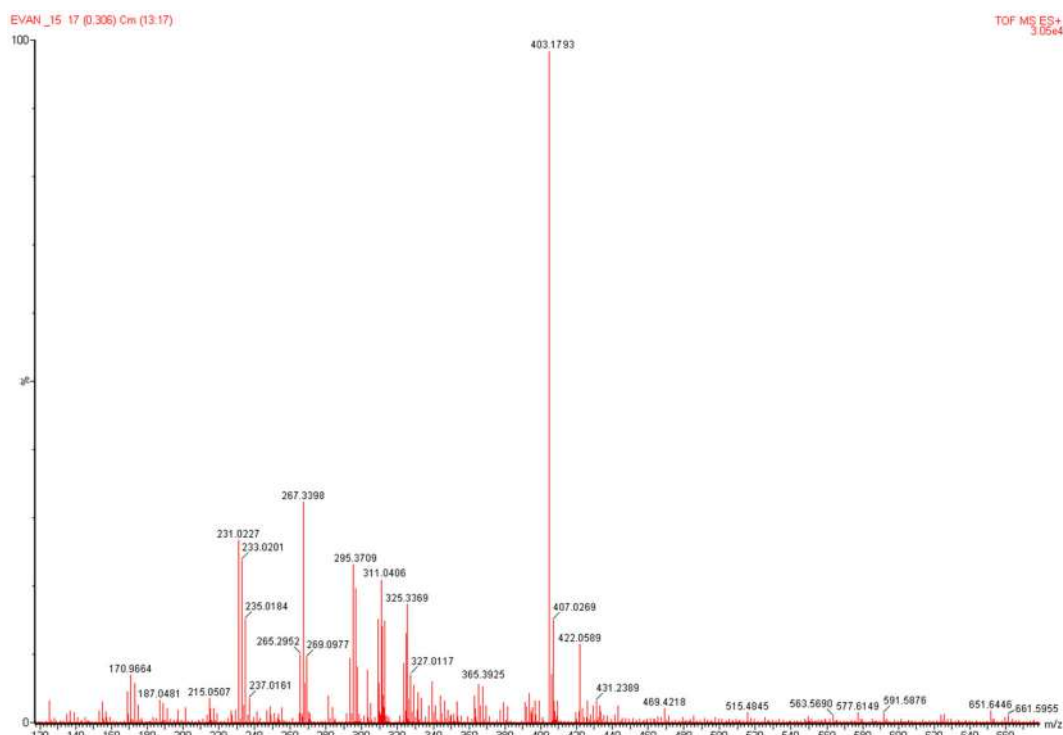


Fig S36. HRTOF-MS spectra of **7**

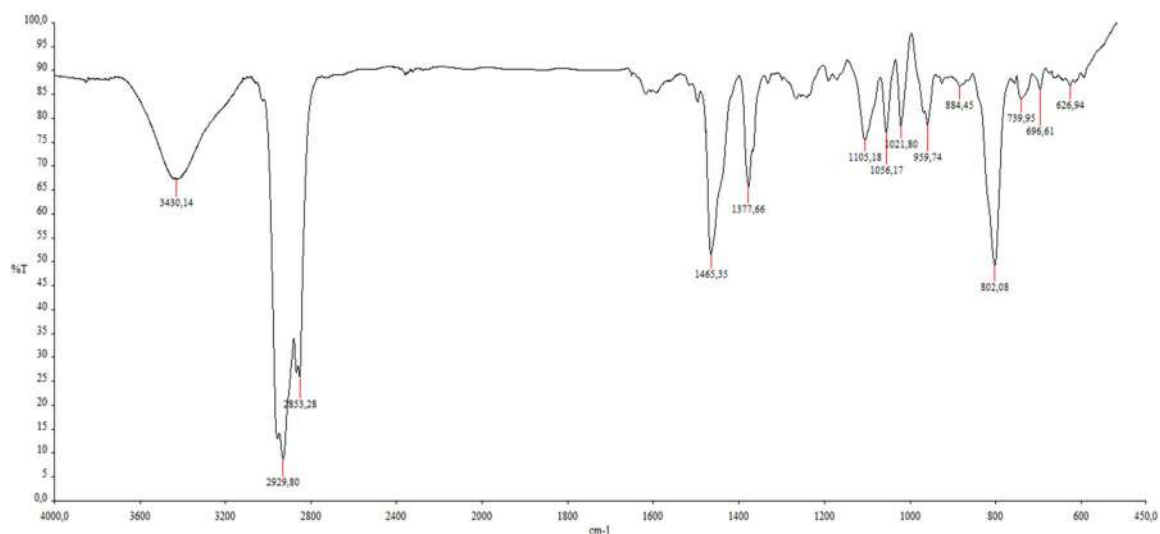
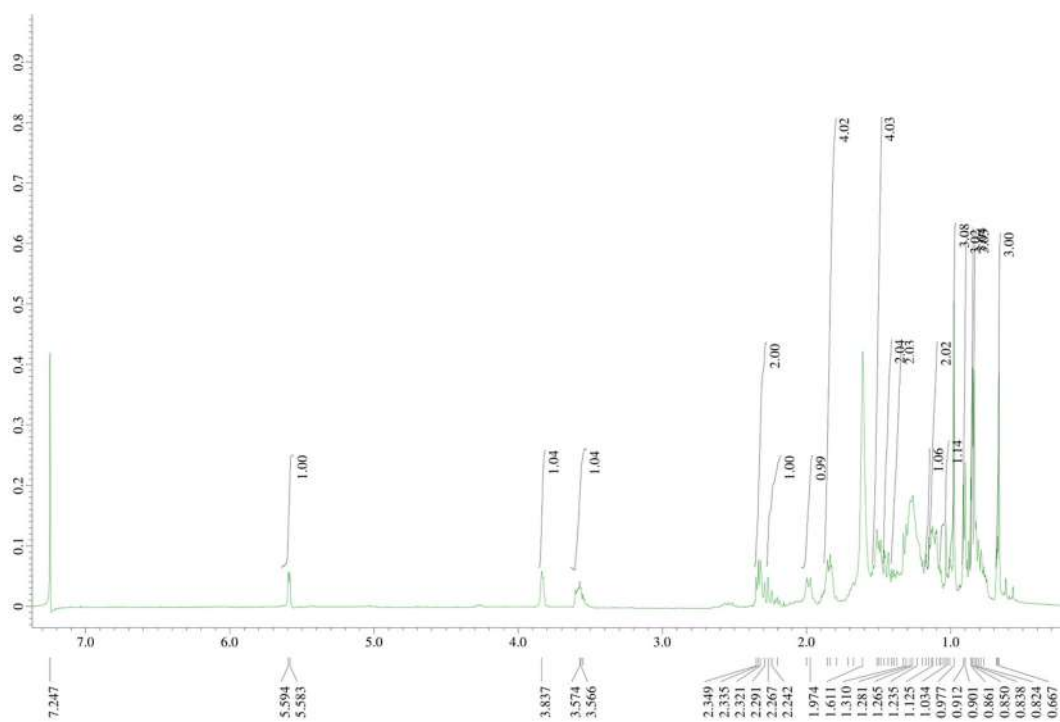


Fig S37. FTIR spectra of 7

Fig S38. ¹H-NMR spectra of 7 (500 MHz in CDCl₃)

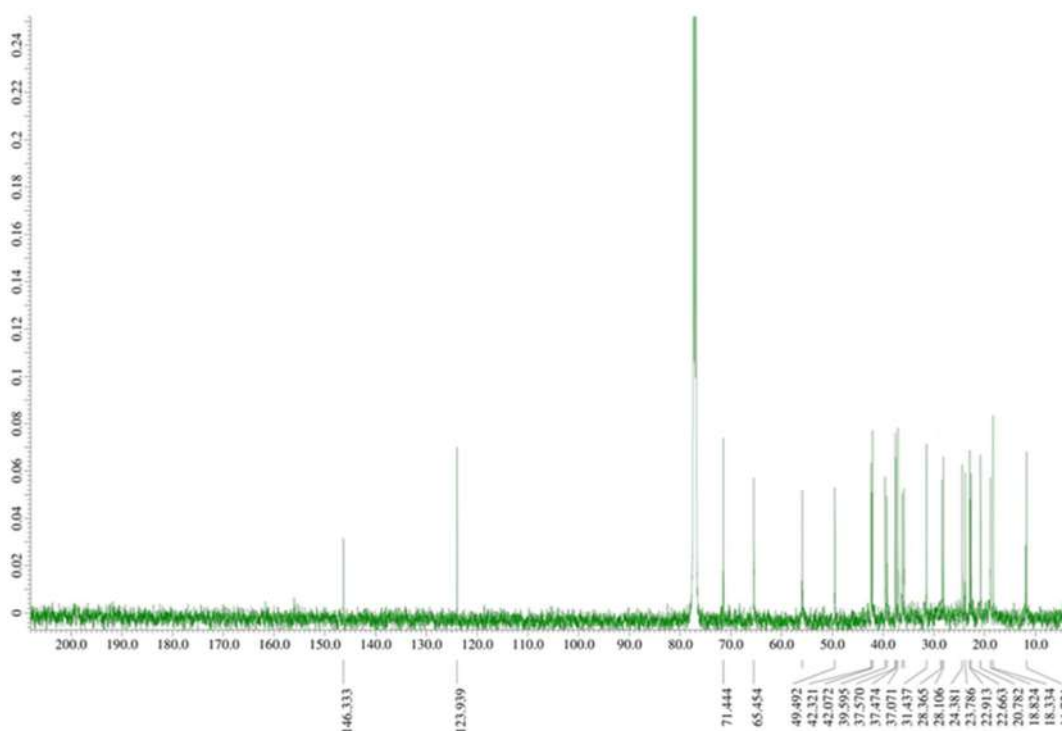


Fig S39. ^{13}C -NMR spectrum of 7 (125 MHz in CDCl_3)

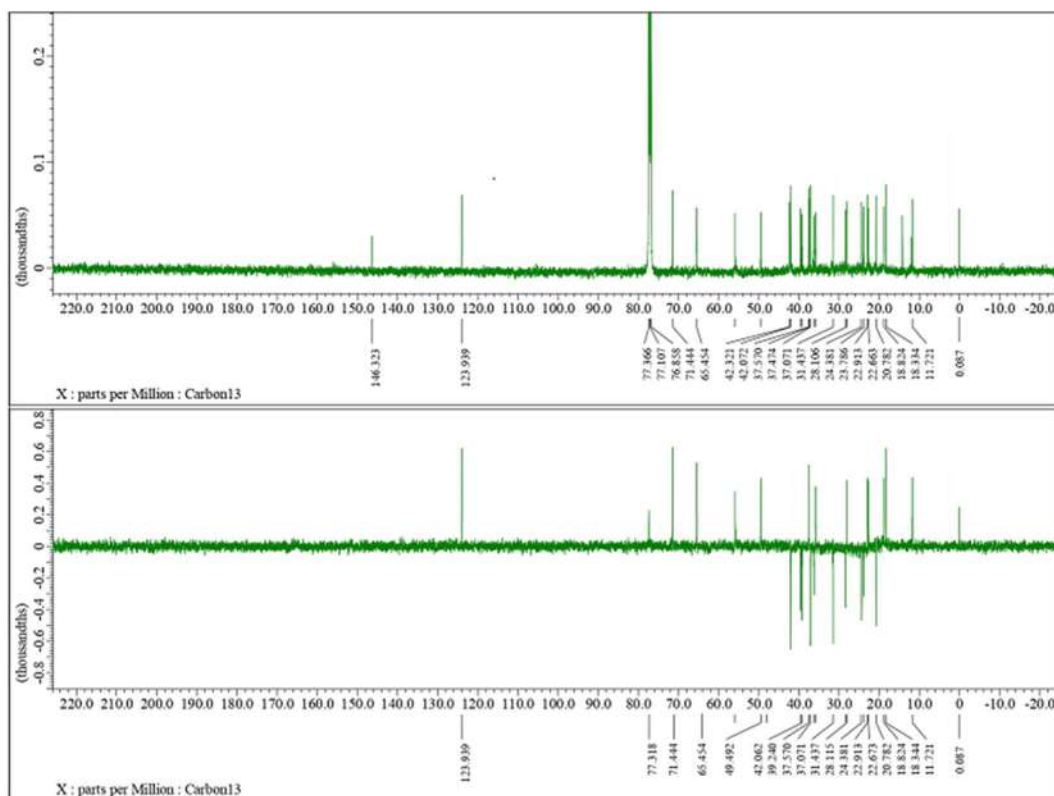


Fig S40. DEPT-135° spectrum of 7 (125 MHz in CDCl_3)

Steroids from *Atactodea striata* and Their Cytotoxic Activity against MCF-7 Breast Cancer Cell Lines

Evan Hadrian¹, Aprilia Permata Sari¹, Tri Mayanti¹, Desi Harneti¹, Rani Maharani¹, Darwati Darwati¹, Kindi Farabi¹, Unang Supratman^{1,2*}, Celcius Waranmaselebun³, Supriatno Salam⁴, Sofa Fajriah⁵, and Muhamad Nurul Azmi⁶

¹Department of Chemistry, Faculty of Mathematics and Natural Sciences, Universitas Padjadjaran, Jl. Raya Bandung-Sumedang Km. 21, Jatinangor, Sumedang 45363, Indonesia

²Central Laboratory, Universitas Padjadjaran, Jl. Raya Bandung-Sumedang Km. 21, Jatinangor, Sumedang 45363, Indonesia

³Department of Fisheries Biotechnology, State Fisheries Polytechnic of Tual, Tual 97613, Southeast Maluku, Indonesia

⁴Faculty of Pharmacy, Universitas Mulawarman, Samarinda, 75123, East Kalimantan, Indonesia

⁵Research Center for Raw Materials for Medicine and Traditional Medicine, National Research and Innovation Agency (BRIN), Tangerang Selatan, Banten 15314, Indonesia

⁶School of Chemical Sciences, Universiti Sains Malaysia, 11800 Minden, Penang, Malaysia

* Corresponding author:

email: unang.supratman@unpad.ac.id

Received: July 21, 2022

Accepted: November 14, 2022

DOI: 10.22146/ijc.76438

Abstract: Marine environment is known as a source of potential steroids with multiple biological activities, one of which is an anticancer agent. *Atactodea striata* are one of the seashells distributed in Indonesia located in the Kei Islands, Southeast Maluku. During the course of our continuing search for biologically active substances from Indonesia seashells, seven steroids have been isolated from the n-hexane fraction of *A. striata* and they were identified as 7 β -hydroxy-sitosterol (1), campesterol (2), β -sitosterol (3), cholesterol (4), 5 α ,8 α -epidioxycholest-6-en-3- β -ol (5), 7-keto-cholesterol (6), and 7 α -hydroxy-cholesterol (7). The structure was identified by spectroscopic methods including 2D NMR techniques, FTIR, HRTOFMS, and chemical shift comparison with previously reported spectral data. Compounds 1-7 were evaluated for their cytotoxic effects against MCF-7 breast cancer cells and showed weak or no anticancer activity.

Keywords: *Atactodea striata*; cytotoxic activity; MCF-7; steroids

■ INTRODUCTION

Sterol belongs to steroid group and is widely distributed in plants, animals, and marines [1]. Marine is known as a source of interesting secondary metabolites, especially as a natural resource of sterols. Several studies indicate that sterols, isolated from marine products, exhibit several bioactivities such as anti-inflammation, antimicrobial, anti-HIV, and anticancer [2-5]. Several sterols with various structures have been isolated from the seashells of *Villorita cyprinoides*, which are two new cholestane type (22E),(24¹E)-24¹,24²-dihomocholesta-5,22,24¹-trien-3 β -ol and (22E)-24¹-homocholesta-5,22-dien-(3 β ,24¹ β)-diol showed interesting bioactivity as

antioxidant and anti-inflammation agents against DPPH and COX-1 with the IC₅₀ values of 0.91 and 0.93 μ g/mL (DPPH), 1.16 and 1.19 μ g/mL (COX-1), respectively [6].

The *Atactodea striata*, known as Mas Ngur shells in Indonesia, are one of the seashell groups belonging to the mollusc phylum, geographically distributed in the Indo-Pacific from East Africa, including Madagascar and the Red Sea, to eastern Polynesia, to northern Japan, and also distributed in Indonesia located in the Kei Islands, Southeast Maluku [7-8]. *A. striata* are small, short-lived bivalves, have a high population, and are usually found in the intertidal zone along sandy beaches [9]. Previously reported that secondary metabolites have

been isolated from Mas Ngur Shells are vicenin-2 and apigenin. Both vicenin-2 and apigenin showed potent cytotoxic activity against breast cancer cells: MCF-7, MDA-MB-231, and Hs578T [10-12].

In our continuous search for biologically active compounds from marine sources, we have isolated two known stigmastane-type steroids (**1-2**), one known campestane-type steroid (**3**), and four known cholestane-type steroids (**4-7**) from the *n*-hexane fraction of *A. striata*. Compounds **1-7** showed weak activity and no cytotoxic activity against MCF-7 breast cancer cells through *in vitro* assay. Here, we report the isolation and structure elucidation of compounds **1-7** along with their cytotoxic activity against MCF-7 breast cancer cells.

■ EXPERIMENTAL SECTION

Materials

The meat of *Atactodea striata* was collected in Ohoi, Kei Island, Southeast Maluku, Indonesia in June 2019. The animal sample was identified and classified by Deep Sea Research Center BRIN, with a voucher B-1209/III/DI/2/2022.

Instrumentation

IR spectra were recorded by Perkin Elmer Spectrum 100 FTIR spectrometer (Shelton, Connecticut, USA) using a NaCl plate. High-resolution mass spectra (HR-TOFMS) were determined on a Waters Xevo Q-TOF direct probe/MS system, utilizing ESI mode and microchannel plates MCPs detector (Milford, MS, USA). The NMR spectra were recorded on JEOL JNM-ECX500R/S1 spectrometer (Tokyo, Japan) at 500 MHz for ¹H and 125 MHz for ¹³C with TMS as an internal standard. The column chromatography was conducted on silica gel 60 (70–230 and 230–400 mesh, Merck, Darmstadt, Germany). The TLC analysis was implemented with silica GF₂₅₄ (Merck, 0.25 mm) and spot detection was obtained by spraying with 10% H₂SO₄ in EtOH, followed by heating and irradiating under ultraviolet-visible light (λ 254 and 365 nm).

Procedure

Extraction and isolation

Dried meat of Mas Ngur shells (*A. striata*) 1.2 kg was

extracted with ethanol (10 L) at room temperature for 3 d and then concentrated under vacuum to yield EtOH extract (407.7 g). The concentrated extract was suspended in H₂O and then partitioned with *n*-hexane, EtOAc and *n*-BuOH.

The *n*-hexane fraction (168.8 g) was subjected to vacuum liquid chromatography in silica gel 60 using a gradient of elution of *n*-hexane-EtOAc-MeOH (10% stepwise) to obtain eight fractions (A-H) combined according to TLC profile. Fraction B (10.2 g) was chromatographed on a column of silica gel, eluted with a gradient of elution of *n*-hexane-EtOAc-MeOH (10% stepwise) to give thirteen subfractions (B1-B13) combined based on TLC control. Fraction B3 and B4 were combined (921.9 mg) and then chromatographed on a column of silica gel, eluted with a gradient of eluent of *n*-hexane:EtOAc (9:1) to obtain **1** (62.2 mg), *n*-hexane:EtOAc (7:3) to obtain **2** (12.5 mg), *n*-hexane:EtOAc (8:2) to obtain **3** (14.7 mg), *n*-hexane:EtOAc (6:4) to obtain **4** (11.8 mg). Fraction B7 (408.5 mg) was separated using column chromatography on silica gel (230–400 mesh) and eluted using 1% gradient of elution of *n*-hexane:EtOAc to yield **5** (15.2 mg). Fractions B8 and B9 were combined (943.4 mg) and then separated using column chromatography on silica gel (230–400 mesh) eluted with *n*-hexane:DCM:EtOAc (8:1:1) to give ten subfractions (B8.9a-j). Fractions B8.9g-h were combined (23.1 mg) and then separated using column chromatography on silica gel (230–400 mesh) eluted with *n*-hexane:DCM:EtOAc (7:2:1) to yield **6** (6.8 mg). Fractions C and D were combined (8.1 g) then chromatographed on a column of silica gel (70–230 mesh), eluted with a gradient of *n*-hexane-EtOAc-MeOH (10% stepwise) to give ten subfractions (CD1-10). Fraction CD4 (263.4 mg) was separated using column chromatography on silica gel (230–400 mesh) eluted using 1% gradient of elution of *n*-hexane:EtOAc to give nine subfractions (CD4.a-i). Fraction CD4.i (35 mg) was separated using column chromatography on silica gel (230–400 mesh) eluted with *n*-hexane:acetone (9:1) to obtain **7** (4.4 mg).

7β-Hydroxy-sitosterol (1). White solid, IR ν_{\max} 3409, 2853, 1458, 1084 cm⁻¹; ¹H-NMR (CDCl₃, 500 MHz), δ_{H} (ppm): 1.18 (1H, m, H-1a), 1.89 (1H, m, H-1b), 1.85 (1H,

m, H-2a), 1.56 (1H, m, H-2b), 3.53 (1H, m, H-3), 2.28 (2H, m, H-4), 5.35 (1H, d, $J = 3.5$ Hz, H-6), 4.01 (1H, d, $J = 3.5$ Hz, H-7), 1.93 (1H, m, H-8), 0.98 (1H, m, H-9), 1.51 (1H, 2H, H-11), 1.19 (1H, m, H-12a), 2.03 (1H, m, H-12b), 1.00 (1H, m, H-14), 1.13 (1H, m, H-15a), 1.61 (1H, m, H-15b), 1.35 (1H, m, H-16a), 1.86 (1H, m, H-16b), 1.10 (1H, m, H-17), 0.68 (3H, s, CH₃-18), 1.01 (3H, s, CH₃-19), 1.37 (1H, m, H-20), 0.99 (3H, d, $J = 6.0$ Hz, CH₃-21), 1.04 (1H, m, H-22), 1.20 (2H, m, H-23), 0.97 (1H, m, H-24a), 1.70 (1H, m, H-24b), 1.35 (1H, m, H-25), 0.82 (3H, d, $J = 4.0$ Hz, CH₃-26), 0.79 (3H, d, $J = 6.5$ Hz, CH₃-27), 1.27 (2H, m, H-28), 0.83 (3H, t, $J = 6.5$ Hz, CH₃-29); ¹³C-NMR (CDCl₃, 125 MHz) see Table 1; HRTOF-MS (positive ion mode) m/z 431.3669 [M+H]⁺, (calculated C₂₉H₅₁O₂, m/z 431.3660).

β-Sitosterol (2). White amorphous solid, IR ν_{\max} 3409, 2853, 1459, 1084 cm⁻¹; ¹H-NMR (CDCl₃, 500 MHz) δ_{H} (ppm): 1.18 (1H, m, H-1a), 1.89 (1H, m, H-1b), 1.85 (1H, m, H-2a), 1.56 (1H, m, H-2b), 3.53 (1H, m, H-3), 2.28 (2H, m, H-4), 5.35 (1H, d, $J = 3.5$ Hz, H-6), 1.53 (2H, m, H-7), 1.93 (1H, m, H-8), 0.98 (1H, m, H-9), 1.51 (2H, m, H-11), 1.19 (1H, m, H-12a), 2.03 (1H, m, H-12b), 1.00 (1H, m, H-14), 1.13 (1H, m, H-15a), 1.61 (1H, m, H-15b), 1.35 (1H, m, H-16a), 1.86 (1H, m, H-16b), 1.10 (1H, m, H-17), 0.68 (3H, s, CH₃-18), 1.01 (3H, s, CH₃-19), 1.37 (1H, m, H-20), 0.99 (3H, d, $J = 6.0$ Hz, CH₃-21), 1.04 (1H, m, H-22a), 1.35 (1H, m, H-22b), 1.20 (2H, m, H-23), 0.97 (1H, m, H-24a), 1.70 (1H, m, H-24b), 1.35 (1H, m, H-25), 0.82 (3H, d, $J = 6.5$ Hz, CH₃-26), 0.79 (3H, d, $J = 6.5$ Hz, CH₃-27), 1.27 (2H, m, H-28), 0.83 (3H, t, $J = 6.5$ Hz, CH₃-29); ¹³C-NMR (CDCl₃, 125 MHz) see Table 1; HRTOF-MS (positive ion mode) m/z 415.3744 [M+H]⁺, (calculated C₂₉H₅₁O, m/z 415.3790).

Campesterol (3). White waxy solid, IR ν_{\max} 3380, 2890, 1459, 1084 cm⁻¹; ¹H-NMR (CDCl₃, 500 MHz) δ_{H} (ppm): 1.15 (1H, m, H-1a), 1.89 (1H, m, H-1b), 1.85 (1H, m, H-2a), 1.56 (1H, m, H-2b), 3.53 (1H, m, H-3), 2.28 (2H, m, H-4), 5.34 (1H, d, $J = 5.0$ Hz, H-6), 1.53 (2H, m, H-7), 1.93 (1H, m, H-8), 0.98 (1H, m, H-9), 1.51 (2H, m, H-11), 1.19 (1H, m, H-12a), 2.03 (1H, m, H-12b), 1.00 (1H, m, H-14), 1.13 (1H, m, H-15a), 1.61 (1H, m, H-15b), 1.35 (1H, m, H-16a), 1.86 (1H, m, H-16b), 1.10 (1H, m, H-17), 0.68 (3H, s, CH₃-18), 1.00 (3H, s, CH₃-19), 1.37 (1H, m, H-20), 0.92 (3H, d, $J = 7.0$ Hz, CH₃-21), 1.04 (1H, m, H-22a), 1.35

(1H, m, H-22b), 1.20 (2H, m, H-23), 0.97 (1H, m, H-24), 1.70 (1H, m, H-25), 0.82 (3H, d, $J = 6.5$ Hz, CH₃-26), 0.85 (3H, d, $J = 6.5$ Hz, CH₃-27), 0.84 (3H, d, $J = 6.5$ Hz, CH₃-28); ¹³C-NMR (CDCl₃, 125 MHz) see Table 1; HRTOF-MS (positive ion mode) m/z 401.3744 [M+H]⁺, (calculated C₂₈H₄₉O, m/z 401.3790).

Cholesterol (4). White amorphous solid, IR ν_{\max} 3409, 2853, 1459, 1084 cm⁻¹; ¹H-NMR (CDCl₃, 500 MHz) δ_{H} (ppm): 1.15 (1H, m, H-1a), 1.83 (1H, m, H-1b), 1.81 (1H, m, H-2a), 1.56 (1H, m, H-2b), 3.53 (1H, m, H-3), 2.28 (2H, m, H-4), 5.34 (1H, d, $J = 5.5$ Hz, H-6), 1.58 (2H, m, H-7), 1.93 (1H, m, H-8), 1.93 (1H, m, H-9), 1.51 (2H, m, H-11), 1.16 (1H, m, H-12a), 2.00 (1H, m, H-12b), 1.04 (1H, m, H-14), 1.13 (1H, m, H-15a), 1.77 (1H, m, H-15b), 1.85 (2H, H-16), 1.10 (1H, m, H-17), 0.66 (3H, s, CH₃-18), 0.99 (3H, s, CH₃-19), 1.36 (1H, m, H-20), 0.90 (3H, d, $J = 6.5$ Hz, CH₃-21), 1.06 (1H, m, H-22a), 1.32 (1H, m, H-22b), 1.25 (2H, m, H-23), 0.94 (2H, m, H-24), 1.80 (1H, m, H-25), 0.85 (3H, s, CH₃-26), 0.83 (3H, s, CH₃-27); ¹³C-NMR (CDCl₃, 125 MHz) see Table 1; HRTOF-MS (positive ion mode) m/z 387.3669 [M+H]⁺, (calculated C₂₇H₄₇O, m/z 387.3680).

5α,8α-Epidioxycholest-6-en-3-β-ol (5). White solid, IR ν_{\max} 3383, 2866, 1459, 1070, 930 cm⁻¹; ¹H-NMR (CDCl₃, 500 MHz) δ_{H} (ppm): 1.95 (1H, m, H-1a), 1.68 (1H, m, H-1b), 1.51 (m, H-2a), 1.82 (1H, m, H-2b), 3.93 (1H, m, H-3), 1.90 (1H, m, H-4a), 2.10 (H-4b), 6.22 (1H, d, $J = 8.5$ Hz, H-6), 6.49 (1H, d, $J = 8.5$ Hz, H-7), 1.48 (1H, m, H-9), 1.01 (1H, m, H-11a), 1.60 (1H, m, H-11b), 1.20 (2H, m, H-12), 1.57 (1H, m, H-14), 1.21 (1H, m, H-15a), 1.50 (1H, m, H-15b), 1.42 (2H, m, H-16), 1.95 (1H, m, H-17), 0.78 (3H, s, CH₃-18), 0.85 (3H, s, CH₃-19), 1.32 (1H, m, H-20), 0.88 (3H, d, $J = 6.5$ Hz, CH₃-21), 1.51 (2H, m, H-22), 1.25 (2H, m, H-23), 1.33 (2H, m, H-24), 1.49 (1H, m, H-25), 0.85 (3H, d, $J = 6.5$ Hz, CH₃-26), 0.84 (3H, d, $J = 6.5$ Hz, CH₃-27); ¹³C-NMR (CDCl₃, 125 MHz) see Table 1; HRTOF-MS (positive ion mode) m/z 439.3188 [M+Na]⁺, (calculated C₂₇H₄₄O₃Na, m/z 439.3188).

7-keto-cholesterol (6). White solid, IR ν_{\max} 3430, 2853, 1674 cm⁻¹; ¹H-NMR (CDCl₃, 500 MHz) δ_{H} (ppm): 1.15 (1H, m, H-1a), 1.83 (1H, m, H-1b), 1.81 (1H, m, H-2a), 1.56 (1H, m, H-2b), 3.67 (1H, m, H-3), 2.50 (1H, m, H-4a), 2.38 (1H, m, H-4b), 5.68 (1H, d, $J = 2.0$ Hz, H-6),

2.23 (1H, dd, $J = 10.5$ and 8.5 Hz, H-8), 0.97 (1H, m, H-9), 1.51 (2H, m, H-11), 1.16 (1H, m, H-12a), 2.00 (1H, m, H-12b), 1.03 (1H, m, H-14), 1.13 (1H, m, H-15a), 1.76 (1H, m, H-15b), 1.33 (1H, m, H-16a), 1.85 (1H, m, H-16b), 1.10 (1H, m, H-17), 0.67 (3H, s, CH₃-18), 1.18 (3H, s, CH₃-19), 1.35 (1H, m, H-20), 0.90 (3H, d, $J = 6.5$ Hz, CH₃-21), 1.06 (1H, m, H-22a), 1.32 (1H, m, H-22b), 1.25 (2H, m, H-23), 0.95 (1H, m, H-24a), 1.80 (1H, m, H-24b), 1.37 (1H, m, H-25), 0.84 (3H, d, $J = 6.5$ Hz, CH₃-26), 0.86 (3H, d, $J = 6.5$ Hz, CH₃-27); ¹³C-NMR (CDCl₃, 125 MHz) see Table 1; HRTOF-MS (positive ion mode) m/z 401.3439 [M+H]⁺, (calculated C₂₇H₄₅O₂, m/z 401.3420).

7 α -Hydroxy-cholesterol (7). White solid, IR ν_{\max} 3430, 2850 cm⁻¹, ¹H-NMR (CDCl₃, 500 MHz) δ_{H} (ppm): 1.13 (1H, m, H-1a), 2.02 (1H, m, H-1b), 1.52 (1H, m, H-2a), 1.82 (1H, m, H-2b), 3.57 (1H, m, H-3), 2.33 (2H, m, H-4), 5.58 (1H, d, $J = 5.5$ Hz, H-6), 3.83 (1H, m, H-7), 1.39 (1H, m, H-8), 1.04 (1H, m, H-9), 1.51 (2H, m, H-11), 1.02 (2H, m, H-12), 1.16 (1H, m, H-14a), 1.43 (1H, m, H-14b), 1.80 (1H, m, H-15a), 1.29 (1H, m, H-15b), 1.30 (2H, m, H-16) 1.41 (1H, m, H-17), 1.00 (3H, s, CH₃-18), 0.66 (3H, s, CH₃-19), 1.35 (1H, m, H-20), 0.92 (3H, d, $J = 6.5$ Hz, CH₃-21), 1.05 (1H, m, H-22a), 1.86 (1H, m, H-22b), 1.15 (1H, m, H-23a), 1.14 (1H, m, H-23b), 1.15 (2H, m, H-24), 1.44 (1H, m, H-25), 0.86 (3H, d, $J = 6.5$ Hz, CH₃-26), 0.84 (3H, d, $J = 6.5$ Hz, CH₃-27); ¹³C-NMR (CDCl₃, 125 MHz) see Table 1; HRTOF-MS (positive ion mode) m/z 403.1793 [M+H]⁺, (calculated C₂₇H₄₇O₂, m/z 403.1793).

Cytotoxic activity test by PrestoBlue assay

The cytotoxicity of all isolated compounds against MCF-7 human breast cancer cells was measured using the

PrestoBlue cells viability assay [13]. The cells were maintained in a Roswell Park Memorial Institute (RPMI) medium supplemented with 10% (*v/v*) Fetal Bovine Serum (FBS) and 1 $\mu\text{L/mL}$ antibiotic. Cultures were incubated at 37°C in a humidified atmosphere of 5% CO₂. The cells were seeded in 96-well microliter plates at 1.7×10^4 cells per well. After 24 h, compounds 1-7 were separately added to the wells. After 96 h, cell viability was determined by measuring the metabolic conversion of resazurin substrate into pink fluorescent resorufin product resulting from the reduction in viable cells. The PrestoBlue assay results were read using a multimode reader at 570 nm. IC₅₀ values were taken from the plotted graph of the percentage of living cells compared to control (%), receiving DMSO, versus the tested concentration of compounds ($\mu\text{g/mL}$). The IC₅₀ values mean concentration required for 50% growth inhibition. PrestoBlue assay and analysis were run in triplicate and averaged. The crude extract of ethanol (407.7 g), *n*-hexane (168.8 g), EtOAc (1.7 g), and *n*-butanol (42.2 g) were tested for their cytotoxic activity against MCF-7 breast cancer cells and showed cytotoxic activity with IC₅₀ values of were 450.90, 176.02, 580.32 and 5,088.12 $\mu\text{g/mL}$, respectively.

RESULTS AND DISCUSSION

The *n*-hexane extract of *A. striata* was separated and purified using the column chromatography method repeatedly, to obtain compounds 1-7 (Fig. 1).

Compound 1 was obtained as a white solid with the yield of mass 62.2 mg (6.74%) of B3-4 fraction (921.9 mg).

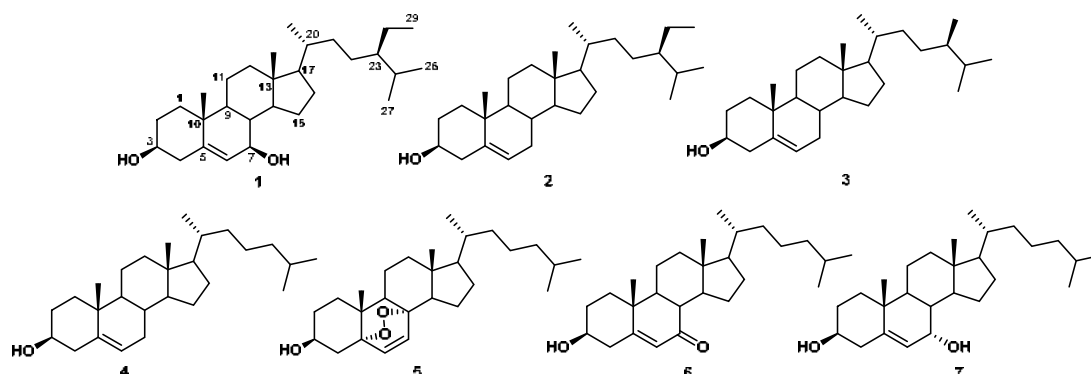


Fig 1. Structures of steroids 1-7

Result of HRTOF-MS spectra (Fig. S1), obtained the molecular weight of **1** $[M+H]^+$ m/z 431.3669 (calculated m/z 431.3680) with molecular formula $C_{29}H_{50}O_2$ indicating five degrees of unsaturation, consisting of 1 double bond and tetracyclic ring system. The FTIR spectrum of **1** (Fig. S2) showed the absorption of the hydroxyl group (3409 cm^{-1}), CH sp^3 (2853 cm^{-1} and 1458 cm^{-1}) and C-O stretching (1084 cm^{-1}). The $^1\text{H-NMR}$ spectrum of **1** (Fig. S3) showed the presence of two tertiary methyl groups at δ_{H} 0.68 (s, CH_3 -18) and 1.01 (s, CH_3 -19), three secondary methyl groups at 0.79 (d, $J = 6.5$, CH_3 -27), 0.82 (d, $J = 6.5$, CH_3 -26) and 0.99 (d, $J = 6.0$, CH_3 -21), one primary methyl group at 0.83 (t, $J = 6.5$, CH_3 -29) indicating the presence of sitosterol groups [14], ten methylene protons sp^3 and also seven methine protons, two oxygenated methine protons at δ_{H} 3.53 (m, H-3), 4.01 (d, $J = 3.5$, H-7), and one olefinic methine at δ_{H} 5.35 (d, $J = 3.5$, H-6). The ^{13}C (Fig. S4) and DEPT 135° (Fig. S5) NMR spectrum of compound **1** showed 29 signals of carbons, presence of six methyl carbons sp^3 at δ_{C} 12.0 (C-29), 12.1 (C-18), 18.9 (C-21), 19.1 (C-27), 19.5 (C-19), and 20.0 (C-26), ten methylene carbons sp^3 , seven methine carbons, two oxygenated methine carbons at δ_{C} 71.9 (C-3); 75.0 (C-7), one olefinic methine carbon at δ_{C} 121.9 (C-6), two quaternary carbons sp^3 at δ_{C} 36.6 (C-10), 45.8 (C-13) and one quaternary carbon olefinic at δ_{C} 140.9 (C-5).

The HMBC correlation of **1** (Fig. S7) showed the correlation of H-3 (δ_{H} 3.53) to C-4 (δ_{C} 42.4), C-2 (δ_{C} 31.8), and C-1 (δ_{C} 37.4), correlation of H-6 (δ_{H} 5.35) to C-8 (δ_{C} 31.8), C-10 (δ_{C} 36.6) and C-4 (δ_{C} 42.4), correlation between H-21 (δ_{H} 0.99) to C-17 (δ_{C} 56.1), C-20 (δ_{C} 36.3), and C-22 (δ_{C} 34.0), correlation of H-25 (δ_{H} 1.70) with C-26 (δ_{C} 20.0) and C-27 (δ_{C} 19.1), correlation between H-29 (δ_{H} 0.83) to C-28 (δ_{C} 23.2) and C-24 (42.5), correlation of H-18 (δ_{H} 0.68) to C-12 (δ_{C} 39.9) and C-13 (45.9), H-19 (δ_{H} 1.01) to C-10 (δ_{C} 36.6) and C-11 (21.2) showed the characteristic of tetracyclic of stigmastane-type steroid. The presence of hydroxyl group at C-7 showed by correlation of H-7 (δ_{H} 4.01) to C-8 (δ_{C} 31.8), C-6 (δ_{C} 121.9) and C-5 (δ_{C} 140.9). The cross peak of $^1\text{H-}^1\text{H-COSY}$ (Fig. S8) spectra observed that H1/H2/H3/H4 and H6/H7/H8, indicate that hydroxy group at C-3 and C-7 also confirm that double bond at C-5/C-6, observed that H25/H24/H28/H29 confirm that

primary methyl group at C-29, H17/20/21 and H26/H25/H27 indicated that secondary methyl group at C-21, C-26, and C-27. A comparison with the previous NMR data of **1** with β -sitosterol [15] revealed that the structures of the two compounds were very similar, except for C-7, the β oriented of hydroxyl at C-7 confirmed with the literature [16]; thus, compound **1** was identified as 7β -hydroxy-sitosterol.

Compound **2** was obtained as a white solid, with the yield of the mass 14.7 mg (1.59%) from B3-4 fraction (921.9 mg). The result of HRTOF-MS spectra (Fig. S9) obtained molecular weight of **2** $[M+H]^+$ m/z 415.3744, (calculated m/z 415.3790), with molecular formula $C_{29}H_{50}O$, which required five degrees of unsaturation consisting of 1 double bond and tetracyclic ring system. The FTIR spectrum of **2** (Fig. S10) showed the absorption of the hydroxyl group (3409 cm^{-1}), CH sp^3 (2870 and 1459 cm^{-1}), and C-O stretching (1084 cm^{-1}). The ^1H , ^{13}C , and DEPT 135° NMR spectrum of **3** (Fig. S11-S13) similar with **1**, the main difference was that **2** was not substituted with hydroxyl at C-7, proved by the absence of an oxygenated methine (δ_{C} 75.0) replaced by methylene carbon sp^3 (δ_{C} 32.0). The selected HMBC correlation (Fig. 2) of **2** showed the correlation of H-3 (δ_{H} 3.53) to C-4 (δ_{C} 42.4), C-2 (δ_{C} 31.6 ppm) and C-1 (δ_{C} 37.2 ppm), correlation of H-6 (δ_{H} 5.35) to C-7 (δ_{C} 32.0), C-8 (δ_{C} 32.0); C-10 (δ_{C} 36.6) and C-4 (δ_{C} 42.4), correlation between H-21 (δ_{H} 0.99) to C-17 (δ_{C} 56.1), C-20 (δ_{C} 36.3), and C-22 (δ_{C} 34.0), H-25 (δ_{H} 1.70) to C-26 (δ_{C} 20.0) and C-27 (δ_{C} 19.1), correlation of H-29 (δ_{H} 0.83) with C-28 (δ_{C} 23.2) and C-24 (42.5), correlation CH_3 -18 (δ_{H} 0.68) to C-12 (δ_{C} 39.9 ppm) and C-13 (45.8 ppm), CH_3 -19 (δ_{H} 1.01) to C-10 (δ_{C} 36.6) and C-11 (21.1) showed the characteristic of tetracyclic of stigmastane-type steroid. The cross peak of $^1\text{H-}^1\text{H-COSY}$ spectra (Fig. 2) observed that H1/H2/H3/H4 indicate that hydroxy group at C-3, observed that H6/H7/H8 confirm that double bond at C5/C6, H25/H24/H28/H29 confirm that primary methyl at C-29; H17/20/21 and H26/H25/H27 indicated that secondary methyl group at C21, C-26, and C-27. Compound **2** was confirmed by data comparison with previously isolated compound and identified as β -sitosterol [15].

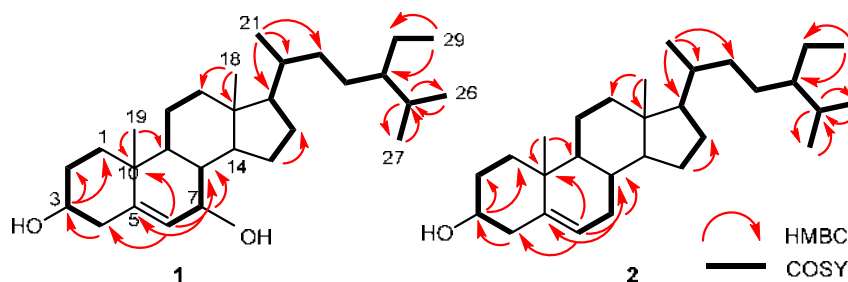


Fig 2. Selected HMBC and ^1H - ^1H -COSY Correlations for 1 and 2

Compound 3 was obtained as a white waxy solid, with the yield of mass 12.2 mg (1.36%) from B3-4 fraction (921.9 mg). Result of HRTOF-MS spectra (Fig. S17), obtained molecular weight of 3 $[\text{M}+\text{H}]^+$ m/z 401.3744, (calculated m/z 401.3790) with molecular formula $\text{C}_{28}\text{H}_{48}\text{O}$, which required five degrees of unsaturation consisting of 1 double bond and tetracyclic ring system. The FTIR spectrum of 3 (Fig S.18) showed the absorption of the hydroxyl group (3380 cm^{-1}), $\text{CH } sp^3$ (2890 and 1459 cm^{-1}), and C-O stretching (1084 cm^{-1}). The ^1H -NMR (Fig. S19) spectrum of compound 3 showed the presence of two tertiary methyl groups at δ_{H} 0.68 (s, CH_3 -18) and 1.00 (s, CH_3 -19), four secondary methyl groups at δ_{H} 0.82 (d, $J = 6.5$, CH_3 -27), 0.84 (d, $J = 6.5$, CH_3 -26), 0.85 (d, $J = 6.5$, CH_3 -28) and 0.92 (d, $J = 7.0$, CH_3 -21), ten methylene protons sp^3 , seven methine protons sp^3 , one oxygenated methine proton at δ_{H} 3.53 (m, H-3), and one olefinic methine at δ_{H} 5.34 (br.d, $J = 5.0$, H-6). The ^{13}C (Fig. S20) and DEPT 135° (Fig. S21) NMR spectra of compound 3 showed 28 signals of carbons, presence of six methyl sp^3 carbons at δ_{C} 11.9 (C-18), 18.8 (C-21), 19.4 (C-26, C-19), 22.6 (C-27), 22.8 (C-28), ten methylene sp^3 carbons, seven methine sp^3 carbons, one oxygenated methine carbon at δ_{C} 71.9 (C-3), one olefinic methine carbon at δ_{C} 121.8 (C-6), two quaternary sp^3 carbons at δ_{C} 36.6 (C-10), 42.3 (C-13) and one quaternary olefinic carbon at δ_{C} 140.8 (C-5). Compound 3 was confirmed with data from the literature identified as a campesterol [17].

Compound 4 was obtained as a white solid, with the yield of mass 15.2 mg (1.65%) from B3-4 fraction (921.9 mg). The result of HRTOF-MS spectra (Fig. S22), obtained molecular weight of 4 $[\text{M}+\text{H}]^+$ m/z 387.3669, (calculated m/z 387.3680), with molecular formula $\text{C}_{27}\text{H}_{46}\text{O}$, which required five degrees of unsaturation

consisting of 1 double bond and tetracyclic ring system. The FTIR spectrum of 4 (Fig. S23) showed the absorption of the hydroxyl group (3409 cm^{-1}), $\text{CH } sp^3$ (2853 and 1459 cm^{-1}), and C-O stretching (1084 cm^{-1}). The ^1H , ^{13}C , and DEPT 135° NMR spectrum of 4 similar with 2, the main difference was that 4 was not substituted with methyl at C-24. The ^1H -NMR spectrum (Fig. S24) of compound 4 showed the presence of two tertiary methyl groups at δ_{H} 0.66 (s, CH_3 -18), and 0.99 (s, CH_3 -19), three secondary methyl groups at δ_{H} 0.83 (d, $J = 6.5$, CH_3 -27), 0.85 (d, $J = 6.5$, CH_3 -26), and 0.90 (d, $J = 6.5$, CH_3 -21), eleven sp^3 methylene protons, and also six sp^3 methine protons, one oxygenated methine proton at δ_{H} 3.53 (m, H-3), and one olefinic methine at δ_{H} 5.34 (d, $J = 5.5$, H-6). The ^{13}C -NMR spectrum (Fig. S25) of compound 4 showed 27 signals of carbons, presence of five sp^3 methyl carbons at δ_{C} 11.9 (C-18), 18.8 (C-21), 19.5 (C-19), 22.6 (C-26), and 22.9 (C-27), eleven sp^3 methylene carbons, six sp^3 methine carbons at δ_{C} 31.9, 50.2, 56.9, 56.2, 36.2 and 28.1, one oxygenated methine carbon at δ_{C} 71.9 (C-3), one olefinic methine carbon at δ_{C} 121.8 (C-6), two sp^3 quaternary carbons at δ_{C} 36.6 (C-10), 42.4 (C-13) and one olefinic quaternary carbon at δ_{C} 140.8 (C-5). Compound 4 was confirmed with data from the literature identified as a cholesterol [18].

Compound 5 was obtained as a white solid, with the yield of mass 15.2 mg (3.72%) from B7 fraction (408.5 mg). The result of HRTOF-MS spectra (Fig. S26), obtained molecular weight of 5 $[\text{M}+\text{Na}]^+$ m/z 439.3188, (calculated m/z 439.3188), with molecular formula $\text{C}_{27}\text{H}_{44}\text{O}_3$, which required six degrees of unsaturation consisting of 1 double bond and pentacyclic ring system. The FTIR of 5 (Fig. S27) spectrum showed the absorption of the hydroxyl group (3383 cm^{-1}), $\text{CH } sp^3$

(2866 and 1459 cm^{-1}), C-O stretching (1070 cm^{-1}), and C-O-O of peroxide stretching (930 cm^{-1}). Compound **5** have same skeleton with **4**, the main difference was **5** have double bond at C-6 and C-7, addition of one peroxide cyclic at C-5 and C-8. The $^1\text{H-NMR}$ spectrum (Fig. S28) of compound **5** showed the presence of two tertiary methyl groups at δ_{H} 0.78 (s, CH_3 -18), and 0.85 (s, CH_3 -19), three secondary methyl groups at δ_{H} 0.84 (d, $J = 6.5$, CH_3 -27), 0.85 (d, $J = 6.5$, CH_3 -26), and 0.88 (d, $J = 6.5$, CH_3 -21), ten methylene protons sp^3 , five methine protons sp^3 , one oxygenated methine proton at δ_{H} 3.93 (m, H-3), and two olefinic methine protons at δ_{H} 6.22 (d, $J = 8.5$, H-7) and 6.49 (d, $J = 8.5$, H-6). The $^{13}\text{C-NMR}$ (Fig. S29) and DEPT 135° (Fig. S30) spectra of compound **5** showed 27 carbon signals, presence of five methyl sp^3 carbons at δ_{C} 12.7 (C-18), 18.2 (C-21), 18.6 (C-19), 22.6 (C-26), and 22.8 (C-27), ten methylene sp^3 carbons, five methine sp^3 carbons, one oxygenated methine carbon at δ_{C} 66.5 (C-3), two olefinic methine carbons at δ_{C} 130.8 (C-7), 135.5 (C-6), two quaternary sp^3 carbons at δ_{C} 37.0 (C-10), 44.8 (C-13) and two oxygenated quaternary carbons at δ_{C} 79.5 (C-8), 82.2 (C-5). Compound **5** was confirmed by data comparison with previously isolated compound, identified as a 5 α ,8 α -epidioxycholest-6-en-3 β -ol [19].

Compound **6** was obtained as a white solid, with the yield of mass 6.8 mg (29.44%) from B8.9g-h fraction (23.1 mg). The result of HRTOF-MS spectra (Fig. S31), obtained molecular weight of **6** $[\text{M}+\text{H}]^+$ m/z 401.3439, (calculated m/z 401.3420), with molecular formula $\text{C}_{27}\text{H}_{44}\text{O}_2$, which required six degrees of unsaturation consisting of 1 double bound, 1 carbonyl, and tetracyclic ring system. The FTIR spectrum of **6** (Fig. S32) showed the absorption of the hydroxyl group (3430 cm^{-1}), CH sp^3 (2853 cm^{-1}), and C=O stretching (1674 cm^{-1}). Compound **6** have same skeleton with **4**, the main difference that **6** was substituted with carbonyl at C-7, the presence of carbonyl confirmed with $^{13}\text{C-NMR}$ spectrum of **6** at δ_{C} 202.4 ppm. The $^1\text{H-NMR}$ (Fig. S33) spectrum of compound **6** showed the presence of two tertiary methyl groups at δ_{H} 0.67 (s, CH_3 -18), and 1.18 (s, CH_3 -19), three secondary methyl groups at δ_{H} 0.84 (d, $J = 6.5$, CH_3 -27), 0.86 (d, $J = 6.5$, CH_3 -26), and 0.90 (d, $J = 6.5$, CH_3 -21), ten methylene sp^3 protons, six methine sp^3 protons, one oxygenated

methine proton at δ_{H} 3.67 (m, H-3), and one olefinic methine at δ_{H} 5.68 (d, $J = 2.0$, H-6). The $^{13}\text{C-NMR}$ (Fig. S34) and DEPT 135° (Fig. S35) spectrum of compound **6** showed 27 signals of carbons, presence of five methyl sp^3 carbons at δ_{C} 12.0 (C-18), 17.9 (C-19), 18.9 (C-21), 22.7 (C-26), and 22.9 (C-27), ten methylene sp^3 carbons, six methine sp^3 carbons, one oxygenated methine carbon at δ_{C} 70.6 (C-3), one olefinic methine carbon at δ_{C} 126.2 (C-6), two quaternary sp^3 carbons at δ_{C} 38.4 (C-10), 43.2 (C-13), one olefinic quaternary carbon at δ_{C} 165.3 (C-5), and one quaternary carbon of carbonyl at δ_{C} 202.4 (C-5). Compound **6** was confirmed with data from the literature identified as a 7-keto-cholesterol [20].

Compound **7** was obtained as a white solid, with the yield of mass 4.4 mg (12.57%) from CD4i fraction (35 mg). The result of HRTOF-MS spectra (Fig. S36), obtained molecular weight of **7** $[\text{M}+\text{H}]^+$ m/z 403.1793, (calculated m/z 403.1793), with molecular formula $\text{C}_{27}\text{H}_{46}\text{O}_2$, which required five degrees of unsaturation consisting of 1 double bound and tetracyclic ring system. The FTIR spectrum of **7** (Fig. S37), showed the absorption of the hydroxyl (3430 cm^{-1}) and CH sp^3 (2850 cm^{-1}) groups. Compound **7** have same skeleton with **4**, the main difference that **7** was substituted with hydroxyl at C-7. The $^1\text{H-NMR}$ (Fig. S38) spectrum of compound **7** showed the presence of two tertiary methyl groups at δ_{H} 0.66 (s, CH_3 -18) and 1.00 (s, CH_3 -19), three secondary methyl groups at δ_{H} 0.84 (d, $J = 6.5$, CH_3 -26), 0.86 (d, $J = 6.5$, CH_3 -27) and 0.92 (d, $J = 6.5$, CH_3 -21), ten methylene sp^3 protons, six methine sp^3 protons, two oxygenated methine protons at δ_{H} 3.57 (m, H-3) and 3.83 (bs, H-7), and one olefinic methine at δ_{H} 5.58 (d, $J = 5.5$, H-6). The $^{13}\text{C-NMR}$ (Fig. S39) and DEPT 135° (Fig. S40) spectra (Fig. S33) of compound **7** showed 27 signals of carbons, presence of five methyl sp^3 carbon at δ_{C} 11.9 (C-18), 18.3 (C-19), 18.8 (C-21), 22.6 (C-27), and 22.9 (C-26), ten methylene sp^3 carbons, six methine sp^3 carbons, two oxygenated methine carbons at δ_{C} 65.4 (C-7) and 70.6 (C-3), one olefinic methine carbon at δ_{C} 123.9 (C-6), two quaternary sp^3 carbons at δ_{C} 37.4 (C-10) and 42.1 (C-13), one olefinic quaternary carbon at δ_{C} 146.3 (C-5). A comparison with the previous NMR data of **7** with 7 β -hydroxy-cholesterol [21], that the structures of

Table 1. ^{13}C NMR data (125 MHz for ^{13}C , in CDCl_3) for 1-7

Position	1	2	3	4	5	6	7
Carbon	δ_c (mult.)	δ_c (mult.)	δ_c (mult.)	δ_c (mult.)	δ_c (mult.)	δ_c (mult.)	δ_c (mult.)
1	37.4 (t)	37.2 (t)	37.3 (t)	37.3 (t)	34.7 (t)	36.4 (t)	39.5 (t)
2	31.8 (t)	31.6 (t)	31.7 (t)	31.7 (t)	30.1 (t)	31.2 (t)	31.4 (t)
3	71.9 (d)	71.8 (d)	71.9 (d)	71.9 (d)	66.5 (d)	70.6 (d)	71.4 (d)
4	42.4 (t)	42.4 (t)	42.3 (t)	42.4 (t)	37.0 (t)	41.9 (t)	42.0 (t)
5	140.9 (s)	140.9 (s)	140.8 (s)	140.8 (s)	82.2 (s)	165.2 (s)	146.3 (s)
6	121.9 (d)	121.9 (d)	121.8 (d)	121.8 (d)	135.5 (d)	126.2 (d)	123.9 (d)
7	75.0 (d)	32.0 (t)	31.9 (t)	31.9 (t)	130.8 (t)	202.4 (s)	65.4 (s)
8	31.8 (d)	32.0 (d)	31.9 (d)	31.9 (d)	79.5 (s)	45.9 (d)	37.5 (d)
9	50.2 (d)	50.2 (d)	50.1 (d)	50.2 (d)	51.1 (d)	50.0 (d)	49.5 (d)
10	36.6 (s)	36.6 (s)	36.6 (s)	36.6 (s)	37.0 (s)	38.4 (s)	37.4 (s)
11	21.2 (t)	21.1 (t)	21.1 (t)	21.2 (t)	23.4 (t)	21.3 (t)	20.7 (t)
12	39.9 (t)	39.9 (t)	39.5 (t)	39.9 (t)	39.5 (t)	38.8 (t)	36.2 (t)
13	45.9 (s)	45.8 (s)	42.3 (s)	42.4 (s)	44.8 (s)	43.2 (s)	42.3 (s)
14	45.9 (d)	56.9 (d)	56.8 (d)	56.9 (d)	51.7 (d)	50.0 (d)	55.9 (d)
15	24.4 (t)	24.4 (t)	24.3 (t)	24.4 (t)	20.6 (t)	26.4 (t)	24.3 (t)
16	28.4 (t)	28.4 (t)	28.3 (t)	28.3 (t)	28.3 (t)	28.7 (t)	28.3 (t)
17	56.1 (d)	56.1 (d)	56.2 (d)	56.2 (d)	56.5 (d)	54.9 (d)	55.9 (d)
18	12.1 (q)	12.1 (q)	11.9 (q)	11.9 (q)	12.7 (q)	12.0 (q)	11.9 (q)
19	19.5 (q)	19.5 (q)	19.4 (q)	19.5 (q)	18.6 (q)	17.3 (q)	18.3 (q)
20	36.3 (d)	36.3 (d)	36.3 (d)	36.2 (d)	35.3 (d)	35.8 (d)	35.8 (d)
21	18.9 (q)	18.9 (q)	18.8 (q)	18.8 (q)	18.2 (q)	18.9 (q)	18.8 (q)
22	34.0 (t)	34.0 (t)	34.0 (t)	35.9 (t)	36.0 (t)	36.3 (t)	37.0 (t)
23	26.1 (t)	26.1 (t)	23.9 (t)	23.9 (t)	23.8 (t)	23.9 (t)	23.8 (t)
24	42.5 (t)	42.5 (t)	39.4 (t)	39.6 (t)	39.5 (t)	39.6 (t)	39.2 (t)
25	29.2 (d)	29.2 (d)	28.1 (d)	28.1 (d)	28.0 (d)	28.1 (d)	28.1 (d)
26	20.0 (q)	20.0 (q)	19.4 (q)	22.6 (q)	22.6 (q)	22.7 (q)	22.9 (q)
27	19.1 (q)	19.1 (q)	22.6 (q)	22.9 (q)	22.8 (q)	22.9 (q)	22.6 (q)
28	23.2 (t)	23.2 (q)	22.8 (q)	-	-	-	-
29	12.0 (q)	12.0 (q)	-	-	-	-	-

the two compounds were very similar, except for C-7, the α oriented of hydroxyl at C-7 confirmed with the literature, compound 7 was identified as a 7 α -hydroxy-cholesterol [22].

The cytotoxic activity of the steroids 1-7 was tested against the MCF-7 cancer cell according to a method described [13]. Cisplatin (53 μM) was used as a positive control. Among all steroid compounds, 5 α ,8 α -epidioxycholest-6-en-3 β -ol (5) showed the highest cytotoxic activity with IC_{50} value of 164.08 μM , followed by campesterol (3), β -sitosterol (2), 7 β -hydroxy-sitosterol (1), 7 α -hydroxy-cholesterol (7), cholesterol (4) and 7-keto-cholesterol (6) with IC_{50} of 256.36, 264.83, 282.33,

439.17, 517.39, and 4246.01 μM , respectively (Table 2). Based on the results, the cytotoxic activity value of the steroids 1-7 against MCF-7 breast cancer cells is affected by the skeleton type of steroids and changes in substituents can reduce the IC_{50} value, the resonance of double bond at C-6, C-7, and addition of one peroxide cyclic at C-5 and C-8 of (5) significantly increased cytotoxic activity, compared to compound 1-4, 6-7 which has double bond at C-5 and C-6 reduced cytotoxic activity, the α and β -oriented of hydroxyl group at C-7 of (7) and (1) gives significant difference of cytotoxic activity with α -oriented decreases the cytotoxic activity, the presence of carbonyl at C-7 of (6) showed the weakest activity.

Table 2. Cytotoxic activity of compounds 1-7 against MCF-7 cells

Compounds	IC ₅₀ (μM)
7β-hydroxy-sitosterol (1)	282.33
β-Sitosterol (2)	264.83
Campesterol (3)	256.36
Cholesterol (4)	517.39
5α,8α-epidioxycholest-6-en-3β-ol (5)	164.08
7-keto-cholesterol (6)	4246.01
7α-hydroxy-cholesterol (7)	439.17
Cisplatin*	53.00

*Positive control

■ CONCLUSION

Seven steroids have been isolated from the *n*-hexane fraction of *Atactodea striata*, two known stigmastane-type steroids, 7β-hydroxy-sitosterol (1) and β-sitosterol (2), one known campestane-type steroid, campesterol (3), and four known cholestane-type steroids, cholesterol (4), 5α,8α-epidioxycholest-6-en-3β-ol (5), 7-keto-cholesterol (6) and 7α-hydroxy-cholesterol (7). All compounds were firstly reported from genus *Atactodea*. The cytotoxic activity of the steroids 1-7 was tested against the MCF-7 cancer cell. Compound (5) showed the highest cytotoxic activity, followed by campesterol (3), β-sitosterol (2), 7β-hydroxy-sitosterol (1), 7α-hydroxy-cholesterol (7), cholesterol (4) and 7-keto-cholesterol (6). The resonance of double bond at C-6, C-7, and addition of one peroxide cyclic at C-5 and C-8 of (5) significantly increased cytotoxic activity, compared to compounds 1-4, 6-7 which has double bond at C-5 and C-6 reduced cytotoxic activity, the α and β-oriented of hydroxyl group at C-7 of (7) and (1) gives significant difference of cytotoxic activity with α-oriented decreases the cytotoxic activity, the presence of carbonyl at C-7 of (6) showed the weakest activity. One of these steroids showed weak activity (5) and the remaining had no activity. The recommendation for future study is the isolated steroids need further research to determine other bioactivities including other cytotoxic activities, such as antioxidant and anti-inflammation activities.

■ ACKNOWLEDGMENTS

This research was financially supported by Universitas Padjadjaran, through the Academic Leadership Grant (No: 1959/UN6.3.1/PT.00/2022 by Unang Supratman).

■ REFERENCES

- [1] Saeidnia, S., Manayi, A., Gohari, A.R., and Abdollahi, M., 2014, The story of beta-sitosterol- A review, *Eur. J. Med. Plants*, 4 (5), 590–609.
- [2] Fernando, I.P.S., Sanjeewa, K.K.A., Kim, H.S., Kim, S.Y., Lee, S.H., Lee, W.W., and Jeon, Y.J., 2017, Identification of sterols from the soft coral *Dendronephthya gigantea* and their anti-inflammatory potential, *Environ. Toxicol. Pharmacol.*, 55, 37–43.
- [3] Cheng, Z.B., Xiao, H., Fan, C.Q., Lu, Y.N., Zhang, G., and Yin, S., 2013, Bioactive polyhydroxylated sterols from the marine sponge *Haliclona crassiloba*, *Steroids*, 78 (14), 1353–1358.
- [4] Carvalhal, F., Correia-da-Silva, M., Sousa, E., Pinto, M., and Kijjoo, A., 2018, Sources and biological activities of marine sulfated sterols, *J. Mol. Endocrinol.*, 61 (2), T211–T231.
- [5] Tung, N.H., Minh, C.V., Ha, T.T., Kiem, P.V., Huong, H.T., Dat, N.T., Nhiem, N.X., Tai, B.H., Hyun, J.H., Kang, H.K., and Kim, Y.H., 2009, C₂₉ sterols with a cyclopropane ring at C-25 and 26 from the Vietnamese marine sponge *Lanthella* sp. and their anticancer properties, *Bioorg. Med. Chem. Lett.*, 19 (16), 4584–4588.
- [6] Joy, M., and Chakraborty, K., 2018, Previously undisclosed bioactive sterols from corbiculid bivalve clam *Villorita cyprinoides* with anti-inflammatory and antioxidant potentials, *Steroids*, 135, 1–8.
- [7] Heryanto, H., and Radjab, A.W., 2013, Dinamika populasi *Atactodea striata* (Gmelin, 1791) (Mollusca: Mesodesmatidae) di pantai berpasir Ohoider, Kep. Kei Kecil, Maluku Tenggara, *Jurnal Biologi Indonesia*, 10 (1), 57–65.

- [8] Hasan, T., Patong, A.R., Wahab, A.W., and Djide, M.N., 2014, Isolasi dan implementasi protein bioaktif Kepah (*Atactodea striata*) sebagai bahan obat antibakteri, *Al-Kimia*, 2 (2), 47–57.
- [9] Shofia, V., Waranmasalembun, C., Prasetyawan, S., and Aulanni'am, A., 2015, Methanol extracts potential of Mas Ngur shells (*Atactodea striata*) against protease profile and description of histopathology of Jejunum rats exposed by Indomethacin, *J. Pure Appl. Chem. Res.*, 4 (2), 77–81.
- [10] Yang, D., Zhang, X., Zhang, W., and Rengarajan, T., 2018, Vicenin-2 inhibits Wnt/ β -catenin signaling and induces apoptosis in HT-29 human colon cancer cell line, *Drug Des., Dev. Ther.*, 12, 1303–1310.
- [11] Lin, C.H., Chang, C.Y., Lee, K.R., Lin, H.J., Chen, T.H., and Wan, L., 2015, Flavones inhibit breast cancer proliferation through the Akt/FOXO3a signaling pathway, *BMC Cancer*, 15 (1), 958.
- [12] Khoja, K.K., Howes, M.J.R., Hider, R., Sharp, P.A., Farrell, I.W., and Latunde-Dada, G.O., 2022, Cytotoxicity of fenugreek sprout and seed extracts and their bioactive constituents on MCF-7 breast cancer cells, *Nutrients*, 14 (4), 784.
- [13] Hutagaol, R.P., Harneti, D., Hidayat, A.T., Nurlelarsari, N., Maharani, R., Katja, D.G., Supratman, U., Awang, K., and Shiono, Y., 2020, (22E,24S)-24-propylcholest-5en-3 α -acetate: A new steroid from the stem bark *Aglaia angustifolia* (Miq.) (Meliaceae), *MolBank*, 2020 (1), M1112.
- [14] Chaturvedula, V.S.P., and Prakash, I., 2012, Isolation of stigmaterol and β -sitosterol from the dichloromethane extract of *Rubus suavissimus*, *Int. Curr. Pharm. J.*, 1 (9), 239–242.
- [15] Farabi, K., Harneti, D., Nurlelarsari, N., Maharani, R., Hidayat, A.T., Supratman, U., Awang, K., and Shiono, Y., 2017, Cytotoxic steroids from the bark of *Aglaia argentea* (Meliaceae), *Chiang Mai Univ. J. Nat. Sci.*, 16 (4), 293–306.
- [16] Tseng, W.R., Huang, C.Y., Tsai, Y.Y., Lin, Y.S., Hwang, T.L., Su, J.H., Sung, P.J., Dai, C.F., and Sheu, J.H., 2016, New cytotoxic and anti-inflammatory steroids from the soft coral *Klyxum flaccidum*, *Bioorg. Med. Chem. Lett.*, 26 (14), 3253–3257.
- [17] Correia, F.C.S., Targanski, S.K., Bomfim, T.R.D., da Silva, Y.S.A.D., Violante, I.M.P., de Carvalho, M.G., Sousa, P.T., Silva, V.C.P., and Ribeiro, T.A.N., 2020, Chemical constituents and antimicrobial activity of branches and leaves of *Cordia insignis* (Boraginaceae), *Rev. Virtual Quim.*, 12 (3), 809–816.
- [18] Sun, B.N., Shen, H.D., Wu, H.X., Yao, L.X., Cheng, Z.Q., and Diao, Y., 2014, Determination of chemical constituents of the marine pulmonate slug, *Paraoncidium reevesii*, *Trop. J. Pharm. Res.*, 13 (12), 2071–2074.
- [19] Pereira, R.B., Pereira, D.M., Jiménez, C., Rodríguez, J., Nieto, R.M., Videira, R.A., Silva, O., Andrade, P.B., and Valentão, P., 2019, Anti-inflammatory effects of 5 α ,8 α -epidioxycholest-6-en-3 β -ol, a steroidal endoperoxide isolated from *Aplysia depilans*, based on bioguided fractionation and NMR analysis, *Mar. Drugs*, 17 (6), 330.
- [20] Notaro, G., Picciali, V., and Sica, D., 1992, New steroidal hydroxyketones and closely related diols from the marine sponge *Cliona copiosa*, *J. Nat. Prod.*, 55 (11), 1588–1594.
- [21] Giorgi, V., Chaves, M., Menéndez, P., and García Carnelli, C., 2019, Bioprospecting of whole-cell biocatalysts for cholesterol biotransformation, *World J. Microbiol. Biotechnol.*, 35 (1), 12.
- [22] Tasyriq, M., Najmuldeen, I.A., In, L.L.A., Mohamad, K., Awang, K., and Hasima, N., 2012, 7 α -Hydroxy- β -sitosterol from *Chisocheton tomentosus* induces apoptosis via dysregulation of cellular Bax/Bcl-2 ratio and cell cycle arrest by downregulating ERK1/2 activation, *Evidence-Based Complementary Altern. Med.*, 2012, 765316.

Supplementary Data

This supplementary data is a part of a paper entitled “Synthesis, Characterization and Antimicrobial Activity of Complexes Metal Ions Ni(II), Zn(II), Pd(II) and Pt(IV) with Polydentate 1,2,4-Triazole Ligand”.

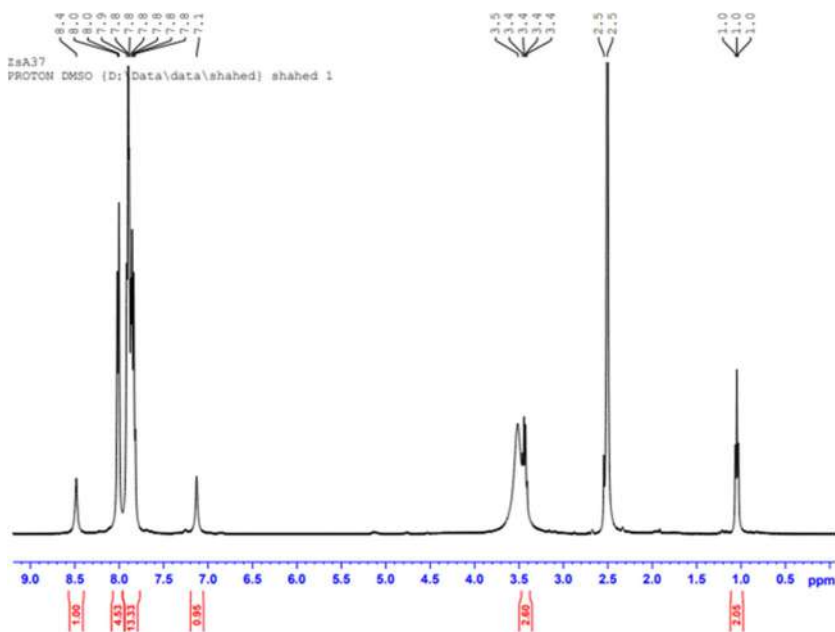


Fig S1. ¹H-NMR of 1,2,4-triazole (L)

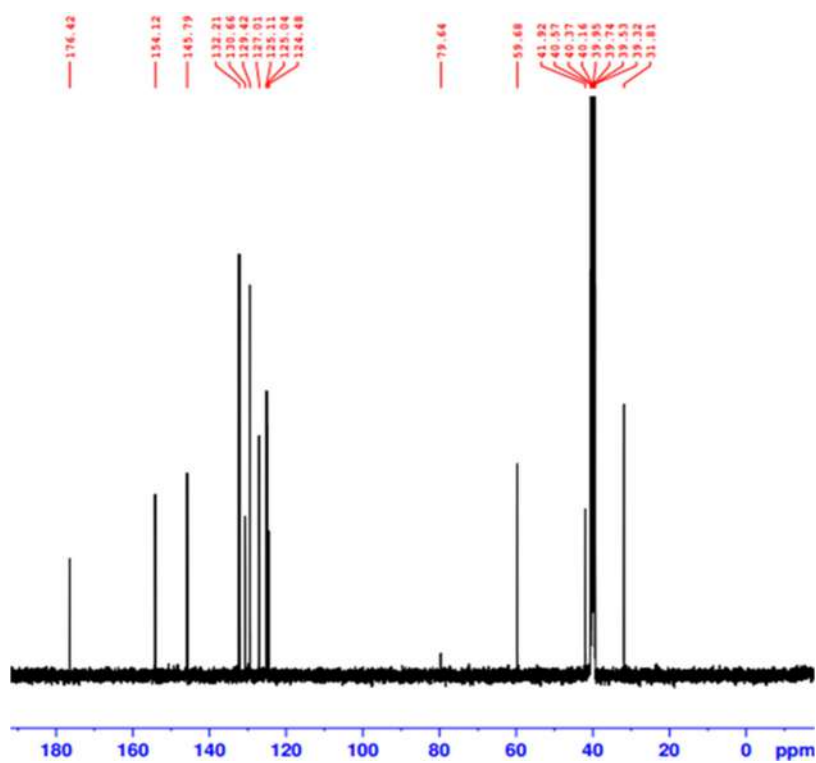


Fig S2. ¹³C-NMR spectrum of ligand L

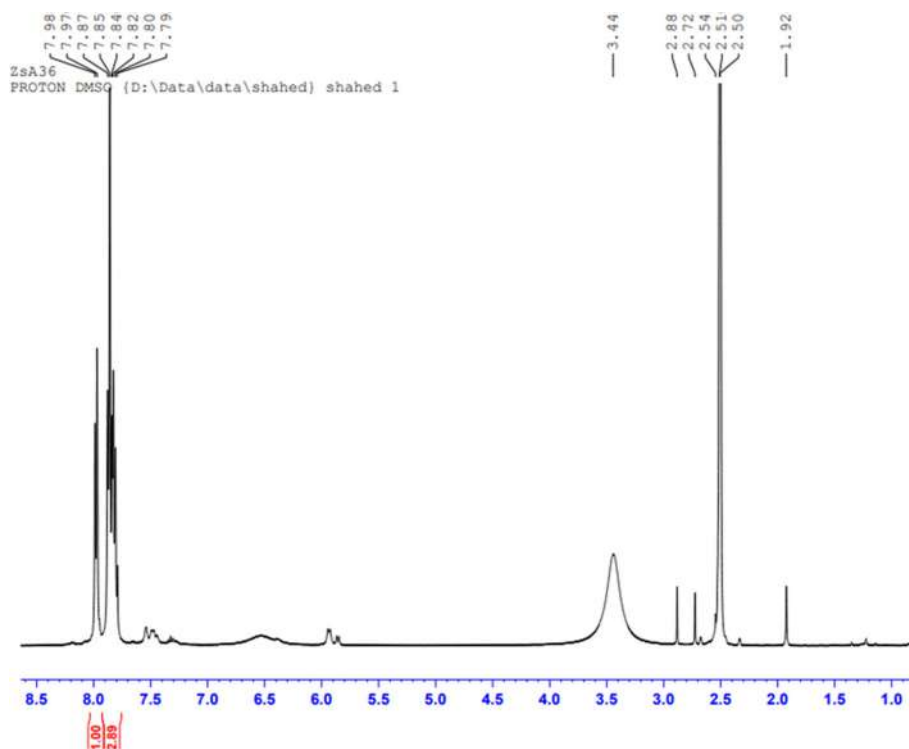
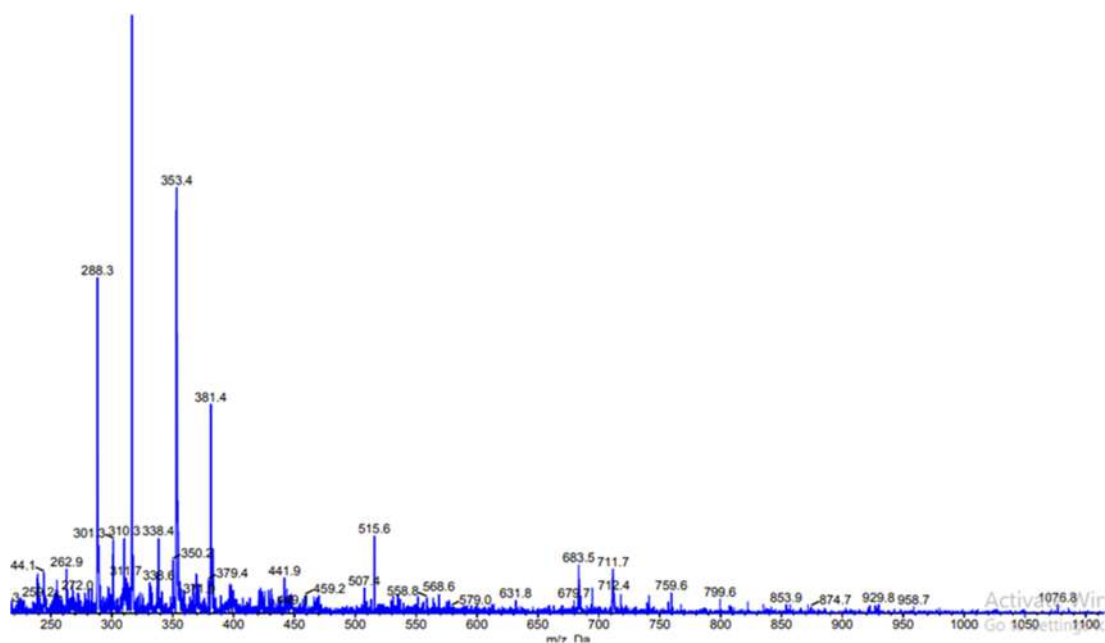
Fig S3. ¹H-NMR spectrum of PdL complex

Fig S4. Mass spectra of Pt-L complex

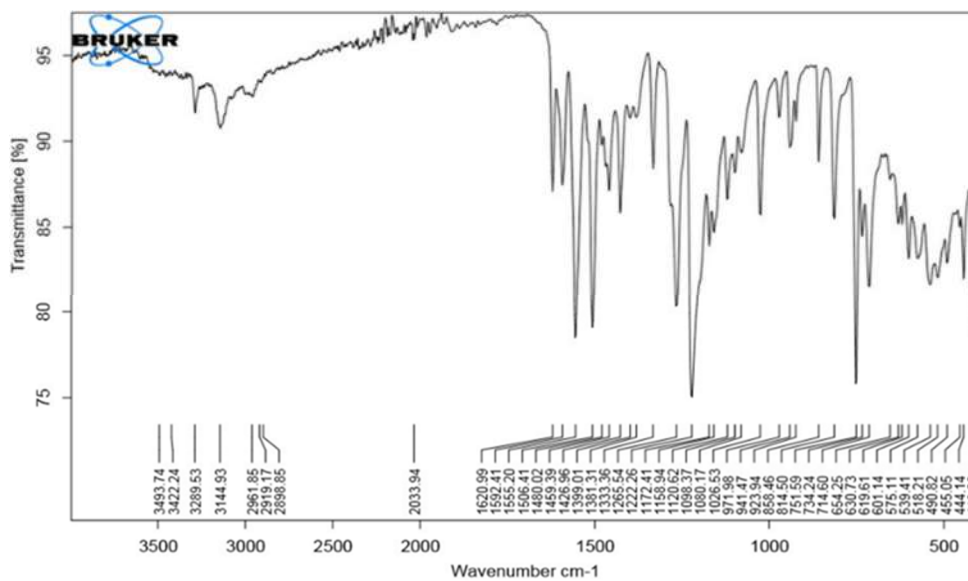


Fig S5. IR spectrum of triazole ligand (L)

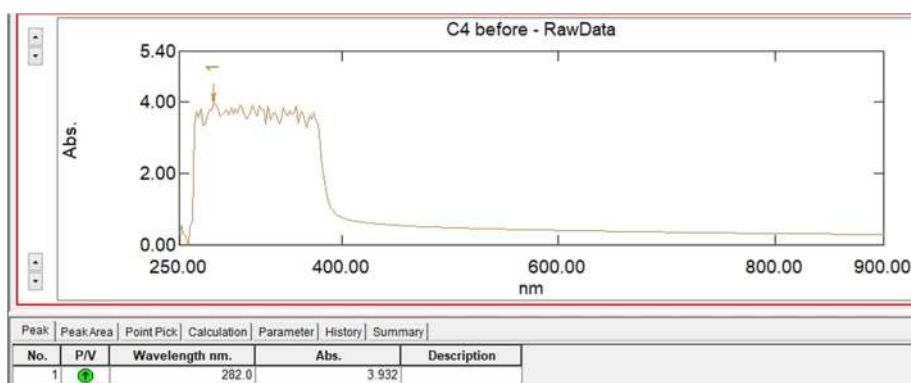


Fig S6. The UV-Visible spectrum of PdL in EtOH solvent

Synthesis, Characterization and Antimicrobial Activity of Complexes Metal Ions Ni(II), Zn(II), Pd(II) and Pt(IV) with Polydentate 1,2,4-Triazole Ligand

Sarab Mahdi Al-Alzawi, Mahmoud Najim Al-Jibouri*, Anaam Majeed Rasheed, and Sinan Midhat Al-Bayati

Department of Chemistry, College of Science, Mustansiriyah University, Baghdad 10052, Iraq

* **Corresponding author:**

tel: +964-7713460946

email:

Mahmoud_inor71@uomustansiriyah.edu.iq

Received: July 30, 2022

Accepted: September 25, 2022

DOI: 10.22146/ijc.76716

Abstract: A new ligand of 1,2,4-triazole derivative was produced by cyclization of sodium dithiocarbamate derivative of ethyl 4-ethoxy-3-nitrobenzoate with carbon disulfide in an alkaline medium. The new ligand, entitled name: L: 4-amino-5-(3-ethoxy-5-nitrophenyl)-2,4-dihydro-3H-1,2,4-triazole-3-thione, was fully characterized depending on HPLC-MS, FTIR, ¹H-NMR and ¹³C-NMR spectroscopies. In addition, the elemental microanalysis was carried out to confirm the skeletal structure of the ligand L. A library of complexes with Ni(II), Zn(II), Pd(II), and Pt(IV) metal ions was prepared by coordination with the ligand. These complexes were characterized by using FTIR, UV-Vis, ¹H-NMR, ¹³C-NMR, spectrophotometric techniques, elemental analysis C.H.N.S, and FAAS. The physicochemical properties of these complexes were determined at 25 °C, such as melting point, magnetic susceptibility and molar conductivity. The microbial study confirmed that the novel ligand and its complexes have the potential to be applied as antimicrobial agents.

Keywords: 1,2,4-triazole ligands; platinum(IV); palladium(II) complexes of triazole; microbial activity

■ INTRODUCTION

1,2,4-Triazole moiety and their derivatives have attracted great attention in the last decade due to their unique properties [1]. The triazole ring is easily formed and many of these functionalized compounds are readily accessible; thus they are talented rich and flexible coordination chemistry. Triazole rings contain π -conjugated systems with easy coordination abilities to metal ions, and they have the ability to exhibit phosphorescence properties. They own nitrogen atoms as hydrogen bond acceptors and aromatic systems, which correspond to π - π stacking [2]. The 1,2,4-triazole moiety contains three atoms of nitrogen in a five-membered aromatic ring, each two atoms are adjacent for stability, increasing the solubility in water. It is able to get two isomers of tautomerism, 1H-isomer 1 and 4H-isomer 2 (Fig. 1). The preferred and more stable structure is the 1H-tautomer was confirmed by both DFT and empirical study. The carbon atom is connected to both nitrogen

atoms in 1,2,4-triazole and thus, the ring of triazole has a deficit in electrons. It was illustrated that the electrophilic reaction with the triazole ring is deactivated. In the parent, the compound is not responsive to the nitration or other common carbon reactions of aromatic chemistry. Though electrophilic attacks on the nitrogen atom are widely mentioned in literature [3-5].

The literature study demonstrated that 1,2,4-triazole derivatives exhibited a wide variety of bioactivities, including antimicrobial, anticancer, anti-inflammatory, analgesic, antiviral, antidepressant, insecticide and plant growth regulator bacteria [6-9]. 1,2,4-Triazole derivatives,

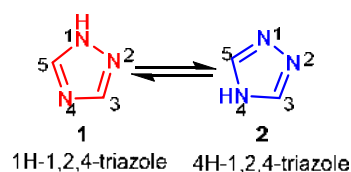


Fig 1. Tautomerism of (1H- and 4H-) 1,2,4-triazoles

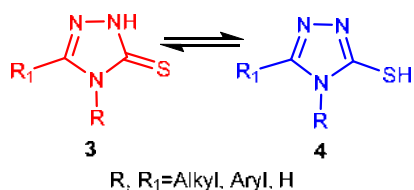


Fig 2. Thione-thiol tautomeric forms

including the -SH group, are one of the subclasses of 1,2,4-triazoles and are considered one of the most interesting compounds due to their biological activity [9-10]. It was found that the main component of mercapto-1,2,4-triazole is in most natural products and pharmaceuticals (Fig. 2).

The presence of active sites in triazole derivatives has intensively enhanced the researchers to synthesize metal complexes with such types of ligands [11-13]. Kanagarajan et al. [13-14] have studied two biologically active Schiff base ligands derived from 1,2,4-triazole in equimolar reaction of 4-amino-5-(pyridin-4-yl)4*H*-1,2,4-triazole-3-thiol with thiophene-2-carbaldehyde and furan-2-carbaldehyde. Furthermore, Co(II), Ni(II) and Cu(II) metal complexes were isolated in their solid state and spectroscopically identified. The anti-proliferative reactivity against many cancer cells has been described for Pt(II), Pd(II), Ni(II), Co(II), and Sn(IV) chelates derived from 4,5-diphenyl-1,2,4-triazole-3-thione as a primary ligand and 1,2-bis(diphenylphosphanyl) ethane as a secondary ligand. The results explained that Pt(II) complex had an important antitumor activity with IC₅₀ values 0.4–0.8 μM. The 1,2,4-triazoles have been explored for linking ligands among transition metal ions.

In recent years, there is much attention to preparing coordination ligands using 1,2,4-triazole moiety particularly, those consisting of S and N in their construction due to their biological activities compared with native ligands [15-16]. A few complexes, including 1,2,4-triazole moiety with two sites for coordination with metal ions, including S and N atoms have been reported. In the current work, we designed and synthesized new derivatives for the triazole ligand as a bidentate ligand as well as its complexes with transition metal ions such as Ni(II), Zn(II), Pd(II) and Pt(IV). The novel prepared complexes were characterized by diverse spectroscopic

methods to find out the potential of these new metal complexes as antimicrobials.

■ EXPERIMENTAL SECTION

Materials

All starting materials and solvents were obtained from commercial companies and used without further purification. Metal chlorides, NiCl₂·6H₂O, ZnCl₂, K₂PtCl₆ and PdCl₂, were supplied from Sigma Aldrich. Hydrazine hydrate, carbon disulfide, absolute ethanol and dimethyl sulfoxide (DMSO) were supplied from Fluka Company with 99% purity.

Instrumentation

A Stuart melting point (digital) SMP30 apparatus was used to record the Melting point. FTIR spectra were measured by a Shimadzu (FTIR) model 4800 s Spectrophotometer between the ranges (4000–400) cm⁻¹ as KBr discs. UV-Vis 16 ultraviolet Spectrophotometer model Shimadzu is used to measure the UV-visible spectra at R.T.°C using 1 cm quartz cell and examined between 200–1100 nm at 10⁻³ M in DMSO. The atomic absorption (A.A.) technique has been measured using a Shimadzu AA680G atomic absorption spectrophotometer at the laboratories of Ibn-Sinaa Company. Elemental analysis is used to determine (C, H, N) for the new ligand [L] and its complexes by Linear Regression Euro EA elemental analysis. Mass spectra were performed for a ligand on GC-MS (DIRECT PROBE) via the ES technique. The ¹H- and ¹³C-NMR spectrum of ligand was recorded at a Bruker DMX-500 spectrophotometers (400 MHz) by using DMSO-*d*₆. Measurement of Conductivity was carried out at room temperature in DMSO using an Inolab multi 740, WTW 82362-Germany. Magnetic susceptibility of novel synthesized complexes was recorded at room temperature by Auto magnetic susceptibility Balance in Al-Mustansiriyah University, College of Science, Chemistry Department.

Procedure

Synthesis of benzamide derivative, A1

Hydrazine hydrate (5 mL, 1 mmol) was added to

the solution of ethyl 4-ethoxy-3-nitrobenzoate (135 mg, 5 mmol) in 15 mL of absolute ethanol. The mixture was refluxed for 10 h, and the TLC was used to monitor the reaction. After that, the mixture reaction was allowed to cool down to room temperature. A final product was isolated by filtered and then washed the ice cold water three times, dried and recrystallized using hot ethanol to obtain compound A1 (Fig. 3); m.p. 124–126 °C; Color white crystal; Yield 95%; FTIR ν (cm⁻¹): 3320 (NH₂, asym.), 3185 (NH₂, sym.), 1670 (C=O, amide); R_f = 0.37 (chloroform:ethyl acetate; 3:2), ¹H-NMR (400 MHz, DMSO-*d*₆), 8.05 (d, 1H, 10-NH), 7.96 (s, 1H, 1-CH), 7.78 (d, 1H, 6-CH), 7.22 (d, 1H, 7-CH), 4.45 (d, 2H, 10-NH), 4.25 (m, 2H, 4-CH), 2.09 (t, 3H, 5-CH₃), ¹³C-NMR (100 MHz, DMSO), 188.4 (9-C=O), 140.09 (3-C), 137.7 (2-C), 133.6 (7-C), 132.3 (8-C), 130.9 (1-C), 127 (6-C), 58.8 (4-C), 30.8 (5-C).

Synthesis of sodium 2-(4-ethoxy-3-nitrobenzoyl)hydrazine-1-carbodithioate (A2)

Compound A1 (2.50 g, 11 mmol) was added to the solution of sodium hydroxide (1.50 g, 20 mmol) in methanol 20 mL at 0 °C with stirring, then carbon

disulfide (5 mL, 13 mmol) was added as a drop-wise and the reaction mixture was stirred for 18 h at room temperature. The reaction was allowed to cool down, and then adding 100 mL of diethyl ether with stirring for 20 min. The solid precipitate was isolated and then washed with the cold methanol to produce compound A2 (Fig. 4). Color yellow powder; m.p. (170–172) °C; Yield 95%; FTIR ν (cm⁻¹): 3400 (N-H), 3178 (N-H), 1656 (C=O), 1270 (C=S); m/z 300.

Synthesis of 4-amino-5-(3-ethoxy-5-nitrophenyl)-2,4-dihydro-3H-1,2,4-triazole-3-thione (L)

Compound A2 (323 mg, 11 mmol) was mixed with the excess amount of hydrazine hydrate (about 20 mL) and refluxed for 8 h. A color change from black-green to light yellow was observed; due to liberating hydrogen sulfide gas and changing the color of lead acetate paper from black to white, TLC is used to monitor the reaction. The final solution was poured into ice-cold water of about 25 mL and acidified with conc. HCl (pH = 3–5). The solid precipitate was isolated, washed by adding cold water, and then dried by vacuum, purified by recrystallized with ethanol to give compound L (Fig. 5).

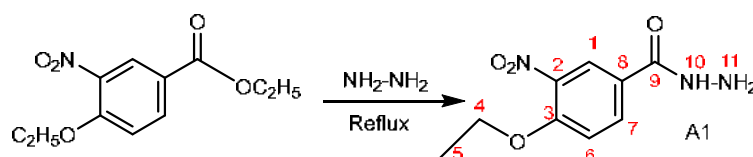


Fig 3. Synthesis of ligand A1

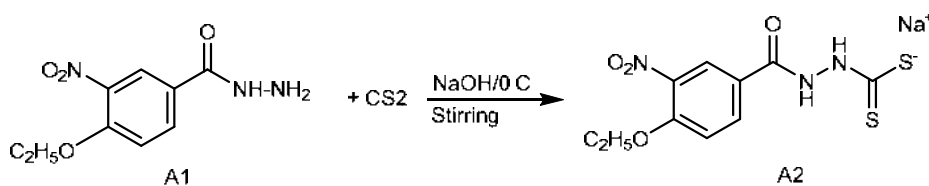


Fig 4. Synthesis of dithiocarbamate salt derivative A2

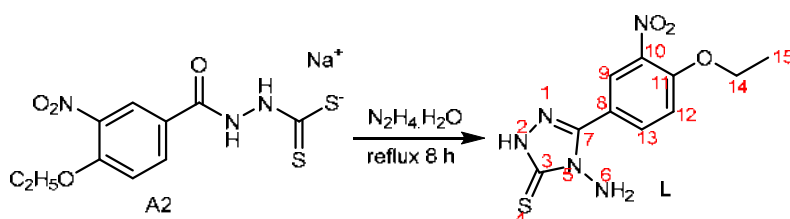


Fig 5. Cyclization reaction to synthesis 4-amino-5-(3-ethoxy-5-nitrophenyl)-2,4-dihydro-3H-1,2,4-triazole-3-thione (L)

Pale yellow solid; Yield 70 %; m.p. 188–190 °C, FTIR ν (cm⁻¹): 3290 (NH₂, asym), 3300 (NH₂, sym.), 3190 (N-H), 1280 (C=S) and 1620 (N-NH₂); R_f = 0.32 (*n*-hexane: methanol; 3:1). ¹H-NMR (400 MHz, DMSO-*d*₆), 8.59 (d, 1H, 2-NH_{triazol}), 7.86 (d, 1H, 13-CH), 7.71 (d, 1H, 12-CH), 7.36 (s, 1H, 9-CH), 5.69 (s, 2H, NH₂-N_{triazol}), 4.25 (m, 2H, 14-CH₂), 2.08 (t, 3H, 15-CH), ¹³C-NMR (100 MHz, DMSO-*d*₆), 176.4 (3-C), 154.1 (11-C), 145.7 (7-C), 132.12 (10-C), 130.6 (13-C), 129.4 (9-C), 127.01 (4-C), 125 (12-C), 79.6 (14-C), 31.8 (15-C); *m/z* 282.

Metals complexes synthesis

To a solution of the metal salts in ethanol, where the salts of (NiCl₂·2H₂O, ZnCl₂, PdCl₂ and PtCl₄) were added to (562 mg, 2.00 mmol) of the ligand L. Mixed solution was reflux using a water bath as long as 3 h. The product was isolated and washed with ethanol, then dried at room temperature. The color, melting point, yield, metal analysis and solubility of the ligand and its complexes are given in Table 1.

RESULTS AND DISCUSSION

¹H-NMR Characterization

The identification of the intermediates, the free 1,2,4-triazole ligand and some selected metal complexes

were carried out with ¹H- and ¹³C-NMR spectra, and the results are summarized in Table 2.

¹H-NMR spectrum for ligand A1

The NMR spectrum of A1 exhibited three signals in the aromatic region between (8.05–7.2) ppm corresponding to the aromatic ring. The new signal was observed at 9.01 ppm corresponding to NH adjacent to the C=O group, which confirmed the formation of a compound with title A1. Also, the NMR spectrum shows a doublet signal with two integrals at 4.45 ppm corresponding to the NH₂ group.

¹H-NMR spectra for ligand L

Compound L was characterized by NMR and mass spectroscopy in addition to IR and UV-Vis spectrometry. The ¹H-NMR spectrum shows the characteristic of a singlet at 8.59 ppm due to the -NH of triazole ring; but no signal was shown in the NMR spectrum for A1 or A2 compound. Thus, giving further evidence to the formation of ligand L. Another signal around 3.5 ppm attributed to the NH₂ group closer to the N-triazole ring confirmed the formation of this ligand. Also, multiples signal at (1.19 ppm) attributed to the ethyl group (Fig. S1 and S2). The spectrum of ¹³C-NMR showed peaks at 174, 154 and 145 ppm corresponding –C=S thione moiety

Table 1. Physical properties and elemental analyses of the prepared compounds

Compound	Color	m.p (°C)	M.wt (g/mol)	Elemental analysis %			M% Obs. (cal.)	M:L	Chemical formula
				Found (cal.)					
				C	H	N			
A1	White	124–126	225	47.70 (48.0)	3.85 (4.88)	17.94 (18.7)			C ₉ H ₁₁ N ₃ O ₄
A2	Yellow	170–172	300	36.11 (40.0)	3.00 (3.33)	12.26 (14.0)			C ₁₀ H ₁₀ N ₃ O ₄ S ₂ Na
L	Pale yellow	188–190	281	41.90 (42.7)	3.08 (3.91)	24.60 (24.9)			C ₁₀ H ₁₁ N ₅ O ₃ S
Ni-L	Dark brown	280–282	692	33.88 (34.7)	3.07 (3.18)	18.64 (20.24)	7.66 (8.48)	1:2	[Ni(C ₁₀ H ₁₁ N ₅ O ₃ S) ₂]Cl ₂
Zn-L	Yellow	278d*	769	30.40 (28.7)	3.04 (2.60)	17.20 (16.7)	16.70 (15.5)	1:1	[Zn(C ₁₀ H ₁₁ N ₅ O ₃ S)Cl ₂]
Pd-L	Pale orange	290d*	739	35.10 (32.4)	3.10 (2.97)	19.72 (18.93)	13.74 (14.4)	1:2	[Pd(C ₁₀ H ₁₁ N ₅ O ₃ S) ₂]Cl ₂
Pt-L	Dark yellow	315d*	900	27.76 (26.7)	2.19 (2.44)	15.30 (15.55)	4.55 (5.17)	1:2	[Pt(C ₁₀ H ₁₁ N ₅ O ₃ S) ₂]Cl ₂

d*: dissociation, obs.: observed

Table 2. ^1H -NMR data of compounds and ^{13}C -NMR of ligand L in $\text{DMSO}-d_6$

Compound	^1H -NMR	^{13}C
A1	8.05-7.2 ppm aromatic ring; 9.01 ppm NH adjacent to the C=O group; a doublet signal 4.45 ppm (NH_2 group)	
L	a singlet at 8.59 ppm -NH of triazole ring; 3.5 ppm NH_2 group closer to the N-triazole ring; multiples signal at (1.19 ppm) ethyl group	174, 154 and 145 ppm -C=S thione moiety; -C=N- of triazole ring (124–120) ppm of aromatic carbon atoms; 39 and 59 ppm (CH_3 , CH_2)
Ni-L	6.22 ppm NH protons	
Zn-L	6.23 ppm NH proton close to triazole ring	
Pd-L	6.28 ppm NH proton close to triazole ring	
Pt-L	6.28 ppm NH proton close to triazole ring	

and -C=N- of triazole ring, at 124–120 ppm of aromatic carbon atoms, and 39 and 59 ppm from methyl and methylene groups, respectively.

^1H -NMR of complexes

A comparison between ^1H -NMR spectra of complexes and with the corresponding ligand clearly indicated the coordination of ligands to metals. The ^1H -NMR spectrum of Ni(II) complexes in $\text{DMSO}-d_6$ showed the chemical shift of amino protons at 6.22 ppm. Whereas these signals appear at 6.23 ppm in Zn(II) complex and 6.28 ppm in both Pd(II), Pt(IV) complex, respectively. These chemical shifts indicate the amino protons close to the triazole ring in the metal complexes are located in different chemical environments and confirm the contribution of the NH_2 group with metal ions. Also, the ^1H -NMR spectrum of these complexes showed a small shift to the downfield in the aromatic regions, which refers to the coordination of ligands to metals. The ^1H -NMR spectrum of complexes illustrated that the peak at 2.8 ppm corresponding to methyl group also appeared in the spectrum of complexes without any change (Fig. S3).

Mass Spectra (MS)

The mass spectral of Ni(II) complexes exhibited main molecular ions plus H_2O bands at m/z 700 [$\text{M}+\text{H}_2\text{O}$] with other bands at 551, 530, 445, and 288 which correspond to the fragmentation of complexes as shown in Fig. 6.

The mass spectra of the Pd(II) complex displayed a mother peak at 739 [M] m/z , which indicated the molecular ion of the Pd(II) complex with many other

peaks at 513, 397, 355, and 288 corresponding to the fractions of Pd(II) complex. While the mass spectral of Pt(IV) complex showed a main peak at 930 [$\text{M}+2\text{H}_2\text{O}$] m/z attributed to a molecular weight of Pt(IV) complex and two molecules of H_2O , a variety of fractions at 712, 515, and 353 m/z correspond to another component of Pt(IV) complex. The mass spectrum of the ligand exhibited the main peak at 281 m/z , which agreed with elemental analyses and confirmed the formation of the ligand (Fig. S4).

FT-IR Spectrum for Ligand and Its Complexes

The main bands of the FTIR spectrum of the ligand and its complexes are presented in Table 3. The free ligand shows strong bands at 1280 and 1620 cm^{-1} assigning to the vibrations of thioamide -C=S and -C=N- of the triazole ring (Fig. S5). The chelation of Ni(II), Zn(II), Pd(II) and Pt(IV) ions to the active sites -C=S and - NH_2 groups have been observed from the lowering in their absorptions to the regions of 3100–3250 and 1250–1275 cm^{-1} . As well as the weak to medium bands at around 520–422 and 389–320 cm^{-1} are associated with the coordination bonds of M-N and M-S, respectively [17-19]. The Zn-L and Pt-L complexes exhibit weak bands at 250–290 cm^{-1} , revealing the presence of M-Cl moieties in the structure of complexes [20-21].

Electronic Spectra and Magnetic Susceptibility of Complexes

The UV-Vis absorption data of triazole ligand were carried out in absolute ethanol at room temp. This study

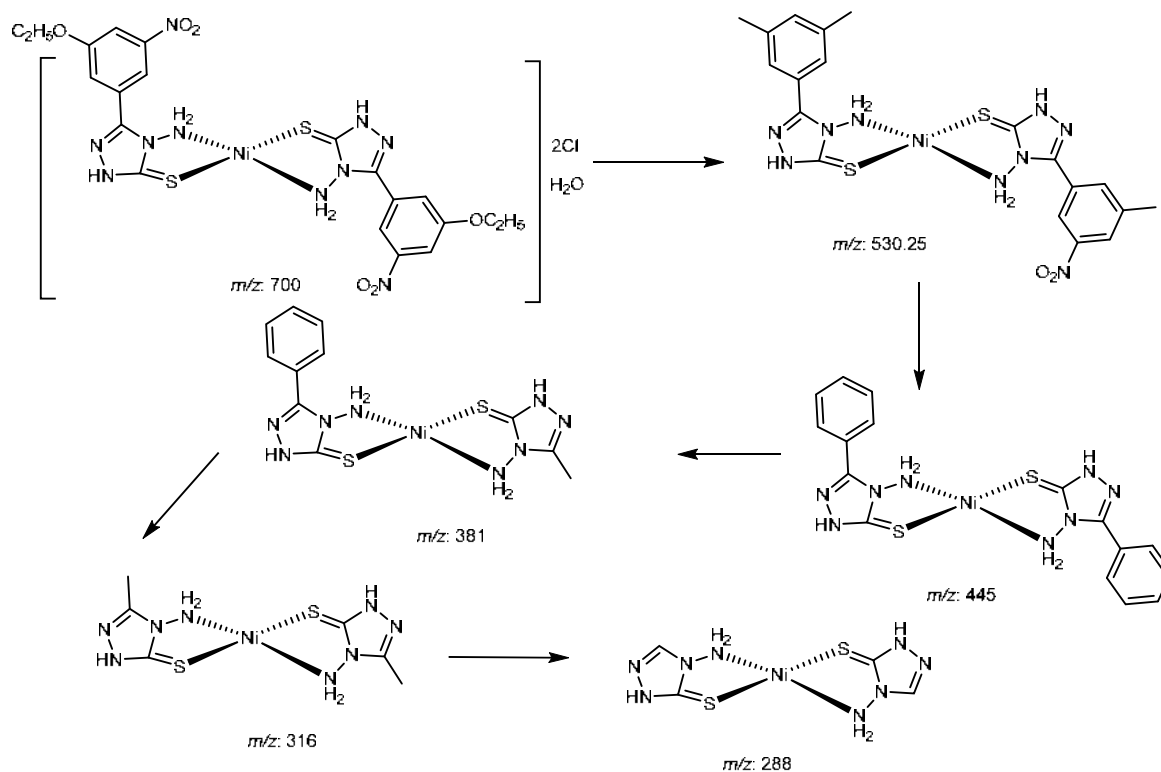


Fig 6. Fragmentation pattern of Ni(II) complexes

Table 3. IR spectrum of triazole ligand and its corresponding metal complexes

No.	Compound	$\nu\text{NH}_{2\text{asy}}, \text{NH}_{2\text{sym}}$	νNH	$\nu\text{C}=\text{S}$	$\nu\text{N}-\text{NH}_2$	M-N	M-S	M-Cl
1	L	3290, 3300	3190	1280	1620			
2	Ni-L	3200(br)	3150	1275	1610(s)	490(m)	389	-
3	Zn-L	3300	3200	1268	1590(s)	422(w)	350(w)	275, 290(w)
4	Pd-L	3400(br)	3120	1250	1566(sh)	520(m)	320(w)	-
5	Pt-L	3360(br)	3209	1269	1605(s)	488(m)	370(w)	250, 288(w)

exhibited three absorption bands, two bands at (210 nm, 47619 cm^{-1}) and (275 nm, 36080 cm^{-1}) were indicated to $\pi-\pi^*$ transition and observed at (380 nm, 26315 cm^{-1}), which is assigned to L-M C.T transition [19]. The solutions of NiL, PdL and PtL complexes in ethanol (10^{-3} M) displayed weak absorptions at (400–800) nm assigning to d-d spectra. The square planar complexes of Ni(II) and Pd(II) recorded weak bands at 450–380 and 350–310 nm, which are mainly attributed to $^1\text{A}_{1g}\rightarrow^1\text{B}_{1g}$ and $^1\text{A}_{1g}\rightarrow^1\text{E}_g$ transitions, respectively (Fig. S6). Furthermore, the diamagnetic properties of all complexes are in well-agreement of low-spin state of the Pd(II) complex having a d^8 configuration favors the formation of complexes with square planar geometry and d^6

configuration with a strong field of the triazole ligand [21].

Molar Conductance for Synthesized Complexes

The molar conductivity of complexes was recorded at 298 K temperature (0.001 M) in DMF solution. The finding suggested that the complexes with a 2:1 ratio are electrolytes due to the presence of two chloride ions in the outer sphere of the complexes structure except for Zn(II) complex, which showed a different manner as a neutral complex with the chemical formula ZnLCl_2 . The following Fig. 7 represents the octahedral geometry of the Pt(IV) complex, square-planar of Ni(II) and Pd(II) complexes, whereas the tetrahedral environment around Zn(II) ions was adopted.

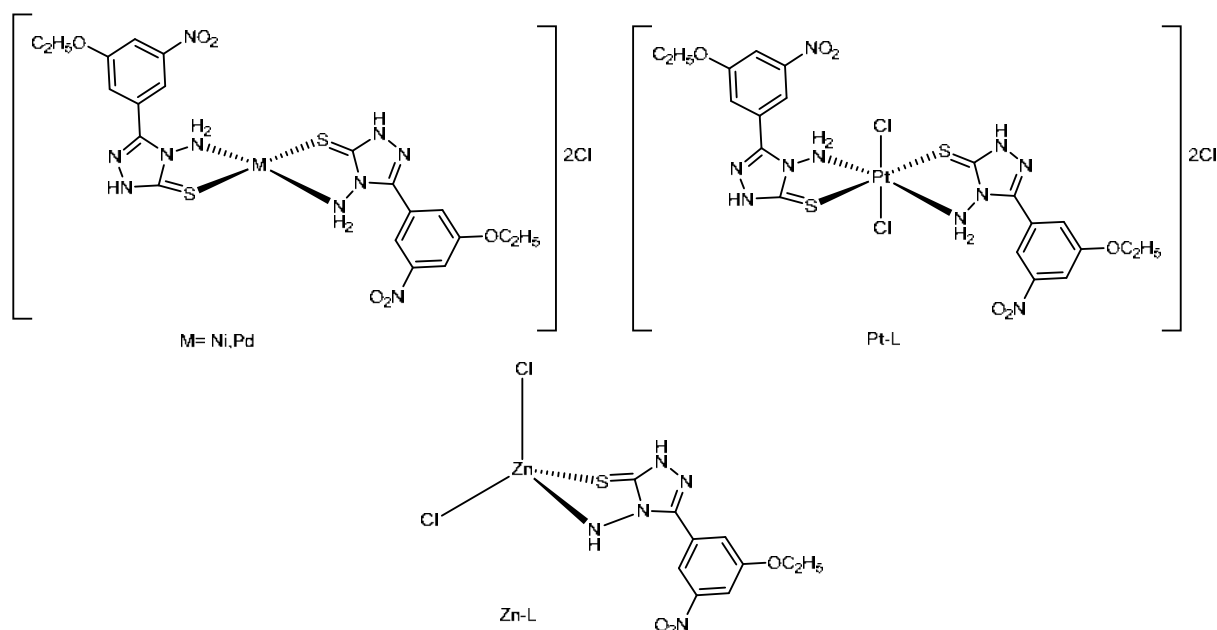


Fig 7. Suggested geometry of the prepared metal complexes

Antimicrobial Study

The inhibition zones (mm) of DMSO solutions of triazole ligand and metal complexes are shown in Table 4. The observed data revealed that Pd(II) and Pt(IV) complexes showed the highest activity against all microorganisms due to the high penetration of the lipoprotein of the bacteria and fungi [20-21]. As well as the free ligand solution in blank DMSO exhibits medium inhibition zones (10–17) mm toward *Staphylococcus aureus* and *Escherichia coli* bacteria, whereas no remarkable antifungal, which may be reasonable in high

polarity of the triazole structure [22]. Furthermore, the solutions of Ni(II) and Zn(II) displayed the lowest activity toward the *E. coli* and *S. aureus* bacteria compared with the control drug of azithromycin (10 ppm), which mainly resulted from the ionic character of chloride ions in the outer sphere of their chemical structures [10,21]. It is observed that the solutions of Pt(IV) and Pd(II) showed greater activity against *Candida albicans* and *Aspergillums favus* which are close to the activity of control Miconazole antifungal drug of 10 ppm concentration. These data on biological

Table 4. Biological activity of the ligand and its metal complexes

Compound		Zone of Inhibition in mm			
		<i>S. aureus</i>	<i>E. Coli</i>	<i>C. albicans</i>	<i>A. favus</i>
L	10 µg/mL	8	8	-	-
	20 µg/mL	10	12	-	-
[NiL ₂]Cl ₂	10 µg/mL	6	8	-	-
	20 µg/mL	8	12	-	-
[ZnCl ₂]	10 µg/mL	4	5	5	-
	20 µg/mL	6	8	7	-
[PdL ₂]Cl ₂	10 µg/mL	12	11	13	18
	20 µg/mL	17	18	17	20
Azithromycin	10 µg/mL	18	22	-	-
	20 µg/mL	25	30	-	-
Miconazole	10 µg/mL	-	-	17	23

activity would have encouraged us in the future to do a wide spectrum of *in vivo* studies for the new complexes.

■ CONCLUSION

In conclusion, the new derivative of 1,2,4-triazole ligand was synthesized, and fully characterized, and its complexes Ni(II), Zn(II), Pd(II) and Pt(IV) complexes were synthesized and characterization via different spectroscopic techniques. It was found that ligand coordinate with metals *via* S and N to form Ni(II) and Pd(II) complexes with square planer geometry and Pt(IV) complex show octahedral geometry while Zn(II) different exhibit shapes by forming tetrahedral geometry. This study suggested that the ligand and its complexes showed moderate activity against bacteria and had the potential as antimicrobial. The PdL and PtL complexes are in good agreement with the antimicrobial activity of expectations due to their *cis*-platinum structures compared with other Ni(II) and square planer NiL complexes. The inhibition zones (mm) of Pt(IV) and Pd(II) complexes in blank DMSO exhibited great antifungal against the two fungi studied, and they are so close to the Miconazole control drug.

■ ACKNOWLEDGMENTS

The authors wish to articulate their thanks and gratefulness to the Chemistry Department in Mustansiriyah University for carrying out the measurements of molar conductivity and magnetic susceptibility of complexes as well as authors are thankful to the members of the service laboratory of the Chemistry Department, College of Science, Yarmook University, Jordan, for performing the NMR analysis of the prepared compounds. We also extend our thanks to the service center of the College of Science, Albait University, Amman, Jordan, for carrying out elemental microanalyses and LC-MS spectra for the prepared metal complexes.

■ REFERENCES

- [1] Ju, F.Y., Li, G.L., Li, X.L., Yin, W.D., and Liu, G.Z., 2019, Syntheses, structures, and properties of two Cd(II)/Zn(II) complexes with 1,2,4-triazole derivatives, *Russ. J. Coord. Chem.*, 45 (8), 600–607.
- [2] Liu, K., Shi, W., and Cheng, P., 2011, The coordination chemistry of Zn(II), Cd(II) and Hg(II) complexes with 1,2,4-triazole derivatives, *Dalton Trans.*, 40 (34), 8475–8490.
- [3] Kargar, H., Torabi, V., Akbari, A., Behjatmanesh-Ardakani, R., Sahraei, A., and Tahir, M.N., 2020, Pd(II) and Ni(II) complexes containing an asymmetric Schiff base ligand: Synthesis, X-ray crystal structure, spectroscopic investigations and computational studies, *J. Mol. Struct.*, 1205, 127642.
- [4] Adachi, J., Mori, T., Inoue, R., Naito, M., Le, N.H.T., Kawamorita, S., Hill, J.P., Naota, T., and Ariga, K., 2020, Emission control by molecular manipulation of double-paddled binuclear Pt^{II} complexes at the air-water interface, *Chem. - Asian J.*, 15 (3), 406–414.
- [5] Yang, G.H., Li, Y.J., Liu, D., and Cui, G.H., 2020, Dual-responsive luminescent sensor based on a water-stable Cd(II)-MOF for the highly selective and sensitive detection of acetylacetone and Cr₂O₇²⁻ in aqueous solutions, *CrystEngComm*, 22 (7), 1166–1175.
- [6] Tenorio, K.V., Fortunato, A.B., Moreira, J.M., Roman, D., D'Oliveira, K.A., Cuin, A., Brasil, D.M., Pinto, L.M.C., Colman, T.A.D., and Carvalho, C.T., 2020, Thermal analysis combined with X-ray diffraction/Rietveld method, FT-IR and UV-vis spectroscopy: Structural characterization of the lanthanum and cerium(III) polycrystalline complexes, *Thermochim. Acta*, 690, 178662.
- [7] Djunaidi, M.C., Pardoyo, P., Widodo, D.S., Lusiana, R.A., and Yuliani, A., 2020, *In-situ* ionic imprinted membrane (IIM) synthesis based on acetic polyeugenoxo acetyl tiophen methanolate for gold(III) metal ion transports, *Indones. J. Chem.*, 20 (6), 1323–1331.
- [8] Omar, S.A.E., Scattergood, P.A., McKenzie, L.K., Bryant, H.E., Weinstein, J.A., and Elliott, P.I.P., 2016, Towards water soluble mitochondria-targeting theranostic osmium(II) triazole-based complexes, *Molecules*, 21 (10), 1382.
- [9] Bisceglie, F., Bacci, C., Vismarra, A., Barilli, E., Pioli, M., Orsoni, N., and Pelosi, G., 2020, Antibacterial

- activity of metal complexes based on cinnamaldehyde thiosemicarbazone analogues, *J. Inorg. Biochem.*, 203, 110888.
- [10] Shukla, S.N., Gaur, P., Raidas, M.L., and Bagri, S.S., 2021, Synthesis, spectroscopic characterization, DFT, oxygen binding, antioxidant activity on Fe(III), Co(II) and Ni(II) complexes with a tetradentate ONNO donor Schiff base ligand, *J. Serb. Chem. Soc.*, 86 (10), 941–954.
- [11] Rasyda, Y.A., Widowati, M.K., Marliyana, S.D., and Rahardjo, S.B., 2021, Synthesis, characterization and antibacterial properties of nickel(II) complex with 4-aminoantipyrine ligand, *Indones. J. Chem.*, 21 (2), 391–399.
- [12] Idrees, M., Nasare, R.D., and Siddiqui, N.J., 2016, Synthesis of S-phenacylated trisubstituted 1,2,4-triazole incorporated with 5-(benzofuran-2-yl)-1-phenyl-1*H*-pyrazol-3-yl moiety and their antibacterial screening, *Chem. Sin.*, 7, 28–35.
- [13] Özadali, K., Özkanlı, F., Jain, S., Rao, P.P.N., and Velázquez-Martínez, C.A., 2012, Synthesis and biological evaluation of isoxazolo[4,5-*d*]pyridazin-4-(5*H*)-one analogues as potent anti-inflammatory agents, *Bioorg. Med. Chem.*, 20 (9), 2912–2922.
- [14] Kanagarajan, V., Thanusu, J., and Gopalakrishnan, M., 2012, Synthesis and in vitro microbiological evaluation of novel 2,4-diaryl-3-azabicyclo[3.3.1]nonan-9,5'-spiro-1',2',4'-triazolidine-3'-thiones, *Med. Chem. Res.*, 21 (12), 3965–3972.
- [15] Bharty, M.K., Bharti, A., Chaurasia, R., Chaudhari, U.K., Kushawaha, S.K., Sonkar, P.K., Ganesan, V., and Butcher, R.J., 2019, Synthesis and characterization of Mn(II) complexes of 4-phenyl(phenyl-acetyl)-3-thiosemicarbazide, 4-amino-5-phenyl-1,2,4-triazole-3-thiolate, and their application towards electrochemical oxygen reduction reaction, *Polyhedron*, 173, 114125.
- [16] Bhale, S.P., Yadav, A.R., Pathare, P.G., Tekale, S.U., Franguelli, F.P., Kótai, L., and Pawar, R.P., 2020, Synthesis, characterization and antimicrobial activity of transition metal complexes of 4-[(2-hydroxy-4-methoxyphenyl) methyleneamino]-2,4-dihydro-3*H*-1,2,4-triazole-3-thione, *Eur. Chem. Bull.*, 9 (12), 430–435.
- [17] Yousif, E.A., Hameed, A.S., and Ameer, A.A., 2005, Synthesis and characterization of complexes of some transition metals with 2-amino-5-(4-hexyloxyphenyl)-1,3,4-thiadiazole, *Al-Nahrain J. Sci.*, 8 (1), 9–11.
- [18] Narayana, B., and Gajendragad, M.R., 1997, Complexes of Zn(II), Pd(II), Hg(II), Pb(II), Cu(I), Ag(I), and Ti(I) with 4-amino-5-mercaptato-3-(o-tolyloxymethyl)-1,2,4-troazol, *Turk. J. Chem.*, 21 (1), 71–76.
- [19] Sliverstein, R.M., Webster, F.X., and Kiemle, D., 2005, *Spectrometric Identification of Organic Compounds*, 7th Ed., Hoboken, NJ.
- [20] Flifel, I.A., and Kadhim, S.H., 2012, Synthesis and Characterization of 1,3,4-oxadiazole derivatives with some new transition metal complexes, *J. Kerbala Univ.*, 10 (3), 197–209.
- [21] Manjunatha, M., Srinivasan, V., and Buvabi, S.H., 2021, Biological studies of novel 22-membered N₂O₂ diazadioxo macrocyclic bis-triazoles transition metal complexes: Synthesis and physicochemical studies, *Mater. Today: Proc.*, 47, 4538–4547.
- [22] Lupaşcu, G., Pahonţu, E., Shova, S., Bărbuceanu, Ş.F., Badea, M., Paraschivescu, C., Neamţu, J., Dinu, M., Ancuceanu, R.V., Drăgănescu, D., and Dinu-Pîrvu, C.E., 2021, Co(II), Cu(II), Mn(II), Ni(II), Pd(II), and Pt(II) complexes of bidentate Schiff base ligand: Synthesis, crystal structure, and acute toxicity evaluation, *Appl. Organomet. Chem.*, 35 (4), e6149.

κ -Carrageenan/Sodium Alginate: A New Synthesis Route and Rapid Adsorbent for Hydroxychloroquine Drug

Mohammed Kassim Al-Hussainawy^{1*} and Layth Sameer Al-Hayder²

¹Department of Chemistry, College of Education, University of Al-Qadisiyah, 58002 Diwaniya, Iraq

²Department of Chemistry, College of Education, University of Al-Qadisiyah, 58002 Al-Muthanna City, Iraq

* **Corresponding author:**

email: kassim1316@gmail.com

Received: August 3, 2022

Accepted: November 5, 2022

DOI: 10.22146/ijc.76819

Abstract: In recent years, the huge amounts of chemicals that are used as drugs and their derivatives have been exposed to the environment due to the COVID-19 pandemic. Some of these drugs (i.e. hydroxychloroquine (HCQ)) have a serious risk on aquatic media. In this study, carrageenan/sodium alginate (κ C/Sa) was investigated as a biopolymer, environmentally friendly, and rapidly adsorbent to eliminate HCQ from its aqueous solution. The biopolymer (κ C/Sa) was synthesized by free radical polymerization assisted by ultrasound in the presence of acrylic acid as cross-linkage and potassium persulfate as an initiator. The natural κ C/Sa was characterized by FTIR, XRD, BET, BJH, and SEM techniques. The produced co-polymer had a mesoporous surface with high purity and significant thermal stability. The best parameters were determined to be 0.05 g biopolymer, 200 ppm initial HCQ concentration, salts, and pH = 7. The adsorption mechanism follows a pseudo second-order kinetic model, and the adsorption isotherm follows a Freundlich model, with q_e reaching 89.8 mg/g at 500 ppm HCQ. Thermodynamic studies indicated that the adsorption of hydroxychloroquine drugs was an exothermic spontaneous process.

Keywords: biopolymer; drug adsorption; pollution removal; hydroxychloroquine; κ -carrageenan/sodium alginate; aqueous media

■ INTRODUCTION

Due to the extensive use of medicines, nutritional supplements, and other drugs in our daily lives, the removal of these substances from aqueous media has become a crucial environmental procedure in recent years [1-2]. Anticoagulants, analgesics, antibiotics, antidepressants, and anti-disease agents are based primarily on organic compounds with acid functional groups and amines linked to aromatic rings. They are intended for hospital, infirmary, and clinical pharmacy use. Their chemical structures are based primarily on organic compounds with acid functional groups and amines attached to aromatic rings [3-4]. One of these medicines, hydroxychloroquine (HCQ), is used in enormous amounts to treat a number of disorders (i.e., malaria and autoimmune diseases) all over the world [5]. One of the most frequently used antiviral medications in

hospitals in recent months is hydroxychloroquine, which has received recommendations from numerous international organizations, including the FDA (World Health Organization), WHO, and the US Food and Drug Administration. This is particularly true given the coronavirus pandemic (SAR-CoV-2/COVID-19) and its recurrent use [6-7]. This medication's toxicity, chemical, and biological characteristics are only a few of its many drawbacks. Sadly, there are not many investigations into the elimination, oxidation, and fate (hydroxychloroquine in aqueous solution after use in different environments) of hydroxychloroquine in aqueous environments in the literature. Significant environmental contaminants include quinoline and its derivatives because of their persistence, carcinogenicity, and toxicity, even if the medicine is a quinoline derivative and the dangers to the environment remain unknown. Therefore, because of their high solubility and poor biodegradability, HCQ

and its derivative products both pose a risk to ecosystems and public health [8-9].

Among wastewater treatments are advanced oxidation processes (ultrasound degradation and photodegradation) and traditional methods (reverse osmosis, membrane separation, and adsorption). The adsorption process is the most effective, low-cost, and easily available method that has been successfully employed for removing pollutants from wastewater, so adsorption technology is critical to reduce adsorbates (dyes, medicines, organic compounds, factory, and hospital waste, etc.) because of rising environmental pollution and contaminants. Because biopolymers can achieve promising qualities and can be utilized again after filtration [10], we chose to employ them in our investigation, in particular for high molecular weight drugs and chemicals [11]. Numerous studies have focused on HCQ removal from aqueous solutions, such as through photodegradation [12], electrochemical oxidation [8], and gamma-irradiation [13]. On the other hand, there are many disadvantages to adsorbents. For example, clay has many disadvantages, such as pH-controlled adsorption, separating adsorbate-adsorbent mixture after adsorption, and it is not possible to regenerate the adsorbent through desorption. Although biomass in its natural state has been investigated as a potential adsorbent, its limited practical use is due to its low adsorption capability. The most popular adsorbent is activated carbon, although its use has been constrained by its expensive cost. Natural fibers are also expensive and can be shrunk after adsorption [11,14-15].

Brown algae can be used to extract the natural polymer sodium alginate. Outstanding qualities of sodium alginate include its great biocompatibility, biodegradability, and capacity for regeneration. Furthermore, carboxyl and hydroxyl groups that are plentiful have a strong adsorption affinity. However, sodium alginate has relatively low mechanical strength, stability, and heat resistance [16-18]. Therefore, to improve their suitability for adsorption, physical or chemical changes are typically used. Surface grafting, cross-linking, and compounding with other components

have been used to modify sodium alginate-based adsorbents [19-20]. Additionally, combining alginate with other components can improve the chemical and physical adsorption properties of the composite. In order to change the physical and chemical characteristics of alginates and boost their adsorption capacity, alginates' physical and chemical characteristics were modified by carrageenan to enhance their adsorption ability [21-22]. Many academics have extensively researched how sodium alginate and carrageenan adhere to medicinal molecules [23-24]. This study aims to synthesize κ -Carrageenan/alginate hydrogel as an environmentally friendly and biodegradable adsorbent for the rapid adsorption of HCQ from its aqueous medium. Synthesis κ -Carrageenan/alginate hydrogel is a new method based on a closed glass tube in nitrogen and a water bath. The product was diagnosed by thermal and morphological measurements.

■ EXPERIMENTAL SECTION

Materials

Hydroxychloroquine (HCQ) was assayed at 98.4% and was equipped with Sigma (Shanghai, China). Aladdin (Shanghai, China) supplied κ -Carrageenan (κ C), sodium alginate (Sa) purity 98%, and zinc oxide (ZnO) purity 99.0%. Also, acrylic acid (AA) at 99.5%, *N,N'*-methylenebisacrylamide (96%), and potassium persulfate > 98.5% were purchased from Aladdin. Commercial suppliers Sigma-Aldrich (Germany) provided calcium chloride (CaCl_2) and sodium chloride (94–97%). ddH₂O stands for double-distilled water it was used to prepare all solutions.

Procedure

Calibration curve

Hydroxychloroquine sulfate concentrations over the range of 1–10 ppm were prepared. However, analysis was done using a 340 nm wavelength by UV-visible spectroscopy, as shown in Fig. 1. Standard curves were produced twice in order to determine the differences that appeared. The stock solution was stored at 25 °C and protected from light before use.

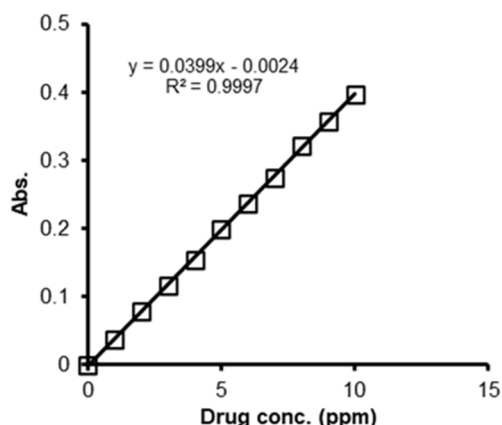


Fig 1. Calibration curve of HCQ drug

κ C/Sa Dual hydrogel

The copolymer of κ C/Sa hydrogel was prepared by solvating 1:1 w/w of carrageenan and alginate in double distilled water (ddH₂O) at a heat range (55–60 °C) for 25 min to form a κ C/Sa solution in a homogenized shape with vigorous stirring until a vortex forms. The cross-linked 50 mg (*N,N'*-methylenebisacrylamide), 10 mg of initiator potassium persulfate (KPS), and 5 mL of acrylic

acid (AA) were added to the homogenous solution (κ C/Sa). These solutions were poured into glass tubes [25]. After that, the ultrasound is used to remove bubbles and the sample is placed in a water bath to complete the polymerization process. Finally, the prepared copolymer was washed with ddH₂O and dried at 65 °C in the oven. The κ C/Sa hydrogel rocks were ground into tiny bits and sieved through a sieve with a mesh size of 150 mesh. The synthesis process is illustrated in Fig. 2 [26].

Characterization of κ C/Sa hydrogel

The amorphous content of the κ C/Sa adsorbent hydrogel was characterized by XRD using (XRD-6000, Shimadzu, Japan), and the radiation by CuK α (0.15040 nm). The XRD pattern was recorded in the range of 10°–80°. To determine the functional groups, spectra of the κ C/Sa adsorbent hydrogel were performed using FTIR (Shimadzu, Japan, 8400 s). The morphology of the κ C/Sa adsorbent hydrogel was observed by SEM (Scanning Electron Microscope) (MIRA3, Tescan, Czech Republic, Iran) with a voltage of 25 kV. The average pore

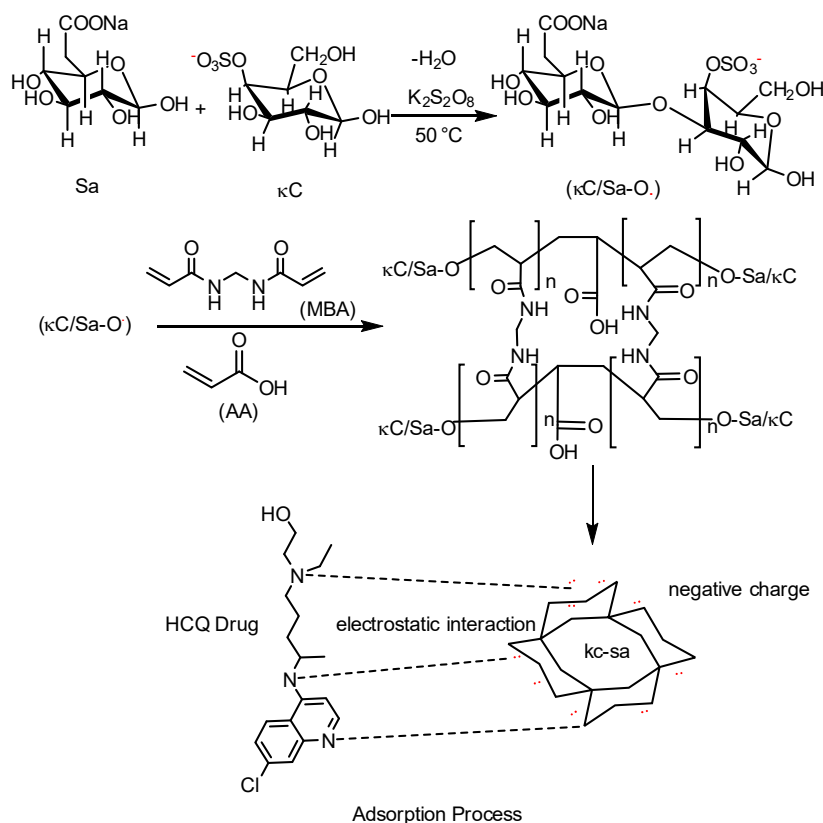


Fig 2. Mechanism of HCQ adsorption by active sites of alginate/carrageenan hydrogel

diameter and pore volume were observed by BET-BJH analysis (NOVA 2200e/Quantachrome/USA) of the κ C/Sa hydrogel. The UV-1800 UV/Visible Scanning Spectrophotometer was performed using Shimadzu (Japan), and the thermogravimetric analysis (TGA, DTA) was done using Perkin Elmer (USA) (TGA 4000).

Protocol of adsorption

All adsorption tests were carried out in 50 mL cube tubes by combining and stirring 10 mL of an aqueous solution contaminated with HCQ with 50 mg of a hydrogel. The solution was centrifuged at 150 rpm after the recommended amount of contact time and filtered. Shaking 50 mg of hydrogel with 10 mL of HCQ solution at an initial pH of 7 and a temperature of 25 °C for varied contact periods between 1 and 180 min was used to conduct adsorption kinetics studies in flasks. By mixing 50 mg of hydrogel with 10 mL of HCQ solution in a 50 mL cube tube and adjusting the temperature from 10 °C to 40 °C, isotherm and thermodynamic parameter tests were also carried out. With a maximum wavelength of 340 nm, a UV-Vis spectrophotometer was used to measure residual HCQ concentrations [27]. Equations were used to determine the quantity of adsorbed HCQ per gram of adsorbent at equilibrium.

$$q_e = \frac{C_0 - C_e}{X} \quad (1)$$

$$R\% = \frac{C_0 - C_e}{C_0} \times 100 \quad (2)$$

where, q_e = Amount of drug adsorbed per unit mass of adsorbent (mg/g), C_0 = Initial drug concentration (mg/L),

C_e = Final drug concentration (mg/L), X = Dose of adsorbent (g/L), and $R\%$ = removal percentage of dye.

Equilibration time for adsorption

Hydroxychloroquine was done with 50 mg of κ C/Sa hydrogel in a 10 mL solution at a 200 ppm concentration. For periods of 1, 2, 4, 6, 10, 15, 30, 45, 60, 90, 120, and 180 min, separate tubes were equilibrated. The samples were separated by filtered paper after each equilibration period, and the HCQ content in the supernatant was calculated by comparing them to the standard curve using UV/vis spectrophotometry at 340 nm.

RESULTS AND DISCUSSION

Adsorbent Characterization

FTIR analysis

The FTIR spectra of the κ C/Sa hydrogel before adsorption in the 4000–400 cm^{-1} wavelength range are displayed in Fig. 3. The OH absorption vibration peak at 3440–3150 cm^{-1} is due to the overlapping that occurred between the two O–H bands of the carboxyl and hydroxyl groups and the N–H group of the MBA crosslinker; the peaks at 1044 cm^{-1} correspond to glycosidic linkage; a peak formed at 1719 cm^{-1} can be attributed to the carbonyl group. The characteristic peak at 1455 cm^{-1} is caused by the symmetric stretching of the COOH groups. Peaks (S=O) appear at 1250 cm^{-1} and 2680 cm^{-1} , which correspond to CH asymmetric stretch [28-29]. The retention of carrageenan and sodium alginate's distinctive absorption peaks in the κ C/Sa hydrogel demonstrated

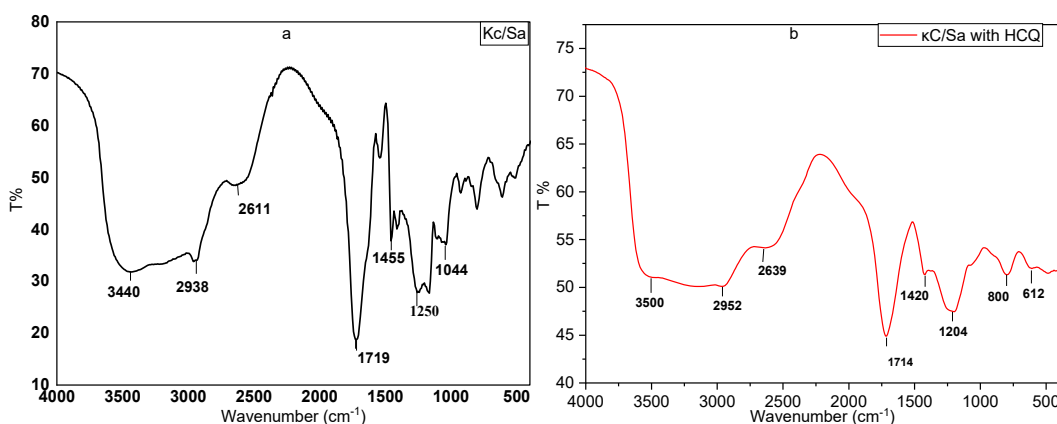


Fig 3. FTIR of κ C/Sa hydrogel: (a) before adsorption, (b) after adsorption

Table 1. FTIR of κ C/Sa hydrogel: (a) before adsorption, (b) after adsorption

Assignment group	a	b
$\nu(\text{O-H, N-H})$ Overlapping	3440–3000	3000–3500
$\nu(\text{C-H})$ Symmetric	2938	2952
$\nu(\text{C-H})$ Asymmetric	2680	2639
$\nu(\text{CO}_2)$	-	-
$\nu(\text{C=O})(-\text{COOH})$ and $(-\text{CONH})$	1540–1719	1714
$\nu(\text{C-N})$	1395	1420
$\nu(\text{S=O})$	1180–1250	1204
$\nu(\text{C-O-C})$	1044	-
$\nu(\text{OH})$ Wag	612	612

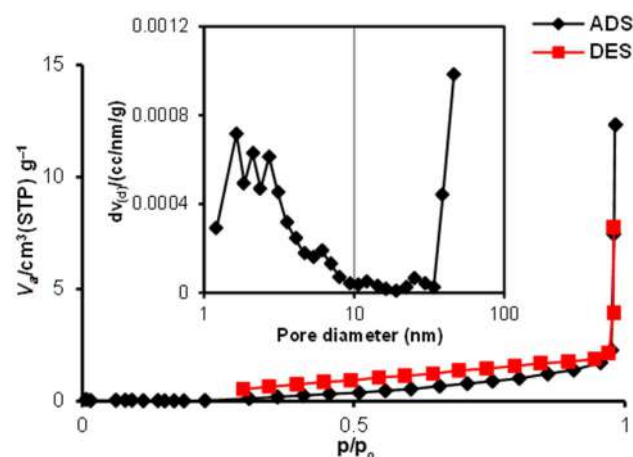
that the final result was a composite biopolymer containing both substances. The various functional groups on the surface, including the hydroxyl, carboxyl, and amino groups, have a significant impact on the adsorption of HCQ medication from an aqueous solution by κ C/Sa hydrogel. Upon protonation and deprotonation, hydrogel functional groups' surfaces may become charged (negative and positive) or neutral. The FTIR spectral data shown in Fig. 3 supports the different interactions between the adsorbent and adsorbate, including electrostatic attractions and hydrogen bonding interactions, which are supported by the FTIR spectral data. Additionally, after HCQ drug adsorption, a broadband of 3400 cm^{-1} was moved to a higher wavenumber of 3500 cm^{-1} due to the weakened κ C/Sa wavenumber of intermolecular hydrogen bonding between its molecules [30].

Specific surface area "BET and BJH"

According to the BET analysis, the composite hydrogel possesses a microporous structure. Simultaneous BJH analysis revealed the surface to have a mesoporous structure. The microporous limit is, however, quite near 437.44 and 46.13 in the BET-BJH analysis, as shown in Table 2. The pores visible in the SEM pictures confirm the BET-BJH analysis' findings. One of the crucial metrics to describe the adsorbents' quality is their surface area and pore size. Table 2 displays the BET-BJH specific surface area, pore size, and overall pore volume of κ C/Sa adsorbed hydrogels. The majority of κ C/Sa adsorption hydrogels have a microporous structure. Fig. 4 displays the nitrogen gas adsorption-desorption isotherms of κ C/Sa adsorbed hydrogels. It was discovered that the BET-BJH isotherms had a relatively

Table 2. Results of the κ C/Sa adsorbent hydrogel's of BET-BJH analysis

	Surface area (m^2/g)	Average pore size (nm)	Pore volume (cm^3/g)
BET	0.17442	437.44	0.019075
BJH	2.1088	46.13	0.013739

**Fig 4.** Adsorption-desorption isotherms and pore size distribution (inset) for the κ C/Sa adsorbent hydrogel

large surface area. It is the adsorbate uptake grows exponentially in type III isotherms of κ C/Sa because of the weak contact between the adsorbate (N_2 gas) and the adsorbent isotherm. The isotherm in Fig. 4 displays the H3 hysteresis loop, which denotes the presence of micropores [31]. The BJH result indicated that the surface has two different types of pores; mesopores (diameter 2–50 nm) and micropores (diameter < 2 nm).

XRD analysis

In Fig. 5, the XRD patterns for κ C/Sa are displayed. The single broad peak in Fig. 5 at 2θ of 21.1068 indicates

that κ C/Sa is semicrystalline in nature with a high concentration of amorphous material. Two peaks in the XRD pattern of κ C/Sa indicate semi-crystallinity: one at 21.1068° , which pertains to a hydrated crystalline structure, and the other at 37.7643° , which is related to an amorphous state [32]. Table 3 shows the XRD analysis results of the κ C/Sa hydrogel.

SEM characterization

The cross-linked κ C/Sa composite hydrogels feature rough surfaces and many folds and are well cross-linked, as shown in the SEM images shown in Fig. 6. These characteristics are crucial for improving the availability of more adsorption sites and a specified surface area for drug pollutants. Adsorbents' adsorption qualities are significantly influenced by their structure and surface characteristics. Additionally, the properties of the contaminants affect how the adsorbents and pollutants interact. In general, surface characteristics of adsorbents have the greatest impact on physical adsorption, whereas surface functional groups have the greatest impact on chemical adsorption.

In addition, alginate/carrageenan utilizing energy dispersive EDX [33] spectroscopy was further studied (Fig. 7). A mixed display of C, O, and S signals the presence of S

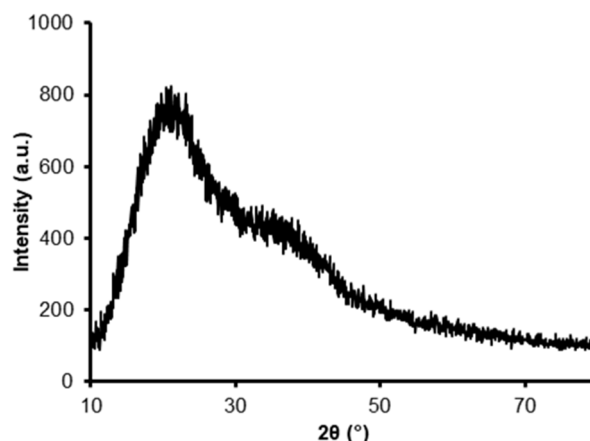


Fig 5. XRD patterns of κ C/Sa hydrogel

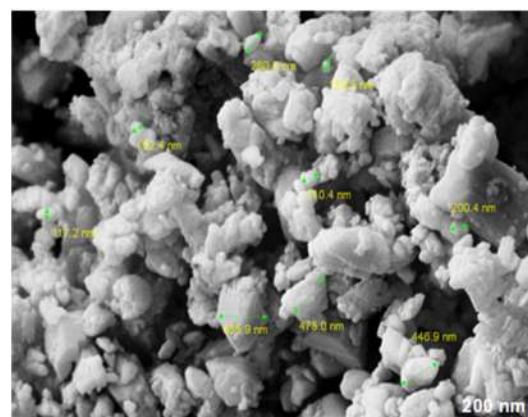


Fig 6. SEM image of κ C/Sa hydrogel

Table 3. XRD analysis results of κ C/Sa adsorbent hydrogel

Position 2θ ($^\circ$)	Height (cts)	FWHM left 2θ ($^\circ$)	d -spacing	Rel. int. (%)	Tip width	D (nm)
21.1068	446.61	0.1476	4.20927	96.10	0.1771	55.266
37.7643	41.64	0.1476	2.32303	8.96	0.1771	53.19

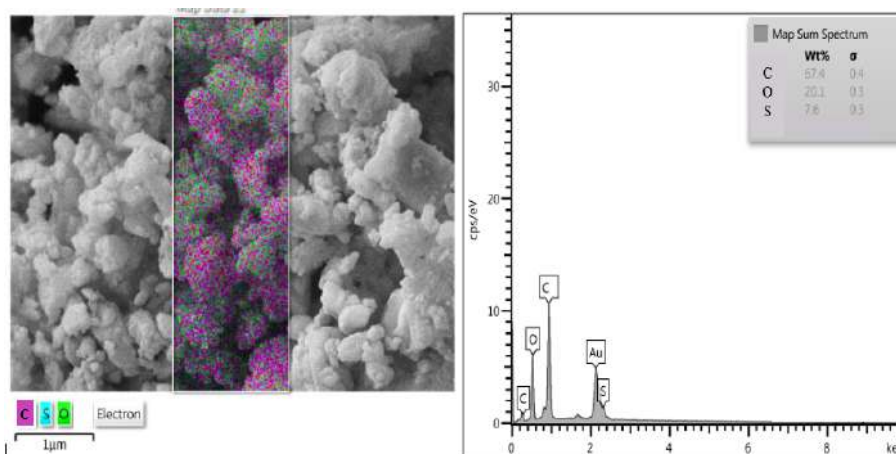


Fig 7. EDX map of composite of κ C/Sa hydrogel

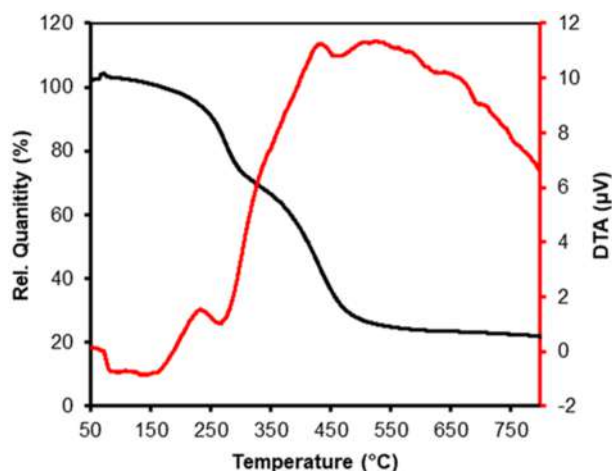


Fig 8. Thermogravimetric analysis (TGA/DTG) of κ C/Sa hydrogel

of the sulfate ion. However, C is derived from natural polymers, and S is derived from potassium persulfate, which is used as an initiator [34].

Thermogravimetric analysis (TGA/DTG)

The relative stability of hydrogels could be evaluated by thermogravimetric analysis, and to demonstrate the purity of the produced hydrogels, thermogravimetric analysis of the κ C/Sa hydrogel was carried out throughout a temperature range at a heating rate of 2 °C/min from 30 °C to 820 °C. The TGA curve (Fig. 8) shows three stages of weight loss, the first in the range of 5% weight loss at 110–200 °C involving evaporation of free water in the porous hydrogel. The second weight loss of 28% was observed at the temperature range of 200–300 °C, indicating the temperature corresponding to 10% weight loss of polymer as a result of thermal degradation of κ C/Sa hydrogel. The last stage of weight loss was the κ C/Sa polymer structural decomposition observed over the range of (320–500°).

DTA curves show four endothermic peaks at 150, 425, 500, and 650 °C, the first peak explains the physical water loss. The endothermic peaks located between 425 and 650 °C have been assigned to different stages of thermal hydrogel degradation [35–36].

Adsorption Properties of κ C/Sa Hydrogel

For batch HCQ adsorption experiments, place 0.05 g of sorbent in a 10 mL batch bottle at pH 7.4 and temperature 25 °C. The concentration of hydroxychloroquine solution

was 200 ppm in adsorption kinetic experiments and 50–500 mg/L in adsorption isotherm experiments. In the investigation, the greatest adsorption capacity of κ C/Sa biopolymer to HCQ drug reached 89 mg/g, and the adsorption reached a situation of equilibrium after about 1 h.

Fig. 9(a) and 9(b) depict, respectively, how pH and the concentrations of CaCl₂ and NaCl affect the adsorption of HCQ on κ C/Sa hydrogels using 0.1 mol/L of NaOH and HCl. The pH was changed from 2 to 11. The pH serves as the basis for determining the substance's adsorption on the surface of the gel since it affects the form in which HCQ is present [36]. Fig. 9(d) shows the influence of the contact time on the removal percentage of HCQ on κ C/Sa hydrogel at natural pH of 25 °C. As presented in Fig. 9(c), the adsorption of κ C/Sa hydrogel on HCQ increased with the drug's starting concentration at various temperatures. Based on the evaluation of the experimental results, at pH 4–9, the κ C/Sa hydrogel is comparatively stable. The adsorption capacity reached a maximum of 89 mg/g at pH 8. This is because HCQ is most commonly in cationic form at pH 7–8. The hydrogel's zeta potential research reveals that it is negatively charged. Therefore, the κ C/Sa hydrogel has a strong electrostatic adsorption capacity for HCQ under alkaline conditions [37–38]. During the adsorption process, when adding different concentrations of NaCl and CaCl₂ (0.001, 0.005, 0.01, 0.05, 0.1, and 0.15 mg/L⁻¹), adsorption capacity can be significantly impacted by ionic strength by managing electrostatic interactions during the process [39]. The equilibrium adsorption capacity was only 26.1 mg/g when the ionic strength was 0.15 mg/L⁻¹, as shown in Fig. 9(b), whereas the adsorption capacities for NaCl and CaCl₂ were 34.1–34.4 at 0.001 mg/L⁻¹. This is because an increase in ionic strength may reduce electrostatic interaction by concealing the surface charge, which can be either attracting or repulsive [40–41]. Specifically, HCQ is prevented from reaching the surface of hydrogels by the competing adsorption of positively charged Na⁺, Ca²⁺, and HCQ particles.

To clarify the dynamics of adsorption of HCQ on κ C/Sa hydrogels, two recognizable kinetic models (pseudo-first-order and pseudo-second-order models)

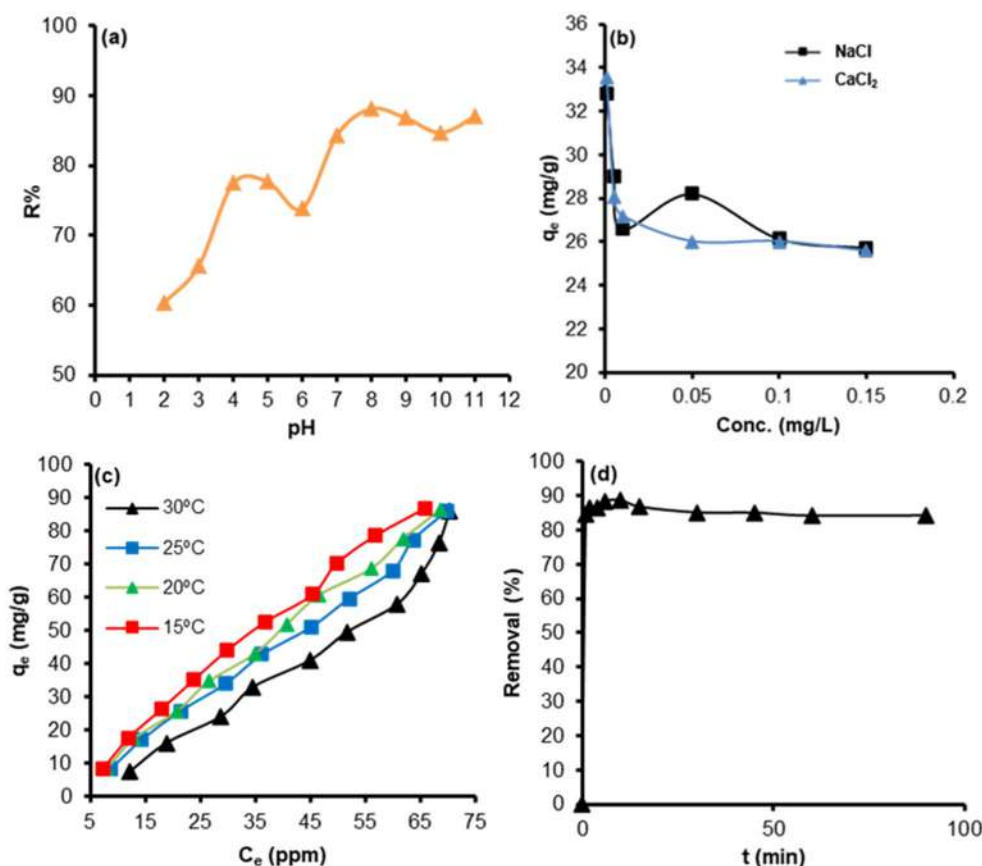


Fig 9. (a) Effects of pH on HCQ adsorption on κ C/Sa hydrogel; (b) Influence of concentration of salts on HCQ adsorption; (c) Influence of temperature on HCQ adsorption (d) Influence of the contact period on the adsorption of HCQ on κ C/Sa hydrogel

were used to survey the dynamic adsorption properties. Table 4 displays the parameters of the two kinetic models. The effect of contact time on the adsorption of κ C/Sa the two kinetic models' parameters In Fig. 10(a), the effect of contact time on κ C/Sa hydrogel adsorption hydrogel on HCQ is shown. Fig. 10(b) shows the fitted curves for different kinetic models. The pseudo-second-order and pseudo-first-order kinetic models displayed greater R^2 scores than the other models (Table 4), showing that the adsorption process is a heterogeneous diffusion process and that κ C/Sa hydrogels contain several types of binding sites. There is contact between HCQ and the adsorbent, and near the border of the adsorbent particle, the adsorption resistance is concentrated [42]. It is discovered by fitting that the adsorption of κ C/Sa hydrogel on HCQ is in good agreement with a more precise forecast of adsorption capacity is made when using a pseudo-second-

Table 4. Kinetic parameter of HCQ on κ C/Sa hydrogel using two model

Model	Parameter	κ C/Sa hydrogel
Pseudo-first-order	R^2	0.8708
	q_e ppm	2.6695
	K_1	0.0756
Pseudo-second-order	R^2	1
	q_e ppm	35.335689
	K_2	0.109711

order kinetic model and a correlation coefficient of 100%. Furthermore, the κ C/Sa hydrogel was compared to earlier reported adsorbents for removing HCQ. As shown in Table 5, adsorption isotherm models are frequently used to symbolize the properties and mechanisms of the phases of liquid and solid during adsorption. The Langmuir [43] and Freundlich [44] isotherms are usually chosen to study the adsorption

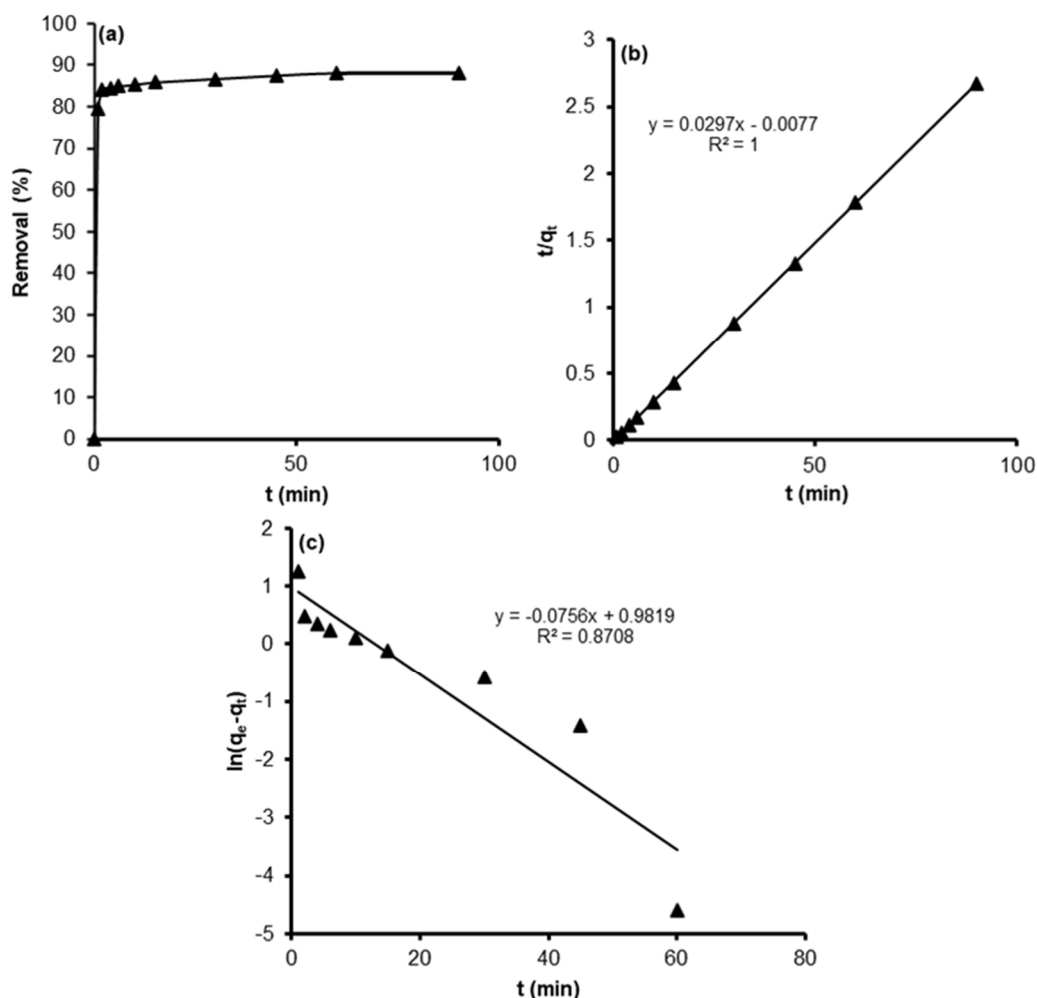


Fig 10. Kinetics curve: (a) κ C/Sa hydrogel, and the adsorption kinetic model fitting graphs, (b) pseudo-second-order, (c) pseudo-first-order (adsorbent dosage): 0.05 g, HCQ: 10 mL and 200 mg/L)

Table 5. Isotherm parameters of HCQ adsorption on κ C/Sa hydrogel using different models

Model	Parameter	κ C/Sa hydrogel
Freundlich	k_F	1.32801
	n_F	0.984446
	R^2	0.9902
Temkin	B	35.556
	K_T	0.136709
Langmuir	R^2	0.9463
	q_m	625
	K_L	0.0025
	R^2	0.8131

attitude of HCQ on hydrogel. Fig. 11 a shows the adsorption isotherm of HCQ at the overfit.

It was found that the adsorption of κ C/Sa hydrogel on HCQ was in good agreement with the pseudo-second-order kinetics, and the correlation coefficient was 100%. Three isotherm models (Freundlich, Langmuir, and Temkin models) were adopted for dataset fitting in order to better explain the adsorption process, as illustrated in Fig. 11. Table 4 displays the evaluation parameters for the model. The Langmuir model, however, cannot accurately predict the adsorption behavior of hydrogels in real-world studies [45], which should be attributed to the gel's structure and frequently misunderstood isotherm features. In the adsorption procedure itself, the gel adsorption data was found to best fit the Freundlich model based on the

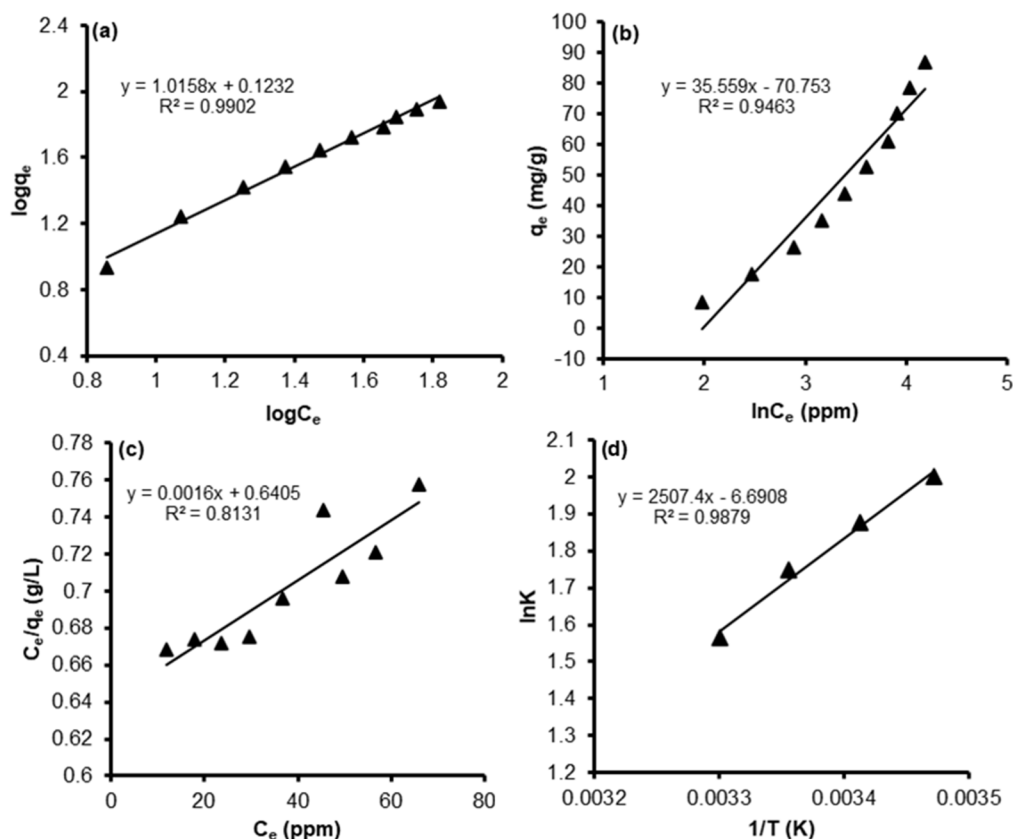


Fig 11. Adsorption isotherms on HCQ adsorption of κ C/Sa hydrogel, graphical graphs showing the fits of various models for adsorption isotherms: (a) Freundlich, (b) Temkin, (c) Langmuir, (d) Van Hove plot of κ C/Sa hydrogel

Table 6. Thermodynamic parameters of κ C/Sa hydrogel

Temperature (K)	ΔG° (kJ mol ⁻¹)	ΔH° (kJ mol ⁻¹)	ΔS° (J mol ⁻¹)
288	-4.79126		
293	-4.57189		
298	-4.32841	-20.8465	-55.4299
303	-3.94154		

isotherm fitting results. Additionally, a good fit with the Freundlich model was attained, illuminating the gel's extremely uneven surface. These findings imply the existence of several adsorption sites in the κ C/Sa hydrogel and the possibility of physical and chemical interactions between HCQ and the hydrogel [46-47]. Fig. 11(c) and 11(d) show the Temkin and Van Hove plots, respectively, of κ C/Sa hydrogel, which explain the negative value of ΔH (-20.8465236 kJ mol⁻¹) as shown in Table 6, which indicates the exothermic nature of adsorption.

CONCLUSION

The polysaccharide-based hydrogel κ C/Sa was prepared by cross-linking with *N,N'*-methylenebisacrylamide and exhibited high mechanical properties and excellent HCQ adsorption performance. It was found that due to the sulfate group (OSO₃) to Carrageenan molecule, κ -carrageenan can effectively improve the adsorption capacity of 500 ppm HCQ (89 mg/g) and the adsorption capacity of alginate/carrageenan composite gel for HCQ removal rate. The compressive strength and elasticity of Carrageenan composite gel can be successfully improved by sodium alginate, as well as its other mechanical characteristics. The combined gels' yield stress and storage modulus both dramatically increased. Carrageenan and sodium alginate's distinctive peaks remained in the FTIR spectrum, demonstrating that the

two materials were successfully bonded together. Because HCQ existed in various forms at various pHs, the results demonstrated that the pH of the solution had a significant impact on the adsorption process of the κ C/Sa hydrogel. Additionally, the hydrogel's carboxyl groups have a significant function. This study shows better mechanical and adsorption characteristics of natural of biopolymer and offers a theoretical and practical foundation for the creation of alternative systems.

■ ACKNOWLEDGMENTS

Authors would like to thank the University of Al-Qadisiyah, College of Education for Pure Sciences morale and self-help the professors for the laboratories used inside the university that is affiliated to the Iraqi Ministry of Education.

■ AUTHOR CONTRIBUTIONS

Mohammed Kassim Al-Hussainawy: performing simulation, methodology, data collection, conceptualization, investigation, formal analysis and visualization, writing (original draft), supervised. Layth Sameer Al-Hayder: formal analysis, visualization, investigation, writing (original draft), writing (review and editing), methodology, writing (review and editing), conceptualization, data collection. The whole manuscript was approved by all authors.

■ REFERENCES

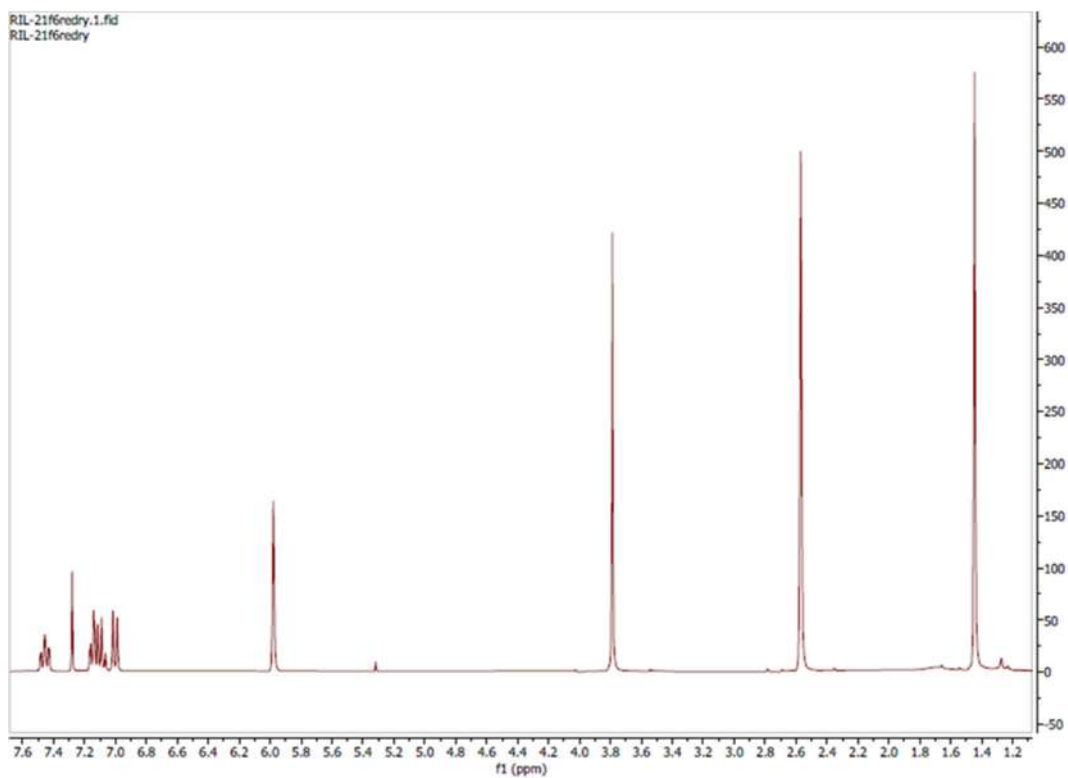
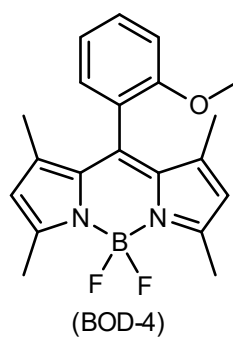
- [1] de Franco, M.A.E., de Carvalho, C.B., Bonetto, M.M., de Pelegrini Soares, R., and Féris, L.A., 2018, Diclofenac removal from water by adsorption using activated carbon in batch mode and fixed-bed column: Isotherms, thermodynamic study and breakthrough curves modeling, *J. Cleaner Prod.*, 181, 145–154.
- [2] Babić, S., Dabić, D., and Ćurković, L., 2017, Fate of hydroxychloroquine in the aquatic environment, *Proceedings of the 15th International Conference on Environmental Science and Technology*, Rhodes, Greece.
- [3] Kebede, T.G., Seroto, M.B., Chokwe, R.C., Dube, S., and Nindi, M.M., 2020, Adsorption of antiretroviral (ARVs) and related drugs from environmental wastewaters using nanofibers, *J. Environ. Chem. Eng.*, 8 (5), 104049.
- [4] Parvinizadeh, F., and Daneshfar, A., 2019, Fabrication of a magnetic metal–organic framework molecularly imprinted polymer for extraction of anti-malaria agent hydroxychloroquine, *New J. Chem.*, 43 (22), 8508–8516.
- [5] Nuri, E., Taraborelli, M., Andreoli, L., Tonello, M., Gerosa, M., Calligaro, A., Argolini, L.M., Kumar, R., Pengo, V., Meroni, P.L., Ruffatti, A., and Tincani, A., 2017, Long-term use of hydroxychloroquine reduces antiphospholipid antibodies levels in patients with primary antiphospholipid syndrome, *Immunol. Res.*, 65 (1), 17–24.
- [6] Mahase, E., 2020, Covid-19: WHO halts hydroxychloroquine trial to review links with increased mortality risk, *BMJ*, 369, m2126.
- [7] Li, X., Wang, Y., Agostinis, P., Rabson, A., Melino, G., Carafoli, E., Shi, Y., and Sun, E., 2020, Is hydroxychloroquine beneficial for COVID-19 patients?, *Cell Death Dis.*, 11 (7), 512.
- [8] Bensalah, N., Midassi, S., Ahmad, M.I., and Bedoui, A., 2020, Degradation of hydroxychloroquine by electrochemical advanced oxidation processes, *Chem. Eng. J.*, 402, 126279.
- [9] Gümüş, D., and Gümüş, F., 2022, Removal of hydroxychloroquine using engineered biochar from algal biodiesel industry waste: Characterization and design of experiment (DoE), *Arabian J. Sci. Eng.*, 47 (6), 7325–7334.
- [10] Özçimen, D., İnan, B., Morkoç, O., and Efe, A., 2017, A review on algal biopolymers, *J. Chem. Eng. Res. Updates*, 4, 7–14.
- [11] Jadhav, A.C., and Jadhav, N.C., 2021, "Treatment of textile wastewater using adsorption and adsorbents" in *Sustainable Technologies for Textile Wastewater Treatments*, Eds. Muthu, S.S., Woodhead Publishing, Sawston, United Kingdom, 235–273.
- [12] Dabić, D., Babić, S., and Škorić, I., 2019, The role of photodegradation in the environmental fate of hydroxychloroquine, *Chemosphere*, 230, 268–277.
- [13] Zauoak, A., Jebali, S., Chouchane, H., and Jelassi, H., 2022, Impact of gamma-irradiation on the

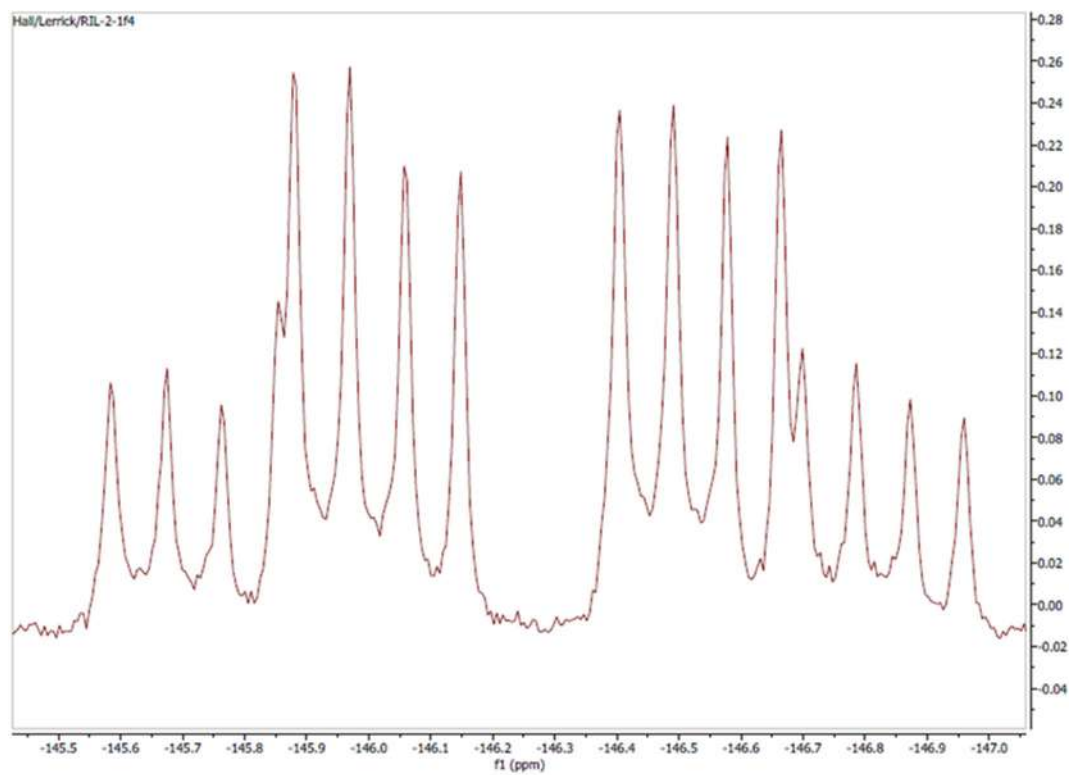
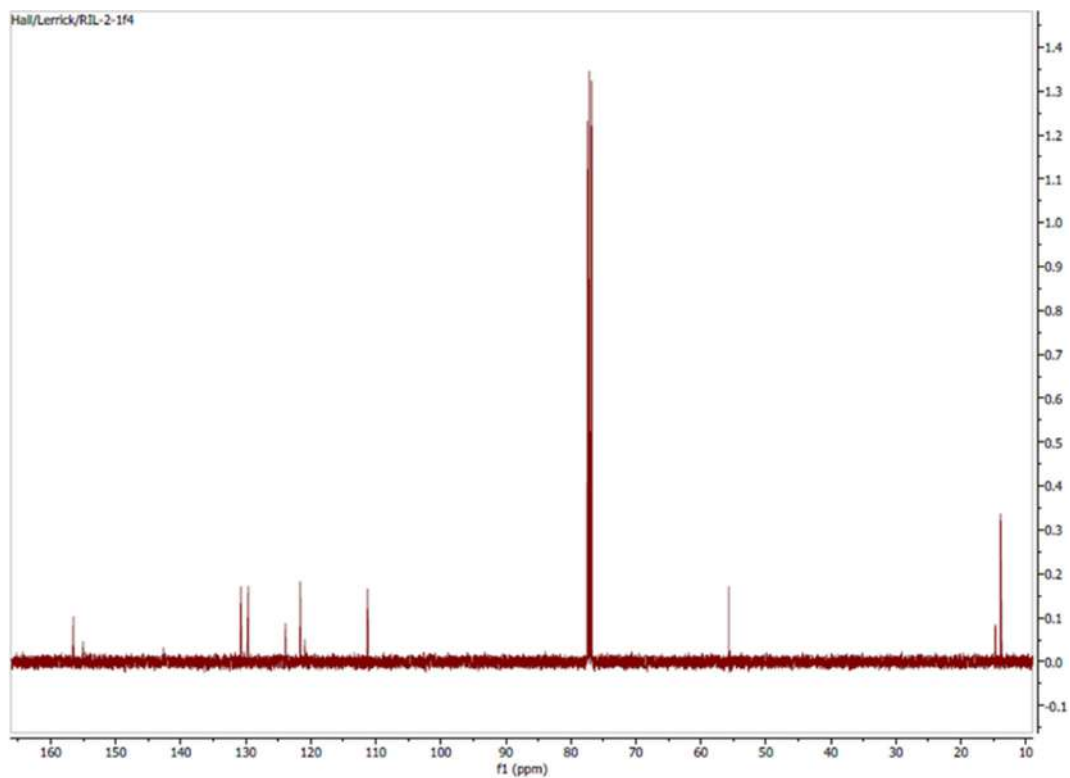
- degradation and mineralization of hydroxychloroquine aqueous solutions, *Int. J. Environ. Sci. Technol.*, 2022, 1–10.
- [14] Dias, J.M., Alvim-Ferraz, M.C.M., Almeida, M.F., Rivera-Utrilla, J., and Sánchez-Polo, M., 2007, Waste materials for activated carbon preparation and its use in aqueous-phase treatment: A review, *J. Environ. Manage.*, 85 (4), 833–846.
- [15] Yadav, A., Bagotia, N., Sharma, A.K., and Kumar, S., 2021, Advances in decontamination of wastewater using biomass-based composites: A critical review, *Sci. Total Environ.*, 784, 147108.
- [16] Gao, X., Zhang, Y., and Zhao, Y., 2017, Biosorption and reduction of Au (III) to gold nanoparticles by thiourea modified alginate, *Carbohydr. Polym.*, 159, 108–115.
- [17] Wang, S., Vincent, T., Faur, C., and Guibal, E., 2018, A comparison of palladium sorption using polyethylenimine impregnated alginate-based and carrageenan-based algal beads, *Appl. Sci.*, 8 (2), 264.
- [18] Ates, B., Koytepe, S., Ulu, A., Gurses, C., and Thakur, V.K., 2020, Chemistry, structures, and advanced applications of nanocomposites from biorenewable resources, *Chem. Rev.*, 120 (17), 9304–9362.
- [19] Thakur, S., Sharma, B., Verma, A., Chaudhary, J., Tamulevicius, S., and Thakur, V.K., 2018, Recent progress in sodium alginate based sustainable hydrogels for environmental applications, *J. Cleaner Prod.*, 198, 143–159.
- [20] He, J., and Chen, J.P., 2014, A comprehensive review on biosorption of heavy metals by algal biomass: Materials, performances, chemistry, and modeling simulation tools, *Bioresour. Technol.*, 160, 67–78.
- [21] Pan, L., Wang, Z., Zhao, X., and He, H., 2019, Efficient removal of lead and copper ions from water by enhanced strength-toughness alginate composite fibers, *Int. J. Biol. Macromol.*, 134, 223–229.
- [22] Wen, R., Tu, B., Guo, X., Hao, X., Wu, X., and Tao, H., 2020, An ion release controlled Cr(VI) treatment agent: Nano zero-valent iron/carbon/alginate composite gel, *Int. J. Biol. Macromol.*, 146, 692–704.
- [23] Shamsudin, M.S., Azha, S.F., Sellaoui, L., Badawi, M., Bonilla-Petriciolet, A., and Ismail, S., 2022, Performance and interactions of diclofenac adsorption using alginate/carbon-based films: Experimental investigation and statistical physics modelling, *Chem. Eng. J.*, 428, 131929.
- [24] Yadav, S., Asthana, A., Singh, A.K., Chakraborty, R., Vidya, S.S., Susan, M.A.B.H., and Carabineiro, S.A.C., 2021, Adsorption of cationic dyes, drugs and metal from aqueous solutions using a polymer composite of magnetic/ β -cyclodextrin/activated charcoal/Na alginate: Isotherm, kinetics and regeneration studies, *J. Hazard. Mater.*, 409, 124840.
- [25] Mandal, B., and Ray, S.K., 2014, Swelling, diffusion, network parameters and adsorption properties of IPN hydrogel of chitosan and acrylic copolymer, *Mater. Sci. Eng., C*, 44, 132–143.
- [26] Abate, G.Y., Alene, A.N., Habte, A.T., and Getahun, D.M., 2020, Adsorptive removal of malachite green dye from aqueous solution onto activated carbon of *Catha edulis* stem as a low cost bio-adsorbent, *Environ. Syst. Res.*, 9 (1), 29.
- [27] Hosseini, S.M., Farmany, A., Alikhani, M.Y., Taheri, M., Asl, S.S., Alamian, S., and Arabestani, M.R., 2022, Co-delivery of doxycycline and hydroxychloroquine using CdTe-labeled solid lipid nanoparticles for treatment of acute and chronic brucellosis, *Front. Chem.*, 10, 890252.
- [28] Abdala Díaz, R.T., Casas Arrojo, V., Arrojo Agudo, M.A., Cárdenas, C., Dobretsov, S., and Figueroa, F.L., 2019, Immunomodulatory and antioxidant activities of sulfated polysaccharides from *Laminaria ochroleuca*, *Porphyra umbilicalis*, and *Gelidium corneum*, *Mar. Biotechnol.*, 21 (4), 577–587.
- [29] Thangeeswari, T., George, A.T., and Kumar, A.A., 2016, Optical properties and FTIR studies of cobalt doped ZnO nanoparticles by simple solution method, *Indian J. Sci. Technol.*, 9 (1), 1–4.
- [30] Al-Hussainawy, M.K., Mehdi, Z.S., Jasim, K.K., Alshamsi, H.A., Saud, H.R., and Kyhoiesh, H.A.K., 2022, A single rapid route synthesis of magnetite/chitosan nanocomposite: Competitive study, *Results Chem.*, 4, 100567.

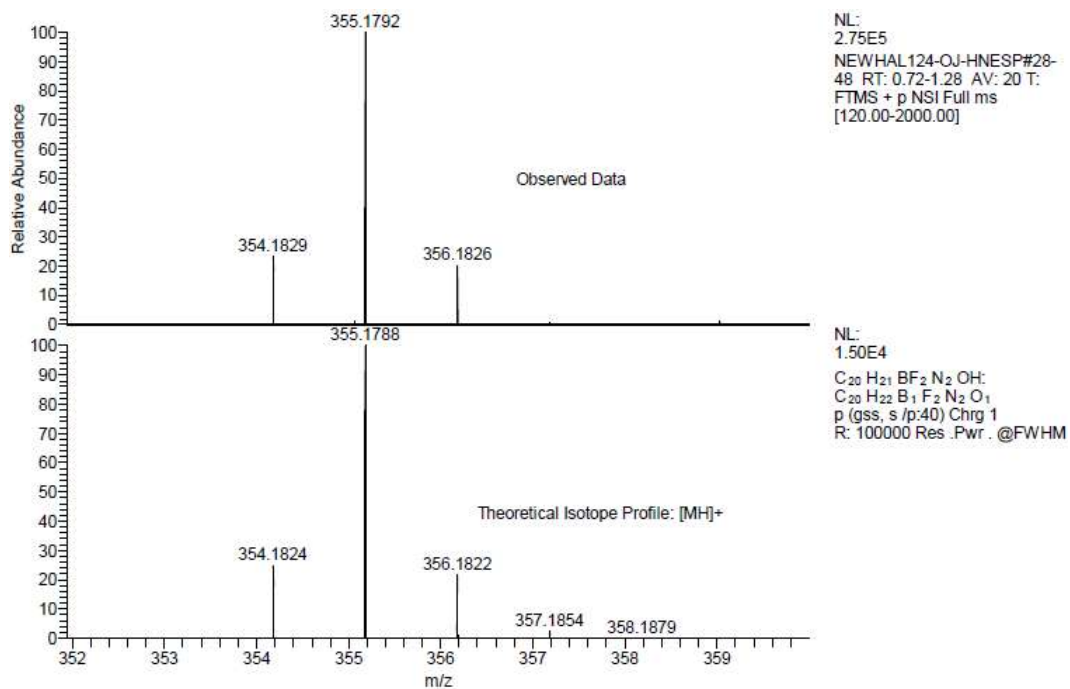
- [31] Işık, B., and Uğraşkan, V., 2021, Adsorption of methylene blue on sodium alginate–flax seed ash beads: Isotherm, kinetic and thermodynamic studies, *Int. J. Biol. Macromol.*, 167, 1156–1167.
- [32] Al-Taweel, S.S., Saud, H.R., Kadhum, A.A.H., and Takriff, M.S., 2019, The influence of titanium dioxide nanofiller ratio on morphology and surface properties of TiO₂/chitosan nanocomposite, *Results Phys.*, 13, 102296.
- [33] Jebur, M.H., Albdere, E.A., Al-Hussainawy, M.K., and Alwan, S.H., 2022, Synthesis and characterization of new 1,3-oxazepine-4,7-dione compounds from 1,2-diaminobenzene, *Int. J. Health Sci.*, 6 (S4), 4578–4589.
- [34] Smith, B.C., 2019, Organic nitrogen compounds V: Amine salts, *Spectroscopy*, 34 (9), 30–37.
- [35] Nadeem, U., and Datta, M., 2014, Adsorption studies on zinc(II) ions on biopolymer composite beads of alginate-fly ash, *Eur. Chem. Bull.*, 3 (7), 682–691.
- [36] Riyandari, B.A., Suherman, S., and Siswanta, D., 2018, The physico-mechanical properties and release kinetics of eugenol in chitosan-alginate polyelectrolyte complex films as active food packaging, *Indones. J. Chem.*, 18 (1), 82–91.
- [37] Yu, F., Cui, T., Yang, C., Dai, X., and Ma, J., 2019, κ -Carrageenan/sodium alginate double-network hydrogel with enhanced mechanical properties, anti-swelling, and adsorption capacity, *Chemosphere*, 237, 124417.
- [38] Gu, L., McClements, D.J., Li, J., Su, Y., Yang, Y., and Li, J., 2021, Formulation of alginate/carrageenan microgels to encapsulate, protect and release immunoglobulins: Egg Yolk IgY, *Food Hydrocolloids*, 112, 106349.
- [39] El Badawy, A.M., Luxton, T.P., Silva, R.G., Scheckel, K.G., Suidan, M.T., and Tolaymat, T.M., 2010, Impact of environmental conditions (pH, ionic strength, and electrolyte type) on the surface charge and aggregation of silver nanoparticles suspensions, *Environ. Sci. Technol.*, 44 (4), 1260–1266.
- [40] Gao, L., Wang, Y., Yan, T., Cui, L., Hu, L., Yan, L., Wei, Q., and Du, B., 2015, A novel magnetic polysaccharide–graphene oxide composite for removal of cationic dyes from aqueous solution, *New J. Chem.*, 39 (4), 2908–2916.
- [41] Lei, C., Wen, F., Chen, J., Chen, W., Huang, Y., and Wang, B., 2021, Mussel-inspired synthesis of magnetic carboxymethyl chitosan aerogel for removal cationic and anionic dyes from aqueous solution, *Polymer*, 213, 123316.
- [42] Tang, J., Huang, J., Tun, T., Liu, S., Hu, J., and Zhou, G., 2021, Cu(II) and Cd(II) capture using novel thermosensitive hydrogel microspheres: Adsorption behavior study and mechanism investigation, *J. Chem. Technol. Biotechnol.*, 96 (8), 2382–2389.
- [43] Rahimi, R., Solimannejad, M., and Farghadani, M., 2021, Adsorption of chloroquine and hydroxychloroquine as potential drugs for SARS-CoV-2 infection on BC₃ nanosheets: A DFT study, *New J. Chem.*, 45 (38), 17976–17983.
- [44] Chen, T., Da, T., and Ma, Y., 2021, Reasonable calculation of the thermodynamic parameters from adsorption equilibrium constant, *J. Mol. Liq.*, 322, 114980.
- [45] Liao, Q., Rong, H., Zhao, M., Luo, H., Chu, Z., and Wang, R., 2022, Strong adsorption properties and mechanism of action with regard to tetracycline adsorption of double-network polyvinyl alcohol-copper alginate gel beads, *J. Hazard. Mater.*, 422, 126863.
- [46] Wang, C.J., Li, Z., and Jiang, W.T., 2011, Adsorption of ciprofloxacin on 2:1 dioctahedral clay minerals, *Appl. Clay Sci.*, 53 (4), 723–728.
- [47] Han, D., Zhao, H., Gao, L., Qin, Z., Ma, J., Han, Y., and Jiao, T., 2021, Preparation of carboxymethyl chitosan/phytic acid composite hydrogels for rapid dye adsorption in wastewater treatment, *Colloids Surf., A*, 628, 127355.

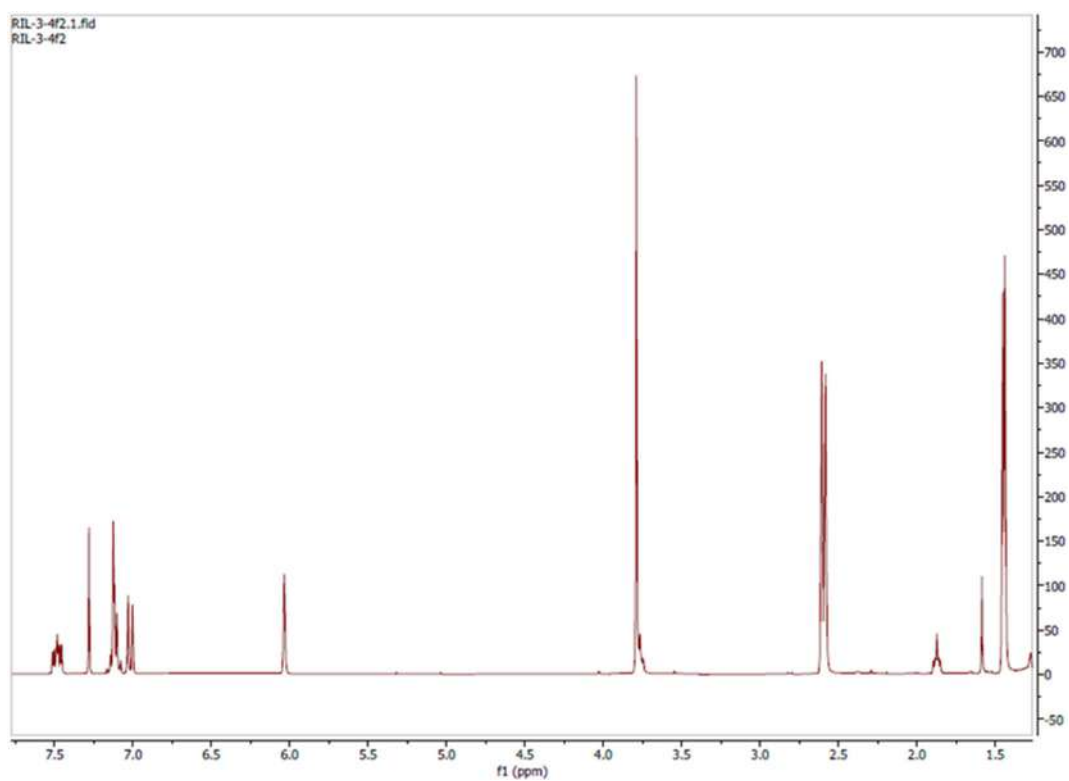
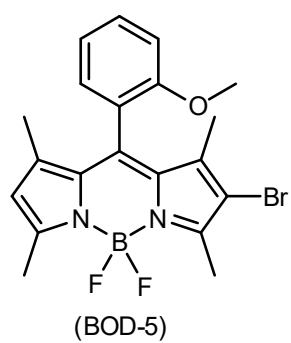
Supplementary Data

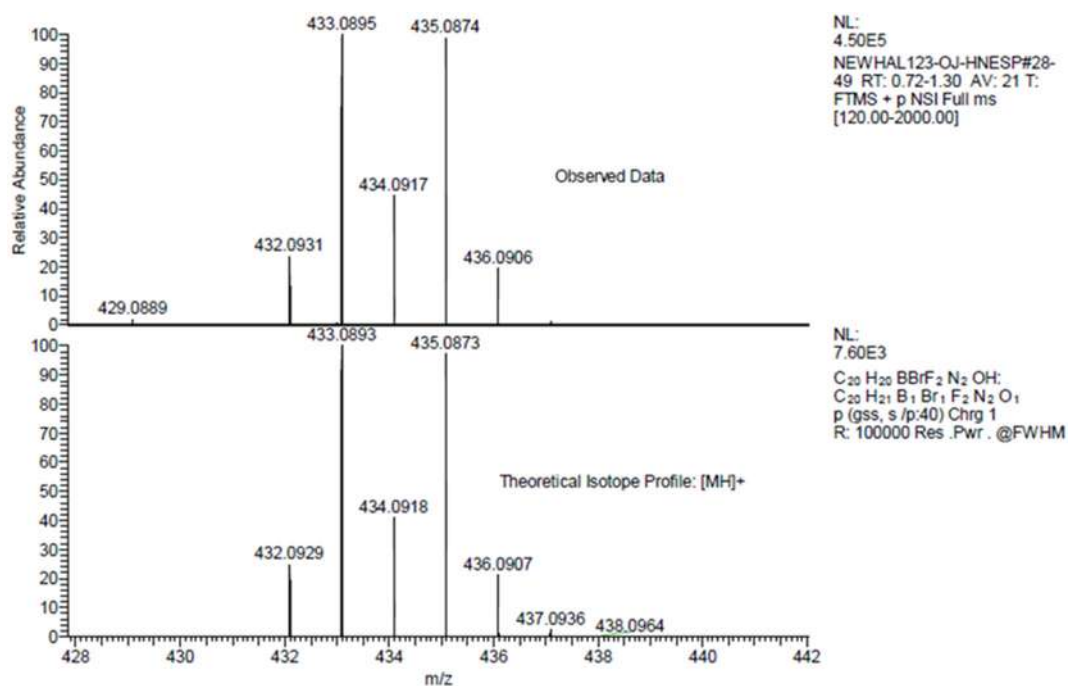
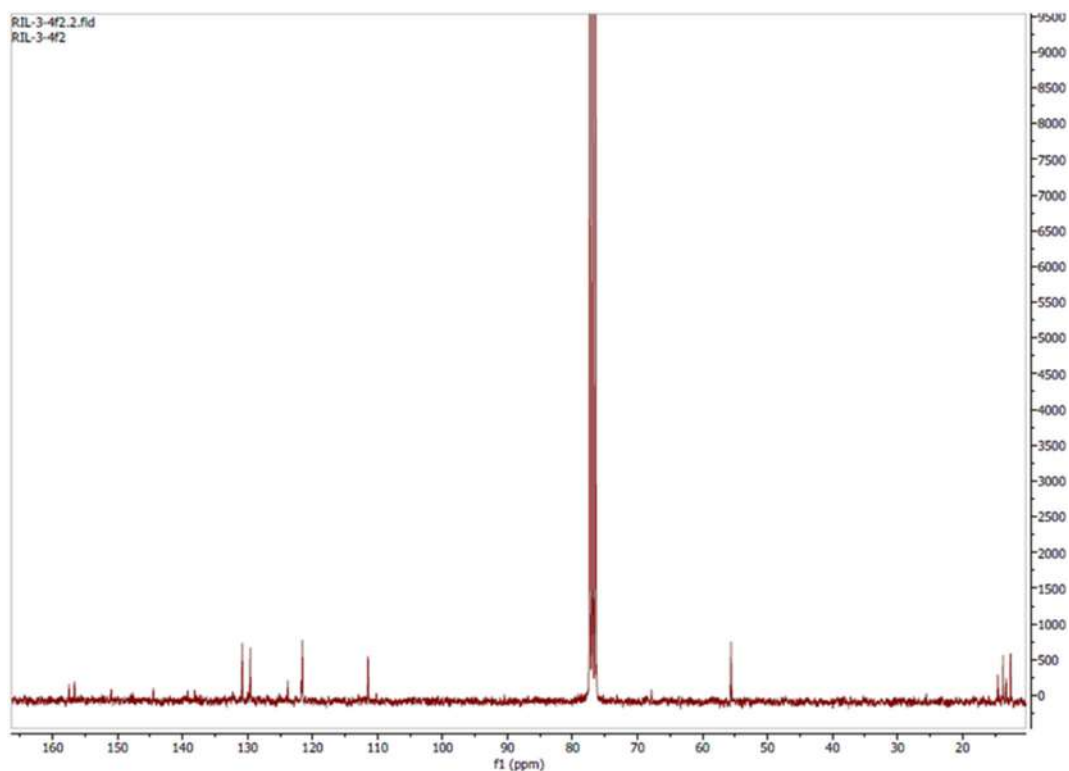
This supplementary data is a part of a paper entitled “T-grafting BODIPY-Based Photosensitizers: The Synthesis of 2,6-Diethylacrylic-8-(*o*-methoxyphenyl)BODIPY and Its DSSC Performance”.

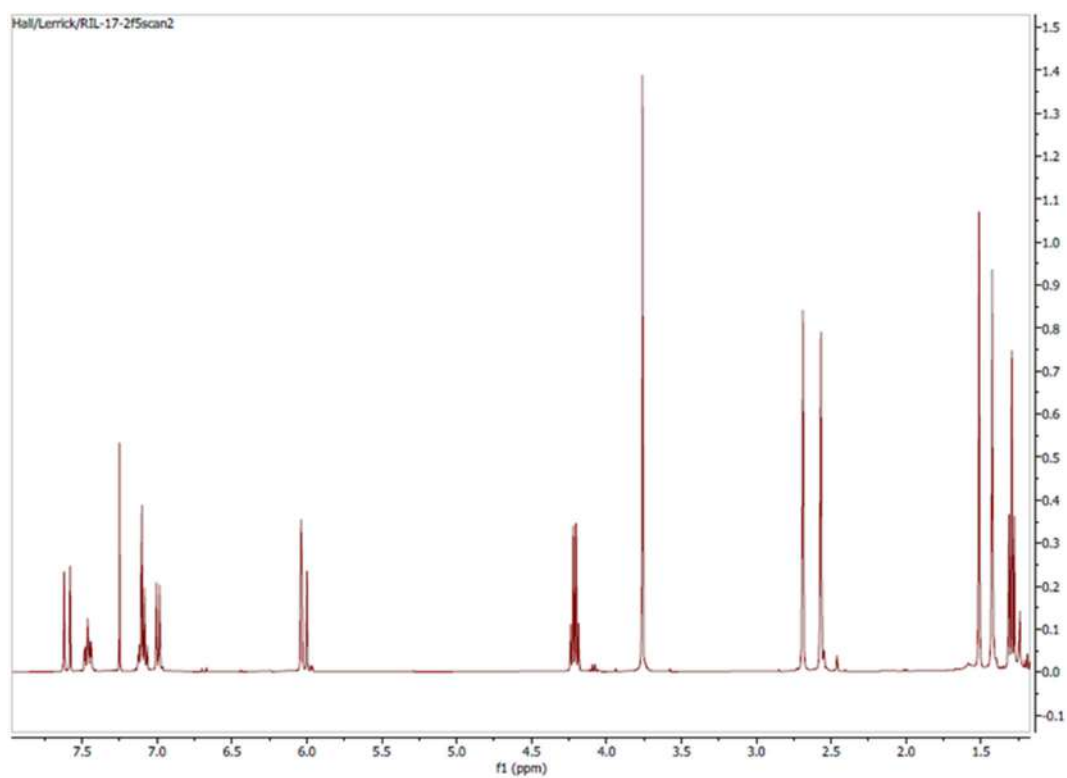
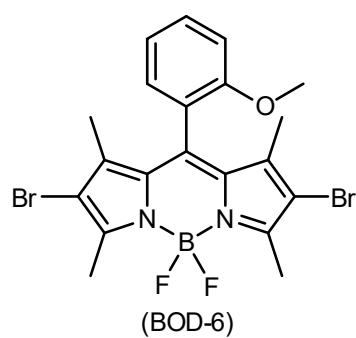


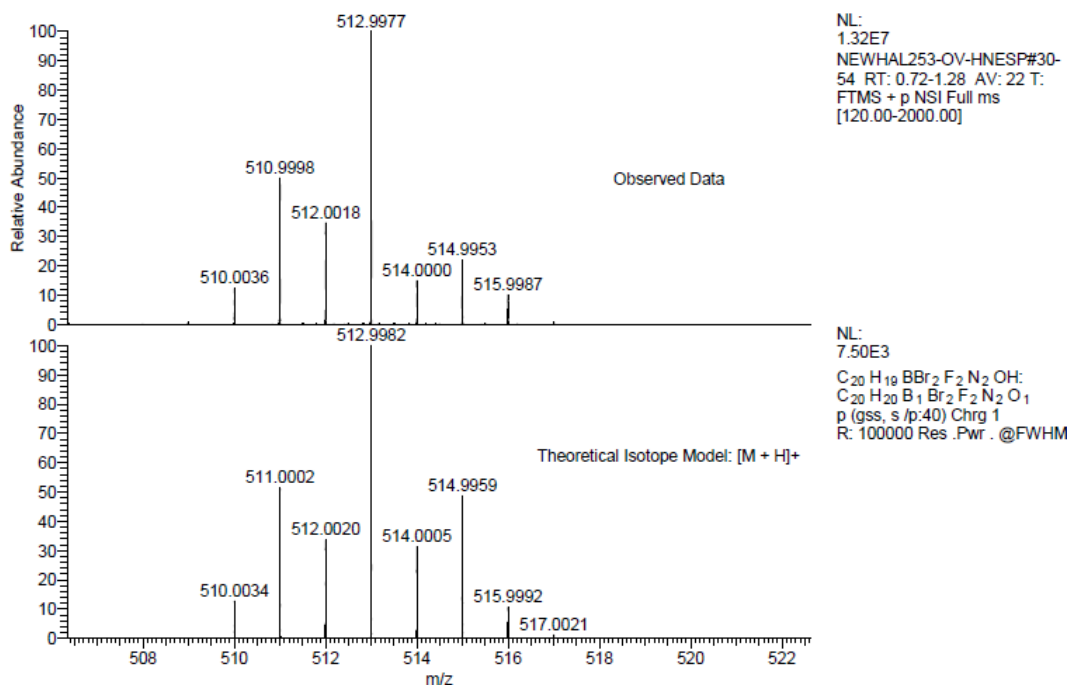
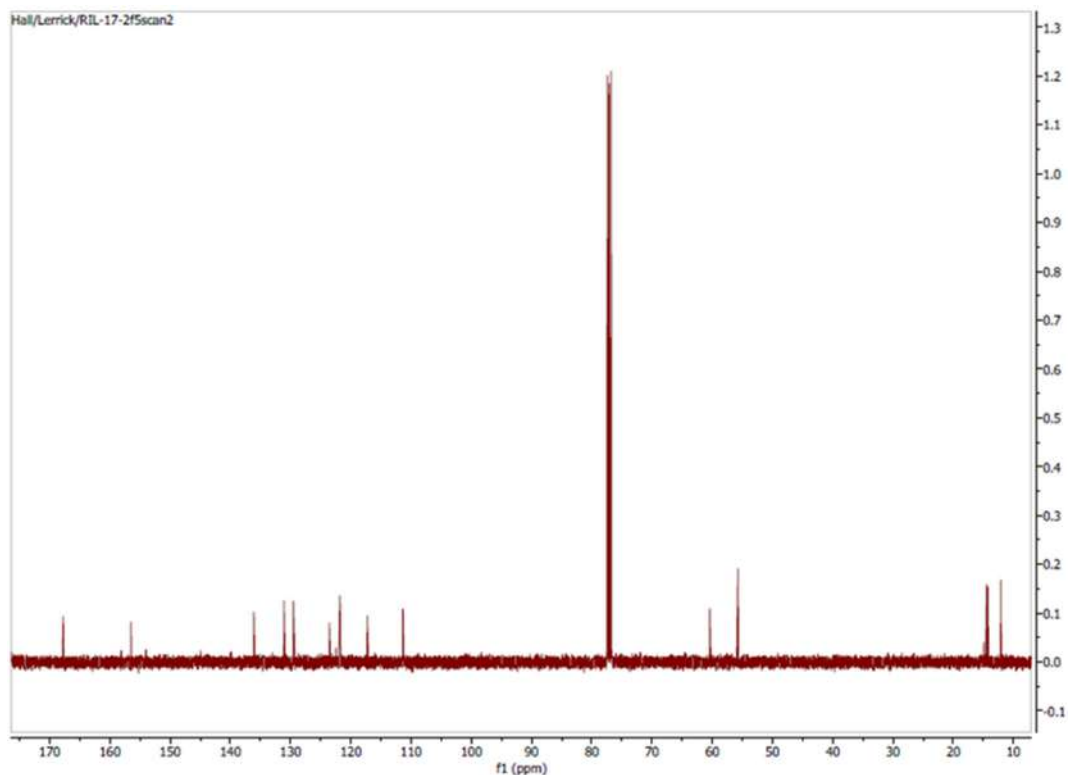


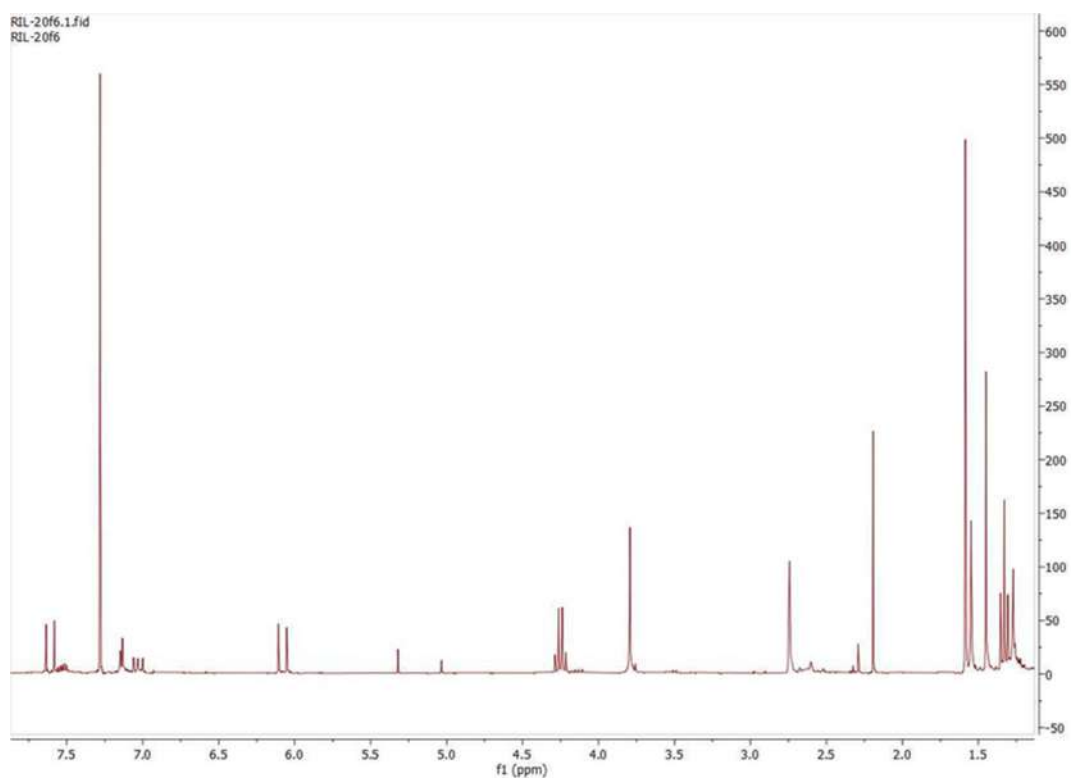
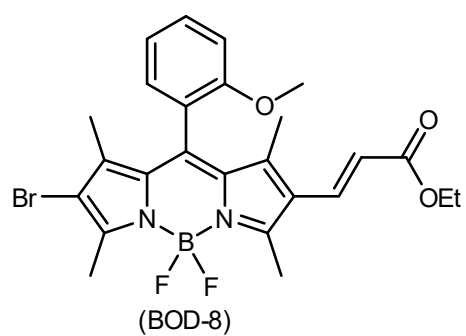


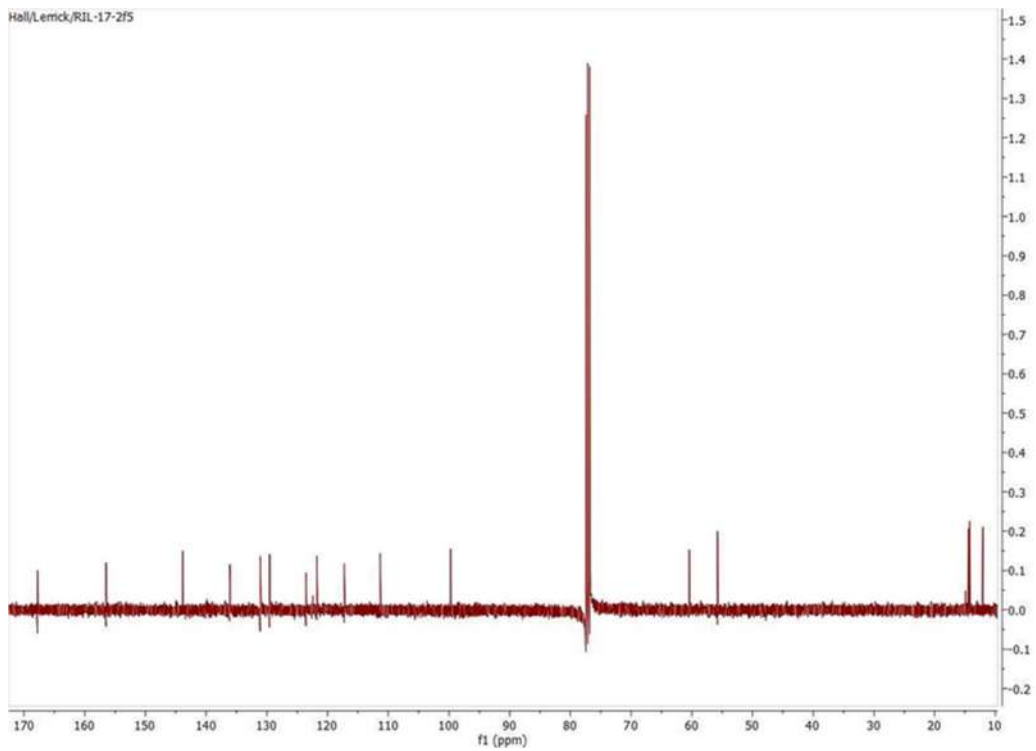


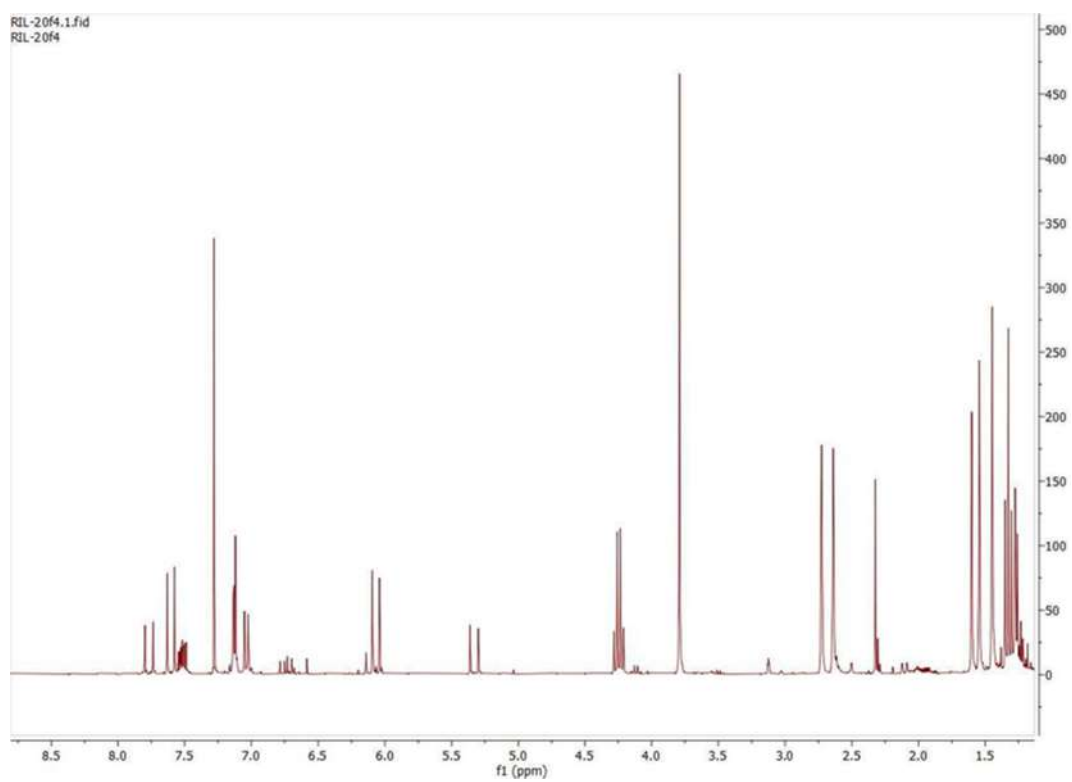
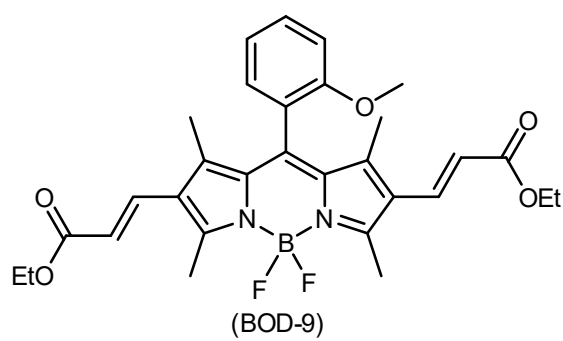


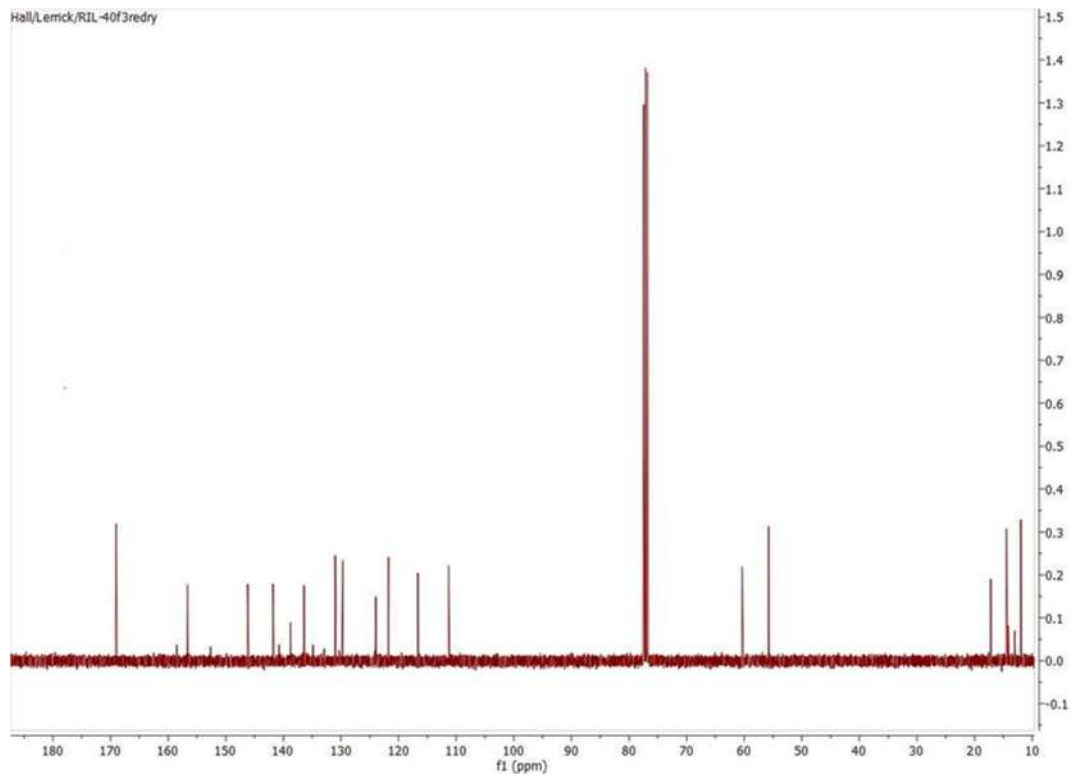




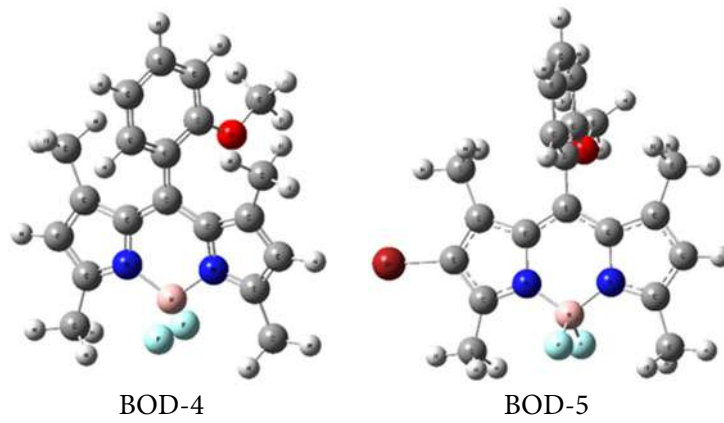








COMPUTATIONAL STUDY



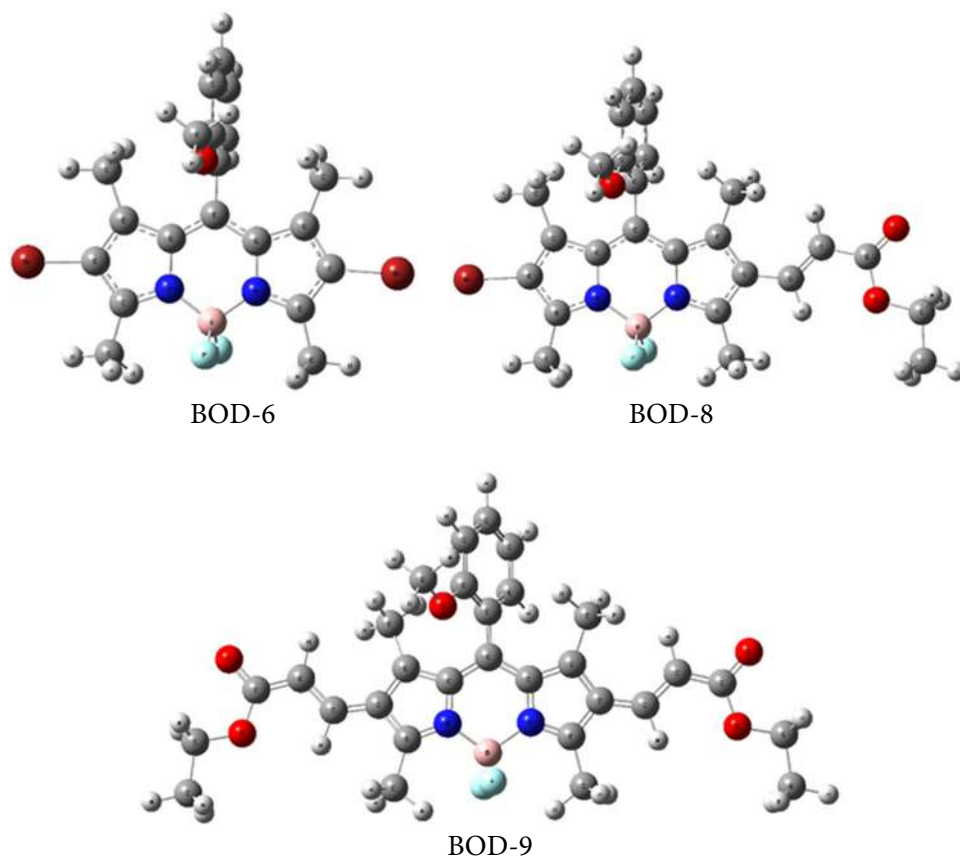
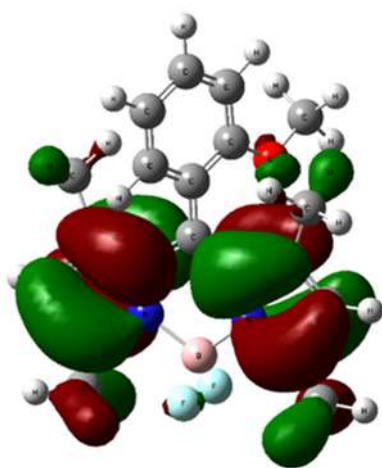
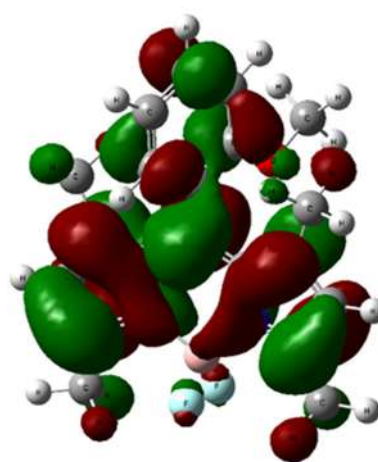


Table 1. The energy values, the MO energy of HOMO, LUMO levels, ΔE (in eV), and dipole moment μ (in Debye's) for BOD-4, 5, 6, 8, and 9

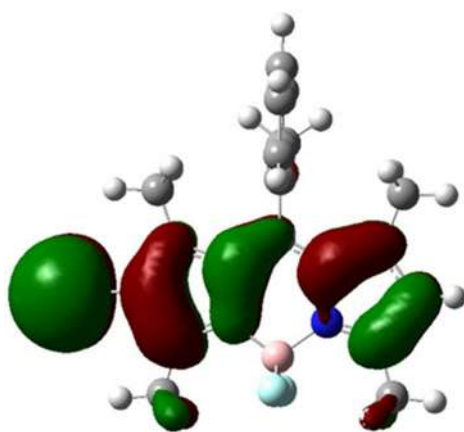
Quantity	BOD-4	BOD-5	BOD-6	BOD-8	BOD-9
Total energy (a.u.)	-1177.59	-1196.87	-1209.63	-1541.42	-1873.20
HOMO	-0.214 au (-5.82337 eV)	-0.210 au (-5.71431 eV)	-0.21696 au (-5.90370 eV)	-0.216 au (-5.877576 eV)	-0.21658 au (-5.893358 eV)
LUMO	-0.095 au (-2.58514 eV)	-0.102 au (-2.775522 eV)	-0.1103 au (-2.99321 eV)	-0.113 au (-3.074843 eV)	-0.11595 au (-3.155115 eV)
ΔE	3.23823 eV	2.938788 eV	2.91049 eV	2.802733 eV	2.738243 eV
M (Debye)	7.3033	8.0650	7.8595	5.7075	3.0751



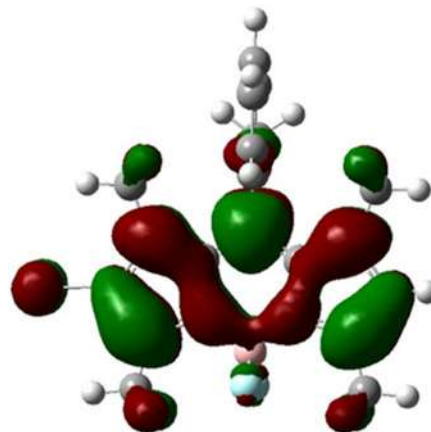
HOMO (BOD-4)



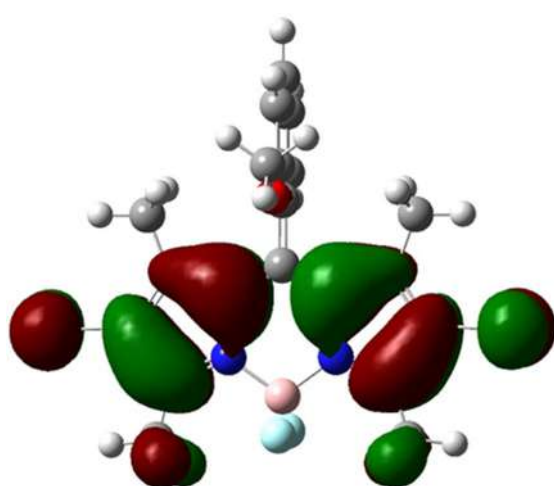
LUMO (BOD-4)



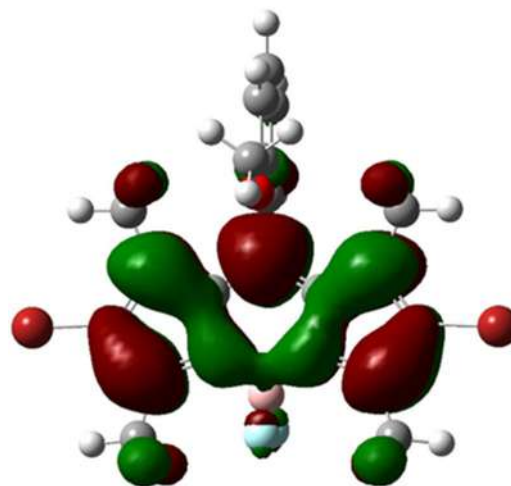
HOMO (BOD-5)



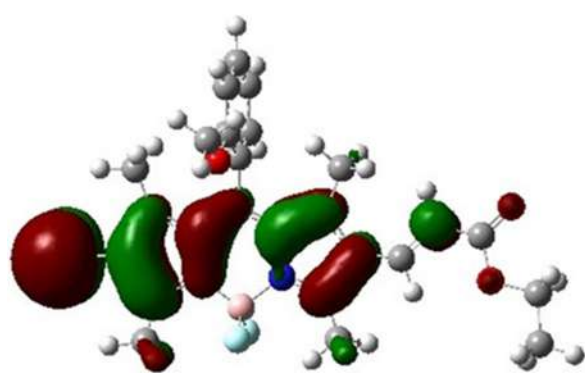
LUMO (BOD-5)



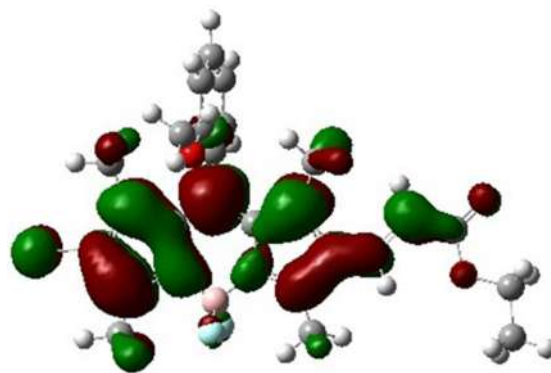
HOMO (BOD-6)



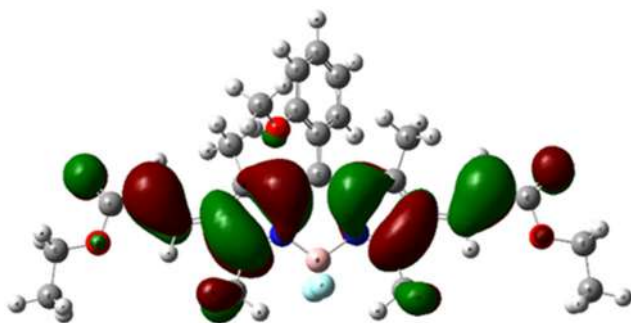
LUMO (BOD-6)



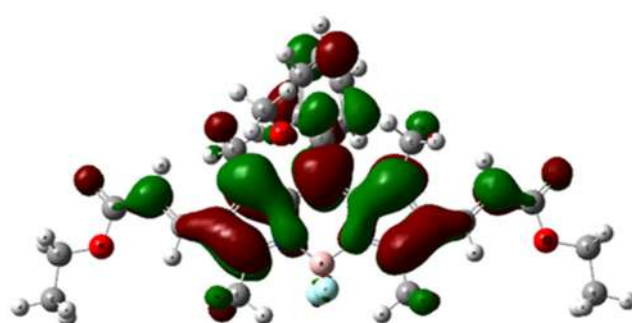
HOMO (BOD-8)



LUMO (BOD-8)



HOMO (BOD-9)



LUMO (BOD-9)

T-grafting BODIPY-Based Photosensitizers: The Synthesis of 2,6-Diethylacrylic-8-(*o*-methoxyphenyl)BODIPY and Its DSSC Performance

Reinner Ishaq Lerrick^{1*}, Wastiana Bere¹, Meliana Da Silva Braga¹, Agus Supriyanto², and Ali Hashem Essa³

¹Department of Chemistry, Faculty of Science and Engineering, University of Nusa Cendana, Jl. Adi Sucipto, Penfui-Kupang 85118, NTT, Indonesia

²Department of Physics, Faculty of Mathematics and Natural Sciences, Universitas Sebelas Maret, Jl. Ir. Sutami 36A, Kentingan, Surakarta 57126, Indonesia

³Department of Chemistry, College of Science, University of Basrah, Basrah 61004, Iraq

* Corresponding author:

tel: +62-8113837791

email: reinner_lerrick@staf.undana.ac.id

Received: August 7, 2022

Accepted: November 22, 2022

DOI: 10.22146/ijc.76919

Abstract: A new T-grafting photosensitizer of Dye-Sensitized Solar Cell (DSSC) has been developed by aligning Donor-Acceptor (D-A) group in an axially chiral BODIPY. Synthesis of the dye was conducted over a linear approach involving one-pot, non-oxidative synthesis of 1,3,5,7-tetramethyl-8-(*o*-methoxyphenyl)BODIPY, bromination, and finally C2/C6 ethyl acrylate Pd-Heck coupling to produce 65% of 2-ethylacrylic-1,3,5,7-tetramethyl-8-(*o*-methoxyphenyl)BODIPY (BOD-8) and 35% of 2,6-diethylacrylic-1,3,5,7-tetramethyl-8-(*o*-methoxyphenyl)BODIPY (BOD-9), both characterized by the appearance of acrylic alkenes at 6.05, and 7.63 ppm for BOD-8, and the additional 5.43, 7.80 ppm doublet peaks for BOD-9. The resulting dye showed excellent photon harvesting-related photovoltaic properties and electronic injection and regeneration processes where the acrylic esters were found to be the Donor and the aryl was the Acceptor. Eventually, the dye produced a current at 0.5% efficiency, similar to the horizontal D-A DSSC photosensitizer design.

Keywords: DSSC photosensitizer; T-grafted alignment; axially chiral BODIPY

■ INTRODUCTION

Boron DiPyrromethanes (BODIPYs, (BOD-1), Fig. 1), 4,4-difluoro-4-bora-3a,4a-diaza-s-indacene an IUPAC name, are among the most versatile organic photoluminescence compound commonly applied in optoelectronic based organic semiconductors [1], chemical and biochemical sensors [2], molecular probes, photo dynamic therapy (PDT) [3] and Photo Thermal Therapy (PTT), and photo Acoustic Imaging (PAI) [4]. These facts are driven by their ease of accessible spectroscopic fine-tuned properties through the structure derivatizations, high photophysical properties, and high stabilities.

Recently, we developed axially chiral BODIPY (Ax*-BODIPY, (BOD-2)) from rotational-locked meso-aryl BODIPYs [5], those in which the perpendicular ortho-substituted phenyl moiety at C8 of the dipyrromethene

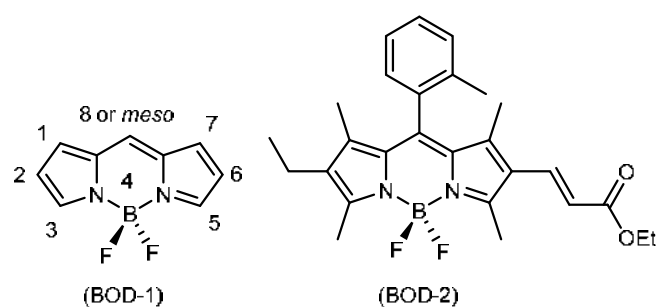


Fig 1. General structure and numbering of BODIPY (BOD-1) and Ax*-BODIPY developed (BOD-2)

core could not intramolecularly rotate, generating high quantum yield and longer lifetime rotor-based fluorophores for intracellular pH and viscosity sensing [6]. Meanwhile, the chemically distinguished acrylate group attached to the dipyrromethene proved to be a π -extended-based red-shift [7] and HOMO-LUMO band

gap (E_g) energy modifier due to its electron-withdrawing characteristic (EWG), and an anchoring group functioned essentially in Dye-Sensitized Solar Cell (DSSC) [8]. All these features allow for further organic photovoltaic (OPV) solar cell-related modifications of the molecules.

We, therefore, intend to employ further such orientation of the meso-aryl-lateral acrylate in the Ax^+ -BODIPY to design T-grafting DSSC photosensitizers (Fig. 2), a new Donor (D)-Acceptor (A) alignment on the BODIPY scaffold in which the aryl (proposed to be the D) at C8 and two acrylates (proposed to be the A) at C2 and C6, resembling that of current Akkaya's vertical (C8-D to C3 or C5-A), horizontal (C2-D to C-6-A), cross-conjugated BODIPY (C3, C5, and C7-D to C2-A) [9], and the pioneering Fukuzumi's D-A design [10], those which have been proven to increase the incident photon-to-current efficiency (IPCE) of the DSSC dyes.

EXPERIMENTAL SECTION

Materials

All the chemicals used in this research were obtained from Sigma Aldrich, TCI and Alfa Aesar in pure (99.9%) grade compounds. The solvents used in the reactions were dried, while the *n*-hexane (95% purity) used for column chromatography was re-distilled. The purification was done using silica gel column chromatography (flash, Kieselgel 60).

Instrumentation

The ^1H and ^{13}C -NMR spectra were obtained using 300.13 MHz and 75.47 MHz, respectively, on a Bruker Avance BVT3200 spectrometer, or 399.78 MHz and 100.53 MHz, respectively, using a Jeol JNM ECS400 spectrometer. The ^{19}F -NMR spectra were recorded at 376.17 MHz on a Jeol JNM ECS400 spectrometer. The Infrared analysis was performed using a Varian 800 FTIR Scimitar Series spectrometer scanning from 4000–600 cm^{-1} . The mass spectrometry analysis was done using a Micromass LCT Premier Mass Spectrometer in Electron Spray (ES) mode.

The UV-Vis and fluorescence spectra were recorded using a PerkinElmer Lambda 35 and DIGILAB HITACHI F-2500 FL spectrophotometer, respectively. The slit width was 2.5 nm for both excitation and emission. The DSSC solar cell performances were measured using Keithley type 2400A sourcemeter in the I-V parameter.

Procedure

Synthesis of 1,3,5,7-tetramethyl-8-(*o*-methoxyphenyl)BODIPY (BOD-4)

To a 50 mL round bottom flask was added 2-methoxybenzoylchloride (0.179 g, 1 mmol), DCM (25 mL) and 2,4-dimethylpyrrole (0.190 g, 2 mmol)

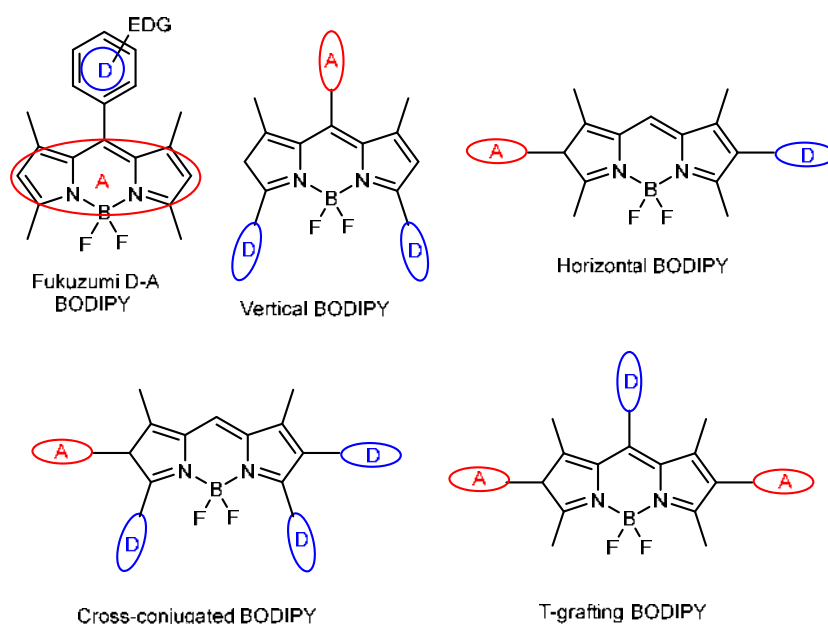


Fig 2. General type of D-A alignment on BODIPYs and the intent T-shape DSSC dye

sequentially. The solution was stirred overnight at room temperature under a nitrogen atmosphere. A 1 mL of *N,N*-diisopropyl-*N*-ethylamine was slowly added to the solution over 5 min, followed by 1 mL of $\text{BF}_3 \cdot \text{Et}_2\text{O}$ at 0 °C. The solution was further stirred for 3 h. The solution was washed with 2×25 mL of water and dried using MgSO_4 . The solvent was removed under reduced pressure to yield a dark brown solid residue. The crude product was then purified through column chromatography (*n*-hexane: ether = 15:1) to obtain an orange solid (BOD-4), 0.088 g (25%). R_f : 0.33 (UV active, petrol 40/60:ether = 1:1), m.p. = 242–243 °C, $^1\text{H-NMR}$ (300 MHz, CDCl_3): δ_{H} 1.45 (s, 6H, 2 Pyrrole CH_3), 2.57 (s, 6H, 2 Pyrrole CH_3), 3.79 (s, 3H, CH_3), 5.98 (s, 2H, 2 Pyrrole H), 7.00 (dd, $J = 8.4$, 0.9 Hz, 1H, ArH), 7.09 (td, $J = 7.3$, 0.9 Hz, 1H, ArH), 7.15 (dd, $J = 7.4$, 2.1 Hz, 1H, ArH), 7.46 (ddd, $J = 8.3$, 7.2, 2.1 Hz, 1H, ArH), $^{13}\text{C-NMR}$, (100 MHz, CDCl_3): δ_{C} 13.8 (2 Pyrrole CH_3), 14.6 (2 Pyrrole CH_3), 55.6 (OCH_3), 111.1 (2 Pyrrole CH), 120.8 (ArCH), 121.4 (ArCH), 123.9 (2 Pyrrole C), 129.5 (ArCH), 130.6 (ArCH), 131.6 (ArC), 139.0 (2 Pyrrole C- CH_3), 142.6 (2 Pyrrole C- CH_3), 154.9 (C_{meso}), 156.4 (ArC- OCH_3), $^{19}\text{F-NMR}$ (376 MHz, CDCl_3): $J(^{19}\text{F}_{\text{A}}-^{11}\text{B}) = 33.7$ Hz, $J(^{19}\text{F}_{\text{B}}-^{11}\text{B}) = 32.8$ Hz, $J(^{19}\text{F}_{\text{A}}-^{19}\text{F}_{\text{B}}) = 110.7$ Hz, IR(neat): $\nu_{\text{max}}/\text{cm}^{-1}$ 2980.9, 1540.0, 1505.3, 1463.0, 1307.0, 1187.6, 1156.6, 971.2, HRMS: calcd. for $\text{C}_{20}\text{H}_{22}\text{BF}_2\text{N}_2\text{O}$ (M+H)⁺: 355.1788, found 355.1792.

Synthesis of 2-bromo-(BOD-5) and 2,6-dibromo-1,3,5,7-tetramethyl-8-(*o*-methoxyphenyl)BODIPY (BOD-6)

BOD-4 (0.285 g, 0.8 mmol), DCM (300 mL) and bromine (16.35 μL , 0.8 mmol) was added to a round bottom flask sequentially. The solution was stirred for 48 h at room temperature under a nitrogen atmosphere. The solution was washed with 2×25 mL of water and dried using MgSO_4 . The remaining solvent was removed under reduced pressure to obtain a solid brown residue. The crude product was then purified through column chromatography (*n*-hexane:ether = 15:1) to give red solid (BOD-5), 0.190 g (55%) and (BOD-6). 0.190 g (46%).

BOD-5. R_f : 0.40 (UV active, petrol 40/60:ether = 7:3), m.p. = 204–206 °C, $^1\text{H-NMR}$ (300 MHz, CDCl_3): δ_{H} 1.44 (s, 3H, Pyrrole CH_3), 1.45 (s, 3H, Pyrrole CH_3), 2.58 (s, 3H, Pyrrole CH_3), 2.61 (s, 3H, Pyrrole CH_3), 3.79 (s, 3H, OCH_3), 6.03 (s, 1H, Pyrrole CH), 7.02 (d, $J = 8.4$ Hz, 1H,

ArH), 7.06–7.14 (m, 2H, 2 ArH), 7.48 (ddd, $J = 8.3$, 6.3, 2.9 Hz, 1H, ArH), $^{13}\text{C-NMR}$, (100 MHz, CDCl_3): δ_{C} 12.8 (Pyrrole CH_3), 13.5 (Pyrrole CH_3), 13.9 (Pyrrole CH_3), 14.7 (Pyrrole CH_3), 55.6 (OCH_3), 110.3 (Pyrrole C-Br), 111.2 (Pyrrole CH), 121.6 (ArCH), 121.7 (Pyrrole C- CH_3), 123.4 (Unbrominated pyrrole C- C_{meso}), 129.3 (ArCH), 129.9 (Pyrrole C- CH_3), 130.9 (ArCH), 132.2 (ArC), 138.1 (ArCH), 139.2 (Pyrrole C- CH_3), 144.6 (Pyrrole C- CH_3), 150.8 (Brominated pyrrole C- C_{meso}), 156.2 (C_{meso}), 157.4 (ArC- OCH_3), $^{19}\text{F-NMR}$ (376 MHz, CDCl_3): $J(^{19}\text{F}_{\text{A}}-^{11}\text{B}) = 32.5$ Hz, $J(^{19}\text{F}_{\text{B}}-^{11}\text{B}) = 31.8$ Hz, $J(^{19}\text{F}_{\text{A}}-^{19}\text{F}_{\text{B}}) = 107.2$ Hz, IR(neat): $\nu_{\text{max}}/\text{cm}^{-1}$ 2980.8, 1538.2, 1497.3, 1463.3, 1304.5, 1176.0, 1157.2, 975.8, 707.5, HRMS: calcd. for $\text{C}_{20}\text{H}_{21}\text{BBrF}_2\text{N}_2\text{O}$ (M+H)⁺: 433.0893, found 433.0895.

BOD-6. R_f : 0.54 (UV active, petrol 40/60:ether = 7:3), m.p. = 231–233 °C, $^1\text{H-NMR}$ (300 MHz, CDCl_3): δ_{H} 1.44 (s, 6H, 2 Pyrrole CH_3), 2.62 (s, 6H, 2 Pyrrole CH_3), 3.79 (s, 3H, OCH_3), 7.03 (d, $J = 8.3$ Hz, 1H, ArH), 7.10–7.14 (m, 2H, 2 ArH), 7.51 (ddd, $J = 8.3$, 5.8, 3.4 Hz, 1H, ArH), $^{13}\text{C-NMR}$, (100 MHz, CDCl_3): δ_{C} 13.0 (2 Pyrrole CH_3), 13.7 (2 Pyrrole CH_3), 55.7 (OCH_3), 100.0 (2 Pyrrole C-Br), 111.3 (ArCH), 121.7 (ArCH), 123.3 (2 Pyrrole C- CH_3), 129.2 (ArCH), 130.6 (2 Pyrrole C- CH_3), 131.2 (ArCH), 139.7 (ArC), 140.2 (Pyrrole C- C_{meso}), 153.5 (C_{meso}), 156.4 (ArC- OCH_3), IR(neat): $\nu_{\text{max}}/\text{cm}^{-1}$ 2924.5, 1541.3, 1460.6, 1401.2, 1350.0, 1178.5, 991.8, 756.5, HRMS: calcd. for $\text{C}_{20}\text{H}_{20}\text{BBr}_2\text{F}_2\text{N}_2\text{O}$ (M+H)⁺: 512.9982, found 512.9977.

Synthesis of 2-bromo-6-ethylacrylaic-(BOD-8) and 2,6-diethylacrylaic-1,3,5,7-tetramethyl-8-(*o*-methoxyphenyl)BODIPY (BOD-9)

To a Schlenk tube was added (BOD-6) (175 mg g, 0.400 mmol), Pd(II) acetate (3 mg, 0.012 mmol), triphenylphosphine (7 mg, 0.028 mmol) and 5 mL DMF. The mixture was stirred for 10 min and followed by the addition of ethyl acrylate (92 mg, 0.922 mmol) and triethylamine (185 mg, 1.832 mmol) in DMF (7 mL). The solution was then warmed for 24 h. A 50 mL DCM was added to the solution and washed with 2×200 mL water. The organic phase was dried using MgSO_4 , and the remaining solvent was removed under reduced pressure to yield a red solid residue. The crude product

was then purified through column chromatography (petrol 40/60:ether = 10:1) to give red solid (BOD-8), 0.137 g (64.6%) and (BOD-9), 0.077 (35%).

BOD-8. ¹H-NMR (300 MHz, CDCl₃): δ_H 1.32 (t, *J* = 7.1 Hz, 3H, CH₃), 1.44 (s, 3H, Pyrrole CH₃), 1.54 (s, 3H, Pyrrole CH₃), 2.64 (s, 3H, Pyrrole CH₃), 2.72 (s, 3H, Pyrrole CH₃), 3.79 (s, 3H, OCH₃), 4.24 (q, *J* = 7.1 Hz, 2H, CH₂), 6.05 (d, *J* = 16.2 Hz, 1H, CH), 6.06 (s, 1H, Pyrrole H), 7.02(d, *J* = 8.3 Hz, 1H, ArH), 7.08–7.21 (m, 2H, 2 ArH), 7.49 (ddd, *J* = 8.3, 5.2, 4.0 Hz, 1H, ArH), 7.63 (d, *J* = 16.2 Hz, 1H, CH), ¹³C-NMR, (100 MHz, CDCl₃): δ_C 11.9 (Br-substituted pyrrole CH₃), 13.9 (Br-substituted pyrrole CH₃), 14.2 (Acrylic CH₂CH₃), 14.4 (Substituted pyrrole CH₃), 14.9 (Substituted pyrrole CH₃), 55.6 (OCH₃), 60.2 (Acrylic CH₂CH₃), 99.3 (Br-substituted pyrrole C-Br), 111.2 (ArCH), 117.1 (=CHCO and Br-substituted C-CH₃), 121.6 (ArCH), 122.4 (Br-substituted pyrrole C-C_{meso}), 123.6 (Br-substituted pyrrole C-CH₃), 129.4 (ArCH), 130.7 (Substituted pyrrole C-CH), 130.9 (ArC), 132.9 (C_{meso}), 135.9 (ArCH and Substituted C-C_{meso}), 144.9 (=CH), 156.4 (2 Substituted pyrrole C-CH₃), 1587.0 (ArC-OCH₃), 167.7 (Acrylic C=O).

BOD-9. ¹H-NMR (300 MHz, CDCl₃): δ_H 1.33 t, *J* = 7.1 Hz, 6H, 2 CH₃), 1.45 (s, 3H, Pyrrole CH₃), 1.54 (s, 3H, Pyrrole CH₃), 2.64 (s, 3H, Pyrrole CH₃), 2.72 (s, 3H, Pyrrole CH₃), 3.79 (s, 3H, OCH₃), 4.25 (q, *J* = 7.1 Hz, 4H, 2 CH₂), 5.43 (d, *J* = 16.3 Hz, 1H, CH), 6.06 (d, *J* = 16.3 Hz, 1H, CH), 6.08 (s, 1H, ArH), 7.13–7.16 (m, 2H, 2 ArH), 7.52 (ddd, *J* = 8.3, 5.6, 3.7 Hz, 1H, ArH), 7.60 (d, *J* = 16.2 Hz, 1H, CH), 7.80 (d, *J* = 16.2 Hz, 1H, CH), ¹³C-NMR, (100 MHz, CDCl₃): δ_C 11.4 (Pyrrole CH₃), 11.9 (Pyrrole CH₃), 14.5 (Pyrrole CH₃), 14.9 (2 Acrylic CH₂CH₃), 17.2 (Pyrrole CH₃), 55.2 (OCH₃), 60.3 (2 Acrylic CH₂CH₃), 111.3 (ArCH and pyrrole C-CH), 116.6 (=CHCO), 121.7 (ArCH and =CHCO), 122.4 (Pyrrole C-C_{meso} and ArCH), 123.9 (Pyrrole C-C_{meso}), 129.6 (ArCH and pyrrole CCH), 130.7 (C_{meso}), 130.9 (ArC), 136.4 (ArCH), 143.0 (Pyrrole C-CH₃ and =CH), 144.9 (=CH and pyrrole C-CH₃), 156.6 (ArCOCH₃), 167.8 (2 Acrylic C=O).

Spectroscopic measurement

The absorption properties of the BODIPYs were

measured by scanning a serial concentration of the samples in organic solvent from 250–700 nm. A plot of concentration vs. absorption was made to produce a linear regression curve used to generate the extinction coefficient (ε). Meanwhile, the fluorescence quantum yield (φ) was determined over scanning of a series of the dilute sample within the absorbance range 0.01 < A < 0.05 followed by calculation through φ equation:

$$\phi_{\text{sample}} = \phi_{\text{standard}} \times \frac{F_{\text{sample}}}{F_{\text{standard}}} \times \frac{A_{\text{standard}}}{A_{\text{sample}}} \times \left(\frac{n_{\text{sample}}}{n_{\text{standard}}} \right)^2$$

where F stands for the area under the sample and standard emission spectrum, A is for the sample and standard absorbance, and n denotes the refractive index of the solvent used to dilute the sample and the standard. Here we used Rhodamine-B (φ = 0.70 in MeOH, λ_{ex} = 512 nm) and the well-known BOD-4 photophysics data (λ_{ex} = 485 nm) as the standard.

Computational calculation

All dyes were submitted to Gaussian 09 package to calculate their band gap energy (E_g) and the HOMO-LUMO model using the density functional theory (B3LYP) method with the SDD basis set level [11].

DSSC fabrication

A TiO₂ slurry in ethanol was leveled using the doctor Blade technique onto the 2.5 × 2.5 mm conductive surface of FTO glass to make a 2.0 × 2.0 mm working electrode. The electrode was sintered under 250 °C and left to cool at room temperature. A dye solution was then slowly dropped to the TiO₂ surface (ca. 13 μm) and was left to dry overnight at room temperature. Meanwhile, the carbon counter electrode was prepared by coating the conductive site of another 2.0 × 2.0 mm FTO glass with candle soot. The KI/I₂ electrolyte was dropped onto the working electrode, and the counter electrode was then covered to make a sandwich-like DSSC cell.

I-V measurement

The organic photovoltaic (OPV) performances were measured using 2602A Keithley under adjusted 1000 Watt/m² of xenon lamp illumination and non-illumination (Dark condition) of the fabricated cells, and all were at room temperature.

■ RESULTS AND DISCUSSION

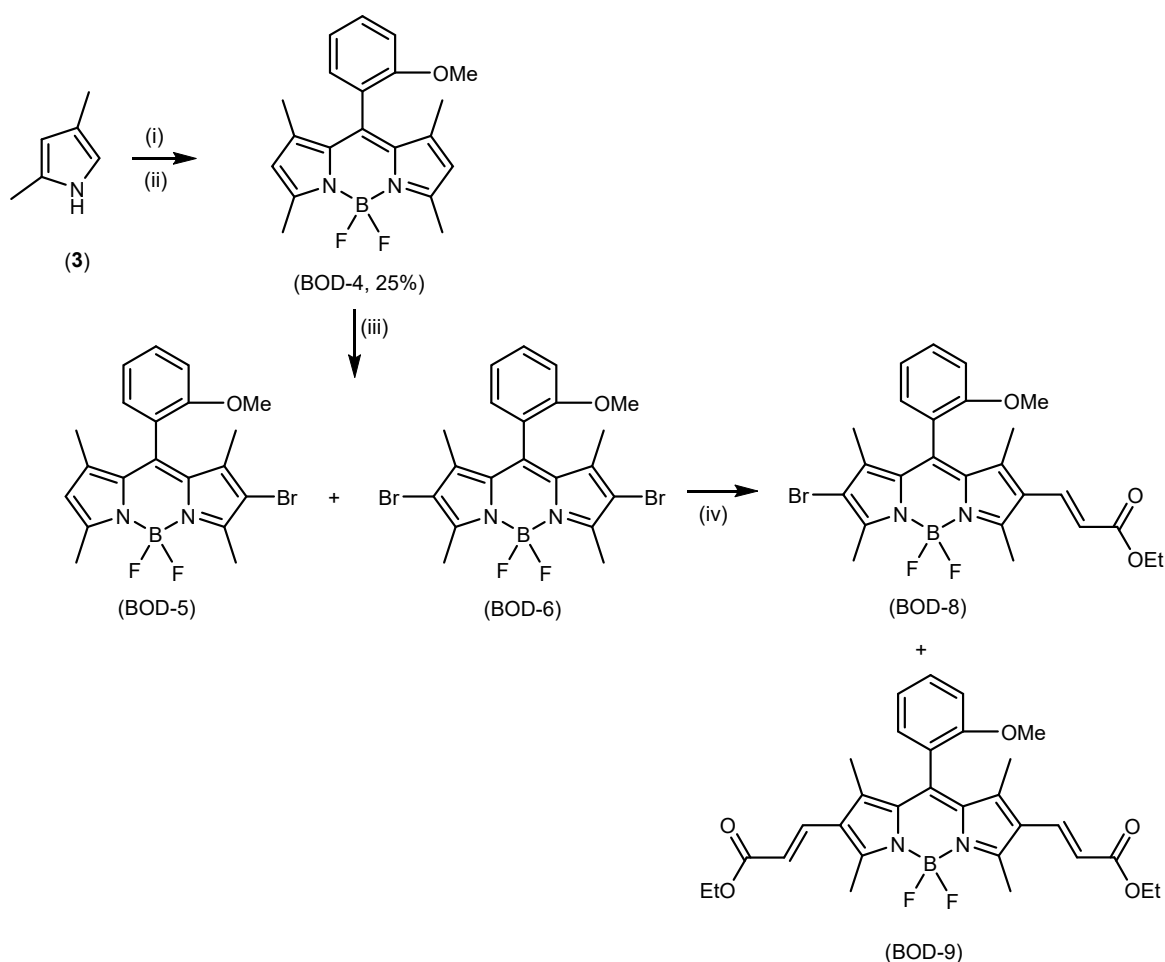
Synthesis of 2,6-Diethylacrylaic-8-(*o*-methoxyphenyl) BODIPY

To access the desired T-grafting BODIPYs, we opted to introduce the *o*-methoxyphenyl group as the Donor unit [12] at C8 due to its effective electron-hole separation upon photoexcitation of the dyes leading to electron current injection to the TiO₂ conduction band [18] and its biocompatibility [13], one of the required photosensitizer properties due to the typical low light energy conversion efficiency (η)-ascribed dyes aggregation on the TiO₂ surface [9]. Accordingly, we submitted *o*-methoxybenzoylchloride to 2,4-dimethylpyrrole (3) in the presence of Grignard reagent as a base catalyst following

modified Sunahara's procedure [14] (Fig. 3). This one-pot non-oxidative in-situ dipyrromethene production was followed by adding Hünig's amine and BF₃·OEt₂ to obtain an orange solid in 25% yield confirmed spectroscopically as (BOD-4) based on Sunahara's ¹H and ¹³C-NMR [14] spectra agreement.

Furthermore, the intent high emission-driven rotational lock *meso*-aryl substituent design was asserted by the appearance of two double-quartet (dq) AMX splitting patterns ascribed to the two quartets (q) 33.7 and 32.8 Hz of ¹¹B-¹⁹F and one double 110.8 Hz of ¹⁹F-¹⁹F coupling (Fig. 4).

The next step was to halogenate the BODIPY (BOD-4). As the C2/C6 is the only available position, such bromine (Br₂) addition would then produce the desired



(i) 2-methoxybenzoylchloride, PhMgBr, DCM, r.t., over night; (ii) *N,N*-diisopropyl-*N*-ethylamine, BF₃OEt₂, 0 °C, 3 h, r.t.; (iii) Br₂, DCM, r.t., 48 h; (iv) ethyl acrylate, Pd(OAc)₂, PPh₃, DMF, triethylamine, 24 h

Fig 3. Synthesis of (BOD-9)

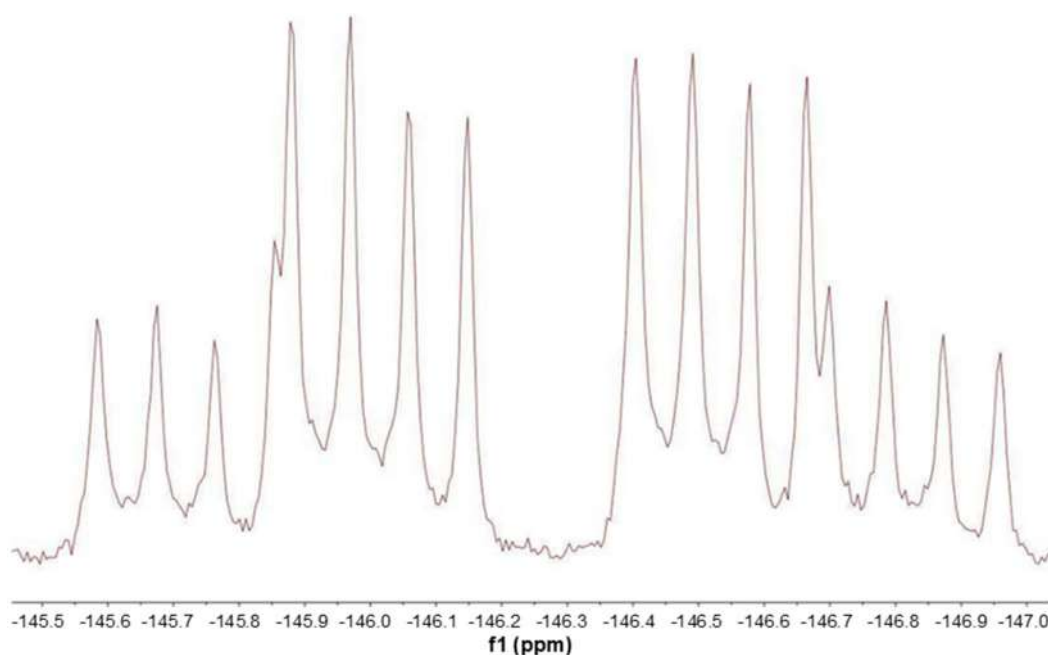


Fig 4. ¹⁹F-NMR spectrum of (BOD-4)

halogenated BODIPY, a required precursor for the late-stage Heck coupling reaction using ethyl acrylate (Fig. 3). Thereby, submission of bromine into the solution of (BOD-4) in DCM produced two separable red solids, which spectroscopically proved to be mono (BOD-5) and dibrominated (BOD-6) product in referring to its singlet, one pyrrole proton peak at 6.03 ppm and no pyrrole peak at ~6 ppm, respectively (see Supplementary Information, SI). The method is even mole ratio control, where the optimum dibromination was achieved at a 1:2 mole ratio (Table 1 entry 4).

Finally, conducting a facile, high-yield, and

straightforward palladium Heck coupling reaction of (BOD-6) to the mixture of ethyl acrylate in DMF produced two red solids, beneficially catalyst-based reaction control (Table 2). The ¹H-NMR spectrum analysis for those two products showed one typical alkenes doublet (d) 'roofing' AA' pattern at 6.05 and 7.63 ppm ($J = 16.2$ Hz) corresponding to mono acrylated (BOD-8) and another additional one at 5.43 and 7.60 ppm ($J = 16.3$ Hz) confirming the desired product (BOD-9), along with the ester's -CH₃ at 1.33 ppm (t, $J = 7.1$ Hz) and -CH₂- group at 4.25 ppm (q, $J = 7.1$ Hz) at both products (see SI).

Table 1. Mole ratio control of bromination reaction of (BOD-4)

Entry	Ratio (BOD-4) to Br ₂	Time (h)	Yield (BOD-5):(BOD-6)(%)
1	1:1	24	40:20
2	1:1	48	55:46
3	1:1.1	48	44:45
4	1:2	24	20:80

Table 2. Optimization of Heck coupling of (BOD-6) with ethyl acrylate

Entry	Pd ²⁺ (mol%)	PPh ₃ (mol%)	Time (h)	Yield (BOD-8):(BOD-9)(%)
1	3	7	24	65:35
2	3.5	7	24	30:70

Photophysical and Electrochemical Properties and Photovoltaic Performance

Before employing the BODIPYs as the DSSC photosensitizers, the incident photon-to-current efficiency (IPCE)-related photophysics and electrochemical properties of those synthesized BODIPYs were evaluated to ensure that the designed dyes work correctly. As shown in Fig. 5, all BODIPYs gave typical BODIPYs' 0-1 vibronic signature spectrum [9], a so-called 'shoulder' due to $S_0 \rightarrow S_2$ electronic transition and weaker $S_0 \rightarrow S_n$ ($n \geq 2$) bands at shorter wavelength [11] which exhibited a Bathochromic effect as their π -extended C2/C6 modification [15], the desired effect in optimizing the absorption of mainly Near Infra-Red (NIR) spectrum of the sun by the dyes [10,19]. Meanwhile, the increase of the relative area of those BOD-8 and BOD-9 $S_0 \rightarrow S_1$ bands to that of the unsubstituted BOD-4 indicates proportionally the mono- and the di- β -substituted, respectively [16]. All the fluorophores' fluorescence spectra were also a mirror image of that of the absorption.

As predicted, the BOD-4 gave typical high absorptivity, narrow Stokes shift ($\lambda_{Em} - \lambda_{Abs} = 10$ nm), and high ϕ (up to 90%), BODIPYs' typical photophysics [11], ascribed from the effective non-radiative relaxation

blocked at the aryl *meso* functional group (Table 1, entry 1). The red-shift absorption and emission found in both the brominated BOD-5 (12 nm) and BOD-6 (27 nm) (Table 3, entry 2 and 3) and the ethyl acrylate substituted BOD-8 (40 nm) and BOD-9 (52 nm) corresponds to the Inter-system Crossing (ISC) process over the heavy atom effect, also proven by the drastic decrease of their quantum yield, and the π -extended effect, respectively. The rotational restriction of the orthogonal (*o*-methoxyphenyl) at C8 compensates substantially [17] for the Br heavy atom effect in BOD-8 as well as in the BOD-9 (Table 3, entry 4 and 5) resulted in exceptionally high ϕ .

As the photon harvesting-related photophysical properties of the dyes have satisfactorily been confirmed, we then conducted the electron injecting and regenerating-related electronic properties of the designed dyes, those two primary parameters in producing high ICPE. We then conducted DFT (B3LYP/SDD) calculation using the Gaussian 09 package of the dyes. Instead of laying on the intended *o*-methoxyphenyl donor group [16], we found that the electrons are otherwise delocalized mostly in the dipyrromethene ring (BOD-4 HOMO) and surprisingly in the excited state (LUMO), this *meso* orthogonal aryl group

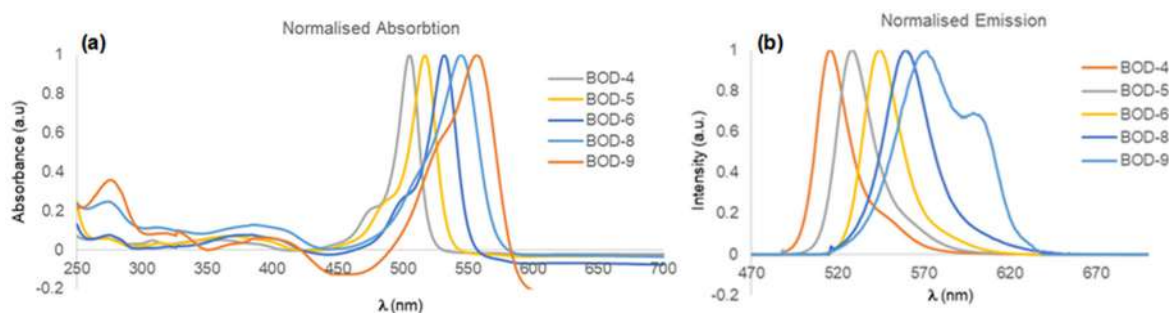


Fig 5. Absorption (a) and Emission spectra (b) of the prepared BODIPYs

Table 3. Optical density and fluorescence properties of the synthesized BODIPYs

Entry	Compound	ϵ ($L \text{ mol}^{-1} \text{ cm}^{-1}$)	λ_{Abs} (nm)	λ_{Em} (nm)	ϕ
1	BOD-4	110,900	505 ^a	515 ^a	0.889 ^a
2	BOD-5	70,000	517	528	0.17 ^b
3	BOD-6	52,500	532	544	0.05 ^b
4	BOD-8	72000	545	559	0.060 ^c
5	BOD-9	92500	557	571	0.502 ^c

^a: reference [14] ^b: BOD-4 was the standard in DCM ($\lambda_{ex} = 485$ nm) ^c: Rhodamine-B was the standard in MeOH ($\phi = 0.70$, $\lambda_{ex} = 512$ nm)

'pulls' the charge density through a mesomeric effect [11]. The effect commonly plays by acceptor groups (see SI). Similarly, the ethyl acrylate group (BOD-8 and BOD-9), expected to be the acceptor group over its π -extended 'pull' effect, is found to bear electron density in their ground state (HOMO) substantially and otherwise 'pushes' the electron to the *o*-methoxyphenyl [11], suitable to be a donor group (see SI). This reverse effect could plausibly cause by the use of the ester of acrylate instead of the acid one [18]. Thereby, our revised T-designed DSSC photosensitizer is like in Fig. 6.

Hitherto our photosensitizers are still found to comply with the electronic driving force requirement (Fig. 7). Those LUMO energies lie upper the TiO₂ conduction band (-4.2 eV) whilst the HOMO levels are below then the electrolyte (I₃⁻/I⁻) redox potential (-5.2 eV), indicating efficient electron injection of the dyes upon photoexcitation to the TiO₂ and efficient dyes regeneration over the electrolyte-cationic dye redox process, respectively [9-10]. The 'push-pull'-related ethyl acrylate C2/C6 introduction effect has also been observed by the reduction of the dyes band gap (E_g) (Table 4), one of the recommended strategies

in the high IPCE organic photovoltaic (OPV) design [20].

Finally, upon halogen lamp illumination to the fabricated DSSC cells, our dyes produced current (Fig. 8). Meanwhile, the T-grafted dye produced a 0.5% ratio of electrical power to the incident sunlight conversion (η) (Table 4 entry 4), similar to the horizontal D-A DSSC photosensitizers alignment. This achievement is much better than its corresponding D-A Fukuzumi-designed dyes [10].

Through these results, we have also seen the heavy atom-related quenching effect on the photosensitizing ability (Entry 1 and 2) and the significant contribution of the acrylate, as a donor, to resolve this effect found in BOD-8 (Entry 3).

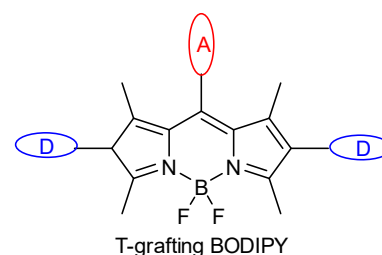


Fig 6. The revised T-grafting photosensitizer

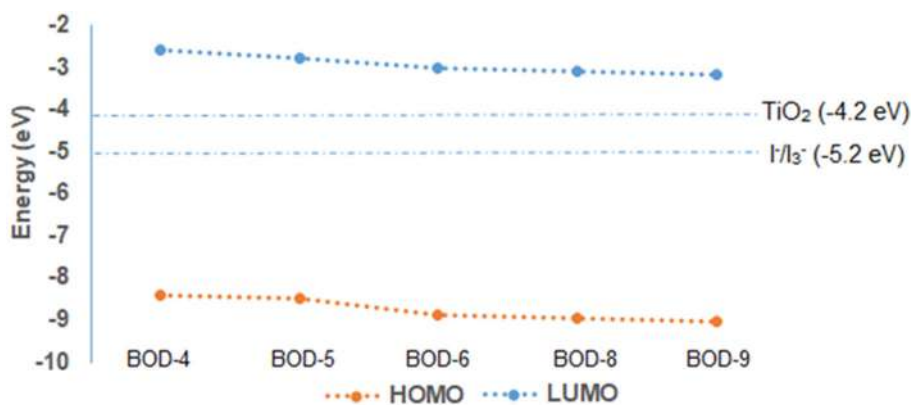


Fig 7. Energy level diagram of those synthesized BODIPY

Table 4. Photovoltaic properties of the prepared dyes

Entry	Dye	E _g (eV)	V _{oc} (mV) ^a	J _{sc} (mA cm ⁻²) ^b	FF ^c	H (%) ^d	Dye amount (10 ⁻⁷ mol cm ⁻²)
1	BOD-5	2.94	0.3333	0.000016	0.259	0.000354	0.1542
2	BOD-6	2.91	n.d.	n.d.	-	-	0.6536
3	BOD-8	2.80	0.075707	0.000116	0.277	0.000121	0.1634
4	BOD-9	2.74	0.1817	0.13240	0.517	0.497	0.6845

^a: Open-circuit voltage, ^b: Short-circuit current, ^c: Fill factor, ^d: Power conversion efficiency, n.d.: not detected

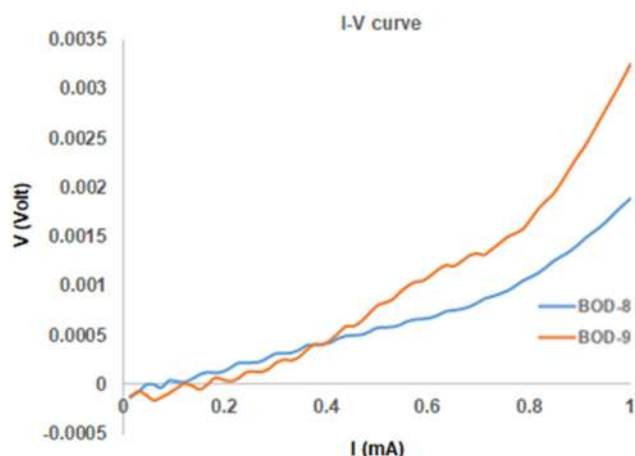


Fig 8. The I-V curve of the fabricated dye sensitizer

CONCLUSION

A new potent DSSC photosensitizer has been achieved by utilizing *meso*-substituted *o*-methoxyphenyl-1,3,5,7-tetramethyl BODIPY. Incorporating ethyl acrylate at C2/C6 of the BODIPY produced a T-grafting DSSC photosensitizer which was photophysical and electronic satisfactorily in conducting photovoltaic processes. The dye had typical horizontal D-A alignment current efficiency (η) of 0.5% in fabrication.

ACKNOWLEDGMENTS

The author(s) thank the Faculty of Science and Engineering, University of Nusa Cendana, for the research grant (Number: 16/UN15.15.2.PPK/SPP/FST/III/2022).

AUTHOR CONTRIBUTIONS

Reinner Ishaq Lerrick conducted the syntheses and the spectroscopy analysis and wrote this manuscript. Meliana Da Silva Braga and Wastiana Bere carried out the DSSC fabrications. Agus Supriyanto performed I-V measurements of the DSSCs. Ali Hashem Essa did the calculations for the DFT. All authors approved this manuscript's final version.

REFERENCES

- [1] Squeo, B.M., Ganzer, L., Virgili, T., and Pasini, M., 2020, BODIPY-based molecules, a platform for photonic and solar cells, *Molecules*, 26 (1), 153.
- [2] Saravanan, V., Ganesan, S., and Rajakumar, P., 2020, Synthesis and DSSC application of BODIPY decorated triazole bridged and benzene nucleus cored conjugated dendrimers, *RSC Adv.*, 10 (31), 18390–18399.
- [3] Awuah, S.G., and You, Y., 2012, Boron dipyrromethene (BODIPY)-based photosensitizers for photodynamic therapy, *RSC Adv.*, 2 (30), 11169–11183.
- [4] Merkes, J.M., Lammers, T., Kancherla, R., Rueping, M., Kiessling, F., and Banala, S., 2020, Tuning optical properties of BODIPY dyes by pyrrole conjugation for photoacoustic imaging, *Adv. Opt. Mater.*, 8 (11), 1902115.
- [5] Lerrick, R.I., Winstanley, T.P.L., Haggerty, K., Wills, C., Clegg, W., Harrington, R.W., Bultinck, P., Herrebout, W., Benniston, A.C., and Hall, M.J., 2014, Axially chiral BODIPYs, *Chem. Commun.*, 50 (36), 4714–4716.
- [6] Radunz, S., Kraus, W., Bischoff, F.A., Emmerling, F., Tschiche, H.R., and Resch-Genger, U., 2020, Temperature- and structure-dependent optical properties and photophysics of BODIPY dyes, *J. Phys. Chem. A*, 124 (9), 1787–1797.
- [7] Feng, Z., Jiao, L., Feng, Y., Yu, C., Chen, N., Wei, Y., Mu, X., and Hao, E., 2016, Regioselective and stepwise syntheses of functionalized BODIPY dyes through palladium-catalyzed cross-coupling reactions and direct C-H arylations, *J. Org. Chem.*, 81 (15), 6281–6291.
- [8] Klifout, H., Stewart, A., Elkhalfifa, M., and He, H., 2017, BODIPYs for dye-sensitized solar cells, *ACS Appl. Mater. Interfaces*, 9 (46), 39873–39889.
- [9] Shah, M.F., Mirlop, A., Chowdhury, T.H., Sutter, A., Hanbazazah, A.S., Ahmed, A., Lee, J.J., Abdel-Shakour, M., Leclerc, N., Kaneko, R., and Islam, A., 2020, Cross-conjugated BODIPY pigment for highly efficient dye sensitized solar cells, *Sustainable Energy Fuels*, 4 (4), 1908–1914.
- [10] Mao, M., and Song, Q.H., 2016, The structure-property relationships of D- π -A BODIPY dyes for dye-sensitized solar cells, *Chem. Rec.*, 16 (2), 719–733.
- [11] Lu, H., Mack, J., Yang, Y., and Shen, Z., 2014, Structural modification strategies for the rational design of red/NIR region BODIPYs, *Chem. Soc. Rev.*, 43 (13), 4778–4823.

- [12] Hosseinnzhad, M., Gharanjig, K., and Moradian, S., 2020, New D-A- π -A organic photo-sensitizer with thioindoxyl group for efficient dye-sensitized solar cells, *Chem. Pap.*, 74 (5), 1487–1494.
- [13] Liu, M., Ma, S., She, M., Chen, J., Wang, Z., Liu, P., Zhang, S., and Li, J., 2019, Structural modification of BODIPY: Improve its applicability, *Chin. Chem. Lett.*, 30 (10), 1815–1824.
- [14] Sunahara, H., Urano, Y., Kojima, H., and Nagano, T., 2007, Design and synthesis of a library of BODIPY-based environmental polarity sensors utilizing photoinduced electron-transfer-controlled fluorescence ON/OFF switching, *J. Am. Chem. Soc.*, 129 (17), 5597–5604.
- [15] Ren, W., Xiang, H., Peng, C., Musha, Z., Chen, J., Li, X., Huang, R., and Hu, Y., 2018, Direct C-H functionalization of difluoroboron dipyrromethenes (BODIPYs) at β -position by iodonium salts, *RSC Adv.*, 8 (10), 5542–5549.
- [16] Chen, J., Mizumura, M., Shinokubo, H., and Osuka, A., 2009, Functionalization of boron dipyrin (BODIPY) dyes through iridium and rhodium catalysis: A complementary approach to α - and β -substituted BODIPYs, *Chem. - Eur. J.*, 15 (24), 5942–5949.
- [17] Farfán-Paredes, M., González-Antonio, O., Tahuilan-Anguiano, D.E., Peón, J., Ariza, A., Lacroix, P.G., Santillan, R., and Farfán, N., 2020, Physicochemical and computational insight of ^{19}F NMR and emission properties of *meso*-(*o*-aryl)-BODIPYs, *New J. Chem.*, 44 (45), 19459–19471.
- [18] Hattori, S., Ohkubo, K., Urano, Y., Sunahara, H., Nagano, T., Wada, Y., Tkachenko, N.V., Lemmetyinen, H., and Fukuzumi, S., 2005, Charge separation in a nonfluorescent donor-acceptor dyad derived from boron dipyrromethene dye, leading to photocurrent generation, *J. Phys. Chem. B*, 109 (32), 15368–15375.
- [19] Cui, Y., Yao, H., Zhang, J., Zhang, T., Wang, Y., Hong, L., Xian, K., Xu, B., Zhang, S., Peng, J., Wei, Z., Gao, F., and Hou, J., 2019, Over 16% efficiency organic photovoltaic cells enabled by a chlorinated acceptor with increased open-circuit voltages, *Nat. Commun.*, 10 (1), 2515.
- [20] Bessette, A., and Hanan, G.S., 2014, Design, synthesis and photophysical studies of dipyrromethene-based materials: Insights into their applications in organic photovoltaic devices, *Chem. Soc. Rev.*, 43 (10), 3342–3405.

Synthesis of Powdered $[Mn(bipy)_3](CF_3SO_3)_2 \cdot 5.5H_2O$: The Physical Properties and Antibacterial Activity

Kristian Handoyo Sugiyarto*, Dwi Anggi Marini, Hari Sutrisno, Dyah Purwaningsih, and Cahyorini Kusumawardani

Department of Chemistry Education, Universitas Negeri Yogyakarta, Jl. Colombo No. 1, Yogyakarta 55281, Indonesia

* **Corresponding author:**

tel: +62-8157935534

email: sugiyarto@uny.ac.id

Received: September 6, 2022

Accepted: December 15, 2022

DOI: 10.22146/ijc.77565

Abstract: The synthesis of the complex containing manganese(II), bipyridine (bipy) as a ligand, and an anionic trifluoromethane sulfonate (triflate) is reported. The corresponding metal content, conductance, and DTG-TGA of the complex lead to the formula of $[Mn(bipy)_3](triflate)_2 \cdot 5.5H_2O$. The fully high-spin magnetic moment is observed, corresponding to five unpaired electrons in the metal ion. The electronic spectral bands suggest the three possible spin-forbidden transitions of the sextet to quartet states. The mode of vibrations of the IR spectrum supports the typical ring of bipy, and the triflate. The images of SEM-EDX indicate the presence of the corresponding elemental content and reflect the relatively high crystallinity, as it is evidenced in the profile of the corresponding powdered diffractogram. The refinement of powdered XRD following the Le Bail program suggests being structurally triclinic symmetry of P_{21}/c . This complex shows inhibition of bacterial activity against *S. aureus* and *E. coli*.

Keywords: manganese(II); bipyridine; triflate; PXRD; antibacterial

■ INTRODUCTION

The chemistry of six coordinated bidentate, phenanthroline (*phen*), and bipyridine (*bipy*), of divalent metals such as Mn(II), Co(II), Ni(II), and Cu(II) with various counterpart anions have been much well studied concerning P-XRD [1-7]. Among the divalent metal complexes, not many detailed physical properties are previously reported, and Mn(II) might exhibit an important role in the development of metal-based drugs. The development of chemotherapeutic organic bases and their metal complexes is now attracting the attention of medicinal chemists [8]. A possible idea for the toxicity of the complexes has been proposed in terms of the chelation theory [9]. Thus, preparation of solid Mn(II) containing *tris-bipy* with triflate anion is a challenge, and the results in its magnetism, IR-UV-Vis spectral properties, Powder-XRD, and anti-bacterial-activity against *Staphylococcus aureus* (*S. aureus*) and *Escherichia coli* (*E. coli*) are reported. The characteristics of the two bacteria represent the two types of gram-positive and gram-negative, respectively. They have been long recognized to be a pathogen, very

famous, and easily found in the surrounding of human life causing disease, skin, and soft tissue infections. In particular, the *E. coli* infection leads to (bloody) diarrhea, vomiting, stomach pains, and cramps. Therefore, the anti-bacterial activity of the complex will be readily known being able to kill both or only one of them, or only inhibit the growth of both or only one of them.

■ EXPERIMENTAL SECTION

Materials

The main reagents, manganese(II) nitrate tetrahydrate- $Mn(NO_3)_2 \cdot 4H_2O$ (97%), 2,2'-bipyridine (99%), and potassium trifluoromethanesulfonate- KCF_3SO_3 (98%), for the complex preparation, and sodium sulfate- Na_2SO_4 (99.99%), ammonium chloride- NH_4Cl (99.5%), manganese(II) sulfate monohydrate- $MnSO_4 \cdot H_2O$ (99.99%), aluminum nitrate nonahydrate- $Al(NO_3)_3 \cdot 9H_2O$ (98%), iron(III) chloride- $FeCl_3$ (reagent grade, 97%), and potassium chloride-KCl (99.09%), for conductivity measurement, were obtained from Aldrich-Sigma, and directly used without special treatment. The Nutrient

Agar (NA), Nutrient Broth (NB), Chloramphenicol, bacteria *E. coli* and *S. aureus*, for antibacterial testing, were obtained from the Microbiological Laboratory, Department of Biology, Yogyakarta State University.

Instrumentation

The instrumentations used in this study were UV-Vis spectrophotometer (Pharmaspec UV 1700), Magnetic Susceptibility Balance (Auto Sherwood Scientific 240V-AC), Fourier-Transformed Infrared Spectrophotometer (FTIR-ABB MB3000 Specord 100), Atomic Absorption Spectrophotometer (PinAAcle 900T Perkin Elmer), Thermogravimetric and differential thermal analyses (NETZSCH STA 409C/CO thermal analyzer), and X-ray diffractometer (Rigaku Miniflex 600).

Procedure

Preparation of complex

The $[\text{Mn}(\text{bipy})_2][\text{CF}_3\text{SO}_3]_2 \cdot n\text{H}_2\text{O}$ complexes were prepared by the anionic replacement method. A warmed ethanolic solution of *bipy* (0.47 g; 3 mmol, ~4 mL) was added by an aqueous solution of $\text{Mn}(\text{NO}_3)_2 \cdot 4\text{H}_2\text{O}$ (0.251 g; 1 mmol; ~3 mL). The mixture was filtered, and the aqueous solution of KCF_3SO_3 in a slight excess amount (0.75 g; 4 mmol, ~3 mL) was added to the filtrate whereupon the dully greenish precipitate resulted in reducing volume and scratching. The solid was filtered, washed with a minimum of cold water, dried in aeration, and stored in a desiccator.

Physical measurements

Magnetism. The Magnetic Susceptibility Balance (MSB) of Auto Sherwood Scientific 240V-AC was used to record the magnetic susceptibility in mass (χ_g) of samples. This instrument was calibrated with $\text{CuSO}_4 \cdot 5\text{H}_2\text{O}$ before running the samples. The powder complex was tightly packed in the Gouy tube till the sign of volume. The difference in mass without and with (electro-)magnet, which reflects the magnetic susceptibility in mass, was then administered. It was converted into molar magnetic susceptibility (χ_M) and then corrected for diamagnetism using Pascal's constant [10-11] to get corrected molar magnetic susceptibility (χ_M'). The effective magnetic moment (μ_{eff}) was then calculated from the general relationship of the following equation,

$$\mu_{\text{eff}} = 2.828 \sqrt{(\chi_M' \cdot T)} \text{ BM}$$

where T is the temperature of the sample [12-16].

UV-Vis electronic and infrared spectra. The spectrophotometer model of Pharmaspec UV 1700 was used to record the UV-Vis electronic spectrum. The sample was spread on a white filter paper closed with a particular thin glass (2 × 2 cm). The fitting was then set in the cell holder, and the spectrum was recorded at 200–1100 nm. An Infrared Spectrophotometer of the FTIR-ABB MB3000 model was used to record the spectrum of the sample. The powdered sample, which was mixed with KBr, was pressed on the cell, and then the spectrum was recorded at 500–4000 cm^{-1} .

Metal content and ionic property. The Atomic Absorption Spectrophotometer of the PinAAcle 900T Perkin Elmer model was used to record the metal content. A conductometer of the Lutron CD-4301 model was used to estimate the conductance property of the complex. It was calibrated with an aqueous solution of 1 M KCl at 25 °C, and several known ionic solutions, $\text{Ca}(\text{NO}_3)_2$, Na_2SO_4 , MnSO_4 , $\text{Mn}(\text{NO}_3)_2$, FeCl_3 , and $\text{Al}(\text{NO}_3)_3$, were also recorded for comparison.

DTG-TGA (Thermogravimetric and differential thermal analyses). The loss of water molecules and the decomposition of the complex were generated on the Diamond (Perkin Elmer Instruments), and simultaneous DTG-TGA were recorded by a NETZSCH STA 409C/CO thermal analyzer model with the rate of 10 °C/min.

Powder diffraction. The Rigaku Miniflex 600 40 kW 15 mA Benchtop Diffractometer with $\text{CuK}\alpha$, $\lambda = 1.5406 \text{ \AA}$ was used to record the diffractogram of the complex. The sample was spread on a special glass plate and set on the cell holder. The diffractogram was then recorded in a scan mode at 2–90° of 2θ within the interval of 0.04 steps per 4 sec for 2 h. The recorded diffractogram was then refined following the Le Bail method within 10–50° of 2θ , which was run within 50 cycles.

Determination of antibacterial activity

Antibacterial activity of the complex was tested against *S. aureus* (ATCC 25924) and *E. coli* (ATCC 35218) according to the agar disk-dilution method in Nutrient Agar (NA) and Nutrient Broth (NB) as media and chloramphenicol as a standard antibacterial agent

(positive control). It was performed at various concentrations of the complex, 125, 250, 500, and 1000 µg/mL. The observation of the inhibition zone (in mm) was done every 3 h during 24 h of incubation. The diameter of the inhibition zone was measured by measuring the distance from the edge of the test sample to the circular boundary of the inhibition zone using a caliper (accuracy 0.02 mm) on 3 sides of the sample [17-18].

■ RESULTS AND DISCUSSION

Conductance, AAS, DTG-TGA and Chemical Formula

The interactions of the clear solutions of *bipy* and manganese(II) produced a dully-greenish solution of the corresponding new compound, which is precipitated by the addition of the saturated excessive triflate solution. The equivalent electrical conductance of this compound was measured together with some other known simple salts, and the results are collected in Table 1.

It is observed that the complex might be classified in the range of the three ions per molecule, and therefore the stoichiometric empirical formula of $[\text{Mn}(\text{bipy})_n](\text{CF}_3\text{SO}_3)_2 \cdot x\text{H}_2\text{O}$ (where $n = 3$) is then worth proposed, reflecting the uncoordinated anionic triflate.

As shown in Fig. 1 and Table 2, the loss of mass of about 10.59% in the first stage at 100–160 °C is believed to be due to the loss of water lattice [19], being 5.5 H₂O (ca. 10.75%). While the remaining stages are not particularly analyzed, the DTG curve suggests that 3-*bipy* is lost in three stages, and the residue at above 540 °C is believed to be manganese oxides as the slow conversion Mn₂O₃ to Mn₃O₄ [20]. Together with the metal content, Mn, obtained from atomic absorption spectral data, 0.05976% (ca. 0.05967%), this suggests confirming the proposed formula of $[\text{Mn}(\text{bipy})_3](\text{CF}_3\text{SO}_3)_2 \cdot 5.5\text{H}_2\text{O}$.

Magnetism

The magnetic moment of the complex is calculated from the molar magnetic susceptibility data which were collected by the measurement for the two separated preparation (Sample 1 and 2) was found to be 6.17 and 5.87 BM at 298 K, respectively (Table 3), being normal paramagnetic nature. This reflects the spin-only value (μ_s), corresponding to five unpaired electrons in the metal ion, and it is the normal value in an octahedral geometry, as observed in some literature to be 5.89–6.16 BM for various compounds [1,9,21-23].

Table 1. Equivalent electric conductance of the aqueous solutions of $[\text{Mn}(\text{bipy})_n](\text{CF}_3\text{SO}_3)_2 \cdot x\text{H}_2\text{O}$ and some known salts (some data, NH₄⁺, Ca²⁺, Al³⁺, and Fe³⁺, are confirmed to references)

Compounds	Equivalent conductance (Λc) Ω ⁻¹ cm ² mol ⁻¹	Ratio of cation/anion	Number of ions per molecule	Reference
NH ₄ Cl	70–78	1:1	2	[4]
MnSO ₄	112.366	1:1	2	
Ca(NO ₃) ₂	379.355	1:2	3	[5]
Mn(NO ₃) ₂	207.777	1:2	3	
Na ₂ SO ₄	214.39	2:1	3	
Al(NO ₃) ₃	510–519	1:3	4	[5-7]
FeCl ₃	477–573	1:3	4	[5-7]
$[\text{Mn}(\text{bipy})_n](\text{CF}_3\text{SO}_3)_2 \cdot x\text{H}_2\text{O}$	261.202	1:2	3	

Table 2. The detailed formula of the complex following the metal TGA content

Proposed complex	H ₂ O content		AAS-Mn content (mg/g)	
	Calculated	TGA (%)	Calculated	Found
$[\text{Mn}(\text{bipy})_3](\text{CF}_3\text{SO}_3)_2 \cdot 5\text{H}_2\text{O}$	9.87		60.26	
$[\text{Mn}(\text{bipy})_3](\text{CF}_3\text{SO}_3)_2 \cdot 5.5\text{H}_2\text{O}$	10.75	10.59	59.67	59.76
$[\text{Mn}(\text{bipy})_3](\text{CF}_3\text{SO}_3)_2 \cdot 6\text{H}_2\text{O}$	11.61		59.09	

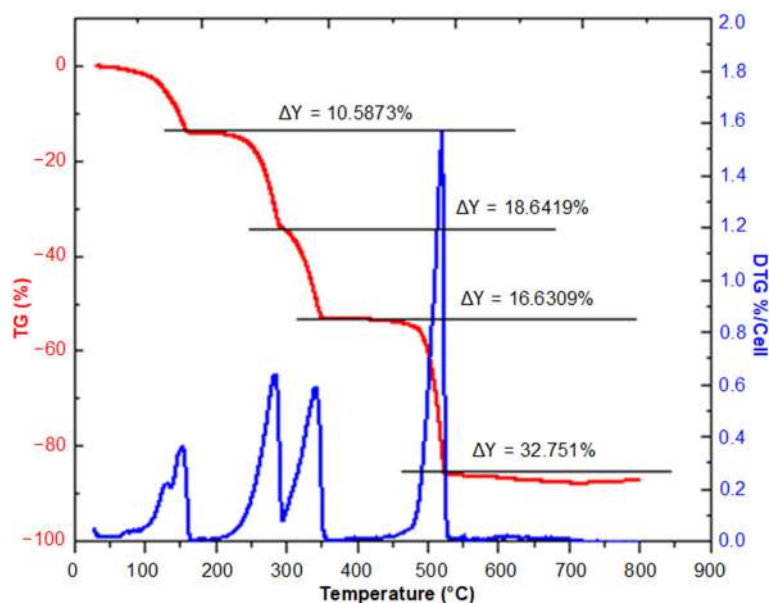


Fig 1. The DTG-TGA of $[\text{Mn}(\text{bipy})_3](\text{CF}_3\text{SO}_3)_2 \cdot x\text{H}_2\text{O}$ at 30–900 °C

Much lower values of several Mn(II) complexes, however, have been reported to be only 4.24 to 4.34 BM at 77–303 K [24], 4.65 BM [25], and 5.12 BM [26].

Electronic Spectrum

The normal high-spin nature, as confirmed by the magnetic data, suggests to the ground state of the sextet, ${}^6A_{1g}$, and as no other sextet excited state is possible, there are no spin-allowed transitions, but the spin-forbidden transitions to quartet states perform the absorption bands and consequently giving rise to very low intensities. The UV-Vis spectra of the powder complex and its solution (inset), as depicted in Fig. 2, exhibit strong ligand absorptions of the $\pi \rightarrow \pi^*$ and $n \rightarrow \pi^*$ at ~ 250 nm (40000 cm^{-1}) and 290 nm (34500 cm^{-1}), respectively, being comparable to the 1,10-phenanthroline ligand [26]. This strong ligand absorption is down to the visible area, and as a result, the $d-d$ spin-forbidden ligand field transitions, which are very low intensities, are not well resolved due to the mask of the tail absorption band as reported by Hariyanto et al. [27].

Following the Tanabe-Sugano diagram for MnF_2 and comparably observed for other literature at the range 19500 – 42000 cm^{-1} [28–29], those two strong ligand bands should mask all possible $d-d$ spin-forbidden transitions [ν_1 – ν_6 : ${}^6A_{1g} \rightarrow {}^4T_{1g}({}^4G)$; ${}^6A_{1g} \rightarrow {}^4T_{2g}({}^4G)$; ${}^6A_{1g} \rightarrow {}^4E_g({}^4G)$, ${}^4A_{1g}({}^4G)$; ${}^6A_{1g} \rightarrow {}^4T_{2g}({}^4D)$; and ${}^6A_{1g} \rightarrow {}^4E_g({}^4D)$, ${}^4T_{1g}({}^4P)$; and

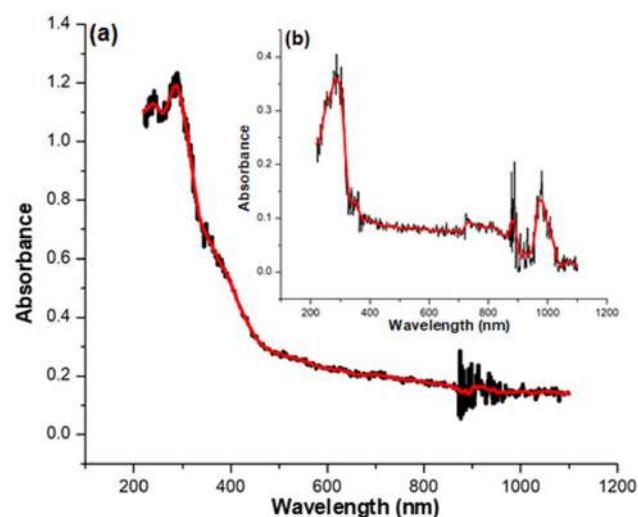


Fig 2. Electronic spectra of $[\text{Mn}(\text{bipy})_3](\text{CF}_3\text{SO}_3)_2 \cdot 5.5\text{H}_2\text{O}$: (a) powder; (b) in solution (inset)

${}^6A_{1g} \rightarrow {}^4T_{1g}({}^4F)$, respectively] which are presumably in the range 19000 – 21000 cm^{-1} (ν_1), 24000 – 25000 cm^{-1} (ν_2), 26000 – 28000 cm^{-1} (ν_3), ~ 30000 , ~ 33500 cm^{-1} (ν_4), ~ 36500 cm^{-1} (ν_5), and 39000 – 41000 cm^{-1} (ν_6), respectively. However, the strong-broad shoulder centered at about 355 nm (28160 cm^{-1}) for the solid spectrum, which might be split into two at 355 nm (28160 cm^{-1}) and 385 nm (25970 cm^{-1}) in the solution spectrum (Fig. 2b), strongly suggest to be ν_3 and ν_2 , respectively [30]. The similarity of the spectral pattern of

the powder and that in solution reflects the stability of this complex.

Infrared Spectra

The IR spectral profile of the complex and the anionic triflate (CF_3SO_3) are shown in Fig. 3. Direct comparison of the two might be made, and thus, the main modes of triflate should be readily assigned in the range of about $1200\text{--}500\text{ cm}^{-1}$, in which the detailed modes of vibrations, symmetric-/asymmetric-stretching modes of SO_3 ($\sim 1250\text{ cm}^{-1}$) and CF_3 (1000 cm^{-1}), symmetry deformations of C-F_3 ($\sim 750\text{ cm}^{-1}$) and SO_3 ($\sim 625\text{ cm}^{-1}$) have been reported in the previous references [2,4-5,27,31-32]. No indicative coordination with the metal is suggested for this anion, consistent with the formula proposed.

In the case of *bipy*-chelation, the typical ring modes ($\nu_{\text{C-C}}$; $\nu_{\text{C-N}}$; C-H ; *bipy* 'breathing') are to be in the range of $1625\text{--}800\text{ cm}^{-1}$. The broad stretching mode at $3500\text{--}3600\text{ cm}^{-1}$ is due to the symmetric-/anti symmetric-stretching modes of -OH of the H_2O lattice as indicated in the TG-DTA data. Another band at 3000 cm^{-1} is due to the stretching vibration of C-H bonds of pyridine rings [20,33].

SEM, EDX, and Powder XRD

As shown in Fig. 4, the complex indicates more or less the bulky poly-crystalline rather than amorphous type (SEM, (a)), with all main elemental content (C, N, O, F, S, and Mn) except for hydrogen (EDX, (b)). It is confirmed by the corresponding diffractogram profile (Fig. 5), showing no broad but sharp peaks.

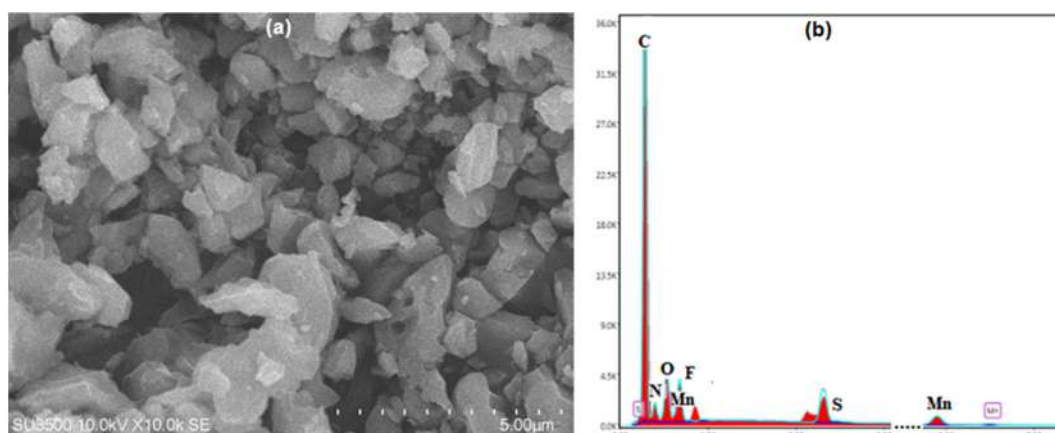


Fig 4. SEM photograph of $[\text{Mn}(\text{bipy})_3](\text{CF}_3\text{SO}_3)_2 \cdot 5.5\text{H}_2\text{O}$ at a magnification of $50.000\times$ (a) showing the crystalline type and EDX (b) showing elemental content

X-Ray Powder Diffraction and Structural Refinement

The crystal structure of $[\text{Mn}(\text{bipy})_3](\text{ClO}_4)_2$ has been established through different preparation of single crystal to signify the coordination of $\text{Mn-N}(\text{bipy})$. Surprisingly, two types of symmetry and space groups are observed [17,34-35]. For this reason, those data might be employed as references to refine the P-XRD of $[\text{Mn}(\text{bipy})_3](\text{CF}_3\text{SO}_3)_2 \cdot 5.5\text{H}_2\text{O}$, as recorded in Fig. 5.

The corresponding diffractogram is shown in Fig. 5. It can be seen that the red-full line of the Le Bail refinement program does touch almost all black points (+)

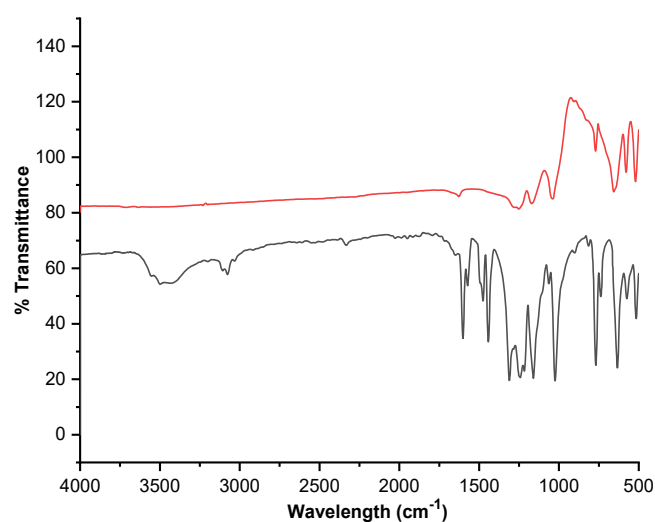


Fig 3. IR Spectra of $[\text{Mn}(\text{bipy})_3](\text{CF}_3\text{SO}_3)_2 \cdot 5.5\text{H}_2\text{O}$ (black) and KCF_3SO_3 (red). Note: Relative transmittance (in %) only significant for each spectrum

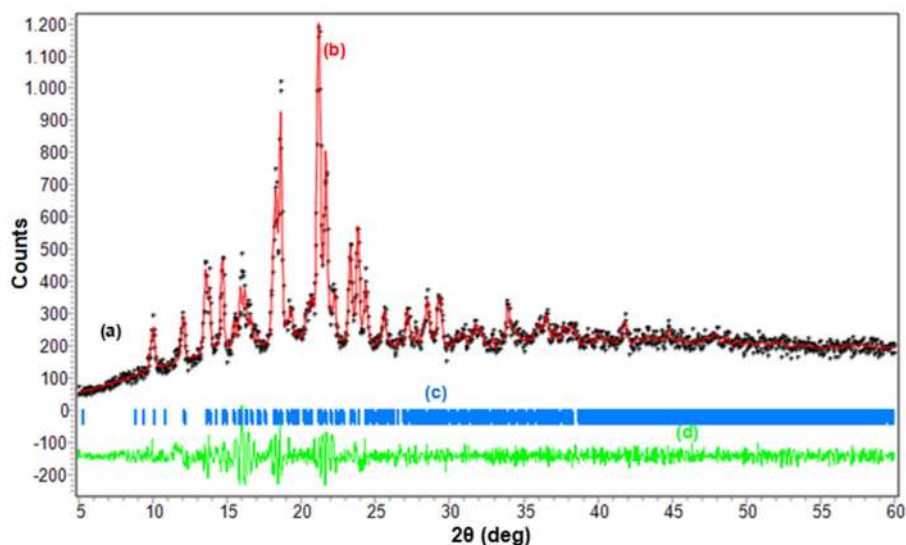


Fig 5. P-XRD profile of $[\text{Mn}(\text{bipy})_3](\text{CF}_3\text{SO}_3)_2 \cdot 5.5\text{H}_2\text{O}$ (a-black), the refinement on monoclinic symmetry of P_{21}/c (b-red) with its position of 2θ (c-blue), and the intensity difference between the black and the red lines (d-green)

Table 4. Crystallography data of $[\text{Mn}(\text{bipy})_3] \text{X}_2^{\text{a}}$ and $[\text{Mn}(\text{bipy})_2 \text{X}_2]^{\text{b}}$; ($\text{X} = \text{CF}_3\text{SO}_3$; ClO_4)

Complex	$\text{X} = \text{CF}_3\text{SO}_3^{\text{a}}$	$\text{X} = \text{ClO}_4^{\text{a}}$ [17]	$\text{X} = \text{ClO}_4^{\text{b}}$ [17]	$\text{X} = \text{ClO}_4^{\text{a}}$ [34]	$\text{X} = \text{ClO}_4^{\text{a}}$ [35]
Color	Greenish-yellowish	Yellow	Green	Golden yellow	Pale yellow
Symmetry	Monoclinic	Monoclinic	Monoclinic	Triclinic	Triclinic
Space Group	P_{21}/c	P_{21}/c	P_{21}/n	$P\bar{1}$	$P\bar{1}$
a (Å)	18.63498	18.6642	8.2272	8.133 (2)	9.535(2)
b (Å)	7.10764	7.932	13.3691(9)	11.056(2)	13.194(3)
c (Å)	21.4993	21.4812	21.0132(14)	18.658(5)	14.854(3)
a (°)	90.0	90.0	90.0	91.02(2)	107.26(3)
β (°)	99.6889	102.9	100.1(3)	91.02(2)	107.26(3)
γ (°)	90.0	90.0	90.0	99.77(2)	91.19(3)
V (Å ³)	2806.9936	3099.3	2275.8(3)	1613.1(7)	1770.2(7)
Z	4			2	2
The figure of Merit:					
R_p	6.07	-			
R_{wp}	9.25	-			
R_{exp}	8.47	-			
GOF	1.192	1.025	1.062	-	1.020
Bragg R-Factor	0.03	-		-	

of experimental data within the expected symmetry and space group model (blue-bar lines). The different intensity between the two experimental points and the refinement line is almost flat green-line, and this demonstrates an acceptable fitting model. The detailed lattice parameters of the structure due to the fitting are then collected in Table 4, together with the relevant data for some known single crystals of the same cations [17,34-

35]. The low figures of merit strongly suggest acceptable refinement, and thus, this complex prepared in this work might be classified as monoclinic symmetry of P_{21}/c .

Antibacterial Activity Test

Antibacterial activities of the complex were tested against *S. aureus* and *E. coli* bacteria with chloramphenicol as a positive control according to the

agar disc-dilution method in Nutrient Agar (NA) and Nutrient Broth (NB) [18]. A total number of 53 bacterial incubations in Petri dishes were prepared, and the two selected inhibition zone sizes of images of them for *S. aureus* at 250 µg/mL are shown in Fig. 6.

All numeric data of the concentration of the complex, and the diameter of the inhibition zone (in mm) with time (in h) are summarized and described graphically in Fig. 7 and Fig. 8.

It was found that the complex exhibits inhibition of the growth activity for both bacteria, *S. aureus* and *E. coli*. After the *two-way* ANOVA followed by Duncan (multiple distances) test, it can be concluded that the concentration of complex as a bacterial inhibitor, and incubation time, both affect the activity of the two bacteria simultaneously. Following the Duncan (multiple distances) test, it was found that the most effective in inhibiting bacterial growth is at 1000 µg/mL as the minimum inhibition

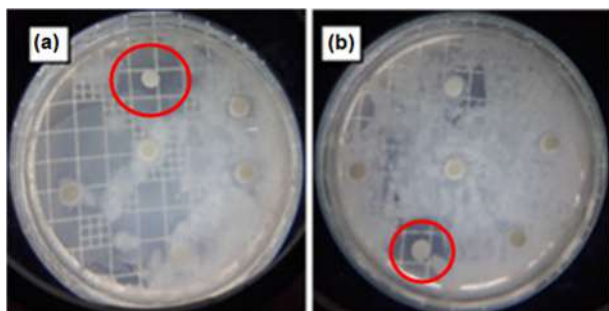


Fig 6. Selected images of bacterial incubation in petri dishes with a clear inhibition zone (red circle) for *S. aureus* at 250 µg/mL

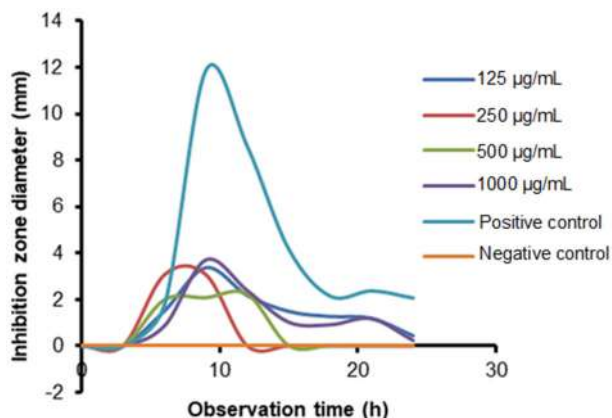


Fig 7. Graph of a diameter of the inhibition zone (in mm) at various concentrations of the complex against the time of *S. aureus* activity (in h)

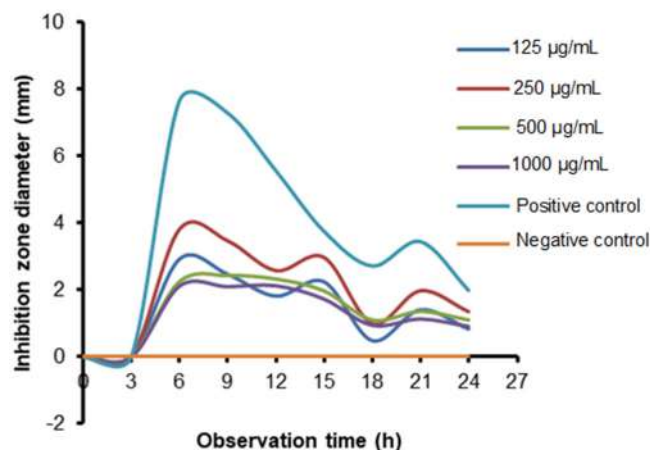


Fig 8. Graph of the diameter of the inhibition zone (in mm) at various concentrations of the complex against the time of *E. coli* activity (in h)

concentration (MIC) with the death phase within 9 h against the *S. aureus*, and at 250 µg/mL (MIC) with the death phase within 6–15 h against the *E. coli*.

In comparison to the simple compound, MnCO_3 [8] and $\text{Mn}(\text{ClO}_4)_2$ [17], for example, there is no antibacterial activity. Thus, in the light of chelation theory, it has been proposed that chelation of *bipy* might considerably reduce the charge of the metal ion, while the formation of a hydrogen bond through the anionic triflate might result in interference with the normal cell process [8-9].

CONCLUSION

In this work, the powdered complex of $[\text{Mn}(\text{bipy})_3](\text{CF}_3\text{SO}_3)_2 \cdot 5.5\text{H}_2\text{O}$, has been isolated as strongly confirmed by AAS, DTG-TGA, conductance, magnetism, UV-Vis and IR spectral properties. The corresponding cell parameters have been reviewed by Le-Bail refinement to the P-XRD diffractogram, which is found to fit the monoclinic symmetry of the P_{21}/c space group. Its antibacterial activity against *S. aureus* and *E. coli* bacteria is found to show inhibition of bacterial growth.

ACKNOWLEDGMENTS

Authors greatly acknowledge the Faculty of Mathematics and Science, Yogyakarta State of University, due to the financial support (Contract Number: B/186/UN34.13/PM.01.01/2020).

■ REFERENCES

- [1] Sugiyarto, K.H., Saputra, H.W., Permanasari, L., and Kusumawardani, C., 2017, Structural analysis of powder complex of $[\text{Mn}(\text{phen})_3](\text{CF}_3\text{SO}_3)_2 \cdot 6.5\text{H}_2\text{O}$, *AIP Conf. Proc.*, 1847, 040006.
- [2] Sugiyarto, K.H., Kusumawardani, C., Sutrisno, H., and Wibowo, M.W.A., 2018, Structural analysis of powdered manganese(II) of 1,10-phenanthroline (phen) as ligand and trifluoroacetate (TFA) as counter anion, *Orient. J. Chem.*, 34 (2), 735–742.
- [3] Kusumawardani, C., Kainastiti, F., and Sugiyarto, K.H., 2018, Structural analysis of powder complex of $\text{Cu}(\text{bipy})_3(\text{CF}_3\text{SO}_3)_2(\text{H}_2\text{O})_x$ ($x = 0.5, 1$), *Chiang Mai J. Sci.*, 45 (4), 1944–1952.
- [4] Sugiyarto, K.H., Kusumawardani, C., and Wulandari, K.E., 2018, Synthesis and structural analysis of powder complex of tris(bipyridine)cobalt(II) trifluoromethanesulfonate octahydrate, *Indones. J. Chem.*, 18 (4), 696–701.
- [5] Sutrisno, H., Kusumawardani, C., Rananggana, R.Y., and Sugiyarto, K.H., 2018, Structural analysis of powder tris(phenanthroline)nickel(II) trifluoroacetate, *Chiang Mai J. Sci.*, 45 (7), 2768–2778.
- [6] Sugiyarto, K.H., Kusumawardani, C., Wigati, H., and Sutrisno, H., 2019, Structural study of the powder complex of Cu(II)-1,10-phenanthroline-trifluoroacetate, *Orient. J. Chem.*, 35 (1), 325–331.
- [7] Sugiyarto, K.H., Louise, I.S.Y., and Wilujeng, S.S., 2020, Preparation and powder XRD analysis of tris(2,2'-bipyridine)nickel(II) trifluoroacetate, *Indones. J. Chem.*, 20 (4), 833–841.
- [8] Uddin, S., Saddam Hossain, M., Abdul Latif, M., Rabiul karim, M., Mohapatra, R.K., and Kudrat-E-Zahan, 2019, Antimicrobial activity of Mn complexes incorporating Schiff bases: A short review, *Am. J. Heterocycl. Chem.*, 5 (2), 27–36.
- [9] Singh, B.K., Mishra, P., Prakash, A., and Bhojak, N., 2017, Spectroscopic, electrochemical and biological studies of the metal complexes of the Schiff base derived from pyrrole-2-carbaldehyde and ethylenediamine, *Arabian J. Chem.*, 10, S472–S483.
- [10] Bain, G.A., and Berry, J.F., 2008, Diamagnetic corrections and Pascal's constants, *J. Chem. Educ.*, 85 (4), 532–536.
- [11] Dalal, M.A., 2017, "Magnetic Properties of Transition Metal Complexes" in *Textbook of Inorganic Chemistry*, Volume 1, Dalal Institute, India, 342–386.
- [12] e-PG Pathshala, 2021, *Inorganic Chemistry-II: Metal-Ligand Bonding, Electronic Spectra and Magnetic Properties of Transition Metal Complexes*, http://epgp.inflibnet.ac.in/epgpdata/uploads/epgp_content/chemistry/07.inorganic_chemistry-ii/33_anomalous_magnetic_moment/et/8821_et_et.pdf, accessed 15 December 2021.
- [13] Chemistry LibreTexts, 2020, *Magnetism*. [https://chem.libretexts.org/Bookshelves/Inorganic_Chemistry/Supplemental_Modules_and_Websites_\(Inorganic_Chemistry\)/Crystal_Field_Theory/Magnetism](https://chem.libretexts.org/Bookshelves/Inorganic_Chemistry/Supplemental_Modules_and_Websites_(Inorganic_Chemistry)/Crystal_Field_Theory/Magnetism), accessed 15 December 2021.
- [14] Chemistry LibreTexts, 2021, *Magnetic Susceptibility and the Spin-only Formula*, [https://chem.libretexts.org/Bookshelves/Inorganic_Chemistry/Map%3A_Inorganic_Chemistry_\(Houusecroft\)/20%3A_d-Block_Metal_Chemistry_-_Coordination_Complexes/20.10%3A_Magnetic_Properties/20.10A%3A_Magnetic_Susceptibility_and_the_Spin-only_Formula](https://chem.libretexts.org/Bookshelves/Inorganic_Chemistry/Map%3A_Inorganic_Chemistry_(Houusecroft)/20%3A_d-Block_Metal_Chemistry_-_Coordination_Complexes/20.10%3A_Magnetic_Properties/20.10A%3A_Magnetic_Susceptibility_and_the_Spin-only_Formula), accessed 15 December 2021.
- [15] Chemistry LibreTexts, 2020, *Magnetic Moments of Transition Metals*, [https://chem.libretexts.org/Bookshelves/Inorganic_Chemistry/Supplemental_Modules_and_Websites_\(Inorganic_Chemistry\)/Crystal_Field_Theory/Magnetic_Moments_of_Transition_Metals](https://chem.libretexts.org/Bookshelves/Inorganic_Chemistry/Supplemental_Modules_and_Websites_(Inorganic_Chemistry)/Crystal_Field_Theory/Magnetic_Moments_of_Transition_Metals), accessed 15 December 2021.
- [16] LibreTexts™, 2021, *Jahn-Teller Effect*, [https://chem.libretexts.org/Bookshelves/Inorganic_Chemistry/Book%3A_Introduction_to_Inorganic_Chemistry_\(Wikibook\)/05%3A_Coordination_Chemistry_and_Crystal_Field_Theory/5.08%3A_Jahn-Teller_Effect](https://chem.libretexts.org/Bookshelves/Inorganic_Chemistry/Book%3A_Introduction_to_Inorganic_Chemistry_(Wikibook)/05%3A_Coordination_Chemistry_and_Crystal_Field_Theory/5.08%3A_Jahn-Teller_Effect), accessed 27 January 2022.
- [17] Kani, I., Atlier, O., and Güven, K., 2016, Mn(II) complexes with bipyridine, phenanthroline and benzoic acid: Biological and catalase-like activity, *J. Chem. Sci.*, 128 (4), 523–536.

- [18] Balouiri, M., Sadiki, M., and Ibsouda, S.K., 2016, Methods for *in vitro* evaluating antimicrobial activity: A review, *J. Pharm. Anal.*, 6 (2), 71–79.
- [19] Dubey, R.K., Paswan, S., Anjum, A., and Singh, A.P., 2019, Synthesis and spectroscopic characterization of lanthanide complexes derived from 9,10-phenanthrenequinone and Schiff base ligands containing N, O donor atoms, *Indian J. Chem., Sect. A*, 58 (4), 446–453.
- [20] Czakis-Sulikowska, D., and Czyłkowska, A., 2003, Thermal and other properties of complexes of Mn(II), Co(II) and Ni(II) with 2,2'-bipyridine and trichloroacetates, *J. Therm. Anal. Calorim.*, 74 (1), 349–360.
- [21] Verma, R., 2017, Synthesis and characterisation of manganese(II) complexes with semicarbazide and thiosemicarbazide based ligands, *Int. J. Pharm. Sci. Res.*, 8 (3), 1504–1513.
- [22] Waheed, E.J., Farhan, M.A., and Hameed, G.F., 2019, Synthesis and characterization of new manganese(II), cobalt(II), cadmium(II) and mercury(II) complexes with ligand [*N*-(3-acetylphenylcarbamoithiyl)-2-chloroacetamide] and their antibacterial studies, *J. Phys.: Conf. Ser.*, 1234, 012096.
- [23] Fayyadh, B.M., Basim Abd, N.A., and Sarhan, B.M., 2022, Synthesis and characterization of new Mn(II), Co(II), Cd(II) and Hg(II) complexes with ligand [*N*-(pyrimidin-2-ylcarbamoithiyl)benzamide] and their anti-bacterial study, *IOP Conf. Ser.: Earth Environ. Sci.*, 1029, 012030.
- [24] Ferenc, W., Dariusz, O., Sarzyński, J., and Gluchowska, H., 2020, Complexes of Mn(II), Co(II), Ni(II), Cu(II) and Zn(II) with ligand formed by condensation reaction of isatin with glutamic acid, *Eletica Quim.*, 45 (3), 12–27.
- [25] Shaker, S.A., Khaledi, H., Cheah, S.C., and Mohd Ali, H., 2016, New Mn(II), Ni(II), Cd(II), Pb(II) complexes with 2-methylbenzimidazole and other ligands. Synthesis, spectroscopic characterization, crystal structure, magnetic susceptibility and biological activity studies, *Arabian J. Chem.*, 9, S1943–S1950.
- [26] Fayad, N.K., Al-Noor, T.H., Mahmood, A.A., and Malih, I.K., 2013, Synthesis, characterization, and antibacterial studies of Mn(II), Fe(II), Co(II), Ni(II), Cu(II) and Cd(II) mixed- ligand complexes containing amino acid (L-Valine) and (1,10-phenanthroline), *Chem. Mater. Res.*, 3 (5), 66–73.
- [27] Hariyanto, N.A., Hanapi, A., Ningsih, R., and Solawati, W., 2021, Synthesis and Characterization of Mn(II) Complex Compounds with Ligand Schiff Base 2-methoxy-6((4-methoxyphenylimino)methyl)phenol, *The 11th International Conference on Green Technology*, Universitas Islam Negeri Maulana Malik Ibrahim Malang, 26 October 2021, 29–32.
- [28] Lever, A.B.P., 1968, “Crystal Field Spectra” in *Inorganic Electronic Spectroscopy*, 1st Ed., Elsevier Science Publisher, Amsterdam, 249–360.
- [29] Dalal, M.A., 2017, “Electronic Spectra of Transition Metal Complexes” in *Textbook of Inorganic Chemistry*, Volume 1, Dalal Institute, India, 214–341.
- [30] Chandra, S., and Pipil, P., 2013, Spectral studies of transition metal complexes with 25,26-dioxo-1,6,12,17,23,24-hexaazacyclohexacosane-1,5,12,16-tetraene macrocyclic ligand (L), *Open J. Inorg. Chem.*, 3 (4), 38775.
- [31] Ignat'ev, N.V., Barthen, P., Kucheryna, A., Willner, H., and Sartori, P., 2012, A convenient synthesis of triflate anion ionic liquids and their properties, *Molecules*, 17 (5), 5319–5338.
- [32] Kusumawardani, C., Permanasari, L., Fatonah, S.D., and Sugiyarto, K.H., 2017, Structural analysis of powder complex of tris(1,10-phenanthroline)copper(II) trifluoromethane sulfonate dihydrate, *Orient. J. Chem.*, 33 (6), 2841–2847.
- [33] Czakis-Sulikowska, D., and Czyłkowska, A., 2005, New 2,2'-bipyridine-chloroacetato complexes of transition metals(II), *J. Therm. Anal. Calorim.*, 82 (1), 69–75.
- [34] Chen, X.M., Wang, R.Q., and Xu, Z.T., 1995, Tris(2,2'-bipyridine)manganese(II) perchlorate hemihydrate, *Acta Crystallogr., Sect. C: Struct. Chem.*, 51 (5), 820–822.
- [35] Yu, X.L., Tong, Y.X., Chen, X.M., and Mak, T.C.W., 1997, Crystal structure of [Mn(bpy)₃](ClO₄)₂·0.5(bpy) (bpy=2,2'-bipyridine), *J. Chem. Crystallogr.*, 27 (7), 441–444.

Review:**Status and Research Gaps of Microplastics Pollution in Indonesian Waters: A Review****Corry Yanti Manullang^{1,2*}, Mufti Petala Patria¹, Agus Haryono³, Sabiqah Tuan Anuar^{4,5},
Suyadi Suyadi⁶, and Rafidha Dh Ahmad Opier²**¹Department of Biology, Faculty of Mathematics and Natural Science, Universitas Indonesia, Depok 16424, Indonesia²Research Center for Deep Sea, National Research and Innovation Agency (BRIN), Ambon 97233, Indonesia³Research Center for Chemistry, National Research and Innovation Agency (BRIN), Serpong 15314, Indonesia⁴Faculty of Science and Marine Environment, Universiti Malaysia Terengganu, 21030 Kuala Nerus, Terengganu, Malaysia⁵Microplastic Research Interest Group, Universiti Malaysia Terengganu, 21030 Kuala Nerus, Terengganu, Malaysia⁶Research Center for Biology, National Research and Innovation Agency (BRIN), Bogor 16911, Indonesia*** Corresponding author:**

tel: +62-911322676

email: corr001@brin.go.id

Received: March 10, 2022

Accepted: July 3, 2022

DOI: 10.22146/ijc.73485

Abstract: This study is the first review of current research on microplastics (MPs) in the marine environments at the national scale in Indonesia from 2015 to 2022. This review was conducted to measure the environmental risk and highlight the waste management issue in Indonesian waters. Our literature study found that: (1) the MPs research was mainly conducted in the western part of Indonesia, especially in Java Island; (2) current research has primarily focused on coastal waters (98%) rather than the deep-sea area (2%); (3) the comparability of data is still hampered by difference in quality, about 67% of articles published have not carried out the polymer confirmation; (4) MPs concentrations reported on the articles that did not carry out the polymer identification tended to report higher MPs concentrations. Finally, we propose to have a standard guideline for MPs analysis at a national level and to do more research in the eastern part of Indonesia and deep-sea areas. Further research is required to fill research gaps on plastic distribution and density in deep-sea areas in the eastern part of Indonesia.

Keywords: MPs; seawater; marine sediment; marine biota; Indonesia

■ INTRODUCTION

Plastics are widely used in packaging, followed by building and construction, automotive, electrical and electronics, agricultural household, leisure, and sport [1]. Plastic is preferred over other materials because it has several advantages: strong, light, cheap, easy to form, can be made transparent, and can be colored. In addition, it does not rust after being left in open air and water [2]. Since the first mass production started in the 1950s, plastic production rose to 368 million tons in 2019 [1]. Plastic fabrication is predicted to continue to grow along with the development of technological advances in plastic polymers. Most plastic products are single-use items designed to be thrown out after one time use. It is reported

that 40% of plastic produced was plastic packaging that will only be used once [1]. If plastic waste is not adequately managed, it can end up in the ocean. Millions of tons of plastic entered the ocean from 192 coastal nations and are predicted to increase in connection with the increase in plastic production every year [3-5]. The ever-increasing amount of plastic waste in the oceans has attracted researchers worldwide to uncover the extent to which plastic pollution has entered the waters. Plastic waste has been detected in coastal areas of all continents, even in highly isolated areas such as the Arctic Ocean [6] and the Mariana deepest trough at a depth of 10908 meters in the Pacific Ocean [7].

Indonesia is the second-largest contributor to plastic

waste in the world's ocean. Indonesia was estimated to produce 3.2 million tons of unmanaged plastic waste a year, of which about 1.29 million tons end up in the sea [4]. In 2017, the Ministry of Industry of the Republic of Indonesia estimated that every year, 4.8 million tons of plastic waste in Indonesia is considered mismanaged in various ways such as being openly burned (48%), dumped on land, in poorly managed official dumpsites (13%), or leaking into rivers, lakes and the ocean (9%) [8]. The latest report of the World Bank in 2021 showed that the number has increased to 4.9 million tons [9]. In a meeting of G20 leaders conducted in Germany, the Indonesian government has a target to decrease waste by reducing solid waste from its source by 30% and adequately handling 70% of solid waste by 2025, 70% of marine plastic litter by 2025 in order to minimize the impacts of plastic pollution. The basic strategy used to minimize plastic waste was by establishing a National Plan of Action (NPOA) on Marine Plastic Debris from 2017 to 2025 [8]. The main objective of this NPOA is to overcome the impacts of plastic waste pollution in the sea and reduce plastic waste in the sea by 70% in 2025. Since 2017, referring to this action plan, many activities have been organized to clean up beaches and rivers in various regions.

In the past decade, scientists have been concerned about microplastics (MPs) which are plastics under 5 mm in size that are often invisible to the naked eye [10]. This increasing concern is highly due to its significant impact on marine biota [11]. The small sizes of MPs can be mistaken as food for various marine species. As a result, MPs have been found in megafauna to planktonic marine biota [12-17]. MPs have been discovered in seawater, sediment, and marine biota in Indonesian waters. In order to explore the topic of MPs' studies in Indonesia, here, we reviewed publications regarding MPs' from Indonesian marine waters from 2015 to 2022. Subsequently, we also identified research gaps about MPs pollution in Indonesian waters. The data and information provide an overview of the degree of plastic pollution across Indonesia and the requirement for better marine environmental management and further research.

Data Collection and Review of Content

In this study, we collected the references (papers) from Indonesia that have been indexed in Scopus. Recent

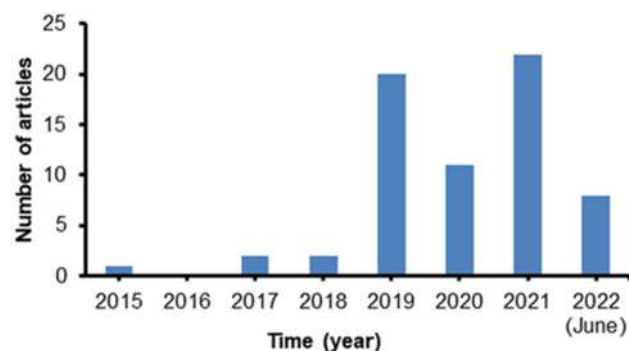


Fig 1. Number of papers on microplastics published between 2015 and 2022 (June) in Indonesia

references published between 2015 (first MPs paper) and 2022 were retrieved using some keywords: “microplastic”, “plastic”, “debris”, “litter”, and “Indonesia”. The references are reviewed critically, and the data collected from the references are entered into MS Excel for data analysis. The papers include 66 published articles (35 journal articles and 31 conference papers) (Fig. 1). The MPs assessment is focused on three major matrices: seawater, marine sediment, and marine biota. This article provides information on MP concentration from Indonesian marine waters, the sampling and extraction methods, the shape of MPs, and the plastic polymers identification. We also highlighted research gaps and management challenges regarding MP pollution in Indonesian waters.

RESULTS AND DISCUSSION

Determination of MPs in Indonesia

Sampling procedures

The instrument and methods used for collecting MPs for seawater, marine sediment, and marine biota in Indonesia have not been standardized. From the literature published in Indonesia, it was discovered that manta and plankton nets were commonly used to collect water samples in coastal waters with mesh sizes of 200 or 300 μm (Table 1). A new development has been conducted through simultaneous grading size samples in sea surface sampling. The water samples were directly divided into sizes 0.5 \times 0.5 cm; 500–1000 μm ; 300–500 μm ; 100–300 μm [18]. In Indonesia, the volume of a water sample taken by plankton nets varied from 0.1 to 10 L. Relatively, no data was found regarding the volume

of a water sample taken by a manta net. For the deep-sea waters, the water sample was collected using a rosette water sampler from certain layers with 10 L per layer [19]. Meanwhile, pipe, Ekman grab, and shovel was commonly used to collect the marine sediment samples, which varied from 100 to 1000 g (Table 2). Some studies used a transect (0.5×0.5 m; 1×1 m) to grab the sediment samples [20-23]. Marine biota was generally collected from the markets and in which the entire gastrointestinal tract was taken for MPs analysis. However, for the small biota (e.g., anchovies, *blue panchax* fish), the entire body of the biota was used [24-28]. The number of samples varied from 2 to 60 individuals. It is suggested that 50 or more individuals per research unit are defined as a suitable sample size for the number of biota samples [29]. Unfortunately, most studies in Indonesia have not exceeded this number of samples. Out of 39 studies, only three (7%) completed this threshold [24,30-31].

Laboratory methodologies for MP extraction

The methods and techniques to isolate MPs from other non-plastic materials such as biological tissues, organic matter, and other non-plastic materials were varied. There are four common types of digestion solutions used to extract and purify the MP from samples, namely acids (nitric acid (HNO_3), hydrochloric acid (HCl), per-chloric acid (HClO_4), etc.), bases (sodium hydroxide (NaOH), potassium hydroxide (KOH)), Oxidant (hydrogen peroxide (H_2O_2)), and enzymes (trypsin, proteinase K, etc.) [12-13,32-34]. However, H_2O_2 30% and KOH 10% were mainly used to remove non-plastic materials in most sample matrices (water, sediment, and biota) to digest biological tissues, organic matter, and other non-plastic materials without damaging the MPs. HNO_3 , HCl, and NaOH were reported to alter plastic's physical state or cause the loss of some plastic-type features [32-33]. The other reagent that can be considered in the extraction process of MP is the enzyme solution. An enzyme (trypsin, proteinase-K) has the advantage of ensuring MPs integrity, short digestion time, and is less harmful to human and environmental health [32-33]. However, this method is rarely used because of the higher price compared to the chemical reagents. In Indonesia, MPs in the seawater and marine sediment

samples were isolated mainly using the sodium chloride (NaCl) solution using the flotation separation method (density). However, few studies used H_2O_2 30% to purify the MPs in seawater and marine sediment, especially when the size of the MP of interest was less than 1 mm [19-20,24]. For larger MPs (1-5 mm) in beach sand and coastal sediment, the MPs were directly separated using a 1-mm² stainless steel sieve, followed by visual sorting [21].

Physical and chemical characterizations

In general, the MPs were physically categorized based on shape, size, color, and type of polymers under the observation of a stereomicroscope. To date, most MP research in Indonesia used visual identification based on size (< 200 μm , 200-500 μm , 500-1000 μm , 1000-5000 μm) and shape (fragment, fiber, foam, film, and granule). Regarding the color of MPs, most studies of MPs in Indonesia did not include the analysis of the color of plastics. The polymer type of the plastics can be further identified either by Fourier transform infrared spectroscopy (FTIR), thermal desorption gas chromatography with mass spectrometry (TDS-GC/MS), pyrolysis gas chromatography with mass spectrometry (Pyr-GC/MS), or Raman spectroscopy. Plastic polymer identification is a crucial protocol to examine the chemical characteristic of MP particles obtained from the visual calculation results (physical analysis) since it will highly be susceptible to misidentifying non-polymer fiber as a plastic material. This type of material is difficult to distinguish through microscopy alone. Additionally, the airborne contamination of fiber types is likely to happen in MP research if a proper cross-contamination protocol is not followed [35]. Previously, research on MPs in sediment samples from the North Sea measured using micro-FTIR showed that only 1.4% of particles visually resembling MPs came from synthetic polymers [36]. The literature data showed that most studies on MPs in Indonesia (over 60%) do not provide polymer analysis. This may be caused by the limited resources of analytical instrumentation that are not easily/readily available in Indonesia. We highlighted a tendency for the reported MPs value to be higher in articles that did not pass the plastic polymer conformation. Due to these

cases, in regards to comparing studies in Indonesia with studies in other countries, we only included the articles that had performed the polymer identification test.

Size and unity

The commonly used units for the study of MPs in Indonesia were n/L (number per liter) for seawater, n/g (number per gram) for marine sediment, and n/ind (number per individual) for marine biota. Some studies that used transect to collect samples in the marine sediment expressed the MPs found with the unit item per m² or item per m³ [21]. In Indonesia, the size of MPs was varied; however, most of the studies did not inform the specific size of MPs, but instead gave general size information of < 5 mm. Nonetheless, some studies classified the MPs in size ranges: < 0.1 mm; 0.3 to 0.5 mm; 0.5 to 1 mm; > 1 mm; and 1 to 5 mm [24,37-38].

Quality control

MP studies are very susceptible to contamination, such as airborne contamination, research equipment, and research materials. The airborne contaminant has been confirmed as fiber, which can indirectly contaminate the sample [35]. Some controls are highly recommended to minimize the contamination during analytical procedures in the laboratory. First, airborne contamination in the laboratory can be minimized by separating the sample processing process from other laboratory activities. Secondly, the air intake from the outside of the analysis room can be reduced by closing air vents to prevent contamination from outside. Thirdly, the destruction process should be carried out in a fume hood or laminar flow chamber to minimize airborne contamination sources [39]. Lastly, samples should always be kept closed to minimize exposure to air. Research equipment is also a significant source of contamination in MP research. Therefore, it is suggested to use metal and glass research apparatus rather than plastic research equipment. Another recommendation was to heat all the research apparatus at 450 °C for 5 h to remove all plastic before using it in MP analysis [40]. Washing research equipment repeatedly with distilled water has effectively removed plastic fibers up to 88 to 98%. However, an experimental study stated no significant difference between repeated rinsing of the

research apparatus with heating at high temperatures [41]. In Indonesia, only a few studies provided information about quality control during the sampling and analysis in the laboratory, e.g., leaving a bare Petri dish or a sterilized filter paper near the sample during the digestion process until the identification is completed [24,37]. They also used either liquid water purified by a reverse-osmosis technique or double-distilled deionized water 3–5 times in their washing procedure, including during the sample clean-up and glassware/sample bottle washing. They found no MP contamination on the blank sample by applying these controls.

The Occurrence of MPs in the Marine Environment in Indonesia

MPs in seawater

A total of 26 data on MPs in seawater have been reported from 2017 to 2022. Among these, about 96% of the data reported was conducted in coastal areas, including estuaries, seagrass habitats, mangrove areas, and coral reef areas. However, we also identified that 48% of the articles did not identify the plastic polymer. The MP abundance in seawater of coastal areas in Indonesia ranged from 0.00004 to 110737 n/L (for the studies without polymer identification) and 0.000023 to 11100 n/L (for studies with polymer identification) (Table 1). The highest concentration of 11100 n/L was found in a small-scale estuary in Central Java [42]. The river receives a large amount of domestic waste without any treatment process. The type of polymer found was polyethylene where this plastic material is widely used in household goods which are easily degraded. We also observed that the value of MP tends to be higher in estuary areas and mangrove ecosystems. This might be due to the ability of mangrove branches and roots to act as trash traps in the water. Trapped trash tends to get stuck in the mangrove area [43]. Meanwhile, the lowest MP concentration was found in the seagrass ecosystem area of the Sulawesi Island [44].

The MP concentration in the coastal areas of Indonesia varied widely. The MPs content with a polymer conformation in Sulawesi Island was 0.000023 up to 55 n/L, followed by 0.00046 ± 0.00025 n/L in Sumatra Island;

0.00054 in Bali Island and 0.00848 ± 0.00943 to 11100 n/L in Java Island (Table 1). The highest MPs content was found in a small-scale estuary in Central Java Island. It is remarkable that this value has far exceeded the MPs content in the estuary of Yellow River, China (930 n/L) [45], Changjiang Estuary, China (0.045 to 0.122 n/L) [46], Yangtse Estuary, China (4.13 n/L) [47], Goiana Estuary, Brazil 0.00026 n/L [48], Urban Estuary in South Africa (0.001 to 0.007 n/L) [49] and Tamar Estuary, England (0.00028 n/L) [50].

The first available data of MPs on the Indonesian deep-sea area was reported from the water column of Sumba waters (300 m) $0.044 \pm 0.024.59$ n/L [19]. These concentrations were far lower than in coastal areas. The MPs concentration reported in Indonesia is relatively lower than the average concentration of MPs in the world's open sea, which is 0.07 to 13.51 n/L [7,51]. The MPs concentration in Sumba Waters decreased in line with the depth and has relatively high concentrations in the thermocline area. Otherwise, the concentration of MPs in the Mariana Trench is linear with their depth levels [7].

MPs in coastal sediments

Studies regarding the concentrations of MPs in sediments have been carried out in Indonesian waters since 2017 (Table 2). Unfortunately, about 70% of the studies conducted did not carry polymer tests on the plastics found. The MPs abundance in marine sediment of coastal areas in Indonesia ranged from 2.96 to 111680 n/Kg dry weight (DW) (for studies without polymer identification) and 0 to 49000 n/Kg DW (for studies with polymer identification) (Table 2). The highest MPs concentration (49000 n/Kg) was found in Central Java [42]. This unrealistic value is found in a small-scale estuary used as a dumping area by the local community. Notably, this concentration is higher than in other regions around the world. For instance, the MPs found in Changjiang Estuary, China, was reported in the range of 20 to 340 n/Kg [52], Haihe Estuary, China (96.7 to 333.3 n/Kg) [53], Yondingxinhe Estuary, China (56.7 to 113.3 n/Kg) [53] and in coastal mangrove, Singapore (12 to 62.7 n/Kg) [54]. However, these findings were not consistent across Indonesia. Some studies also reported that MPs concentration in some estuaries in Indonesia was lower than in other regions.

For instance, a lower concentration of MPs was found in mangrove sediment from Jakarta Bay in the range of 28.09 ± 10.28 n/Kg [37].

MPs in marine biota

Entanglement and plastic consumed by marine biota when consuming food have been frequently reported as the effects of large-sized plastics on wildlife and other aquatic biotas. Wildlife entangled in plastic may become immobile, bound, and eventually die. Animals that consume plastic may experience intestinal obstructions or even suffocate [2]. However, reports of microplastics in biota are far more widespread. Marine biota is more likely to consume smaller microplastics than larger macroplastics. Microplastics have been discovered in marine organisms of all sizes, from zooplankton to whales [12-17]. However, based on experiments in the laboratory, the presence of microplastics in the marine biota did not directly cause any deaths. Studies that documented mortality from exposure to microplastics found that the death of marine biota were typically caused by unreasonable intake of microplastics that also exceeds the expected concentration of microplastics in the environment [55-56]. Plastic can pass through the digestive tract but cannot be digested like food. This situation can change eating patterns, impede physical growth and physiological processes, and damage biota immunological systems [57-59]. It is recognized that exposure to microplastics in the biota can facilitate the entrance of hazardous chemicals into the biota [60].

MPs studies in Indonesia on biota have been conducted on various species such as fish (demersal and pelagic) and benthic biota (sea cucumber, shellfish, sea urchins) (Table 3 and Table 4). Thirty-eight papers report the presence of MPs and anthropogenic waste in marine biota. Of the 38 articles, only eight articles reported the polymer composition in their studies. Plastics are generally identified in the digestive tract. The MPs abundance in fish ranged from 0 to 246 and 0 to 688 n/ind (for studies with polymer identification) (Table 3). The highest MPs concentration was found in the anchovy species *Stolephorus* spp., which is caught in the waters around Sulawesi (688 n/ind) [61]. Based on

FTIR results, it was suspected that the type of MPs found was polystyrene, polyamide. Generally, the higher MPs concentration was recorded in the pelagic fish (Table 3). MPs studies on benthic biota have been reported on shellfish, sea cucumbers, and sea urchins. However, only three studies provided data with polymer identification. The MPs abundance in benthic organisms ranged from 0.5 to 2175 and 0.29 to 3.2 n/ind (for studies with polymer identification) (Table 4).

The MP content found in marine biota from Indonesia was significantly varied. The lower MP concentration in demersal fish were recorded from Sulawesi Island (0.17 to 0.8 n/ind) [44] and Jakarta Bay (1.97 n/ind) [24]. Both of these values were below MP content in fish estuarine from England (0.69 n/ind) [62] and China (2.5 n/ind) [63]. The low range of MPs on benthic biota was recorded in Sulawesi Island (0.29 to

0.5 n/ind) [64]. This range was lower than France (2.1 n/ind) [65], and Canada (6.1 to 15.4 n/ind) [66]. Nevertheless, few studies reported a much higher concentration in fish, for instance, 366 ± 3.51 n/ind in a small pelagic fish, *Stolephorus* spp. [26].

Research Gaps on MPs Research in Indonesia

We highlight the limited resources (expensive chemical reagents and analytical instrumentation that are not easily/readily available in Indonesia) that caused most studies on MPs in Indonesia (64%) not to provide polymer analysis. It is found that MPs concentration in most studies without polymer identification can be overestimated. Consequently, the MPs' concentration in Indonesian waters is widely varied. Furthermore, these studies did not provide the blank procedure during the sampling and laboratory analysis, so it is challenging to do

Table 1. The concentration of MPs in seawater of Indonesia

Location	Sampling devices	Volume sample (L)	MPs extraction	Concentration (n/L)	Shape dominancy	Chemical form	Quality control	Ref.
Bali	Manta net	*NI	H ₂ O ₂ 30%	0.00054 to 0.0007	Fragment	PP, PE, PS	Yes	[67]
Bali	Plankton net	35800	Gravimetrically	0.00004 to 0.00090	Film	NA	NA	[68]
ENT	Rosette sampler	10	H ₂ O ₂ 30%	0.044 ± 0.024	Fiber	NA	NA	[19]
ENT	Plankton net	1	H ₂ O ₂ 30%	2 to 28	Fiber	NA	NA	[69]
Java	Pipette	0.2	NaCl	156 ± 13.46	Fiber	NA	NA	[70]
Java	Plankton net	20	NaCl	13.15	Fiber	NA	NA	[71]
Java	Plankton net	20	NaCl	90.7 to 103.8	Fiber	NA	NA	[72]
Java	Plankton net	10	NaCl	15460	Film	NA	NA	[73]
Java	Plankton net	20	NaCl	248.5 ± 3.81	Fiber	NA	NA	[74]
Java	Manta net	*NI	H ₂ O ₂ 30%	0.66 to 3.00	Fragment	PP, PE	Yes	[75]
Java	*NI	5	NaCl	700 to 11100	Fiber	PP, PE	Yes	[42]
Java	*NI	20	H ₂ O ₂ 30%	0.38 to 0.61	Foam	PE, PS	Yes	[76]
Java	Manta net	*NI	H ₂ O ₂ 30%	0.00848 to 0.00937	Fragment	PE, PP, PS	Yes	[24]
Java	Manta net	270000	ZnCl ₂	16.8 to 41.6 (in n/m ²)	*NI	PP, LDPE	NA	[77]
Java	Plankton net	20	NaCl	87626 to 110737	Fiber	NA	NA	[78]
Java	Manta trawl	0.15	NaCl	57530	Fiber	NA	NA	[79]
Java	Manta trawl	*NI	NaCl	70.9 ± 27.1	Film, fiber	PP, PE	Yes	[80]
Java	Plankton net	5000	*NI	12.6	Fiber	Nylon, PP, PS	NA	[81]
Molucca	Manta Net	21829	H ₂ O ₂ 30%	0.0146 to 0.4331	Fiber	NA	NA	[82]
Sulawesi	Vacuum pump	10	ZnCl ₂	7 to 55	*NI	PS	NA	[83]
Sulawesi	Manta net	*NI	ZnCl ₂	0.000023	*NI	LDPE, PS	NA	[44]
Sulawesi	Neuston net	*NI	KOH 10%	0.00178 to 0.00183	Fiber	NA	NA	[84]
Sulawesi	Neuston net	*NI	H ₂ O ₂ 30%	0.056	Fragment	PS	NA	[85]
Sulawesi	Neuston net	10	Gravimetrically	6.9 to 7.7	Fiber	PS, PE	Yes	[86]
Sumatra	Plankton net	5	NaCl	283.9 ± 2.63	Fiber	NA	NA	[87]
Sumatra	Manta net	*NI	H ₂ O ₂ 30%	0.00046 ± 0.00025	Fragment	PE, LDPE, PP	Yes	[18]

*ENT: East Nusa Tenggara; NI: Not Informed; NA: Not Available; n/L: item per liter; n/m²: item per meter square; PP: polypropylene, PS: Polystyrene; PE: polyethylene; LDPE: Low-Density PE

Table 2. The concentration of MPs in marine sediment of Indonesia

Location	Sampling devices	Volume sample (g)	MPs extraction	Concentration (n/Kg)	Shape dominancy	Chemical form	Quality control	Ref.
Java	Transect	250	H ₂ O ₂ 30%	28.09 ± 10.28	Foam	PP, PE	Yes	[37]
Java	Gravity corer	500	NaCl	800 to 49000	Fragment	PP, PE	Yes	[42]
Java	*NI	500	NaCl	31700	Film	NA	NA	[73]
Java	*NI	500	H ₂ O ₂ 30%	206.04 to 896.96	Fragment	NA	NA	[88]
Java	Transect	2000	NaCl	145 to 354	Fragment	NA	NA	[89]
Java	*NI	250	NaCl	87.4 to 99.88	Fiber	NA	NA	[78]
Java	Eckman grab	*NI	H ₂ O ₂ 30%	3.35 to 13.33	Fragment	PP, PE	Yes	[75]
Java	Grab sampler	*NI	NaCl	590	Fiber	PP, LDPE	*NI	[90]
Java	*NI	*NI	NaCl	18405 to 38790	Fragment	NA	NA	[91]
Java	Sediment grab	*NI	NaCl	82480 to 111680	Fiber	NA	NA	[72]
Java	Pipe	*NI	NaCl	169.2 ± 5.184	Fiber	NA	NA	[74]
Java	Smith-McIntyre	10 cm depth	NaCl	267 ± 98	Foam	CP, PS	Yes	[38]
Java	Grabs	500 to 1000	NaCl	920	Fiber	NA	NA	[71]
Java	Eckman grab	20	SI	34666 to 45066	Fiber	PE, PP, PS	NA	[92]
Java	Grab sampler	35 mL	ZnCl ₂	0 to 8	Fiber	PP	Yes	[93]
Java	Van Veen grab	600 to 880	NaCl	166.9	Film, fiber	PP, PE, PS	Yes	[80]
Java	*NI	*NI	H ₂ O ₂ 10%	28500 to 43000	Film	NA	NA	[94]
Molucca	Transect	0.0125 m ³	gravimetrically	68.8 N/m ²	Film	NA	NA	[21]
Papua	Transect		H ₂ O ₂ 30%	1140 to 1998	Fiber	NA	NA	[20]
Sumatra	Transect	250	NaCl	11200 ± 263	Fiber	NA	NA	[23]
Sumatra	Transect	250	NaCl	3700 ± 0.28	Film	NA	NA	[87]
Sumatra	Shovel	250	NaCl	906	Film	NA	NA	[95]
Sumatra	*NI	100	NaCl	1976 to 2203	Fiber	NA	NA	[96]
Sumatra	Van Veen grab	250	H ₂ O ₂ 30%	72.64 ± 25.28	Fragment	PE, PP	Yes	[97]
Sulawesi	*NI	100	ZnCl ₂	2.96 to 28.29	*NI	NA	NA	[83]
Sulawesi	*NI	120	ZnCl ₂	14.6 to 50	Fiber	PE	NA	[64]
Sulawesi	Corer	100	ZnBr ₂	195 ± 66.98	Fiber	NA	NA	[98]
Sulawesi	Transect	150	H ₂ O ₂ 30%	165 to 217	Fiber	NA	NA	[22]
WNT	Transect	1500	NaCl	116.41 ± 80.78	Fragment	NA	NA	[99]
WNT	Van Veen grab	250	H ₂ O ₂ 30%	44.19 ± 12.40	Fragment	PE, PP	Yes	[97]

*ENT: East Nusa Tenggara; NI: Not Informed; NA: Not Available; n/Kg: item per kilogram; n/m²: item per meter square; n/m³: item per meter cubic; PP: polypropylene; PS: Polystyrene; PE: polyethylene; LDPE: Low-Density PE; ABS: Acrylonitrile Butadiene Styrene; PC: Polycarbonates; CP: cellulose propionate; PVC: Polyvinyl Chloride; PA: polyamide

Table 3. The abundance of MPs in fish from Indonesia

Location	Species	Number of samples	MPs extraction	Concentrations	Physical shape	Chemical form	Quality control	Ref
ENT	<i>Stolephorus spp.</i>	15	NaOH	302 ± 1.0	Film	NA	NA	[25]
Java	<i>Mugil dussumieri</i>	15	HNO ₃ 65%	297	Fiber	NA	NA	[79]
Java	<i>Aplocheilus sp.</i>	60	H ₂ O ₂ 30%	1.97	Fiber	PP, PS	Yes	[24]
Java	<i>Various fishes</i>	25	HNO ₃ 65%	16.28	Fiber	NA	NA	[100]
Java	<i>Oreochromis mossambicus</i>	10	NaCl	4.30 ± 4.7	Fiber	NA	NA	[101]
Java	<i>Scatophagus argus</i>	35	NaCl	5.22 ± 4.3	Fiber	NA	NA	[101]
Java	<i>S. canaliculatus</i>	30	NaCl	17.97 ± 5.8	Fiber	NA	NA	[101]
Java	<i>Crenimugil seheli</i>	12	NaCl	8.42 ± 11.9	Fiber	NA	NA	[101]
Java	<i>M. cephalus</i>	27	NaCl	9.26 ± 6.1	Fiber	NA	NA	[101]
Java	<i>C.chanos</i>	10	NaCl	8 ± 6.3	Fiber	NA	NA	[101]
Java	<i>Anodontostoma chacunda</i>	10	NaCl	12.50 ± 6.7	Fiber	NA	NA	[101]
Java	<i>Abalistes stellaris</i>	30	NaCl	16.07 ± 11.05	Fiber	NA	NA	[101]

Location	Species	Number of samples	MPs extraction	Concentrations	Physical shape	Chemical form	Quality control	Ref
Java	<i>C. chanos</i>	6	HNO ₃ 65%	8.8 to 9.58 (n/g)	Fiber	NA	NA	[72]
Java	<i>C. chanos</i>	3	H ₂ O ₂ 30%	1.16 to 2.66	Fragment	PP, PE	Yes	[75]
Java	<i>Euthynnus affinis</i>	*NI	KOH 15%	1 to 9	*NI	NA	NA	[102]
Java	<i>S. commersonnii</i>	15	H ₂ O ₂ 30%	1.87 ± 0.64	Fiber	NA	NA	[28]
Java	<i>S. insularis</i>	15	H ₂ O ₂ 30%	6.8 ± 1.62	Fiber	NA	NA	[28]
Java	<i>S. indicus</i>	15	H ₂ O ₂ 30%	3.66 ± 2.41	Fiber	NA	NA	[28]
Java	<i>S. indicus</i>	*NI	NaOH	246.10 ± 32.25	Fiber	NA	NA	[70]
Java	<i>S. fimbriata</i>	10	NaCl	14.6 ± 6.09	Fiber	NA	NA	[70]
Java	<i>Stolephorus</i> spp.	15	NaOH	42 to 131	Fiber	PP, PA	Yes	[61]
Java	<i>L. vitta</i>	3	NaCl	15 to 26	Fiber	NA	NA	[103]
Java	<i>Cephalopholis boenak</i>	2	NaCl	8 to 10	Fiber	NA	NA	[103]
Java	<i>C. formosa</i>	1	NaCl	8	Fiber	NA	NA	[103]
Java	<i>Plectorhinchus gibbosus</i>	1	NaCl	7	Fiber	NA	NA	[103]
Java	<i>Cyprinus</i> sp.	1	NaCl	11	Fiber	NA	NA	[103]
Java	Genera <i>Epinephelus</i>	20	HNO ₃ 65%	82.4	Fiber	NA	NA	[94]
Kalimantan	<i>Stolephorus</i> spp.	15	NaOH	130 ± 1.73	Fiber	NA	NA	[25]
Kalimantan	<i>Stolephorus</i> spp.	16	NaOH	366 ± 3.51	Fragment	PE, HDPE	NA	[26]
Molucca	<i>Epinephelus fuscoguttatus</i>	29	NaCl	3.07	Fragment	NA	NA	[31]
Molucca	<i>E. coioides</i>	36	NaCl	2.64	Fragment	NA	NA	[31]
Molucca	<i>E. suillus</i>	65	NaCl	1.51	Fragment	NA	NA	[31]
Molucca	<i>S. canaliculatus</i>	47	NaCl	2.47	Fragment	NA	NA	[31]
Molucca	<i>Synanceia</i>	27	NaCl	5.93	Film	NA	NA	[31]
Molucca	<i>Scarus psittacus</i>	16	NaCl	2.25	Fragment	NA	NA	[31]
Molucca	<i>Stolephorus</i> spp.	15	NaOH	277 ± 1.15	Fiber	PA	Yes	[61]
Papua	<i>Stolephorus</i> spp.	15	NaOH	59 to 290	Fiber	HDPE, PA	Yes	[61]
Sumatra	Various fishes	25	KOH 10%	62.96	Film	NA	NA	[104]
Sumatra	<i>Stolephorus</i> spp.	15	NaOH	246 to 645	Fiber	PS, PS, HDPE	Yes	[61]
Sulawesi	<i>Oreochromis niloticus</i>	5	KOH 10%	0			NA	[34]
Sulawesi	Family Carangidae	7	KOH 10%	5.9 ± 5.1	Fragment	NA	NA	[34]
Sulawesi	<i>S. argenteus</i>	2	KOH 10%	0.5 ± 0.7	Fragment	NA	NA	[34]
Sulawesi	<i>S. fuscescens</i>	2	KOH 10%	0			NA	[34]
Sulawesi	<i>S. canaliculatus</i>	3	KOH 10%	0.3 ± 0.6	Fiber	NA	NA	[34]
Sulawesi	<i>Lutjanus gibbus</i>	5	KOH 10%	0.00			NA	[34]
Sulawesi	<i>Katsuwonus pelamis</i>	9	KOH 10%	0			NA	[34]
Sulawesi	<i>Rastrelliger kanagurta</i>	9	KOH 10%	1 ± 1.1	Fragment	NA	NA	[34]
Sulawesi	<i>Decapterus macrosoma</i>	17	KOH 10%	2.5 ± 6.3	Foam	NA	NA	[34]
Sulawesi	<i>Spratelloides gracilis</i>	10	KOH 10%	1.1 ± 1.7	Fragment	NA	NA	[34]
Sulawesi	<i>S. canaliculatus</i>	10	KOH 10%	0.8	*NI	LDPE, Nylon, PS	NA	[44]
Sulawesi	<i>Gerres longirostris</i>	10	KOH 10%	0.5	*NI	LDPE, Nylon, PS	NA	[44]
Sulawesi	<i>Selaroides leptolepis</i>	14	KOH 10%	0.43	*NI	LDPE, Nylon, PS	NA	[44]
Sulawesi	<i>Lethrinus ornatus</i>	12	KOH 10%	0.17	*NI	LDPE, Nylon, PS	NA	[44]
Sulawesi	<i>Oreochromis niloticus</i>	25	KOH 10%	1.6 to 3.5	*NI	NA	Yes	[84]
Sulawesi	<i>Megalops cyprinoides</i>	12	KOH 10%	1.83 to 3.5	*NI	NA	Yes	[84]
Sulawesi	<i>Barbonymus gonionotus</i>	23	KOH 10%	0.91 to 2	*NI	NA	Yes	[84]
Sulawesi	<i>Chanos chanos</i>	50	KOH 10%	3.5 ± 2.87	*NI	NA	Na	[30]
Sulawesi	<i>Stolephorus</i> spp.	15	NaOH	95 to 688	Fiber	PS, PA	Yes	[61]
WNT	<i>Stolephorus</i> spp.	16	NaOH	88 ± 2.89	Fiber	PP, PS, LDPE, Nylon	NA	[27]
WNT	<i>Stolephorus</i> spp.	15	NaOH	48 ± 2.31	Fiber	PS	Yes	[61]

*WNT: West Nusa Tenggara; NI: Not Informed; NA: Not Available; n/ind: item per individual; n/g: item per gram; PP: polypropylene; PA: polyamide; PS: Polystyrene; PVC: Polyvinyl Chloride; HDPE: High-density polyethylene

Table 4. The abundance of MPs in benthos from Indonesia

Location	Species	Number of samples	Mps Extraction	Concentrations (n/ind)	Physical shape	Chemical form	QC	Ref.
Java	<i>Perna viridis</i>	30	HNO ₃ 65%	23	Fiber	NA	NA	[71]
Java	<i>Littoraria scabra</i>	10	HNO ₃ 65%	75.5	Fiber	NA	NA	[105]
Java	<i>Metopograpsus quadridentata</i>	9	HNO ₃ 65%	328.56	Fiber	NA	NA	[105]
Java	<i>Telescopium telescopium</i>	27	HNO ₃ 65%	764.81	Film	NA	NA	[73]
Java	<i>Anadara granosa</i>	15	HNO ₃ 65%	618.8 ± 121.4	Fiber	NA	NA	[74]
Java	<i>Diadema setosum</i>	15	HNO ₃ 65%	1,786 to 2,175	Fiber	NA	NA	[78]
Java	<i>Holothuria leucospilota</i>	15	HNO ₃ 65%	8.44 (n/g)	Fiber	NA	NA	[106]
Java	<i>Paracaudina sp</i>	20	KOH 10%	289 to 1380	Fiber	NA	NA	[107]
Java	<i>Dolabella auricularia</i>	8	HNO ₃ 65%	40.1 to 73.7 (n/g)	Fiber	NA	NA	[108]
Java	<i>Placuna placenta</i>	6	H ₂ O ₂ 30%	1	Fiber	PP, Nylon	NA	[81]
Sumatra	<i>A. granosa</i>	10	HNO ₃ 65%	434 ± 97.05	Fiber	NA	NA	[23]
Sumatra	<i>Cerithidea obtusa</i>	*NI	HNO ₃ 65%	167 ± 16.01	Film	NA	NA	[87]
Sumatra	<i>Laevistrombus turturella</i>	*NI	HNO ₃ 65%	489	Film	NA	NA	[95]
Sumatra	<i>H. scabra</i>	28	H ₂ O ₂ 30%	3.21 ± 0.07	Fragment	PE, PP	Yes	[97]
Sumatra	<i>Various species</i>	*NI	H ₂ O ₂ 30%	32 to 52	Fiber	NA	NA	[109]
Sulawesi	<i>Marcia hiantina</i>	22	KOH 20%	1.10 to 3.08	Fiber	NA	NA	[110]
Sulawesi	<i>Tripneustes gratilla</i>	17	KOH 10%	0.53	*NI	NA	NA	[64]
Sulawesi	<i>Pinna sp.</i>	6	KOH 10%	0.5	*NI	NA	NA	[64]
Sulawesi	<i>Pinctada sp.</i>	12	KOH 10%	0.3	*NI	NA	NA	[64]
Sulawesi	<i>Cypraea tigris</i>	10	KOH 10%	0.3	*NI	NA	NA	[64]
Sulawesi	<i>Nudi Branch</i>	6	KOH 10%	0			NA	[64]
Sulawesi	<i>Tripneustes gratilla</i>	14	KOH 10%	0.5	*NI	LDPE, PS	NA	[44]
Sulawesi	<i>Cypraea tigris</i>	14	KOH 10%	0.36	*NI	LDPE, PS	NA	[44]
Sulawesi	<i>Pinctada sp.</i>	14	KOH 10%	0.29	*NI	LDPE, PS	NA	[44]
Sulawesi	<i>D. setosum</i>	10	KOH 10%	23.70 ± 2.99	Fiber	NA	NA	[98]
WNT	<i>H. scabra</i>	54	H ₂ O ₂ 30%	1.39 ± 0.86	Fragment	PE, PP	Yes	[99]

*NI: Not Informed; NA: Not Available; n/ind: item per individual; n/g: item per gram; PS: Polystyrene; LDPE: Low-Density polyethylene; PA: polyamide

comparative studies among other studies across Indonesia.

The MPs' research in Indonesia primarily focused on the western part of Indonesia (65%), including Java Island. About 50% of studies were conducted on Java Island (Fig. 2). Over 60% of data came from the western part of Indonesia. Meanwhile, research conducted in the eastern part of Indonesia were predominantly in rural areas and small islands that are very vulnerable to marine plastic waste due to limited waste management. Over 70% of plastic pollution in Indonesia originates in rural regions and small to medium-sized cities [8-9]. It is reported that plastic waste in mangrove areas of small islands such as the Ambon Island (Molucca) negatively impacts mangrove health [43]. Plastic waste is trapped in mangrove areas due to limited waste management on small islands.

It is also observed that limited data is available regarding the distribution of MPs in Indonesia's deep-sea waters. The lack of study in the deep-sea area of Indonesia is something that is worth noting. Essentially, if we refer to the deep-sea's definition as a sea with a depth of more than 200 meters vertically and horizontally [111], then 68% (4.1 million km²) of Indonesia's marine area is classified as deep-sea waters [112]. Although very limited data is available from the deep sea area, several studies predicted potentially large quantities accumulating in the deep sea ocean. This is expected after a higher concentration of MP is found in line with their depth [7,112]. It is reported that the increase in the value of MP in the water column and marine sediment in Mariana Trench is in conformity with its depth [7]. However, our knowledge about microplastic pollution from deep-sea oceans is relatively

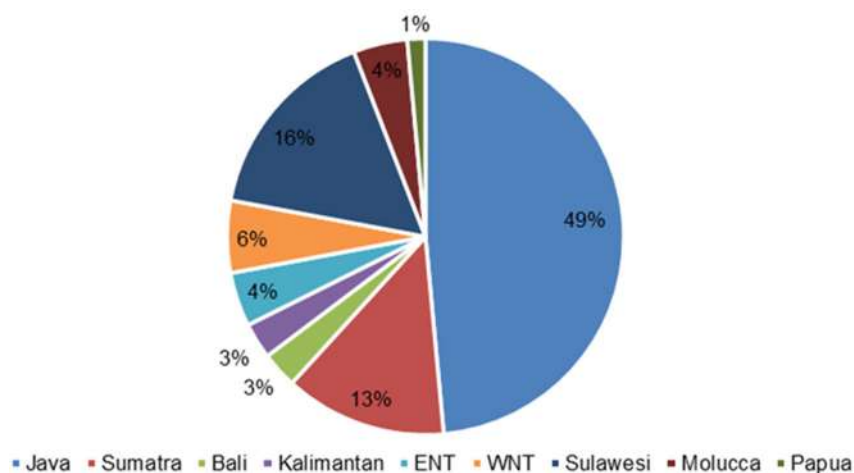


Fig 2. Number of papers on microplastics published between 2015 and 2022 (June) in Indonesia based on locations

little. We need more data from deep-sea areas.

This brief review also highlights that the dominant research in Indonesia is still related to the distribution and concentration of MPs. Information on MPs fate analysis until it reaches the body of organisms or humans and research related to the mechanism of transportation of microplastics does not appear to be widely available in Indonesia. Furthermore, due to the higher MPs concentration in Indonesian waters in some locations, we proposed to do research about remediating MP from the environment. The MPs remediation technologies such as electrocoagulation, sediment-MP isolation (SMI), cellulose nitrate filter membrane, fluidization and flotation, nanoparticle and sol-gel method have been widely used in the remediation of MPs [114].

■ CONCLUSION

This brief review summarizes the milestones that have been made in microplastic research in the Indonesian waters over the last decade. Lack of polymer analysis in the research in Indonesia due to the limited resources (expensive chemical reagents and analytical instrumentation that is not easily/readily available) led to many unconfirmed studies regarding the type of polymer, thus can also undermine the result. It is noteworthy that most studies on MP in Indonesia (64%) do not provide polymer identification and lack a blank/control procedure during the sampling until the identification process, thus impeding data quality. Consequently, the

estimation of MP concentration is overestimated, and comparative studies are challenging. The MP research was mainly conducted in the western part of Indonesia, especially on Java Island. Data and information about MP pertaining to the eastern part of Indonesia are very limited. Current research has primarily focused on coastal waters rather than the deep-sea area. Thus, we propose to have a standard guideline for MPs analysis at a national level and future work should focus on conducting more research in the eastern part of Indonesia, which is mainly dominated by deep-sea areas.

■ ACKNOWLEDGMENTS

The authors thank Dr. Muhammad Reza Cordova from the Research Center for Oceanography, National Research and Innovation Agency (BRIN) and Dr.rer.nat. Yasman, M.Sc. from Universitas Indonesia (UI) for providing helpful comments on earlier drafts of the manuscript. The authors would like to thank the 2022-2023 Hibah PUTI Q2 of Universitas Indonesia (NKB-656/UN2.RST/HKP.05.00/2022) and LIPI COREMAP-CTI 2021–2022 (17/A/DK/2021) for funding this study.

■ AUTHOR CONTRIBUTIONS

Corry Yanti Manullang: Writing – original draft, Writing – Review & editing, Conceptualization, Resources, Investigation, Methodology, Analysis. Rafidha Dh Ahmad Opier: Data curation. Suyadi, Mufti Petala Patria, Agus Haryono, Sabiqah Tuan Anuar:

Supporting the study and revising the substantial content.

■ REFERENCES

- [1] Plastics Europe, 2020, *Plastics—the Facts 2020*, <https://plasticseurope.org/knowledge-hub/plastics-the-facts-2020/>, accessed on 1 March 2021.
- [2] Thevenon, F., Carroll, C., and Sousa, J., 2014, *Plastic Debris in the Ocean: The Characterization of Marine Plastics and their Environmental Impacts, Situation Analysis Report*, IUCN, Gland, Switzerland.
- [3] Geyer, R., Jambeck, J.R., and Law, K.L., 2017, Production, use, and fate of all plastics ever made, *Sci. Adv.*, 3 (7), e1700782.
- [4] Jambeck, J., Geyer, R., Wilcox, C., Siegler, T.R., Perryman, M., Andrady, A., Narayan, R., and Law, K.L., 2015, Plastic waste inputs from land into the ocean, *Science*, 347 (6223), 768–771.
- [5] Meijer, L.J.J., van Emmerik, T., van der Ent, R., Schmidt, C., and Lebreton, L., 2021, More than 1000 rivers account for 80% of global riverine plastic emissions into the ocean, *Sci. Adv.*, 7 (18), eaaz5803.
- [6] Lusher, A.L., Tirelli, V., O'Connor, I., and Officer, R., 2015, Microplastics in Arctic polar waters: The first reported values of particles in surface and sub-surface samples, *Sci. Rep.*, 5 (1), 14947.
- [7] Peng, X., Chen, M., Chen, S., Dasgupta, S., Xu, H., Ta, K., Du, M., Li, J., Guo, Z., and Bai, S., 2018, Microplastics contaminate the deepest part of the world's ocean, *Geochem. Perspect. Lett.*, 9, 1–5.
- [8] Government Republic of Indonesia, 2020, *Indonesia's Plan of Action on Marine Plastic Debris 2017-2025*, https://maritim.go.id/konten/unggahahan/2018/03/NAP_Marine_Plastic_Debris_Indonesia_Summary.pdf, accessed on 1 August 2021.
- [9] World Bank, 2021, *Plastic Waste Discharges from Rivers and Coastlines in Indonesia*, Marine Plastics Series, East Asia and Pacific Region, Washington DC.
- [10] GESAMP, 2015, *Sources, fate and effects of microplastics in the marine environment: A global assessment*, Eds. Kershaw, P.J., IMO/FAO/UNESCO-IOC/UNIDO/WMO/IAEA/UN/UNEP/UNDP Joint Group of Experts on the Scientific Aspects of Marine Environmental Protection, Rep. Stud., GESAMP No. 90, 96 p.
- [11] Kühn, S., Bravo Rebolledo, E.L., and van Franeker, J.A., 2015, "Deleterious Effects of Litter on Marine Life" in *Marine Anthropogenic Litter*, Eds. Bergmann, M., Gutow, L., and Klages, M., Springer International Publishing, Cham, Switzerland, 75–116.
- [12] Besseling, E., Wegner, A., Foekema, E.M., van den Heuvel-Greve, M.J., and Koelmans, A.A., 2013, Effects of microplastic on fitness and PCB bioaccumulation by the lugworm *Arenicola marina* (L.), *Environ. Sci. Technol.*, 47 (1), 593–600.
- [13] Cole, M., Lindeque, P., Fileman, E., Halsband, C., Goodhead, R., Moger, J., and Galloway, T.S., 2013, Microplastic ingestion by zooplankton, *Environ. Sci. Technol.*, 47 (12), 6646–6655.
- [14] Desforges, J.P.W., Galbraith, M., and Ross, P.S., 2015, Ingestion of microplastics by zooplankton in the northeast Pacific Ocean, *Arch. Environ. Contam. Toxicol.*, 69 (3), 320–330.
- [15] Md Amin, R., Sohaimi, E.S., Anuar, S.T., and Bachok, Z., 2020, Microplastic ingestion by zooplankton in Terengganu coastal waters, southern South China Sea, *Mar. Pollut. Bull.*, 150, 110616.
- [16] Sun, X., Li, Q., Zhu, M., Liang, J., Zheng, S., and Zhao, Y., 2017, Ingestion of microplastics by natural zooplankton groups in the northern South China Sea, *Mar. Pollut. Bull.*, 115 (1-2), 217–224.
- [17] Wicczorek, A.M., Croot, P.L., Lombard, F., Sheahan, J.N., and Doyle, T.K., 2019, Microplastic ingestion by gelatinous zooplankton may lower efficiency of the biological pump, *Environ. Sci. Technol.*, 53 (9), 5387–5395.
- [18] Syakti, A.D., Hidayati, N.V., Jaya, Y.V., Siregar, S.H., Yude, R., Suhendy, S., Asia, L., Wong-Wah-Chung, P., and Doumenq, P., 2018, Simultaneous grading of microplastic size sampling in the Small Islands of Bintan water, Indonesia, *Mar. Pollut. Bull.*, 137, 593–600.
- [19] Cordova, M.R., and Hernawan, U.E., 2018, Microplastics in Sumba waters, East Nusa

- Tenggara, *IOP Conf. Ser.: Earth Environ. Sci.*, 162, 012023.
- [20] Marei, I.C.A., Saleh, F.I.E., Manullang, C.Y., Soamole, A., and Rehalat, I., 2021, Occurrence and distribution of microplastics in the beach sediment of Anday Beach, West Papua (Indonesia), *IOP Conf. Ser.: Earth Environ. Sci.*, 944, 012070.
- [21] Manullang, C.Y., 2019, The abundance of plastic marine debris on beaches in Ambon Bay, *IOP Conf. Ser.: Earth Environ. Sci.*, 253, 012037.
- [22] Widiastuti, I.M., Serdiati, N., and Tahya, A.M., 2021, Study of microplastic sediment abundance in Palu Bay, Central Sulawesi, Indonesia, *AACL Bioflux*, 14 (5), 2857–2865.
- [23] Fitri, S., and Patria, M.P., 2019, Microplastic contamination on *Anadara granosa* Linnaeus 1758 in Pangkal Babu mangrove forest area, Tanjung Jabung Barat district, Jambi, *J. Phys.: Conf. Ser.*, 1282, 012109.
- [24] Cordova, M.R., Riani, E., and Shiomoto, A., 2020, Microplastics ingestion by blue panchax fish (*Aplocheilichthys* sp.) from Ciliwung Estuary, Jakarta, Indonesia, *Mar. Pollut. Bull.*, 161, 111763.
- [25] Ningrum, E.W., and Patria, M.P., 2019, Microplastics and mercury detection on anchovy from Alor and Balikpapan harbors, Indonesia, *2019 IEEE R10 Humanitarian Technology Conference (R10-HTC)(47129)*, November 12-14, 2019, Depok, Indonesia, 254–257.
- [26] Ningrum, E.W., Patria, M.P., and Sedayu, A., 2019, Ingestion of microplastics by anchovies from Talisayan harbor, East Kalimantan, Indonesia, *J. Phys.: Conf. Ser.*, 1402, 033072.
- [27] Ningrum, E.W., and Patria, M.P., 2019, Ingestion of microplastics by anchovies from east Lombok Harbour, Lombok Island, Indonesia, *AIP Conf. Proc.*, 2120 (1), 040002.
- [28] Guntur, G., Asadi, M.A., and Purba, K., 2021, Ingestion of microplastics by anchovies of the Madura Strait, Indonesia, *AACL Bioflux*, 14 (3), 1163–1170.
- [29] ICES, 2015, OSPAR request on development of a common monitoring protocol for plastic particles in fish stomachs and selected shellfish on the basis of existing fish disease surveys, *ICES Special Request Advice Northeast Atlantic and Arctic Ocean*, 1–6.
- [30] Amelinda, C., Werorilangi, S., Burhanuddin, A.I., and Tahir, A., 2021, Occurrence of microplastic particles in milkfish (*Chanos chanos*) from brackishwater ponds in Bonto Manai Village, Pangkep Regency, South Sulawesi, Indonesia, *IOP Conf. Ser.: Earth Environ. Sci.*, 763, 012058.
- [31] Al Muhdhar, M.H.I., Sumberartha, I.W., Hassan, Z., Rahmansyah, M.S., and Tamalene, M.N., 2021, Examination of microplastic particles in reef fish food in Ternate Island waters, Indonesia, *Jordan J. Biol. Sci.*, 14 (4), 853–858.
- [32] Catarino, A.I., Thomson, R., Sanderson, W., and Henry, T.B., 2017, Development and optimization of a standard method for extraction of microplastics in mussels by enzyme digestion of soft tissues, *Environ. Toxicol. Chem.*, 36 (4), 947–951.
- [33] Cole, M., Webb, H., Lindeque, P.K., Fileman, E.S., Halsband, C., Galloway, T.S., 2014, Isolation of microplastics in biota-rich seawater samples and marine organisms, *Sci. Rep.*, 4 (1), 4528.
- [34] Rochman, C.M., Tahir, A., Williams, S.L., Baxa, D.V., Lam, R., Miller, J.T., Teh, F.C., Werorilangi, S., and Teh, S.J., 2015, Anthropogenic debris in seafood: Plastic debris and fibers from textiles in fish and bivalves sold for human consumption, *Sci. Rep.*, 5 (1), 14340.
- [35] Dris, R., Gasperi, J., Mirande, C., Mandin, C., Guerrouache, M., Langlois, V., and Tassin, B., 2017, A first overview of textile fibers, including microplastics, in indoor and outdoor environments, *Environ. Pollut.*, 221, 453–458.
- [36] Shim, W.J., Hong, S.H., and Eo, S.E., 2017, Identification methods in microplastic analysis: A review, *Anal. Methods*, 9 (9), 1384–1391.
- [37] Cordova, M.R., Ulumuddin, Y.I., Purbonegoro, T., and Shiomoto, A., 2021, Characterization of microplastics in mangrove sediment of Muara Angke Wildlife Reserve, Indonesia, *Mar. Pollut. Bull.*, 163, 112012.

- [38] Falahudin, D., Cordova, M.R., Sun, X., Yogaswara, D., Wulandari, I., Hindarti, D., and Arifin, Z., 2020, The first occurrence, spatial distribution and characteristics of microplastic particles in sediments from Banten Bay, Indonesia, *Sci. Total Environ.*, 705, 135304.
- [39] Claessens, M., Van Cauwenberghe, L., Vandegehuchte, M.B., and Janssen, C.R., 2013, New techniques for the detection of microplastics in sediments and field collected organisms, *Mar. Pollut. Bull.*, 70 (1-2), 227–233.
- [40] Zhao, S., Ward, J.E., Danley, M., and Mincer, T.J., 2018, Field-based evidence for microplastic in marine aggregates and mussels: Implications for trophic transfer, *Environ. Sci. Technol.*, 52 (19), 11038–11048.
- [41] Song, J., Hou, C., Zhou, Y., Liu, Q., Wu, X., Wang, Y., and Yi, Y., 2020, The flowing of microplastics was accelerated under the influence of artificial flood generated by hydropower station, *J. Cleaner Prod.*, 255, 120174.
- [42] Khoironi, A., Hadiyanto, H., Anggoro, S., and Sudarno, S., 2020, Evaluation of polypropylene plastic degradation and microplastic identification in sediments at Tambak Lorok coastal area, Semarang, Indonesia, *Mar. Pollut. Bull.*, 151, 110868.
- [43] Suyadi, S., and Manullang, C.Y., 2020, Distribution of plastic debris pollution and its implications on mangrove vegetation, *Mar. Pollut. Bull.*, 160, 111642.
- [44] Tahir, A., Soeprapto, D.A., Sari, K., Wicaksono, E.A., and Werorilangi, S., 2020, Microplastic assessment in seagrass ecosystem at Kodingareng Lompo island of Makassar City, *IOP Conf. Ser.: Earth Environ. Sci.*, 564, 012032.
- [45] Han, M., Niu, X., Tang, M., Zhang, B.T., Wang, G., Yue, W., Kong, X., and Zhu, J., 2019, Distribution of microplastics in surface water of the lower Yellow River near estuary, *Sci. Total Environ.*, 707, 135601.
- [46] Zhao, S., Wang, T., Zhu, L., Xu, P., Wang, X., Gao, L., and Li, D., 2019, Analysis of suspended microplastics in the Changjiang Estuary: Implications for riverine plastic load to the ocean, *Water Res.*, 161, 560–569.
- [47] Zhao, S., Zhu, L., Wang, T., and Li, D., 2014, Suspended microplastics in the surface water of the Yangtze Estuary System, China: First observations on occurrence, distribution, *Mar. Pollut. Bull.*, 86 (1-2), 562–568.
- [48] Lima, A.R.A., Costa, M.F., and Barletta, M., 2014, Distribution patterns of microplastics within the plankton of a tropical estuary, *Environ. Res.*, 132, 146–155.
- [49] Naidoo, T., Glassom, D., and Smit, A.J., 2015, Plastic pollution in five urban estuaries of KwaZulu-Natal, South Africa, *Mar. Pollut. Bull.*, 101 (1), 473–480.
- [50] Sadri, S.S., and Thompson, R.C., 2014, On the quantity and composition of floating plastic debris entering and leaving the Tamar Estuary, Southwest England, *Mar. Pollut. Bull.*, 81 (1), 55–60.
- [51] Courtene-Jones, W., Quinn, B., Gary, S.F., Mogg, A.O.M., and Narayanaswamy, B.E., 2017, Microplastic pollution identified in deep-sea water and ingested by benthic invertebrates in the Rockall Trough, North Atlantic Ocean, *Environ. Pollut.*, 231, 271–280.
- [52] Peng, G., Xu, P., Zhu, B., Bai, M., and Li, D., 2017, Microplastics in freshwater river sediments in Shanghai, China: A case study of risk assessment in mega-cities, *Environ. Pollut.*, 234, 448–456.
- [53] Wu, N., Zhang, Y., Zhang, X., Zhao, Z., He, J., Li, W., Ma, Y., and Niu, Z., 2019, Occurrence and distribution of microplastics in the surface water and sediment of two typical estuaries in Bohai Bay, China, *Environ. Sci.: Processes Impacts*, 21 (7), 1143–1152.
- [54] Mohamed Nor, N.H., and Obbard, J.P., 2013, Microplastics in Singapore's coastal mangrove ecosystems, *Mar. Pollut. Bull.*, 79 (1-2), 278–283.
- [55] Oliveira, M., Ribeiro, A., Hylland, K., and Guilhermino, L., 2013, Single and combined effects of microplastics and pyrene on juveniles (0+ group) of the common goby *Pomatoschistus*

- microps* (Teleostei, Gobiidae), *Ecol. Indic.*, 34, 641–647.
- [56] Rist, S.E., Assidqi, K., Zamani, N.P., Appel, D., Perschke, M., Huhn, M., and Lenz, M., 2016, Suspended micro-sized PVC particles impair the performance and decrease survival in the Asian green mussel *Perna viridis*, *Mar. Pollut. Bull.*, 111 (1-2), 213–220.
- [57] Derraik, J.G.B., 2002, The pollution of the marine environment by plastic debris: A review, *Mar. Pollut. Bull.*, 44 (9), 842–852.
- [58] Wright, S.L., Thompson, R.C., and Galloway, T.S., 2013, The physical impacts of microplastics on marine organisms: A review, *Environ. Pollut.*, 178, 483–492.
- [59] von Moos, N., Burkhardt-Holm, P., and Köhler, A., 2012, Uptake and effects of microplastics on cells and tissue of the blue mussel *Mytilus edulis* L. after an experimental exposure, *Environ. Sci. Technol.*, 46 (20), 11327–11335.
- [60] Rochman, C.M., Hoh, E., Kurobe, T., and Teh, S.J., 2013, Ingested plastic transfers hazardous chemicals to fish and induces hepatic stress, *Sci. Rep.*, 3 (1), 3263.
- [61] Ningrum, E.W., and Patria, M.P., 2022, Microplastic contamination in Indonesian anchovies from fourteen locations, *Biodiversitas*, 23, 125–134.
- [62] Horton, A.A., and Barnes, D.K.A., 2020, Microplastic pollution in a rapidly changing world: Implications for remote and vulnerable marine ecosystems, *Sci. Total Environ.*, 738, 140349.
- [63] Jabeen, K., Su, L., Li, J., Yang, D., Tong, C., Mu, J., and Shi, H., 2017, Microplastics and mesoplastics in fish from coastal and fresh waters of China, *Environ. Pollut.*, 221, 141–149.
- [64] Tahir, A., Samawi, M.F., Sari, K., Hidayat, R., Nimzet, R., Wicaksono, E.A., Asrul, L., and Werorilangi, S., 2019, Studies on microplastic contamination in seagrass beds at Spermonde Archipelago of Makassar Strait, Indonesia, *J. Phys.: Conf. Ser.*, 1341, 022008.
- [65] Phuong, N.N., Poirier, L., Pham, Q.T., Lagarde, F., and Zalouk-Vergnoux, A., 2018, Factors influencing the microplastic contamination of bivalves from the French Atlantic coast: Location, season and/or mode of life?, *Mar. Pollut. Bull.*, 129 (2), 664–674.
- [66] Davidson, K., and Dudas, S.E., 2016, Microplastic ingestion by wild and cultured Manila clams (*Venerupis philippinarum*) from Baynes Sound, British Columbia, *Arch. Environ. Contam. Toxicol.*, 71 (2), 147–156.
- [67] Suteja, Y., Atmadipoera, A.S., Riani, E., Nurjaya, I.W., Nugroho, D., and Cordova, M.R., 2021, Spatial and temporal distribution of microplastic in surface water of tropical estuary: Case study in Benoa Bay, Bali, Indonesia, *Mar. Pollut. Bull.*, 163, 111979.
- [68] Germanov, E.S., Marshall, A.D., Hendrawan, I.G., Admiraal, R., Rohner, C.A., Argeswara, J., Wulandari, R., Himawan, M.R., and Loneragan, N.R., 2019, Microplastics on the menu: Plastics pollute Indonesian manta ray and whale shark feeding grounds, *Front. Mar. Sci.*, 6, 679.
- [69] Kisnarti, E.A., Ningsih, N.S., Putri, M.R., Hendriati, N., and Box, C., 2021, Microplastic observations in the waters of Labuan Bajo-Gili Trawangan, Indonesia, *IOP Conf. Ser.: Earth Environ. Sci.*, 925, 012043.
- [70] Hardianti, E., Wardhana, W., and Patria, M.P., 2021, Microplastic abundance in anchovy *Stolephorus indicus* (Van Hasselt, 1823) in the Lada Bay, Pandeglang, Banten, *J. Phys.: Conf. Ser.*, 1725, 012050.
- [71] Fathoniah, I., and Patria, M.P., 2021, Abundance of microplastic in green mussel *Perna viridis*, water, and sediment in Kamal Muara, Jakarta Bay, *J. Phys.: Conf. Ser.*, 1725, 012042.
- [72] Priscilla, V., and Patria, M.P., 2019, Comparison of microplastic abundance in aquaculture ponds of milkfish *Chanos chanos* (Forsskål, 1775) at Muara Kamal and Marunda, Jakarta Bay, *IOP Conf. Ser.: Earth Environ. Sci.*, 404, 012027.

- [73] Putri, F.T., and Patria, M.P., 2021, Microplastic in mangrove horn snail *Telescopium telescopium* (Linnaeus, 1758) at mangrove ecosystem, Rambut Island, Jakarta Bay, Indonesia, *J. Phys.: Conf. Ser.*, 1725, 012045.
- [74] Ukhrowi, H.R., Wardhana, W., and Patria, M.P., 2021, Microplastic abundance in blood cockle *Anadara granosa* (Linnaeus, 1758) at Lada Bay, Pandeglang, Banten, *J. Phys.: Conf. Ser.*, 1725, 012053.
- [75] Sembiring, E., Fareza, A.A., Suendo, V., and Reza, M., 2020, The presence of microplastics in water, sediment, and milkfish (*Chanos chanos*) at the downstream area of Citarum River, Indonesia, *Water, Air, Soil Pollut.*, 231 (7), 355.
- [76] Cordova, M.R., Purwiyanto, A.I.S., and Suteja, Y., 2019, Abundance and characteristics of microplastics in the northern coastal waters of Surabaya, Indonesia, *Mar. Pollut. Bull.*, 142, 183–188.
- [77] Syakti, A.D., Bouhroum, R., Hidayati, N.V., Koenawan, C.J., Boulkamh, A., Sulisty, I., Lebarillier, S., Akhlus, S., Doumenq, P., and Wong-Wah-Chung, P., 2017, Beach macro-litter monitoring and floating microplastic in a coastal area of Indonesia, *Mar. Pollut. Bull.*, 122 (1-2), 217–225.
- [78] Huseini, D.R., Suryanda, A., and Patria, M.P., 2021, Comparative analysis of microplastic content in water, sediments, and digestive traces of sea urchin *Diadema setosum* (Leske, 1778) on Untung Jawa Island and Tidung Island, Seribu Islands, Jakarta, *IOP Conf. Ser.: Mater. Sci. Eng.*, 1098, 052051.
- [79] Rahmawati, N.H.F., and Patria, M.P., 2019, Microplastics dissemination from fish *Mugil dussumieri* and mangrove water of Muara Teluknaga, Tangerang, Banten, *J. Phys.: Conf. Ser.*, 1282, 012104.
- [80] Takarina, N.D., Purwiyanto, A.I.S., Rasud, A.A., Arifin, A.A., and Suteja, Y., 2022, Microplastic abundance and distribution in surface water and sediment collected from the coastal area, *Global J. Environ. Sci. Manage.*, 8 (2), 183–196.
- [81] Tielman, E.M., Indriana, L.F., Widowati, I., and Ambariyanto, A., 2022, Presence of microplastics in windowpane oyster *Placuna placenta* and the waters from the Tambak Lorok Coastal Area in Central Java, Indonesia, *IJMS*, 27 (1), 53–60.
- [82] Manullang, C.Y., Opier, R.D.A., Suyadi, S., Rehalat, I., Soamole, A., and Tatipatta, W.M., 2022, Floating microplastics on the sea surface of semi-closed and open bays of small islands, *AACL Bioflux*, 15 (1), 454–61.
- [83] Tahir, A., Taba, P., Samawi, M.F., and Werorilangi, S., 2019, Microplastics in water, sediment and salts from traditional salt producing ponds, *Global J. Environ. Sci. Manage.*, 5 (4), 431–440.
- [84] Wicaksono, E.A., Tahir, A., and Werorilangi, S., 2020, Preliminary study on microplastic pollution in surface-water at Tallo and Jeneberang Estuary, Makassar, Indonesia, *AACL Bioflux*, 13 (2), 902–909.
- [85] Kama, N.A., Rahim, S.W., and Yaqin, K., 2021, Microplastic concentration in column seawater compartment in Burau, Luwu Regency, South Sulawesi, Indonesia, *IOP Conf. Ser.: Earth Environ. Sci.*, 763, 012061.
- [86] Sawalman, R., Putri Zamani, N., Werorilangi, S., and Samira Ismet, M., 2021, Spatial and temporal distribution of microplastics in the surface waters of Barranglompo Island, Makassar, *IOP Conf. Ser.: Earth Environ. Sci.*, 860, 012098.
- [87] Fitri, S., and Patria, M.P., 2019, Microplastic contamination on *Cerithidea obtusa* (Lamarck 1822) in Pangkal Babu mangrove forest area, Tanjung Jabung Barat District, Jambi, *AIP Conf. Proc.*, 2168, 020075.
- [88] Yona, D., Sari, S.H.J., Iranawati, F., Bachri, S., and Ayuningtyas, W.C., 2019, Microplastics in the surface sediments from the eastern waters of Java Sea, Indonesia, *F1000Research*, 8, 98.
- [89] Asadi, M.A., Hertika, A.M.S., Iranawati, F., and Yuwandita, A.Y., 2019, Microplastics in the sediment of intertidal areas of Lamongan, Indonesia, *AACL Bioflux*, 12 (4), 1065–1073.
- [90] Firdaus, M., Trihadiningrum, Y., and Lestari, P., 2020, Microplastic pollution in the sediment of Jagir Estuary, Surabaya City, Indonesia, *Mar. Pollut. Bull.*, 150, 110790.

- [91] Manalu, A.A., Hariyadi, S., and Wardiatno, Y., 2017, Microplastics abundance in coastal sediments of Jakarta Bay, Indonesia, *AACL Bioflux*, 10 (5), 1164–1173.
- [92] Azizi, A., Setyowati, W.N., Fairus, S., Puspito, D.A., and Irawan, D.S., 2021, Microplastic pollution in the sediment of Jakarta Bay, Indonesia, *IOP Conf. Ser.: Earth Environ. Sci.*, 930, 012010.
- [93] Utami, D.A., Reuning, L., Konechnaya, O., and Schwarzbauer, J., 2021, Microplastics as a sedimentary component in reef systems: A case study from the Java Sea, *Sedimentology*, 68 (6), 2270–2292.
- [94] Mardiansyah, M., Utomo, A.B., and Putri, L.S.E., 2022, Microplastics in grouper fish (*Genera epinephelus*) gastrointestinal tract from Pramuka Island, Seribu Islands, Indonesia, *J. Ecol. Eng.*, 23 (3), 194–205.
- [95] Al Hamra, A.J., and Patria, M.P., 2019, Microplastic in gonggong snails (*Laevistrombus turturella*) and sediment of Bintan Island, Kepulauan Riau Province, Indonesia, *AIP Conf. Proc.*, 2202, 020079.
- [96] Amin, B., Galib, M., and Setiawan, F., 2020, Preliminary investigation on the type and distribution of microplastics in the west coast of Karimun Besar Island, *IOP Conf. Ser.: Earth Environ. Sci.*, 430, 012011.
- [97] Riani, E., and Cordova, M.R., 2022, Microplastic ingestion by the sandfish *Holothuria scabra* in Lampung and Sumbawa, Indonesia, *Mar. Pollut. Bull.*, 175, 113134.
- [98] Sawalman, R., Werorilangi, S., Ukkas, M., Mashoreng, S., Yasir, I., and Tahir, A., 2021, Microplastic abundance in sea urchins (*Diadema setosum*) from seagrass beds of Barranglompo Island, Makassar, Indonesia, *IOP Conf. Ser.: Earth Environ. Sci.*, 763, 012057.
- [99] Asadi, M.A., Ritonga, Y.A.P., Yona, D., and Hertika, A.M.S., 2019, Vertical distribution of microplastics in coastal sediments of Bama Resort, Baluran National Park, Indonesia, *Nat. Environ. Pollut. Technol.*, 18 (4), 1169–1176.
- [100] Efadeswarni, E., Andriantoro, A., Azizah, N., and Saragih, G.S., 2019, Microplastics in digestive tracts of fishes from Jakarta Bay, *IOP Conf. Ser.: Earth Environ. Sci.*, 407, 012008.
- [101] Hastuti, A.R., Lumbanbatu, D.T.F., and Wardiatno, Y., 2019, The presence of microplastics in the digestive tract of commercial fishes off Pantai Indah Kapuk coast, Jakarta, Indonesia, *Biodiversitas*, 20 (5), 1233–1242.
- [102] Andreas, A., Hadibarata, T., Sathishkumar, P., Prasetia, H., Hikmat, H., Pusfitasari, E.D., Tasfiyati, A.N., Muzdalifah, D., Waluyo, J., Randy, A., Ramadhaningtyas, D.P., Zuas, O., and Sari, A.A., 2021, Microplastic contamination in the Skipjack Tuna (*Euthynnus affinis*) collected from Southern Coast of Java, Indonesia, *Chemosphere*, 276, 130185.
- [103] Susanti, N.K.Y., Mardiasuti, A., and Hariyadi, S., 2022, Microplastics in fishes as seabird preys in Jakarta Bay area, *IOP Conf. Ser.: Earth Environ. Sci.*, 967, 012033.
- [104] Amin, B., Febriani, I.S., Nurrachmi, I., and Fauzi, M., 2020, Microplastics in gastrointestinal track of some commercial fishes from Bengkalis waters, Riau Province Indonesia, *J. Phys.: Conf. Ser.*, 1655, 012122.
- [105] Patria, M.P., Santoso, C.A., and Tsabita, N., 2020, Microplastic ingestion by periwinkle snail *Littoraria scabra* and mangrove crab *Metopograpsus quadridentata* in Pramuka Island, Jakarta Bay, Indonesia, *Sains Malays.*, 49 (9), 2151–2158.
- [106] Wicaksono, K.B., Patria, M.P., and Suryanda, A., 2021, Microplastic ingestion in the black sea cucumber *Holothuria leucospilota* (Brandt, 1835) collected from Rambut Island, Seribu Islands, Jakarta, Indonesia, *IOP Conf. Ser.: Mater. Sci. Eng.*, 1098, 052049.
- [107] Amin, B., Rukim, M., and Nurrachmi, I., 2021, Presence of microplastics in sea cucumber *Paracaudina* sp from Karimun Island, Kepulauan Riau, Indonesia, *IOP Conf. Ser.: Earth Environ. Sci.*, 934, 012053.
- [108] Priscilla, V., Sedayu, A., and Patria, M.P., 2019, Microplastic abundance in the water, seagrass, and sea hare *Dolabella auricularia* in Pramuka Island,

- Seribu Islands, Jakarta Bay, Indonesia, *J. Phys.: Conf. Ser.*, 1402, 033073.
- [109] Idris, F., Febrianto, T., Hidayati, J.R., Rajib, R., and Nugraha, A.H., 2022, Microplastic abundance in sea cucumber at seagrass ecosystem of Bintan Island and surrounding area, Indonesia, *IOP Conf. Ser.: Earth Environ. Sci.*, 967, 012009.
- [110] Wicaksono, E.A., Werorilangi, S., and Tahir, A., 2021, Microplastic occurrence in Venus clam *Marcia hiantina* (Veneridae) in Tallo Estuary, Makassar, Indonesia, *AACL Bioflux*, 14 (3), 1651–1657.
- [111] Rogers, A.D., 2015, Environmental change in the deep ocean, *Annu. Rev. Environ. Resour.*, 40, 1–38.
- [112] Indonesian Institute of Sciences, 2019, *Academic draft of Research Center for Deep-Sea*, Indonesian Institute of Sciences, Ambon.
- [113] Woodall, L.C., Sanchez-Vidal, A., Canals, M., Paterson, G.L.J., Coppock, R., Sleight, V., Calafat, A., Rogers, A.D., Narayanaswamy, B.E., and Thompson, R.C., 2014, The deep sea is a major sink for microplastic debris, *R. Soc. Open Sci.*, 1 (4), 140317.
- [114] Chellasamy, G., Kiriyanthan, R.M., Maharajan, T., Radha, A., and Yun, K., 2022, Remediation of microplastics using bionanomaterials: A review, *Environ. Res.*, 208, 112724.

Review:**An Overview of the Current State and Prospects for Oil Recovery from Oily Sludge**

Chinakulova Aigerim Nurlankyzy^{1*}, Niyazbekova Rimma Kalmanbayevna¹, Khaldun Mohammad Al Azzam², Mukhambetov Gabit Mukhambetovich³, Aimagambetova Raushan Zhanatovna⁴, El-Sayed Negim⁵, and Serekpayeva Mira¹

¹S. Seifullin Kazakh Agro Technical University, Nur-Sultan, Zhengis Ave 62, 010000, Kazakhstan

²Pharmacological and Diagnostic Research Center (PDRC), Department of Pharmaceutical Sciences, Faculty of Pharmacy, Al-Ahliyya Amman University, Amman 19328, Jordan

³Economics, Kazakhstan Institute of Standardization and Metrology, Nur-Sultan, Prospekt Mangilik Yel. 11, 010016, Kazakhstan

⁴Department of Strategic Development and Science of the Kazakhstan Institute of Metrology and Standardization, Nur-Sultan, Astana, 010000, Kazakhstan

⁵School of Petroleum Engineering, Satbayev University, 22 Satpayev Street, 050013 Almaty, Kazakhstan

*** Corresponding author:**

email: aigera_chinakulova@mail.ru

Received: August 24, 2022

Accepted: September 25, 2022

DOI: 10.22146/ijc.77253

Abstract: Oily sludge is a solid emulsified waste created by the petroleum industry. Solid particles, crude oil, and water comprise most of their composition. Because it contains high concentrations of cycloalkanes, benzene series, polycyclic aromatic hydrocarbons, and other harmful and hazardous substances, it poses a severe risk to human health and the environment. It must be treated to reduce its toxicity. However, crude oil is a significant component of oily sludge and has a high recycling value. As a result, numerous procedures for extracting crude oil from oily sludge have been developed, including solvent extraction, pyrolysis, centrifugation, ultrasonic treatment, electronic treatment, flotation, supercritical treatment, and combination processes. The primary purpose of this review is to describe the evolution of various recycling technologies and to compare their benefits, drawbacks, and ways of action. This concept is expected to be the cornerstone for future recycling technology development.

Keywords: oily sludge; petroleum industry; hazardous; crude oil; toxicity

■ INTRODUCTION

Energy is increasingly in demand globally because of the fourth industrial revolution's expanding economy. Most of the world's energy demands are met by fossil fuels, especially oil. With the accelerated expansion of industry and energy, consumption and demand for oil are rising drastically. As a result, refineries generate more oil sludge, which collects at the bottom of tanks when oil is being stored. This sludge negatively affects the tank's capacity and operational safety [1-5]. When discussing the production, exploration, storage, transportation, and processing of crude oil, the term "oil sludge" refers to a thick, viscous, and challenging-to-handle fluid [6-10].

A complex physicochemical combination of oil products, water, and mechanical contaminants, including clay, sand, and metal oxides, make up oil sludge. Oil sludge is mainly developed during producing, processing, storing, and transporting of oil. It comprises drilling fluid, waste oil in the well, emulsified solids produced during crude oil processing, and sediment found in the storage tank [11-14]. When oil is cleaned of pollutants and water, for example, oil sludge can occur as a consequence of natural, regulated processes, as well as other kinds of accidents (spills). The environment might sustain severe harm in the latter scenario due to a large-scale disaster or late identification. The primary

goal of this review is to describe the evolution of various recycling technologies and compare their advantages, disadvantages, and methods of operation.

■ FORMATION OF OIL SLUDGE

During transportation to the refinery, the heavier and lighter crude oil hydrocarbons often separate. This problem is usually exacerbated by storing crude at low temperatures, removing volatile components, and using cool temperatures. The thick fractions that separate from crude oil and settle at the bottom of storage tanks are referred to as sludge [1,15]. Both upstream and downstream oil industry operations can generate large volumes of oil waste. While downstream activities refer to crude oil refining, upstream operations refer to crude oil extraction, transportation, and storage. Oil sludge sources in upstream operations include slop oil in oil wells, oil left in tank bottoms, and drilling mud deposits.

Crude oil is temporarily stored in storage tanks before being converted into petroleum products, where it usually separates into heavier and lighter petroleum hydrocarbons. Heavy hydrocarbons frequently sink with water and other particulates. Oil sludge is a substance that collects at the bottom of storage tanks and combines oil, sediments, and water. These are taken out through tank

cleaning procedures and shipped for additional processing or disposal [16-17].

The amount of sludge created during the refining process is determined by various factors, including the crude oil's properties (such as density and viscosity), the way the refinery processes the crude, how oil is stored, and—most importantly—the capacity of the refinery [18-24]. The production of more oil sludge is typically correlated with cleaning higher power. One ton of oil sludge is generated for every 500 tons of crude oil treated, according to estimations [25-27]. According to assessments, more than 60 million tons of oily sludge can produce each year, and more than 1 billion tons of oily sludge have accumulated as a whole [28-30]. Fig. 1 shows the schematic diagram of the oily sludge sources. Furthermore, it is predicted that the total output of oily sludges will rise in response to the rising global demand for refined goods [29,31].

According to the physicochemical composition and method of formation, oil sludge is divided into five groups [32-34]:

- (i) Natural oil sludge - waste generated at the bottom of various water bodies after an oil spill.
- (ii) Oil sludge - waste generated during well drilling, various drilling fluids.

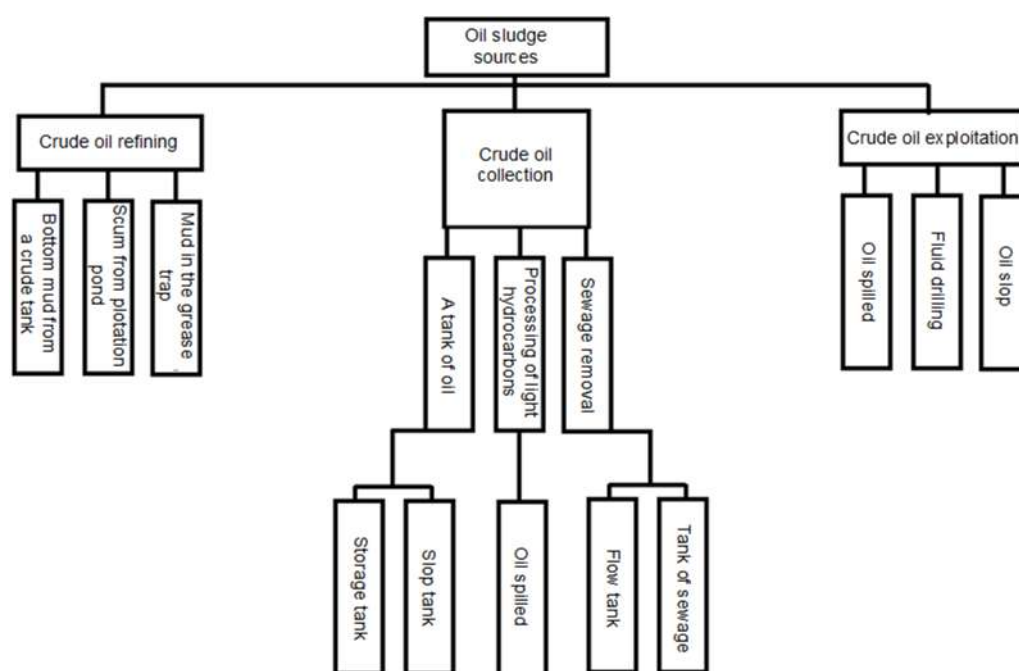


Fig 1. Schematic diagram of the oily sludge source

- (iii) Oil sludge - waste produced during the purification of oil from solid hydrocarbons and mechanical impurities.
- (iv) Tank oil sludge is waste generated throughout the transportation and storage of oil in various tanks.
- (v) Ground oil sludge - is a product of the combination of soil and oil spilled on it; the reason for this can be both a technological process and an accident.

According to the state of aggregation, oil sludge is divided into liquid, solid and highly viscous, gaseous

■ CHARACTERISTICS OF OILY SLUDGE

Depending on its origin, oil sludge can have a vast array of constituents. The hydrocarbon component of oil waste comprises a variety of compounds that can be transformed into other compounds during long-term storage via condensation, isomerization, and polymerization. However, all oil sludge contains water and other impurities. Long-term storage of oil sludge changes over time due to precipitation accumulation, the advancement of microorganisms, the incidence of oxidative processes, and other processes. In some cases, oil sludge is a stable emulsion that cannot be separated into various components [35-36]. Oil sludge consists of organic constituents (72%), moisture (19.2%), sulfur (1.8%), and mineral part (16%). According to Alexandrovich and Sergeevich [37], the mineral composition of oil sludge was SiO₂: 4.55%, CaO: 3.14%, Fe₂O₃: 1.65%, Al₂O₃: 2.36%, MgO: 2.36%, and others: 3.3%.

Both inorganic and organic pollutants can be found in petroleum sludge. Metal compounds, including zinc, copper, lead, chromium, nickel, and mercury, are examples of inorganic pollutants. Total petroleum hydrocarbon measurements of organic pollutants in the sludge vary from 510,000 to 640,000 mg/kg [38]. Oil sludge has 15 to 50% petroleum hydrocarbons (in percent by weight), 30 to 85% water, and 5 to 46% solids. Petroleum hydrocarbons (PHCs) and further organic compounds in oily sludge are categorized into four types: Asphaltenes, aliphatic and aromatic chemicals, and compounds comprising nitrogen, sulfur, and oxygen (NSO) [39].

Alkanes, cycloalkanes, benzene, toluene, xylenes, naphthalene, phenols, and other polycyclic aromatic

hydrocarbons, for instance, methylation derivatives of fluorine, phenanthrene, anthracene, chrysene, and pyrene account for up to 75% of PHCs in oily sludge [17]. Polar molecules such as naphthenic acids, mercaptans, thiophenes, and pyridines are noticed in the NSO fraction. The quantity of nitrogen (N) in oily sludge is less than 3%, with the bulk found in the distillate residue as a component of the asphalt and resin fraction [17].

In contrast to the oxygen concentration, typically less than 4.8%, sulfur (S) level can range from 0.3 to 10%. Asphaltenes are mixes of colloidal and pentane-insoluble chemicals that contain polyaromatic and alicyclic molecules with alkyl replacements (often methyl groups), and their molecular weights range from 500 to several thousand [40]. Since these components include hydrophilic functional groups and can thus act as lipophilic emulsifiers, asphaltenes and resins can be accountable for the oily sludge emulsion's stability. Oily sludge typically contains 40 to 52% alkanes, 28 to 31% aromatics, 8 to 10% asphaltenes, and 7 to 22.4% resins by mass [41]. The pH of oil sludge is typically between 6.5 and 7.5.

A recent study has identified significant amounts of Fe (60, 200 mg/kg), Zn (1.299 mg/kg), Cu (500 mg/kg), Ni (480 mg/kg), Cr (480 mg/kg), and Pb (565 mg/kg) in oil refinery sludges [41-44]. Additionally, oil sludge contains polycyclic aromatic hydrocarbons (PAHs), which are hazardous and cancer-causing-mutagenic, at amounts of 550 mg/kg or less.

The US Environmental Protection Agency (USEPA) has reported 16 PAHs as priority pollutants, namely: naphthalene, acenaphthylene, acenaphthene, fluorene, phenanthrene, anthracene, fluoroanthene, pyrene, benzo[a]anthracene, chrysene, benzo[b]fluoranthene, benzo[k]fluoranthrene, benzo[a]pyrene, indeno[1,2,3-cd]pyrene, dibenzo[a,h]anthracene, and benzo[g,h,i]perylene [45-46].

■ DANGER OF OIL SLUDGE TO THE ENVIRONMENT

Oily sludge is considered hazardous waste. If this is not handled and disposed of appropriately, it will have significant harmful effects. There are three possible ways

that adverse consequences could manifest themselves. (1) Inadequately treated oily sludge pollutes surface waters, even groundwaters, and causes a severe excess of COD and oily substances in water; (2) The volatilization of oil components in oil sludge will result in an excessive concentration of total hydrocarbons in the air of nearby areas; and (3) Oily sludge comprises of an actual amount of toxic and harmful organic compounds, for instance, hydrocarbons, phenols, anthracene, and benzene ring compounds. As a result, oil sludge is classified on the National Inventory of Hazardous Wastes [36,47].

When oil sludge is subjected to environmental factors, it can expand, evaporate, be absorbed by living organisms, and undergo transformation [35]. The processes of oil-containing compound degradation are markedly accelerated by sunlight. In contrast, the spread of oil-derived products in the soil is markedly slowed down by the evaporation of light fractions. Heavy oil fractions eventually produce emulsions that are difficult to separate. The exposure temperature affects how quickly petroleum products decompose. Lower temperatures slow down the rate of decomposition. Therefore, bacterial, chemical, and photochemical breakdown processes, as well as some organisms' and plants' activities, all contribute to the degradation of petroleum products [48].

PHCs and other flame-retardant substances are present in large amounts. Oil sludge is categorized as hazardous waste in various countries; hence, incorrect removal or poor treatment can damage the environment and people's health. Oil sludge is categorized as a material of the third class of hazards or one with a medium environmental impact. The direct damage that oil sludge may do to the environment and humans is [49]:

- (i) Chemicals from the first and second classes of hazards can be found in oil slime. Some examples include phenanthrenes, benzopyrene, and other pyrene derivatives. These compounds cause malignant tumors in animals, similar to those in people.
- (ii) It damages the liver, heart, and brain. The oil contains harmful heavy metal ions that can enter human food systems and cause harm.
- (iii) They cause slow seed germination and germination rate. According to laboratory tests, the seeds are

entirely incapable of germination at a concentration of oil sludge of 6–8%. Because of their smaller size and underdeveloped root systems, the above-ground sections of plants in polluted soils seem weaker.

- (iv) Animals that reside in soil polluted with oil waste, such as moles and mice, are doomed. Several oil compounds accumulate in the organisms of animals and have mutagenic effects, causing severe diseases, infertility, and affecting behavior.

■ OVERVIEW OF OIL SLUDGE DISPOSAL METHODS

Proper handling of oil waste is receiving more consideration due to expanded production and its hazardous nature. Numerous ways have been developed to control it to lower the concentration of harmful pollutants or immobilize them, limiting the impact of unfriendly material on the environment and health [50]. Among them are farming/burial, photocatalysis, incineration, curing/stabilization, sonication, solvent extraction, chemical processing, pyrolysis, and biodegradation [51-56].

The three waste management phases are used in most remediation methods: (1) reducing oil sludge creation through technology, (2) recovering oil from oily sludge, and (3) disposing of non-recoverable oil sludge [50]. Various techniques for treating oily sludge have been developed, as detailed below.

Because of the dangerous nature of oil sludge and its potential environmental effect, its safe disposal poses various difficulties and challenges. In general, no solution can fulfill all the requirements for the reuse and disposal of different types of oil sludge waste. Some treatments may show tremendous promise for fuel recovery or decontamination of non-recoverable remnants. However, their capital or operating costs may be prohibitively costly, or their adoption in a large-scale treatment may be difficult. A wide range of applications and cheap operating costs may be provided by other processing techniques, such as farming and composting, although their microbial breakdown processes may take some time [17].

The properties of the sludge, processing capacity, cost, disposal requirements, and time limitations should all be considered when selecting oily sludge treatment systems. Centrifugation, surfactant recovery, freeze/thaw, froth flotation, and biological sludge treatment are a few procedures that may be better adapted to handle oily sludges with high moisture content. Other processes need pre-treating the sludge to lower its moisture level, including incineration, pyrolysis, and stabilization/solidification. Fig. 2 compares oily sludge treatment and its application level and the average oil recovery rate percentage extracted from different papers [50,57-63]. Because technology selection incorporates several factors, assessing the overall performance of available technologies is challenging. Some multi-criteria assessment analysis methodologies can aid in developing a standard technology evaluation system and selecting the most appropriate disposal methods by researchers [17].

The advantages of many new oily sludge recovery and treatment systems include speed, high efficiency, and energy savings. At the same time, the disadvantages involve high maintenance and operating cost, high running cost, low efficiency, and environmental pollution [50]. Researchers' efforts and accomplishments have been

effective in improving efficiency and lowering processing costs. However, most novel approaches are still in the laboratory, far from pilot testing or large-scale technical implementation. Researchers will thus focus on a long experiment to explore new technologies [64].

■ APPLICATIONS OF OIL SLUDGE

The utilization of oil sludge as a secondary raw material appears to be one of the primary developments in the processing of oil sludge [65-68]. This strategy improves the environmental condition in oil refining zones leads to the most efficient use of natural resources.

The selection of the most appropriate technique for the disposal of oil sludge is a difficult task. The disposal and neutralization of highly hazardous waste generated in large cities present several challenges to improving environmental safety. Second, the adaptation and selection of technology for a particular location or territory are determined by the morphological and quantitative composition of the generated waste.

In general, the appropriateness of oil sludge for secondary raw material should be established by its composition, characteristics, and environmental danger. Oil sludge is commonly processed in batches according to

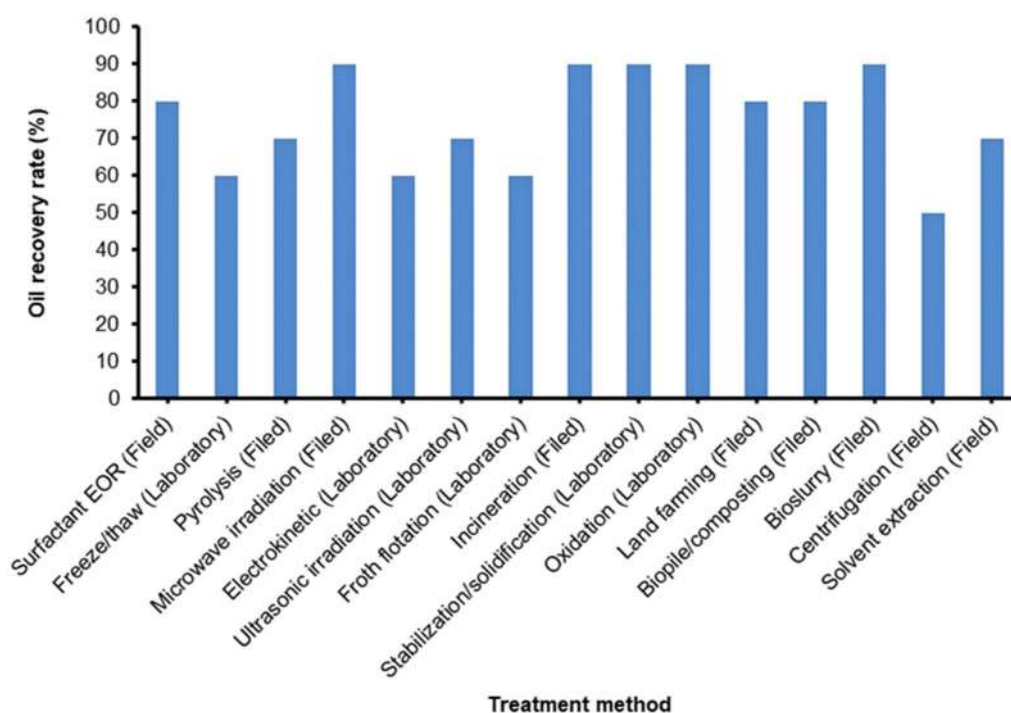


Fig 2. Comparison of oil sludge treatment and disposal methods

to the method used to create it. This approach to the existing situation solves the environmental and rational usage of oil sludge problems. Whether or not oil sludge causes pollution depends on some factors, many of which have to do with its composition and physical characteristics. The processing technique is determined by the consistency of the oil sludge and the organic matter, mechanical impurities, and water content [69-71].

Oil sludge applications are classified based on their technological nature and composition. For example, in the application of road construction, the types of oily waste used are oil sludge refinery (organic part 8–10%; mineral part 70–75%, and water 17–20%) and oil production sludge (organic part 6–40%; mineral part 50–87% and water 5–10%). Another application is oil sludge condensed (organic part 20–25%; mineral part 55–65%; and water 10–25%) and oil sludge refineries (organic part 13–28%; mineral part 59–77%; and water 10–22%) are the types of oily waste used in the application of construction materials. Additionally, the types of oily waste used in the fuel industry are refinery liquid waste (organic part 60–90%; mineral part 5–10% and water 10–20%) and waste from the production of petroleum oils (organic part 77–90%; mineral part 10–14% and water 4–7%). Moreover, the types of oily waste used in bitumen production are the top layer of the acid tar storage (organic part 9–15%; mineral part 65–78% and water 11–26%) and bottom acid tar (organic part 20–26%; mineral part 54–69% and water 18–20%) [69].

■ CONCLUSION

The three essential components of oil sludge are, as previously stated, the organic portion, the mineral portion, and water. Depending on the type of oil, the organic sludge-mass fraction ranges from 6 to 90%; the mineral sludge-mass fraction ranges from 5 to 87%, and water content ranges from 4 to 25%. Oil sludge with a high mineral concentration is used in road construction, building material manufacturing, and bitumen production. Oil sludge with a high organic matter concentration is used as a fuel component in the petroleum industry.

■ ACKNOWLEDGMENTS

The research was carried out following the Program BR12967699, "Creation of regulatory documentation, scientific and technical foundations for effective composite smart materials based on industrial waste."

■ AUTHOR CONTRIBUTIONS

All authors played significant roles in the conceptualization and design, data gathering, and analysis. They also contributed to the article's development and revision and decided to submit it to the current journal. They approved the final version to be released and agreed to be responsible for all parts of the effort.

■ REFERENCES

- [1] Souas, F., 2022, Rheological behavior of oil sludge from Algerian refinery storage tanks, *Pet. Res.*, 2022, In Press, Corrected Proof.
- [2] Jiang, H., Wang, Y., Nie, C., Yan, F., Ouyang, X., and Gong, J., 2021, Oil sludge deposition in storage tanks: A case study for Russian crude oil in Mo-he station, *Appl. Sci.*, 11 (1), 321.
- [3] Ba, S.F., Li, Y.L., Qu, Y.D., Zhang, D., Pang, L., Chen, W.W., Wang, Y.Q., and Lu, F., 2016, Deposition law of oil sludge in crude oil storage tank and countermeasures for jet cleaning, *Plant Maint. Eng.*, 2, 68–70.
- [4] Mansur, A.A., Pannirselvam, M., Al-Hothaly, K.A., Adetutu, E.M., and Bal, A.S., 2015, Recovery and characterization of oil from waste crude oil tank bottom sludge from Azzawiya oil refinery in Libya, *J. Adv. Chem. Eng.*, 5 (1), 1000118.
- [5] Lee, C.L., Tsai, C.H., and Jou, C.H.G., 2020, Energy and resource utilization of refining industry oil sludge by microwave treatment, *Sustainability*, 12 (17), 6862.
- [6] Islam, B., 2015, Petroleum sludge, its treatment and disposal: A review, *Int. J. Chem. Sci.*, 13 (4), 1584–1602.
- [7] Hassanzadeh, M., Tayebi, L., and Dezfouli, H.,

- 2018, Investigation of factors affecting on viscosity reduction of sludge from Iranian crude oil storage tanks, *Pet. Sci.*, 15 (3), 634–643.
- [8] Tang, X., Wei, X., and Chen, S., 2019, Continuous pyrolysis technology for oily sludge treatment in the chain-slap conveyors, *Sustainability*, 11 (13), 3614.
- [9] Ren, H., Zhou, S., Wang, B., Peng, L., and Li, X., 2020, Treatment mechanism of sludge containing highly viscous heavy oil using biosurfactant, *Colloids Surf., A*, 585, 124117.
- [10] Gopang, I.A., Mahar, H., Jatoi, A.S., Akhtar, K.S., Omer, M., and Azeem, M.S., 2016, Characterization of the sludge deposit in crude oil storage tanks, *J. Fac. Eng. Technol.*, 23 (1), 57–64.
- [11] Olajire, A.A., 2020, Recent advances on the treatment technology of oil and gas produced water for sustainable energy industry-mechanistic aspects and process chemistry perspectives, *Chem. Eng. J. Adv.*, 4, 100049.
- [12] Maia de Medeiros, A.D., da Silva Junior, C.J.G., de Amorim, J.D.P., Durval, I.J.B., de Santana Costa, A.F., and Sarubbo, L.A., 2022, Oily Wastewater treatment: Methods, challenges, and trends, *Processes*, 10 (4), 743.
- [13] Rocha e Silva, F.C.P., Rocha e Silva, N.M.P., Luna, J.M., Rufino, R.D., Santos, V.A., and Sarubbo, L.A., 2018, Dissolved air flotation combined to biosurfactants: A clean and efficient alternative to treat industrial oily water, *Rev. Environ. Sci. Bio/Technol.*, 17 (4), 591–602.
- [14] Galdino, C.J.S., Maia, A.D., Meira, H.M., Souza, T.C., Amorim, J.D.P., Almeida, F.C.G., Costa, A.F.S., and Sarubbo, L.A., 2020, Use of a bacterial cellulose filter for the removal of oil from wastewater, *Process Biochem.*, 91, 288–296.
- [15] Hart, A., 2014, A review of technologies for transporting heavy crude oil and bitumen via pipelines, *J. Petrol. Explor. Prod. Technol.*, 4 (3), 327–336.
- [16] Chrysalidis, A., and Kyzas, G.Z., 2020, Applied cleaning methods of oil residues from industrial tanks, *Processes*, 8 (5), 569.
- [17] Hu, G., 2016, Development of novel oil recovery methods for petroleum refinery oily sludge treatment, *Thesis*, University of Northern British Columbia, British Columbia.
- [18] Mora, V.C., Morelli, I.S., and Rosso, J.A., 2020, Co-treatment of an oily sludge and aged contaminated soil: Permanganate oxidation followed by bioremediation, *J. Environ. Manage.*, 261, 110169.
- [19] Liu, C., Xu, Q., Hu, X., Zhang, S., Zhang, P.Y., and You, Y., 2020, Optimization of process parameters of rhamnolipid treatment of oily sludge based on response surface methodology, *ACS Omega*, 5 (45), 29333–29341.
- [20] Das, S., Kuppanan, N., Channashettar, V.A., and Lal, B., 2018, “Remediation of Oily Sludge- and Oil-Contaminated Soil from Petroleum Industry: Recent Developments and Future Prospects” in *Advances in Soil Microbiology: Recent Trends and Future Prospects. Microorganisms for Sustainability*, Vol. 3, Eds., Adhya, T., Lal, B., Mohapatra, B., Paul, D., and Das, S., Springer, Singapore, 165–177.
- [21] Chen, L., Zhang, X., Sun, L., Xu, H., Si, H., and Mei, N., 2016, Study on the fast pyrolysis of oil sludge and its product distribution by PY-GC/MS, *Energy Fuels*, 30 (12), 10222–10227.
- [22] Hu, G., Li, J., Huang, S., and Li, Y., 2016, Oil recovery from petroleum sludge through ultrasonic assisted solvent extraction, *J. Environ. Sci. Health, Part A: Toxic/Hazard. Subst. Environ. Eng.*, 51 (11), 921–929.
- [23] Liang, J., Zhao, L., and Hou, W., 2017, Solid effect in chemical cleaning treatment of oily sludge, *Colloids Surf., A*, 522, 38–42.
- [24] Duan, M., Wang, X., Fang, S., Zhao, B., Li, C., and Xiong, Y., 2018, Treatment of Daqing oily sludge by thermochemical cleaning method, *Colloids Surf., A*, 554, 272–278.
- [25] da Silva, L.J., Alves, F.C., and de França, F.P., 2012, A Review of the technological solutions for the treatment of oily sludges from petroleum refineries, *Waste Manage. Res.*, 30 (10), 1016–1030.
- [26] Kuranchie, F.A., Attiogbe, F., and Quarshie, A.M., 2017, A review of the impacts and management of oily sludge in the oil and gas industry, *Int. J. Res. Eng. Technol.*, 6 (7), 32–37.

- [27] Pazoki, M., and Hasanidarabadi, B., 2017, Management of toxic and hazardous contents of oil sludge in Siri Island, *Global J. Environ. Sci. Manage.*, 3 (1), 33–42.
- [28] British Petroleum Company, 2012, *BP Statistical Review of World Energy June 2012*, British Petroleum Co., London, 16.
- [29] Ramirez, D., Shaw, L.J., and Collins, C.D., 2021, Oil sludge washing with surfactants and co-solvents: oil recovery from different types of oil sludges, *Environ. Sci. Pollut. Res.*, 28 (5), 5867–5879.
- [30] Ayol, A., and Yurdakoş, Ö.T., 2019, Chemical and thermal characteristics of petrochemical industrial sludge, *Desalin. Water Treat.*, 172, 29–36.
- [31] Adeola, A.O., Akingboye, A.S., Ore, O.T., Oluwajana, O.A., Adewole, A.H., Olawade, D.B., and Ogunyeye, A.C., 2022, Crude oil exploration in Africa: Socio-economic implications, environmental impacts, and mitigation strategies, *Environ. Syst. Decis.*, 42 (1), 26–50.
- [32] El Mahdi, A.M., Aziz, H.A., and Eqab, E.S., 2017, Review on innovative techniques in oil sludge bioremediation, *AIP Conf. Proc.*, 1892, 040026.
- [33] Chu, Z., Gong, Z., Wang, Z., Zhang, H., Wu, J., Wang, Z., Guo, Y., Zhang, J., Li, G., Zhang, L., and Wang, H., 2021, Experimental study on kinetic characteristics of oil sludge gasification, *Asia-Pac. J. Chem. Eng.*, 16 (2), e2616.
- [34] Wdowczyk, A., Szymańska-Pulikowska, A., and Domańska, M., 2022, Analysis of the bacterial biocenosis of activated sludge treated with leachate from municipal landfills, *Int. J. Environ. Res. Public Health*, 19 (3), 1801.
- [35] Goverdovskaya, L.G., Klimavichus, Y.E., and Nosarev, N.S., 2021, Development of mobile technology for the disposal of oily waste, *E3S Web Conf.*, 266, 06011.
- [36] Li, X., Zhang, F., Guan, B., Sun, J., and Liao, G., 2020, Review on oily sludge treatment technology, *IOP Conf. Ser.: Earth Environ. Sci.*, 467, 012173.
- [37] Alexandrovich, D.R., and Sergeevich, M.S., 2018, Innovations aimed at the secondary use of waste of PJSC "RN-Komsomolsk Oil Refinery, *Scientific and Technical Conference of Students of the 10th and 11th grades of ROSNEFT*, <https://www.rosneft.com/business/Downstream/Neftepererabotka/OilRefineries/KomsomolskRefinery/>, accessed on July 20, 2022.
- [38] Al-Mebayedh, H., Niu, A., and Lin, C., 2022, Petroleum hydrocarbon composition of oily sludge and contaminated soils in a decommissioned oilfield waste pit under desert conditions, *Appl. Sci.*, 12 (3), 1355.
- [39] Jafarinejad, S., 2017, "Solid-Waste Management in the Petroleum Industry" in *Petroleum Waste Treatment and Pollution Control*, Butterworth-Heinemann, Oxford, UK, 269–345.
- [40] Zheng, F., Shi, Q., Vallverdu, G.S., Giusti, P., and Bouyssièrè, B., 2020, Fractionation and characterization of petroleum asphaltene: Focus on metalopetroleomics, *Processes*, 8 (11), 1504.
- [41] Hamadani, M.A., and Al Ghazi, A.A., 2015, Isolation and identification of hydrocarbon degrading bacteria from oil sludge in oil producing area of Basrah, Iraq, *Int. J. Eng. Tech. Res.*, 3 (2), 22–27.
- [42] Gbarakoro, T.N., and Bello, A.D., 2022, Assessment of the concentration of petroleum hydrocarbon in oily wastes residual ash at Bodo-Ogoni remediation site, Nigeria, *J. Geosci. Environ. Prot.*, 10, 1–15.
- [43] Jasmine, J., and Mukherji, S., 2015, Characterization of oily sludge from a refinery and biodegradability assessment using various hydrocarbon degrading strains and reconstituted consortia, *J. Environ. Manage.*, 149, 118–125.
- [44] Pakpahan, E.N., Shafiq, N., Isa, M.H., Kutty, S.R.M., and Mustafa, M.R., 2016, Petroleum sludge thermal treatment and use in cement replacement – A solution towards sustainability, *Proceedings of the 3rd International Conference on Civil, Offshore and Environmental Engineering (ICCOEE 2016)*, 1st ed., Malaysia, 15-17 Aug 2016, CRC Press, 251–256.
- [45] Ji, L., Li, W., Li, Y., He, Q., Bi, Y., Zhang, M., Zhang, G., and Wang, X., 2022, Spatial distribution, potential sources, and health risk of polycyclic aromatic hydrocarbons (PAHs) in the surface soils

- under different land-use covers of Shanxi Province, North China, *Int. J. Environ. Res. Public Health*, 19 (19), 11949.
- [46] Zelinkova, Z., and Wenzl, T., 2015, The occurrence of 16 EPA PAHs in food – A review, *Polycyclic Aromat. Compd.*, 35 (2-4), 248–284.
- [47] Aminova, A.S., Gaibullaev, S.A., and Juraev, K.A., 2015, Tech. The use of oil sludge is a rational way of their disposal, *Young Sci.*, 2, 124–126.
- [48] Oil sludge: What it is, how it is formed, types, methods of processing and disposal, <https://cleanbin.ru/terms/oil-sludge>, accessed on June 15, 2022.
- [49] Mitra, S., Chakraborty, A.J., Tareq, A.M., Bin Emran, T., Nainu, F., Khusro, A., Idris, A.M., Khandaker, A.U., Osman, H., Alhumaydhi, F.A., and Simal-Gandara, J., 2022, Impact of heavy metals on the environment and human health: Novel therapeutic insights to counter the toxicity, *J. King Saud Univ., Sci.*, 34 (3), 101865.
- [50] Johnson, O.A., and Affam, A.C., 2019, Petroleum sludge treatment and disposal: A review, *Environ. Eng. Res.*, 24 (2), 191–201.
- [51] Zhao, S., Zhou, X., Wang, C., and Jia, H., 2018, Dewatering and low-temperature pyrolysis of oily sludge in the presence of various agricultural biomasses, *Environ. Technol.*, 39 (21), 2715–2723.
- [52] Al-Doury, M.M.I., 2019, Treatment of oily sludge using solvent extraction, *Pet. Sci. Technol.*, 37 (2), 190–196.
- [53] Han, M., Yu, L., and Chen, Y.H., 2016, Study on treatment of petrochemical sludge by advanced oxidation process, *Oxid. Commun.*, 39 (2), 1663–1669.
- [54] Roldán-Carrillo, T., Castorena-Cortés, G., Zapata-Pefinasco, I., Reyes-Avila, J., and Olguin-Lora, P., 2012, Aerobic biodegradation of sludge with high hydrocarbon content generated by a Mexican natural gas processing facility, *J. Environ. Manage.*, 95, 93–98.
- [55] Yan, P., Lu, M., Yang, Q., Zhang, H.L., Zhang, Z.Z., and Chen, R., 2012, Oil recovery from refinery oily sludge using a rhamnolipid biosurfactant-producing *Pseudomonas*, *Bioresour. Technol.*, 116, 24–28.
- [56] De Almeida, D.G., Soares Da Silva, R.C.F., Luna, J.M., Rufino, R.D., Santos, V.A., Banat, I.M., and Sarubbo, L.A., 2016, Biosurfactants: Promising molecules for petroleum biotechnology advances, *Front. Microbiol.*, 7, 01718.
- [57] Chen, H.S., Zhang, Q.M., Yang, Z.J., and Liu, Y.S., 2020, Research on treatment of oily sludge from the tank bottom by ball milling combined with ozone-catalyzed oxidation, *ACS Omega*, 5 (21), 12259–12269.
- [58] Han, M., Zhang, J., Chu, W., Chen, J., and Zhou, G., 2019, Research progress and prospects of marine oily wastewater treatment: A review, *Water*, 11 (12), 2517.
- [59] Fonts, I., Gea, G., Azuara, M., Ábrego, J., and Arauzo, J., 2012, Sewage sludge pyrolysis for liquid production: A review, *Renewable Sustainable Energy Rev.*, 16 (5), 2781–2805.
- [60] Hu, G., Li, J., and Zeng, G., 2013, Recent development in the treatment of oily sludge from petroleum industry: A review, *J. Hazard. Mater.*, 261, 470–490.
- [61] Li, J., Song, X., Hu, G., and Thring, R.W., 2013, Ultrasonic desorption of petroleum hydrocarbons from crude oil contaminated soils, *J. Environ. Sci. Health, Part A: Toxic/Hazard. Subst. Environ. Eng.*, 48 (11), 1378–1389.
- [62] Zhang, J., Li, J.B., Thring, R.W., Hu, X., and Song, X.Y., 2012, Oil recovery from refinery oily sludge via ultrasound and freeze/thaw, *J. Hazard. Mater.*, 203-204, 195–203.
- [63] Gong, Z., Wang, Z., and Wang, Z., 2018, Study on migration characteristics of heavy metals during oil sludge incineration, *Pet. Sci. Technol.*, 36 (6), 469–474.
- [64] Hui, K., Tang, J., Lu, H., Xi, B., Qu, C., and Li, J., 2020, Status and prospect of oil recovery from oily sludge: A review, *Arabian J. Chem.*, 13 (8), 6523–6543.
- [65] Yang, Q., Zhang, C., Li, L., and Xu, W., 2020, Anaerobic co-digestion of oil sludge with corn stover for efficient biogas production, *Sustainability*, 12 (5), 1861.

- [66] Kankia, M.U., Baloo, L., Mohammed, B.S., Hassan, S.B., Ishak, E.A., and Zango, Z.U., 2020, Review of petroleum sludge thermal treatment and utilization of ash as a construction material, a way to environmental sustainability, *Int. J. Adv. Appl. Sci.*, 7 (12), 68–81.
- [67] Srivastava, N., Srivastava, M., Gupta, V.K., Manikanta, A., Mishra, K., Singh, S., Singh, S., Ramteke, P.W., and Mishra, P.K., 2018, Recent development on sustainable biodiesel production using sewage sludge, *3 Biotech*, 8 (5), 245.
- [68] Bora, R.R., Richardson, R.E., and You, F., 2020, Resource recovery and waste-to-energy from wastewater sludge via thermochemical conversion technologies in support of circular economy: A comprehensive review, *BMC Chem. Eng.*, 2 (1), 8.
- [69] Kozlova, H.O., 2019, Improving the technology for obtaining building materials from oil sludge, *Thesis*, Institute of Chemistry and Engineering Ecology, Togliatti State University, Samara, Russia.
- [70] Bao, Q., Huang, L., Xiu, J., Yi, L., Zhang, Y., and Wu, B., 2022, Study on the thermal washing of oily sludge used by rhamnolipid/sophorolipid binary mixed bio-surfactant systems, *Ecotoxicol. Environ. Saf.*, 240, 113696.
- [71] Liu, C., Zhang, Y., Sun, S., Huang, L., Yu, L., Liu, X., Lai, R., Luo, Y., Zhang, Z., and Zhang, Z., 2018, Oil recovery from tank bottom sludge using rhamnolipids, *J. Pet. Sci. Eng.*, 170, 14–20.

NOTE:**Enhancing the Amino Acid and Reducing the Metal Ions Contents in the Hydrolysate Resulting from Hydrothermal Carbonization of Chicken Feather Waste by Chemical Phosphorylation****Agus Kuncaka^{1*}, Wahyu Tri Supardi², Winarto Haryadi¹,
Adhitasari Suratman¹, and Priatmoko Priatmoko¹**¹Department of Chemistry, Faculty of Mathematics and Natural Sciences, Universitas Gadjah Mada, Sekip Utara, Yogyakarta 55281, Indonesia²Department of Computer Science and Electronics, Faculty of Mathematics and Natural Sciences, Universitas Gadjah Mada, Sekip Utara, Yogyakarta 55281, Indonesia*** Corresponding author:**

email: akuncaka@ugm.ac.id

Received: March 23, 2022

Accepted: December 13, 2022

DOI: 10.22146/ijc.73725

Abstract: Chemical phosphorylation of hydrolysate resulting from hydrothermal carbonization of chicken feather waste was performed to enhance the amino acids and reduce the metal ions content. The aim of this research is to improve the functional properties of chicken feathers hydrolysate without impairing the nutritional availability thereof with the cheapest chemical method by phosphorylation. Phosphorylated hydrolysate can function as animal feed and fertilizer. The hydrolysate of chicken feathers was obtained by hydrothermal carbonization in an alkaline condition using a CaO and KOH catalyst, by the ratio of water:dry matter of chicken feathers is 5:1, at 9–10 atm pressure, and in a temperature of 190–200 °C during 3 h. Phosphorylation has been carried out by reacting the hydrolysate with H₃PO₄ 85% in pH of 5, 6, 7 and using the original hydrolysate as control. The sample that has been prepared was characterized and semi-quantitative analyzed by HPLC and AAS. The phosphorylation results showed that the total maximum protein of soluble protein, their minimum metal ions, and anion in soluble protein was obtained at pH 7, while the higher the pH, the lower the liquid protein that was obtained.

Keywords: hydrothermal carbonization; phosphorylation; liquid protein

■ INTRODUCTION

The non-composting method was proposed for the treatment of chicken feather pathogenic waste [1]. Chicken feathers are the main by-product waste in the poultry industry that constitute about 5–7% of the total chicken weight [2-3]. Based on Central Statistics Agency (BPS) data, broiler chicken production in Indonesia reached 3,495,090.5 tons in 2019, with 6% of the live weight produced being feathers. So, it is assumed that the production of chicken feathers in 2019 reached 236,705.4 tons [4]. It can be estimated about several million tons of chicken feathers were discarded for years. Therefore, chicken feathers storage is quite important instead of

collecting them in an abundant area without treatment to avoid the risk of microbial growth and infections that may become hazardous to the environment and affect human health due to their keratin content [5-7]. Chicken feathers contain 91% keratin, 8% water, and 1% lipid [8]. Keratin has a high protein and amino acids content that can be a low-cost source of nitrogen (up to 15% total N) [9-10], but keratin is difficult to digest by the organism and it needs a long time to be degraded in the environment [3,11]. Keratin is an insoluble protein in polar solutions such as water, weak acids and weak bases, and even in some organic solvents, which makes them resistant to microbial degradation and proteolytic enzymes such as pepsin and trypsin [12-14]. The

presence of cross bonds from disulfide bonds caused by the contains of sulfur amino or cysteine, hydrogen bonds, and hydrophobic interactions are driving the stability of keratin [15].

Keratin in chicken feather waste can potentially be converted into raw material for animal feed and fertilizer through chemical treatment for application in agricultural and food fields [16-18]. To be converted as raw material, the cystine bond of keratin in chicken feathers must be broken down [19]. Hydrothermal carbonization (HTC) is the thermochemical method that involves the application of high temperature and high pressure to convert biomass into a solid product called hydrochar, liquid product and gaseous product that is rich in organic and inorganic compounds in the sub-critical water environment [20-21]. The liquid product must be separated from the hydrochar using phosphorylation. KOH catalyst can be used as an activation agent in the HTC process, which has an effect on the change of morphology and chemical functional group in the product, and also can enhance the degree of carbonization [22-23]. Production of organic fertilizer from poultry feather wastes excluding the composting process was investigated by several researchers [24-28]. This research reports the combination of HTC and phosphorylation to convert the chicken feather pathogenic waste into valuable liquid protein, simultaneously to get digestible feed animals, and organic fertilizer by non-composting method.

■ EXPERIMENTAL SECTION

Materials

The materials used were hydrolysate, H_3PO_4 85% (Brataco Chemical), KOH (Brataco Chemical), CaO (Brataco Chemical), distilled water, and filter paper.

Instrumentation

The equipment used in this research were laboratory glassware, Buchner filter, Atomic Absorption Spectroscopy (AAS, Contra A 300 Analytik Jena), High-Performance Liquid Chromatography (HPLC, LiChrospher 100 RP-18 column with Thermo Ultimate 3000 RS Fluorescence detector), UV-Vis spectrophotometer (Shimadzu UV-

1800) and Hydrothermal carbonization (HTC reactor of 1145 L capacity).

Procedure

HTC of chicken feathers

The hydrolysate of chicken feathers was obtained using hydrothermal carbonization 1145 L HTC reactor. First, as much as 200 kg of wet chicken feathers containing 25% of dry matter of chicken feathers was put in the HTC reactor and then added to 100 L of water. The ratio of water:dry matter of chicken feathers is 5:1. After that, as much as 7.50 kg of CaO and 2.25 kg of KOH were added. The HTC reactor was heated up to a temperature of 190–200 °C for 3 h, and the pressure was controlled at 9–10 atm. The hydrolysate obtained from the HTC process was then phosphorylated by H_3PO_4 85% in various pH of 5, 6, and 7.

Sample preparation of phosphorylated hydrolysate for AAS analysis

The emulsion of hydrolysate was moved into a 100 mL beaker glass; it was reacted with 0.5 mL of H_3PO_4 85% and then repeated by adding 1 and 2 mL of H_3PO_4 85%. Each result of phosphorylation was vacuumed using a Buchner funnel that was covered using Whatman 40 filter paper. After the liquid fraction was filtered, the liquid fraction and the residue were analyzed using the AAS spectrophotometer to prove the content of Cu, Fe, Mn, Mg, Zn, Ca, and K. The content of P was analyzed using a UV-Vis spectrophotometer, and the profile of amino acids in liquid protein was analyzed using HPLC.

Characterization of profile amino acids

The characterization by HPLC was done for all samples. Each sample was weighed for 60 mg and then added with 4 mL of HCl 6 M. The sample was heated for 24 h at a temperature of 110 °C, then cooled down to room temperature and neutralized (pH 7) using NaOH 6 M. After that, the sample was added with distilled water until the volume reached 10 mL and then filtered with 0.2 mm Whatman filter paper. Characterization of profile amino acids in the sample was carried out by HPLC. The HPLC instrument that was used was LiChrospher 100 RP-18 (5 μm) column with Thermo Ultimate 3000 RS Fluorescence detector. The sample

was taken around 50 μL , and as much as 300 μL of OPA was added. The sample was stirred for 5 min before 10 μL of the sample was injected into the HPLC injector.

RESULTS AND DISCUSSION

This research aimed to conduct the chemical phosphorylation of hydrolysate resulting from HTC of chicken feather waste, to enhance the proteins and reduce the metal ions content. The product obtained was liquid hydrolysate and its solid phase that separated using phosphorylation. Phosphorylation was conducted to enhance the quality of protein without impairing the soluble protein that was available. The results of HPLC analysis of phosphorylated hydrolysate in various pH solutions are given in Table 1. It is worthy of being noted here that there is no free amino acid detected in the hydrolysate resulting from the HTC of chicken feather waste. Analysis of HPLC conducted the profile of amino acids of protein hydrolysate.

Table 1 shows that the optimum pH for the highest concentration of dissolved protein was obtained at pH 7. These phenomena conduct that phosphorylation enhances the reaction between dihydrogen phosphate ion and a group of amino acids in proteins of hydrolysate. It is also generally conducts protein in essential amino acids with maximum concentration at pH 7 except threonine.

The results indicate that the lower the pH, the higher the liquid protein that is obtained. The variation of solubility of protein reveals that the interaction between dihydrogen phosphate ion and amino acids group facilitated by hydrogen bonding force to form an ion protein phosphate that is more soluble in water at pH 7 [29-31]. The product of the reaction between the ion dihydrogen phosphate and amino acid is shown in Fig. 1 [32].

The content of metals (Fe, Mn, Zn, and Mg) in all pH can be seen in Fig. 2. These results show that the protein dihydrogen phosphate anion precipitates Fe, Mn, Zn, and Mg ions in their protein biphosphate neutral salt [13]. Except for the Cu ion, with a pH of 7, which formed a complex of copper ions in the form of ions copper protein dihydrogen phosphate. The concentration of Cu in liquid protein at different pH showed in Fig. 3.

A comparison of Ca, P, and K concentrations in liquid protein at different pH can be seen in Fig. 4. The

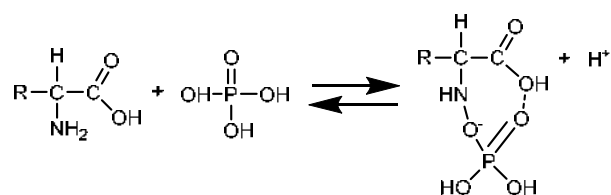


Fig 1. Phosphorylation reaction of a hydrolysate

Table 1. Amino acid profile of hydrolysate protein before and after phosphorylation

Amino acid	Before phosphorylation		After phosphorylation					
	pH 8-9		pH 7		pH 6		pH 5	
	weight	% AA	weight	% AA	weight	% AA	weight	% AA
Aspartic acid	0.51	0.85	0.48	0.80	0.46	0.76	0.48	0.80
Glutamic acid	0.90	1.51	0.94	1.56	0.87	1.45	0.89	1.49
Serin	0.48	0.80	0.51	0.85	0.48	0.79	0.48	0.80
Glycine	0.63	1.05	0.72	1.20	0.68	1.14	0.73	1.22
Threonine*	0.22	0.37	0.20	0.34	0.20	0.33	0.18	0.30
Arginine*	0.61	1.01	0.68	1.13	0.65	1.09	0.67	1.12
Alanine	0.55	0.91	0.65	1.08	0.61	1.02	0.65	1.08
Tyrosine	0.50	0.83	0.53	0.89	0.48	0.81	0.48	0.81
Valine	0.73	1.21	0.84	1.40	0.79	1.32	0.78	1.31
Phenylalanine*	0.61	1.01	0.66	1.10	0.62	1.04	0.61	1.02
L-Leucine*	0.55	0.92	0.63	1.05	0.60	0.99	0.60	1.00
Leucine*	0.77	1.28	0.89	1.48	0.82	1.37	0.84	1.40
Total	7.12	11.86	7.80	13.00	7.33	12.22	7.46	12.47

*essential amino acid

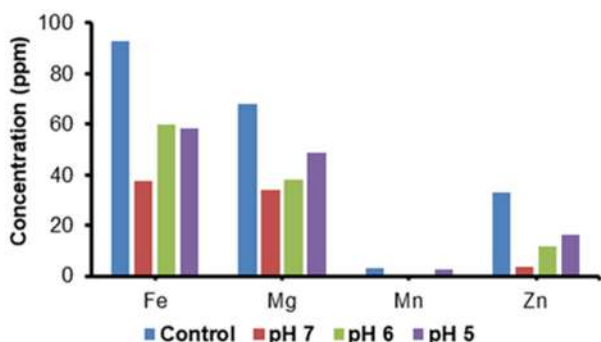


Fig 2. Comparison of Fe, Mg, Mn, and Zn concentrations in liquid protein at different pH

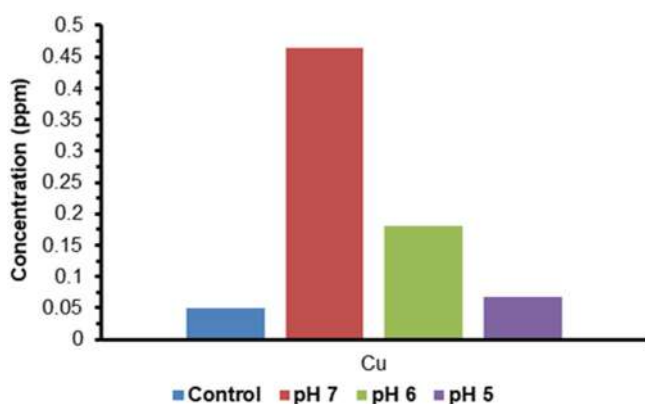


Fig 3. Comparison of Cu concentration in liquid protein at different pH

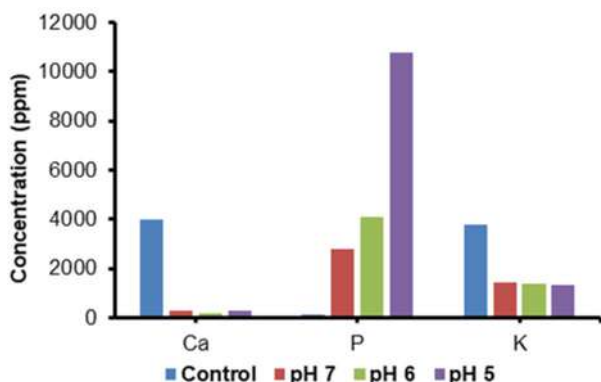


Fig 4. Comparison of Ca, P, and K concentrations in liquid protein at different pH

maximum Ca and K ions concentration was conducted at its origin hydrolysate. This concentration was obtained due to their solubilization of catalysis Ca and K utilized during HTC. The decreasing of pH conducts the diminution of concentration Ca and K ions in the liquid phase to form their neutral protein phosphate, except for the concentration of P ion. It indicates that the higher of

H⁺ conducted, the higher the phosphate concentration can be obtained in the liquid phase.

The profile concentration of metals contained in dry matter of solid precipitate can be shown in Fig. 5 and 6. This figure showed the diminution of concentration of metals observed by decreasing its pH value.

Fig. 7 shows that the concentration of K in the dry matter is relatively stable on various pH, while the

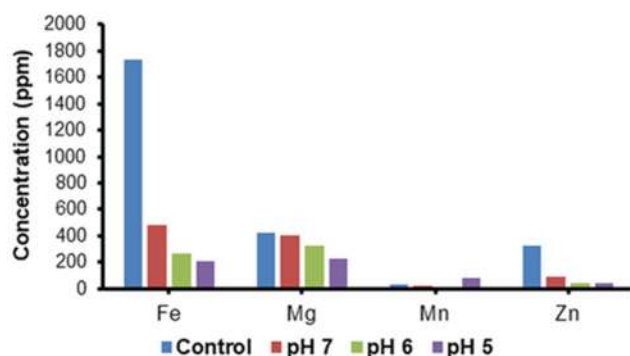


Fig 5. Comparison of Fe, Mg, Mn, and Zn concentration in solid humus at different pH

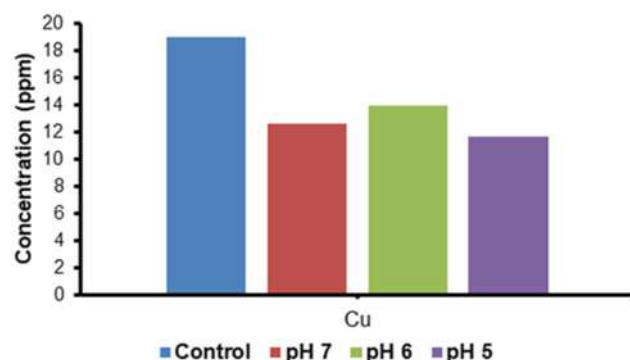


Fig 6. Comparison of Cu concentration in solid humus at different pH

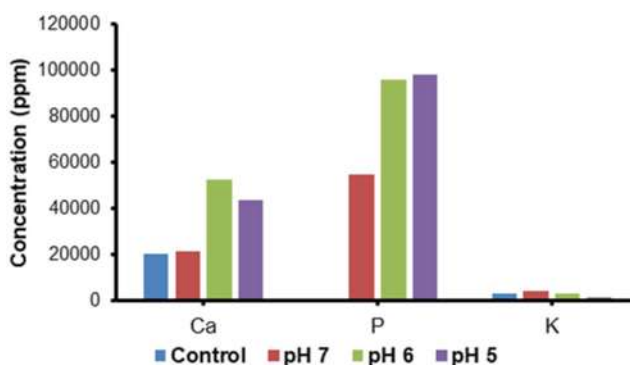


Fig 7. Comparison of Ca, P, and K concentrations in solid humus at different pH

concentration of Ca and P ions in the diminution of pH conduct the augmentation of their content in dry matter.

The results of this research show that chemical phosphorylation can enhance the protein content and reduce the metal ions content in the hydrolysate. The maximum soluble protein and minimum metal ions condition of hydrolysate was obtained at pH 7 and indicating the higher the pH, the lower the liquid protein that was obtained. The enhancement of soluble protein in hydrolysate had advantages as a source of nitrogen that can be functioned as a digestible animal feed and potential organic fertilizer, while the reduction of metal ions content in hydrolysate is suitable with minimum heavy metals content requirements of feed animals and organic fertilizer.

■ CONCLUSION

Based on the results of this research, the optimum phosphorylation condition to produce maximal soluble protein and minimum concentration of metal content in chicken feather hydrolysate has been obtained at pH 7. It can be concluded that chemical phosphorylation constitutes the simple and cheapest method to improve the functional properties of chicken feathers hydrolysate resulting from HTC without impairing the nutritional availability. This research opened the opportunity to easily get proteins with a smaller chain that can be used as digestible animal feed and organic fertilizer.

■ ACKNOWLEDGMENTS

This research has been funded by the PPTI 2021 project with Contract Number of 2821/UN1.DITLIT/DIT-LIT/PT/2021 and Matching Fund by the Directorate General Higher Education (DGHE) through the Kedaireka 2022 project with Contract Number 5974/UN1.P/Dit-PUI/HK.08.00/2022.

■ REFERENCES

- [1] Ayilara, M.S., Olanrewaju, O.S., Babalola, O.O., and Odeyemi, O., 2020, Waste management through composting: Challenges and potentials, *Sustainability*, 12 (11), 4456.
- [2] da Silva, R.R., 2018, Keratinases as an alternative method designed to solve keratin disposal on the environment: Its relevance on agricultural and environmental chemistry, *J. Agric. Food Chem.*, 66 (28), 7219–7221.
- [3] Said, M.I., 2020, Potential development of poultry feather waste resources as raw material in industry: A review, *IOP Conf. Ser.: Earth Environ. Sci.*, 492, 012089.
- [4] Azizah, A., Nurhayati, N., Hendalia, E., and Maghfiro, S.R., 2021, Solubility of dry matter and protein of hydrolyzed feather meal fermented by *Lactobacillus casei* Shirota, *J. Hunan Univ. Nat. Sci.*, 48 (11), 174–179.
- [5] Lange, L., Huang, Y., and Busk, P.K., 2016, Microbial decomposition of keratin in nature—a new hypothesis of industrial relevance, *Appl. Microbiol. Biotechnol.*, 100 (5), 2083–2096.
- [6] Endo, R., Kamei, K., Iida, I., and Kawahara, Y., 2008, Dimensional stability of waterlogged wood treated with hydrolyzed feather keratin, *J. Archaeol. Sci.*, 35 (5), 1240–1246.
- [7] Poole, A.J., and Church, J.S., 2015, The effects of physical and chemical treatments on Na₂S produced feather keratin films, *Int. J. Biol. Macromol.*, 73, 99–108.
- [8] Arifin, T., 2008, Pemanfaatan Limbah Bulu Ayam Potong Metode Pengukusan untuk Bahan Ransum Ayam Potong, *Thesis*, Pengelolaan Sumber Daya Alam dan Lingkungan, Universitas Sumatera Utara, Medan, Indonesia.
- [9] Joardar, J.C., and Rahman, M.M., 2018, Poultry feather waste management and effects on plant growth, *Int. J. Recycl. Org. Waste Agric.*, 7 (3), 183–188.
- [10] Jeong, J.H., Lee, O.M., Jeon, Y.D., Kim, J.D., Lee, N.R., Lee, C.Y., and Son, H.J., 2010, Production of keratinolytic enzyme by a newly isolated feather-degrading *Stenotrophomonas maltophilia* that produces plant growth-promoting activity, *Process Biochem.*, 45 (10), 1738–1745.
- [11] Joshi, S.G., Tejashwini, M.M., Revati, N., Sridevi, R., and Roma, D., 2007, Isolation, identification, and characterization of a feather degrading bacterium, *Int. J. Poult. Sci.*, 6 (9), 689–693.

- [12] Parry, D.A.D., and North, A.C.T., 1998, Hard α -keratin intermediate filament chains: Substructure of the N and C terminal domains and the predicted structure and function of the C-terminal domains of type I and type II chains, *J. Struct. Biol.*, 122 (1), 67–75.
- [13] Zhao, W., Yang, R., Zhang, Y., and Wu, L., 2012, Sustainable and practical utilization of feather keratin by an innovative physicochemical pretreatment: High density steam flash-explosion, *Green Chem.*, 14 (12), 3352–3360.
- [14] Vidmar, B., and Vodovnik, M., 2018, Microbial keratinases: Enzymes with promising biotechnological applications, *Food Technol. Biotechnol.*, 56 (3), 312–328.
- [15] Mazotto, A.M., de-Melo, A.C.N., Macrae, A., Rosado, A.S., Peixoto, R., Cedrola, S., Couri, S., Zingali, R.B., Villa, A.L.V., Rabinovitch, L., Chaves, J.Q., and Vermelho, A.B., 2011, Biodegradation of feather waste by extracellular keratinases and gelatinases from *Bacillus* spp., *World J. Microbiol. Biotechnol.*, 27 (6), 1355–1365.
- [16] Li, Q., 2022, Perspectives on converting keratin-containing wastes into biofertilizers for sustainable agriculture, *Front. Microbiol.*, 13, 918262.
- [17] Al Mousa, A.A., Moubayed, N.M.S., Al Jaloud, A.M., Al Khattaf, F.S., and Dahmasha, N.D., 2021, Chicken feathers waste management by microbial as a sustainable and tool environmental friendly, *J. Environ. Prot.*, 12 (9), 639–653.
- [18] Ramnani, P., Singh, R., and Gupta, R., 2005, Keratinolytic potential of *Bacillus licheniformis* RG1: Structural and biochemical mechanism of feather degradation, *Can. J. Microbiol.*, 51 (3), 191–196.
- [19] Adiati, U., Puastuti, W., Mathius, I., 2004, Peluang pemanfaatan tepung bulu ayam sebagai bahan pakan ternak ruminansia, *Wartazoa*, 14 (1), 39–44.
- [20] Aragón-Briceño, C.I., Pozarlik, A.K., Bramer, E.A., Niedzwiecki, L., Pawlak-Kruczek, H., and Brem, G., 2021, Hydrothermal carbonization of wet biomass from nitrogen and phosphorus approach: A review, *Renewable Energy*, 171, 401–415.
- [21] Ischia, G., and Fiori, L., 2021, Hydrothermal carbonization of organic waste and biomass: A review on process, reactor, and plant modeling, *Waste Biomass Valorization*, 12 (6), 2797–2824.
- [22] Chaiammart, N., Eiad-ua, A., and Panomsuwan, G., 2020, Hydrothermal carbonization synthesis and KOH activation of porous carbons from waste marigold flowers, *IOP Conf. Ser.: Mater. Sci. Eng.*, 773, 012048.
- [23] Sengottian, M., Venkatachalam, C.D., and Ravichandran, S.R., 2022, Optimization of alkali catalyzed hydrothermal carbonization of *Prosopis juliflora* woody biomass to biochar for copper and zinc adsorption and its application in supercapacitor, *Int. J. Electrochem. Sci.*, 17, 220938.
- [24] Tronina, P., and Bubel, F., 2008, Production of organic fertilizer from poultry feather wastes excluding the composting process, *Pol. J. Chem. Technol.*, 10 (2), 33–36.
- [25] Onifade, A.A., Al-Sane, N.A., Al-Musallam, A.A., and Al-Zarban, S., 1998, A review: Potentials for biotechnological applications of keratin-degrading microorganisms and their enzymes for nutritional improvement of feathers and other keratins as livestock feed resources, *Bioresour. Technol.*, 66 (1), 1–11.
- [26] Yang, F., and Antonietti, M., 2020, Artificial humic acids: Sustainable materials against climate change, *Adv. Sci.*, 7 (5), 1902992.
- [27] Alhnidi, M.J., Körner, P., Wüst, D., Pfersich, J., and Kruse, A., 2020, Nitrogen-containing hydrochar: The influence of nitrogen-containing compounds on the hydrochar formation, *ChemistryOpen*, 9 (8), 864–873.
- [28] Kruse, A., and Dahmen, N., 2015, Water – A magic solvent for biomass conversion, *J. Supercrit. Fluids*, 96, 36–45.
- [29] Neal, J.F., Zhao, W., Grooms, A.J., Smeltzer, M.A., Shook, B.M., Flood, A.H., and Allen, H.C., 2019, Interfacial supramolecular structures of amphiphilic receptors drive aqueous phosphate recognition, *J. Am. Chem. Soc.*, 141 (19), 7876–7886.

- [30] Hargrove, A.E., Nieto, S., Zhang, T., Sessler, J.L., and Anslyn, E.V., 2011, Artificial receptors for the recognition of phosphorylated molecules, *Chem. Rev.*, 111 (11), 6603–6782.
- [31] Jastrzab, R., Nowak, M., Zabizak, M., Odani, A., and Kaczmarek, M.T., 2021, Significance and properties of the complex formation of phosphate and polyphosphate groups in particles present in living cells, *Coord. Chem. Rev.*, 435, 213810.
- [32] Gowri, S., Uma Devi, T., Alen, S., Sajan, D., Surendra Dilip, C., and Vinitha, G., 2018, Synthesis, crystal structure, optical and third order nonlinear optical properties of phosphoric acid pyridine-1-ium-2-carboxylate, *J. Mater. Sci.: Mater. Electron.*, 29 (23), 19710–19723.